Mathematical Modelling of Biological Variations due to Application of Nanofluids in Body Fluids

Submitted to

University of Calicut

in partial fulfillment of the requirements

for the award of the Degree of

Doctor of Philosophy
in
Mathematics

By

SUJESH A S

Under the guidance of

Dr. Alphonsa Mathew

Assistant Professor



Research and Postgraduate Department of Mathematics

St. Thomas' College (Autonomous)

Thrissur - 680001, Kerala.

December 2022

DECLARATION

I, **Sujesh A S**, hereby declare that the thesis entitled, ***"Mathematical Modelling of Biological Variations due to Application of Nanofluids in Body Fluids"***, submitted to the **University of Calicut** in partial fulfillment of the requirements for the award of the Degree of ***Doctor of Philosophy in Mathematics*** is a bonafide research work done by me under the supervision and guidance of **Dr. Alphonsa Mathew**, Assistant Professor, Department of Mathematics, St. Thomas' College (Autonomous), Thrissur, Kerala. I further declare that this thesis has not previously formed the basis of any degree, diploma or any other similar title.

Thrissur **Sujesh A S**

12 December, 2022



CERTIFICATE

This is to certify that the thesis titled ***"Mathematical Modelling of Biological Variations due to Application of Nanofluids in Body Fluids"*** submitted by **Sujesh A S** to the **University of Calicut** in partial fulfillment of the requirements for the award of the Degree of ***Doctor of Philosophy in Mathematics*** is a record of original research work carried out by him under my supervision. The content of this thesis, in full or in parts, has not been submitted by any other candidate to any other University for the award of any degree or diploma.

Thrissur
12 December, 2022

Dr. Alphonsa Mathew
Research Supervisor



CERTIFICATE

I hereby certify that, this is the revised version of the thesis entitled ***"Mathematical Modelling of Biological Variations due to Application of Nanofluids in Body Fluids"*** submitted by **Sujesh A S**, under my guidance, after incorporating the necessary corrections/suggestions made by the adjudicators. I also certify that the contents in the thesis and the soft copy are one and the same.

Thrissur
20 March, 2023

Dr. Alphonsa Mathew
Research Supervisor

ABSTRACT

A substance capable of flowing is termed as a fluid. Fluids are of two types, namely liquids and gases. The study of fluid's behaviour at rest (termed fluid statics) and in motion (termed fluid dynamics) is combinedly known as fluid mechanics.

The fluid produced and circulated within the human body or secreted outside the human body is known as body fluid. Blood, saliva, urine, tears, sweat, and breast milk are a few examples of body fluid. Water is the basis of all body fluids and the human body is composed of about 60% of water.

Nanofluid is a colloidal mixture in which a base fluid (water, oil, ethylene glycol, etc.) is mixed with nanometer-sized particles (metals, carbides, oxides or carbon nanotubes). Fluids constituting two nanometer-sized particles are termed hybrid nanofluids. Nanofluids tend to upgrade and stabilize the thermal properties of the fluid which marked a revolution in the field of fluid dynamics.

The description of a system using mathematical concepts and language is known as mathematical model and the process of developing a mathematical model is known as mathematical modelling. Mathematical models find its use in natural sciences, engineering disciplines and social sciences. A mathematical model helps to explain a system and to study the effects of different components and also to make predictions about its behaviour.

The thesis entitled *Mathematical Modelling of Biological Variations due to Application of Nanofluids in Body Fluids* has been arranged into 12 chapters. Chapter 1 introduces the basic concepts, preliminaries and definitions to the reader. An extensive review of related literature has been presented in Chapter 2. Owing to the practical applications (like biomedical imaging, hyperthermia, pharmaceuticals, biosensors, medical instruments, bio-chromatography, microchip pump, theranostic, biomedical science, targeted drug delivery, and cancer therapy), nine fluid flow problems are modelled and investigated in this thesis.

In Chapter 3, the bioconvective stagnation point flow involving carbon nanotubes along a lengthening sheet subject to induced magnetic field and multiple stratification effects is investigated. The dynamics of water conveying single-wall

carbon nanotubes (SWCNTs) and magnetite nanoparticles on the bioconvective stagnation-point flow along a stretching sheet subject to chemical reaction, viscous dissipation, induced magnetic field, and stratification effects is investigated in Chapter 4. Non-spherical nanoparticles have gained popularity for their ability in changing the thermophysical properties of a nanofluid. Chapter 5 elucidates the significance of multiple slip and nanoparticle shape on stagnation point flow of blood-based silver nanofluid considering chemical reaction, induced magnetic field, thermal radiation, nanoparticle shape and linear heat source.

The numerical study on the stratification effects of bioconvective electromagnetohydrodynamic (EMHD) flow past a stretching sheet using water-based CNT has been presented in Chapter 6. The focal concern of Chapter 7 is to numerically scrutinize the consequences of multiple slip, linear radiation and chemically reactive species on MHD convective Carreau nanoliquid flow over an elongating cylinder. Moreover, statistical scrutiny on the impact of Hartmann number, thermal radiation and thermal slip parameter over heat transfer rate employing Response Surface Methodology (RSM) and sensitivity analysis is also performed. The nanomaterial flow of Chapter 8 has been modelled using the modified Buongiorno nanofluid model. The impact of the stratification constraints and magnetic field are also accounted. Further, the influence of magnetic field parameter, thermal stratification parameter, volume fraction of magnetite nanoparticles, and velocity ratio parameter on the heat transfer rate has been scrutinized statistically using a five-level four-factor response surface optimized model.

In Chapter 9, the dynamics of the $TiO_2 - H_2O$ nanomaterial over a nonlinearly stretched surface and modelled using modified Buongiorno model is investigated. Experimentally derived correlations of the thermal conductivity and dynamic viscosity of the nanomaterial are utilized. The hydromagnetic bioconvective flow of a nanomaterial over a lengthening surface is investigated in Chapter 10. Realistic nanomaterial modelling is achieved by incorporating passive control of the nanoparticles at the boundary. The impact of the Newtonian heating and Stefan blowing constraints are also accounted. The sensitivity

of heat transport rate is also computed. Chapter 11 numerically elucidates the dynamics of electro-magnetohydrodynamic flow of blood-gold nanomaterial over a nonlinearly stretching surface utilizing the Casson model. The impact of second-order hydrodynamic-slip, nanoparticle radius, first-order thermal-slip, inter-particle spacing and non-uniform heat source are also accounted.

Lastly, Chapter 12 presents the concluding remarks of the thesis and proposals for future work.

I dedicate this work

to my parents who paved the way for me during their lifetime and

to my beloved teachers and friends for their unconditional love and support.

ACKNOWLEDGEMENT

This thesis would not have been possible without the guidance and the help of several individuals who in one way or another contributed and extended their valuable assistance in the preparation and completion of the study.

My greatest regards to the Almighty for bestowing upon me the courage and strength to face the complexities of life and complete this research work successfully.

I wish to express my heartfelt gratitude to my Research Supervisor and my Mentor, Dr. Alphonsa Mathew, Assistant Professor, Department of Mathematics, St. Thomas' College (Autonomous), Thrissur. Her guidance, suggestions and constant support have sustained me through this work. I would always cherish this experience for the rest of my life. It's my great privilege to have worked under her guidance.

I am forever indebted to Dr. Rakesh Kumar, Professor, Srinivasa Ramanujan Department of Mathematics, Central University of Himachal Pradesh and Dr. B. Mahanthesh, Associate Professor, Department of Mathematics, CHRIST (Deemed to be University), Bangalore for sharing their expertise and knowledge on the subject. Special thanks to Joby Mackolil, A.S. Sabu, Ravinder Kumar and Dr. Arshad Mohammed Ali for their constant guidance and support, which helped me greatly during the research period. I personally acknowledge the support and help rendered by my research colleagues of Mathematics and Statistics Departments, St. Thomas' College (Autonomous), Thrissur. It was an honour to work with them.

St. Thomas' College (Autonomous), Thrissur is sincerely acknowledged for providing me the resources and facilities required for the completion of my research. I express my sincere thanks to Dr. Fr. Martin K A (Principal), Dr. Joy K L (Former Principal), Dr. Ignatius Antony (Former Principal) and non-teaching staffs of St. Thomas' College (Autonomous), Thrissur. I am highly grateful to Dr. Saju M I (Head of the Department), Prof. Vincent Joseph Pulikkottil (Former Head of the Department) and all the faculty members of the Mathematics Department.

I would like to express my sincere gratitude for the support and help rendered by my co-authors. I also recall, with gratitude, the support and the motivation rendered by my beloved parents and my dear teachers, friends, and relatives.

Sujesh A S

Contents

Declaration i
Certificate iii
Abstract vii
Acknowledgements xiii
List of Figures xxi
List of Tables xxvii

1 **Introduction** 1
1.1 Fluid 1
1.2 Density 1
1.3 Viscosity 1
1.4 Newton's Law of Viscosity 1
1.5 Thermal Conductivity 2
1.6 Types of Fluid 2
1.7 Dilatant Fluid 3
1.8 Pseudoplastic Fluid 3
1.9 Casson Fluid 3
1.10 Carreau Fluid 3
1.11 Laminar Fluid Flow 4
1.12 Steady and Unsteady Fluid Flow 4
1.13 Rotational and Irrotational flow 4
1.14 Mathematical Model 4
1.15 Fundamental Equations of Fluid Flow 4
1.16 Boundary Conditions 5
1.17 Bioconvection 7
1.18 Magnetic Field 8
1.19 Induced Magnetic Field 8

1.20 Dimensional Analysis 8
1.21 Non-Dimensional Parameters 8
1.22 Body Fluid 10
1.23 Nanofluid 10
1.24 Volume Fraction of Nanoparticle 10
1.25 Thermophysical Properties of Nanofluid 10
1.26 Khanafer-Vafai-Lightstone Model 12
1.27 Buongiorno Model 12
1.28 Modified Buongiorno Model 13
1.29 Solution Methodology 13
1.30 Motivation 16
1.31 Objectives 17
1.32 Overview of the Thesis 17

2 **Review of Related Literature** 23
2.1 Nanofluid 23
2.2 Hybrid Nanofluid 25
2.3 Blood-based Nanofluid 27
2.4 Nanoparticle Shape and Radius 27
2.5 Carreau Nanofluid 28
2.6 Casson Nanofluid 29
2.7 Nanofluid Flow Model 30
2.8 Magnetohydrodynamics 32
2.9 Induced Magnetic Field 32
2.10 Electromagnetohydrodynamics 33
2.11 Bioconvection 34
2.12 Stratification 35
2.13 Flow past a Stretching Sheet 36
2.14 Flow over a Rotating Disk 37
2.15 Stagnation Flow 37
2.16 Slip Boundary Constraint 38
2.17 Heat Source 39
2.18 Passive Control of Nanoparticles 40

2.19 Thermal Radiation 40
2.20 Newtonian Boundary Constraint 41
2.21 Stefan Blowing 41
2.22 Statistical Techniques 42
2.23 Need for the Study 43

3 **Bioconvective stagnation-point flow due to induced magnetic field** 45
3.1 Introduction 45
3.2 Mathematical Frame 46
3.3 Numerical Frame & Validation 49
3.4 Results & Discussion 50
3.5 Conclusion 63

4 **Bioconvectice hybrid stagnation-point flow due to induced magnetic field** 67
4.1 Introduction 67
4.2 Mathematical Frame 68
4.3 Numerical Frame & Validation 72
4.4 Results & Discussion 73
4.5 Conclusion 83

5 **Significance of nanoparticle shape on stagnation-point flow in the presence of induced magnetic field** 87
5.1 Introduction 87
5.2 Mathematical Frame 88
5.3 Numerical Frame & Validation 92
5.4 Results & Discussion 93
5.5 Conclusion 108

6 **Bioconvective EMHD nanofluid flow past a stretching sheet** 113
6.1 Introduction 113
6.2 Mathematical Frame 114
6.3 Numerical Frame & Validation 117
6.4 Results & Discussion 118
6.5 Statistical Frame 128

6.6 Conclusion 132

7 **Hydromagnetic Carreau nanoliquid flow over an elongating cylinder** 135
7.1 Introduction 135
7.2 Mathematical Frame 136
7.3 Numerical Frame & Validation 139
7.4 Results & Discussion 140
7.5 Statistical Frame 152
7.6 Conclusion 164

8 **Bioconvective stagnation-point flow over a rotating stretchable disk** 169
8.1 Introduction 169
8.2 Mathematical Frame 170
8.3 Numerical Frame & Validation 174
8.4 Results & Discussion 176
8.5 Statistical Frame 186
8.6 Conclusion 192

9 **Nanoliquid flow with irregular heat source and realistic boundary conditions** 195
9.1 Introduction 195
9.2 Mathematical Frame 197
9.3 Numerical Frame & Validation 199
9.4 Results & Discussion 201
9.5 Statistical Frame 209
9.6 Conclusion 217

10 **Bioconvective magnetized nanomaterial flow subjected to convective thermal heating and Stefan blowing** 221
10.1 Introduction 221
10.2 Mathematical Frame 222
10.3 Numerical Frame & Validation 225
10.4 Results & Discussion 227
10.5 Statistical Frame 239

10.6 Conclusion 247

11 **Electro-magnetohydrodynamic Casson nanomaterial flow over a nonlinearly stretched surface** 251
11.1 Introduction 251
11.2 Mathematical Frame 252
11.3 Numerical Frame & Validation 255
11.4 Results & Discussion 257
11.5 Conclusion 267

12 **Conclusion and Future Scope** 271
12.1 Concluding Remarks 271
12.2 Future Research Work 274

List of Publications 275

List of Presentations 277

Bibliography 279
Bibliography 279

List of Figures

3.1 Geometrical Frame 46
3.2 $f'(\zeta)$ for differing A values 53
3.3 $f'(\zeta)$ for differing β values 54
3.4 $g'(\zeta)$ for differing A values 54
3.5 $g'(\zeta)$ for differing β values 55
3.6 $g'(\zeta)$ for differing λ values 55
3.7 $\theta(\zeta)$ for differing A values 56
3.8 $\theta(\zeta)$ for differing Ec values 56
3.9 $\theta(\zeta)$ for differing ϕ values 57
3.10 $\theta(\zeta)$ for differing s_1 values 57
3.11 $\psi(\zeta)$ for differing A values 58
3.12 $\psi(\zeta)$ for differing Kr values 58
3.13 $\psi(\zeta)$ for differing s_2 values 59
3.14 $\chi(\zeta)$ for differing A values 59
3.15 $\chi(\zeta)$ for differing s_3 values 60
3.16 Parallel effect of ϕ & β on $Cf_x Re_x^{1/2}$ 60
3.17 Parallel effect of ϕ & Ec on $Nu_x Re_x^{-1/2}$ 61
3.18 Parallel effect of ϕ & s_1 on $Nu_x Re_x^{-1/2}$ 61
3.19 Parallel effect of Kr & s_2 on $Sh_x Re_x^{-1/2}$ 62
3.20 Parallel effect of Kr & s_3 on $Nn_x Re_x^{-1/2}$ 62

4.1 Geometrical Frame 68
4.2 Variation of A on $f'(\zeta)$ & $g'(\zeta)$ 76
4.3 Variation of β on $f'(\zeta)$ 76
4.4 Variation of β on $g'(\zeta)$ 77
4.5 Variation of λ on $g'(\zeta)$ 77
4.6 Parallel effect of β & $\phi_{Fe_3O_4}$ on $Cf_x Re_x^{1/2}$ 78

4.7 Parallel effect of β & ϕ_{SWCNT} on $Cf_x Re_x^{1/2}$ 78
4.8 Variation of $\phi_{Fe_3O_4}$ & ϕ_{SWCNT} on $\theta(\zeta)$ 79
4.9 Variation of S_1 & Ec on $\theta(\zeta)$ 79
4.10 Parallel effect of S_1 & $\phi_{Fe_3O_4}$ on $Nu_x Re_x^{-1/2}$ 80
4.11 Parallel effect of Ec & ϕ_{SWCNT} on $Nu_x Re_x^{-1/2}$ 80
4.12 Variation of Kr, Le, & S_2 on $\psi(\zeta)$ 81
4.13 Variation of Pe & S_3 on $\chi(\zeta)$ 81
4.14 Parallel effect of (a) S_2 & Le on $Sh_x Re_x^{-1/2}$ and (b) S_3 & Lb on $Nn_x Re_x^{-1/2}$ 82
4.15 Parallel effect of (a) S_2 & Kr on $Sh_x Re_x^{-1/2}$ and (b) S_3 & Kr on $Nn_x Re_x^{-1/2}$ 82

5.1 Geometrical Frame 88
5.2 $f'(\eta)$ for differing A values 96
5.3 $f'(\eta)$ for differing β values 97
5.4 $f'(\eta)$ for differing ϕ values 97
5.5 $f'(\eta)$ for differing nanoparticle shapes 98
5.6 $Cf_x\ Re_x^{1/2}$ for differing nanoparticle shapes β values 98
5.7 $Cf_x\ Re_x^{1/2}$ for differing nanoparticle shapes ϕ values 99
5.8 $g'(\eta)$ for differing A values 99
5.9 $g'(\eta)$ for differing β values 100
5.10 $g'(\eta)$ for differing λ values 100
5.11 $g'(\eta)$ for differing nanoparticle shapes 101
5.12 $\theta(\eta)$ for differing A values 101
5.13 $\theta(\eta)$ for differing ϕ values 102
5.14 $\theta(\eta)$ for differing Q_T values 102
5.15 $\theta(\eta)$ for differing R_d values 103
5.16 $\theta(\eta)$ for differing T_{slip} values 103
5.17 $\theta(\eta)$ for differing nanoparticle shapes 104
5.18 $Nu_x Re_x^{-1/2}$ for differing nanoparticle shapes and ϕ values 104
5.19 $Nu_x Re_x^{-1/2}$ for differing nanoparticle shapes and Q_T values 105
5.20 $Nu_x Re_x^{-1/2}$ for differing nanoparticle shapes and R_d values 105
5.21 $Nu_x Re_x^{-1/2}$ for differing nanoparticle shapes and T_{slip} values . . . 106
5.22 $\psi(\eta)$ for differing A values 106

5.23 $\psi(\eta)$ for differing Le values 107
5.24 $\psi(\eta)$ for differing Kr values 107
5.25 $\psi(\eta)$ for differing C_{slip} values 108

6.1 Geometrical Frame 114
6.2 $f'(\eta)$ for differing M values 120
6.3 $f'(\eta)$ for differing E values 120
6.4 $\theta(\eta)$ for differing ϕ values 121
6.5 $\theta(\eta)$ for differing Ec values 121
6.6 $\theta(\eta)$ for differing s_1 values 122
6.7 $\psi(\eta)$ for differing Kr values 122
6.8 $\psi(\eta)$ for differing s_2 values 123
6.9 $\chi(\eta)$ for differing s_3 values 123
6.10 Variation of $Nn_x\ Re_x^{-1/2}$ with Kr & Lb 124
6.11 Variation of $Nn_x\ Re_x^{-1/2}$ with s_3 & Le 124
6.12 Actual versus Estimated $Cf_x\ Re_x^{1/2}$ 131
6.13 Actual versus Estimated $Nu_x\ Re_x^{-1/2}$ 131

7.1 Geometrical Frame 136
7.2 $f'(\eta)$ for differing K values 142
7.3 $f'(\eta)$ for differing We values 142
7.4 $f'(\eta)$ for differing M values 143
7.5 $f'(\eta)$ for differing b_1 values 143
7.6 $\theta(\eta)$ for differing K values 144
7.7 $\theta(\eta)$ for differing M values 144
7.8 $\theta(\eta)$ for differing Rd values 145
7.9 $\theta(\eta)$ for differing b_1 values 145
7.10 $\theta(\eta)$ for differing b_2 values 146
7.11 $\phi(\eta)$ for differing K_r values 146
7.12 $\phi(\eta)$ for differing Nt values 147
7.13 $\phi(\eta)$ for differing Nb values 147
7.14 $\phi(\eta)$ for differing b_3 values 148
7.15 Simultaneous effect of Rd & b_2 on $Nu_x\ Re_x^{-1/2}$ $(n = 0.7)$ 148
7.16 Simultaneous effect of Rd & b_2 on $Nu_x\ Re_x^{-1/2}$ $(n = 1.4)$ 149

7.17 Simultaneous effect of K_r & b_3 on $Sh_x\ Re_x^{-1/2}$ $(n = 0.7)$ 149
7.18 Simultaneous effect of K_r & b_3 on $Sh_x\ Re_x^{-1/2}$ $(n = 1.4)$ 150
7.19 Residual plots for $Nu_{0.7}$ 156
7.20 Residual plots for $Nu_{1.4}$ 156
7.21 Contour plots for $Nu_{0.7}$ 157
7.22 Surface plots for $Nu_{0.7}$ 158
7.23 Contour plots for $Nu_{1.4}$ 159
7.24 Surface plots for $Nu_{1.4}$ 160
7.25 Bar charts showcasing the sensitivity of $Nu_{0.7}$ 161
7.26 Bar charts showcasing the sensitivity of $Nu_{1.4}$ 162

8.1 Geometrical Frame 170
8.2 Impression of S on $F(\eta)$ 177
8.3 Impression of S on $G(\eta)$ 178
8.4 Impression of M on $F(\eta)$ 178
8.5 Impression of M on $G(\eta)$ 179
8.6 Impression of ω on $G(\eta)$ 179
8.7 Impression of ϕ on $\theta(\eta)$ 180
8.8 Impression of S_1 on $\theta(\eta)$ 180
8.9 Impression of Kr on $\psi(\eta)$ 181
8.10 Impression of S_2 on $\psi(\eta)$ 181
8.11 Impression of S_3 on $\chi(\eta)$ 182
8.12 Simultaneous impression of ω and M on $C_f\ Re^{1/2}$ 182
8.13 Simultaneous impression of ϕ and S on $C_f\ Re^{1/2}$ 183
8.14 Simultaneous impression of S_1 and M on $Nu_r\ Re^{-1/2}$ 183
8.15 Simultaneous impression of ϕ and S on $Nu_r\ Re^{-1/2}$ 184
8.16 Simultaneous impression of S_2 and Kr on $Sh_r\ Re^{-1/2}$ 184
8.17 Simultaneous impression of S_2 and Kr on $Nn_r\ Re^{-1/2}$ 185
8.18 Simultaneous impression of S_3 and Lb on $Nn_r\ Re^{-1/2}$ 185
8.19 Residual versus Predicted value 188
8.20 Surface plots for $Nu_r\ Re^{-1/2}$ 191

9.1 Geometrical Frame 196
9.2 $f'(\zeta)$ for distinct values of n 202

9.3 $f'(\zeta)$ for distinct values of M . . . 202
9.4 $\theta(\zeta)$ for distinct values of n . . . 203
9.5 $\theta(\zeta)$ for distinct values of M . . . 203
9.6 $\theta(\zeta)$ for distinct values of R_d . . . 204
9.7 $\theta(\zeta)$ for distinct values of Q_E . . . 204
9.8 $\theta(\zeta)$ for distinct values of Nt . . . 205
9.9 $\psi(\zeta)$ for distinct values of n . . . 205
9.10 $\psi(\zeta)$ for distinct values of Nt . . . 206
9.11 $\psi(\zeta)$ for distinct values of Nb . . . 206
9.12 Simultaneous effect of M and ϕ on $Cf_x\ Re_x^{1/2}$ . . . 207
9.13 Simultaneous effect of M and ϕ on $Nu_x\ Re_x^{-1/2}$ . . . 207
9.14 Simultaneous effect of R_d and Q_E on $Nu_x\ Re_x^{-1/2}$ . . . 208
9.15 Residual plots . . . 212
9.16 Contour plots for on $Nu_x\ Re_x^{-1/2}$ . . . 213
9.17 Surface plots for on $Nu_x\ Re_x^{-1/2}$ . . . 214
9.18 Bar charts showcasing the sensitivity of on $Nu_x\ Re_x^{-1/2}$ . . . 215

10.1 Geometrical Frame . . . 222
10.2 $f'(\xi)$ for distinct n values . . . 228
10.3 $f'(\xi)$ for distinct M values . . . 229
10.4 $\theta(\xi)$ for distinct n values . . . 229
10.5 $\theta(\xi)$ for distinct M values . . . 230
10.6 $\theta(\xi)$ for distinct Q_T values . . . 230
10.7 $\theta(\xi)$ for distinct Q_E values . . . 231
10.8 $\theta(\xi)$ for distinct Rd values . . . 231
10.9 $\theta(\xi)$ for distinct Bi values . . . 232
10.10 $\psi(\xi)$ for distinct n values . . . 232
10.11 $\psi(\xi)$ for distinct Kr values . . . 233
10.12 $\psi(\xi)$ for distinct Le values . . . 233
10.13 $\chi(\xi)$ for distinct Pe values . . . 234
10.14 $\chi(\xi)$ for distinct Ω values . . . 234
10.15 $\chi(\xi)$ for distinct Lb values . . . 235
10.16 Simultaneous impact of M and n on $Cf_x\ Re_x^{1/2}$ . . . 235
10.17 Simultaneous impact of M and n on $Nu_x\ Re_x^{-1/2}$ . . . 236

10.18 Simultaneous impact of Q_T and Q_E on $Nu_x\ Re_x^{-1/2}$ 236
10.19 Simultaneous impact of Rd and Bi on $Nu_x\ Re_x^{-1/2}$ 237
10.20 Simultaneous impact of Lb and Kr on $Nn_x\ Re_x^{-1/2}$ 237
10.21 Simultaneous impact of Pe and Ω on $Nn_x\ Re_x^{-1/2}$ 238
10.22 Residual plots 242
10.23 Contour plots for on $Nu_x\ Re_x^{-1/2}$ 243
10.24 Surface plots for on $Nu_x\ Re_x^{-1/2}$ 244
10.25 Bar charts showcasing the sensitivity of on $Nu_x\ Re_x^{-1/2}$ 245

11.1 Geometrical Frame 252
11.2 Deviations in $f'(\eta)$ with m 257
11.3 Deviations in $f'(\eta)$ with M 258
11.4 Deviations in $f'(\eta)$ with E 258
11.5 Deviations in $f'(\eta)$ with β 259
11.6 Deviations in $f'(\eta)$ with ϕ 259
11.7 Deviations in $f'(\eta)$ with h 260
11.8 Deviations in $f'(\eta)$ with R_{np} 260
11.9 Deviations in $f'(\eta)$ with L_1 261
11.10 Deviations in $f'(\eta)$ with L_2 261
11.11 Deviations in $\theta(\eta)$ with M 262
11.12 Deviations in $\theta(\eta)$ with ϕ 262
11.13 Deviations in $\theta(\eta)$ with h 263
11.14 Deviations in $\theta(\eta)$ with R_{np} 263
11.15 Deviations in $\theta(\eta)$ with L_3 264
11.16 Deviations in $\theta(\eta)$ with A^* 264
11.17 Deviations in $Cf_xRe_x^{1/2}$ with differing parameters 265
11.18 Deviations in $Nu_xRe_x^{-1/2}$ with differing parameters 265

List of Tables

3.1 Comparison of drag coefficient $\left(Cf_x Re_x^{1/2}\right)$ for different A values between the present study and the works of Iqbal, Azhar, et al., 2017 and Hayat et al., 2015, 2016 when $\phi = \beta = 0$ 51

3.2 Comparison of $Nu_x Re_x^{-1/2}$ and $-Cf_x Re_x^{1/2}$ for differing ϕ, β, λ values between the present study and (Iqbal, Azhar, et al., 2017) 51

3.3 Thermophysical properties of water and SWCNT 51

4.1 Comparison of drag coefficient $\left(Cf_x Re_x^{1/2}\right)$ with Hayat et al., 2015, 2016; Iqbal, Azhar, et al., 2017 for different A values when $\phi_{Fe_3O_4} = \phi_{SWCNT} = \beta = \lambda = 0$ 73

4.2 Thermophysical properties of water, Fe_3O_4 and $SWCNT$ 74

5.1 Comparison of drag coefficient $\left(Cf_x Re_x^{1/2}\right)$ for different A values between the present study and the works of Iqbal, Azhar, et al., 2017 and Hayat et al., 2015, 2016 when $\phi = \beta = 0$ 94

5.2 Thermophysical properties of blood and silver 94

5.3 Variation in $Sh_x\ Re_x^{-\ 1/2}$ when $A = 0.5$, $\beta = 0.1$, $\lambda = 0.5$ & $\phi = 0.1$ 94

6.1 Comparison of $Nu_x (Re_x)^{-1/2}$ for differing Pr values between the present study and the works of W. A. Khan et al., 2010; Wang, 1989 when $M = E = Kr = Ec = Le = Lb = Pe = \ \Omega = \ s_1 = s_2 = s_3 = 0$ 118

6.2 Thermophysical properties of water and SWCNT 118

6.3 Variation in $Cf_x\ Re_x^{1/2}$ when $Kr = 1,\ Ec = Le = Lb = 0.3,\ Pe = \Omega = 0.5$ & $s_1 = s_2 = s_3 = 0.1$ 125

6.4 Variation in $Nu_x\ Re_x^{-\ 1/2}$ when $Kr = 1,\ Le = Lb = 0.3,\ Pe = \Omega = 0.5$ & $s_2 = s_3 = 0.1$ 126

6.5 Variation in $Sh_x\ Re_x^{-\ 1/2}$ when $M = 1,\ Ec = Lb = 0.3,\ Pe = \Omega = 0.5$ & $s_1 = s_3 = 0.1$ 127

6.6 Correlation Coefficient (r), Probable Error (PE) and $\left|\frac{r}{PE}\right|$ of drag coefficient 129
6.7 Correlation Coefficient (r), Probable Error (PE) and $\left|\frac{r}{PE}\right|$ of heat transfer rate 129

7.1 Comparison of $Nu_x Re_x^{-1/2}$ for different Pr values with the work of W. A. Khan et al., 2010 when $Nb \to 0$ and $M = K = We = Sc = Nt = Rd = K_r = b_1 = b_2 = b_3 = 0$ 140
7.2 Variation in $\frac{1}{2}Cf_x\ Re_x^{1/2}$ for various parameters when $Pr = 4$ and $Sc = 1.2$ 151
7.3 Effectual parameter levels 153
7.4 CCD experimental design and the corresponding responses 154
7.5 ANOVA table ($Nu_{0.7}$) 155
7.6 ANOVA table ($Nu_{1.4}$) 155
7.7 Sensitivity of $Nu_{0.7}$ & $Nu_{1.4}$ when $A = 0$ 164

8.1 Resemblance of $F'(0)$ and $-G'(0)$ with the work of Mustafa et al., 2016 when $S = \phi = Nt = Le = Lb = \Omega = Pe = Kr = S_1 = S_2 = S_3 = 0,\ Nb \to 0$, and $Pr = 1$ 175
8.2 Thermophysical properties of water and magnetite nanoparticles . . 176
8.3 Effectual parameter levels 187
8.4 Four-factor CCD experimental design and the corresponding responses 189
8.5 ANOVA table 190

9.1 Comparison of $Nu_x Re_x^{-1/2}$ for different values of Pr_f with the work of W. A. Khan et al., 2010 when $n = 1$. $Nb \to 0$ and $M = Nt = \phi = R_d = Q_E = Le = 0$ 200
9.2 Thermophysical properties of water and titanium dioxide 201
9.3 Effectual parameter levels 210
9.4 Experimental design with actual and estimated response values . . . 211
9.5 ANOVA table and regression coefficients 212
9.6 Sensitivity of $Nu_x\ Re_x^{-1/2}$ when $A = 0$ 217

10.1 Resemblance of $-\theta'(0)$ for ordinary fluid when $Pr_f = 1$ 226
10.2 Effectual parameter levels 239

10.3 Experimental design with actual and estimated response values . . . 241
10.4 ANOVA table and regression coefficients 242
10.5 Sensitivity of $Nu_x\ Re_x^{-1/2}$ when $A = 0$ 246

11.1 Resemblance of $-\theta'(0)$ for ordinary fluid when $Pr_f = 1$ 256
11.2 Thermophysical properties of blood and gold 256

Chapter 1

Introduction

1.1 Fluid

A substance capable of flowing is termed as a fluid. Fluids are of two types, namely liquids and gases. The study of fluid's behaviour at rest (termed fluid statics) and in motion (termed fluid dynamics) is combinedly known as fluid mechanics.

1.2 Density

The ratio of fluid's mass to its volume is defined as the density (denoted by ρ) of the fluid.

1.3 Viscosity

The internal friction that exhibits resistance to the alterations in fluid's form is known as viscosity. Viscosity can also be conceptualized as the thickness of a fluid.

1.4 Newton's Law of Viscosity

The Newton's law of viscosity states that the shear stress is directly proportional to the velocity gradient. Mathematically,

$$\tau = \mu \frac{du}{dx} \tag{1.4.1}$$

where τ is the shear stress, u is the velocity and μ is the constant of proportionality known as dynamic viscosity. The ratio of dynamic viscosity to the density is known as kinematic viscosity.

1.5 Thermal Conductivity

The measure that quantifies the material's ability to conduct heat is known as thermal conductivity. Alternatively, thermal conductivity can also be defined as the ratio of heat flux to the temperature gradient.

1.6 Types of Fluid

1.6.1 Incompressible Fluid

A fluid whose density remains constant when a force is applied is known as incompressible fluid. Liquids are, generally, regarded as incompressible fluids.

1.6.2 Compressible Fluid

A fluid whose density alters when a force is applied is known as compressible fluid. Gases are, generally, regarded as compressible fluids.

1.6.3 Ideal Fluid

Ideal fluid is an imaginary fluid that is incompressible and having zero viscosity.

1.6.4 Real Fluid

Any fluid having viscosity is known as real fluid. Realistically, all fluids are real fluids.

1.6.5 Newtonian Fluid

The fluid that follows Newton's law of viscosity is known as Newtonian fluid. Alcohol, gases, gasoline and water are a few examples of Newtonian fluid.

1.6.6 Non-Newtonian Fluid

The fluid that doesn't follow Newton's law of viscosity is known as non-Newtonian fluid. Blood, paint, ketchup and toothpaste are a few examples of non-Newtonian fluid.

1.6.7 Ideal Plastic Fluid

A Newtonian fluid whose shear stress exceeds the resultant value is known as ideal plastic fluid.

1.7 Dilatant Fluid

Dilatant (or shear thickening) fluid is a type of non-Newtonian fluid that exhibits a positive functional relationship between shear stress and viscosity. Examples of dilatant fluids include oobleck and quicksand.

1.8 Pseudoplastic Fluid

Pseudoplastic (or shear thinning) fluid is a type of non-Newtonian fluid that exhibits an inverse functional relationship between shear stress and viscosity. Examples of pseudoplastic fluids include blood and ketchup.

1.9 Casson Fluid

Casson fluid is a shear thinning fluid that assumes infinite viscosity at zero shear-rate, and vice versa. The rheological equation for an isotropic and incompressible flow of a Casson fluid is given by (see Isa et al., 2017; Suresh Reddy & Panda, 2022):

$$\tau_{ij} = \begin{cases} 2\left(\mu_B + \frac{P_y}{\sqrt{2\pi}}\right) e_{ij} \ , \ \pi > \pi_c \\ \\ 2\left(\mu_B + \frac{P_y}{\sqrt{2\pi_c}}\right) e_{ij}, \ \pi < \pi_c \end{cases} \tag{1.9.1}$$

where where μ_B is plastic dynamic viscosity of the non-Newtonian fluid, P_y is the yield stress of the fluid, τ_{ij} is $(i,j)^{th}$ component of the stress tensor, $\pi = e_{ij}e_{ij}$, e_{ij} is the $(i,j)^{th}$ component of the deformation rate and π_c is a critical value of π based on the non-Newtonian model. *Human blood*, honey, tomato sauce, jelly, and concentrated fruit juices are examples of Casson fluid.

1.10 Carreau Fluid

Carreau fluid is a generalized Newtonian fluid whose viscosity μ depends on the shear rate, which is based on the equation:

$$\mu\left(\dot{\gamma}\right) = \mu_\infty + \left(\mu_0 - \mu_\infty\right)\left(1 + \left(\lambda\dot{\gamma}\right)^2\right)^{\frac{n-1}{2}} \tag{1.10.1}$$

where λ is the relaxation time, $\dot{\gamma}$ is the generalised shear rate, n is the power-law index, μ_0 represents the zero shear viscosity, and μ_∞ is the infinite shear viscosity. It is noteworthy to mention that the above model with $n < 1$ shows a shear thinning

nature and $n > 1$ shows a shear thickening nature. *Human blood* is an example of Carreau fluid with shear thinning nature.

1.11 Laminar Fluid Flow

Laminar fluid flow corresponds to the smooth movement of fluid particles. It is characterized by the movement of particles in laminas with zero disruption and negligible lateral mixing.

1.12 Steady and Unsteady Fluid Flow

The fluid flow in which the fluid properties (like pressure, velocity, density, etc.) at a point remains unaltered with time is known as steady fluid flow. The case in which the fluid properties at a point alter with time corresponds to the unsteady fluid flow.

1.13 Rotational and Irrotational flow

The curl of velocity (known as vorticity, Ω) measures the fluid's rotation. The type of flow in which the fluid particles rotate about their own axis (when $\Omega \neq 0$) is known as rotational flow. The type of flow in which the fluid particles do not rotate about their own axis (when $\Omega = 0$) is known as irrotational flow.

1.14 Mathematical Model

The description of a system using mathematical concepts and language is known as mathematical model and the process of developing a mathematical model is known as mathematical modelling. Mathematical models find its use in natural sciences, engineering disciplines and social sciences. A mathematical model helps to explain a system and to study the effects of different components and also to make predictions about its behaviour.

1.15 Fundamental Equations of Fluid Flow

1.15.1 Equation of Continuity

The equation of continuity is derived from the law of conservation of mass which states that the rate of increase in the fluid's mass within a considered region is equal to the rate of flow through its boundary. In vector notation it can be written as (see Bansal, 1977):

$$\frac{\partial \rho}{\partial t} + \nabla . \left(\rho \vec{V}\right) = 0 \tag{1.15.1}$$

where $\vec{V}$ is the velocity vector and ρ is the fluid density.

Note:

- In the case of steady compressible flow, the equation of continuity reduces to:

$$\nabla.\left(\rho\vec{V}\right) = 0 \tag{1.15.2}$$

- In the case of incompressible flow, the equation of continuity reduces to:

$$\nabla.\vec{V} = 0 \tag{1.15.3}$$

1.15.2 Equation of Momentum (Navier-Stokes' Equation)

The equation of momentum is derived from the Newton's second law of motion which states that the total force amounts to the rate of change of linear momentum. In vector notation it can be written as (see Bansal, 1977):

$$\rho\frac{D\vec{V}}{Dt} = \rho\vec{F} + \mu\nabla^2\vec{V} - \nabla P \tag{1.15.4}$$

where $\vec{V}$ is the velocity vector, ρ is the fluid density, P is the pressure, $\vec{F}$ is the force, μ is the dynamic viscosity, and $\frac{D}{Dt} \equiv \frac{\partial}{\partial t} + \left(\vec{V}.\nabla\right)$ is known as the material derivative.

1.15.3 Equation of Energy

The equation of energy is derived from the law of conservation of energy which states that the total energy in an isolated system is conserved. It can be written as (see Bansal, 1977):

$$\rho\frac{DE_t}{Dt} = \rho\left(v_i\frac{Dv_i}{Dt} + \frac{DI}{Dt} + v_j\frac{\partial K}{\partial x_j}\right) \tag{1.15.5}$$

where $(v_i\ , v_j)$ are the velocity components, ρ is the fluid density, I is the internal energy, K is the potential energy, and E_t is the total energy.

1.16 Boundary Conditions

The constraints necessary to solve a boundary value problem (BVP) are termed as boundary conditions (see Wazwaz, 2002; Strauss, 2007). BVP is a differential

equation (or system of differential equations) that must be solved in a domain with specified boundaries. BVP is different from the initial value problem (IVP) in which only one extreme of the interval is known.

1.16.1 Dirichlet Boundary Condition

Dirichlet boundary condition (DBC), named after Peter Gustav Lejeune Dirichlet, is a type of boundary condition that specifies the value that the unknown function must take along the domain's boundary.

1.16.2 Neumann Boundary Condition

Neumann boundary condition (NBC), named after Carl Neumann, is a type of boundary condition that specifies the value that the derivative of a solution will take on the domain's boundary.

1.16.3 Robin Boundary Condition

Robin boundary condition (RBC), named after Victor Gustave Robin, is a type of boundary condition that consists of a linear combination of the field's values and its derivative on the boundary.

1.16.4 Mixed Boundary Condition

Mixed boundary condition (MBC) is a type of boundary condition that applies multiple types of boundary conditions in different parts of the domain. It is worth noting that the boundary condition must be applied on the entire boundary. RBC consists of applying different types of boundary conditions to the same boundary region whereas MBC consists of applying different types of boundary conditions to different parts of the boundary.

1.16.5 Cauchy Boundary Condition

Cauchy boundary condition (CBC) is a type of boundary condition that applies on both the unknown field and its derivative. CBC implies the imposition of two constraints (1 DBC + 1 NBC) whereas RBC implies only one constraint.

1.16.6 Slip Boundary Constraint

The relative movement of the fluid with the boundary is characterized with the aid of slip constraint. Multiple slip corresponds to the case when more than one slip (velocity, thermal, or solutal) condition is considered.

The Wu's velocity slip boundary constraint for arbitrary Knudsen number is given by (see Wu, 2008; Fang & Aziz, 2010):

$$U_{slip} = \frac{2}{3}\left[\frac{(3-\alpha f^3)}{\alpha} - \frac{3}{2}\frac{(1-f^2)}{K_n}\right]\lambda\,\frac{\partial u}{\partial y} - \frac{1}{4}\left[f^4 - \frac{2}{K_n^2}\left(1-f^2\right)\right]\lambda^2\,\frac{\partial^2 u}{\partial y^2}$$

$$= A\,\frac{\partial u}{\partial y} + B\,\frac{\partial^2 u}{\partial y^2}$$

where α is the momentum accommodation coefficient with $0 \leq \alpha \leq 1$, λ is the molecular mean free path, K_n is the Knudsen number defined as the mean free path λ divided by a characteristic length for the flow and $f = min\,[1/K_n, 1]$. Based on the definition of f, it is seen that for any given value of K_n, we have $0 \leq f \leq 1$. The molecular mean free path is always positive. Thus, $B < 0$ and A is a positive number.

1.16.7 Newtonian Boundary Constraint

The Newton thermal boundary condition accounts for one of the most common boundary constraints encountered in general practice. The existence of convective heating (or cooling) at the surface due to the surface energy balance is termed Newtonian (or convective) boundary constraint.

1.16.8 Passive Control of Nanoparticles

The boundary constraint when the normal flux of nanoparticles is zero is termed as zero mass flux or passive control of nanoparticles.

1.16.9 Stefan Blowing

The diffusion of nanoparticles (or species) from the lengthening surface to the ambient region creates a blowing effect. This blowing effect, derived from the Stefan problem, is dissimilar from the mass injection or blowing resulting from transpiration on a permeable surface.

1.17 Bioconvection

Bioconvection refers to the convection due to the erratic movement of microorganisms initiated by the unstable density stratification of microorganisms.

1.18 Magnetic Field

The vector field that describes the magnetic influence on a moving electric charge or a magnetic material is termed as magnetic field. This force is measured using the Lorentz force whose formula is given by:

$$\vec{J} = \sigma\left(\vec{E} + \vec{V} \times \vec{B}\right) \tag{1.18.1}$$

The electromagnetic force $\vec{F_m}$ that must be accounted in the momentum equation is given by:

$$\vec{F_m} = \vec{J} \times \vec{B} \tag{1.18.2}$$

where $\vec{J}$ is the current density, σ is the electrical conductivity, $\vec{V}$ is the velocity, $\vec{E}$ is the electrical field intensity and $\vec{B}$ is the magnetic field.

1.19 Induced Magnetic Field

Induced magnetic field is the additional magnetic field that gets induced on electrically conducting fluid in the presence of an external magnetic field. This phenomenon is due to the impact of a larger magnetic Reynolds number.

1.20 Dimensional Analysis

Dimensional analysis is the study of the mathematical correspondence on the quantities of a physical problem based on its units and dimensions.

1.21 Non-Dimensional Parameters

The ratio of one force to the other force yields a dimensionless number known as the non-dimensional parameter.

1.21.1 Reynolds Number

The ratio of inertial force to the viscous force is known as Reynolds number. The flow pattern is determined by the Reynolds number. A high Reynolds number implies an increased inertial force that corresponds to a turbulent flow pattern. A low Reynolds number implies an increased viscous force that corresponds to a laminar flow pattern.

1.21.2 Magnetic Parameter

The ratio of electromagnetic force to viscous force is known as the magnetic parameter. An increase in the magnetic parameter generates Lorentz force that affects the flow profiles.

1.21.3 Eckert Number

The ratio of advective mass transport to the heat dissipation potential is known as Eckert number. The phenomenon of self-heating of a fluid due to viscous dissipation is characterized by Eckert number.

1.21.4 Schmidt Number

The ratio of kinematic viscosity to mass diffusivity is known as Schmidt number.

1.21.5 Prandtl Number

The ratio of kinematic viscosity to thermal diffusivity is known as Prandtl number. It measures the relative importance of heat conduction and fluid's viscosity.

1.21.6 Lewis Number

The ratio of thermal diffusivity to mass diffusivity is known as Lewis number. It can be alternatively defined as the ratio of Schmidt number to Prandtl number.

1.21.7 Péclet Number

The product of Reynolds number and Prandtl number is known as P*é*clet number.

1.21.8 Biot Number

The ratio of resistance to heat transport inside a body and at the surface of a body is known as Biot number.

1.21.9 Skin Friction Coefficient

The dimensionless shearing stress on the surface of a body due to a fluid motion is known as the skin friction coefficient.

1.21.10 Nusselt Number

The ratio of convective heat transport to conductive heat transport is known as Nusselt number. It measures the effectiveness of heat convection at the surface.

1.21.11 Sherwood Number

The ratio of convective mass transport to diffusive mass transport is known as Sherwood number. It measures the effectiveness of mass convection at the surface.

1.21.12 Motile Density Number

The ratio of convective transport of microorganisms to the diffusive transport of microorganisms is known as motile density number.

1.22 Body Fluid

The fluid produced and circulated within the human body or secreted outside the human body is known as body fluid. Blood, saliva, urine, tears, sweat, and breast milk are a few examples of body fluid. Water is the basis of all body fluids and the human body is composed of about 60% of water.

1.23 Nanofluid

Nanofluid is a colloidal mixture in which a base fluid (water, oil, ethylene glycol, etc.) is mixed with nanometer-sized particles (metals, carbides, oxides or carbon nanotubes). Fluids constituting two nanometer-sized particles are termed hybrid nanofluids. Choi & Eastman, 1995 observed that the nanofluid tends to upgrade and stabilize the thermal properties of the fluid which marked a revolution in the field of fluid dynamics.

1.24 Volume Fraction of Nanoparticle

Nanoparticle volume fraction is the ratio between the volume of nanoparticles and the volume of all constituents of the mixture (or nanofluid). It is dimensionless and expressed as a number between 0 and 1.

1.25 Thermophysical Properties of Nanofluid

1.25.1 Dynamic Viscosity of Nanofluid

The effective dynamic viscosity of nanofluid:

- Based on Einstein, 1906 model, is given by

$$\frac{\mu_{nf}}{\mu_f} = 1 + 2.5\ \phi_{np} \tag{1.25.1}$$

- Based on Brinkman, 1952 model, is given by

$$\frac{\mu_{nf}}{\mu_f} = \frac{1}{(1-\phi_{np})^{2.5}} \tag{1.25.2}$$

- Based on Graham, 1981 model, is given by

$$\frac{\mu_{nf}}{\mu_f} = 1 + 2.5\ \phi_{np} + 4.5 \left\{ \frac{1}{\left(\frac{h}{R_{np}}\right)\left(2+\frac{h}{R_{np}}\right)\left(1+\frac{h}{R_{np}}\right)^2} \right\} \tag{1.25.3}$$

where μ_{nf} is the dynamic viscosity of the nanofluid, μ_f is the dynamic viscosity of the base fluid, ϕ_{np} is the nanoparticle volume fraction, h is the inter-particle spacing and R_{np} is the nanoparticle radius.

1.25.2 Thermal Conductivity of Nanofluid

The effective thermal conductivity of nanofluid:

- Based on Maxwell, 1873 model (applicable for spherical-shaped nanoparticles), is given by

$$\frac{k_{nf}}{k_f} = \frac{k_{np} + 2k_f - 2\phi_{np}\left(k_f - k_{np}\right)}{k_{np} + 2k_f + \phi_{np}\left(k_f - k_{np}\right)} \tag{1.25.4}$$

- Based on Hamilton & Crosser, 1962 model (applicable for non-spherical shaped nanoparticles), is given by

$$\frac{k_{nf}}{k_f} = \frac{k_{np} + (\Lambda - 1)\,k_f - (\Lambda - 1)\,\phi_{np}\left(k_f - k_{np}\right)}{k_{np} + (\Lambda - 1)\,k_f + \phi_{np}\ \left(k_f - k_{np}\right)} \tag{1.25.5}$$

- Based on Xue, 2005 model (applicable for carbon nanotubes), is given by

$$\frac{k_{nf}}{k_f} = \frac{(1-\phi_{np}) + 2\phi_{np}\left(\frac{k_{np}}{k_{np}-k_f}\right)\ ln\left(\frac{k_{np}+k_f}{2k_f}\right)}{(1-\phi_{np}) + 2\phi_{np}\left(\frac{k_f}{k_{np}-k_f}\right)\ ln\left(\frac{k_{np}+k_f}{2k_f}\right)} \tag{1.25.6}$$

where k_{nf} is the thermal conductivity of the nanofluid, k_f is the thermal conductivity of the base fluid, k_{np} is the thermal conductivity of the nanoparticle, ϕ_{np} is the nanoparticle volume fraction and Λ is the nanoparticle shape factor.

1.25.3 Density of Nanofluid

Based on mixture theory, the density of nanofluid is given by

$$\rho_{nf} = (1 - \phi_{np})\, \rho_f + \phi_{np}\ \rho_{np} \tag{1.25.7}$$

where ρ_{nf} is the density of the nanofluid, ρ_f is the density of the base fluid, ρ_{np} is the density of the nanoparticle and ϕ_{np} is the nanoparticle volume fraction.

1.25.4 Specific Heat of Nanofluid

Based on mixture theory, the specific heat of nanofluid is given by

$$(\rho C_p)_{nf} = (1 - \phi_{np})\, (\rho C_p)_f + \phi_{np}\ (\rho C_p)_{np} \tag{1.25.8}$$

where $(\rho C_p)_{nf}$ is the specific heat of the nanofluid, $(\rho C_p)_f$ is the specific heat of the base fluid, $(\rho C_p)_{np}$ is the specific heat of the nanoparticle and ϕ_{np} is the nanoparticle volume fraction.

1.25.5 Electrical Conductivity of Nanofluid

Based on mixture theory, the effective electrical conductivity of nanofluid is given by

$$\frac{\sigma_{nf}}{\sigma_f} = 1 + \frac{3\left(\frac{\sigma_{np}}{\sigma_f} - 1\right)\phi_{np}}{\left(\frac{\sigma_{np}}{\sigma_f} + 2\right) - \left(\frac{\sigma_{np}}{\sigma_f} - 1\right)\phi_{np}} \tag{1.25.9}$$

where σ_{nf} is the electrical conductivity of the nanofluid, σ_f is the electrical conductivity of the base fluid, σ_{np} is the electrical conductivity of the nanoparticle and ϕ_{np} is the nanoparticle volume fraction.

1.26 Khanafer-Vafai-Lightstone Model

Khanafer, Vafai, & Lightstone, 2003 proposed a nanofluid transport model accounting the nanoparticle dispersion. It was developed by considering the effective thermophysical properties of nanofluid.

1.27 Buongiorno Model

The non-homogeneous two-component nanomaterial model describes that the base fluid and nanoparticle have different temperatures and velocities. Buongiorno, 2006 proposed a two-phase nanofluid model comprising seven slip mechanisms

(diffusiophoresis, gravity, Brownian diffusion, fluid drainage, thermophoresis, inertia, and Magnus effect). Among the considered slip mechanisms, only Brownian diffusion and thermophoresis were observed to be significant.

1.28 Modified Buongiorno Model

The Buongiorno model excludes the augmentation in the effective thermophysical properties of the fluid due to the addition of nanoparticles. Different nanoparticles exhibit varied changes in the thermophysical properties of nanofluids and hence these attributes must be also heeded. Therefore, the Buongiorno model was modified by including effective thermophysical properties which is known as the modified Buongiorno model (see Yang, Li, & Nakayama, 2013).

1.29 Solution Methodology

The numerical computation on the modelled system has elucidated with the aid of following techniques.

1.29.1 Finite Difference based *bvp5c* Scheme

The *bvp5c* scheme employs a code based on finite differences that implements the Lobatto IIIA formula of the sixth order in four steps (see Kierzenka & Shampine, 2008) which is a positioning formula whose polynomial positioning provides a C^1-continuous solution with uniform precision of the fifth order in the considered closed interval. Lobatto IIIA's sixth-order four-step formula is implemented as an implicit Runge-Kutta formula. The *bvp5c* scheme solves the algebraic equations directly and checks the true error (positive difference between real and approximate solutions). This process is continued until the appropriate level of error tolerance is reached.

1.29.2 Runge-Kutta based *ode45* Scheme

The *ode45* scheme (see Shampine & Reichelt, 1997) is a single-step method that employs a code based on an explicit Runge-Kutta method of orders 4 and 5.

1.29.3 Runge-Kutta-Fehlberg Method & Adaptive Runge-Kutta Method

The general algorithm (based on the Runge-Kutta formulas of orders 5 and 4) is defined as:

$$K_1 = h\ f\left(x, y\right) \tag{1.29.1}$$

$$K_i = h\ f\left(x + A_i\ h, y + \sum_{j=1}^{i-1} B_{ij}\ K_j\right);\quad i = 2, 3, \ldots, 6 \tag{1.29.2}$$

$$y_5\left(x + h\right) = y\left(x\right) + \sum_{i=1}^{6} C_i\ K_i \tag{1.29.3}$$

$$y_4\left(x + h\right) = y\left(x\right) + \sum_{i=1}^{6} D_i\ K_i \tag{1.29.4}$$

The coefficient matrices appearing in the above formulas are not unique.

For Runge-Kutta-Fehlberg method (see Md Basir et al., 2019), the coefficient matrices are given by:

$$A = \begin{bmatrix} 0 & 1/4 & 3/8 & 12/13 & 1 & 1/2 \end{bmatrix}$$

$$B = \begin{bmatrix} 0 & 0 & 0 & 0 & 0 \\ 1/4 & 0 & 0 & 0 & 0 \\ 3/32 & 9/32 & 0 & 0 & 0 \\ 1932/2197 & -7200/2197 & 7296/2197 & 0 & 0 \\ 439/216 & -8 & 3860/513 & -845/4104 & 0 \\ -8/27 & 2 & -3544/2565 & 1859/4104 & -11/40 \end{bmatrix}$$

$$C = \begin{bmatrix} 16/135 & 0 & 6656/12825 & 28561/56430 & -9/50 & 2/55 \end{bmatrix}$$

$$D = \begin{bmatrix} 25/216 & 0 & 1408/2565 & 2197/4104 & -1/5 & 0 \end{bmatrix}$$

For adaptive Runge-Kutta method (see Kiusalaas, 2005), the coefficient matrices are given by:

$$A = \begin{bmatrix} 0 & 1/5 & 3/10 & 3/5 & 1 & 7/8 \end{bmatrix}$$

$$B = \begin{bmatrix} 0 & 0 & 0 & 0 & 0 \\ 1/5 & 0 & 0 & 0 & 0 \\ 3/40 & 9/40 & 0 & 0 & 0 \\ 3/10 & -9/10 & 6/5 & 0 & 0 \\ -11/54 & 5/2 & -70/27 & 35/27 & 0 \\ 1631/55296 & 175/512 & 575/13824 & 44275/110592 & 253/4096 \end{bmatrix}$$

$$C = \begin{bmatrix} 37/378 & 0 & 250/621 & 125/594 & 0 & 512/1771 \end{bmatrix}$$

$$D = \begin{bmatrix} 2825/27648 & 0 & 18575/48384 & 13525/55296 & 277/14336 & 1/4 \end{bmatrix}$$

1.29.4 Bulirsch-Stoer Algorithm

The Bulirsch-Stoer algorithm is a numerical procedure based on the Richardson extrapolation and the midpoint method (see Kiusalaas, 2005 Bulirsch, Stoer, & Stoer, 2002). In place of the original Bulirsch and Stoer technique, a simplified version that holds on to the fundamental ideas of Bulirsch and Stoer has been utilized. The automated step size adjustment has been omitted in the algorithm for increased efficiency. For computations requiring high accuracy solutions involving smooth functions, the Bulirsch-Stoer algorithm has an upper hand.
To compute the solution of the ODE $y'(x) = F(x, y)$ with initial point (x_0) and terminal point $(x_0 + nh)$, where h is the step size and n is the number of steps, the following computations are carried out using the midpoint method:

$$\begin{aligned} y_1 &= y_0 + hF_0 \\ y_2 &= y_0 + 2hF_1 \\ y_3 &= y_1 + 2hF_2 \\ &\vdots \\ y_n &= y_{n-2} + 2hF_{n-1} \end{aligned} \tag{1.29.5}$$

where $y_i = y(x_i)$ and $F_i = F(x_i, y_i)$, $i = 1$ *to* n. Furthermore, the final value $y(x_0 + nh)$ is calculated using the formula $y(x_0 + nh) = \frac{1}{2}[y_n + (y_{n-1} + hF_n)]$ that

has been finalized by averaging the $y_n's$ obtained through the midpoint formula and the Euler formula. The initial application of the midpoint method uses two integration steps. The number of steps is increased by 2 in successive integrations, each integration being followed by Richardson extrapolation. The procedure is stopped when the difference of successive solutions is less than the required tolerance.

1.30 Motivation

Heat and mass transfer plays a pivotal role in many practical applications like cancer therapy, automotive radiators, air conditioning, refrigeration, microwave ovens, blow moulding, and petrochemical refining. Over the years, scientists have been thriving in finding ways to enhance these transfer capabilities. The use of nanofluid in place of conventional fluid by Choi & Eastman, 1995 marked a major breakthrough in the field of fluid dynamics. Nanofluids play a crucial role in medical and engineering applications due to their ability to enhance heat and mass transfer capabilities. Nanofluid involving microorganisms is an advancing field that has intrigued researchers due to its relevance in antibiotics, biofuel, toxin removal, targeted drug delivery and food digestion.

Nanomedicine is a new concept which combines nanotechnology and medicine. Nanomedicine is the application of nanoscale technologies to the practice of medicine. It is used for diagnosis, prevention and treatment of disease and to gain increased understanding of underlying disease mechanisms. The nascent field of nanomedicine has evoked enormous interest among physical and biological scientists. The great appeal of nanomedicine lies in its promise of using the unique properties of nanoscale materials to address some of the most challenging problems of medical diagnosis and therapy. The novel procedure that integrates therapy and diagnosis in a single platform is termed theranostics.

A mathematical model is a description of a system using mathematical concepts and language. The process of developing a mathematical model is termed mathematical modelling. Mathematical models are used in the natural sciences and engineering disciplines as well as social sciences. A model may help to explain a system and to study the effects of different components and to make predictions about behaviour. Based on literature review and practical applications, very less attention is given to the theoretical studies (through mathematical modelling) concerning biological

variations in body fluids due to the application of nanofluid/hybrid nanofluid in various geometries.

1.31 Objectives

The main objectives of this research work are:

- To mathematically model nanofluid flow problems considering their biological application.
- To solve and analyze the modelled flow problems using different numerical methods.
- To work on the mathematical and physical interpretation of results generated using the graphical data.
- To study and evaluate the impact of nanofluids in the biological systems.
- To statistically model the interactive effects of pertinent parameters on the physical quantity of choice.
- To explain the significance of the derived results and to elucidate their biological meaning.

1.32 Overview of the Thesis

The thesis is arranged into 12 chapters. Chapter 1 introduces the basic concepts, preliminaries and definitions to the reader. An extensive review of related literature has been presented in Chapter 2. Owing to their practical applications, nine fluid flow problems are modelled and investigated in this thesis whose summaries are stated below.

Bioconvective stagnation-point flow due to induced magnetic field

For its applications in biomedical imaging, hyperthermia, targeted drug delivery, and cancer therapy, the bioconvective stagnation point flow involving carbon nanotubes along a lengthening sheet subject to induced magnetic field and multiple stratification effects is investigated. Additionally, chemical reaction and viscous dissipation effects are also heeded. Relevant similarity formulas are effectuated in converting the modelled equations into a first-order system of ODEs and are further treated

in MATLAB using *ode45* and Newton Raphson method. Illustrations on the consequence of effectual parameters on the physical quantities and the flow profiles are achieved with the aid of graphs.

Bioconvectice hybrid stagnation-point flow due to induced magnetic field

For its applications in biomedical imaging, hyperthermia, targeted drug delivery, and cancer therapy, the dynamics of water conveying single-wall carbon nanotubes (SWCNTs) and magnetite nanoparticles on the bioconvective stagnation-point flow along a stretching sheet subject to chemical reaction, viscous dissipation, induced magnetic field, and stratification effects is investigated. Relevant similarity formulas are effectuated in converting the governing equations into a system of ODEs and are further treated numerically using the Runge-Kutta-Fehlberg method with the shooting technique. Illustrations on the consequence of effectual parameters on the physical quantities and the flow profiles are achieved with the aid of graphs.

Significance of nanoparticle shape on stagnation-point flow in the presence of induced magnetic field

Non-spherical nanoparticles have gained popularity for their ability in changing the thermophysical properties of a nanofluid. The significance of multiple slip and nanoparticle shape on stagnation point flow of blood-based silver nanofluid considering chemical reaction, induced magnetic field, thermal radiation, and linear heat source which is beneficial in cancer therapy, biomedical imaging, hyperthermia, and tumor therapy is investigated. Relevant similarity transformations are effectuated in converting the mathematically modelled governing equations into a system of ODEs and are then numerically resolved in MATLAB employing the adaptive Runge-Kutta method and the Newton Raphson method. Observations on the consequence of differing parameters on varying attributes are achieved via tables and graphs. Additionally, the shape effect of nanoparticles on various attributes is also evaluated.

Bioconvective EMHD nanofluid flow past a stretching sheet

Carbon nanotubes (CNTs) are highly recognized for their diverse biomedical applications. The present study aims to numerically and statistically study the stratification

effects of bioconvective electromagnetohydrodynamic (EMHD) flow past a stretching sheet using water-based CNT. The current study, with applications ranging from biomedical imaging, targeted drug delivery, and cancer therapy, provides a theoretical perspective that is beneficial in biomedical engineering. The mathematically modelled system of partial differential equations (PDEs) is then transmuted into a system of ordinary differential equations (ODEs) using apposite transformations which are then resolved numerically using *bvp*5*c* (MATLAB built-in function) algorithm. The impact of influential parameters on concentration, velocity, microbial concentration, temperature and physical quantities are illustrated with the aid of graphs and tables. Further, statistical techniques like correlation, the slope of linear regression, probable error and multiple linear regression are employed in scrutinizing the consequence of influential parameters on physical quantities.

Hydromagnetic Carreau nanoliquid flow over an elongating cylinder

The focal concern of this chapter is to numerically scrutinize the consequences of multiple slip, linear radiation and chemically reactive species on MHD convective Carreau nanoliquid flow over an elongating cylinder. The present study has applications in metallurgical procedures, blow molding, glass fibers, and extrusion processes. Relevant transformations are implemented in converting the governing equations into a system of ODEs and are further treated numerically using the Bulirsch-Stoer algorithm coupled with the shooting technique in MATLAB. The Bulirsch-Stoer method is based on two ideas (midpoint method & Richardson extrapolation). Illustrations on the effect of flow profiles due to the varying parameter values are achieved using graphs. Characteristics of skin friction are quantified using linear regression slope. Simultaneous impact of radiation and thermal slip on Nusselt number and the response of solutal slip and chemically reactive species on mass transfer rate is analysed using three-dimensional surface plots. Moreover, statistical scrutiny on the impact of Hartmann number ($1 \leq M \leq 2$), thermal radiation ($1 \leq Rd \leq 2$) and thermal slip parameter ($0.1 \leq b_2 \leq 0.3$) over heat transfer rate employing Response Surface Methodology (RSM) and sensitivity analysis is also performed.

Bioconvective stagnation-point flow over a rotating stretchable disk

Owing to its practical application in pharmaceuticals, biosensors, medical instruments, bio-chromatography, microchip pump, biomedical science, micro-actuators, and aerodynamics, the bioconvective stagnation-point flow over a whirling extendible disk is investigated. Ferro-nanofluid has been particularly chosen in this work since water-based magnetite nanofluid and rotating disk share similar applications. The nanomaterial flow has been modelled using the modified Buongiorno nanofluid model (MBNM). The impact of the stratification constraints and magnetic field are also accounted. Von Kármán's similarity transformations are employed and the transmuted nonlinear ODEs are resolved using the finite-difference based *bvp5c* routine. MATLAB generated flow profiles have been analyzed for augmentations in the influential parameter values. The influence of magnetic field parameter ($0.2 \leq M \leq 1.8$), thermal stratification parameter ($0.1 \leq S_1 \leq 0.5$), volume fraction of magnetite nanoparticles ($0.01 \leq \phi \leq 0.09$), and velocity ratio parameter ($0.1 \leq S \leq 0.5$) on the heat transfer rate has been scrutinized statistically using a five-level four-factor response surface optimized model.

Nanoliquid flow with irregular heat source and realistic boundary conditions

Titanium dioxide plays a vital role in cancer therapy methods (including photothermal therapy and photodynamic therapy), skincare products, heat exchangers, and car radiators. Therefore, the dynamics of the $TiO_2 - H_2O$ nanomaterial over a nonlinearly stretched surface is investigated. For realistic nanoliquid modelling, the conventional Buongiorno model has been improvised (called modified Buongiorno model) by incorporating the effective thermophysical properties of the nanoliquid. Experimentally derived correlations of the thermal conductivity and dynamic viscosity of the nanomaterial are utilized. The significance of passive control of nanoparticles is also studied. The heat transfer analysis includes the mechanism of Rosseland heat flux and exponential heat source. Similarity theory is used to obtain nonlinear ordinary differential equations (ODEs) from the governing partial differential equations which are solved numerically using *bvp*5*c*, a finite difference-based routine in MATLAB. Further, the heat transfer rate is statistically scrutinized for the consequence of magnetic field ($0.5 \leq M \leq 1.5$), thermal radiation ($0.5 \leq R_d \leq 1.5$) and exponential heat source ($0.2 \leq Q_E \leq 0.4$) by employing

Response Surface Methodology (RSM) and sensitivity analysis.

Bioconvective magnetized nanomaterial flow subjected to convective thermal heating and Stefan blowing

Theranostic is a novel procedure that integrates therapy and diagnosis in a single platform. For its application in theranostic and photothermal therapy for melanoma skin cancer, the hydromagnetic bioconvective flow of a nanomaterial over a lengthening surface is investigated. Realistic nanomaterial modelling is achieved by incorporating passive control of the nanoparticles at the boundary. The impact of the Newtonian heating and Stefan blowing constraints are also accounted. Apposite transformations are employed and then transmuted nonlinear ODEs are resolved using the Bulirsch-Stoer and Newton-Raphson methods. The influence of Stefan blowing parameter ($-3 \leq Sb \leq 3$), the magnetic field parameter ($0.8 \leq M \leq 1.2$) and the Biot number ($0.2 \leq Bi \leq 0.4$) on the heat transfer rate has been scrutinized and optimized utilizing the response surface methodology (RSM). The sensitivity of heat transport rate is computed.

Electro-magnetohydrodynamic Casson nanomaterial flow over a nonlinearly stretched surface

For its biomedical applicability, the dynamics of electro-magnetohydrodynamic flow of blood-gold nanomaterial over a nonlinearly stretching surface utilizing the Casson model has been elucidated numerically. The impact of second-order hydrodynamic-slip, nanoparticle radius, first-order thermal-slip, inter-particle spacing and non-uniform heat source are also accounted. The modelled flow equations are transmuted into a nonlinear system of first-order ODEs (with the aid of apposite similarity variables) which are then resolved numerically utilizing the finite-difference based *bvp*5*c* scheme. The current chapter finds its application in radiofrequency ablation, magnetic resonance imaging, cancer therapy, and targeted drug delivery.

Lastly, Chapter 12 presents the concluding remarks of the thesis and proposals for future work. An extensive bibliography follows this chapter.

Chapter 2

Review of Related Literature

2.1 Nanofluid

Nanofluid, a suspension of ultrafine particles (1-100nm) in a base fluid, introduced by Choi & Eastman, 1995, tends to stabilize and upgrade the thermal properties of the fluid that boosted its acceptance. Since then, scientists have been working hard to further enhance heat transfer capabilities. Nanomaterials play a crucial role in medical and engineering applications due to their ability to enhance heat and mass transfer capabilities. According to Song et al., 2021 and Oke et al., 2021, the inherent nature of nanoparticles is bound to affect the temperature distribution. Mackolil & Mahanthesh, 2019 noted that the augmenting nanoparticle volume fraction tends to increase the nanoliquid temperature in an unsteady nanoliquid flow past an inclined plate. Sheikholeslami & Ganji, 2013 studied the heat transfer capabilities of water-based Cu nanomaterial between parallel plates using HPM (homotopy perturbation method). The authors found that the heat transport improved with higher nanoparticle volume fraction. The copper-based nanomaterial flow over an elongated surface was studied by Ahmad, Ijaz Khan, Hayat, & Alsaedi, 2020. The comparative analysis revealed that the nanomaterial temperature and velocity are higher for water-based copper nanomaterial. Further, the authors found that nanoparticle volume fraction has a constructive effect on the heat transfer rate. Hazarika, Ahmed, & Chamkha, 2021 used fourth order RK-shooting technique to numerically investigate the MHD flow of a chemically reacting water based nanofluid over a permeable stretching sheet involving chemical reaction, thermophoresis, heat source and viscous dissipation. Kameswaran, Narayana, Sibanda, & Murthy, 2012 utilized water-based copper and water-based silver nanofluids to investigate

the impact of pertinent parameters on the hydromagnetic nanofluid flow over a lengthening sheet considering chemical reaction and viscous dissipation effects. It is observed that water-based copper nanofluid exhibits better mass and heat transfer rates.

Ferro-nanofluid (fluid suspension of nanosized magnetite particles) spot applications in biosensors, hyperthermia, microchip pump, targeted drug delivery, and micro-actuators [see Rout et al., 2021]. On administering magnetic field, an increase (of nearly 300%) in the heat transport coefficient of ferro-nanofluid was reported by Azizian et al., 2014. An amplification in the thermal conductivity of Jeffery nanofluid on dispensing magnetite nanoparticles was observed by Sandeep, Chamkha, & Animasaun, 2017. The negative effect of the magnetic parameter on the heat transfer rate of the ferro-nanofluid flow on a rotating disk was pointed out by Z. Abbas, Naveed, Tabassum, & Ahmad, 2021.

Particles of silver between 1nm and 100nm, called silver nanoparticles, have been proved to be beneficial in the medical field with their antibacterial properties and also due to their applicability in the treatment of many diseases; namely cancer [see Mathur, Jha, Ramteke, & Jain, 2018; Foulkes, Ali Asgari, Curtis, & Hoskins, 2019; Hepokur et al., 2019]. Abbasi, Hayat, & Ahmad, 2015 examined the peristaltic transport of silver-water nanofluid in the presence of constant applied magnetic field considering Ohmic heating, velocity slip, thermal slip, and Hall effects. The authors observed that the addition of 5% silver nanoparticles reduced the velocity and temperature of the base fluid by 10% and 16%, respectively. The dominating nature of silver nanoliquid over copper nanoliquid on the heat transfer rate was observed by Hayat, Qayyum, Imtiaz, & Alsaedi, 2016 and Sravanthi, 2019. In addition, Hayat, Khan, Qayyum, & Alsaedi, 2018 noted that the Bejan number is more for Ag-water nanofluid. The increment of the average Nusselt number by increasing the volume fraction of nanoparticles for typical nanofluid is more sensible than hybrid nanofluid in an enclosure with rotating heat sources [see Jamiatia, 2019]. The study on the hydrothermal and irreversibility behaviour of a biologically synthesized silver-water nanoliquid in a wavy microchannel heat sink, conducted by Al-Rashed et al., 2019, revealed that the nanoliquid has a better cooling performance in comparison with pure water.

CNT (carbon nanotube) is a graphene sheet rolled up into a tube having a nanoscale

diameter. CNTs are categorised into SWCNT (single-wall carbon nanotubes) and MWCNT (multi-wall carbon nanotubes) based on the number of used graphene sheets. CNT finds its use in structural reinforcement, automotive parts, device modelling, energy storage, electromagnetic shields, etc. CNTs are also proved to be useful in the medical field. CNTs are administered in drug delivery, cancer diagnosis & treatment, thermal ablation, delivery of genetic material, etc. Practically, SWCNTs are preferred over MWCNTs due to the amelioration it provides in the medical field and also due to their lower toxicity level. The significance of nonlinear thermal radiation and quartic chemical reactions on CNT-water nanomaterial flow over a lengthening surface has been explored by R. Kumar, Kumar, Sheikholeslami, & Chamkha, 2019. A higher Nusselt number is noted for SWCNTs than MWCNTs. In addition, the heat transfer growth subject to different CNTs and induced magnetic field (IMF) has been examined by M. Raza et al., 2020. Nadeem, Hayat, & Khan, 2019 conducted a numerical study to reveal that water-based SWCNT-MWCNT hybrid nanoliquid has a better heat transfer rate when balanced against SWCNT-water nanoliquid. Sreedevi & Reddy, 2019 performed a comparative study on the effect of water-based SWCNTs and MWCNTs Maxwell nanoliquid flow between two stretchable rotating disks. M. I. Khan, Hayat, Shah, & Haq, 2019 elucidated the impact of CNTs on stagnation flow over a stretched surface involving quartic chemical reaction and induced magnetic field. Z. Iqbal, Azhar, & Maraj, 2017 conducted a numerical investigation to exploit the response of induced magnetic field on transfer quantities using MWCNT and SWCNT and noted a constructive effect for nanoparticle volume fraction on the induced magnetic field.

2.2 Hybrid Nanofluid

Fluids constituting two or more nanoparticles are termed hybrid nanofluids. Mabood, Yusuf, & Khan, 2021 investigated the significance of melting heat transfer, magnetic field, and nonlinear radiation on hybrid nanoliquid flow over a stretched surface and observed that augmenting nanoparticle volume fraction of copper tends to increase the heat transfer rate. The consequence of the Newtonian heating process and nonlinear thermal radiation effect on water-based $Cu - Ti_2O_3$ hybrid nanofluid flow over an elongating porous surface considering Darcy-Forchheimer's model was analyszed by Yusuf, Mabood, Khan, & Gbadeyan, 2020. The authors noticed that

the rate of entropy generation upsurged for ordinary nanofluid when compared with the hybrid nanofluid. Waini, Ishak, & Pop, 2019a explored the two-dimensional steady flow of water-based $Al_2O_3 - Cu$ hybrid nanoliquid over a nonuniformly shrinking/stretching permeable surface. R. Ali, Asjad, & Akgül, 2021 remarked that the water-based hybrid nanoliquid improved the nanofluid temperature and velocity profiles when compared with engine oil-based nanofluid. Junoh, Ali, Arifin, Bachok, & Pop, 2019 studied the hydromagnetic (MHD) stagnation point hybrid nanofluid flow over a stretching/ shrinking sheet and observed an increased heat transfer rate in the hybrid nanofluid when compared with the normal nanofluid. Subhani & Nadeem, 2019 performed a comparison study on the regular and hybrid nanofluid flow induced by an exponentially stretching surface along with micropolar fluid theory. The authors perceived a higher temperature and heat transfer rate in the case of hybrid nanofluid. Agrawal, Dadheech, Jat, Baleanu, & Purohit, 2021 adopted the Runga-Kutta fourth-order method to investigate the MHD radiative flow through a permeable stretching surface immersed in a porous medium. The authors also conducted a parallel analysis on three types of hybrid nanofluids. Ramesh, Shehzad, & Tlili, 2020 explored the Darcy-Forchheimer hybrid nanomaterial flow in a stretchable convergent and divergent channel. For higher solid volume fractions, an enhancement in the velocity of the convergent channel and a decline in the velocity of the divergent channel were noted. Ramesh, Shehzad, & Izadi, 2020 inquired about the thermal transportation of hybrid and regular nanofluids flow due to a moving thin needle. The authors observed that the temperature profile improved in the hybrid nanofluid case. A reduction in the heat transfer rate (upper branch) on the shrinking sheet was observed by Waini, Ishak, & Pop, 2019b with mounting volume fraction of copper nanoparticles. Aly & Pop, 2020 performed a comparative study between hybrid nanofluid and regular nanofluid on the MHD stagnation-point flow over a stretching/shrinking sheet. The numerical exploration performed by Jamaludin, Naganthran, Nazar, & Pop, 2020 reveals that the hybrid nanofluid exhibited the highest temperature and the lowest heat transfer rate. Lund, Omar, Raza, & Khan, 2021 illustrated the dual solutions for dissipative MHD hybrid nanofluid flow past a stretching/shrinking surface and noticed an escalation in the temperature with augmenting values of Eckert number.

2.3 Blood-based Nanofluid

Blood is a connective tissue in fluid form [see Sembulingam & Sembulingam, 2012]. Blood flow utilizing nanoparticles are important in the medical industry for cancer treatment and drug delivery. The significance of partial slip and buoyancy on the blood-gold Carreau nanofluid flow over an upper horizontal surface of a paraboloid of revolution was investigated by O. K. Koriko et al., 2018. The authors observed that the maximum values for surface drag and the heat transfer rate was showcased by smaller values of Deborah number. The augmentation in the volume fraction of carbon nanotubes increased the blood temperature (see Khalid, Khan, Khan, Shafie, & Tlili, 2018). Dinarvand, Rostami, Dinarvand, & Pop, 2019 pointed out that the use of CuO and Cu hybrid nanoparticles reduced the haemodynamic effect of the capillary relative to the pure blood case. U. Khan, Bilal, Zaib, Makinde, & Wakif, 2022 numerically simulated the nonlinear radiative flow of Casson gold-nanoliquid through a stretched rotating rigid disk subject to Lorentz force utilizing the three-stage Lobatto method. Ashraf, Qasim, Wakif, Afridi, & Animasaun, 2022 utilized the generalized differential quadrature method to explore the peristaltic flow of blood-based Casson nanomaterial containing platelet-shaped magnetite nanoparticles. Eid, Al-Hossainy, & Zoromba, 2019 conducted a numerical study on the MHD blood-based SWCNT nanofluid flow through a circular cylinder considering linear heat source/sink, nonlinear thermal radiation, and nanoparticle shape effect. The authors observed that both velocity and temperature profile increase for augmenting heat source/sink, thermal radiation and SWCNT volume fraction with respect to lamina and cylinder shapes. Further, the significance of partial slip due to lateral velocity and viscous dissipation for blood-gold Carreau nanomaterial and dusty fluid was elucidated by O. K. Koriko, Adegbie, Shah, Animasaun, & Olotu, 2021. A significant difference in the effect of partial slip on the dynamics of dusty fluid and blood-gold nanomaterial was observed.

2.4 Nanoparticle Shape and Radius

Different nanoparticle shape and radius exhibit different thermal properties that are beneficial in industrial and biomedical fields. The nanoparticles can be categorized into spherical and non-spherical nanoparticles based on their physical shape. Different shaped nanoparticle exhibits different properties and different

heat transfer capabilities (see Truong, Whittaker, Mak, & Davis, 2015). Timofeeva, Routbort, & Singh, 2009 analyzed the thermophysical properties of alumina nanofluid with different nanoparticle shapes; namely platelet, blade, brick, and cylinder; both practically and theoretically. Ellahi, Hassan, & Zeeshan, 2017 pointed out that the lowest velocity and highest temperature of the nanoliquid were caused by the sphere and disc-shaped particles, respectively for the mixed convective nanoliquid flow past a vertical lengthening permeable sheet. In addition, Benkhedda, Boufendi, Tayebi, & Chamkha, 2020 reported that the maximum friction factor is exhibited by the platelet-shaped silver-titanium dioxide nanoparticles. The reduction in the temperature profile of $Cu - CuO$/blood with the increasing shape factor values was revealed by Tripathi, Prakash, Tiwari, & Ellahi, 2020. A comparative analysis of $Ti - H_2O$ and $Ag - H_2O$ nanofluids on the effect of nanoparticle shape in a microchannel, conducted by Sindhu & Gireesha, 2021, showcased that the silver nanofluid exhibited higher entropy than the titanium nanofluid. The authors also observed that the entropy generation is high in the case of disc-shaped nanoparticles, followed by needle and sphere-shaped nanoparticles. Elnaqeeb, Animasaun, & Shah, 2021 investigated the dynamics of water conveying nanoparticles with various densities and shapes through a rectangular closed domain and observed that the heat transfer is maximal in the case of ternary-hybrid nanofluid made up of copper oxide, copper, and silver nanoparticles. The changes in the radius of the nanoparticle is proportional to the velocity profile and inversely proportional to the thermal field (see N. A. Shah et al., 2021). Sun et al., 2022 noted that the augmentations in nanoparticle radius tends to magnify the skin friction coefficient whereas Verma, Rajput, Bhattacharyya, & Chamkha, 2022 and Akbar et al., 2022 noticed a decrease in the drag coefficient.

2.5 Carreau Nanofluid

For a generalized Newtonian fluid, the value of shear rate depends only on its current time point, i.e., there is no memory or history of deformation. Carreau fluid is one such fluid whose viscosity μ depends on the shear rate, which is based on the equation:

$$\mu\left(\dot{\gamma}\right) = \mu_{\infty} + \left(\mu_0 - \mu_{\infty}\right)\left(1 + \left(\lambda\dot{\gamma}\right)^2\right)^{\frac{n-1}{2}} \tag{2.5.1}$$

where λ is the relaxation time, $\dot{\gamma}$ is the generalised shear rate, n is the power-law index, μ_0 represents the zero shear viscosity, and μ_∞ is the infinite shear viscosity. Human blood is an example of Carreau fluid with shear thinning nature.

Numerous studies concerning Carreau nanoliquid with variable geometry, boundary conditions and effects have been carried out. Madhu et al., 2020 used FEM to discuss the impact of second law utilization on Carreau fluid flow caused due to a tilted microchannel. The authors observed a decline in temperature due to the augmentation in the Weissenberg number. Carreau nanoliquid flow past a convectively heated expanding surface was numerically studied by Eid, Mahny, Dar, & Muhammad, 2020 using RKF45. A reduction in the mass transfer rate was noted owing to a hike in chemical reaction. Gangadhar, Ramana, Makinde, & Kumar, 2018 explored the consequences of Cattaneo-Christov heat flux on a Carreau fluid past an elongating cylinder. The problem was tackled using the spectral relaxation method and the authors found out that rising magnetic parameter caused an enlargement in the temperature profile. Vinita & Poply, 2020 inspected the response of outer velocity slip flow on an expanding cylinder. The authors noticed shrinkage in the velocity profile due to the increasing velocity slip parameter. Salahuddin, 2020 utilised the Keller box method along with the shooting technique to analyse the Carreau fluid model over an extended cylinder. I. Khan, Malik, Hussain, & Khan, 2017 carried out a study on Carreau nanoliquid flow considering Joule heating over a slanted lengthening cylinder. Salahuddin, Hussain, Malik, Awais, & Khan, 2017 conducted a numerical analysis on the response of chemically reactive species and generalized slip on the MHD Carreau nanoliquid flow induced by a linear expanding cylinder using finite difference method and observed an improvement in the velocity profile with augmenting velocity slip parameter.

2.6 Casson Nanofluid

The fluids whose viscosity alters with stress are termed non-Newtonian fluids. Casson fluid, proposed by Casson, 1959, is a shear thinning fluid that assumes infinite viscosity at zero shear-rate, and vice versa. The rheological equation for an isotropic and incompressible flow of a Casson fluid is given by (see Isa et al., 2017; Suresh Reddy & Panda, 2022):

$$\tau_{ij} = \begin{cases} 2\left(\mu_B + \frac{P_y}{\sqrt{2\pi}}\right) e_{ij} \ , \ \pi > \pi_c \\ \\ 2\left(\mu_B + \frac{P_y}{\sqrt{2\pi_c}}\right) e_{ij}, \ \pi < \pi_c \end{cases} \tag{2.6.1}$$

where where μ_B is plastic dynamic viscosity of the non-Newtonian fluid, P_y is the yield stress of the fluid, τ_{ij} is $(i,j)^{th}$ component of the stress tensor, $\pi = e_{ij}e_{ij}$, e_{ij} is the $(i,j)^{th}$ component of the deformation rate and π_c is a critical value of π based on the non-Newtonian model. Human blood, honey, tomato sauce, jelly, and concentrated fruit juices are a few examples of Casson fluid.

Mukhopadhyay, 2013 observed that the augmentation in Casson parameter suppressed the velocity and enhanced the thermal field. Later, Hussanan, Salleh, Alkasasbeh, & Khan, 2018 extended the work of Mukhopadhyay, 2013 by considering the flow in the presence of Newtonian heating and magnetic field. The consequence of radiation, magnetic field, and non-uniform heat source/sink on the blood-gold Casson nanofluid flow in a slippery curved sheet has been studied by U. Khan, Shafiq, Zaib, Sherif, & Baleanu, 2020. The effectiveness of spherical-shaped gold nanoparticles in the Casson nanofluid flow was pointed out by Nazeer, Irfan, Hussain, & Siddique, 2022. U. Khan, Zaib, Khan, & Nisar, 2021 elucidated the dynamics of blood-based Casson gold nanofluid over a curved elongated/shrinked surface. The negative impact of Casson parameter on the electro-magnetic stagnation flow was noticed by Hussain, Farooq, & Sheremet, 2022.

2.7 Nanofluid Flow Model

Khanafer et al., 2003 proposed a nanoliquid transport model accounting the nanoparticle dispersion. Later, Tiwari & Das, 2007 developed a simpler nanofluid model considering the effective thermophysical properties of a nanofluid. R. Kumar, Kumar, Shehzad, & Sheikholeslami, 2018 utilized the Tiwari-Das nanofluid model to investigate the influence of vibrational rotations and multiple slip conditions on the hydromagnetic nanomaterial flow over an elongating surface. The authors observed a rise in the Nusselt number for augmenting nanoparticle volume fraction. Mustafa, Javed, & Ghaffari, 2016 employed the Tiwari-Das nanoliquid model to mathematically model the magnetohydrodynamic stagnation-point flow of ferro-nanofluid over a spinning disk.

Buongiorno, 2006 proposed a nanofluid model comprising seven slip mechanisms (diffusiophoresis, gravity, Brownian diffusion, fluid drainage, thermophoresis, inertia, and Magnus effect). Among the considered slip mechanisms, only Brownian diffusion and thermophoresis were observed to be significant. Sheikholeslami, Ganji, & Rashidi, 2016 utilized the Buongiorno nanofluid model to investigate the consequence of the magnetic field on the unsteady squeezing flow between two infinite parallel plates. The Bödewadt nanofluid flow employing the Buongiorno nanofluid model was studied by J. Khan, Mustafa, Hayat, & Alzahrani, 2017 with the aid of the Keller-box method. The authors observed that the nanofluid temperature ascended with a larger thermophoretic force. Sadiq, Haider, Hayat, & Alsaedi, 2020 made use of the Tiwari-Das model whereas Hayat, Haider, Muhammad, & Alsaedi, 2020 exercised the Buongiorno nanofluid model to analyze the significance of slip constraints on the Darcy-Forchheimer flow over a spinning disk. Chu et al., 2020 modelled a bioconvective third-grade fluid flow using Buongiorno nanofluid model to investigate the consequence of magnetohydrodynamics (MHD) and activation energy over a lengthening surface.

Buongiorno nanofluid model neglects the nanofluid's effective thermal properties that are dependent on the selected nanoparticle. By including the effective thermophysical characteristics of the nanomaterial in Buongiorno's model, Yang et al., 2013 introduced the modified Buongiorno nanofluid model (MBM). Puneeth, Manjunatha, Madhukesh, & Ramesh, 2021 utilized the RKF-45 scheme and modified Buongiorno nanofluid model to numerically explore the influence of mixed convective hybrid nanomaterial flow past a bidirectional nonlinear expandable sheet. Mahanthesh & Mackolil, 2021 considered the MBM to investigate the consequence of alumina nanomaterial in heat transfer augmentation. The authors established that the random motion and thermophoresis of nanoparticles exhibit a positive effect on the nanomaterial temperature. Rana, Mahanthesh, Mackolil, & Al-Kouz, 2021 investigated the significance of nonlinear convection and aggregation kinematics of nanoparticles on the nanofluid flow (modeled using modified Buongiorno nanofluid model) through a vertical plate.

2.8 Magnetohydrodynamics

Magneto-fluid dynamics (MHD) is the branch in physics which deals with the dynamics of electrically conductive fluids under the influence of a magnetic field. The concept of magnetohydrodynamics was first introduced by Alfvén, 1942. MHD flows have applications in cancer therapy, magnetic cell separation, electromagnetic pump, drug delivery, aeronautics, and magnetic resonance imaging. Sk, Das, & Kundu, 2016 observed that the proficiency of a thermal system can be improved by scheming the strength of the applied magnetic field. An increase in the drag coefficient and a decrease in the heat transfer rate with rise in magnetic parameter values was noted by Jafar, Shafie, & Ullah, 2020. Gholinia, Hoseini, & Gholinia, 2019 numerically investigated the free convective flow of Walter-B nanoliquid over a tilted expanding sheet using RKF45 and noted an increase in the temperature profile due to augmenting magnetic field parameter. Sarkar & Sahoo, 2021 observed a decline in the velocity profiles of the upper solution branch with the augmentation in the intensity of the applied magnetic field. The destructive nature of the magnetic field on the radial and tangential velocity profiles was noted by Upadhya, Devi, Raju, & Ali, 2021. Pal & Mondal, 2018 elucidated the bioconvective MHD nanofluid flow past an exponentially stretching surface and observed a decline in the motile density due to augmenting values of microorganism concentration difference parameter and bioconvection Peclet number. M. A. Kumar, Reddy, Rao, & Goud, 2021 employed a numerical model to investigate the influence of thermal radiation on the nanofluid flow from an infinite vertical plate considering viscous dissipation and magnetic field. It is noted that an augmentation in radiation parameter causes an enhancement in the temperature and velocity profiles.

2.9 Induced Magnetic Field

The magnetic field represents an important characteristic of hydromagnetic problems. In some cases, the magnetic Reynolds number of the flow may not be realistic to be assumed small in magnitude; hence induced magnetic field is not negligible (see O. Koriko, Omowaye, Animasaun, & Bamisaye, 2017). Induced magnetic field (IMF) corresponds to the additional magnetic field that gets induced on electrically conducting fluid when encountered with an external magnetic field caused due to the impact of a larger magnetic Reynolds number. IMF has applications in MRI, glass

manufacturing, geophysics, and MHD generators, etc. IMF paired with blood flow plays a decisive role in blood pumps, treatment of cardiac diseases and has many other biomedical applications. Kumari, Takhar, & Nath, 1990 explored the fluid flow and heat transfer over an elongating sheet heeding IMF. Later, the MHD flow over a lengthening sheet subject to an IMF was reinvestigated by F. M. Ali, Nazar, Arifin, & Pop, 2011a. Investigations on entropy generation and IMF effects on Cu and TiO_2 nanofluid using Keller box method are carried out by Z. Iqbal, Maraj, Azhar, & Mehmood, 2017 and observed an improved thermal conductivity for water-based TiO_2 nanofluid when compared with water based Cu nanofluid. Mehmood & Iqbal, 2016 utilized the fifth-order Runge-Kutta method to examine the consequence of induced magnetic field on stagnation point flow of nanofluid involving gyrotactic microorganisms. F. M. Ali, Nazar, Arifin, & Pop, 2011b developed the study of Mahapatra & Gupta, 2002 to analyze the hydromagnetic stagnation point fluid flow over a lengthening sheet subject to an IMF. Later, Junoh et al., 2019 broadened the work of F. M. Ali et al., 2011b to study the hybrid nanoliquid flow characteristics. Gireesha, Mahanthesh, Shivakumara, & Eshwarappa, 2016 numerically analyzed nanofluid stagnation point flow past a stretching surface attending IMF and found out that the induced magnetic field enhances with the intensifying hydromagnetic field. M. S. Iqbal et al., 2020 scrutinized the influence of induced magnetic field on ferrofluid past a vertical stretching surface and observed that velocity profile enhanced for assisting flow with magnetic parameter. Further, Amjad et al., 2020 studied the influence of Lorentz force and induced magnetic field on Casson micropolar nanoliquid over a permeable curved stretching/shrinking surface.

2.10 Electromagnetohydrodynamics

Electromagnetohydrodynamics (EMHD) is the area that concerns the study of dynamics of electrically conducting fluids under the influence of the magnetic and electric fields. EMHD has raised quite an interest over the years due to its versatile application in geophysics, engineering, biomedical engineering, magnetic drug targeting and many others. Z. Shah, Bonyah, Islam, & Gul, 2019 examined the significance of thermal radiation on the EMHD rotating flow of CNTs over a stretching sheet and noticed that the electric parameters ascend the velocity profile whereas the magnetic parameter descends the velocity profile. Daniel, Aziz,

Ismail, & Bahar, 2020 analysed the two-dimensional unsteady EMHD nanoliquid flow over a lengthening sheet involving multi-slip and dual stratification effects and noticed that the electric field parameter has a constructive effect on velocity. The effect of EMHD in the nanoliquid flow past a porous Riga plate pertaining gyrotactic microorganism was numerically explored by T. Abbas, Hayat, Ayub, Bhatti, & Alsaedi, 2019. Zhang, Bhatti, & Michaelides, 2020 investigated the EMHD behaviour of a third-grade fluid flowing between a pair of parallel plates utilising a Darcy-Brinkman-Forchheimer model. The authors observed an enhancement in the temperature profile for the augmenting magnetic field parameter. Jakeer & Reddy, 2020 examined the impact of viscous dissipation, heat generation, and slip on the entropy generation in electro-magnetohydrodynamic $Ag-Cu-H_2O$ hybrid nanofluid. In addition, Zainal, Nazar, Naganthran, & Pop, 2021 explored the unsteady EMHD stagnation point flow in a hybrid nanofluid concerning a stretching/shrinking sheet. The double stratification effects on EMHD nanoliquid flow over a lengthening sheet involving Joule heating, viscous dissipation and radiation effects were numerically explored by Daniel, Aziz, Ismail, & Salah, 2017b with the aid of an implicit finite difference scheme. Liu, Jian, & Tan, 2018 conducted an entropy generation analysis of EMHD flow in a curved rectangular microchannel. The authors noticed that the electric field parameter had a positive impact on the entropy generation rate.

2.11 Bioconvection

Bioconvection is a routine mechanism caused by the erratic movement of microorganisms. This phenomenon was first noticed by Wager, 1911 and the term bioconvection was given by Platt, 1961. Bioconvective flow problems find their applications in microbial enhanced oil recovery, toxin removal, targeted drug delivery, food digestion, antibiotics, and bio-microsystems. Kuznetsov & Avramenko, 2004 were among the first few to investigate the stability of a suspension containing microorganisms and small particles. M. Uddin, Khan, Qureshi, & Bég, 2017 employed the Runge-Kutta-Fehlberg method to numerically investigate the impact of thermal and hydrodynamic slip constraints on the water-based bio-nanomaterial containing microorganisms. The authors observed that the augmenting bioconvection Peclet number tends to improve the motile microorganism density number. The consequence of multiple slips on bioconvective flow was

studied by Alshomrani, Ullah, & Baleanu, 2020. M. M. Bhatti, Shahid, Abbas, Alamri, & Ellahi, 2020 studied the role of activation energy on a suspension of nanoparticles and microorganisms in a magnetized fluid with the aid of successive local linearization methods. The consequence of hydrodynamic slip and convective boundary conditions on the flow past a lengthening sheet containing microorganisms was examined by Sampath Kumar, Gireesha, Mahanthesh, & Chamkha, 2019. The authors noted a drop in the microbial concentration with a rising bioconvection Peclet number. The outcome of gyrotactic microbes in the nanoliquid flow along a nonlinearly lengthening porous sheet was revealed by Ahmad, Ashraf, & Ali, 2020. Al-Amri & Muthtamilselvan, 2020 explored the significance of thermal radiation, microorganisms, magnetic field, and activation energy on the two-dimensional stagnation point flow of an incompressible nanoliquid and noted an increase in the density of motile microorganisms for larger values of Peclet number. M. Bhatti & Michaelides, 2021 studied the significance of Arrhenius activation energy on the thermo-bioconvection nanofluid flow over a Riga plate and noticed that an augmentation in the bioconvection Rayleigh number weakened the velocity profile. Waqas, Naseem, Muhammad, & Farooq, 2021 observed a shrinkage in the microbial concentration with mounting values of Peclet number. The relevance of three-dimensional bioconvective flow due to an exponentially stretching has been explored by Alqarni, Waqas, Alghamdi, & Muhammad, 2022. The authors noticed that the microbial concentration ascends with microorganism Biot number but descends with Peclet number.

2.12 Stratification

Fluctuations in heat, mass and motile density profiles or the presence of different fluids trigger a formation of layers known as stratification. Alsaedi, Khan, Farooq, Gull, & Hayat, 2017 elucidated the stratification effects of MHD mixed convective nanofluid flow past an elongated surface using homotopy analysis method and observed a decrease in temperature with augmenting thermal stratification parameter. Muhammad, Alamri, Waqas, Habib, & Ellahi, 2021 scrutinized the influence of slip on the bioconvective Carreau nanoliquid flow and observed a decrease in the density of the motile microorganism with augmenting bioconvection Lewis number. A numerical exploration on the impact of swimming gyrotactic microorganisms for hydromagnetic

nanofluid through a stretched porous sheet using the Darcy-Forchheimer model was carried out by Shahid, Huang, Bhatti, Zhang, & Ellahi, 2020. The impression of thermal stratification and Marangoni convection on the hybrid nanofluid flow over a spinning disk has been examined by Manzoor, Muhammad, Farooq, & Waqas, 2022. Tlili et al., 2020 analysed the impact of double stratification and partial slip on the hydromagnetic micropolar nanoliquid flow along a stretched surface containing gyrotactic microorganisms and observed a decline in temperature profile due to augmenting thermal stratification values. Ahmad, Nadeem, Muhammad, & Issakhov, 2020 elucidated the effect of double stratification on carbon nanotube (CNT) nanofluid flow and detected a decrease in the nanofluid temperature and volume fraction concerning thermal and solutal stratification parameters, respectively. Further, Ramzan, Riasat, Shah, Kumam, & Thounthong, 2020 examined the impact of thermal stratification parameter on unsteady ethylene glycol-based nanoliquid flow.

2.13 Flow past a Stretching Sheet

Cortell, 2007 explored the heat transfer and viscous fluid flow over an elongating sheet. The analysis was carried out for two cases (a sheet with prescribed surface temperature and for a sheet with constant surface temperature). W. Khan & Pop, 2010 were among the first to study the laminar nanofluid flow problem on a stretching sheet. Rana & Bhargava, 2012 extended the work of W. Khan & Pop, 2010 to investigate the nanofluid flow past a nonlinearly lengthening sheet. The authors noted an increase in nanofluid temperature and a decrease in velocity for mounting values of stretching ratio. Later, Mabood, Khan, & Ismail, 2015 progressed the work of Rana & Bhargava, 2012 by incorporating viscous dissipation and magnetic field effects. Eid, 2020 numerically investigated the heat transfer characteristics of the shape of gold nanoparticles on the blood flow past an exponentially lengthening sheet using Sisko nanofluid and considering the Biot number effect. The highest heat transfer rate was observed by the blade-shaped nanoparticle (blowing case) and the spherical nanoparticles (suction case). Mabood, Ibrahim, Kumar, & Lorenzini, 2020 numerically explained the consequence of thermal radiation, velocity and thermal slip on an inclined MHD Casson nanofluid flow utilizing the Runge-Kutta-Fehlberg method and observed growth in Nusselt number due to augmenting values of Prandtl

number. Krishnamurthy, Gireesha, Prasannakumara, & Gorla, 2016 performed a numerical analysis to elucidate the effect of chemical reaction on boundary layer slip flow of nanofluid induced by a nonlinear stretching sheet. The destructive effect of chemical reaction parameter on the nanoparticle concentration profile was observed by S. Ibrahim, Lorenzini, Kumar, & Raju, 2017 and Daniel, Aziz, Ismail, & Salah, 2019.

2.14 Flow over a Rotating Disk

Scientists and researchers follow the studies concerning nanofluid flow due to the rotation of the disk for their practical application in centrifugal filtration, pharmaceuticals, biosensors, medical instruments, microchip pumps, biomedical science, micro-actuators, bio-chromatography, and aerodynamics. Kármán, 1921 was the first to investigate the flow over a rotating disk. Pioneering works on the nanoscale fluid flow over a rotating disk were carried out by Bachok, Ishak, & Pop, 2011 and Turkyilmazoglu, 2014. Mahanthesh, Gireesha, Animasaun, Muhammad, & Shashikumar, 2019 proved the amalgam of $SWCNT - H_2O$ nanomaterial improved the thermal field when compared with the water-based MWCNT nanomaterial. Recently, Shehzad, Mabood, Rauf, Izadi, & Abbasi, 2021 exploited the Runge–Kutta-Fehlberg scheme to elucidate the rheological features of Casson-Maxwell fluids over expandable spinning disk. R. Kumar, Bhattacharyya, Seth, & Chamkha, 2021 studied about magnetite water based nanofluid flow over a rotating disk in the presence of external magnetic field and Arrhenius activation energy using fourth order Noumerov's method and noted that the thermophoresis parameter has a negative impact on heat transfer rate. Doh, Muthtamilselvan, Swathene, & Ramya, 2020 employed the semi-analytical homotopy analysis method (HAM) to examine the effect of homogeneous and heterogeneous reactions on a spinning disk with variable thickness. Hayat, Haider, Muhammad, & Alsaedi, 2017 studied the Darcy-Forchheimer nanofluid flow due to a spinning disk and observed a decrease in the velocity profiles with mounting values of porosity parameter and the inertial coefficient.

2.15 Stagnation Flow

The stagnation point corresponds to the point where the fluid's local velocity is zero. It proposes many applications in engineering, industry, and physiological

fluid flows. Hiemenz, 1911 was the first researcher to numerically explore the stagnation-point flow problem. Turkyilmazoglu, 2012 discussed the hydromagnetic stagnation-point due to an expandable whirling disk. R. Kumar, Kumar, Vajravelu, & Sheikholeslami, 2020 explored the stagnation flow of the Casson nanomaterial through Darcy-Forchheimer medium. The authors noted a drop in the velocity profile of Sakiadis flow with the Casson parameter. Mahanthesh, Mackolil, & Shehzad, 2020 statistically surveyed the impact of thermal Biot number and exponential heat source parameter on the heat transfer rate. R. Kumar, Kumar, Sharma, & Sheikholeslami, 2021 employed OHAM to examine the transport of nanomaterial filled in Darcy-Forchheimer medium space. Waini, Ishak, & Pop, 2021 investigated the unsteady stagnation flow of a hybrid nanomaterial on a porous rigid surface and observed an increase in the heat transfer rate with augmenting mass flux parameter. N. Abbas, Malik, Alqarni, & Nadeem, 2020 explored the stagnation-point hybrid nanofluid flow over a slip surface. The authors adopted the Runge-Kutta-Fehlberg method to numerically solve the nonlinear system of differential equations and noted that the velocity is inversely proportional to the velocity ratio parameter. Hafeez, Khan, & Ahmed, 2020 employed the BVP Midrich scheme to numerically survey the hydromagnetic stagnation-point flow of Oldroyd-B nanoliquid.

2.16 Slip Boundary Constraint

The relative movement of the fluid with the boundary is characterized with the aid of slip constraint. Multiple slip corresponds to the case when more than one slip (velocity, thermal, or solutal) condition is considered. Nandeppanavar, Vajravelu, Abel, & Siddalingappa, 2012 employed Wu's velocity-slip model (see Wu, 2008) to investigate the consequence of second-order slip over a lengthening surface. Abdelmalek et al., 2020 utilized HAM to numerically investigate the impact of second-order hydrodynamic-slip parameter and Stefan blowing on the hydromagnetic Casson flow over a linearly extending surface. The dynamics of Casson fluid flow with first-order hydrodynamic-slip over a non-linearly elongating surface was elucidated by Senapati, Parida, Swain, & Ibrahim, 2022. The authors noticed a reduction in the flow velocity with augmentation in the slip-parameter. The ability of the second-order hydrodynamic-slip parameter to increase the Casson nanofluid temperature was pointed out by Obalalu, 2022. Daniel, Aziz, Ismail, &

Salah, 2018 reported that the augmenting velocity slip parameter slows the velocity profile. S. A. Khan, Nie, & Ali, 2020 and Amanulla, Saleem, Wakif, & AlQarni, 2019 noted that multiple slip effects have a positive impact on boundary layer flow. The decrease in the heat transfer rate due to the velocity slip parameter was observed by W. Ibrahim & Negera, 2020. A decrease in the temperature and concentration profile was noted due to the increased thermal and solutal slip parameter values, respectively by Barik, Mishra, Mishra, & Pattnaik, 2020. The temperature and velocity slip effect of Casson nanoliquid flow over a tilted permeable elongating cylinder was examined by Usman, Soomro, Haq, Wang, & Defterli, 2018. The analysis revealed that with increasing slip parameter, Nusselt number shows a decreasing behaviour whereas Sherwood number shows an increasing behaviour.

2.17 Heat Source

Internal heat sources play an important role in various heat transfer applications. A heat source enhances the temperature of working fluid which in return has a considerable effect on the heat transfer rate. The heat generation or absorption parameter plays a key role in medical and industrial fields like cancer therapy, heat pumps, heat exchangers, targeted drug delivery, imaging, and filtration devices. Naramgari & Sulochana, 2016 explored the effect of internal heat generation or absorption parameter on hydromagnetic nanofluid flow over an exponentially stretching sheet. The authors noticed that the heat generation or absorption parameter is capable of enhancing the momentum and thermal boundary layers. The positive impact of nonuniform heat source/sink on the thermal field of a stretching surface was elucidated by Thumma & Mishra, 2020. The impact of an exponential space-based heat source (ESHS) on the Marangoni convection and radiative flow of dusty nanoliquid was explored by Mahanthesh, Gireesha, PrasannaKumara, & Shashikumar, 2017. A positive impact on heat transfer rate and temperature of the dusty nanomaterial is reported due to the presence of the ESHS mechanism. Farooq et al., 2021 explored the impact of ESHS on the bioconvective flow of Carreau nanomaterial over an elongated cylinder and noticed that the temperature profile is directly proportional with the ESHS parameter. The authors concluded that for heating processes the ESHS is deemed to be better suited. The non-uniform heat source (NHS) constitutes a combination of space-dependent heat source (SHS) and

temperature-dependent heat source (THS). Mahanthesh, Animasaun, Rahimi-Gorji, & Alarifi, 2019 carried out a comparative analysis on the impact of NHS on dusty-Casson and dusty-Carreau fluid past an elongated surface. A statistical exploration on the effect of NHS over a plate was executed by Mahanthesh, Thriveni, & Lorenzini, 2021. An enhanced thermal field and a declined heat transfer rate was noted by Li et al., 2022 when the magnitude of SHS and THS parameters were augmented.

2.18 Passive Control of Nanoparticles

The boundary constraint when the normal flux of nanoparticles is zero is termed as zero mass flux or passive control of nanoparticles (see Kuznetsov & Nield, 2013). The passive control of the nanoparticles improves the practicality of the model (see Halim, Sivasankaran, & Noor, 2017; Ramly, Sivasankaran, & Noor, 2017; Abdul Halim & Mohd Noor, 2021). I. Uddin et al., 2018 investigated the buoyancy effect on the stagnation point flow with zero mass flux and convective boundary conditions. ur Rehman et al., 2020 elucidated the consequence of thermal stratification and passive control of nanoparticles of Sutterby nanofluid flow over a linearly stretched sheet.

2.19 Thermal Radiation

The transfer of heat by the means of the electromagnetic radiation generated by the thermal motion of particles in matter is called thermal radiation. The phenomenon of thermal radiation has crucial importance in space technology and intense heat processes such as nuclear power plants, gas turbines, gas-cooled nuclear reactors, and space vehicles. Gireesha, Umeshaiah, Prasannakumara, Shashikumar, & Archana, 2020 elucidated the behavior of radiation in MHD three-dimensional Jeffrey fluid flow through a stretching sheet and observed an increment in fluid temperature and nanoparticle concentration with the changes in the radiation parameter. Nasir et al., 2018 implemented the homotopy analysis method (HAM) to address thermal radiation and thermophoresis effects on the three-dimensional rotating nanofluid flow containing single-wall carbon nanotubes (SWCNT). The authors noticed that the nanofluid temperature is an expanding function of radiation parameter. The significant influence of radiation parameters on heat and mass transfer rate is explored by Besthapu, Haq, Bandari, & Al-Mdallal, 2019. Hady, Ibrahim, Abdel-Gaied, & Eid, 2012 investigated the impact of radiation parameter on the viscous flow of a

nanofluid over a nonlinearly stretching sheet. The authors observed an improvement in the heat transfer rate with escalating values of thermal radiation parameter. The three-dimensional MHD flow of nanofluid over a nonlinearly stretching sheet in the presence of slip and thermal radiation was elucidated by Mahanthesh, Gireesha, Gorla, & Makinde, 2018. The radiation parameter showcased a positive impact on the temperature profile.

2.20 Newtonian Boundary Constraint

The Newton thermal boundary condition accounts for one of the most common boundary constraints encountered in general practice. The existence of convective heating (or cooling) at the surface due to the surface energy balance is termed Newtonian (or convective) boundary constraint. Seth, Bhattacharyya, Kumar, & Chamkha, 2018 examined about the unsteady hydromagnetic boundary layer flow of a thermally radiating nanofluid considering Navier's velocity slip and Newtonian boundary constraint past a non-linear stretching sheet placed in a porous medium using OHAM. A rise in the nanofluid temperature was noticed for augmenting values of the Biot number. The negative effect of the Biot number on the heat transfer rate was discussed by M. Khan, Irfan, & Khan, 2019 whereas A. Kumar, Tripathi, Singh, & Sheremet, 2021 observed an increase in the Nusselt number.

2.21 Stefan Blowing

The diffusion of nanoparticles (or species) from the lengthening surface to the ambient region creates a blowing effect. This blowing effect, derived from the Stefan problem, is dissimilar from the mass injection or blowing resulting from transpiration on a permeable surface. This was initially studied by Spalding, 1954. Fang & Jing, 2014 revealed the improvement in the flow field with increasing values of blowing parameter whereas a decrease in velocity profile with improving Stefan blowing parameter was presented by B. Ali, Hussain, Abdal, & Mehdi, 2020. The consequence of Stefan blowing and thermo-hydrodynamic slip over a linearly lengthening sheet employing Lie group analysis was elucidated by Rana, Shukla, Bég, & Bhardwaj, 2021. The flow was mathematically modeled using the modified Buongiorno model. Gowda, Kumar, Prasannakumara, Nagaraja, & Gireesha, 2021 utilized the Runge-Kutta-Fehlberg 45 (RKF45) procedure to numerically explore the ferromagnetic fluid flow over a flat lengthening sheet considering the magnetic

dipole effect. Bég, Kabir, Uddin, Izani Md Ismail, & Alginahi, 2021 utilized the Chebyshev spectral collocation method to appraise the effect of Stefan blowing and microorganisms on the swirling nanomaterial flow from a whirling disk.

2.22 Statistical Techniques

The inclusion of statistical techniques like regression analysis, response surface methodology and sensitivity analysis for scrutinizing physical quantities like drag coefficients, heat and mass transfer rates has been amply exercised by the researchers recently. Statistical tools like multiple linear regression, correlation, probable error and slope of linear regression prove to be a better methodology in analysing the relationship between the effectual parameters and the dependent variables. The pertinent flow parameters are taken as the independent variables and physical quantities (like drag coefficient, mass transfer rate or heat transfer rate) are chosen as the dependent variable. Response Surface Methodology (RSM) analyses the collaborative outcome of influential parameters (independent variables) on the physical quantity of interest (response or dependent variable). Sensitivity analysis, on the other hand, measures the extent and nature of dependency exhibited by the independent variables on the response variable. Thriveni & Mahanthesh, 2021 utilized RSM and sensitivity analysis to statistically measure the consequence of effectual parameters on the Nusselt number of hybrid nanoliquid flow in a micro-annulus. The authors noted that the quadratic radiation parameter is positive sensitive towards the Nusselt number. Pordanjani et al., 2019 examined the influence of heating length, Richardson number, and Hartmann number on the entropy generation, Nusselt number, and Bejan number of a hybrid nanomaterial in a square diagonal cavity with the aid of RSM and sensitivity analysis. A positive sensitivity for Hartmann number on the Bejan number and a negative sensitivity for Hartmann number on the averaged Nusselt number were observed. Mackolil & Mahanthesh, 2021 performed a sensitivity analysis on the reduced Nusselt number considering magnetic parameter, thermal radiation parameter, and nanoparticle volume fraction. The authors delineated the dominance of the thermal radiation parameter on the reduced Nusselt number. Shafiq, Sindhu, & Khalique, 2020 employed sensitivity analysis on the density of motile microorganisms and Nusselt number considering Lewis number, Brownian motion variable, and thermophoresis number as the influential

parameters on an exponentially stretched surface. The authors noted that the rate of heat transfer of the nanomaterial is maximum when a larger value of Brownian motion and smaller values of Lewis number and thermophoresis aspect are considered. Further, the significance of the applied magnetic field on the Nusselt number and surface friction coefficient in the forced convective nanomaterial flow past a wedge was revealed by Vahedi, Pordanjani, Raisi, & Chamkha, 2019 by employing RSM and sensitivity analysis methods.

2.23 Need for the Study

Based on the literature review, the following gaps have been identified.

- The bioconvective stagnation point flow of CNT over a stretching sheet considering induced magnetic field, microorganisms and stratification effects has not been a topic of study.
- The dynamics of water conveying single-wall carbon nanotubes and magnetite nanoparticles subject to induced magnetic field has not yet been studied.
- The effect of multiple slip, spherical and non-spherical (cylinder, platelet, and blade) nanoparticles on the stagnation point flow of silver-blood nanofluid in the presence of an induced magnetic field has not yet been studied.
- The stratification effects of electromagnetohydrodynamic bioconvective CNT nanofluid flow past a stretching sheet has not yet been studied.
- No attempt to study the consequences of multiple slip on hydromagnetic convective Carreau nanoliquid flow over an elongating cylinder has been carried out.
- The significance of magnetic field and stratification constraints on the bioconvective stagnation-point flow over a rotating stretchable disk has not been considered yet.
- No attempt to study the MHD flow of a nanomaterial over a nonlinearly elongated surface in the presence of radiation and exponential heat source using the modified Buongiorno model and passive control of nanoparticles has been carried out.

- The dynamics of bioconvective magnetized nanomaterial flow over a nonlinearly elongated surface with Stefan blowing and Newtonian boundary constraints has not been considered yet.
- The dynamics of electro-magnetohydrodynamic Casson nanomaterial flow over a nonlinearly stretched surface with second-order hydrodynamic-slip and non-uniform heat source has not yet been studied.

Chapter 3

Bioconvective stagnation-point flow due to induced magnetic field *

3.1 Introduction

The nanofluid studies involving microorganisms is an advancing field that has intrigued researchers due to its relevance in antibiotics, biofuel, toxin removal, targeted drug delivery and food digestion. The magnetic field represents an important characteristic of hydromagnetic problems. However, studies incorporating induced magnetic field (the additional magnetic field that gets induced on electrically conducting fluid when encountered with an external magnetic field caused due to the impact of a larger magnetic Reynolds number) effects are limited in number. For its applications in biomedical imaging, hyperthermia, targeted drug delivery, and cancer therapy, the bioconvective stagnation point flow involving carbon nanotubes along a lengthening sheet subject to induced magnetic field and multiple stratification effects is investigated. Additionally, chemical reaction and viscous dissipation effects are also heeded. Relevant similarity formulas are effectuated in converting the modeled equations into a first-order system of ODEs and are further treated in MATLAB using *ode45* and Newton Raphson method. Illustrations on the consequence of effectual parameters on the physical quantities and the flow profiles are achieved with the aid of graphs.

*Published in: ZAMM - Journal of Applied Mathematics and Mechanics (Wiley), 2021; 101(11); e202000375.

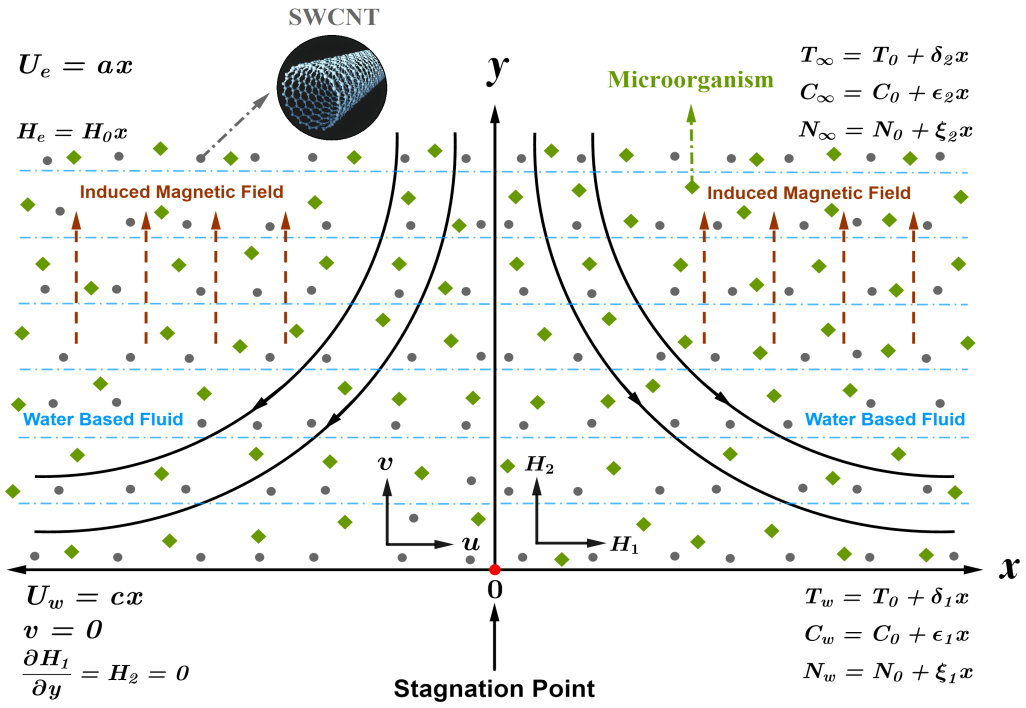

Figure 3.1: Geometrical Frame

3.2 Mathematical Frame

Two-dimensional steady incompressible bioconvective stagnation point flow over a linearly elongating sheet (see Figure 3.1) is considered under the ensuing assumptions:

- The expanding sheet is positioned along x axis and water-based SWCNT nanofluid (containing microorganisms) occupies the region $y > 0$.
- $U_w(x) = cx$ and $U_e(x) = ax$ correspond to the velocity of the lengthening sheet and the free stream, respectively.
- Induced magnetic field vector, $H = (H_1, H_2)$ is considered with H_1 & H_2 being the magnetic integrants along x and y direction, respectively.
- Chemical reaction and viscous dissipation effects are incorporated.
- Motile density, thermal, and solutal stratification effects are also considered.

Following the aforementioned assumptions, the governing equations are written as (see Alsaedi et al., 2017; Z. Iqbal, Azhar, & Maraj, 2017):

$$\frac{\partial u}{\partial x}+\frac{\partial v}{\partial y}=0 \tag{3.2.1}$$

$$\frac{\partial H_1}{\partial x}+\frac{\partial H_2}{\partial y}=0 \tag{3.2.2}$$

$$u\frac{\partial u}{\partial x}+v\frac{\partial u}{\partial y}-\frac{\mu_e}{4\pi\rho_{nf}}\left(H_1\frac{\partial H_1}{\partial x}+H_2\frac{\partial H_1}{\partial y}\right)=U_e\frac{dU_e}{dx} - \frac{\mu_e H_e}{4\pi\rho_{nf}}\frac{dH_e}{dx}+\left(\frac{\mu_{nf}}{\rho_{nf}}\right)\frac{\partial^2 u}{\partial y^2} \tag{3.2.3}$$

$$u\frac{\partial H_1}{\partial x}+v\frac{\partial H_1}{\partial y}-H_1\frac{\partial u}{\partial x}-H_2\frac{\partial u}{\partial y}=\alpha_m\frac{\partial^2 H_1}{\partial y^2} \tag{3.2.4}$$

$$u\frac{\partial T}{\partial x}+v\frac{\partial T}{\partial y}=\alpha_{nf}\frac{\partial^2 T}{\partial y^2}+\frac{\mu_{nf}}{(\rho C_p)_{nf}}\left(\frac{\partial u}{\partial y}\right)^2 \tag{3.2.5}$$

$$u\frac{\partial C}{\partial x}+v\frac{\partial C}{\partial y}=D_B\frac{\partial^2 C}{\partial y^2}-k_r\left(C-C_\infty\right) \tag{3.2.6}$$

$$u\frac{\partial N}{\partial x}+v\frac{\partial N}{\partial y}+\frac{bW_c}{C_w-C_0}\left(\frac{\partial}{\partial y}\left(N\frac{\partial C}{\partial y}\right)\right)=D_m\frac{\partial^2 N}{\partial y^2} \tag{3.2.7}$$

subject to the boundary conditions (see Alsaedi et al., 2017; Z. Iqbal, Azhar, & Maraj, 2017):

$$\begin{gathered} u=U_w(x)=cx,\ v=0,\ \tfrac{\partial H_1}{\partial y}=H_2=0,\ T=T_w=T_0+\delta_1 x, \\ C=C_w=C_0+\epsilon_1 x,\ N=N_w=N_0+\xi_1 x \qquad \text{at } y=0 \end{gathered}$$

$$\begin{gathered} u\to U_e(x)=ax,\ H_1\to H_e(x)=H_0 x,\ T\to T_\infty=T_0+\delta_2 x, \\ C\to C_\infty=C_0+\epsilon_2 x,\ N\to N_\infty=N_0+\xi_2 x \qquad \text{as } y\to\infty \end{gathered}$$

where $\alpha_m=\dfrac{1}{4\pi\mu_e\sigma_{nf}}$ represents the magnetic diffusivity.

Consider the following similarity transformations (see Alsaedi et al., 2017; Z. Iqbal, Azhar, & Maraj, 2017):

$$u=cxf\,'(\zeta),\ v=-\sqrt{c\vartheta_f}f(\zeta),\ H_1=H_0xg\,'(\zeta),\ \zeta=y\sqrt{\frac{c}{\vartheta_f}},\ H_2=-H_0\sqrt{\frac{\vartheta_f}{c}}g(\zeta),$$

$$\theta(\zeta)=\frac{T-T_\infty}{T_w-T_0},\ \psi(\zeta)=\frac{C-C_\infty}{C_w-C_0},\ \chi(\zeta)=\frac{N-N_\infty}{N_w-N_0}$$

Employing the similarity transformations into Equations (3.2.1) – (3.2.7), we get:

$$f\,''' - A_1\,A_2\left\{(\,f\,')^2 - f\,f\,'' - \frac{\beta}{A_2}\left\{(\,g\,')^2 - g\,g\,'' - 1\right\} - A^2\right\} = 0 \tag{3.2.8}$$

$$g\,''' - \frac{A_5}{\lambda}\,\{\,g\,f\,'' - f\,g\,''\,\} = 0 \tag{3.2.9}$$

$$\theta\,'' + \frac{A_3\,Pr}{A_4}\,f\,\theta\,' + \frac{Ec\,Pr}{A_1\,A_4}\,(\,f\,'')^2 = 0 \tag{3.2.10}$$

$$\psi\,'' + Le\,f\,\psi\,' - Kr\,Le\,\psi = 0 \tag{3.2.11}$$

$$\chi\,'' + Lb\,f\,\chi\,' - Pe\,\{\,(\,\chi + \Omega\,)\,\psi\,'' + \chi\,'\,\psi\,'\,\} = 0 \tag{3.2.12}$$

subject to the boundary conditions

$$f(\zeta) = 0, \quad f\,'(\zeta) = 1, \quad g(\zeta) = 0, \quad g\,''(\zeta) = 0, \quad \theta(\zeta) = 1 - s_1,$$
$$\psi(\zeta) = 1 - s_2, \quad \chi(\zeta) = 1 - s_3 \quad \text{when } \zeta = 0$$

$$f'(\zeta) \to A, \quad g\,'(\zeta) \to 1, \quad \theta(\zeta) \to 0,$$
$$\psi(\zeta) \to 0, \quad \chi(\zeta) \to 0 \quad \text{as } \zeta \to \infty$$

where the dimensionless parameters are given in appendix I.

The nanofluid models incorporated are (see Z. Iqbal, Azhar, & Maraj, 2017; Sreedevi & Reddy, 2019):

Effective Dynamic Viscosity : $\dfrac{\mu_{nf}}{\mu_f} = \dfrac{1}{(1-\phi)^{2.5}} = \dfrac{1}{A_1}$

Effective Density : $\dfrac{\rho_{nf}}{\rho_f} = (1-\phi) + \phi\left(\dfrac{\rho_{SWCNT}}{\rho_f}\right) = A_2$

Effective Specific Heat : $\dfrac{(\rho C_p)_{nf}}{(\rho C_p)_f} = (1-\phi) + \phi\left(\dfrac{(\rho C_p)_{SWCNT}}{(\rho C_p)_f}\right) = A_3$

Effective Thermal Conductivity : $\dfrac{k_{nf}}{k_f} = \dfrac{(1-\phi) + 2\phi\,\frac{k_{SWCNT}}{k_{SWCNT}-k_f}\,ln\left(\frac{k_{SWCNT}+k_f}{2k_f}\right)}{(1-\phi) + 2\phi\,\frac{k_f}{k_{SWCNT}-k_f}\,ln\left(\frac{k_{SWCNT}+k_f}{2k_f}\right)} = A_4$

$$\text{Effective Electrical Conductivity} \quad : \quad \frac{\sigma_{nf}}{\sigma_f} = 1 + \frac{3\left(\frac{\sigma_{SWCNT}}{\sigma_f} - 1\right)\phi}{\left(\frac{\sigma_{SWCNT}}{\sigma_f} + 2\right) - \left(\frac{\sigma_{SWCNT}}{\sigma_f} - 1\right)\phi} = A_5$$

The physical quantities are given by (see Alsaedi et al., 2017; Z. Iqbal, Azhar, & Maraj, 2017):

$$\text{Local drag coefficient} \quad : \quad Cf_x = \frac{\tau_\omega}{\rho_f \ (U_w)^2} = \frac{\mu_{nf} \ \frac{\partial u}{\partial y}\Big|_{y=0}}{\rho_f \ (U_w)^2}$$

$$\Rightarrow \ Cf_x \ Re_x^{1/2} = \frac{f\,''(0)}{A_1}$$

$$\text{Local Nusselt number} \quad : \quad Nu_x = \frac{x \ q_\omega}{k_f \ (T_w - T_0)} = \frac{-x \ k_{nf} \ \frac{\partial T}{\partial y}\Big|_{y=0}}{k_f \ (T_w - T_0)}$$

$$\Rightarrow \ Nu_x \ Re_x^{-\ 1/2} = -A_4 \ \theta\,'(0)$$

$$\text{Local Sherwood number} \quad : \quad Sh_x = \frac{x \ q_m}{D_B \ (C_w - C_0)} = \frac{-x \ D_B \ \frac{\partial C}{\partial y}\Big|_{y=0}}{D_B \ (C_w - C_0)}$$

$$\Rightarrow \ Sh_x \ Re_x^{-\ 1/2} = -\ \psi\,'(0)$$

$$\text{Local motile density number} \quad : \quad Nn_x = \frac{x \ q_n}{D_m \ (N_w - N_0)} = \frac{-x \ D_m \ \frac{\partial N}{\partial y}\Big|_{y=0}}{D_m \ (N_w - N_0)}$$

$$\Rightarrow \ Nn_x \ Re_x^{-\ 1/2} = -\ \chi\,'(0)$$

where $Re_x = \frac{xU_w}{\vartheta_f}$ is the local Reynold's number.

3.3 Numerical Frame & Validation

Equations (3.2.8) - (3.2.12) together with the boundary conditions are numerically resolved in MATLAB employing *ode45* (for solving) and Newton Raphson method (for shooting). This is accomplished by initially assuming:

$$\Gamma_1 = f, \quad \Gamma_2 = f\,', \quad \Gamma_3 = f\,'', \quad \Gamma_3{}' = f\,''', \quad \Gamma_4 = g, \quad \Gamma_5 = g\,',$$
$$\Gamma_6 = g\,'', \quad \Gamma_6{}' = g\,''', \quad \Gamma_7 = \theta, \quad \Gamma_8 = \theta\,', \quad \Gamma_8{}' = \theta\,'', \quad \Gamma_9 = \psi,$$
$$\Gamma_{10} = \psi\,', \quad \Gamma_{10}{}' = \psi\,'', \quad \Gamma_{11} = \chi, \quad \Gamma_{12} = \chi\,', \quad \Gamma_{12}{}' = \chi\,''$$

The reduced system of the first-order ODE is given by:

$$\Gamma_1{}' = \Gamma_2 \ , \ \Gamma_2{}' = \Gamma_3 \ ,$$

$$\Gamma_3{}' = A_1 \ A_2 \ \left\{ \ (\Gamma_2)^2 - \Gamma_1 \ \Gamma_3 - \frac{\beta}{A_2} \ \left\{ (\Gamma_5)^2 - \Gamma_4 \ \Gamma_6 - 1 \right\} - A^2 \ \right\} \ ,$$

$$\Gamma_4{}' = \Gamma_5 \ , \ \Gamma_5{}' = \Gamma_6 \ ,$$

$$\Gamma_6{}' = \frac{A_5}{\lambda} \ \{ \ \Gamma_4 \ \Gamma_3 - \Gamma_1 \ \Gamma_6 \ \} \ ,$$

$$\Gamma_7{}' = \Gamma_8 \ , \ \Gamma_8{}' = - \left\{ \frac{A_3 \ Pr}{A_4} \ \Gamma_1 \ \Gamma_8 + \frac{Ec \ Pr}{A_1 \ A_4} \ (\Gamma_3)^2 \right\} \ ,$$

$$\Gamma_9{}' = \Gamma_{10} \ , \ \Gamma_{10}{}' = Kr \ Le \ \Gamma_9 - Le \ \Gamma_1 \ \Gamma_{10} \ ,$$

$$\Gamma_{11}{}' = \Gamma_{12} \ \ , \ \Gamma_{12}{}' = Pe \ \left\{ \ (\Gamma_{11} + \Omega) \ \ \Gamma_{10}{}' + \Gamma_{12} \ \Gamma_{10} \ \right\} - Lb \ \Gamma_1 \ \Gamma_{12} \ .$$

with

$$\begin{gathered} \Gamma_1(0) = 0, \quad \Gamma_2(0) = 1, \quad \Gamma_3(0) = \Lambda_1, \quad \Gamma_4(0) = 0, \\ \Gamma_5(0) = \Lambda_2, \quad \Gamma_6(0) = 0, \quad \Gamma_7(0) = 1 - s_1, \quad \Gamma_8(0) = \Lambda_3, \\ \Gamma_9(0) = 1 - s_2, \quad \Gamma_{10}(0) = \Lambda_4, \quad \Gamma_{11}(0) = 1 - s_3, \quad \Gamma_{12}(0) = \Lambda_5 \end{gathered}$$

where Λ_1 , Λ_2 , Λ_3 , Λ_4 & Λ_5 are estimated by employing the Newton Raphson method with a befitting initial guess.

The above set of equations are then numerically resolved utilizing *ODE45*, a built-in MATLAB function, with an absolute error tolerance of 10^{-6}. *ODE45* employs a fourth-order Runge-Kutta method with a self-adaptive step size for effective computation. The veracity of the code and the validation of this research work have been adjudged through a restrictive comparison of the present work with prior published works of Hayat et al., 2015, 2016; Iqbal, Azhar, et al., 2017 (showcased in Table 3.1 & 3.2).

3.4 Results & Discussion

The consequence of influential parameters on microbial concentration ($\chi(\zeta)$), velocity ($f'(\zeta)$), concentration ($\psi(\zeta)$), temperature ($\theta(\zeta)$) and induced magnetic field ($g'(\zeta)$) profiles are illustrated via Figures 3.2 - 3.15. Changes in the aforementioned profiles due to stretching parameter (A) are graphed in Figures 3.2, 3.4, 3.7, 3.11

Table 3.1: Comparison of drag coefficient $\left(Cf_x Re_x^{1/2}\right)$ for different A values between the present study and the works of Iqbal, Azhar, et al., 2017 and Hayat et al., 2015, 2016 when $\phi = \beta = 0$

A	$\boldsymbol{Cf_x Re_x^{1/2}}$			
	Iqbal et al., 2017	**Hayat et al., 2015**	**Hayat et al., 2016**	**Present study**
0.1	-0.969386	-0.96939	-0.96937	-0.9693860
0.2	-0.918107	-0.91811	-0.91813	-0.9181071
0.5	-0.667263	-0.66726	-0.66723	-0.6672637
0.7	-0.433475	-0.43346	-0.43345	-0.4334755
0.8	-0.299388	-0.29929	-0.29921	-0.2993888
0.9	-0.154716	-0.15458	-0.1545471	-0.1547167
1	0	0	0	0

Table 3.2: Comparison of $Nu_x Re_x^{-1/2}$ and $-Cf_x Re_x^{1/2}$ for differing ϕ, β, λ values between the present study and (Iqbal, Azhar, et al., 2017)

$\boldsymbol{\phi}$	$\boldsymbol{\beta}$	$\boldsymbol{\lambda}$	$\boldsymbol{-Cf_x Re_x^{1/2}}$		$\boldsymbol{Nu_x Re_x^{-1/2}}$	
			Iqbal et al., 2017	**Present study**	**Iqbal et al., 2017**	**Present study**
0.1	0	1	0.8201	0.82011	2.9371	2.93709
0.2	0	1	1.0139	1.01386	3.7139	3.71387
0	0	1	0.6673	0.66726	1.8581	1.85807
0	0.1	1	0.5759	0.57595	1.8771	1.8771
0	0.2	5	0.5129	0.51293	1.8909	1.89091
0	0.2	10	0.5651	0.56507	1.8802	1.88018

Table 3.3: Thermophysical properties of water and SWCNT

Property	**Water (base fluid)**	**SWCNT (nanoparticle)**
$\boldsymbol{\rho}$	997	2600
$\boldsymbol{C_p}$	4179	425
$\boldsymbol{k}$	0.613	6600
$\boldsymbol{\sigma}$	0.05	10^6

& 3.14. It is perceived that augmenting A values produces a constructive effect on $f'(\zeta)$ and destructive effect on $g'(\zeta)$, $\theta(\zeta)$, $\psi(\zeta)$ & $\chi(\zeta)$. Simultaneous effects of parameters on physical quantities are depicted in Figures 3.16 - 3.20. Studies have been carried out for $A = 0.5$ & $A = 1.5$ with Prandtl number(Pr) and infinity fixed at 6.2 and 6, respectively. Thermophysical properties of the conventional fluid (water) and SWCNT (nanofluid) are showcased in Table 3.3.

Figure 3.3 bespeaks the deviations in $f'(\zeta)$ with respect to β (magnetic parameter). It is noted that $f'(\zeta)$ increases for augmenting β values when $A = 0.5$ and a reversed behaviour is observed for $f'(\zeta)$ when $A = 1.5$. Figure 3.5 depicts the influence of β on $g'(\zeta)$. An elevation in $g'(\zeta)$ for $A = 0.5$ and a demotion when $A = 1.5$ are observed for elevating β values. Figure 3.6 explains the mixed effect of λ (reciprocal of magnetic Prandtl number) on $g'(\zeta)$. Initially, elevating λ values decays $g'(\zeta)$ and afterwards, a reversed trend is observed when $A = 0.5$. A similar but inversed impact is perceived when $A = 1.5$.

Variation in $\theta(\zeta)$ due to Eckert number (Ec) is elucidated in Figure 3.8 and it is noted that augmenting Ec numerals fuels an increase in $\theta(\zeta)$. Physically, this result can be associated with the generation of friction forces between the fluid particles which increases the nanomaterial temperature. The ascending nature of $\theta(\zeta)$ with ϕ (volume fraction of nanoparticle) is illustrated in Figure 3.9. This increase in temperature can be physically related to the improvement in the thermal conductivity of the nanoliquid caused by larger nanoparticle occupancy. Figure 3.10 explains the consequence of s_1 (thermal stratification parameter) on $\theta(\zeta)$. A decreasing behaviour is noticed and this is due to the waning temperature differences. Physically, the decrease in the nanofluid temperature is due to the drop in the temperature difference between the surface and away from the surface caused by an increase in s_1.

With a rise in the magnitude of Kr (chemical reaction parameter), depletion in $\psi(\zeta)$ is observed which has been plotted in Figure 3.12. The physical explanation being that the increased chemical reaction eats up the nanoparticle which induces shrinkage in the concentration profile. Figure 3.13 reveals the change in $\psi(\zeta)$ with ascending s_2 (solutal stratification parameter). An increase in s_2 prompts a decrease in the volumetric fraction which sources a fall in $\psi(\zeta)$. Physically, an increase in s_2 descends the concentration profile due to the decrease in the volumetric fraction

between the surface and reference nanoparticles. Figure 3.15 describes the negative influence of s_3 (motile density stratification parameter) on $\chi(\zeta)$. This is because an augmentation in s_3 decreases the concentration difference of microorganisms between the surface and away from the surface and hence the microbial concentration decreases.

One can interpret from Figure 3.16 that $Cf_x Re_x^{1/2}$ increases with β and decreases with ϕ when $A = 0.5$. For $A = 1.5$, $Cf_x Re_x^{1/2}$ improves with ϕ and deteriorates with β. Physically, stretching parameter corresponds to the ratio of free stream velocity to the stretching sheet velocity. For $A > 1$, there is an increase in the straining motion near the stagnation region that results in the acceleration of free stream. However, for $A < 1$, the flow has an inverted boundary layer structure. Hence, the results of skin friction are negative for $A = 0.5$. From Figures 3.17 & 3.18, it is clear that $Nu_x Re_x^{-1/2}$ (both cases) ascends with ϕ and descends with Ec & s_1. Figure 3.19 demonstrates the escalating and declining behaviour of Kr & s_2 on $Sh_x Re_x^{-1/2}$ (both cases), respectively. Figure 3.20 depicts that Kr causes a rise in $Nn_x Re_x^{-1/2}$ (both cases) whereas a fall in $Nn_x Re_x^{-1/2}$ (both cases) is observed due to s_3.

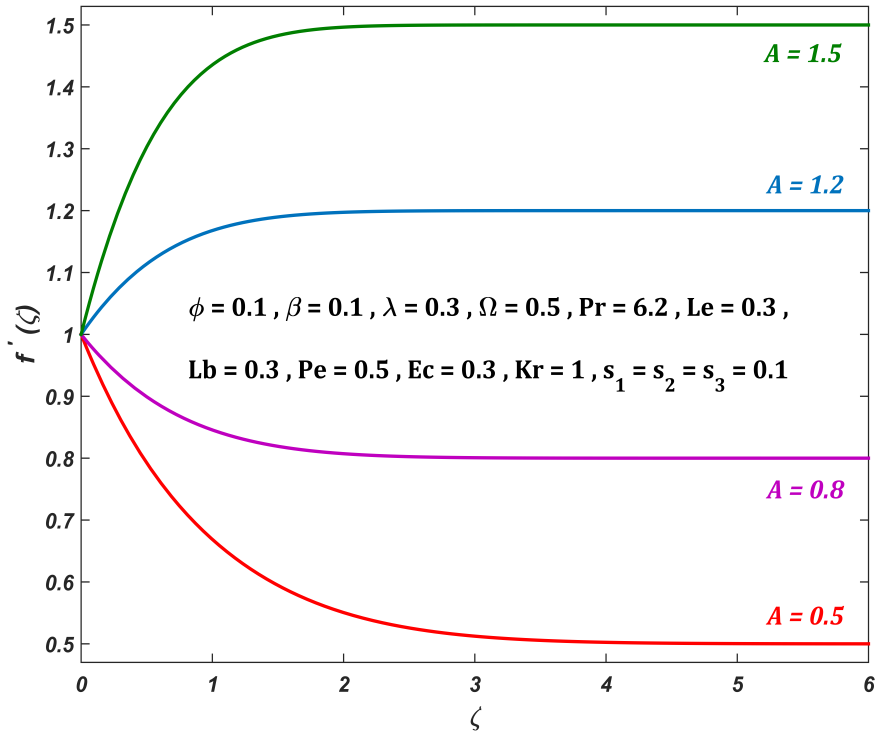

Figure 3.2: $f'(\zeta)$ for differing A values

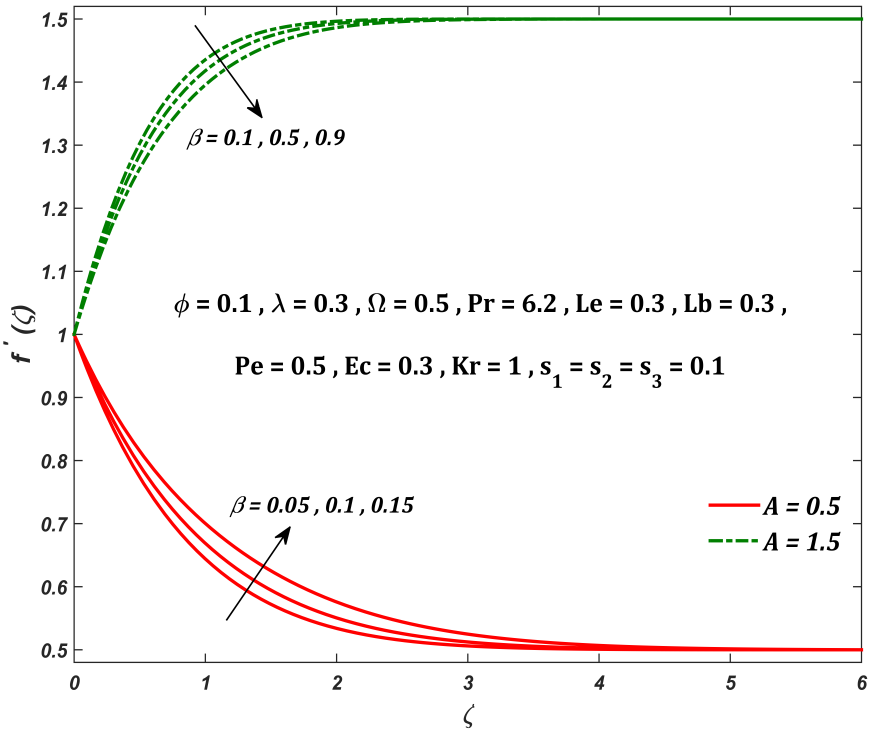

Figure 3.3: $f'(\zeta)$ for differing β values

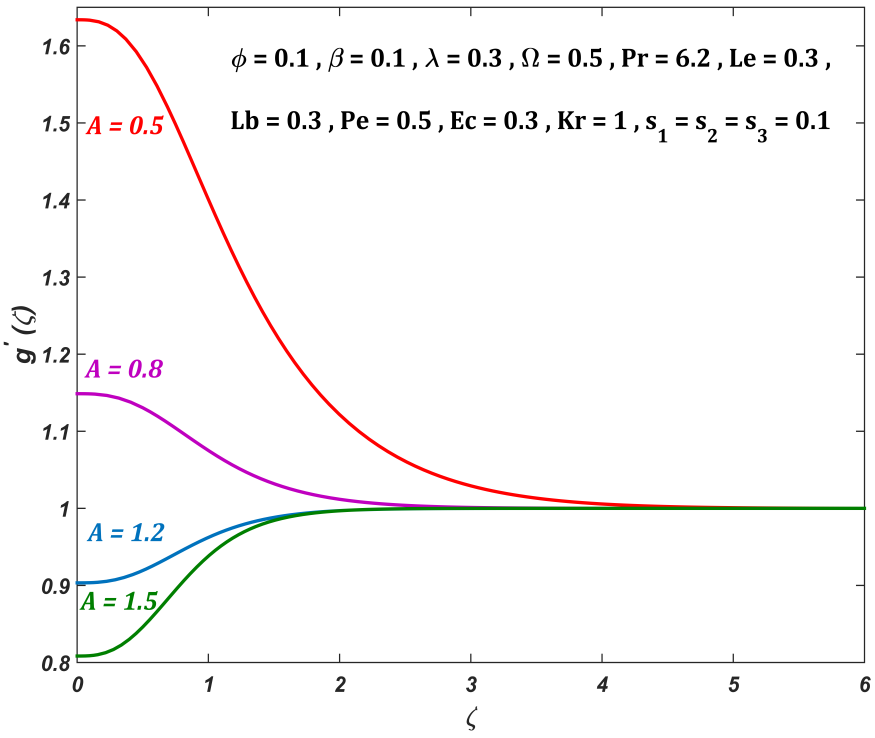

Figure 3.4: $g'(\zeta)$ for differing A values

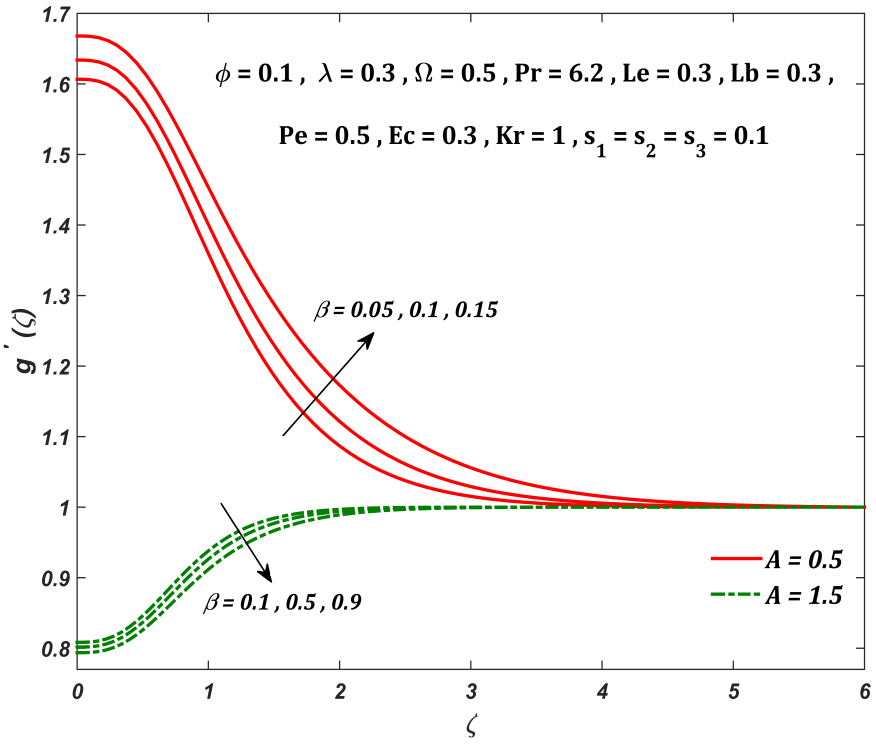

Figure 3.5: $g'(\zeta)$ for differing β values

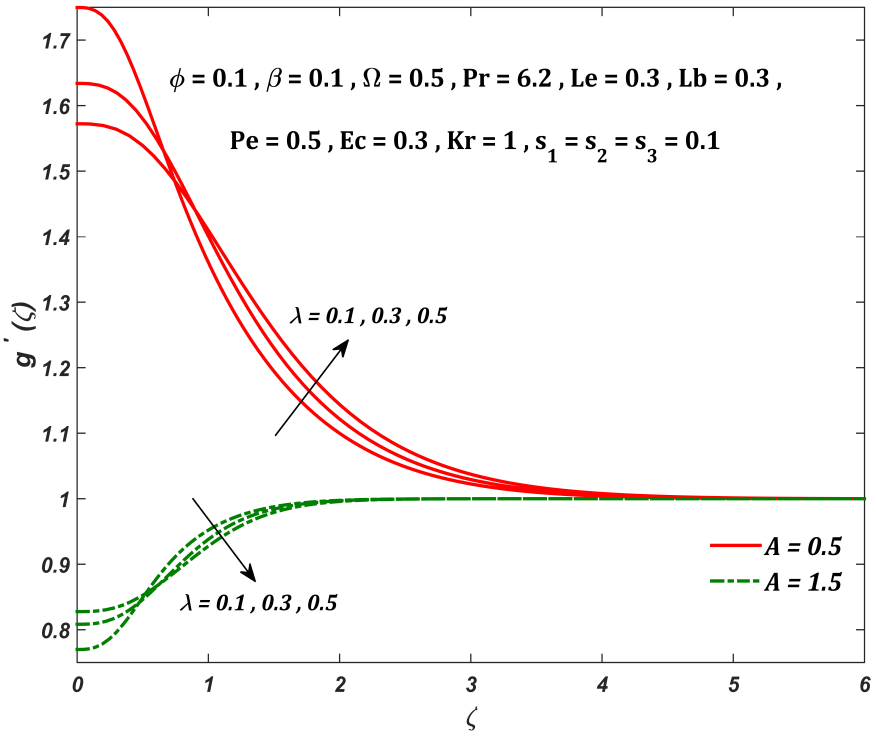

Figure 3.6: $g'(\zeta)$ for differing λ values

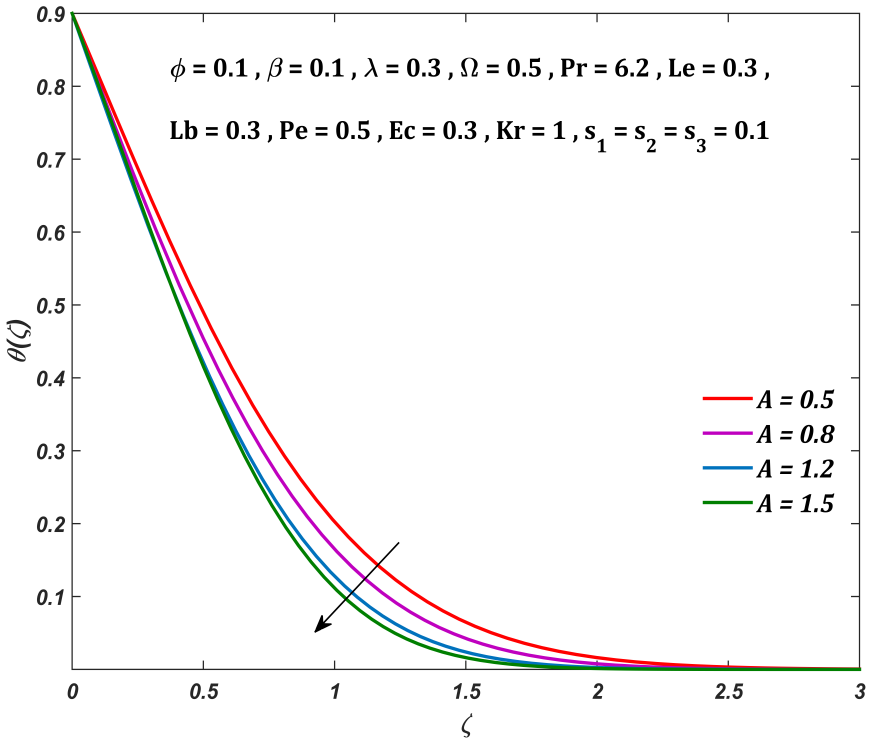

Figure 3.7: $\theta\,(\zeta)$ for differing A values

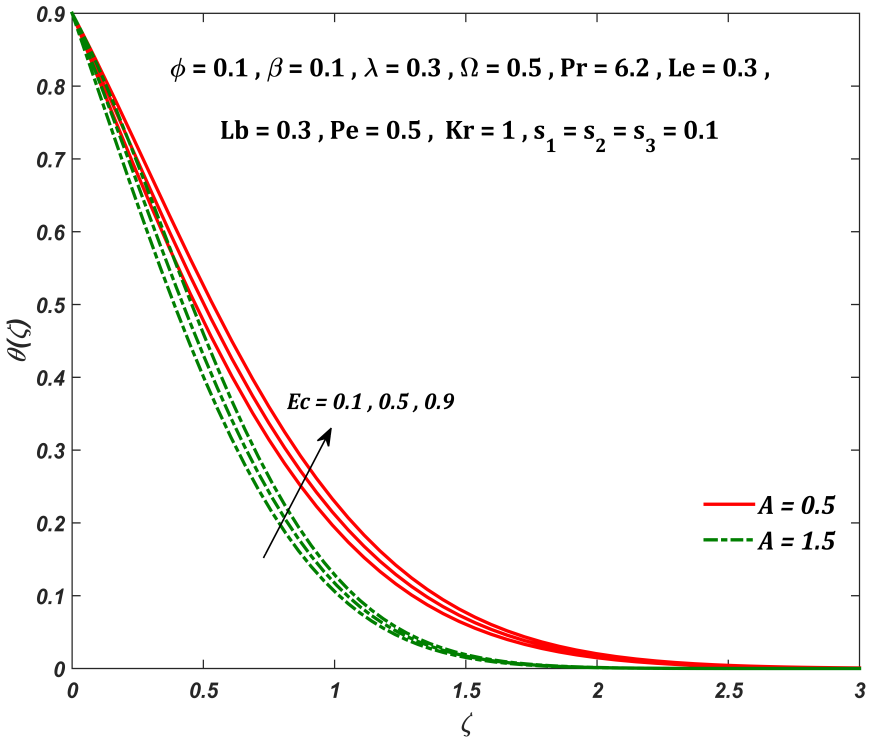

Figure 3.8: $\theta\,(\zeta)$ for differing Ec values

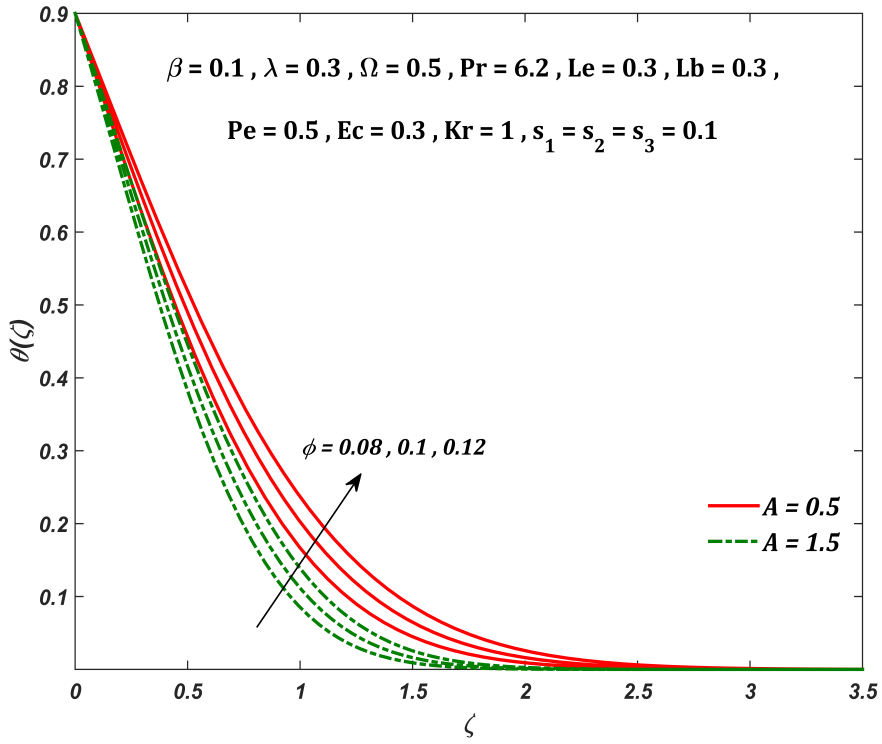

Figure 3.9: $\theta(\zeta)$ for differing ϕ values

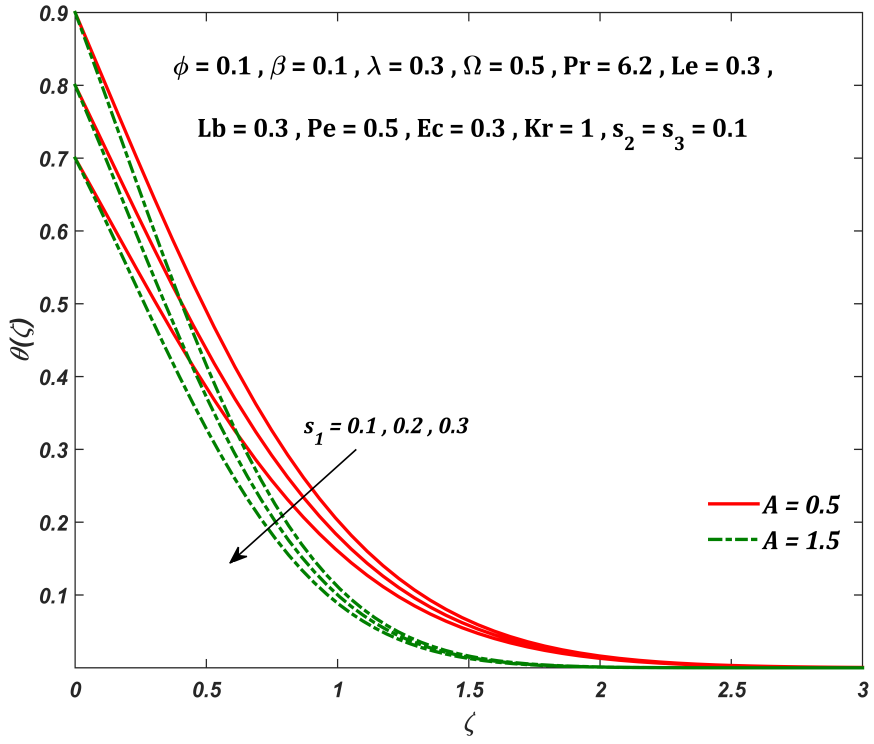

Figure 3.10: $\theta(\zeta)$ for differing s_1 values

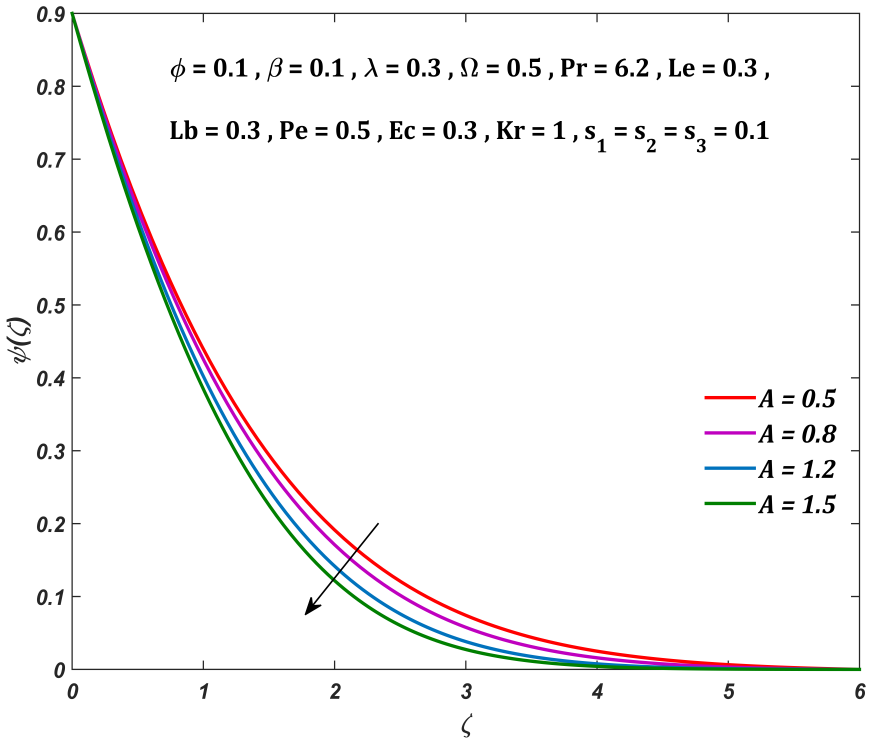

Figure 3.11: $\psi(\zeta)$ for differing A values

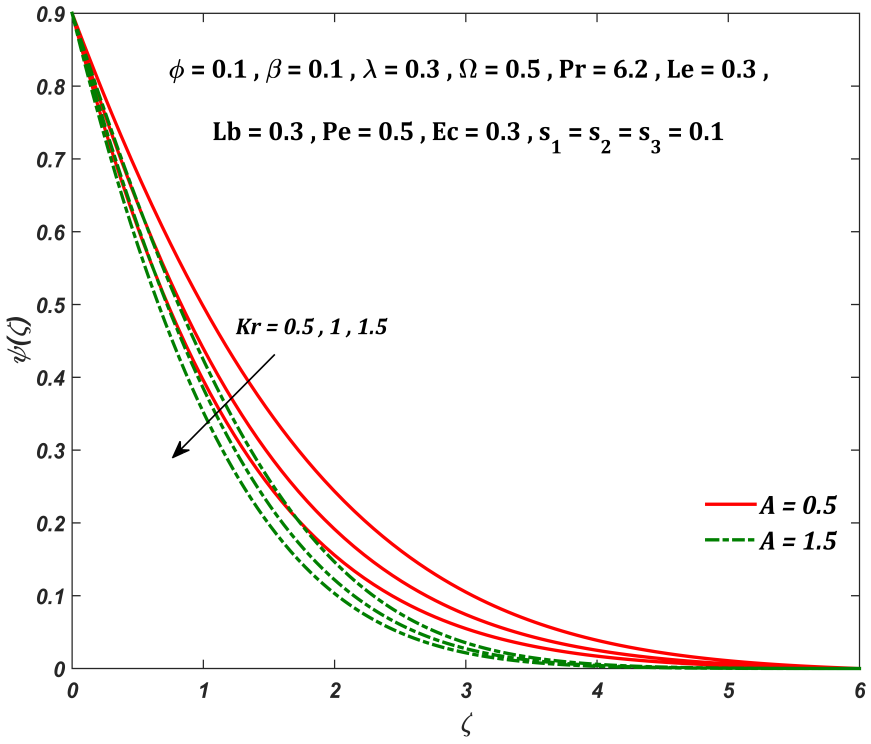

Figure 3.12: $\psi(\zeta)$ for differing Kr values

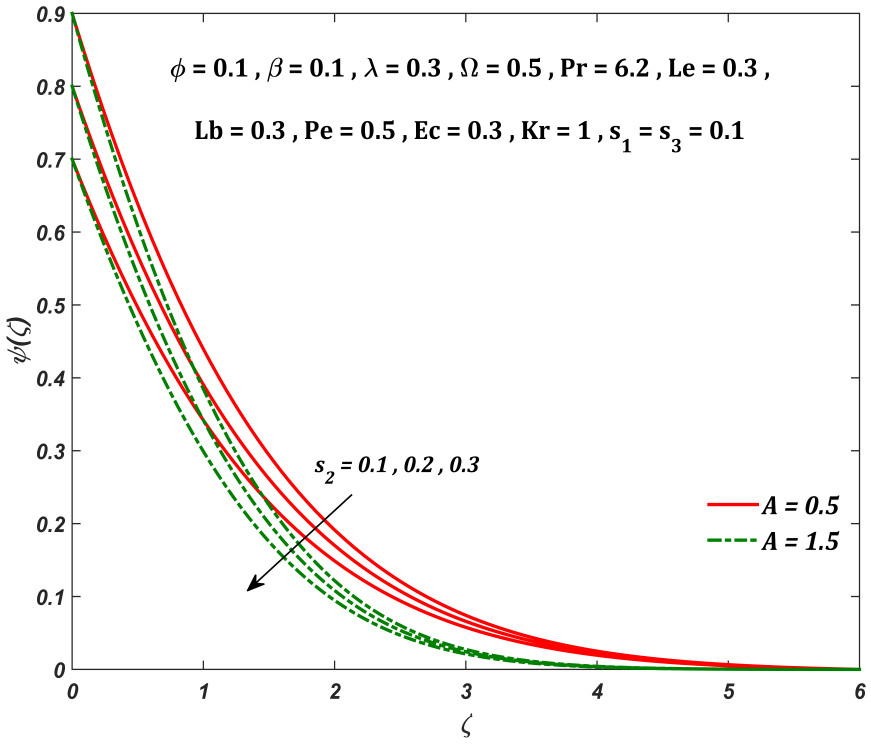

Figure 3.13: $\psi\,(\zeta)$ for differing s_2 values

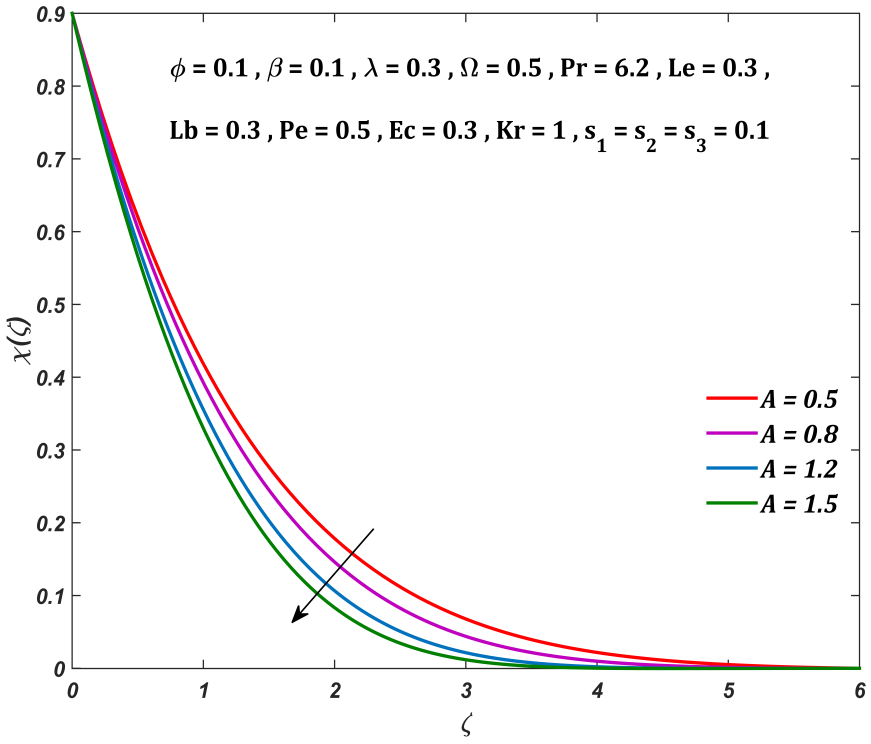

Figure 3.14: $\chi\,(\zeta)$ for differing A values

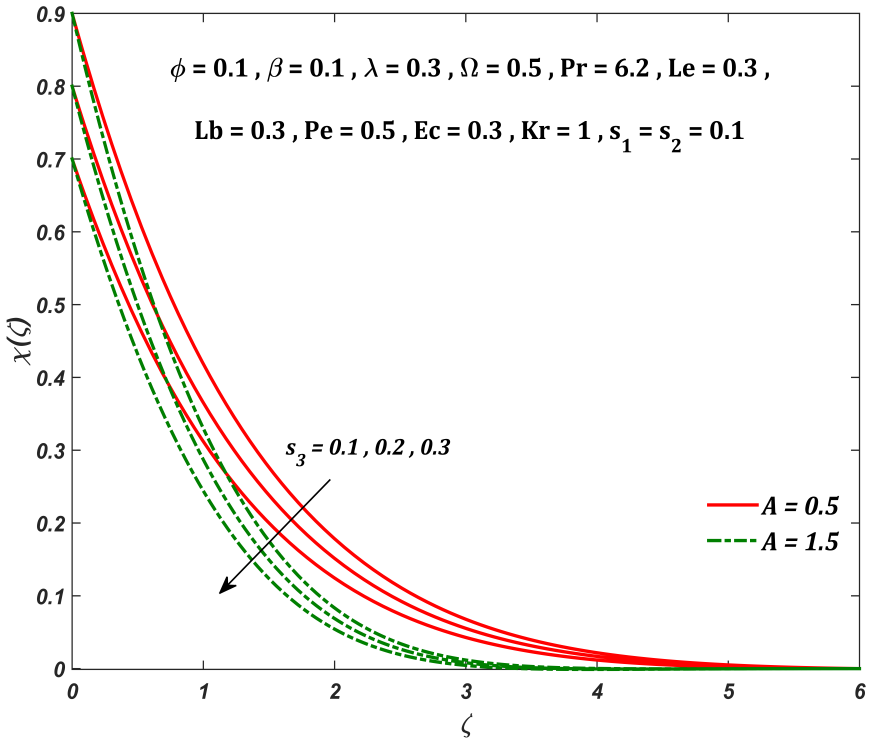

Figure 3.15: $\chi\,(\zeta)$ for differing s_3 values

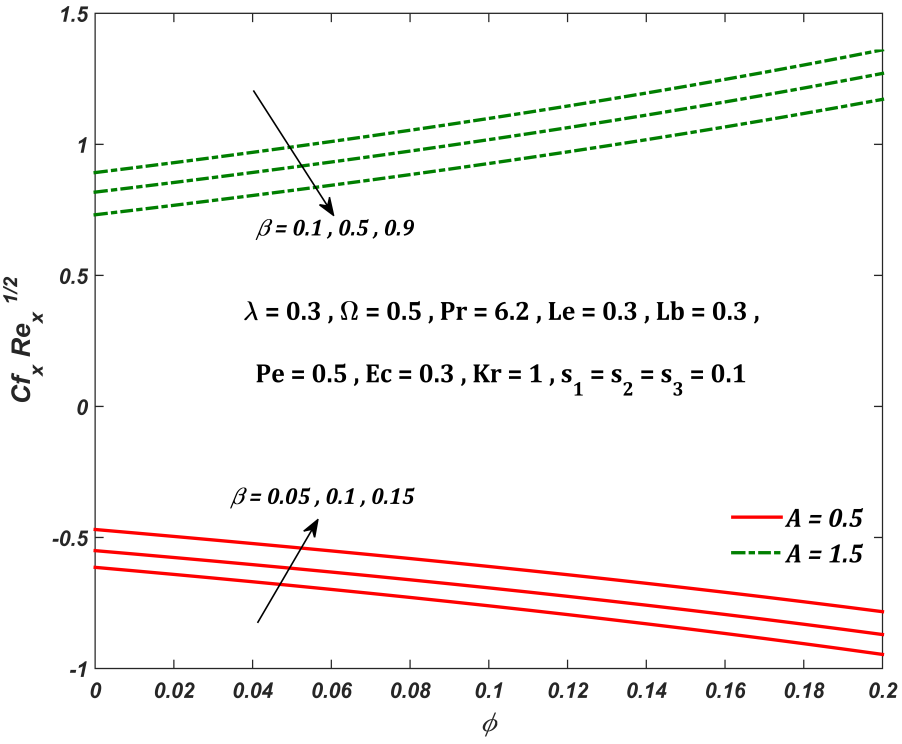

Figure 3.16: Parallel effect of ϕ & β on $Cf_x Re_x^{1/2}$

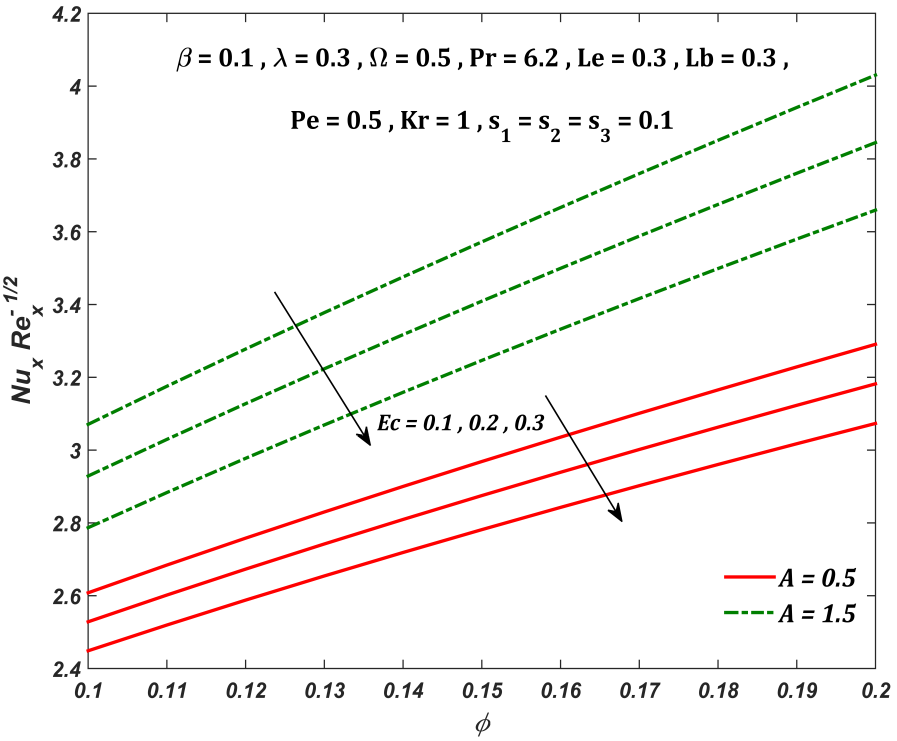

Figure 3.17: Parallel effect of ϕ & Ec on $Nu_x Re_x^{-1/2}$

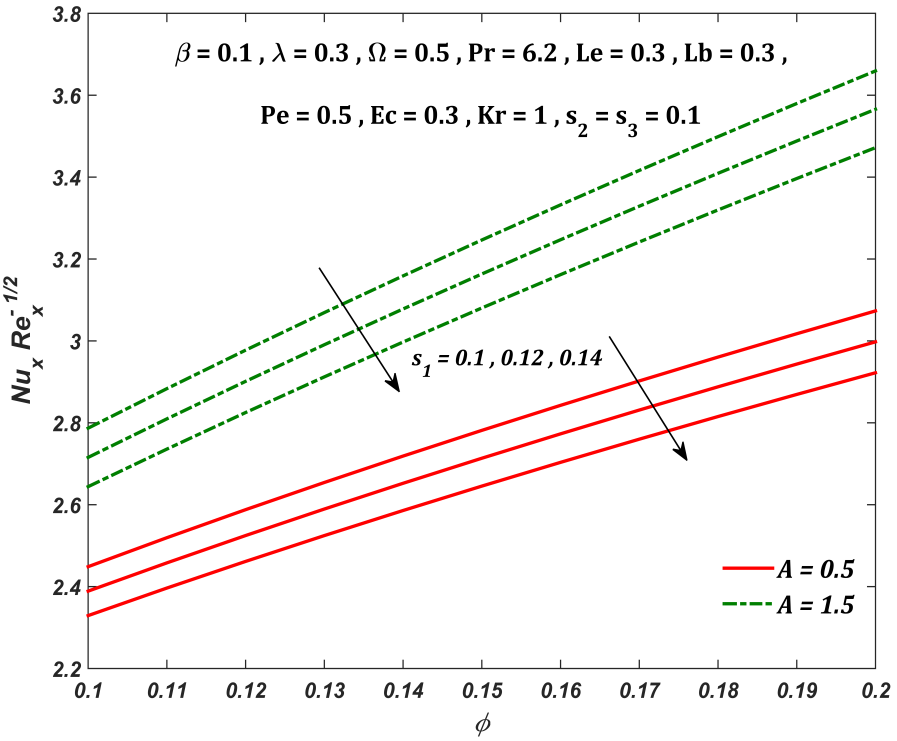

Figure 3.18: Parallel effect of ϕ & s_1 on $Nu_x Re_x^{-1/2}$

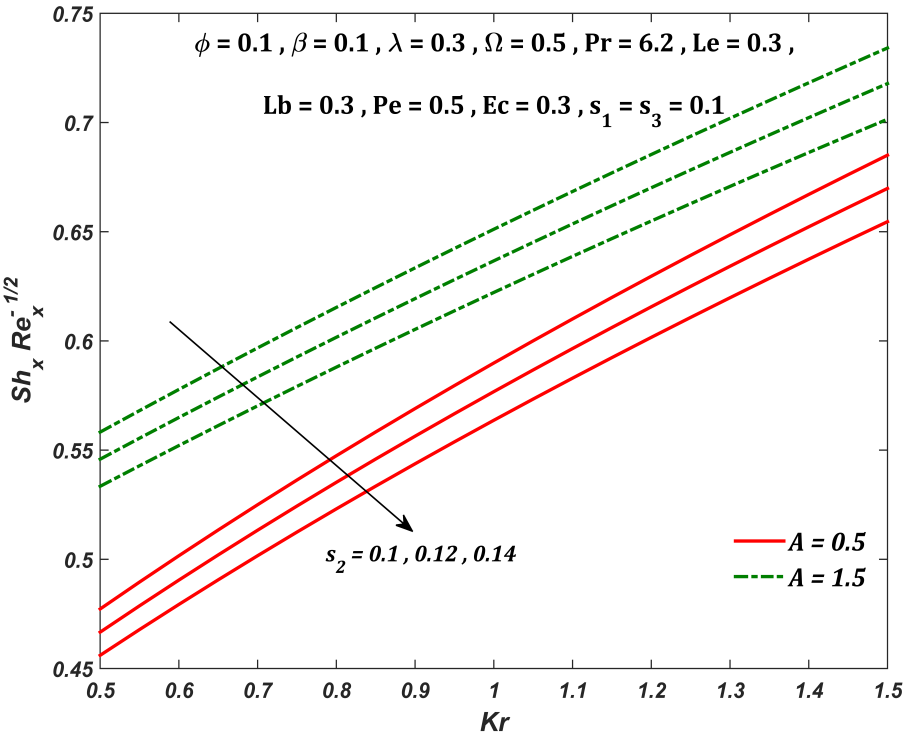

Figure 3.19: Parallel effect of Kr & s_2 on $Sh_x Re_x^{-1/2}$

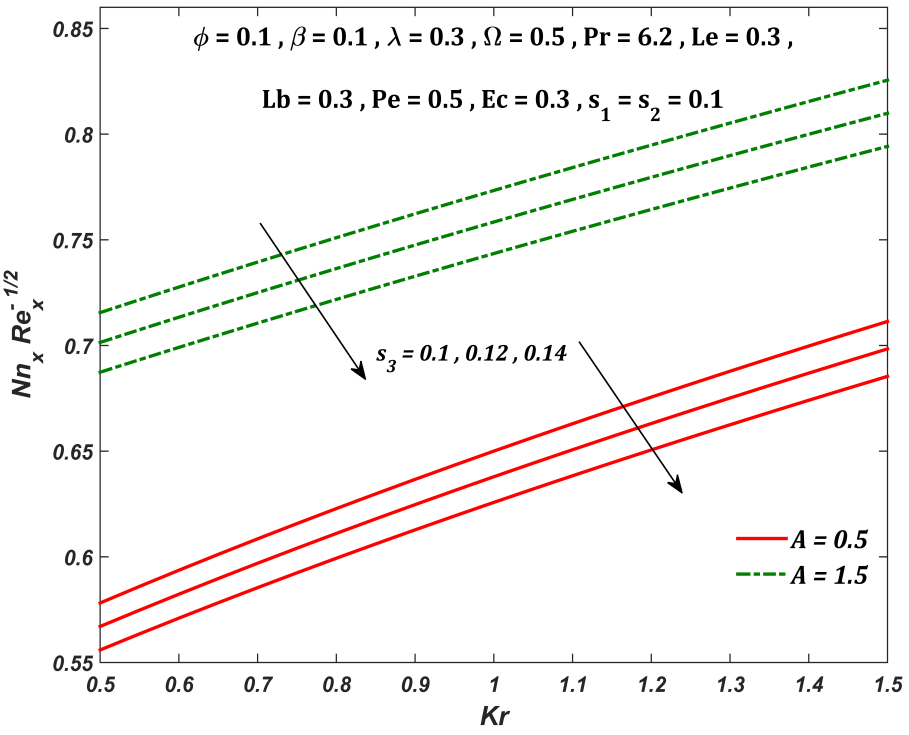

Figure 3.20: Parallel effect of Kr & s_3 on $Nn_x Re_x^{-1/2}$

3.5 Conclusion

The key points noted from the study are:

- The nanomaterial velocity is directly proportional to the magnetic parameter for $A = 0.5$ and inversely proportional when $A = 1.5$.
- Drag coefficient (when $A = 0.5$) ascends with magnetic parameter and descends with nanoparticle volume fraction. However, the results are reversed when $A = 1.5$.
- Eckert number and nanoparticle volume fraction exhibit a constructive effect on the temperature profile.
- Heat transfer is elevated due to nanoparticle volume fraction and lowered with Eckert number and thermal stratification parameter.
- Chemical reaction parameter has a destructive effect on concentration profile.
- Chemical reaction parameter promotes and solutal stratification demotes mass transfer.
- A decline in microorganism, concentration and temperature profiles is observed due to ascending motile density, solutal, thermal stratification parameters, respectively.
- Microorganism density number lowers with motile density stratification parameter.

Appendix I: Non-dimensional qunatities

$A = \frac{a}{c}$	Stretching parameter
$\beta = \frac{\mu_e}{4\pi\rho_f}\left(\frac{H_0}{c}\right)^2$	Magnetic parameter
$\lambda = \frac{1}{4\pi\mu_e\sigma_f\vartheta_f}$	Reciprocal of magnetic Prandtl number
$Pr = \frac{(\mu C_p)_f}{k_f} = \frac{\vartheta_f}{\alpha_f}$	Prandtl number
$Kr = \frac{k_r}{c}$	Chemical reaction parameter
$Ec = \frac{(cx)^2}{(C_p)_f (T_w - T_0)}$	Eckert number
$Le = \frac{\vartheta_f}{D_B}$	Lewis number
$Lb = \frac{\vartheta_f}{D_m}$	Bioconvection Lewis number
$Pe = \frac{bW_c}{D_m}$	Bioconvection Peclet number
$\Omega = \frac{N_\infty}{N_w - N_0}$	Microorganism concentration difference parameter
$s_1 = \frac{\delta_2}{\delta_1}$	Thermal stratification parameter
$s_2 = \frac{\epsilon_2}{\epsilon_1}$	Solutal stratification parameter
$s_3 = \frac{\xi_2}{\xi_1}$	Motile density stratification parameter

Appendix II: Nomenclature

a, c	Dimensional constants	W_c	Maximum cell swimming speed
u, v	Velocity components	H_0	Uniform magnetic field at infinity
Nn_x	Local motile density	T_∞	Ambient fluid temperature
T_0	Reference temperature	N_∞	Ambient microbial concentration
C	Fluid concentration	C_0	Reference nanoparticle concentration
T	Fluid temperature	N_0	Reference microbial concentration
x, y	Cartesian coordinates	N_w	Microbial concentration near wall
b	Chemotaxis constant	C_w	Nanoparticle concentration near wall
T_w	Wall fluid temperature	C_∞	Ambient nanoparticle concentration
C_p	Specific heat	Cf_x	Local drag coefficient
k_r	Reaction rate constant	Nu_x	Local Nusselt number
Sh_x	Local Sherwood number	N	Microorganism concentration
σ	Electrical conductivity	H_e	Magnetic field at free stream
ζ	Dimensionless variable	D_B	Chemical molecular diffusivity
ϑ	Kinematic viscosity	D_m	Microorganism diffusion coefficient
k	Thermal conductivity	Ω	Microorganism concentration difference
μ_e	Magnetic permeability		parameter
ρ	Fluid density	λ	Reciprocal of magnetic Prandtl number
β	Magnetic parameter	ϕ	Nanoparticle volume fraction
α_m	Magnetic diffusivity	α	Thermal diffusivity

Chapter 4

Bioconvectice hybrid stagnation-point flow due to induced magnetic field *

4.1 Introduction

The nanofluid studies involving microorganisms is an advancing field that has intrigued researchers due to its relevance in antibiotics, biofuel, toxin removal, targeted drug delivery and food digestion. The magnetic field represents an important characteristic of hydromagnetic problems. In some cases, the magnetic Reynolds number of the flow may not be realistic to be assumed small in magnitude; hence induced magnetic field (the additional magnetic field that gets induced on electrically conducting fluid in the presence of an external magnetic field.) is not negligible. However, studies incorporating induced magnetic field effects are limited in number. For its applications in biomedical imaging, hyperthermia, targeted drug delivery, and cancer therapy, the dynamics of water conveying single-wall carbon nanotubes (SWCNTs) and magnetite nanoparticles on the bioconvective stagnation-point flow along a stretching sheet subject to chemical reaction, viscous dissipation, induced magnetic field, and stratification effects is investigated. Relevant similarity formulas are effectuated in converting the governing equations into a system of ODEs and are further treated numerically using the Runge-Kutta-Fehlberg method with the shooting technique. Illustrations on the consequence of effectual parameters on the physical quantities and the flow profiles are achieved with the aid of graphs. The main objectives of the current chapter are to:

- Construct the bioconvective model to study the dynamics of water conveying

*Published in: International Communications in Heat and Mass Transfer (Elsevier), 2021; 126; 105484.

single-wall carbon nanotubes and magnetite nanoparticles considering induced magnetic field, thermal stratification, viscous dissipation, chemical reaction, solutal stratification, and motile density stratification effects.

- Provide theoretical knowledge on the consequence of effectual parameters on the flow profiles.
- Explore the significance of pertinent parameters on surface drag, heat transfer rate, mass transfer rate, and microorganism density number.

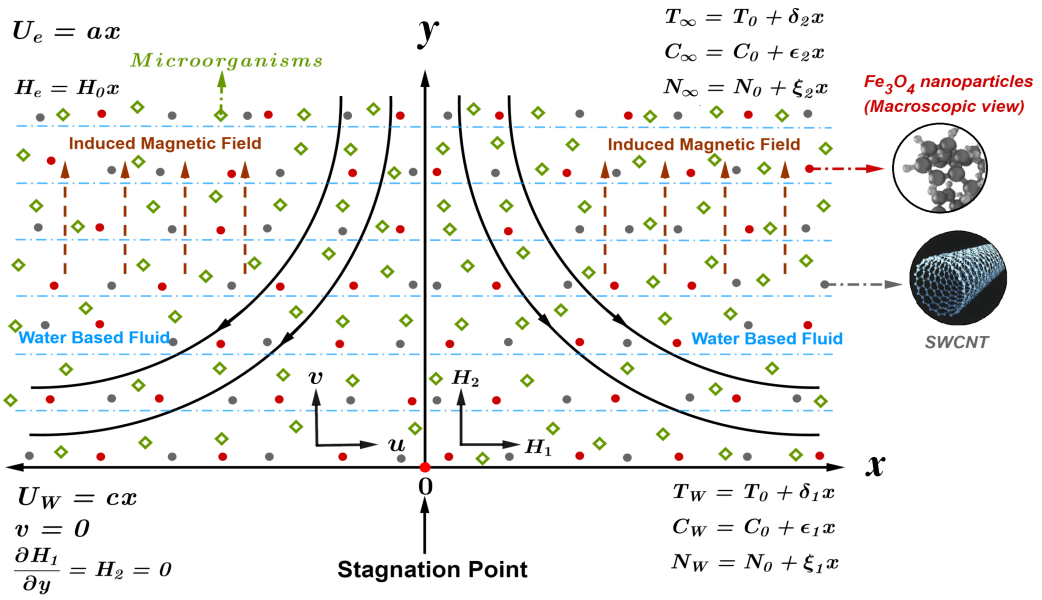

Figure 4.1: Geometrical Frame

4.2 Mathematical Frame

Two-dimensional steady incompressible stagnation point flow over a linearly elongating sheet (see Figure 4.1) is considered under the ensuing assumptions:

- The expanding sheet is positioned along x axis and water-based $Fe_3O_4 - SWCNT$ hybrid nanofluid (containing microorganisms) occupies the region $y > 0$.
- $U_W(x) = cx$ and $U_e(x) = ax$ correspond to the velocity of the lengthening sheet and the free stream, respectively.

- Induced magnetic field vector, $H = (H_1, H_2)$ is considered with H_1 & H_2 being the magnetic integrants along x and y direction, respectively.
- Chemical reaction and viscous dissipation effects are incorporated.
- Thermal, solutal and motile density stratification effects are also considered.

Following the aforementioned assumptions, the governing equations take the form (see Alsaedi et al., 2017; Z. Iqbal, Azhar, & Maraj, 2017):

$$\frac{\partial u}{\partial x} + \frac{\partial v}{\partial y} = 0 \tag{4.2.1}$$

$$\frac{\partial H_1}{\partial x} + \frac{\partial H_2}{\partial y} = 0 \tag{4.2.2}$$

$$u\frac{\partial u}{\partial x} + v\frac{\partial u}{\partial y} - \frac{\mu_e}{4\pi\rho_{hnf}}\left(H_1\frac{\partial H_1}{\partial x} + H_2\frac{\partial H_1}{\partial y}\right) = U_e\frac{dU_e}{dx} - \frac{\mu_e H_e}{4\pi\rho_{hnf}}\frac{dH_e}{dx} + \left(\frac{\mu_{hnf}}{\rho_{hnf}}\right)\frac{\partial^2 u}{\partial y^2} \tag{4.2.3}$$

$$u\frac{\partial H_1}{\partial x} + v\frac{\partial H_1}{\partial y} - H_1\frac{\partial u}{\partial x} - H_2\frac{\partial u}{\partial y} = \alpha_m\frac{\partial^2 H_1}{\partial y^2} \tag{4.2.4}$$

$$u\frac{\partial T}{\partial x} + v\frac{\partial T}{\partial y} = \alpha_{hnf}\frac{\partial^2 T}{\partial y^2} + \frac{\mu_{hnf}}{(\rho C_p)_{hnf}}\left(\frac{\partial u}{\partial y}\right)^2 \tag{4.2.5}$$

$$u\frac{\partial C}{\partial x} + v\frac{\partial C}{\partial y} = D_B\frac{\partial^2 C}{\partial y^2} - k_r\left(C - C_\infty\right) \tag{4.2.6}$$

$$u\frac{\partial N}{\partial x} + v\frac{\partial N}{\partial y} + \frac{bW_c}{C_W - C_0}\left(\frac{\partial}{\partial y}\left(N\frac{\partial C}{\partial y}\right)\right) = D_m\frac{\partial^2 N}{\partial y^2} \tag{4.2.7}$$

subject to the boundary conditions (see Alsaedi et al., 2017; Z. Iqbal, Azhar, & Maraj, 2017):

$$u = U_W(x) = cx,\ v = 0,\ \tfrac{\partial H_1}{\partial y} = H_2 = 0,\ T = T_W = T_0 + \delta_1 x,$$
$$C = C_W = C_0 + \epsilon_1 x,\ N = N_W = N_0 + \xi_1 x \quad \text{at } y = 0$$

$$u \to U_e(x) = ax,\ H_1 \to H_e(x) = H_0 x,\ T \to T_\infty = T_0 + \delta_2 x,$$
$$C \to C_\infty = C_0 + \epsilon_2 x,\ N \to N_\infty = N_0 + \xi_2 x \quad \text{as } y \to \infty$$

where $\alpha_m = \dfrac{1}{4\pi\mu_e\sigma_{hnf}}$ represents the magnetic diffusivity.

Consider the following similarity transformations (see Alsaedi et al., 2017; Z. Iqbal, Azhar, & Maraj, 2017):

$$u = cxf\,'(\zeta),\ v = -\sqrt{c\vartheta_f}f(\zeta),\ H_1 = H_0 x g\,'(\zeta),\ \zeta = y\sqrt{\frac{c}{\vartheta_f}},\ H_2 = -H_0\sqrt{\frac{\vartheta_f}{c}}g(\zeta),$$

$$\theta(\zeta) = \frac{T - T_\infty}{T_W - T_0},\ \psi(\zeta) = \frac{C - C_\infty}{C_W - C_0},\ \chi(\zeta) = \frac{N - N_\infty}{N_W - N_0}$$

Employing the similarity transformations into Equations (4.2.1) – (4.2.7), we get:

$$f\,''' - A_1\,A_2\left\{(f\,')^2 - f\,f\,'' - \frac{\beta}{A_2}\left\{(g\,')^2 - g\,g\,'' - 1\right\} - A^2\right\} = 0 \tag{4.2.8}$$

$$g\,''' - \frac{A_5}{\lambda}\{g\,f\,'' - f\,g\,''\} = 0 \tag{4.2.9}$$

$$\theta\,'' + \frac{A_3\,Pr}{A_4}\,f\,\theta\,' + \frac{Ec\,Pr}{A_1\,A_4}(f\,'')^2 = 0 \tag{4.2.10}$$

$$\psi\,'' + Le\,f\,\psi\,' - Kr\,Le\,\psi = 0 \tag{4.2.11}$$

$$\chi\,'' + Lb\,f\,\chi\,' - Pe\,\{(\chi + \Omega)\,\psi\,'' + \chi\,'\,\psi\,'\} = 0 \tag{4.2.12}$$

subject to the boundary conditions

$$f(\zeta) = 0,\quad f\,'(\zeta) = 1,\quad g(\zeta) = 0,\quad g\,''(\zeta) = 0,\quad \theta(\zeta) = 1 - S_1,$$
$$\psi(\zeta) = 1 - S_2,\quad \chi(\zeta) = 1 - S_3 \quad \text{when } \zeta = 0$$

$$f'(\zeta) \to A,\quad g\,'(\zeta) \to 1,\quad \theta(\zeta) \to 0,$$
$$\psi(\zeta) \to 0,\quad \chi(\zeta) \to 0 \quad \text{as } \zeta \to \infty$$

where the dimensionless parameters are given in appendix I.

The hybrid nanofluid models incorporated are (see Mabood, Ashwinkumar, & Sandeep, 2022; Sreedevi & Reddy, 2019):

$$\frac{\mu_{hnf}}{\mu_f} = \frac{1}{(1-\phi_{Fe_3O_4})^{2.5}\ (1-\phi_{SWCNT})^{2.5}} = \frac{1}{A_1}$$

$$\frac{\rho_{hnf}}{\rho_f} = (1-\phi_{SWCNT})\left\{(1-\phi_{Fe_3O_4}) + \frac{\rho_{Fe_3O_4}}{\rho_f}\ \phi_{Fe_3O_4}\right\} + \frac{\rho_{SWCNT}}{\rho_f}\ \phi_{SWCNT} = A_2$$

$$\frac{(\rho C_p)_{hnf}}{(\rho C_p)_f} = (1-\phi_{SWCNT})\left\{(1-\phi_{Fe_3O_4}) + \frac{(\rho C_p)_{Fe_3O_4}}{(\rho C_p)_f}\ \phi_{Fe_3O_4}\right\} + \frac{(\rho C_p)_{SWCNT}}{(\rho C_p)_f}\ \phi_{SWCNT} = A_3$$

$$\frac{k_{hnf}}{k_{bf}} = \frac{1-\phi_{SWCNT}+2\phi_{SWCNT}\left(\frac{k_{SWCNT}}{k_{SWCNT}-k_{bf}}\right) ln\left(\frac{k_{SWCNT}+k_{bf}}{2k_{bf}}\right)}{1-\phi_{SWCNT}+2\phi_{SWCNT}\left(\frac{k_{bf}}{k_{SWCNT}-k_{bf}}\right) ln\left(\frac{k_{SWCNT}+k_{bf}}{2k_{bf}}\right)}$$

$$\frac{k_{bf}}{k_f} = \frac{k_{Fe_3O_4}+2k_f-2\phi_{Fe_3O_4}\left(k_f-k_{Fe_3O_4}\right)}{k_{Fe_3O_4}+2k_f+\phi_{Fe_3O_4}\left(k_f-k_{Fe_3O_4}\right)}$$

$$\frac{\sigma_{hnf}}{\sigma_f} = 1 + \frac{3\left\{\frac{\phi_{Fe_3O_4}\sigma_{Fe_3O_4}+\phi_{SWCNT}\sigma_{SWCNT}}{\sigma_f} - \left(\phi_{Fe_3O_4}+\phi_{SWCNT}\right)\right\}}{2+\left\{\frac{\phi_{Fe_3O_4}\sigma_{Fe_3O_4}+\phi_{SWCNT}\sigma_{SWCNT}}{\left(\phi_{Fe_3O_4}+\phi_{SWCNT}\right)\sigma_f}\right\} - \left\{\frac{\phi_{Fe_3O_4}\sigma_{Fe_3O_4}+\phi_{SWCNT}\sigma_{SWCNT}}{\sigma_f} - \left(\phi_{Fe_3O_4}+\phi_{SWCNT}\right)\right\}}$$

$$A_4 = \frac{k_{hnf}}{k_f} = \frac{k_{hnf}}{k_{bf}} \times \frac{k_{bf}}{k_f},\ and\ A_5 = \frac{\sigma_{hnf}}{\sigma_f}$$

The physical quantities are given by (see Alsaedi et al., 2017; Z. Iqbal, Azhar, & Maraj, 2017; Mabood et al., 2022):

$$\text{Local drag coefficient} \quad : \quad Cf_x = \frac{\tau_\omega}{\rho_f\ (U_w)^2} = \frac{\mu_{hnf}\ \left.\frac{\partial u}{\partial y}\right|_{y=0}}{\rho_f\ (U_w)^2}$$

$$\Rightarrow\ Cf_x\ Re_x^{1/2} = \frac{f\ ''(0)}{A_1}$$

$$\text{Local Nusselt number} \quad : \quad Nu_x = \frac{x\ q_\omega}{k_f\ (T_w - T_0)} = \frac{-x\ k_{hnf}\ \left.\frac{\partial T}{\partial y}\right|_{y=0}}{k_f\ (T_w - T_0)}$$

$$\Rightarrow\ Nu_x\ Re_x^{-\ 1/2} = -A_4\ \theta\ '(0)$$

Local Sherwood number : $$Sh_x = \frac{x\ q_m}{D_B\ (C_w - C_0)} = \frac{-x\ D_B\ \left.\frac{\partial C}{\partial y}\right|_{y=0}}{D_B\ (C_w - C_0)}$$

$$\Rightarrow\ Sh_x\ Re_x^{-\ 1/2} = -\ \psi\,'(0)$$

Local motile density number : $$Nn_x = \frac{x\ q_n}{D_m\ (N_w - N_0)} = \frac{-x\ D_m\ \left.\frac{\partial N}{\partial y}\right|_{y=0}}{D_m\ (N_w - N_0)}$$

$$\Rightarrow\ Nn_x\ Re_x^{-\ 1/2} = -\ \chi\,'(0)$$

where $Re_x = \frac{xU_W}{\vartheta_f}$ is the local Reynold's number.

4.3 Numerical Frame & Validation

Equations (4.2.8) - (4.2.12) together with the boundary conditions shows a nonlinear nature and it seems to be difficult to find the closed-form or exact solution for the considered problem. Hence, the approximate solutions are computed numerically employing the Runge-Kutta-Fehlberg method cum shooting technique. This is accomplished by initially assuming:

$$\Upsilon_1 = f,\quad \Upsilon_2 = f\,',\quad \Upsilon_3 = f\,'',\quad \Upsilon_3{}' = f\,''',\quad \Upsilon_4 = g,\quad \Upsilon_5 = g\,',$$
$$\Upsilon_6 = g\,'',\quad \Upsilon_6{}' = g\,''',\quad \Upsilon_7 = \theta\,,\quad \Upsilon_8 = \theta\,',\quad \Upsilon_8{}' = \theta\,'',\quad \Upsilon_9 = \psi,$$
$$\Upsilon_{10} = \psi\,',\quad \Upsilon_{10}{}' = \psi\,'',\quad \Upsilon_{11} = \chi\,,\quad \Upsilon_{12} = \chi\,',\quad \Upsilon_{12}{}' = \chi\,''$$

The reduced system of the first-order ODE is given by:

$$\Upsilon_1{}' = \Upsilon_2\ ,\ \Upsilon_2{}' = \Upsilon_3\ ,$$

$$\Upsilon_3{}' = A_1\ A_2\ \left\{\ (\Upsilon_2)^2 - \Upsilon_1\ \Upsilon_3 - \frac{\beta}{A_2}\ \left\{(\Upsilon_5)^2 - \Upsilon_4\ \Upsilon_6 - 1\right\} - A^2\ \right\},$$

$$\Upsilon_4{}' = \Upsilon_5\ ,\ \Upsilon_5{}' = \Upsilon_6\ ,$$

$$\Upsilon_6{}' = \frac{A_5}{\lambda}\ \{\ \Upsilon_4\ \Upsilon_3 - \Upsilon_1\ \Upsilon_6\ \}\ ,$$

$$\Upsilon_7{}' = \Upsilon_8\ ,\ \Upsilon_8{}' = -\left\{\frac{A_3\ Pr}{A_4}\ \Upsilon_1\ \Upsilon_8 + \frac{Ec\ Pr}{A_1\ A_4}\ (\Upsilon_3)^2\right\},$$

$\Upsilon_9{}' = \Upsilon_{10}$, $\Upsilon_{10}{}' = Kr\ Le\ \Upsilon_9 - Le\ \Upsilon_1\ \Upsilon_{10}$,

$\Upsilon_{11}{}' = \Upsilon_{12}$, $\Upsilon_{12}{}' = Pe\ \left\{ (\Upsilon_{11} + \Omega)\ \Upsilon_{10}{}' + \Upsilon_{12}\ \Upsilon_{10} \right\} - Lb\ \Upsilon_1\ \Upsilon_{12}$.

with

$$\Upsilon_1(0) = 0, \quad \Upsilon_2(0) = 1, \quad \Upsilon_3(0) = \Gamma_1, \quad \Upsilon_4(0) = 0,$$
$$\Upsilon_5(0) = \Gamma_2, \quad \Upsilon_6(0) = 0, \quad \Upsilon_7(0) = 1 - S_1, \quad \Upsilon_8(0) = \Gamma_3,$$
$$\Upsilon_9(0) = 1 - S_2, \quad \Upsilon_{10}(0) = \Gamma_4, \quad \Upsilon_{11}(0) = 1 - S_3, \quad \Upsilon_{12}(0) = \Gamma_5$$

where Γ_1 , Γ_2 , Γ_3 , Γ_4 & Γ_5 are estimated using shooting technique with a suitable initial guess.

Accuracy of the code and the validation of the current problem have been accounted for through a restrictive comparison of the present work with prior published works Hayat et al., 2015, 2016; Iqbal, Azhar, et al., 2017 (showcased in Table 4.1 and a commendable agreement is noted.

Table 4.1: Comparison of drag coefficient $\left(Cf_x Re_x^{1/2}\right)$ with Hayat et al., 2015, 2016; Iqbal, Azhar, et al., 2017 for different A values when $\phi_{Fe_3O_4} = \phi_{SWCNT} = \beta = \lambda = 0$

A	$\boldsymbol{Cf_x Re_x^{1/2}}$			
	Iqbal et al., 2017	**Hayat et al., 2015**	**Hayat et al., 2016**	**Present study**
0.1	-0.969386	-0.96939	-0.96937	-0.969386
0.2	-0.918107	-0.91811	-0.91813	-0.918107
0.5	-0.667263	-0.66726	-0.66723	-0.667264
0.7	-0.433475	-0.43346	-0.43345	-0.433476
0.8	-0.299388	-0.29929	-0.29921	-0.299389
0.9	-0.154716	-0.15458	-0.1545471	-0.154717
1	0	0	0	0

4.4 Results & Discussion

The consequence of influential parameters on microbial concentration ($\chi(\zeta)$), velocity ($f'(\zeta)$), concentration ($\psi(\zeta)$), temperature ($\theta(\zeta)$) and induced magnetic field ($g'(\zeta)$) profiles are illustrated via Figures 4.2 - 4.15. Studies have been carried out for water-based $Fe_3O_4 - SWCNT$ hybrid nanofluid and Fe_3O_4 nanofluid with

Prandtl number (Pr) and infinity fixed at 6.2 and 10, respectively. Thermophysical properties of the conventional fluid (water), Fe_3O_4 (nanoparticle 1), and $SWCNT$ (nanoparticle 2) are showcased in Table 4.2.

Table 4.2: Thermophysical properties of water, Fe_3O_4 and $SWCNT$

Property	**Water** *(conventional fluid)*	**Fe_3O_4** *(nanoparticle 1)*	**SWCNT** *(nanoparticle 2)*
$\boldsymbol{\rho}$	997	5180	2600
$\boldsymbol{C_p}$	4179	670	425
$\boldsymbol{k}$	0.613	9.7	6600
$\boldsymbol{\sigma}$	0.05	25000	10^6

Figures 4.2(a) & 4.2(b) illustrate the impact of stretching parameter (A) on $f'(\zeta)$ & $g'(\zeta)$, respectively and it is perceived that augmenting A values produces a constructive effect on $f'(\zeta)$ and destructive effect on $g'(\zeta)$. Figure 4.3 depicts the variations in $f'(\zeta)$ due to β (magnetic parameter). It is observed that $f'(\zeta)$ increases for augmenting β values when $A < 1$ and a reversed behaviour is observed for $f'(\zeta)$ when $A > 1$.

Figure 4.4 bespeaks the deviation in $g'(\zeta)$ concerning β. An increase in $g'(\zeta)$ for $A < 1$ and a decrease $g'(\zeta)$ for $A > 1$ are noted for elevating β values. Figure 4.5 explains the mixed effect of λ (reciprocal of magnetic Prandtl number) on $g'(\zeta)$). Initially, elevating λ values decays $g'(\zeta)$ and afterwards, a reversed trend is observed when $A < 1$. A similar but inversed impact is perceived when $A > 1$.

Figures 4.6 & 4.7 elucidate the simultaneous effect of β, $\phi_{Fe_3O_4}$ & ϕ_{SWCNT} on $Cf_xRe_x^{1/2}$ (drag coefficient). It can be interpreted that $Cf_xRe_x^{1/2}$ improves with β and deteriorates with $\phi_{Fe_3O_4}$ & ϕ_{SWCNT} when $A < 1$. When $A > 1$, $Cf_xRe_x^{1/2}$ increases with $\phi_{Fe_3O_4}$ & ϕ_{SWCNT} and decreases with β. Biologically, a higher drag coefficient implies increased interaction between the fluid and the surface, which is beneficial in targeted drug delivery and biomedical imaging.

Variation in $\theta(\zeta)$ due to $\phi_{Fe_3O_4}$ (volume fraction of nanoparticle 1) and ϕ_{SWCNT} (volume fraction of nanoparticle 2) are illustrated in Figures 4.8(a) & 4.8(b), respectively. It is observed that $\theta(\zeta)$ ascends with augmenting $\phi_{Fe_3O_4}$ & ϕ_{SWCNT}. Physically, this increase in temperature can be related to the improvement in the

thermal conductivity of the nanoliquid caused by larger nanoparticle occupancy. The constructive effect of Ec (Eckert number) is illustrated in Figure 4.9(b). Physically, it is associated with the generation of friction forces between the fluid particles which increases the temperature profile. In addition, the analysis on the significance of $\phi_{Fe_3O_4}$, ϕ_{SWCNT} & Ec on the temperature profile unveils that the nanoliquid can be used for killing tumors or cancerous cells. Figure 4.9(a) depicts a descending nature of $\theta(\zeta)$ for S_1 (thermal stratification parameter). Physically, the decrease in the nanoliquid temperature is due to the decrease in the temperature difference between the surface and away from the surface caused by an increase in S_1.

The simultaneous effect of Ec, S_1, $\phi_{Fe_3O_4}$ & ϕ_{SWCNT} on $Nu_x Re_x^{-1/2}$ (heat transfer rate) has been studied with the aid of Figures 4.10 & 4.11. It can be said that for $A = 0.8$, $Nu_x Re_x^{-1/2}$ decreases with respect to S_1, Ec & ϕ_{SWCNT} and remains almost unchanged with respect to $\phi_{Fe_3O_4}$.

Figure 4.12 explains the consequence of Kr (chemical reaction parameter), Le (Lewis number) and S_2 (solutal stratification parameter) on $\psi(\zeta)$. A decreasing behaviour on the concentration profile is observed for augmenting Kr, Le & S_2 values. Physically, an increase in S_2 descends the concentration profile due to the decrease in the volumetric fraction between the surface and reference nanoparticles. Moreover, an increase in Kr consumes more nanoparticles and hence concentration decreases. Biologically, consumption of more nanoparticles is directly proportional to improved medication and biomedical imaging.

Figure 4.13 discusses the impact of Pe (Peclet number) and S_3 (motile density stratification parameter) on $\chi(\zeta)$. It is observed that the augmenting effectual parameter values tend to decrease $\chi(\zeta)$. Physically, an augmentation in S_3 decreases the concentration difference of microorganisms between the surface and away from the surface and hence the microbial concentration decreases.

Figures 4.14(a) & 4.15(a) bespeak the simultaneous variation of Le, Kr & S_2 on $Sh_x Re_x^{-1/2}$ (mass transfer rate) and Figures 4.14(b) & 4.15(b) depict the simultaneous variation of Lb (bioconvection Lewis number), Kr & S_3 on $Nn_x Re_x^{-1/2}$ (microorganism density number). It can be easily observed that $Sh_x Re_x^{-1/2}$ increases with Kr & Le and decreases due to S_2. Furthermore, it is also noted that $Nn_x Re_x^{-1/2}$ increases with Kr & Lb and decreases due to S_3.

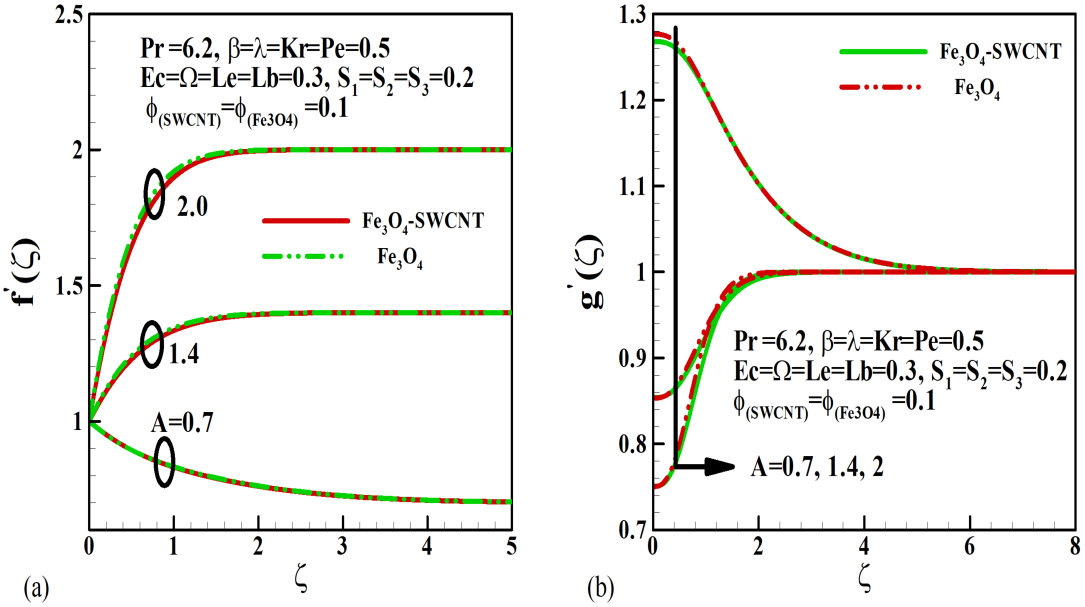

Figure 4.2: Variation of A on $f'(\zeta)$ & $g'(\zeta)$

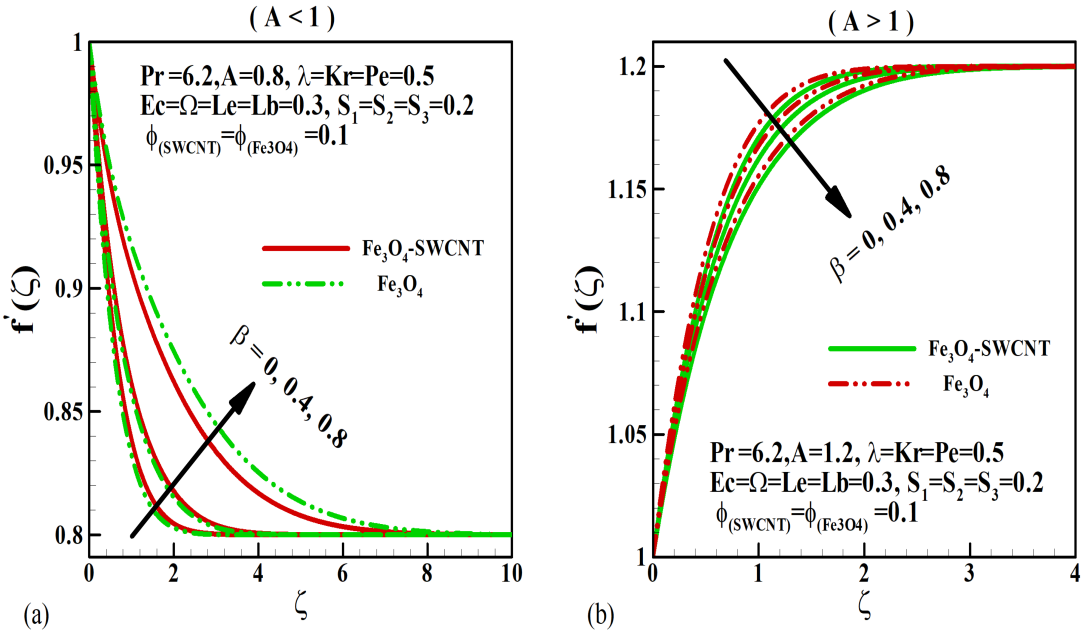

Figure 4.3: Variation of β on $f'(\zeta)$

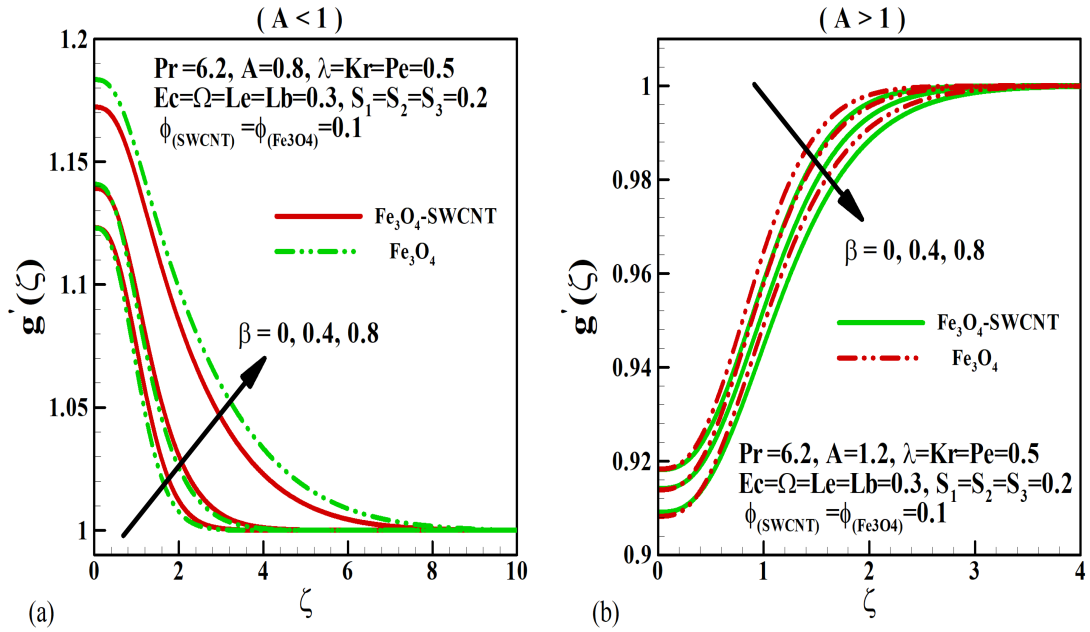

Figure 4.4: Variation of β on $g'(\zeta)$

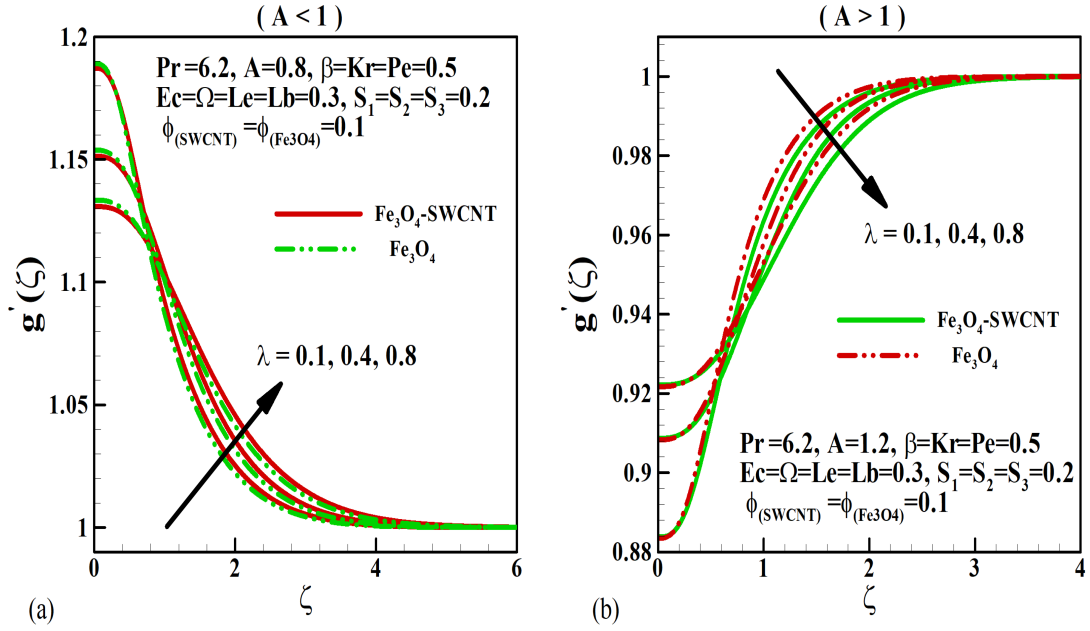

Figure 4.5: Variation of λ on $g'(\zeta)$

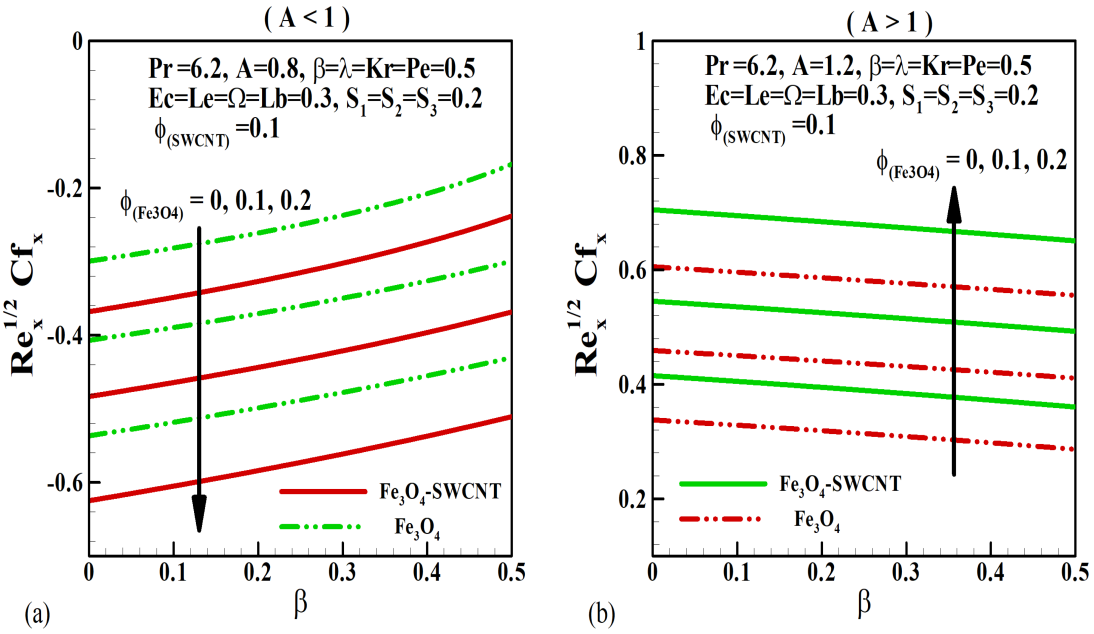

Figure 4.6: Parallel effect of β & $\phi_{Fe_3O_4}$ on $Cf_x Re_x^{1/2}$

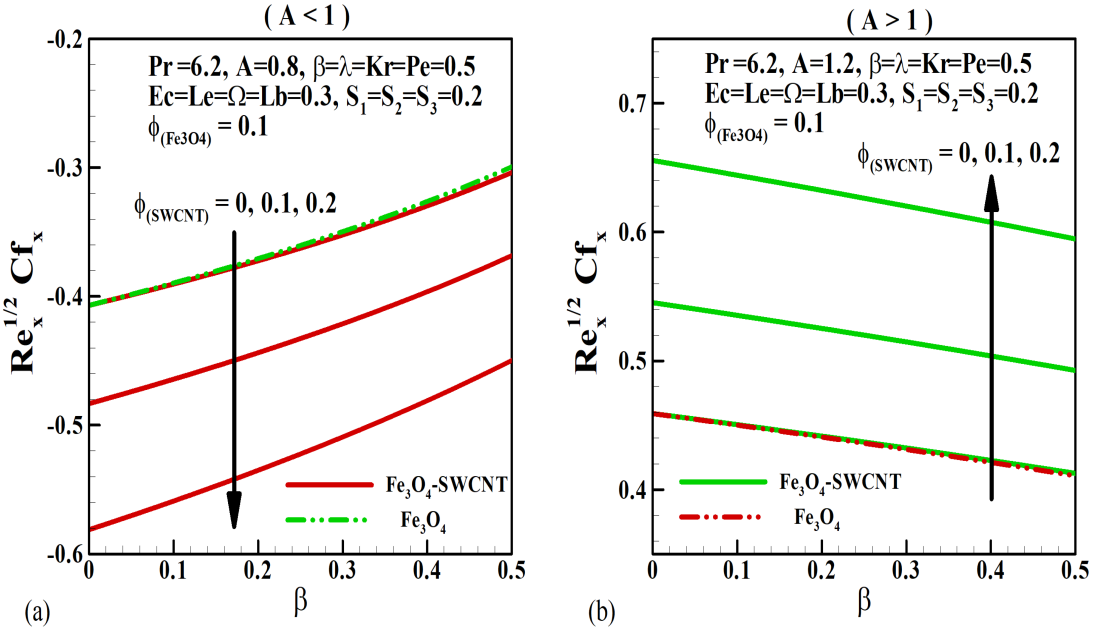

Figure 4.7: Parallel effect of β & ϕ_{SWCNT} on $Cf_x Re_x^{1/2}$

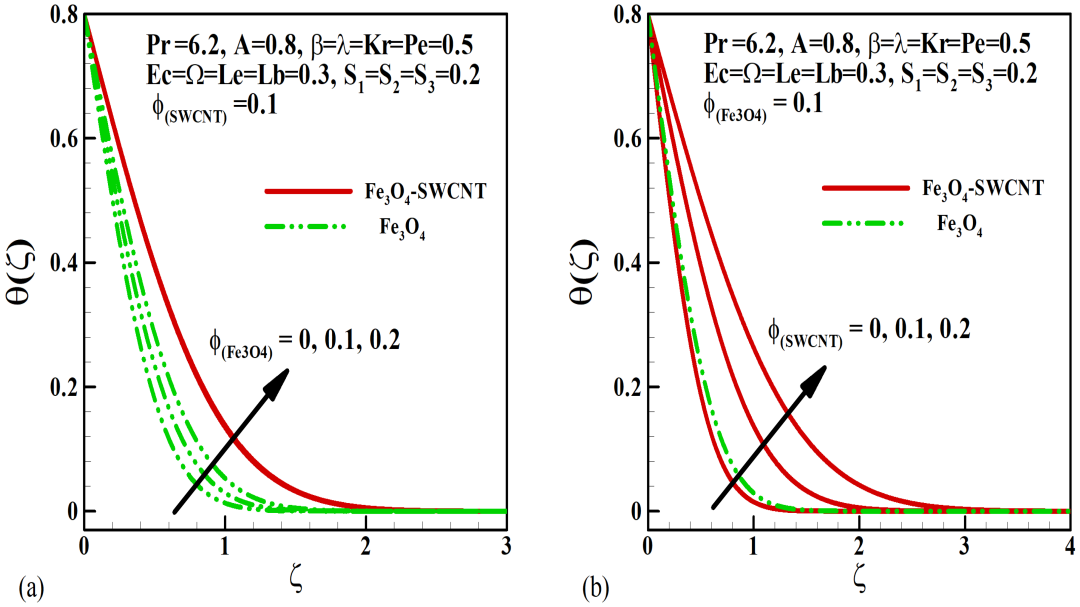

Figure 4.8: Variation of $\phi_{Fe_3O_4}$ & ϕ_{SWCNT} on $\theta\,(\zeta)$

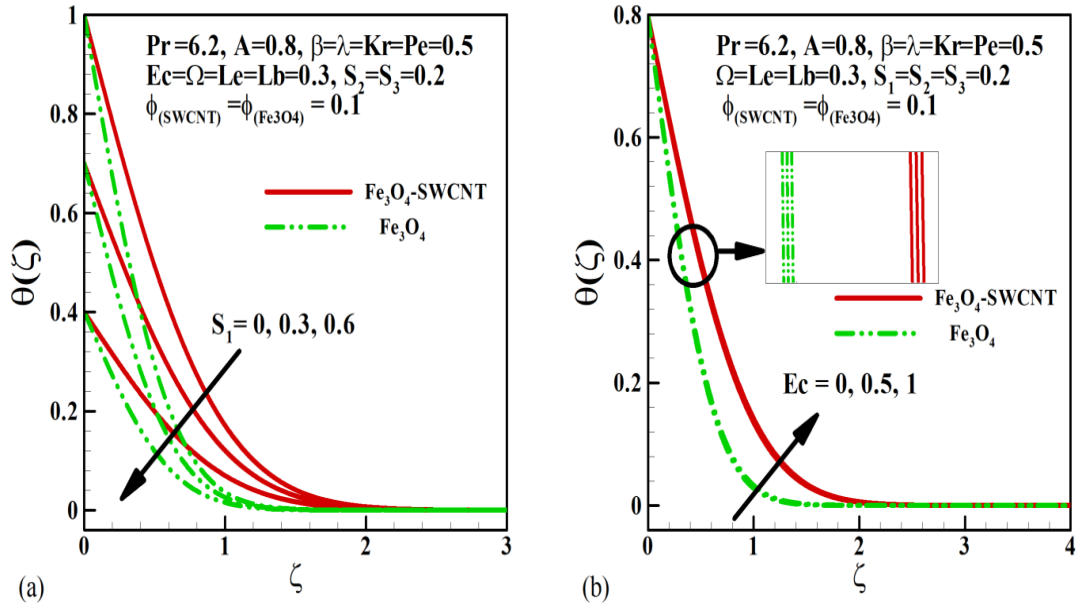

Figure 4.9: Variation of S_1 & Ec on $\theta\,(\zeta)$

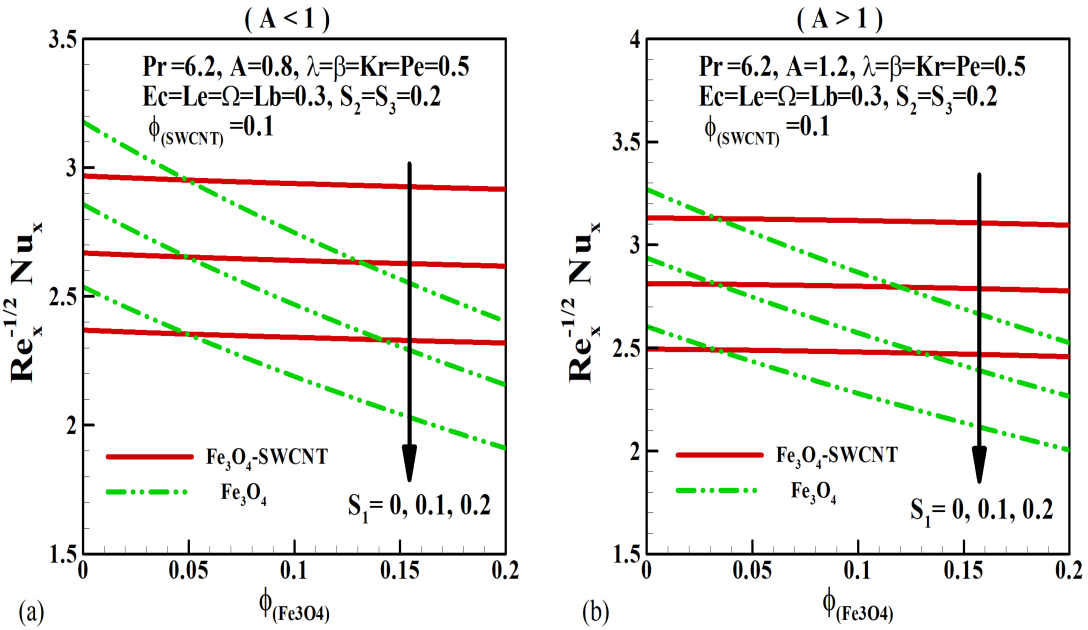

Figure 4.10: Parallel effect of S_1 & $\phi_{Fe_3O_4}$ on $Nu_x Re_x^{-1/2}$

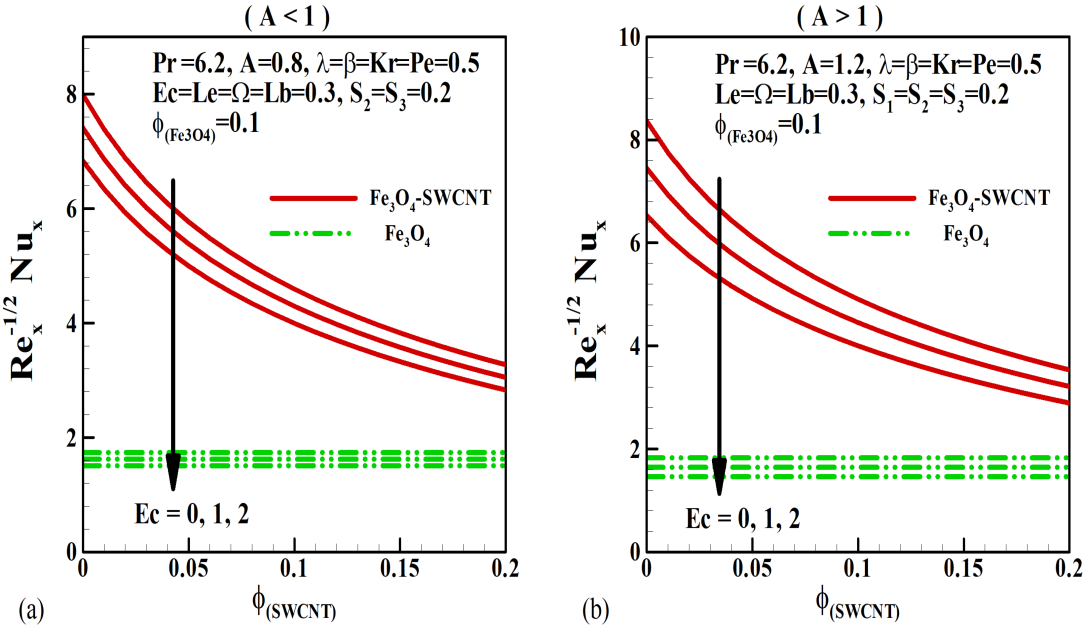

Figure 4.11: Parallel effect of Ec & ϕ_{SWCNT} on $Nu_x Re_x^{-1/2}$

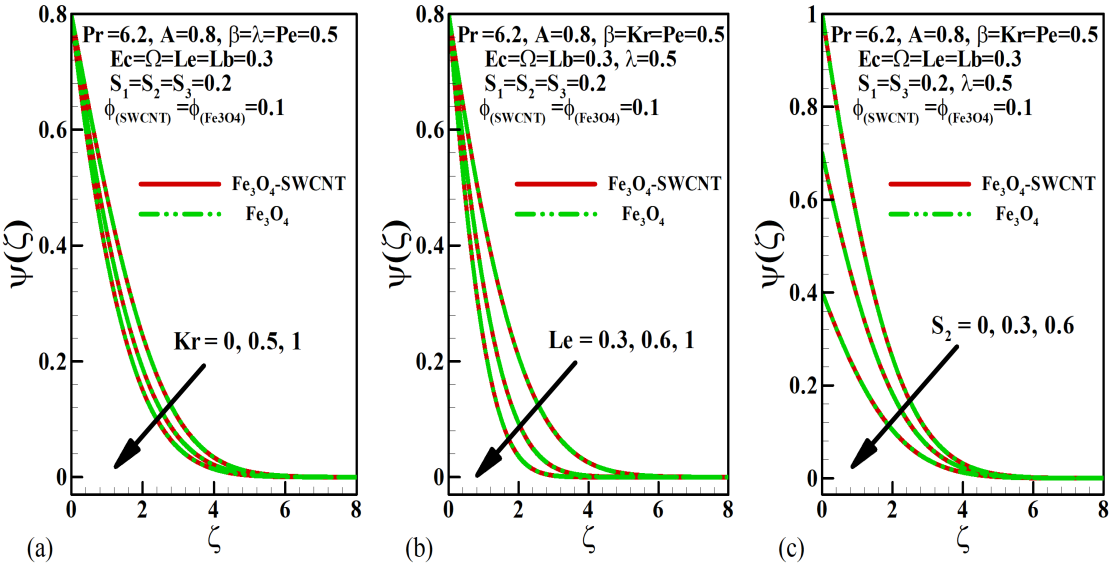

Figure 4.12: Variation of $Kr,\ Le,\ \&\ S_2$ on $\psi\,(\zeta)$

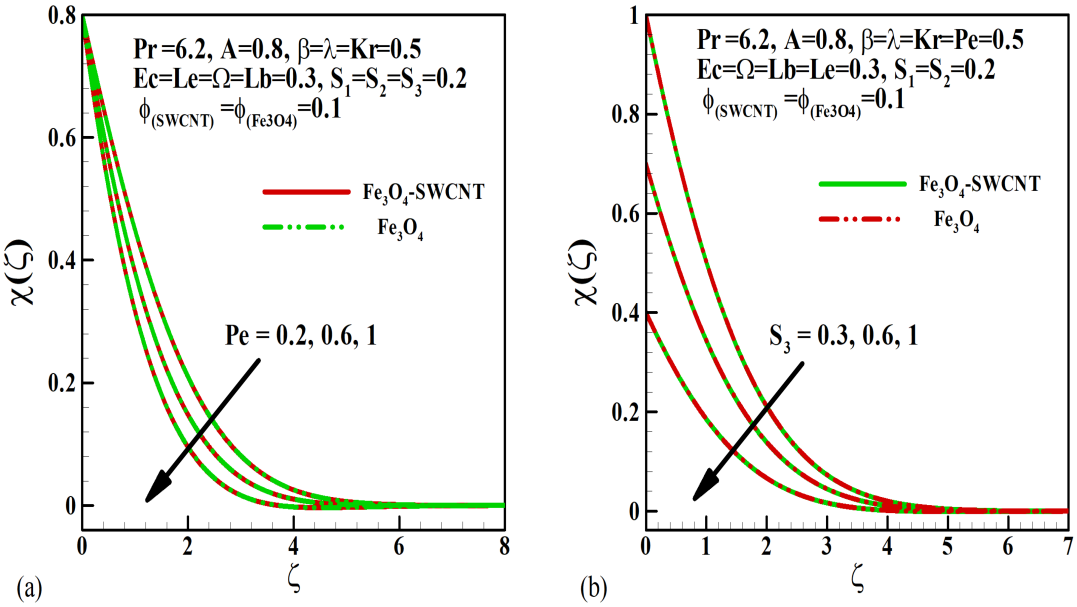

Figure 4.13: Variation of $Pe\ \&\ S_3$ on $\chi\,(\zeta)$

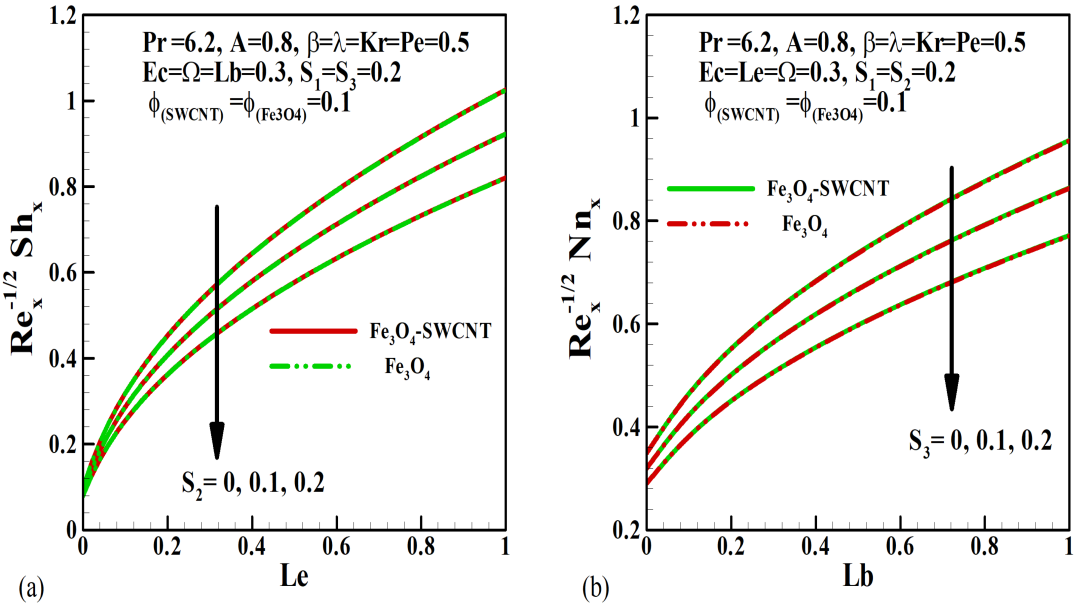

Figure 4.14: Parallel effect of (a) S_2 & Le on $Sh_x Re_x^{-1/2}$ and (b) S_3 & Lb on $Nn_x Re_x^{-1/2}$

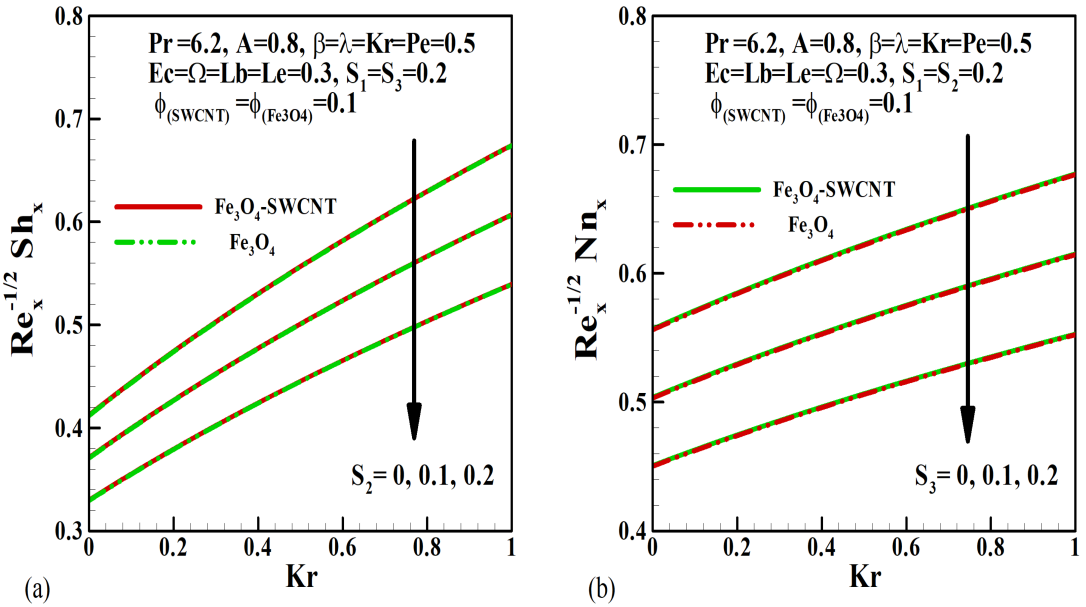

Figure 4.15: Parallel effect of (a) S_2 & Kr on $Sh_x Re_x^{-1/2}$ and (b) S_3 & Kr on $Nn_x Re_x^{-1/2}$

4.5 Conclusion

The dynamics of water conveying single-wall carbon nanotube and magnetite nanoparticles on the stagnation point flow along a stretching sheet subject to chemical reaction, viscous dissipation, induced magnetic field, and stratification effects have been numerically explored using the Runge-Kutta-Fehlberg method combined with the shooting technique. The key points noted from the study are:

- The augmenting volume fraction of single-wall carbon nanotube and magnetite nanoparticles raises the nanofluid temperature. Further, augmenting the Eckert number intensifies the nanofluid temperature. Biologically, the increase in the nanofluid temperature caused by the pertinent parameters is beneficial in killing tumors and cancerous cells.

- The velocity profile is directly proportional to the magnetic parameter when $A < 1$ and inversely proportional to the magnetic parameter when $A > 1$.

- The maximum drag coefficient (when $A = 0.8$) is experienced for higher values of the magnetic parameter and lower volume fraction of single-wall carbon nanotube and magnetite nanoparticles. However, the maximum drag coefficient (when $A = 1.2$) is experienced for lower values of the magnetic parameter and higher volume fraction of single-wall carbon nanotube and magnetite nanoparticles. Biologically, a higher drag coefficient implies increased interaction between the fluid and the surface, which is beneficial in targeted drug delivery and biomedical imaging.

- The mass transfer rate is a decreasing function of the solutal stratification parameter and an increasing function of the chemical reaction parameter.

- Augmenting chemical reaction parameter has a destructive effect on concentration profile that contributes towards improved medication and biomedical imaging.

- The maximum heat transfer rate is observed for smaller values of thermal stratification parameter, Eckert number, and nanoparticle volume fraction of single-wall carbon nanotube.

Appendix I: Non-dimensional qunatities

$A = \frac{a}{c}$	Stretching parameter
$\beta = \frac{\mu_e}{4\pi\rho_f}\left(\frac{H_0}{c}\right)^2$	Magnetic parameter
$\lambda = \frac{1}{4\pi\mu_e\sigma_f\vartheta_f}$	Reciprocal of magnetic Prandtl number
$Pr = \frac{(\mu C_p)_f}{k_f} = \frac{\vartheta_f}{\alpha_f}$	Prandtl number
$Kr = \frac{k_r}{c}$	Chemical reaction parameter
$Ec = \frac{(cx)^2}{(C_p)_f (T_W - T_0)}$	Eckert number
$Le = \frac{\vartheta_f}{D_B}$	Lewis number
$Lb = \frac{\vartheta_f}{D_m}$	Bioconvection Lewis number
$Pe = \frac{bW_c}{D_m}$	Bioconvection Peclet number
$\Omega = \frac{N_\infty}{N_W - N_0}$	Microorganism concentration difference parameter
$S_1 = \frac{\delta_2}{\delta_1}$	Thermal stratification parameter
$S_2 = \frac{\epsilon_2}{\epsilon_1}$	Solutal stratification parameter
$S_3 = \frac{\xi_2}{\xi_1}$	Motile density stratification parameter

Appendix II: Nomenclature

a, c	Dimensional constants	W_c	Maximum cell swimming speed
u, v	Velocity components	H_0	Uniform magnetic field at infinity
Nn_x	Local motile density	T_∞	Ambient fluid temperature
T_0	Reference temperature	N_∞	Ambient microbial concentration
C	Fluid concentration	C_0	Reference nanoparticle concentration
T	Fluid temperature	N_0	Reference microbial concentration
x, y	Cartesian coordinates	N_w	Microbial concentration near wall
b	Chemotaxis constant	C_w	Nanoparticle concentration near wall
T_w	Wall fluid temperature	C_∞	Ambient nanoparticle concentration
C_p	Specific heat	Cf_x	Local drag coefficient
k_r	Reaction rate constant	Nu_x	Local Nusselt number
Sh_x	Local Sherwood number	N	Microorganism concentration
σ	Electrical conductivity	H_e	Magnetic field at free stream
ζ	Dimensionless variable	D_B	Chemical molecular diffusivity
ϑ	Kinematic viscosity	D_m	Microorganism diffusion coefficient
k	Thermal conductivity	Ω	Microorganism concentration difference
μ_e	Magnetic permeability		parameter
ρ	Fluid density	λ	Reciprocal of magnetic Prandtl number
β	Magnetic parameter	ϕ	Nanoparticle volume fraction
α_m	Magnetic diffusivity	α	Thermal diffusivity

Chapter 5

Significance of nanoparticle shape on stagnation-point flow in the presence of induced magnetic field *

5.1 Introduction

The nanoparticles can be categorized into spherical and non-spherical nanoparticles based on their physical shape. Different shaped nanoparticle exhibits different properties and different heat transfer capabilities. Non-spherical nanoparticles have gained popularity for their ability in changing the thermophysical properties of a nanofluid. Blood is a connective tissue in fluid form. Blood flow utilizing nanoparticles are important in the medical industry for cancer treatment and drug delivery. Induced magnetic field paired with blood flow plays a decisive role in blood pumps, treatment of cardiac diseases and has many other biomedical applications. The significance of multiple slip and nanoparticle shape on stagnation point flow of blood-based silver nanofluid considering chemical reaction, induced magnetic field, thermal radiation, and linear heat source which is beneficial in cancer therapy, biomedical imaging, hyperthermia, and tumor therapy is investigated. Relevant similarity transformations are effectuated in converting the mathematically modelled governing equations into a system of ODEs and are then numerically resolved in MATLAB employing the adaptive Runge-Kutta method and the Newton Raphson method. Observations on the consequence of differing parameters on varying attributes are achieved via tables and graphs. Additionally, the shape effect of nanoparticles on various attributes is also evaluated. The current chapter makes

*Published in: Surfaces and Interfaces (Elsevier), 2021; 25; 101267.

an attempt in answering the following research questions:

- What is the significance of thermal slip and solutal slip parameters on the nanofluid temperature and nanofluid concentration, respectively?
- How does the nanoparticle shape affect the flow profiles?
- What is the variation in the nanofluid temperature with linear heat source, thermal radiation, and volume fraction of silver nanoparticles?
- How sensitive are the physical quantities with spherical and non-spherical nanoparticles?

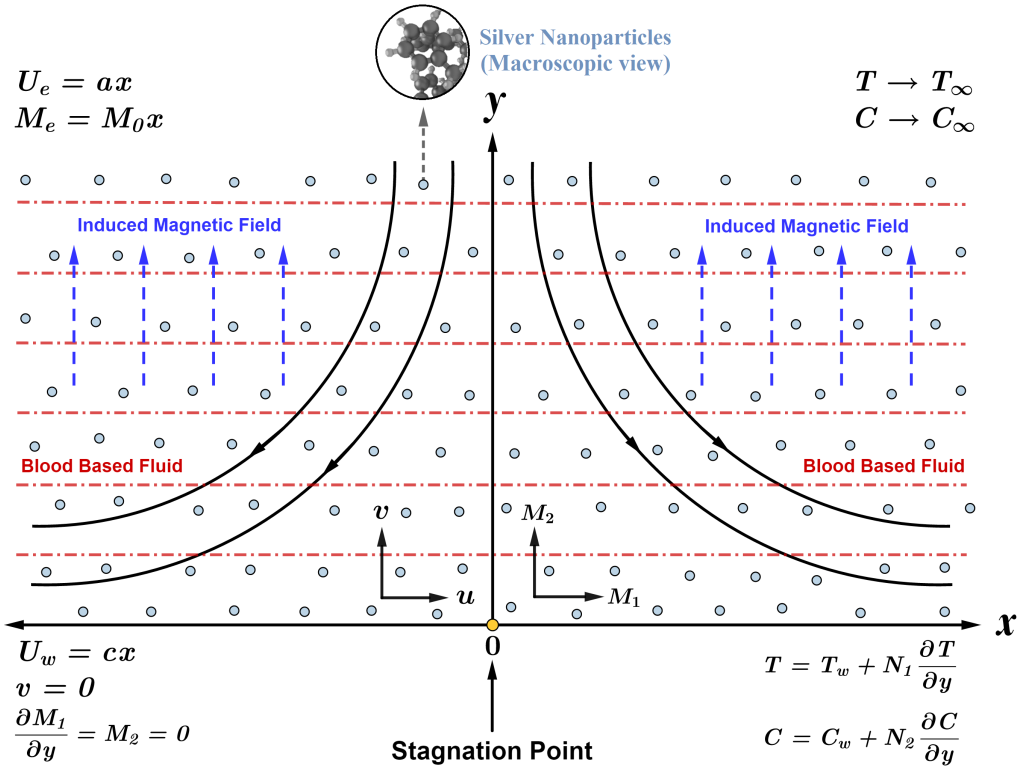

Figure 5.1: Geometrical Frame

5.2 Mathematical Frame

Two-dimensional steady incompressible stagnation point flow over a linearly elongating sheet (see Figure 5.1) is considered under the ensuing assumptions:

- The expanding sheet is positioned along x axis and blood-based silver nanofluid occupies the region $y > 0$.

- $U_w(x) = cx$ and $U_e(x) = ax$ correspond to the velocity of the lengthening sheet and the free stream, respectively.
- Induced magnetic field vector, $M = (M_1, M_2)$ is considered with M_1 & M_2 being the magnetic integrants along x and y direction, respectively.
- Chemical reaction, linear heat source, thermal radiation, and nanoparticle shape (sphere, cylinder, platelet, and blade) effects are incorporated.
- Thermal and solutal slip effects are also considered.

Following the aforementioned assumptions, the governing equations are written as (see El-Aziz & Afify, 2018; Barik et al., 2020):

$$\frac{\partial u}{\partial x} + \frac{\partial v}{\partial y} = 0 \tag{5.2.1}$$

$$\frac{\partial M_1}{\partial x} + \frac{\partial M_2}{\partial y} = 0 \tag{5.2.2}$$

$$u\frac{\partial u}{\partial x} + v\frac{\partial u}{\partial y} - \frac{\mu_e}{4\pi\rho_{nf}}\left(M_1\frac{\partial M_1}{\partial x} + M_2\frac{\partial M_1}{\partial y}\right) = U_e\frac{dU_e}{dx} - \frac{\mu_e M_e}{4\pi\rho_{nf}}\frac{dM_e}{dx} + \left(\frac{\mu_{nf}}{\rho_{nf}}\right)\frac{\partial^2 u}{\partial y^2} \tag{5.2.3}$$

$$u\frac{\partial M_1}{\partial x} + v\frac{\partial M_1}{\partial y} - M_1\frac{\partial u}{\partial x} - M_2\frac{\partial u}{\partial y} = \alpha_m\frac{\partial^2 M_1}{\partial y^2} \tag{5.2.4}$$

$$u\frac{\partial T}{\partial x} + v\frac{\partial T}{\partial y} = \alpha_{nf}\frac{\partial^2 T}{\partial y^2} + \frac{q_T}{(\rho C_p)_{nf}}(T - T_\infty) - \frac{1}{(\rho C_p)_{nf}}\frac{\partial q_r}{\partial y} \tag{5.2.5}$$

$$u\frac{\partial C}{\partial x} + v\frac{\partial C}{\partial y} = D_B\frac{\partial^2 C}{\partial y^2} - k_r(C - C_\infty) \tag{5.2.6}$$

subject to the boundary conditions (see El-Aziz & Afify, 2018; Barik et al., 2020):

$$u = U_w(x) = cx,\ v = 0,\ \tfrac{\partial M_1}{\partial y} = M_2 = 0,\ T = T_w + N_1\tfrac{\partial T}{\partial y},\ C = C_w + N_2\tfrac{\partial C}{\partial y} \ \text{ at } y = 0$$

$$u \to U_e(x) = ax,\ M_1 \to M_e(x) = M_0 x,\ T \to T_\infty, C \to C_\infty \ \text{ as } y \to \infty$$

where $\alpha_m = \dfrac{1}{4\pi\mu_e\sigma_{nf}}$ represents the magnetic diffusivity.

Consider the following similarity transformations (see El-Aziz & Afify, 2018; Barik et al., 2020):

$$u = cxf\,'(\eta),\ v = -\sqrt{c\vartheta_f}f(\eta),\ M_1 = M_0 x g\,'(\eta),\ M_2 = -M_0\sqrt{\frac{\vartheta_f}{c}}g(\eta),$$

$$\eta = y\sqrt{\frac{c}{\vartheta_f}},\ \theta(\eta) = \frac{T-T_\infty}{T_w-T_0},\ \psi(\eta) = \frac{C-C_\infty}{C_w-C_0}$$

Employing the linearized Roseland approximation and the similarity transformations into Equations $(5.2.1)-(5.2.6)$, we get:

$$f\,''' = A_1\ A_2\ \left\{\ (\ f\,'\ )^2 - f\ f\,'' - \frac{\beta}{A_2}\ \left\{\ (\ g\,'\ )^2 - g\ g\,'' - 1\right\} - A^2\ \right\} \tag{5.2.7}$$

$$g\,''' = \frac{A_5}{\lambda}\ \{\ g\ f\,'' - f\ g\,''\ \} \tag{5.2.8}$$

$$\theta\,'' = \frac{-Pr\ \{\ A_3\ f\ \theta\,' + Q_T\ \theta\ \}}{A_4 + \frac{4}{3}R_d} \tag{5.2.9}$$

$$\psi\,'' = Kr\ Le\ \psi - Le\ f\ \psi\,' \tag{5.2.10}$$

subject to the boundary conditions

$$f(0) = 0, f\,'(0) = 1,\ g(0) = 0,\ g\,''(0) = 0,\ \theta(0) = 1 + T_{slip}\ \theta\,'(0),$$

$$\psi(0) = 1 + C_{slip}\ \psi\,'(0)\,,\ f\,'(\infty) \to A,\ g\,'(\infty) \to 1,\ \theta(\infty) \to 0,\ \psi(\infty) \to 0.$$

where the dimensionless parameters are given in appendix I.

The nanofluid models and nanaoparticle shape properties incorporated are given by (see Benkhedda et al., 2020):

Spherical	***Non-spherical***
$\frac{\mu_{nf}}{\mu_f} = \frac{1}{(1-\phi)^{2.5}} = \frac{1}{A_1}$	$\frac{\mu_{nf}}{\mu_f} = 1 + A_{shape}\ \phi + B_{shape}\ \phi^2 = \frac{1}{A_1}$

$$A_2 = \frac{\rho_{nf}}{\rho_f} = (1-\phi) + \phi\left(\frac{\rho_{Ag}}{\rho_f}\right)$$

$$A_3 = \frac{(\rho C_p)_{nf}}{(\rho C_p)_f} = (1-\phi) + \phi\left(\frac{(\rho C_p)_{Ag}}{(\rho C_p)_f}\right)$$

$$A_4 = \frac{k_{nf}}{k_f} = \frac{k_{Ag} + (s-1)\,k_f - (s-1)\,\phi\,(k_f - k_{Ag})}{k_{Ag} + (s-1)\,k_f + \phi\,(k_f - k_{Ag})}$$

$$A_5 = \frac{\sigma_{nf}}{\sigma_f} = 1 + \frac{3\left(\frac{\sigma_{Ag}}{\sigma_f} - 1\right)\phi}{\left(\frac{\sigma_{Ag}}{\sigma_f} + 2\right) - \left(\frac{\sigma_{Ag}}{\sigma_f} - 1\right)\phi}$$

	Sphere	***Cylinder***	***Platelet***	***Blade***
A	-	13.5	37.1	14.6
B	-	904.4	612.6	123.3
Shape factor, s	3	4.9	5.7	8.6

The physical quantities are given by (see Z. Iqbal, Azhar, & Maraj, 2017; M. I. Khan et al., 2019):

$$\text{Local drag coefficient} \quad : \quad Cf_x = \frac{\tau_\omega}{\rho_f\ (U_w)^2} = \frac{\mu_{nf}\ \left.\frac{\partial u}{\partial y}\right|_{y=0}}{\rho_f\ (U_w)^2}$$

$$\Rightarrow\ Cf_x\ Re_x^{1/2} = \frac{f\,''(0)}{A_1}$$

$$\text{Local Nusselt number} \quad : \quad Nu_x = \frac{x\ q_\omega}{k_f\ (T_w - T_\infty)} = \frac{-x\left(k_{nf}\ \frac{\partial T}{\partial y} - q_r\right)\Big|_{y=0}}{k_f\ (T_w - T_\infty)}$$

$$\Rightarrow\ Nu_x\ Re_x^{-\ 1/2} = -\left(A_4 + \frac{4}{3}R_d\right)\ \theta\,'(0)$$

$$\text{Local Sherwood number} \quad : \quad Sh_x = \frac{x\ q_m}{D_B\ (C_w - C_0)} = \frac{-x\ D_B\ \frac{\partial C}{\partial y}\Big|_{y=0}}{D_B\ (C_w - C_0)}$$

$$\Rightarrow\ Sh_x\ Re_x^{-\ 1/2} = -\ \psi\,'(0)$$

where $Re_x = \frac{xU_w}{\vartheta_f}$ is the local Reynold's number.

5.3 Numerical Frame & Validation

Equations (5.2.7) - (5.2.10) together with the boundary conditions are numerically resolved in MATLAB employing the adaptive Runge-Kutta method (for solving) and Newton Raphson (for shooting). Shooting technique involves converting the boundary value problem into an initial value problem and then estimating the unknowns using the far-field boundary conditions. For this, initially assume:

$$\Gamma_1 = f,\quad \Gamma_2 = f\,',\quad \Gamma_3 = f\,'',\quad \Gamma_3{}' = f\,''',\ \Gamma_4 = g,\quad \Gamma_5 = g\,',\ \Gamma_6 = g\,'',$$
$$\Gamma_6{}' = g\,''',\quad \Gamma_7 = \theta\ ,\quad \Gamma_8 = \theta\,',\quad \Gamma_8{}' = \theta\,''\ ,\quad \Gamma_9 = \psi,\ \Gamma_{10} = \psi\,',\quad \Gamma_{10}{}' = \psi\,''$$

The reduced system of the first-order ODE is given by:

$$\Gamma_1{}' = \Gamma_2\ ,\ \Gamma_2{}' = \Gamma_3\ ,$$

$$\Gamma_3{}' = A_1\ A_2\ \left\{\ (\Gamma_2)^2 - \Gamma_1\ \Gamma_3 - \frac{\beta}{A_2}\ \left\{(\Gamma_5)^2 - \Gamma_4\ \Gamma_6 - 1\right\} - A^2\ \right\},$$

$$\Gamma_4{}' = \Gamma_5\ ,\ \Gamma_5{}' = \Gamma_6\ ,$$

$$\Gamma_6{}' = \frac{A_5}{\lambda}\ \{\ \Gamma_4\ \Gamma_3 - \Gamma_1\ \Gamma_6\ \}\ ,$$

$$\Gamma_7{}' = \Gamma_8\ ,\ \Gamma_8{}' = \frac{-Pr\ \{\ A_3\ \Gamma_1\ \Gamma_8 + Q_T\ \Gamma_7\ \}}{A_4 + \frac{4}{3}R_d}\ ,$$

$$\Gamma_9{}' = \Gamma_{10}\ ,\ \Gamma_{10}{}' = Kr\ Le\ \Gamma_9 - Le\ \Gamma_1\ \Gamma_{10}\ .$$

with

$$\Gamma_1(0) = 0\ ,\ \Gamma_2(0) = 1\ ,\ \Gamma_3(0) = \Lambda_1\ ,\ \Gamma_4(0) = 0\ ,\ \Gamma_5(0) = \Lambda_2\ ,\ \Gamma_6(0) = 0,$$
$$\Gamma_7(0) = 1 + T_{slip}\ \Lambda_3\ ,\ \Gamma_8(0) = \Lambda_3\ ,\ \Gamma_9(0) = 1 + C_{slip}\ \Lambda_4\ ,\ \Gamma_{10}(0) = \Lambda_4.$$

where Λ_1 , Λ_2 , Λ_3 & Λ_4 are estimated using the Newton Raphson method with a suitable initial guess.

Validity of the code for the current problem has been adjudged through a restrictive correspondence of the present work with prior published works of Hayat et al., 2015, 2016; Iqbal, Azhar, et al., 2017 (showcased in Table 5.1) and a commendable agreement is noted.

5.4 Results & Discussion

The consequence of influential parameters on velocity ($f'(\eta)$), concentration ($\psi(\eta)$), temperature ($\theta(\eta)$), induced magnetic field ($g'(\eta)$) profiles and physical quantities are illustrated via Figures 5.2 - 5.25. Prandtl number (Pr) and infinity are fixed at 21 and 5, respectively. Thermophysical properties of base fluid (blood) and silver (nanoparticle) are showcased in Table 5.2.

Figure 5.2 elucidates the positive impact of the stretching parameter (A) on $f'(\eta)$ meaning that an augmentation in stretching parameter results in the escalation of $f'(\eta)$. Figure 5.3 describes the deviations in $f'(\eta)$ with β (magnetic parameter). An increase in β tends to increase $f'(\eta)$. Figure 5.4 bespeaks the deviations in $f'(\eta)$ with respect to ϕ (nanoparticle volume fraction). It can be observed that $f'(\eta)$ decreases for augmenting ϕ values. This can be physically associated with the fact that ascending ϕ values increases the nanofluid viscosity which in turn decreases the nanofluid velocity. The nanoparticle shape effect on velocity profile is depicted in Figure 5.5. The highest nanofluid velocity profile is exhibited by cylinder-shaped silver nanoparticles followed by platelet, blade, and spherical-shaped nanoparticles, respectively.

Figures 5.6 & 5.7 elucidate the parallel effect of β & ϕ with the differing nanoparticle shapes on $Cf_x\ Re_x^{1/2}$. It is perceived that $Cf_x\ Re_x^{1/2}$ is a decreasing function of ϕ and an increasing function of β. Further, it can be observed that the drag coefficient is highest for spherical-shaped silver nanoparticles and least for cylindrically shaped silver nanoparticles.

Table 5.1: Comparison of drag coefficient $\left(Cf_x Re_x^{1/2}\right)$ for different A values between the present study and the works of Iqbal, Azhar, et al., 2017 and Hayat et al., 2015, 2016 when $\phi = \beta = 0$

A	$\boldsymbol{Cf_x Re_x^{1/2}}$			
	Iqbal et al., 2017	**Hayat et al., 2015**	**Hayat et al., 2016**	**Present study**
0.1	-0.969386	-0.96939	-0.96937	-0.9693861
0.2	-0.918107	-0.91811	-0.91813	-0.9181071
0.5	-0.667263	-0.66726	-0.66723	-0.6672637
0.7	-0.433475	-0.43346	-0.43345	-0.4334756
0.8	-0.299388	-0.29929	-0.29921	-0.2993888
0.9	-0.154716	-0.15458	-0.1545471	-0.1547167
1	0	0	0	0

Table 5.2: Thermophysical properties of blood and silver

Property	**Blood (base fluid)**	**Silver (nanoparticle)**
$\boldsymbol{\rho}$	1063	10490
$\boldsymbol{C_p}$	3594	235
$\boldsymbol{k}$	0.492	429
$\boldsymbol{\sigma}$	0.8	6.3×10^7

Table 5.3: Variation in $Sh_x\ Re_x^{-\ 1/2}$ when $A = 0.5$, $\beta = 0.1$, $\lambda = 0.5$ & $\phi = 0.1$

Kr	**Le**	$\mathbf{C_{slip}}$	$\mathbf{Sh_x\ Re_x^{-1/2}}$			
			Sphere	***Cylinder***	***Platelet***	***Blade***
1.5	0.3	0.3	0.6166	0.6263	0.6261	0.6217
2.0	0.3	0.3	0.6773	0.6852	0.6850	0.6815
2.5	0.3	0.3	0.7298	0.7363	0.7362	0.7333
2.0	0.2	0.3	0.5737	0.5808	0.5807	0.5774
2.0	0.3	0.3	0.6773	0.6852	0.6850	0.6815
2.0	0.4	0.3	0.7594	0.7675	0.7674	0.7638
2.0	0.3	0.2	0.7265	0.7355	0.7354	0.7313
2.0	0.3	0.3	0.6773	0.6852	0.6850	0.6815
2.0	0.3	0.4	0.6343	0.6412	0.6411	0.6380

Figure 5.8 displays the negative impact of A on $g'(\eta)$ whereas Figure 5.9 displays the positive impact of β on $g'(\eta)$. Figure 5.10 explains the mixed effect of λ (reciprocal of magnetic Prandtl number) on $g'(\eta)$. Initially, elevating λ values decays $g'(\eta)$ and afterwards, a reversed trend is observed. The dual nature is evident from the relation that λ is inversely proportional to the momentum diffusivity. Figure 5.11 represents nanoparticle shape effect on $g'(\eta)$. The highest and lowest induced magnetic field profiles are recorded by cylindrical and spherical shaped silver nanoparticles, respectively.

The consequence of A on $\theta(\eta)$ is graphed in Figure 5.12. A decline in temperature is noted for the increasing A values. Figure 5.13 throws light into the constructive nature of ϕ on $\theta(\eta)$. Physically, the improvement in $\theta(\eta)$ is due to the increased thermal conductivity of fluid caused by the hike in nanoparticle volume fraction. In addition, the inherent nature of nanoparticles is bound to affect the temperature distribution. The influence of Q_T (linear heat source parameter) and R_d (thermal radiation parameter) on $\theta(\eta)$ is analyzed in Figures 5.14 & 5.15, respectively. Both parameters tend to increase $\theta(\eta)$. This can be associated with the fact that an increase in Q_T & R_d supplies supplemental energy to the system which triggers a surge in $\theta(\eta)$. Biologically, the increase in temperature profiles due to augmenting nanoparticle volume fraction, linear heat source, and thermal radiation unveils that the nanofluid can be used for killing tumors or cancerous cells.

The effect of T_{slip} (thermal slip parameter) is analyzed with the aid of Figure 5.16. It is noted that augmenting T_{slip} values lead to a decrease in $\theta(\eta)$. Augmentation in the thermal slip parameter reduces the sensitivity of the fluid flow within the boundary layer, which reduces the amount of heat produced and thereby reduces the temperature. The impact of nanoparticle shape on $\theta(\eta)$ is explained in Figure 5.17. The blade-shaped silver nanoparticles contribute the most towards $\theta(\eta)$ and cylinder-shaped silver nanoparticles contribute the least towards $\theta(\eta)$.

The parallel effect of ϕ, Q_T, R_d & T_{slip} with the differing nanoparticle shapes on $Nu_x\ Re_x^{-1/2}$ is elucidated in Figure 5.18 - 5.21. It is seen that ϕ & R_d promotes $Nu_x\ Re_x^{-1/2}$ whereas Q_T & T_{slip} demotes $Nu_x\ Re_x^{-1/2}$. A significant rise in the heat transfer rate is showcased by the blade-shaped silver nanoparticles followed by platelet, cylinder, and spherical-shaped nanoparticles, respectively.

Variation in $\psi(\eta)$ for differing A values is demonstrated in Figure 5.22 and it is perceived that A has a negative effect on $\psi(\eta)$. Figure 5.23 elucidates the effect of Le (Lewis number) on $\psi(\eta)$. $\psi(\eta)$ decreases with augmenting Le values. Figure 5.24 explains the negative impact of Kr (chemical reaction parameter) on $\psi(\eta)$. This can be associated with the fact that augmenting Kr values eats up the nanoparticle which decreases $\psi(\eta)$. Biologically, consumption of more nanoparticles is directly proportional to improved medication and hyperthermia. The impact of C_{slip} (solutal slip parameter) on $\psi(\eta)$ is graphed in Figure 5.25. It is seen that increasing C_{slip} values help in decreasing $\psi(\eta)$.

The consequence of pertinent parameters on $Sh_x\ Re_x^{-\ 1/2}$ is explained in Table 5.3. It is perceived that Kr & Le have a positive impact on $Sh_x\ Re_x^{-\ 1/2}$ and C_{slip} descends $Sh_x\ Re_x^{-\ 1/2}$. In addition, it is observed that the cylinder-shaped silver nanoparticles offer the highest $Sh_x\ Re_x^{-\ 1/2}$ value.

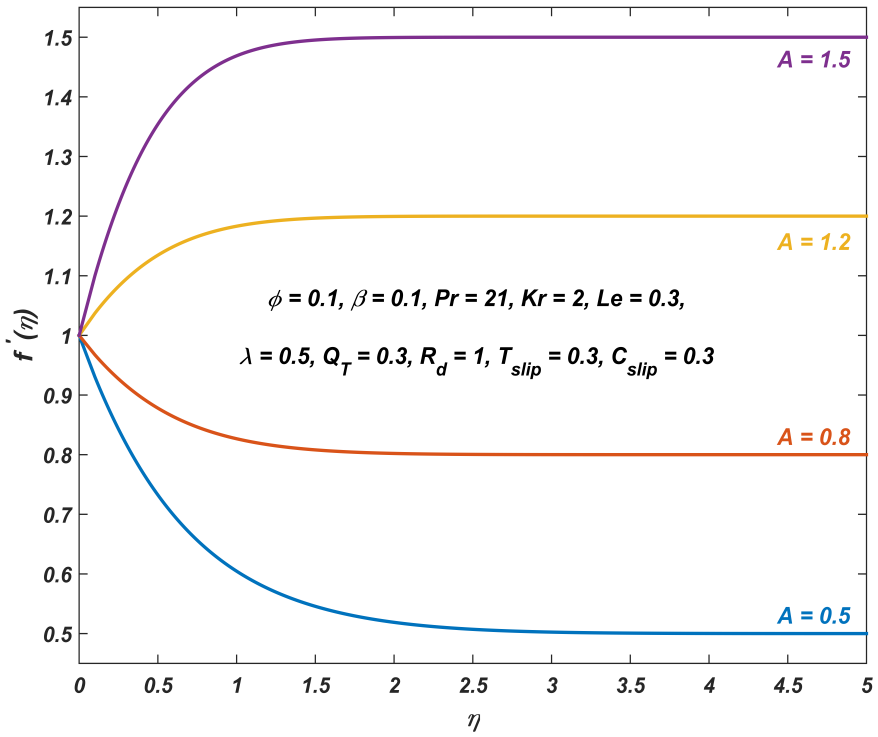

Figure 5.2: $f'(\eta)$ for differing A values

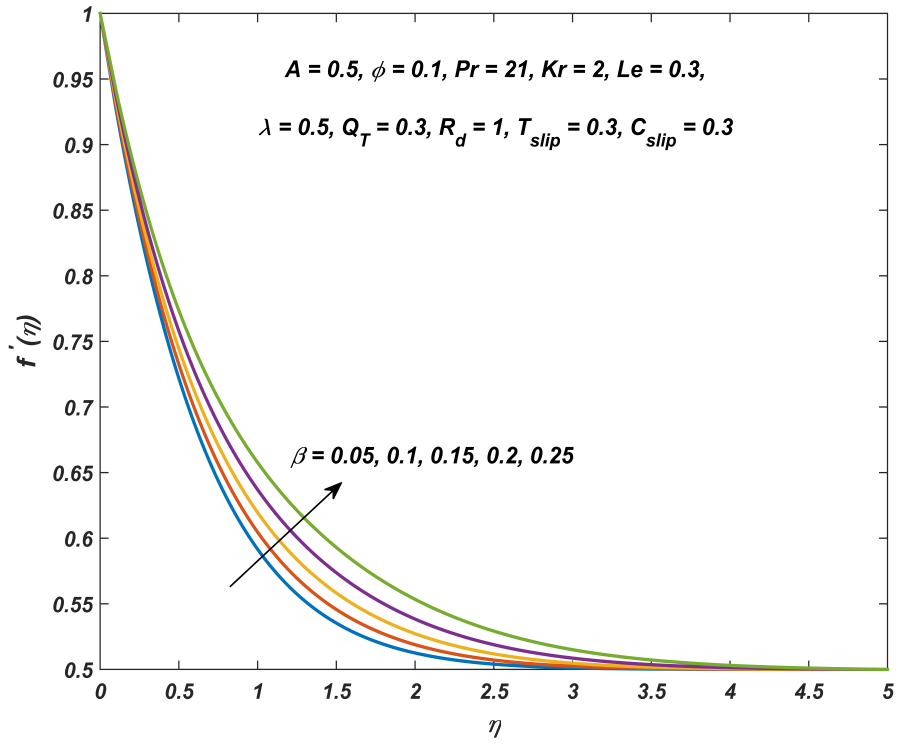

Figure 5.3: $f'(\eta)$ for differing β values

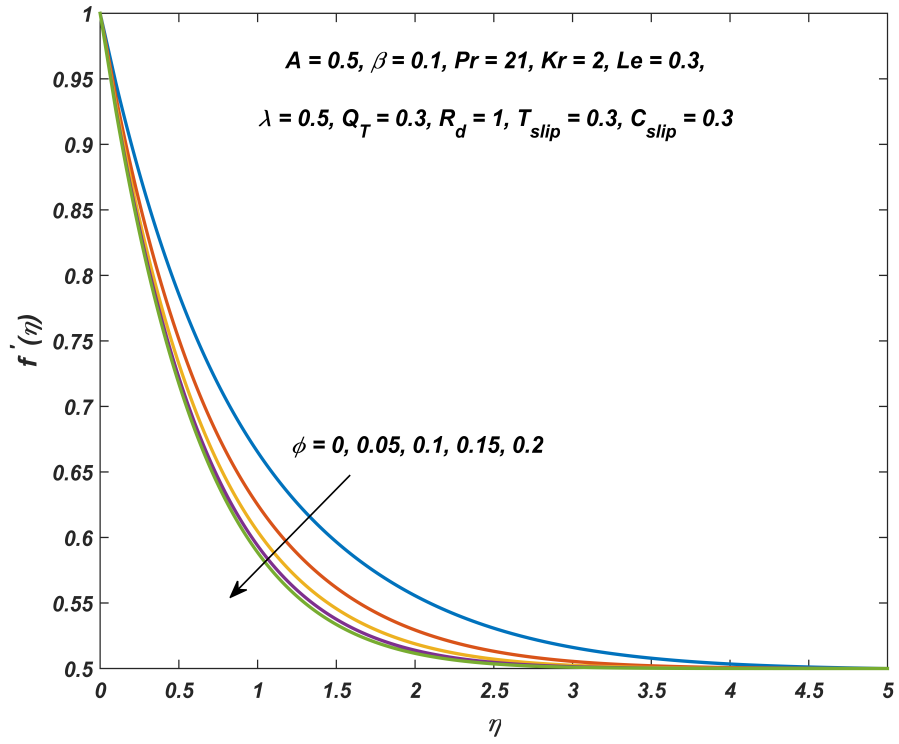

Figure 5.4: $f'(\eta)$ for differing ϕ values

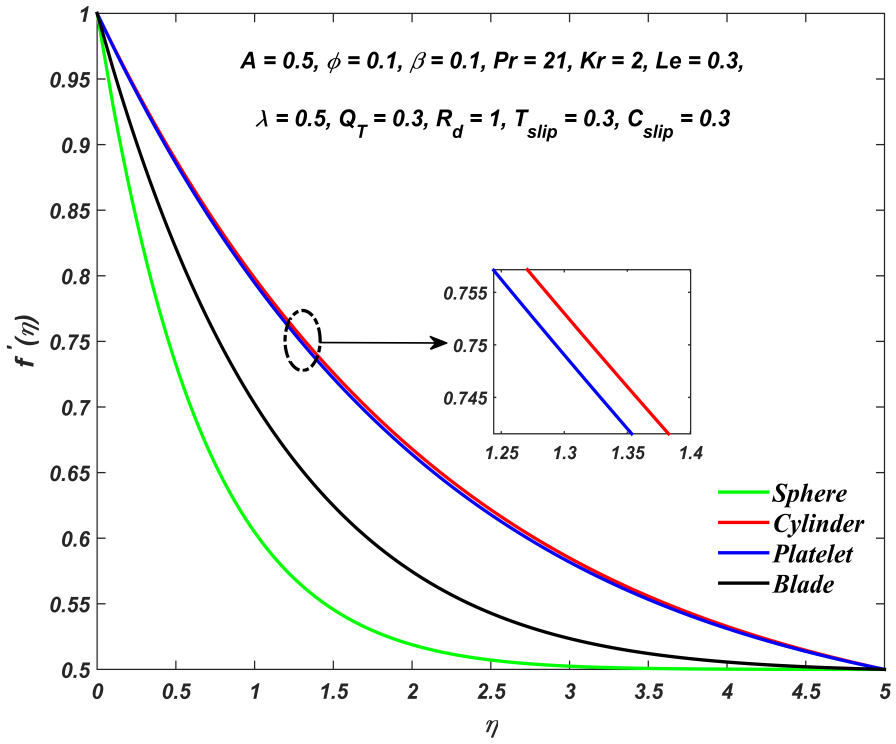

Figure 5.5: $f'(\eta)$ for differing nanoparticle shapes

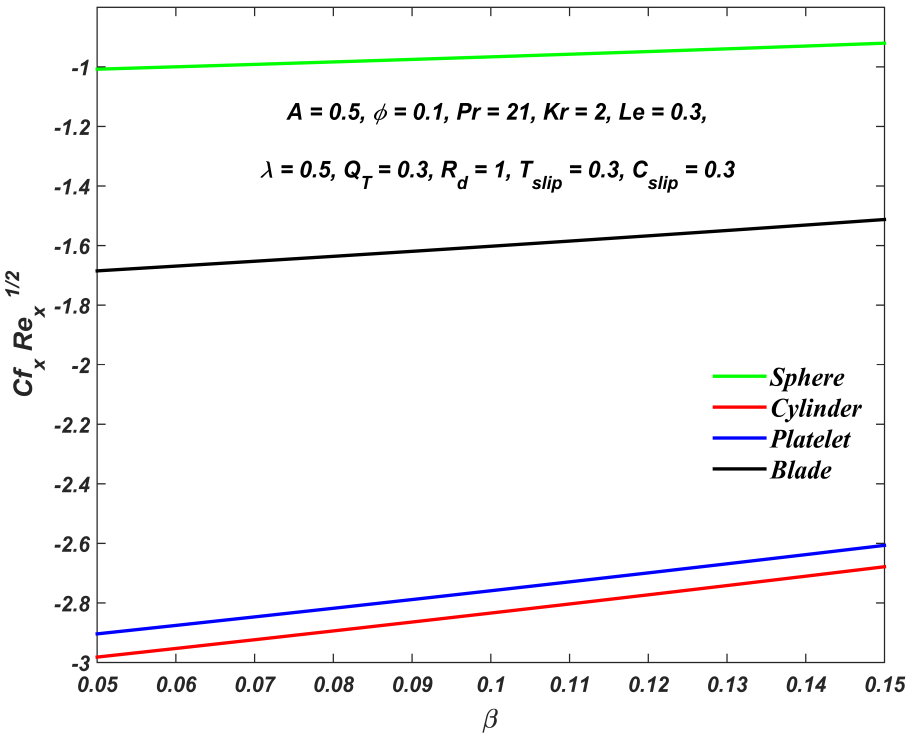

Figure 5.6: $Cf_x\ Re_x^{1/2}$ for differing nanoparticle shapes β values

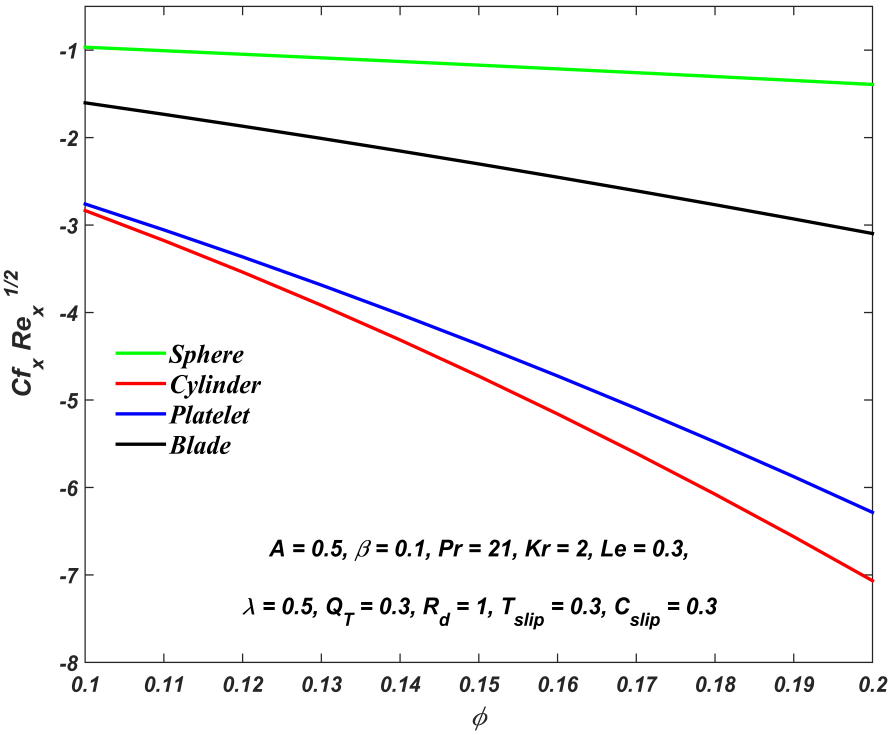

Figure 5.7: $Cf_x\ Re_x^{1/2}$ for differing nanoparticle shapes ϕ values

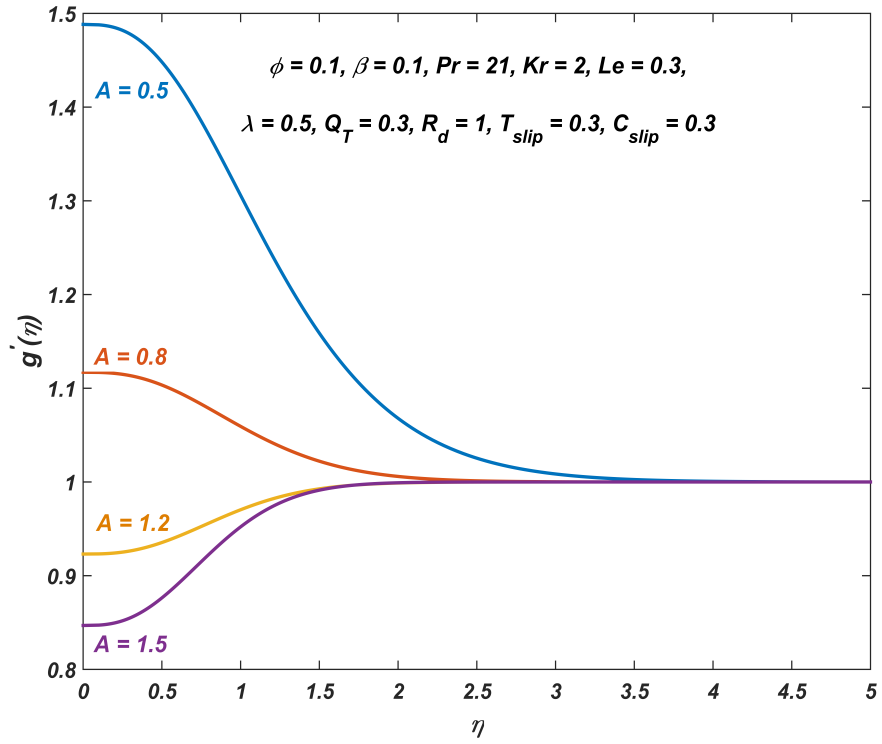

Figure 5.8: $g'(\eta)$ for differing A values

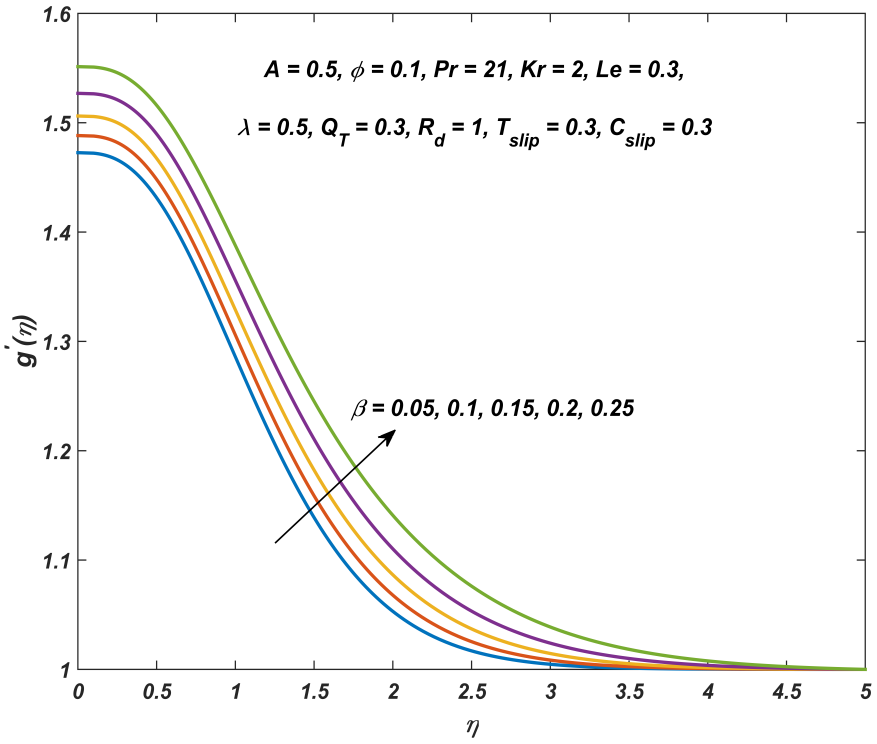

Figure 5.9: $g'(\eta)$ for differing β values

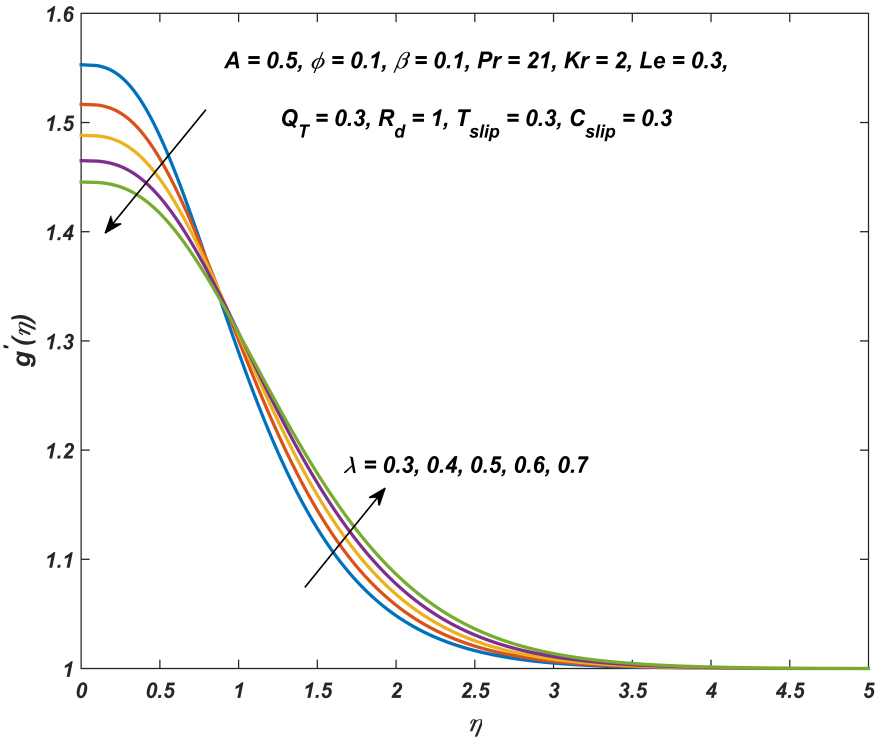

Figure 5.10: $g'(\eta)$ for differing λ values

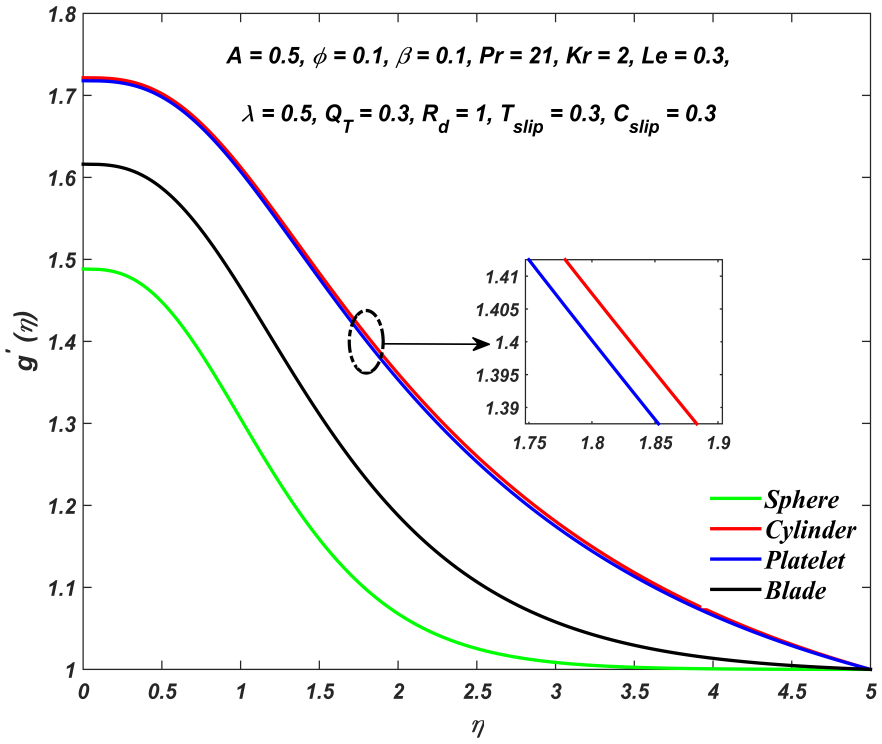

Figure 5.11: $g'(\eta)$ for differing nanoparticle shapes

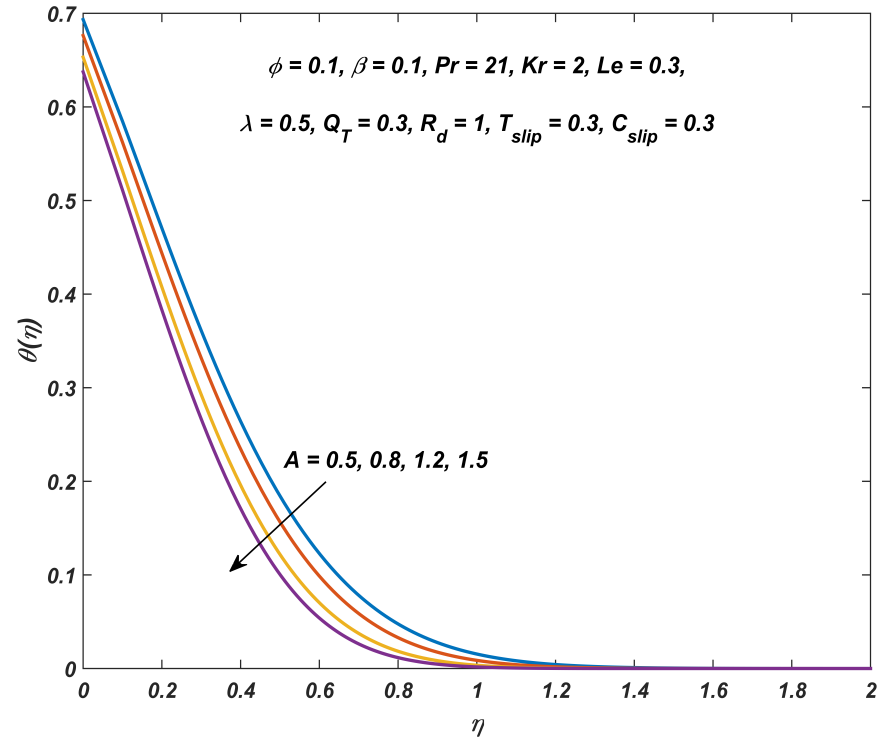

Figure 5.12: $\theta(\eta)$ for differing A values

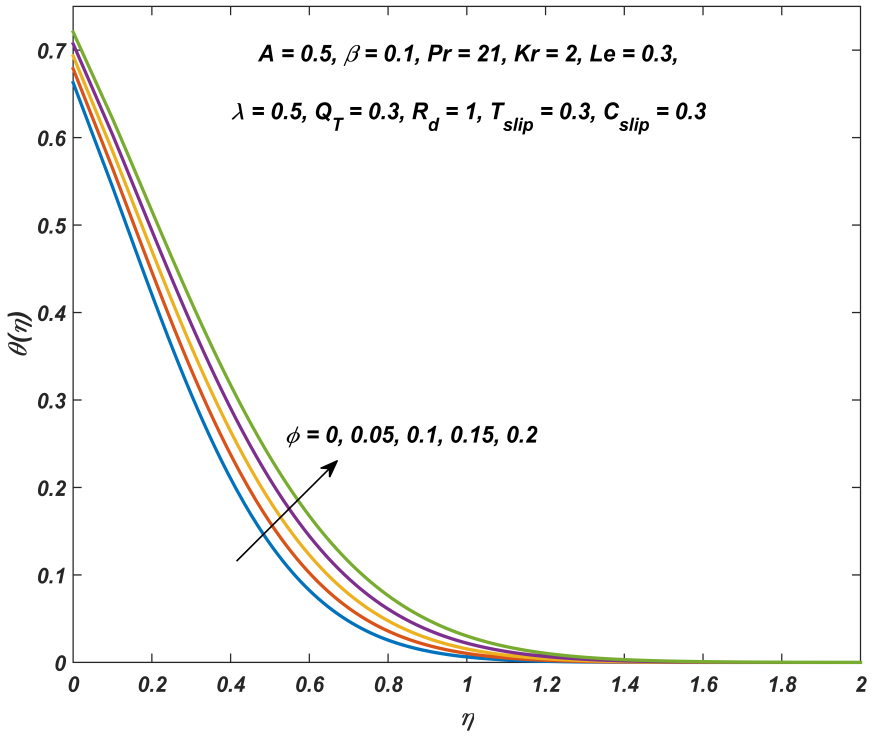

Figure 5.13: $\theta(\eta)$ for differing ϕ values

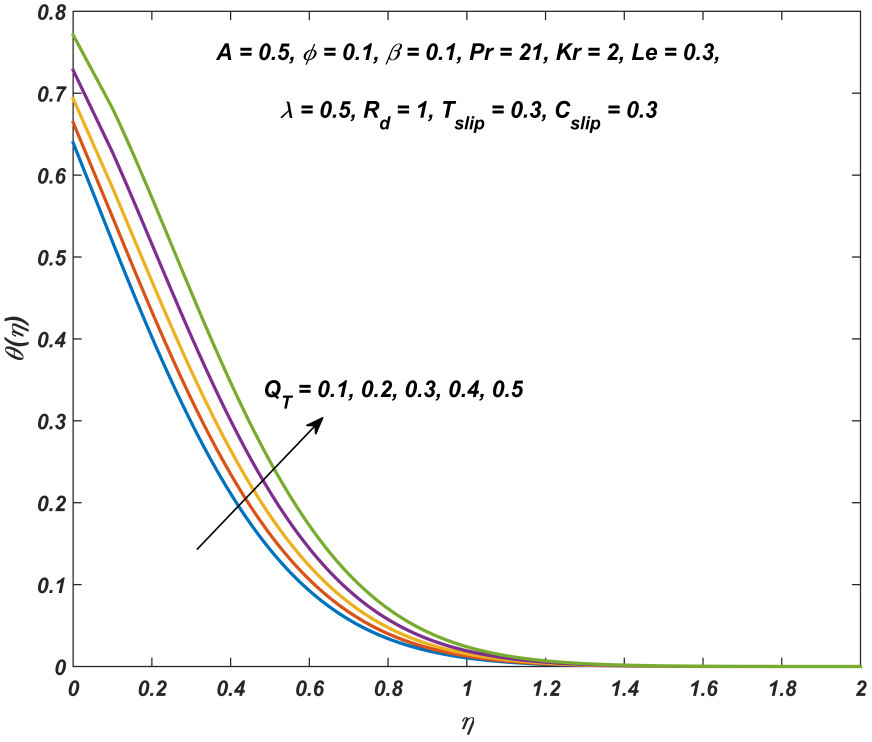

Figure 5.14: $\theta(\eta)$ for differing Q_T values

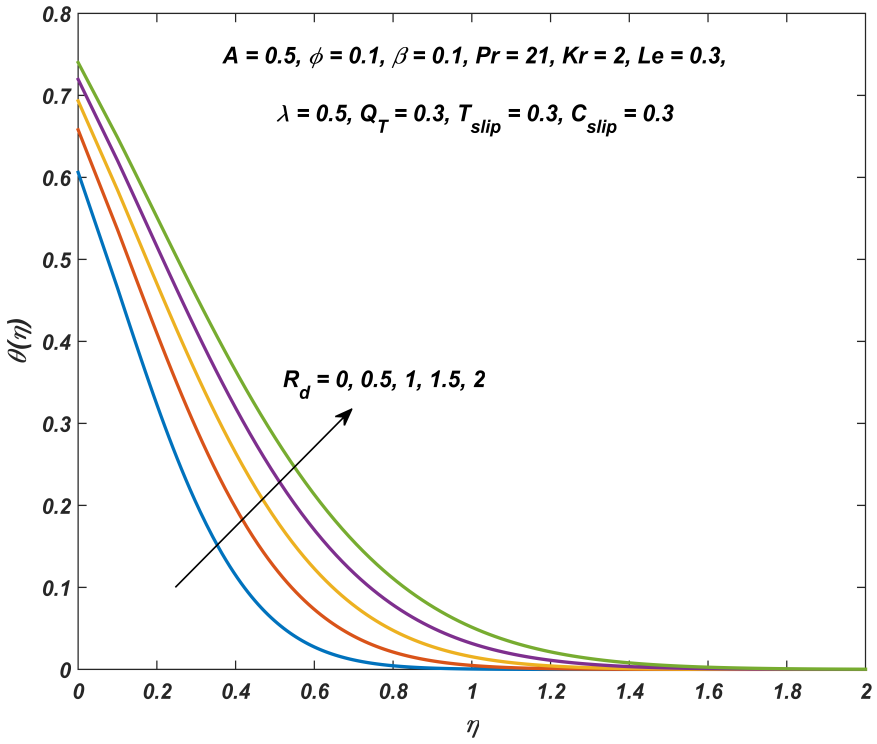

Figure 5.15: $\theta(\eta)$ for differing R_d values

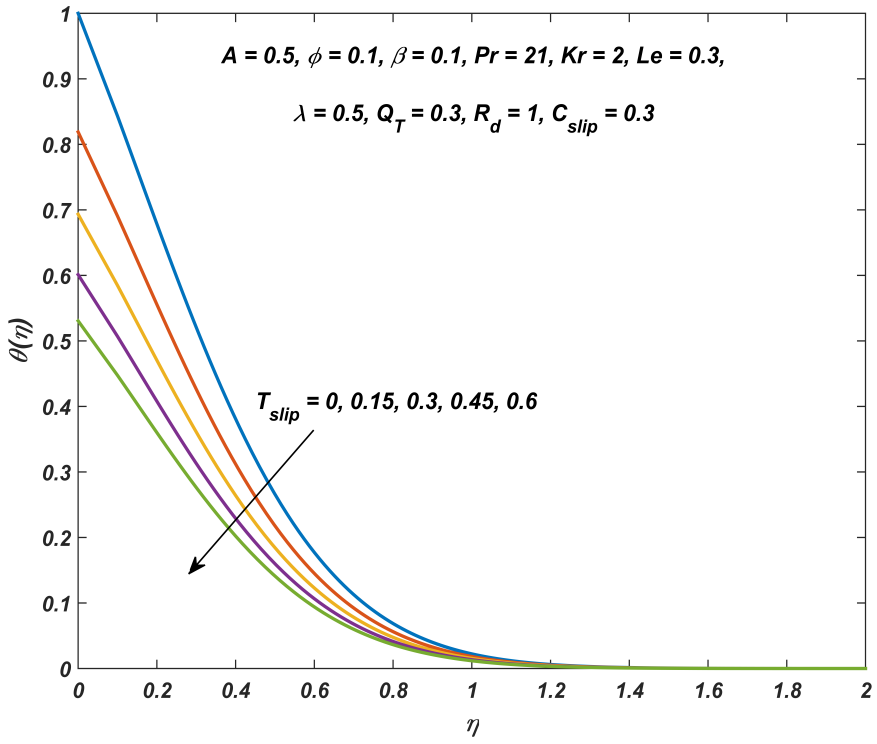

Figure 5.16: $\theta(\eta)$ for differing T_{slip} values

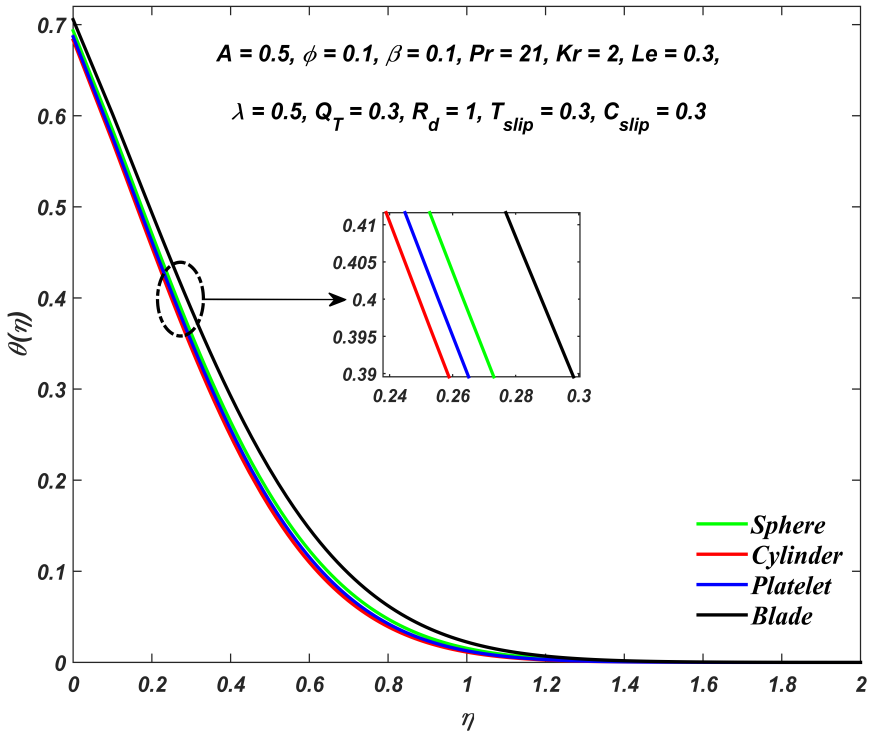

Figure 5.17: $\theta(\eta)$ for differing nanoparticle shapes

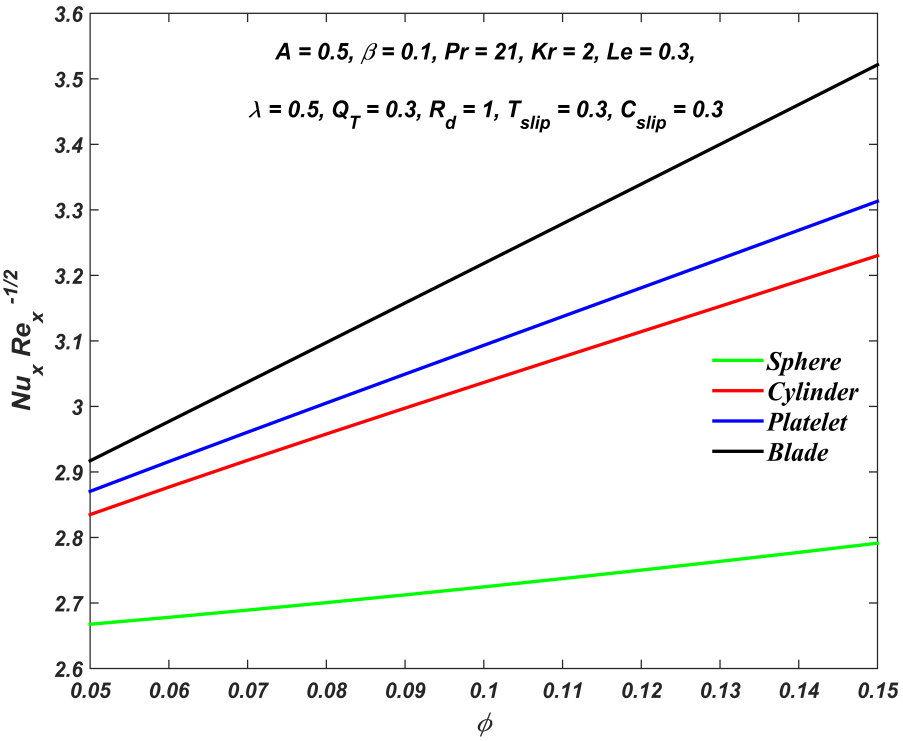

Figure 5.18: $Nu_x Re_x^{-1/2}$ for differing nanoparticle shapes and ϕ values

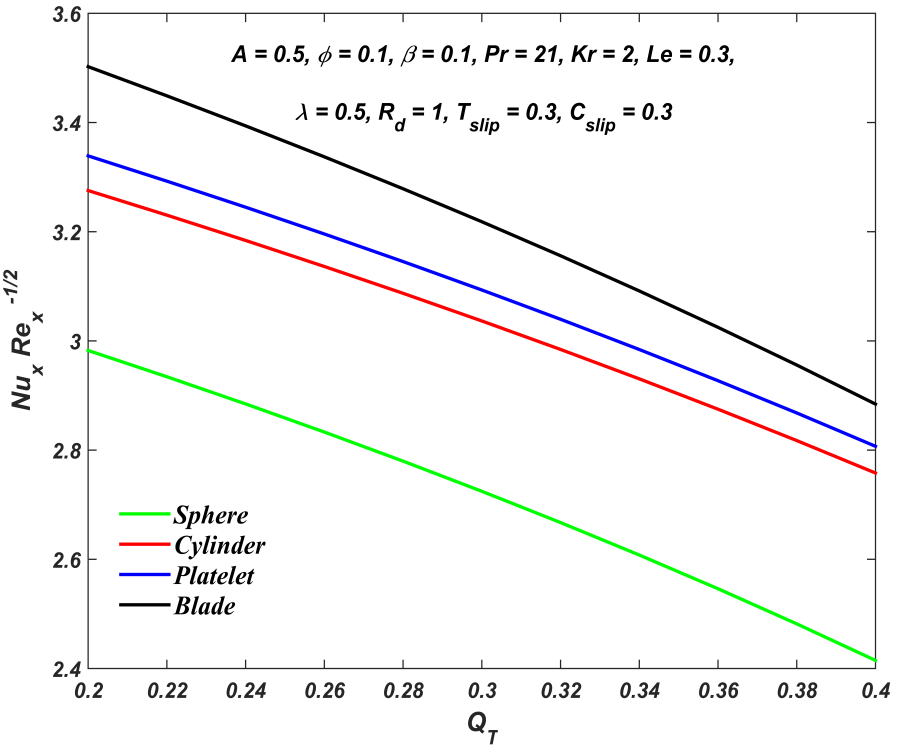

Figure 5.19: $Nu_x Re_x^{-1/2}$ for differing nanoparticle shapes and Q_T values

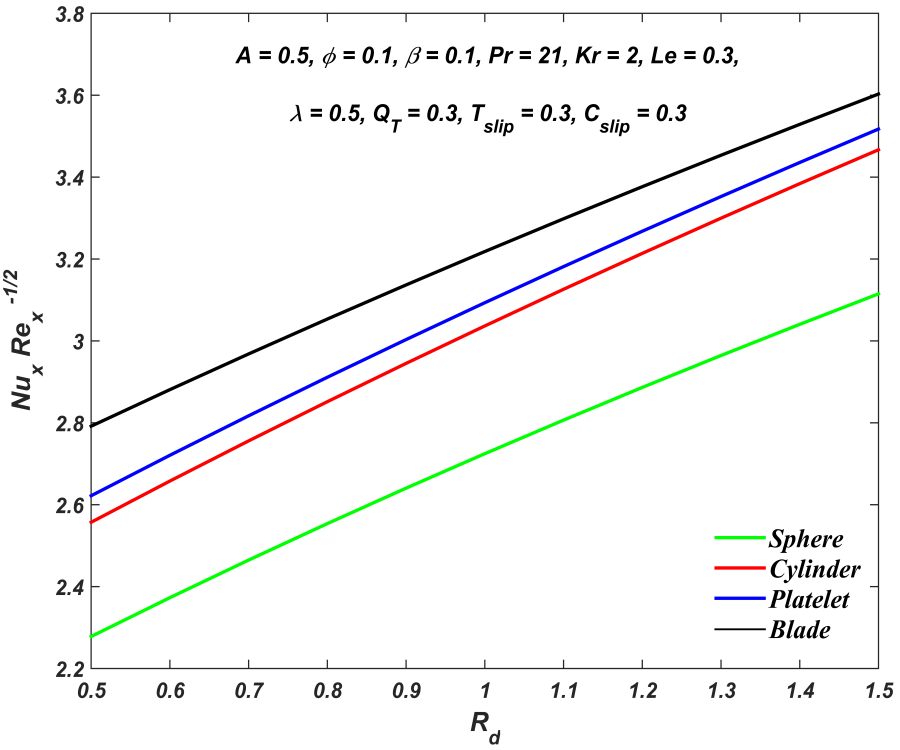

Figure 5.20: $Nu_x Re_x^{-1/2}$ for differing nanoparticle shapes and R_d values

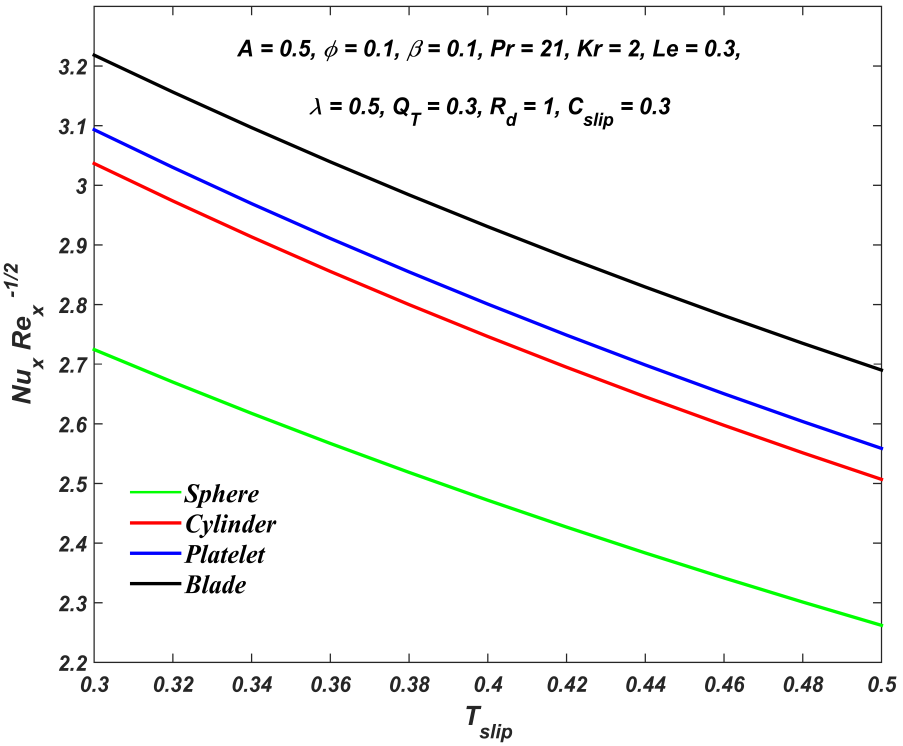

Figure 5.21: $Nu_x Re_x^{-1/2}$ for differing nanoparticle shapes and T_{slip} values

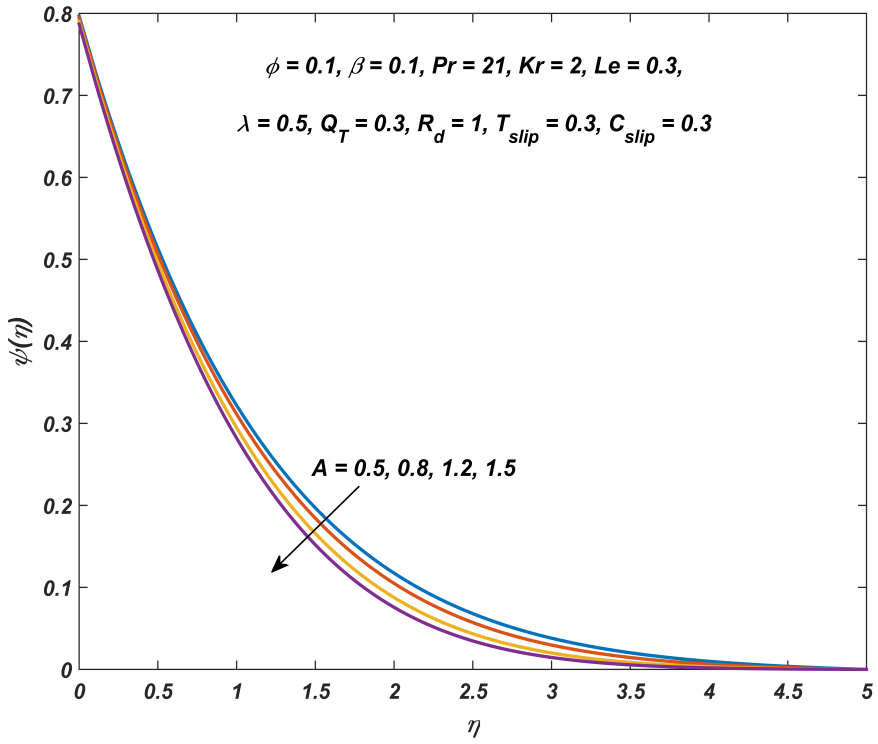

Figure 5.22: $\psi(\eta)$ for differing A values

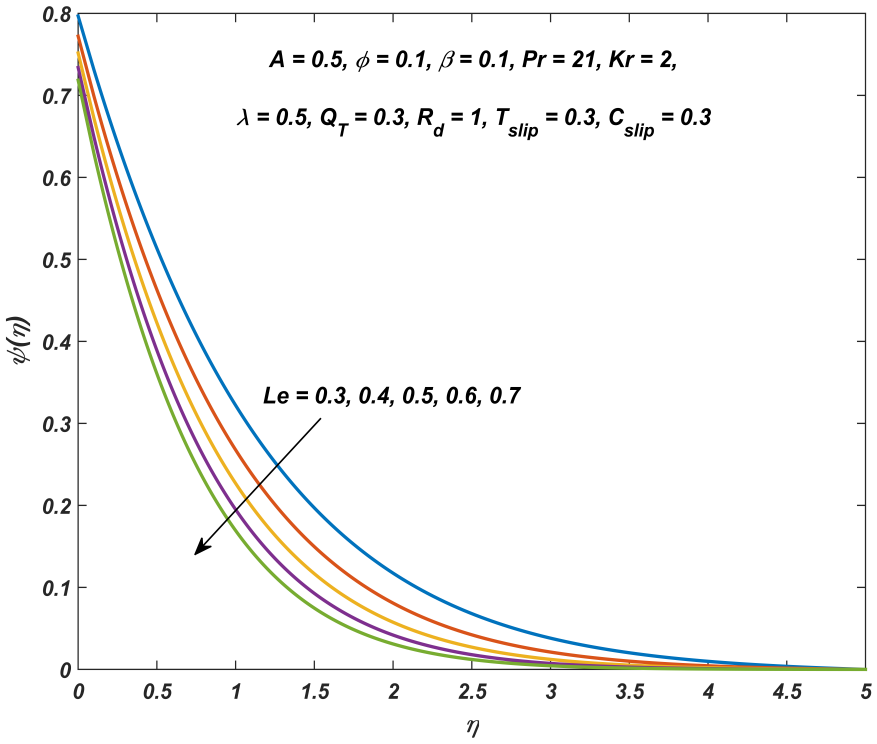

Figure 5.23: $\psi(\eta)$ for differing Le values

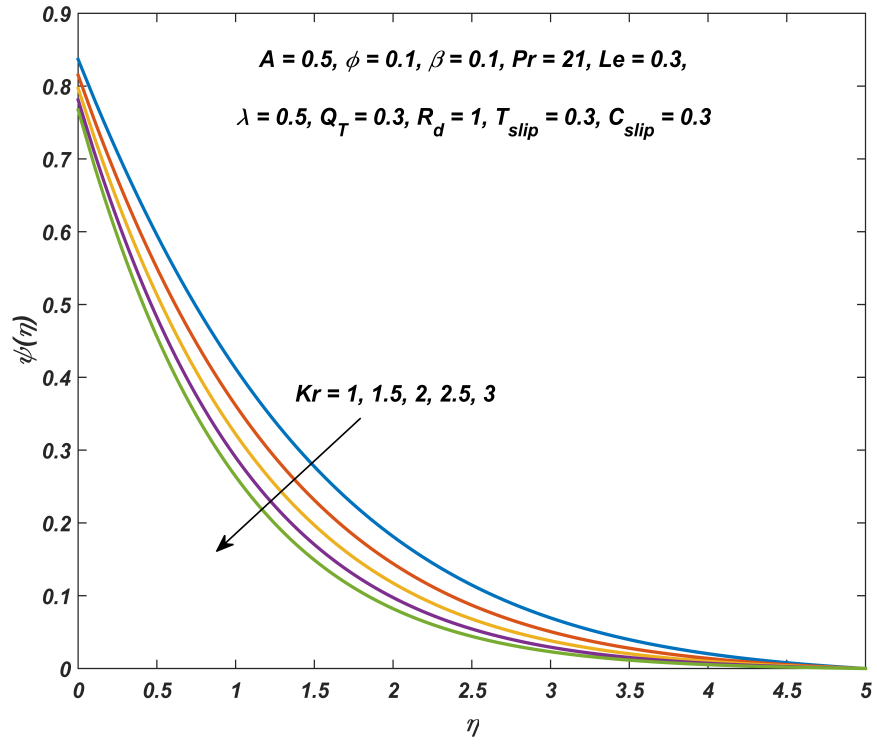

Figure 5.24: $\psi(\eta)$ for differing Kr values

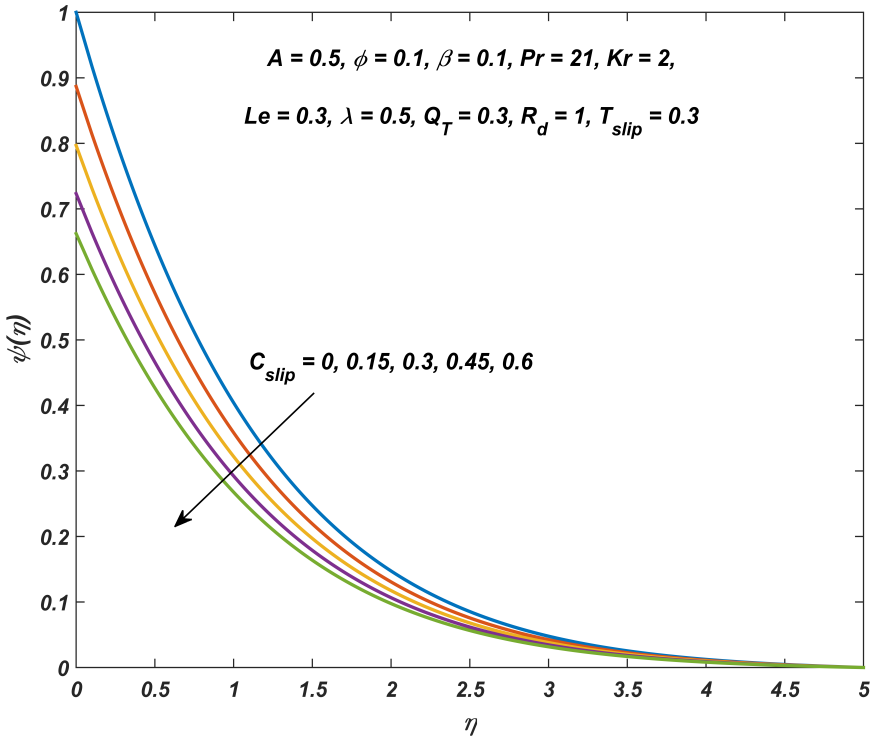

Figure 5.25: $\psi(\eta)$ for differing C_{slip} values

5.5 Conclusion

The influence of thermal and solutal slip on the stagnation point flow of blood-based silver nanomaterial in the presence of an induced magnetic field has been examined. The significance of spherical and non-spherical silver nanoparticles on the flow profiles and physical quantities has been analyzed. The key points drawn from the study are:

- Nanofluid temperature and nanofluid concentration reduce with increasing values of thermal slip and concentration slip parameters, respectively.
- Velocity and induced magnetic field profiles are least affected by spherical-shaped silver nanoparticles and highly affected by cylinder-shaped silver nanoparticles. Blade shaped silver nanoparticles contribute the most whereas cylinder-shaped silver nanoparticles contribute the least towards the nanofluid temperature.
- Nanofluid temperature ascends with augmenting linear heat source, thermal

radiation parameter, and volume fraction of silver nanoparticles.

- Blade shaped silver nanoparticles offer an increased heat transfer rate over the other nanoparticle shapes and cylinder-shaped silver nanoparticles exhibit the highest mass transfer rate. A significant rise in the surface drag is brought out by the spherical-shaped silver nanoparticles followed by blade, platelet, and cylinder-shaped nanoparticles.

Appendix I: Non-dimensional qunatities

$A = \frac{a}{c}$	Stretching parameter
$\beta = \frac{\mu_e}{4\pi\rho_f}\left(\frac{M_0}{c}\right)^2$	Magnetic parameter
$\lambda = \frac{1}{4\pi\mu_e\sigma_f\vartheta_f}$	Reciprocal of magnetic Prandtl number
$Pr = \frac{(\mu C_p)_f}{k_f} = \frac{\vartheta_f}{\alpha_f}$	Prandtl number
$Kr = \frac{k_r}{c}$	Chemical reaction parameter
$R_d = \frac{4\sigma^* {T_\infty}^3}{k^* k_f}$	Thermal radiation parameter
$Le = \frac{\vartheta_f}{D_B}$	Lewis number
$Q_T = \frac{q_T}{c\,(\rho C_p)_f}$	Linear heat source parameter
$T_{slip} = N_1\sqrt{\frac{c}{\vartheta_f}}$	Thermal slip parameter
$C_{slip} = N_2\sqrt{\frac{c}{\vartheta_f}}$	Solutal slip parameter

Appendix II: Nomenclature

a, c	Dimensional constants	q_T	Heat source coefficient
u, v	Velocity components	M_0	Uniform magnetic field at infinity
q_r	Radiative heat flux	T_∞	Ambient fluid temperature
N_1	Temperature slip factor	N_2	Concentration slip factor
C	Fluid concentration	k^*	Mean absorption coefficient
T	Fluid temperature	Q_T	Linear heat source
x, y	Cartesian coordinates	C_w	Nanoparticle concentration near wall
T_w	Wall fluid temperature	C_∞	Ambient nanoparticle concentration
C_p	Specific heat	Cf_x	Local drag coefficient
k_r	Reaction rate constant	Nu_x	Local Nusselt number
Sh_x	Local Sherwood number	R_d	Thermal radiation parameter
σ	Electrical conductivity	M_e	Magnetic field at free stream
η	Dimensionless variable	D_B	Mass diffusivity
ϑ	Kinematic viscosity	σ^*	Stefan- Boltzmann constant
k	Thermal conductivity	μ_e	Magnetic permeability
ρ	Fluid density	λ	Reciprocal of magnetic Prandtl number
β	Magnetic parameter	ϕ	Nanoparticle volume fraction
α_m	Magnetic diffusivity	α	Thermal diffusivity

Chapter 6

Bioconvective EMHD nanofluid flow past a stretching sheet *

6.1 Introduction

Carbon nanotubes (CNTs) are highly recognized for their diverse biomedical applications. Electromagnetohydrodynamics (EMHD) is the area that concerns the study of dynamics of electrically conducting fluids under the influence of the magnetic and electric fields. EMHD has raised quite an interest over the years due to its versatile application in geophysics, engineering, biomedical engineering, magnetic drug targeting and many others. The present study aims to numerically and statistically study the stratification effects of bioconvective EMHD flow past a stretching sheet using water-based CNT. The current study, with applications ranging from biomedical imaging, targeted drug delivery, and cancer therapy, provides a theoretical perspective that is beneficial in biomedical engineering. The mathematically modelled system of partial differential equations (PDEs) is then transmuted into a system of ordinary differential equations (ODEs) using apposite transformations which are then resolved numerically using *bvp*5*c* (MATLAB built-in function) algorithm. The impact of influential parameters on concentration, velocity, microbial concentration, temperature and physical quantities are illustrated with the aid of graphs and tables. Further, statistical techniques like correlation, the slope of linear regression, probable error and multiple linear regression are employed in scrutinizing the consequence of influential parameters on physical quantities. The main objectives of the current chapter are to:

*Published in: Heat Transfer (Wiley), 2021; 50(7); 6680-6702.

- Construct the mathematical model to study the EMHD bioconvective CNT nanofluid flow past a stretching sheet considering thermal, solutal, and motile density stratification effects.
- Provide theoretical knowledge on the consequence of pertinent parameters on flow profiles.
- Predict the formulae for drag coefficient and heat transfer rate using multiple linear regression.

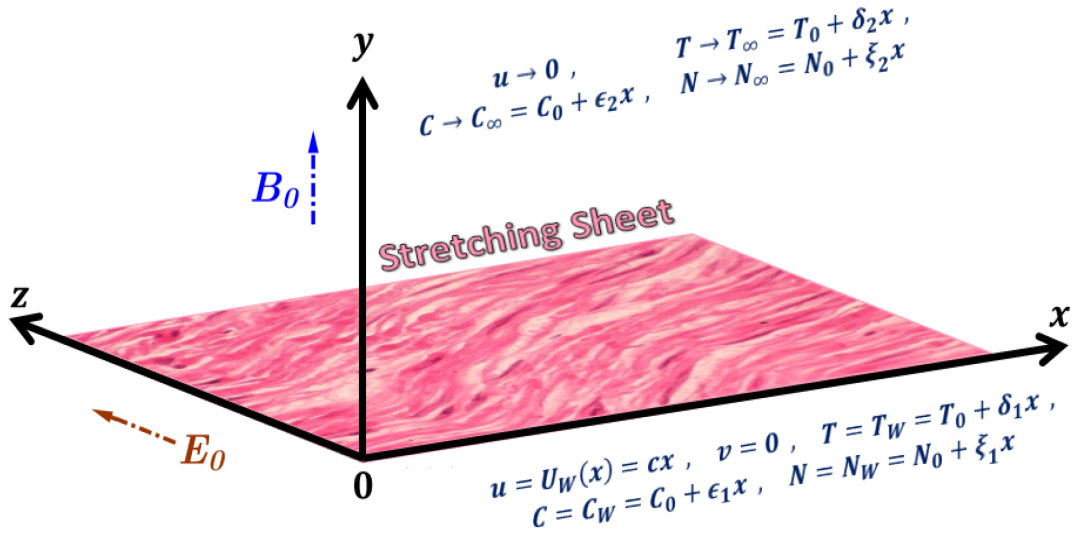

Figure 6.1: Geometrical Frame

6.2 Mathematical Frame

Consider a two-dimensional steady incompressible bioconvective flow over a lengthening sheet positioned along $x-$axis (see Figure 6.1) stretching with a velocity $U_W(x) = cx$. Water-based SWCNT nanofluid (containing microorganisms) occupies the region $y > 0$. A uniform electric field of strength E_0 and a uniform magnetic field of strength B_0 is applied normal to the fluid flow. Thermal, solutal and motile density stratification effects are incorporated. Further, viscous dissipation and chemical reaction effects are also considered.

Under these assumptions, the governing equations take the form (see Daniel et al., 2020; Daniel, Aziz, Ismail, & Salah, 2017a):

$$\frac{\partial u}{\partial x}+\frac{\partial v}{\partial y}=0 \tag{6.2.1}$$

$$u\frac{\partial u}{\partial x}+v\frac{\partial u}{\partial y}=\left(\frac{\mu_{nf}}{\rho_{nf}}\right)\frac{\partial^2 u}{\partial y^2}+\frac{\sigma_{nf}\ \left(E_0\ B_0-{B_0}^2\ u\right)}{\rho_{nf}} \tag{6.2.2}$$

$$u\frac{\partial T}{\partial x}+v\frac{\partial T}{\partial y}=\alpha_{nf}\frac{\partial^2 T}{\partial y^2}+\frac{\mu_{nf}}{(\rho C_p)_{nf}}\left(\frac{\partial u}{\partial y}\right)^2 \tag{6.2.3}$$

$$u\frac{\partial C}{\partial x}+v\frac{\partial C}{\partial y}=D_B\frac{\partial^2 C}{\partial y^2}-k_r\left(C-C_\infty\right) \tag{6.2.4}$$

$$u\frac{\partial N}{\partial x}+v\frac{\partial N}{\partial y}+\frac{bW_c}{C_W-C_0}\left(\frac{\partial}{\partial y}\left(N\frac{\partial C}{\partial y}\right)\right)=D_m\frac{\partial^2 N}{\partial y^2} \tag{6.2.5}$$

subject to the boundary conditions (Daniel et al., 2020, 2017a; Alsaedi et al., 2017):

$$\begin{gathered}u=U_W(x)=cx,\ v=0,\ T=T_W=T_0+\delta_1 x,\\ C=C_W=C_0+\epsilon_1 x,\ N=N_W=N_0+\xi_1 x \qquad \text{at } y=0\end{gathered}$$

$$\begin{gathered}u\to 0,\ T\to T_\infty=T_0+\delta_2 x,\\ C\to C_\infty=C_0+\epsilon_2 x,\ N\to N_\infty=N_0+\xi_2 x \qquad \text{as } y\to\infty\end{gathered}$$

Consider the following similarity transformations (see W. Khan & Pop, 2010; Alsaedi et al., 2017):

$$u=cxf\,'(\eta),\ v=-\sqrt{c\vartheta_f}f(\eta),\ \eta=y\sqrt{\frac{c}{\vartheta_f}},$$

$$\theta(\eta)=\frac{T-T_\infty}{T_W-T_0},\ \psi(\eta)=\frac{C-C_\infty}{C_W-C_0},\ \chi(\eta)=\frac{N-N_\infty}{N_W-N_0}$$

Employing the similarity transformations into Equations (6.2.1) – (6.2.5), we get:

$$f\,'''-A_1\ A_2\ \left\{\ (f\,')^2-f\ f\,''-\frac{A_5}{A_2}\ (M(\ E-f\,'))\ \right\}=0 \tag{6.2.6}$$

$$\theta\,''+\frac{A_3\ Pr}{A_4}\ f\ \theta\,'+\frac{Ec\ Pr}{A_1\ A_4}\ (f\,'')^2=0 \tag{6.2.7}$$

$$\psi\,''+Le\ f\ \psi\,'-Kr\ Le\ \psi=0 \tag{6.2.8}$$

$$\chi\,'' + Lb\ f\ \chi\,' - Pe\ \{\ (\ \chi + \Omega\ )\ \ \psi\,'' + \chi\,'\ \psi\,'\ \} = 0 \tag{6.2.9}$$

subject to the boundary conditions

$$f\,(0) = 0,\ \ f\,'(0) = 1,\ \ \theta\,(0) = 1 - s_1,\ \ \psi\,(0) = 1 - s_2,\ \ \chi\,(0) = 1 - s_3,$$
$$f\,'(\infty) \to 0,\ \ \theta\,(\infty) \to 0,\ \ \psi\,(\infty) \to 0,\ \ \chi\,(\infty) \to 0.$$

where the dimensionless parameters are given in appendix I.
The nanofluid models incorporated are (see Z. Iqbal, Azhar, & Maraj, 2017; Sreedevi & Reddy, 2019):

Effective Dynamic Viscosity : $\dfrac{\mu_{nf}}{\mu_f} = \dfrac{1}{(1-\phi)^{2.5}} = \dfrac{1}{A_1}$

Effective Density : $\dfrac{\rho_{nf}}{\rho_f} = (1-\phi) + \phi\left(\dfrac{\rho_{SWCNT}}{\rho_f}\right) = A_2$

Effective Specific Heat : $\dfrac{(\rho C_p)_{nf}}{(\rho C_p)_f} = (1-\phi) + \phi\left(\dfrac{(\rho C_p)_{SWCNT}}{(\rho C_p)_f}\right) = A_3$

Effective Thermal Conductivity : $\dfrac{k_{nf}}{k_f} = \dfrac{(1-\phi) + 2\phi\ \frac{k_{SWCNT}}{k_{SWCNT}-k_f}\ ln\left(\frac{k_{SWCNT}+k_f}{2k_f}\right)}{(1-\phi) + 2\phi\ \frac{k_f}{k_{SWCNT}-k_f}\ ln\left(\frac{k_{SWCNT}+k_f}{2k_f}\right)} = A_4$

Effective Electrical Conductivity : $\dfrac{\sigma_{nf}}{\sigma_f} = 1 + \dfrac{3\left(\frac{\sigma_{SWCNT}}{\sigma_f} - 1\right)\phi}{\left(\frac{\sigma_{SWCNT}}{\sigma_f} + 2\right) - \left(\frac{\sigma_{SWCNT}}{\sigma_f} - 1\right)\phi} = A_5$

The physical quantities are given by (see Z. Iqbal, Azhar, & Maraj, 2017; Daniel et al., 2020, 2017a; Alsaedi et al., 2017):

Local drag coefficient : $Cf_x = \dfrac{\tau_\omega}{\rho_f\ (U_W)^2} = \dfrac{\mu_{nf}\ \left.\frac{\partial u}{\partial y}\right|_{y=0}}{\rho_f\ (U_W)^2}$

$$\Rightarrow\ Cf_x\ Re_x^{1/2} = \frac{f\,''(0)}{A_1}$$

$$\text{Local Nusselt number} \quad : \quad Nu_x = \frac{x\ q_\omega}{k_f\ (T_W - T_0)} = \frac{-x\ k_{nf}\ \left.\frac{\partial T}{\partial y}\right|_{y=0}}{k_f\ (T_W - T_0)}$$

$$\Rightarrow\ Nu_x\ Re_x^{-\ 1/2} = -A_4\ \theta\,'(0)$$

$$\text{Local Sherwood number} \quad : \quad Sh_x = \frac{x\ q_m}{D_B\ (C_W - C_0)} = \frac{-x\ D_B\ \left.\frac{\partial C}{\partial y}\right|_{y=0}}{D_B\ (C_W - C_0)}$$

$$\Rightarrow\ Sh_x\ Re_x^{-\ 1/2} = -\ \psi\,'(0)$$

$$\text{Local motile density number} \quad : \quad Nn_x = \frac{x\ q_n}{D_m\ (N_W - N_0)} = \frac{-x\ D_m\ \left.\frac{\partial N}{\partial y}\right|_{y=0}}{D_m\ (N_W - N_0)}$$

$$\Rightarrow\ Nn_x\ Re_x^{-\ 1/2} = -\ \chi\,'(0)$$

where $Re_x = \frac{xU_W}{\vartheta_f}$ is the local Reynold's number.

6.3 Numerical Frame & Validation

Equations (6.2.6) – (6.2.9) along with the boundary conditions are resolved numerically manoeuvring *bvp*5*c* solver, a MATLAB built-in function. For this, choose:

$$f = y_1,\ f\,' = y_2,\ f\,'' = y_3,\ \theta = y_4,\ \theta\,' = y_5,\ \psi = y_6,\ \psi\,' = y_7,\ \chi = y_8,\ \chi\,' = y_9$$

Accordingly, the system of first-order ODEs is given by:

$$y_1^{'} = y_2,\ y_2^{'} = y_3,\ y_3^{'} = A_1\ A_2\ \left\{\ (y_2)^2 - y_1\ y_3 - \tfrac{A_5}{A_2}\ (M\,(E - y_2))\ \right\}$$

$$y_4^{'} = y_5,\ y_5^{'} = -\tfrac{A_3\ Pr}{A_4}\ y_1\ y_5 - \tfrac{Ec\ Pr}{A_1\ A_4}\ (y_3)^2$$

$$y_6^{'} = y_7,\ y_7^{'} = Kr\ Le\ y_6 - Le\ y_1\ y_7$$

$$y_8^{'} = y_9,\ y_9^{'} = Pe\ \left\{\ (y_8\ + \Omega)\ y_7^{'} + y_9\ y_7\ \right\} - Lb\ y_1\ y_9.$$

with

$$y_1\,(0) = 0,\ \ y_2\,(0) = 1,\ \ y_4\,(0) = 1 - s_1,\ \ y_6\,(0) = 1 - s_2,\ \ y_8\,(0) = 1 - s_3,$$
$$y_2\,(\infty) \to 0,\ \ y_4\,(\infty) \to 0,\ \ y_6\,(\infty) \to 0,\ \ y_8\,(\infty) \to 0.$$

Validation of the current problem and accuracy of the code have been accounted for through a restrictive comparison of the present work with prior published works of W. A. Khan et al., 2010; Wang, 1989 (showcased in Table 6.1) and a commendable agreement is noted.

Table 6.1: Comparison of $Nu_x(Re_x)^{-1/2}$ for differing Pr values between the present study and the works of W. A. Khan et al., 2010; Wang, 1989 when $M = E = Kr = Ec = Le = Lb = Pe = \Omega = s_1 = s_2 = s_3 = 0$

Pr	$\mathbf{Nu_x(Re_x)^{-1/2}}$		
	W. A. Khan et al., 2010	**Wang, 1989**	**Present study**
0.7	0.4539	0.4539	0.4539
2	0.9113	0.9114	0.9114
7	1.8954	1.8954	1.8954
20	3.3539	3.3539	3.3539
70	6.4621	6.4622	6.4622

Table 6.2: Thermophysical properties of water and SWCNT

Property	**Water (base fluid)**	**SWCNT (nanoparticle)**
$\boldsymbol{\rho}$	997	2600
$\boldsymbol{C_p}$	4179	425
$\boldsymbol{k}$	0.613	6600
$\boldsymbol{\sigma}$	0.05	10^6

6.4 Results & Discussion

The consequence of various influential parameters on microbial concentration ($\chi(\eta)$), velocity ($f'(\eta)$), concentration ($\psi(\eta)$), and temperature ($\theta(\eta)$) profiles are illustrated via Figures 6.2 - 6.9 with Prandtl number and infinity fixed at 6.2 and 3, respectively. Thermophysical properties of SWCNT and water are showcased in Table 6.2.

Figure 6.2 describes the decreasing nature of when magnetic field parameter is increased meaning that the velocity drops when the magnetic field parameter is increased. Physically, it is associated with the generation of Lorentz force (a frictional force) which reduces the velocity. From Figure 6.3, it is observed that the velocity improves due to augmenting electric field parameter. Biologically, magnetic field and electric field parameters play a crucial role since these parameters are responsible for manipulating the transport of nanofluid to the desired location and also for improved biomedical imaging.

Figure 6.4 indicates that nanoparticle volume fraction (ϕ) enhances the temperature profile. This increase in temperature can be related to the improvement in the thermal conductivity of the nanofluid caused by larger nanoparticle occupancy. The analysis on the effect of ϕ on the temperature unveils that the nanofluid can be used for killing tumors or cancerous cells. The impact of Eckert number (Ec) is depicted in Figure 6.5. As Ec is amplified, the temperature profile enlarges. Physically, it is associated with the generation of friction forces between the fluid particles which increases the temperature profile. A decline in temperature is noted when the thermal stratification parameter (s_1) is increased (see Figure 6.6). Physically, the decrease in temperature is due to the decrease in the temperature difference between the surface and away from the surface caused by an increase in s_1.

A decline in concentration is noted (see Figure 6.7) when the chemical reaction parameter (Kr) is increased. Physical reason being that an increase in Kr consumes more nanoparticles and hence concentration decreases. Biologically, consumption of more nanoparticles is directly proportional to improved medication and biomedical imaging. A decline in concentration is noted (due to the decrease in the volumetric fraction between the surface and reference nanoparticles) when the solutal stratification parameter (s_2) is increased (see Figure 6.8). The variation of motile density stratification parameter (s_3) is given in Figure 6.9. A decline in microbial concentration is noted. Physically, an augmentation in s_3 decreases the concentration difference of microorganisms between the surface and away from the surface and hence microbial concentration decreases.

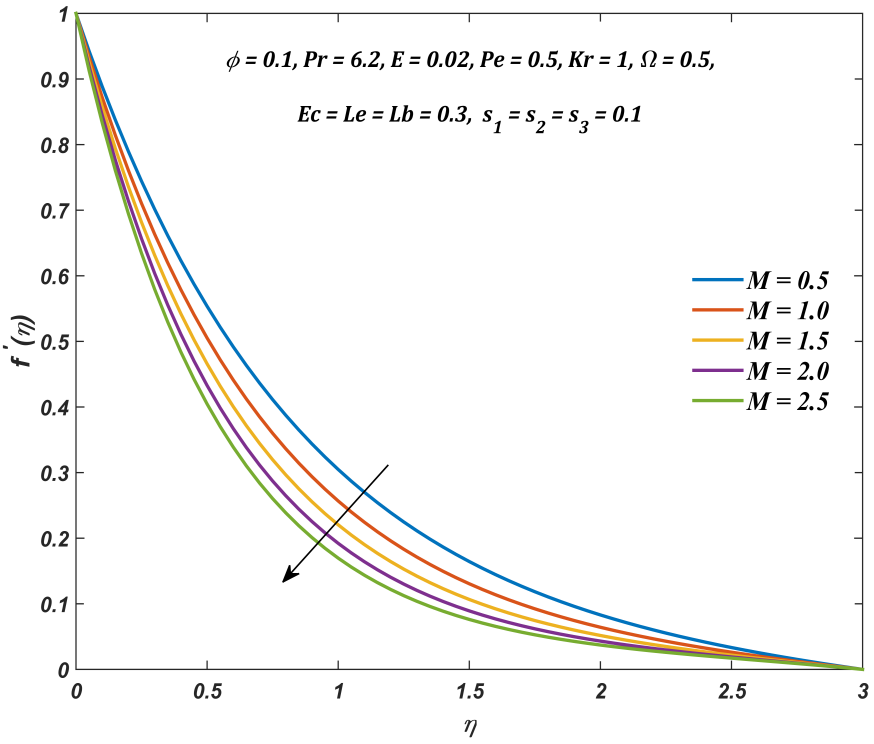

Figure 6.2: $f'(\eta)$ for differing M values

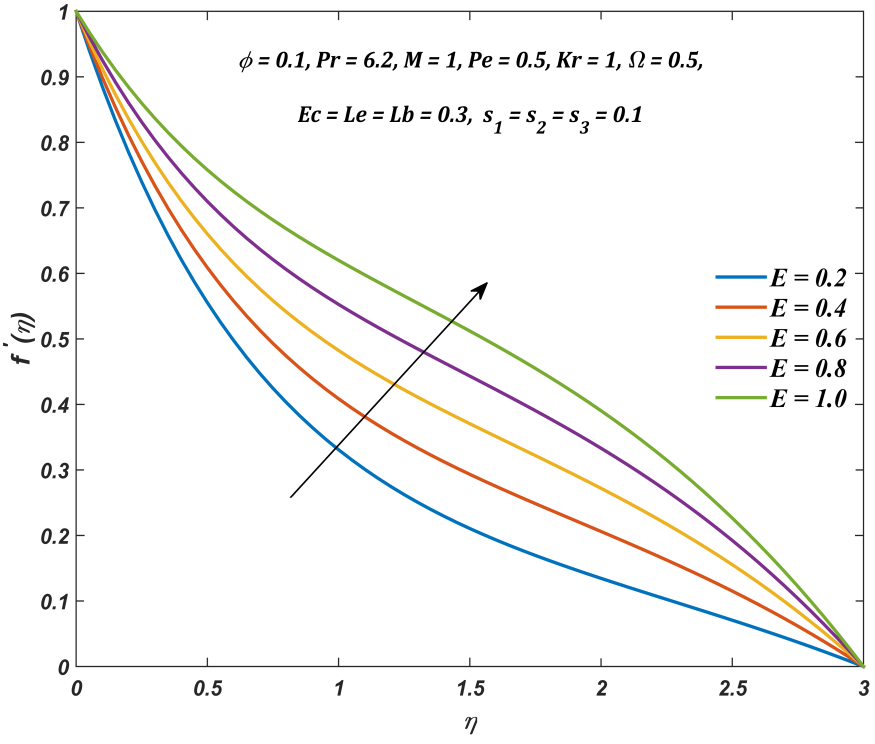

Figure 6.3: $f'(\eta)$ for differing E values

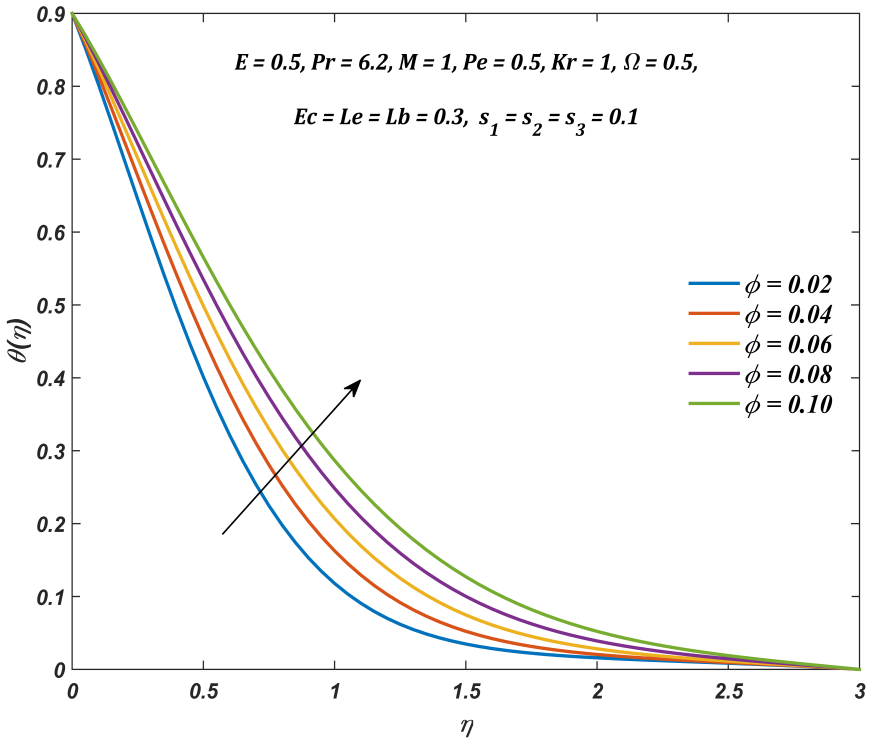

Figure 6.4: $\theta(\eta)$ for differing ϕ values

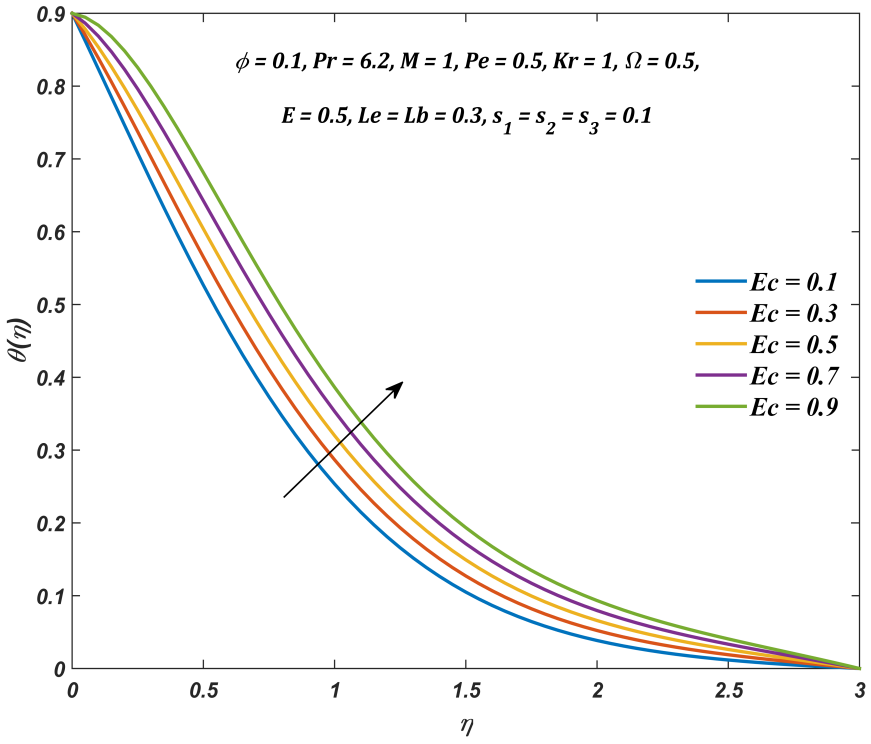

Figure 6.5: $\theta(\eta)$ for differing Ec values

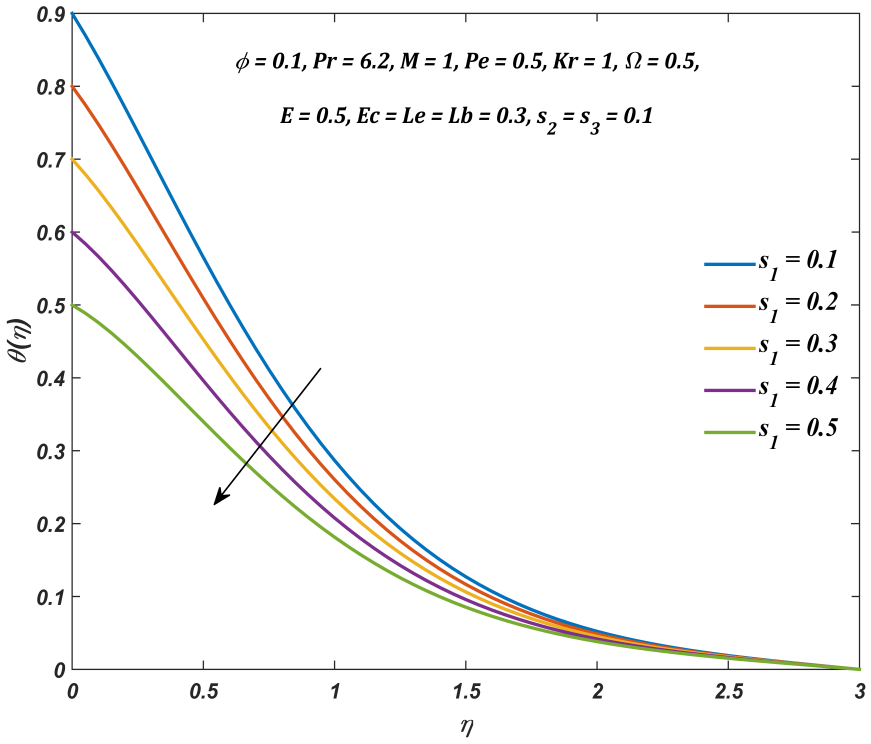

Figure 6.6: $\theta(\eta)$ for differing s_1 values

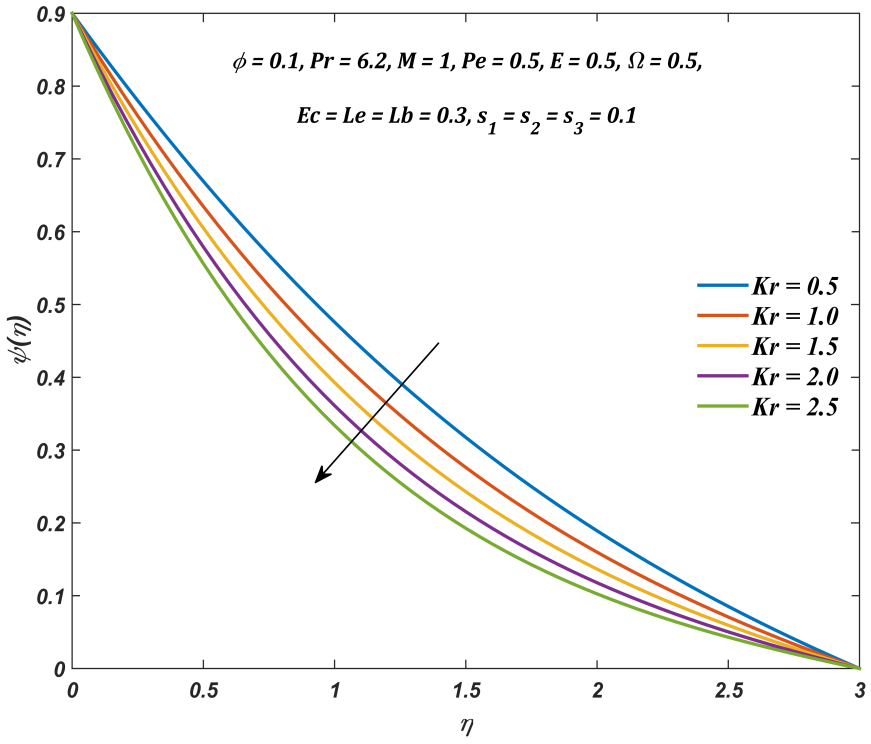

Figure 6.7: $\psi(\eta)$ for differing Kr values

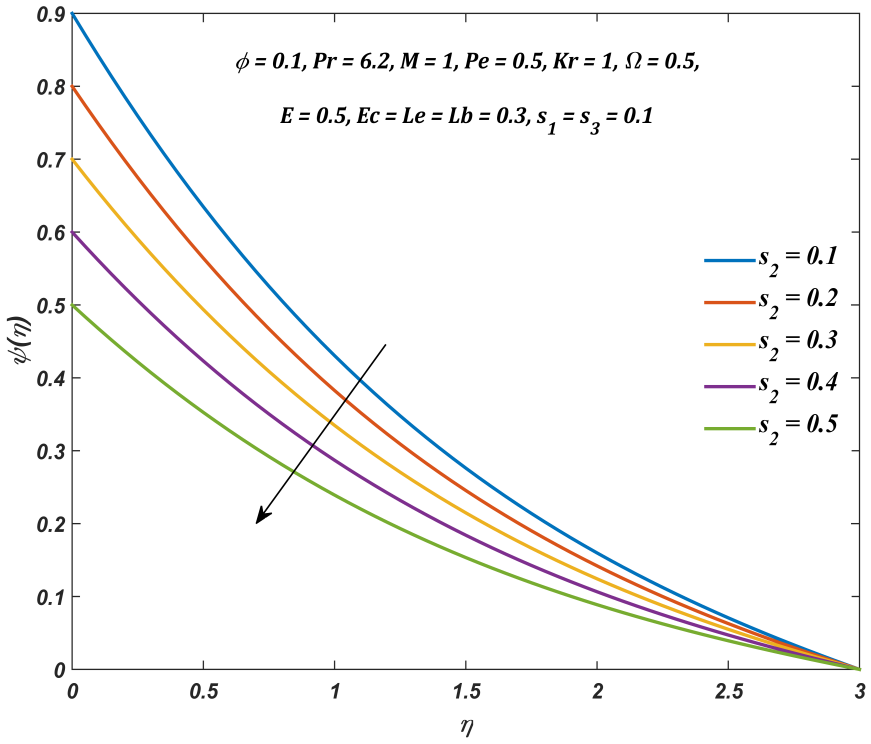

Figure 6.8: $\psi(\eta)$ for differing s_2 values

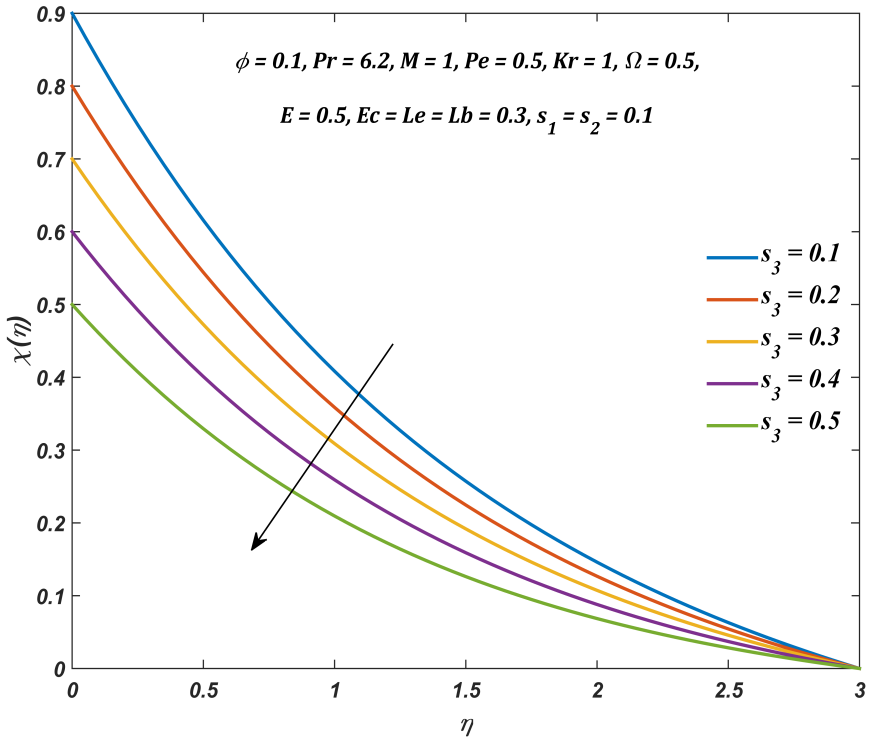

Figure 6.9: $\chi(\eta)$ for differing s_3 values

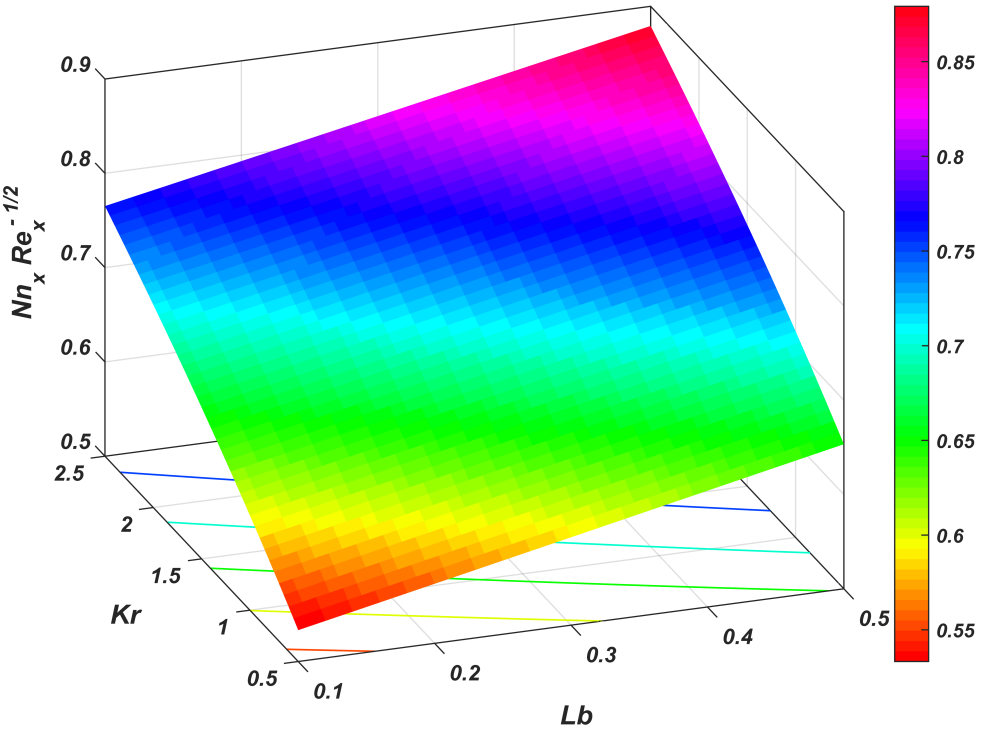

Figure 6.10: Variation of $Nn_x\ Re_x^{-1/2}$ with Kr & Lb

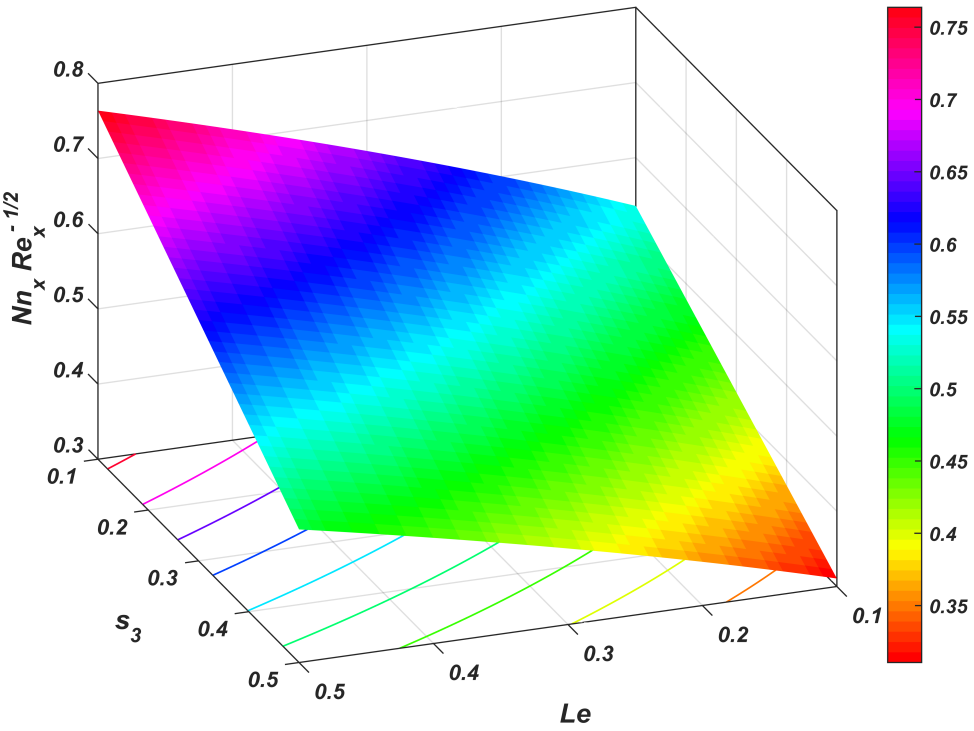

Figure 6.11: Variation of $Nn_x\ Re_x^{-1/2}$ with s_3 & Le

Figures 6.10 & 6.11 explain the simultaneous impact of parameters on microorganism density number. It can be summarised that microorganism density number intensifies with chemical reaction parameter (Kr), Lewis number (Le) & bioconvection Lewis number (Lb). Also, it is perceived that microorganism density number attenuates with motile density stratification parameter (s_3).

Table 6.3: Variation in $Cf_x\ Re_x^{1/2}$ when $Kr = 1,\ Ec = Le = Lb = 0.3,\ Pe = \Omega = 0.5$ & $s_1 = s_2 = s_3 = 0.1$

ϕ	**M**	**E**	$\mathbf{Cf_x\ Re_x^{1/2}}$
0.1	1	0.2	-1.6045
0.1	1	0.4	-1.4112
0.1	1	0.6	-1.2231
0.1	1	0.8	-1.0393
0.1	1	1	-0.8595
Slope			**0.93095**
0.1	0.5	0.5	-1.2699
0.1	1	0.5	-1.3165
0.1	1.5	0.5	-1.3742
0.1	2	0.5	-1.4362
0.1	2.5	0.5	-1.4998
Slope			**-0.1159**
0.02	1	0.5	-1.1016
0.04	1	0.5	-1.1513
0.06	1	0.5	-1.2035
0.08	1	0.5	-1.2585
0.1	1	0.5	-1.3165
Slope			**-2.685**

Table 6.4: Variation in $Nu_x\ Re_x^{-\ 1/2}$ when $Kr = 1,\ Le = Lb = 0.3,\ Pe = \Omega = 0.5$ & $s_2 = s_3 = 0.1$

$\mathbf{s_1}$	ϕ	**Ec**	**M**	**E**	$\mathbf{Nu_x\ Re_x^{-1/2}}$
0.1	0.1	0.3	1	0.2	1.2128
0.1	0.1	0.3	1	0.4	1.5408
0.1	0.1	0.3	1	0.6	1.8084
0.1	0.1	0.3	1	0.8	2.0268
0.1	0.1	0.3	1	1	2.2038
Slope					**1.234**
0.1	0.1	0.3	0.3	0.5	1.5837
0.1	0.1	0.3	0.6	0.5	1.6416
0.1	0.1	0.3	0.9	0.5	1.6743
0.1	0.1	0.3	1.2	0.5	1.6914
0.1	0.1	0.3	1.5	0.5	1.6983
Slope					**0.093**
0.1	0.1	0.1	1	0.5	2.1958
0.1	0.1	0.2	1	0.5	1.9386
0.1	0.1	0.3	1	0.5	1.6814
0.1	0.1	0.4	1	0.5	1.4242
0.1	0.1	0.5	1	0.5	1.167
Slope					**-2.572**
0.1	0.02	0.3	1	0.5	1.2251
0.1	0.04	0.3	1	0.5	1.3626
0.1	0.06	0.3	1	0.5	1.4812
0.1	0.08	0.3	1	0.5	1.5861
0.1	0.1	0.3	1	0.5	1.6814
Slope					**5.6805**
0.1	0.1	0.3	1	0.5	1.6814
0.2	0.1	0.3	1	0.5	1.4088
0.3	0.1	0.3	1	0.5	1.1363
0.4	0.1	0.3	1	0.5	0.8637
0.5	0.1	0.3	1	0.5	0.5912
Slope					**-2.7255**

Table 6.5: Variation in $Sh_x\ Re_x^{-\ 1/2}$ when $M = 1,\ Ec = Lb = 0.3,\ Pe = \Omega = 0.5$ & $s_1 = s_3 = 0.1$

$\mathbf{s_2}$	ϕ	**Kr**	**Le**	**E**	$\mathbf{Sh_x\ Re_x^{-1/2}}$
0.1	0.1	1	0.3	0.2	0.5895
0.1	0.1	1	0.3	0.4	0.5946
0.1	0.1	1	0.3	0.6	0.5994
0.1	0.1	1	0.3	0.8	0.604
0.1	0.1	1	0.3	1	0.6084
Slope					**0.0236**
0.1	0.1	1	0.1	0.5	0.4098
0.1	0.1	1	0.2	0.5	0.508
0.1	0.1	1	0.3	0.5	0.597
0.1	0.1	1	0.4	0.5	0.6785
0.1	0.1	1	0.5	0.5	0.7539
Slope					**0.8587**
0.1	0.1	0.5	0.3	0.5	0.4973
0.1	0.1	1	0.3	0.5	0.597
0.1	0.1	1.5	0.3	0.5	0.6858
0.1	0.1	2	0.3	0.5	0.7663
0.1	0.1	2.5	0.3	0.5	0.8402
Slope					**0.17102**
0.1	0.02	1	0.3	0.5	0.5961
0.1	0.04	1	0.3	0.5	0.5963
0.1	0.06	1	0.3	0.5	0.5965
0.1	0.08	1	0.3	0.5	0.5968
0.1	0.1	1	0.3	0.5	0.597
Slope					**0.0115**
0.1	0.1	1	0.3	0.5	0.597
0.2	0.1	1	0.3	0.5	0.5307
0.3	0.1	1	0.3	0.5	0.4643
0.4	0.1	1	0.3	0.5	0.398
0.5	0.1	1	0.3	0.5	0.3317
Slope					**-0.6633**

Tables 6.3 - 6.5 elucidate the variation of pertinent parameters on drag coefficient, heat transfer and mass transfer rate, respectively. The slope of linear regression (or simply slope) indicates the nature of variation of drag coefficient/heat transfer rate/mass transfer rate. A negative slope implies that the varying parameter has a negative effect on the considered physical quantity. The rate of increase/decrease of physical quantity per unit value of the varying parameter is explained using the slope's magnitude. The main outcomes drawn from Tables 6.3 - 6.5 are:

- The drag coefficient is a decreasing function of M & ϕ and an increasing function of E.
- Mass transfer rate is an increasing function of $E,\ Kr,\ Le$, & ϕ and a decreasing function of s_2.
- Heat transfer rate is a decreasing function of Ec & s_1 and an increasing function of $E,\ M$, & ϕ.

6.5 Statistical Frame

Statistical techniques (like correlation and regression) are largely used by researchers to discover the nature of impact of independent variables (various parameters) on the dependent variable (physical quantities like heat transfer rate/ drag coefficient/ mass transfer rate). Regression analysis aids in quantifying the variation of dependent variable initiated by the change in independent variables. Regression analysis rules out the need for resolving the problem frequently and hence eases the calculation process. For a chosen range of independent variables, an approximate value of the dependent variable can be faultlessly predicted utilizing multiple linear regression.

6.5.1 Correlation and Probable Error

The degree of relationship between two variables is determined with the help of correlation. The sign of correlation coefficient (r) comments on the nature of the relationship while the magnitude of r bespeaks on the dimension of relationship. The positive value of r indicates that an augmentation in the independent variable will beget an improvement in the dependent variable and the negative value of correlation coefficient implies that an augmentation in the independent variable will lower the dependent variable. The reliability of the calculated correlation coefficient

values is guaranteed using probable error (PE). Correlation is said to be significant if $\left|\frac{r}{PE}\right| > 6$; where $PE = \left(\frac{1-r^2}{\sqrt{n}}\right)$ 0.6745 and n is the number of observations [see (Fisher, 1921)].

Table 6.6: Correlation Coefficient (r), Probable Error (PE) and $\left|\frac{r}{PE}\right|$ of drag coefficient

Parameter	**r**	**PE**	$\left\|\frac{\mathbf{r}}{\mathbf{PE}}\right\|$
ϕ	-0.99953	0.000281	3554.453
M	-0.99831	0.001021	977.8618
E	0.999899	6.10E-05	16389.83

Table 6.7: Correlation Coefficient (r), Probable Error (PE) and $\left|\frac{r}{PE}\right|$ of heat transfer rate

Parameter	**r**	**PE**	$\left\|\frac{\mathbf{r}}{\mathbf{PE}}\right\|$
ϕ	0.997314	0.001618	616.3864
Ec	-1	-1.30E-16	7.47E+15
M	0.940793	0.034662	27.14199
E	0.992816	0.004318	229.9108
$\mathbf{s_1}$	-1	1.22E-09	8.21E+08

From Tables 6.6 & 6.7, it is inferred that $Cf_x\ Re_x^{1/2}$ is negatively correlated with M & ϕ and positively correlated with E. Also, it is inferred that $Nu_x\ Re_x^{-1/2}$ is negatively correlated with Ec & s_1 and positively correlated with E, M & ϕ. Further, it is noted that the above results are in good agreement with the numerical results observed in Tables 6.3 & 6.4. Using $\left|\frac{r}{PE}\right|$ values, it can be deduced that all parameters of $Cf_x\ Re_x^{1/2}$ & $Nu_x\ Re_x^{-1/2}$ are significant.

6.5.2 Multiple Linear Regression

Regression analysis is a statistical modelling technique used to establish a relationship between a dependent (drag coefficient or heat transfer rate) and one or more independent (various parameters considered) variables. Since all correlations are significant, multiple linear regression is employed in estimating the drag coefficient and heat transfer rates.

The estimated models are:

$$Cf_{est} = a_\phi \phi + a_M M + a_E E + b$$
$$Nu_{est} = a_\phi \phi + a_M M + a_E E + a_{Ec} Ec + a_{s_1} s_1 + b$$

where $a_\phi,\ a_M,\ a_E,\ a_{Ec},\ a_{s_1}$, and b are the estimated regression coefficients.

Jenkins et al., 2020 elucidated that a sample size of 25 or above would be considered optimal for research based on regressions or meta-regressions. Accordingly, the drag coefficient is estimated from 30 sets of values chosen in the range $[0.02, 0.1]$ for ϕ, $[0.5, 2.5]$ for M & $[0.2, 1]$ for E, and the regression coefficients are calculated using Microsoft Excel. Furthermore, heat transfer rate is also estimated from 30 sets of values chosen in the range $[0.02, 0.1]$ for ϕ, $[0.3, 1.5]$ for M, $[0.2, 1]$ for E, $[0.2, 0.4]$ for Ec, & $[0.1, 0.5]$ for s_1 and the regression coefficients are calculated using Microsoft Excel. Since the p-values for all physical parameters are less than 0.05 the regression coefficients are significant. A negative regression coefficient implies that drag coefficient or heat transfer rate decreases for the corresponding parameter and a positive regression coefficient represents that the corresponding parameter has an increasing effect on drag coefficient or heat transfer rate. The estimated regression models are given below:

$$Cf_{est} = -2.765014142\ \phi - 0.107916023\ M + 0.873312541\ E - 1.370390154$$
$$Nu_{est} = 5.276108658\ \phi + 0.094619221\ M + 1.194981645\ E$$
$$- 2.5720\ Ec - 2.688355065\ s_1 + 1.490951117$$

It is conclusive that E has a positive impact whereas M & ϕ have a negative impact on the drag coefficient. It can also be deduced that E, M, & ϕ have a positive impact while Ec & s_1 descends the heat transfer rate. This is in harmony with the results seen in Tables 6.3 & 6.4.

The original data $\left(Cf_x\ Re_x^{1/2}\ \&\ Nu_x\ Re_x^{-1/2} \right)$ are numerically calculated considering 30 sets of parameter values in the considered range and the estimated data are computed with the aid of estimated regression models (Cf_{est} & Nu_{est}) for the same set of parameter values. Comparison of the estimated data with the original data has been illustrated in Figures 6.12 & 6.13. It is observed that the estimated regression model is capable of predicting the values of drag coefficient and heat transfer rate faultlessly.

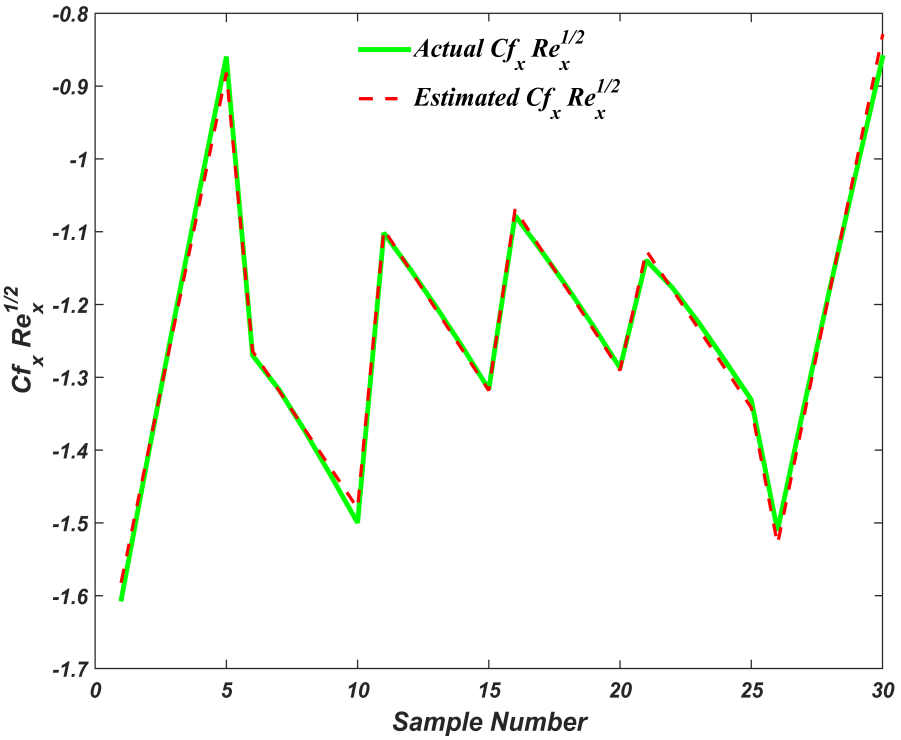

Figure 6.12: Actual versus Estimated $Cf_x\ Re_x^{1/2}$

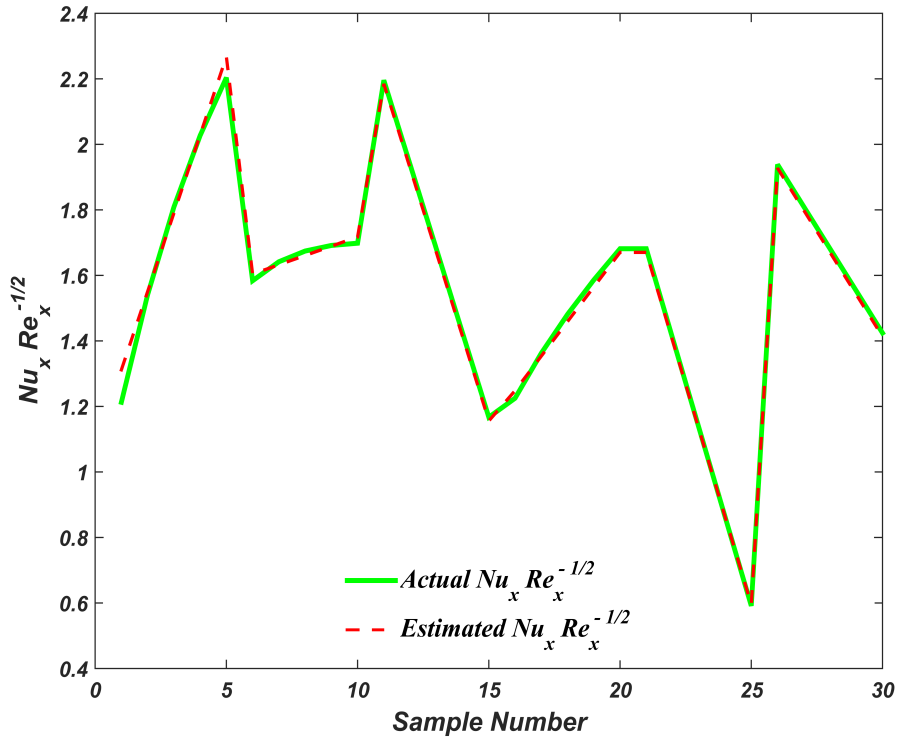

Figure 6.13: Actual versus Estimated $Nu_x\ Re_x^{-1/2}$

6.6 Conclusion

Due to its applications in targeted drug delivery, biomedical imaging, and cancer therapy, the significance of electric and magnetic fields acting on the bioconvective flow considering stratification effects has been examined. The effect of influential parameters on the water-based SWCNT nanofluid flow profiles has been numerically investigated with the aid of the bvp5c scheme. Further, the influence of pertinent parameters on the heat transfer rate and the drag coefficient has been scrutinized utilizing multiple linear regression. In future, the present work can be extended by conducting a detailed theoretical study with more advantageous effects or by considering non-Newtonian fluids. The key points of the present study are:

- Augmenting nanoparticle volume intensifies the nanofluid temperature. This unveils that the nanofluid can be used for killing tumors or cancerous cells.
- Thermal, solutal and motile density stratification parameters exhibit a negative impact on temperature, concentration and microbial concentration, respectively.
- Descending electric field parameter and ascending magnetic field parameter retards the velocity profile, which helps in improving the efficiency of targeted drug delivery and biomedical imaging.
- Microorganism density number is a decreasing function of motile density stratification parameter and an increasing function of chemical reaction parameter.
- The estimated model for drag coefficient, using multiple linear regression, is given by:

$$Cf_{est} = -2.765014142\ \phi - 0.107916023\ M + 0.873312541\ E - 1.370390154$$

- The estimated model for heat transfer rate, using multiple linear regression, is given by:

$$\begin{aligned} Nu_{est} = {} & 5.276108658\ \phi + 0.094619221\ M + 1.194981645\ E \\ & - 2.5720\ Ec - 2.688355065\ s_1 + 1.490951117 \end{aligned}$$

Appendix I: Non-dimensional qunatities

$M = \frac{\sigma_f \ {B_0}^2}{c \ \rho_f}$	Magnetic field parameter
$E = \frac{E_0}{B_0 \ U_W}$	Electric field parameter
$Pr = \frac{(\mu C_p)_f}{k_f} = \frac{\vartheta_f}{\alpha_f}$	Prandtl number
$Kr = \frac{k_r}{c}$	Chemical reaction parameter
$Ec = \frac{(cx)^2}{(C_p)_f (T_W - T_0)}$	Eckert number
$Le = \frac{\vartheta_f}{D_B}$	Lewis number
$Lb = \frac{\vartheta_f}{D_m}$	Bioconvection Lewis number
$Pe = \frac{bW_c}{D_m}$	Bioconvection Peclet number
$\Omega = \frac{N_\infty}{N_W - N_0}$	Microorganism concentration difference parameter
$s_1 = \frac{\delta_2}{\delta_1}$	Thermal stratification parameter
$s_2 = \frac{\epsilon_2}{\epsilon_1}$	Solutal stratification parameter
$s_3 = \frac{\xi_2}{\xi_1}$	Motile density stratification parameter

Appendix II: Nomenclature

c	Dimensional constant	W_c	Maximum cell swimming speed
u, v	Velocity components	B_0	Uniform magnetic field
Nn_x	Local motile density	T_∞	Ambient fluid temperature
T_0	Reference temperature	N_∞	Ambient microbial concentration
C	Fluid concentration	C_0	Reference nanoparticle concentration
T	Fluid temperature	N_0	Reference microbial concentration
x, y	Cartesian coordinates	N_w	Microbial concentration near wall
b	Chemotaxis constant	C_w	Nanoparticle concentration near wall
T_w	Wall fluid temperature	C_∞	Ambient nanoparticle concentration
C_p	Specific heat	Cf_x	Local drag coefficient
k_r	Reaction rate constant	Nu_x	Local Nusselt number
Sh_x	Local Sherwood number	N	Microorganism concentration
σ	Electrical conductivity	E_0	Uniform electric field
η	Dimensionless variable	D_B	Chemical molecular diffusivity
ϑ	Kinematic viscosity	D_m	Microorganism diffusion coefficient
k	Thermal conductivity	Ω	Microorganism concentration difference
α	Thermal diffusivity		parameter
ρ	Fluid density	ϕ	Nanoparticle volume fraction

Chapter 7

Hydromagnetic Carreau nanoliquid flow over an elongating cylinder *

7.1 Introduction

Fluids are categorized into two groups; Newtonian and non-Newtonian. A linear stress-strain relationship is observed in the case of Newtonian fluids. Carreau nanofluid model includes low and high shear rates which is an attracting aspect in non-Newtonian studies. Human blood is an example of Carreau fluid with shear thinning nature. The focal concern of this chapter is to numerically scrutinize the consequences of multiple slip, linear radiation and chemically reactive species on MHD convective Carreau nanoliquid flow over an elongating cylinder. The present study has applications in metallurgical procedures, blow molding, glass fibers, and extrusion processes. Relevant transformations are implemented in converting the governing equations into a system of ODEs and are further treated numerically using the Bulirsch-Stoer algorithm coupled with the shooting technique in MATLAB. The Bulirsch-Stoer method is based on two ideas (midpoint method & Richardson extrapolation). Illustrations on the effect of flow profiles due to the varying parameter values are achieved using graphs. Characteristics of skin friction are quantified using linear regression slope. Simultaneous impact of radiation and thermal slip on Nusselt number and the response of solutal slip and chemically reactive species on mass transfer rate is analysed using three-dimensional surface plots. Moreover, statistical scrutiny on the impact of Hartmann number ($1 \leq M \leq 2$), thermal radiation ($1 \leq Rd \leq 2$) and thermal slip parameter ($0.1 \leq b_2 \leq 0.3$) over heat transfer rate employing response surface methodology and sensitivity analysis is performed.

*Published in: Thermal Science and Engineering Progress (Elsevier), 2021; 25; 101038.

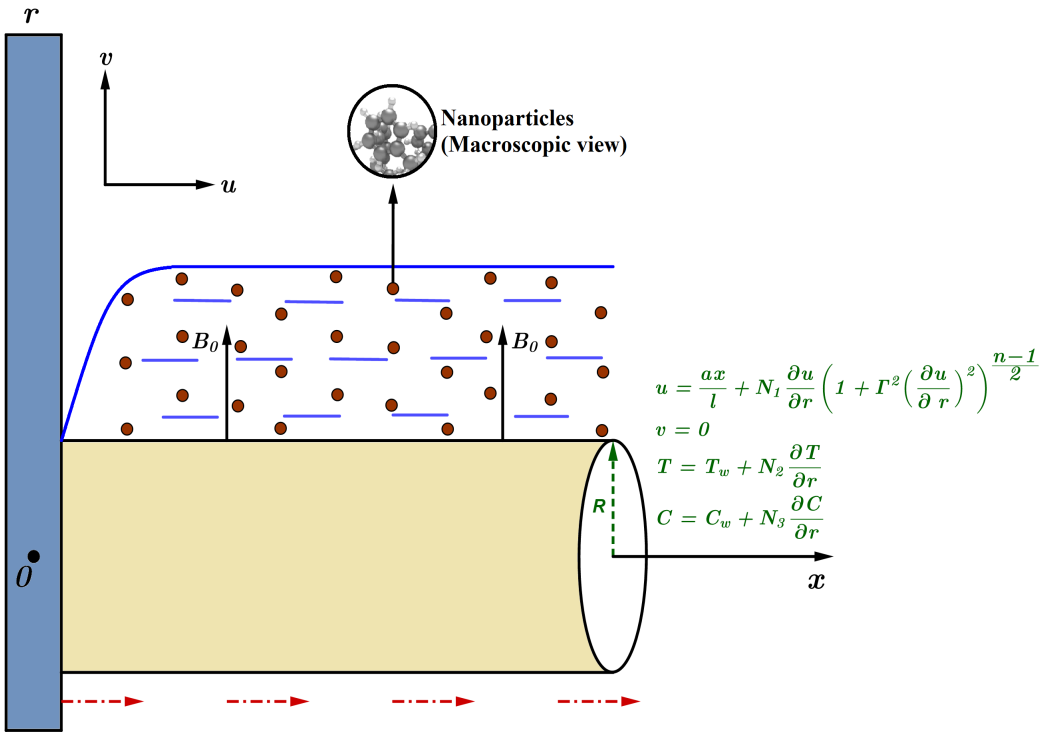

Figure 7.1: Geometrical Frame

7.2 Mathematical Frame

A steady two-dimensional hydromagnetic Carreau nanoliquid flow over an elongating cylinder with $r = R$ fixed at origin, 0 with radiative and chemical reactive effects is analysed (see Figure 7.1). The cylinder is elongated along the $x-$direction with velocity $\frac{ax}{l}$ and a uniform magnetic field (of strength B_0) is administered in the $r-$direction.

The governing equations take the form (see I. Khan et al., 2017):

$$\frac{\partial (ru)}{\partial x} + \frac{\partial (rv)}{\partial r} = 0 \tag{7.2.1}$$

$$u\frac{\partial u}{\partial x} + v\frac{\partial u}{\partial r} = \frac{\vartheta_f}{r}\frac{\partial u}{\partial r}\left(1 + \Gamma^2\left(\frac{\partial u}{\partial r}\right)^2\right)^{\frac{n-1}{2}} + \vartheta_f \frac{\partial^2 u}{\partial r^2}\left(1 + \Gamma^2\left(\frac{\partial u}{\partial r}\right)^2\right)^{\frac{n-1}{2}} - \frac{\sigma_f {B_0}^2 u}{\rho_f} + \vartheta_f (n-1)\Gamma^2\left(\frac{\partial^2 u}{\partial r^2}\right)\left(\frac{\partial u}{\partial r}\right)^2\left(1 + \Gamma^2\left(\frac{\partial u}{\partial r}\right)^2\right)^{\frac{n-3}{2}} \tag{7.2.2}$$

$$u\frac{\partial T}{\partial x}+v\frac{\partial T}{\partial r}=\alpha_f\left(\frac{\partial^2 T}{\partial r^2}+\frac{1}{r}\frac{\partial T}{\partial r}\right)+\frac{(\rho C)_p}{(\rho C)_f}\left(D_B\frac{\partial \mathcal{C}}{\partial r}\frac{\partial T}{\partial r}+\frac{D_T}{T_\infty}\left(\frac{\partial T}{\partial r}\right)^2\right)$$
$$-\frac{1}{(\rho C_p)_f}\frac{\partial q_r}{\partial r} \tag{7.2.3}$$

$$u\frac{\partial \mathcal{C}}{\partial x}+v\frac{\partial \mathcal{C}}{\partial r}=\ D_B\left(\frac{\partial^2 \mathcal{C}}{\partial r^2}+\frac{1}{r}\frac{\partial \mathcal{C}}{\partial r}\right)+\frac{D_T}{T_\infty}\left(\frac{\partial^2 T}{\partial r^2}+\frac{1}{r}\frac{\partial T}{\partial r}\right)-K_l\left(\mathcal{C}-\mathcal{C}_\infty\right) \tag{7.2.4}$$

subject to the boundary conditions (see I. Khan et al., 2017):

$$u=\frac{ax}{l}+N_1\frac{\partial u}{\partial r}\left(1+\Gamma^2\left(\frac{\partial u}{\partial r}\right)^2\right)^{\frac{n-1}{2}},\ v=0,\ T=T_w+N_2\frac{\partial T}{\partial r},$$

$$\mathcal{C}=\mathcal{C}_w+N_3\frac{\partial \mathcal{C}}{\partial r}\qquad \text{at } r=R$$

$$u\to 0,\ \ T\to T_\infty,\ \ \mathcal{C}\to\mathcal{C}_\infty\quad as\ r\to\infty$$

Under Roseland approximation we have:

$$q_r=-\frac{4\sigma^*}{3k^*}\frac{\partial T^4}{\partial r}$$

Using Taylor's series, we get:

$$T^4\cong 4T_\infty^3T-3T_\infty^4$$

Consider the following similarity transformations (see I. Khan et al., 2017; Salahuddin et al., 2017):

$$\eta=\frac{r^2-R^2}{2R}\sqrt{\frac{a}{l\vartheta_f}}\ ,\ \xi=\sqrt{\frac{a\vartheta_f}{l}}xRf\left(\eta\right)\ \ ,\ \theta\left(\eta\right)=\frac{T-T_\infty}{T_w-T_\infty}\ ,$$

$$u=\frac{1}{r}\frac{\partial \xi}{\partial r}\ ,\ v=-\frac{1}{r}\frac{\partial \xi}{\partial x}\ ,\ \phi\left(\eta\right)=\frac{\mathcal{C}-\mathcal{C}_\infty}{\mathcal{C}_w-\mathcal{C}_\infty}\ .$$

u and v are chosen such that Equation (7.2.1) is identically satisfied. Using the above defined similarity transformations, Equations (7.2.2) – (7.2.4) are converted into:

$$f f'' - (f')^2 + (1 + 2\mathrm{K}\eta)\, f'''\left(1 + \mathrm{We}^2 (f'')^2\right)^{\frac{n-1}{2}} + 2K f''\left(1 + \mathrm{We}^2 (f'')^2\right)^{\frac{n-1}{2}} - M f' + (n-1)\,\mathrm{We}^2 K (f'')^3\left(1 + \mathrm{We}^2 (f'')^2\right)^{\frac{n-3}{2}} + (n-1)\,\mathrm{We}^2 (f'')^2\,(1 + 2\mathrm{K}\eta)\, f'''\left(1 + \mathrm{We}^2 (f'')^2\right)^{\frac{n-3}{2}} = 0 \tag{7.2.5}$$

$$(1 + 2\mathrm{K}\eta)\,\theta'' + 2K\theta' + Pr f\theta' + Pr\,(1 + 2\mathrm{K}\eta)\left(Nb\phi'\theta' + Nt(\theta')^2\right) + \frac{4}{3}Rd\left((1 + 2\mathrm{K}\eta)\,\theta'' + K\theta'\right) = 0 \tag{7.2.6}$$

$$(1 + 2\mathrm{K}\eta)\,\phi'' + 2K\phi' + Sc\,(f\phi' - K_r\,\phi) + \frac{Nt}{Nb}\left((1 + 2\mathrm{K}\eta)\,\theta'' + 2K\theta'\right) = 0 \tag{7.2.7}$$

subject to the boundary conditions

$$f(0) = 0,\ f'(0) = 1 + b_1\ f''(0)\left(1 + \mathrm{We}^2\ (f''(0))^2\right)^{\frac{n-1}{2}}\ ,\ f'(\infty) \to 0\ ,$$

$$\theta(0) = 1 + b_2\ \theta'(0)\ \ ,\ \theta(\infty) \to 0,\ \phi(0) = 1 + b_3\ \phi'(0)\ \ ,\ \phi(\infty) \to 0$$

where the dimensionless parameters are given in appendix I.

The physical quantities are given by (see I. Khan et al., 2017; Salahuddin et al., 2017):

Local drag coefficient : $$Cf_x = \frac{\tau_{rx}}{\frac{1}{2}\rho_f\left(\frac{ax}{l}\right)^2}\ ,$$

$$where\ \tau_{rx} = \left(\mu_f \frac{\partial u}{\partial r}\left(1 + \Gamma^2\left(\frac{\partial u}{\partial r}\right)^2\right)^{\frac{n-1}{2}}\right)_{r=R}$$

$$\Rightarrow\ \frac{1}{2}Cf_x\ Re_x^{1/2} = f''(0)\left(1 + \mathrm{We}^2\ (f''(0))^2\right)^{\frac{n-1}{2}}.$$

Local Nusselt number : $$Nu_x = \frac{x q_w}{k_f\,(T_w - T_\infty)}\ ,$$

$$where\ q_w = -\left(k_f \frac{\partial T}{\partial r} - q_r\right)_{r=R}$$

$$\Rightarrow\ Nu_x\ Re_x^{-\,1/2} = -\left(1 + \frac{4}{3}Rd\right)\theta'(0).$$

Local Sherwood number : $Sh_x = \dfrac{x q_m}{D_B\,(\mathcal{C}_w - \mathcal{C}_\infty)}$,

$$where\ q_m = -\Big(D_B \frac{\partial \mathcal{C}}{\partial r}\Big)_{r=R}$$

$$\Rightarrow\ Sh_x\ Re_x^{-\ 1/2} = -\phi\,'(0).$$

7.3 Numerical Frame & Validation

Equations (7.2.5) – (7.2.7) are numerically solved using the Bulirsch-Stoer algorithm with shooting technique. Shooting technique involves converting the boundary value problem into an initial value problem and then estimating the unknowns using the far-field boundary conditions. For this, initially assume:

$$g_1 = f,\ g_2 = f\,',\ g_3 = f\,'',\ g_4 = \theta,\ g_5 = \theta\,',\ g_6 = \phi,\ g_7 = \phi\,'$$

The reduced system of the first-order ODE is given by:

$g_1\,' = g_2$, $g_2\,' = g_3$,

$$g_3\,' = \frac{-\Big(g_1 g_3 - {g_2}^2 - M g_2 + 2K g_3 (1 + \mathrm{We}^2 {g_3}^2)^{\frac{n-1}{2}} + (n-1)\ We^2 K {g_3}^3 (1 + \mathrm{We}^2 {g_3}^2)^{\frac{n-3}{2}}\Big)}{(1 + 2\mathrm{K}\ \eta)\Big\{(1 + \mathrm{We}^2 {g_3}^2)^{\frac{n-1}{2}} + (n-1)\, We^2 {g_3}^2 (1 + \mathrm{We}^2 {g_3}^2)^{\frac{n-3}{2}}\Big\}},$$

$g_4\,' = g_5$,

$$g_5\,' = \frac{-\Big(2\ K\ g_5 + Pr\ g_1\ g_5 + Pr\ \ (1 + 2\ \mathrm{K}\ \eta)\ \ (Nb\ g_5\ g_7 + Nt\ {g_5}^2) + \frac{4}{3} Rd\ K\ g_5\Big)}{(1 + 2\ \mathrm{K}\ \eta)\Big\{1 + \frac{4}{3}\ Rd\Big\}},$$

$g_6\,' = g_7$,

$$g_7\,' = \frac{-\Big(2\ K\ g_7 + Sc\ g_1\ g_7 - Sc\ K_r\ g_6 + \frac{Nt}{Nb}\Big((1 + 2\ \mathrm{K}\ \eta)\ \ g_5' + 2\ K\ g_5\Big)\Big)}{(1 + 2\ \mathrm{K}\ \eta)}$$

with

$$g_1(0) = 0,\ g_2(0) = 1 + b_1\ h_1\ (1 + \mathrm{We}^2\ h_1^2)^{\frac{n-1}{2}}\ ,\ g_3(0) = h_1\ ,$$

$$g_4(0) = 1 + b_2\ h_2\ ,\ g_5(0) = h_2\ ,\ g_6(0) = 1 + b_3\ h_3\ ,\ g_7(0) = h_3\ .$$

where $h_1,\ h_2$ & h_3 are estimated by employing the Newton Raphson method with a suitable initial guess.

The Bulirsch-Stoer method is based on two ideas; the midpoint method and Richardson extrapolation. A simplified version of the original Bulirsch and Stoer technique (a very complex procedure) that retains the essential ideas of Bulirsch and Stoer has been used. The original method involves a few refinements like automatic adjustment of step size which are missing out in the simplified algorithm. The current algorithm has an upper hand in the computation of high accuracy solutions involving smooth functions. The current version of the Bulirsch-Stoer method yields solutions with an accuracy of 10^{-6}. Validation of the numerical method (Bulirsch-Stoer method) has been carried out through a restrictive comparison with the work of W. A. Khan et al., 2010 and a commendable agreement is noted (Table 7.1).

Table 7.1: Comparison of $Nu_x Re_x^{-1/2}$ for different Pr values with the work of W. A. Khan et al., 2010 when $Nb \to 0$ and $M = K = We = Sc = Nt = Rd = K_r = b_1 = b_2 = b_3 = 0$

Pr	$\mathbf{Nu_x Re_x^{-1/2}}$	
	W. A. Khan et al., 2010	**Bulirsch-Stoer algorithm**
0.7	0.4539	0.45393241
2	0.9113	0.911357651
7	1.8954	1.895403242
20	3.3539	3.353904223
70	6.4621	6.462199501

7.4 Results & Discussion

The consequence of pertinent parameters like Hartmann number (M), Weissenberg number (We), chemical reaction parameter (K_r), thermophoresis parameter (Nt), curvature parameter (K), radiation parameter (Rd), Brownian motion parameter (Nb), power-law index (n), and slip parameters (b_1, b_2, b_3) on concentration $(\phi(\eta))$, temperature $(\theta(\eta))$ and axial velocity $(f'(\eta))$ profile is

studied through Figures 7.2 - 7.14. The study has been carried out for pseudo-plastic fluid ($0 < n < 1$) and dilatant fluid ($n > 1$), which are the two types of Carreau fluid based on the power-law index (see Zhang, 2021). Schmidt number (Sc), Prandtl number (Pr), and infinity are locked at 1.2, 4, and 15 respectively.

Variation of $f'(\eta)$ with increasing K values is elucidated in Figure 7.2. It is observed that the axial velocity profile increases with augmenting K values after travelling a certain distance. The consequence of We on the axial velocity for pseudo-plastic fluid ($n = 0.7$) and dilatant fluid ($n = 1.4$) is depicted in Figure 7.3. A differing behaviour is noted on the axial velocity for pseudo-plastic and dilatant fluids. Physically, this is due to the characteristic that We improves the elastic forces causing a depletion in the velocity profile of pseudo-plastic fluid. Lorentz force is generated due to increasing M which reduces the axial velocity profile. This physical effect is represented in Figure 7.4. Figure 7.5 displays the consequence of b_1 on axial velocity. It is observed that $f'(\eta)$ decreases when b_1 is increased. It is also worthwhile mentioning $f'(\eta)$ when $n < 1$ is lower than that of dilatant fluid.

The consequence of K on $\theta(\eta)$ is elucidated in Figure 7.6. It is observed that the curvature parameter has a constructive effect on $\theta(\eta)$. Hartmann number (M) has a positive influence on $\theta(\eta)$ meaning that an increase in M will increase the temperature profile (see Figure 7.7). Radiation parameter enhances $\theta(\eta)$ which is observed in Figure 7.8. The influence of b_1 & b_2 on $\theta(\eta)$ has been studied through Figures 7.9 & 7.10, respectively. It is seen that $\theta(\eta)$ improves with rising b_1 values and impairs with rising b_2 values. It is also noted that $\theta(\eta)$ when $n < 1$ is greater than dilatant fluid.

The consequence of K_r on $\phi(\eta)$ has been graphed in Figure 7.11. It is evident that $\phi(\eta)$ reduces due to an increase in K_r. Figure 7.12 describes the variation of $\phi(\eta)$ with Nt and it is observed that $\phi(\eta)$ has a positive impact on Nt. Figure 7.13 elucidates the effect of Nb on $\phi(\eta)$ and a negative impact is observed. This can be physically ascribed to the characteristic that an improvement in Nb will enhance the random motion of nanoparticles and in return lowers the nanoliquid concentration. The impact of b_3 on $\phi(\eta)$ is discussed in Figure 7.14. It is noted that $\phi(\eta)$ depletes with increasing b_3 values.

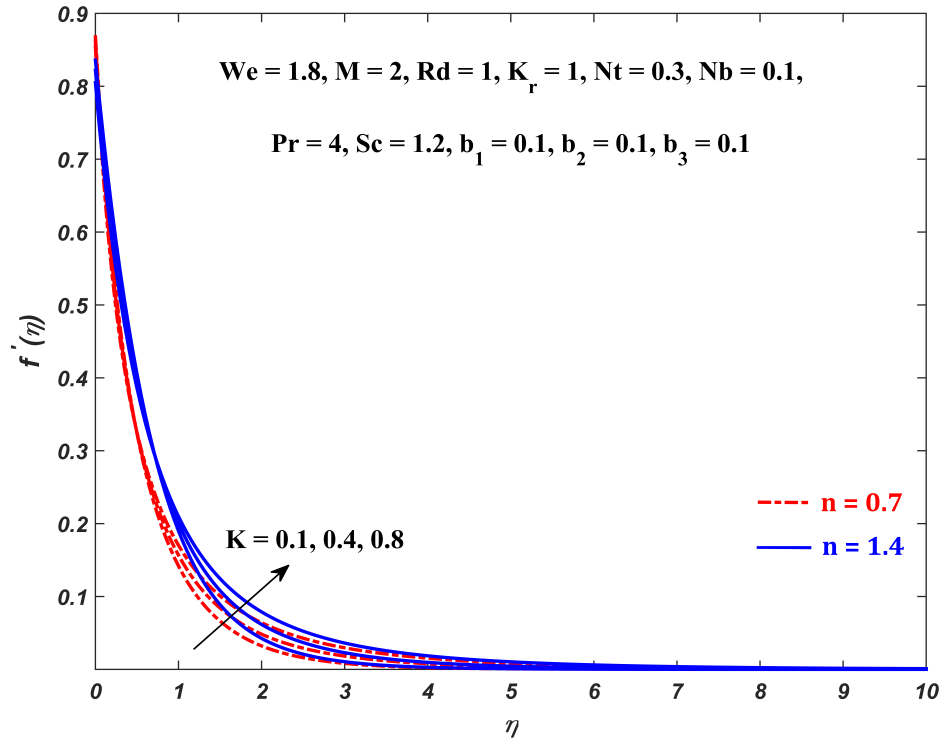

Figure 7.2: $f'(\eta)$ for differing K values

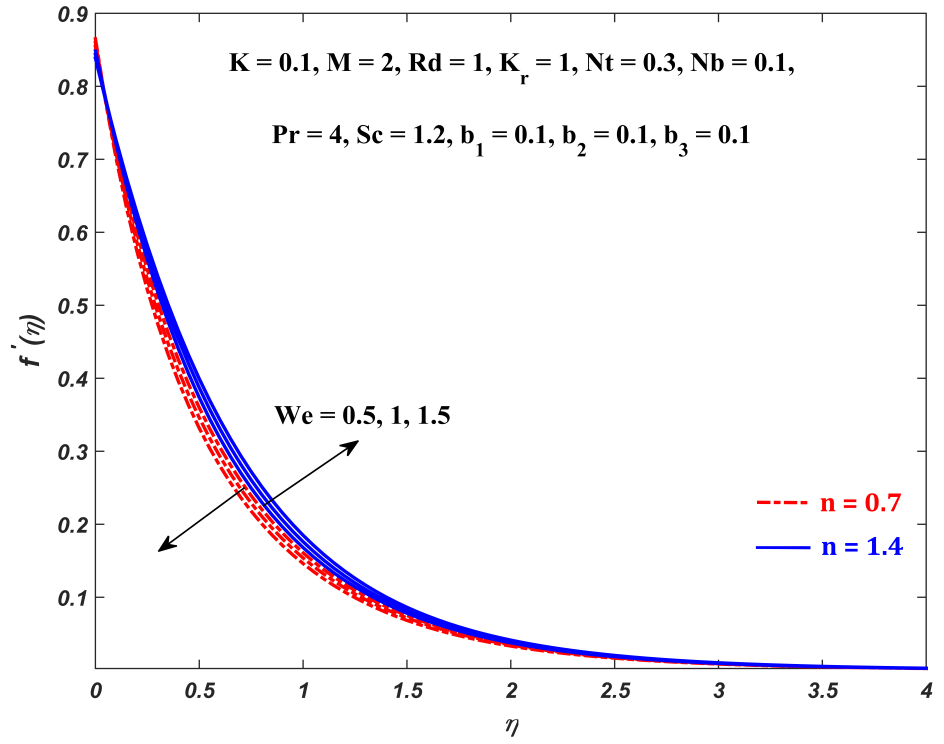

Figure 7.3: $f'(\eta)$ for differing We values

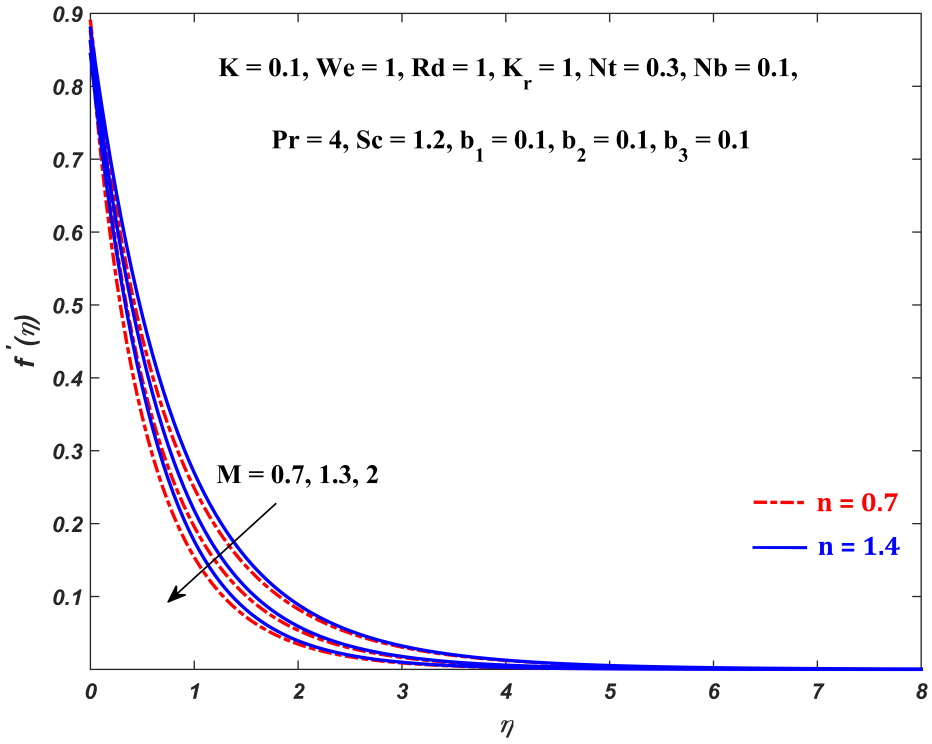

Figure 7.4: $f'(\eta)$ for differing M values

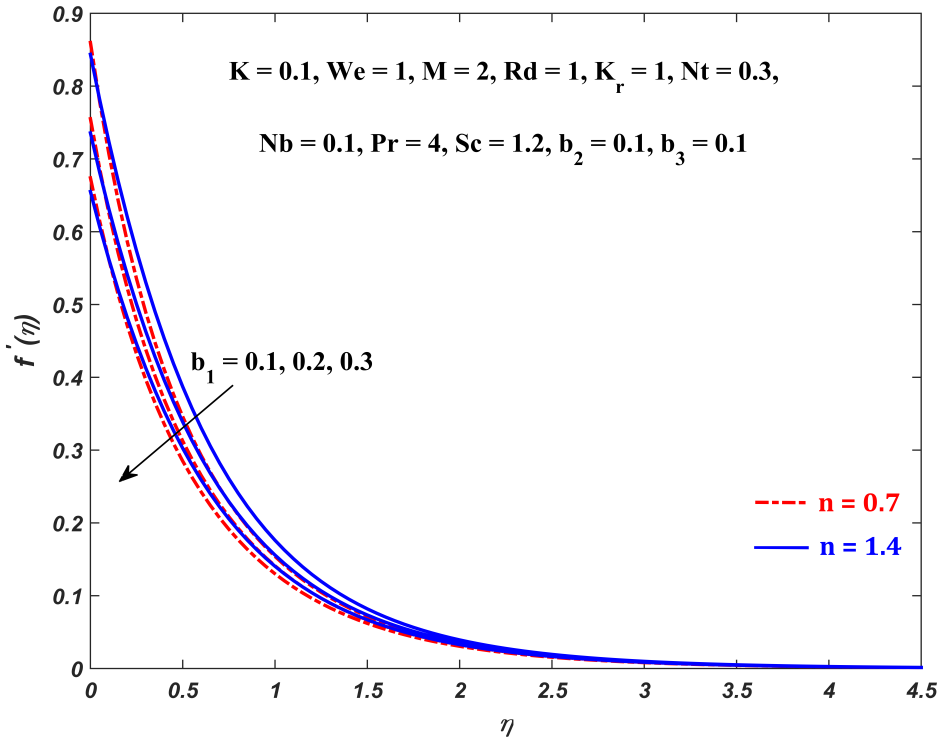

Figure 7.5: $f'(\eta)$ for differing b_1 values

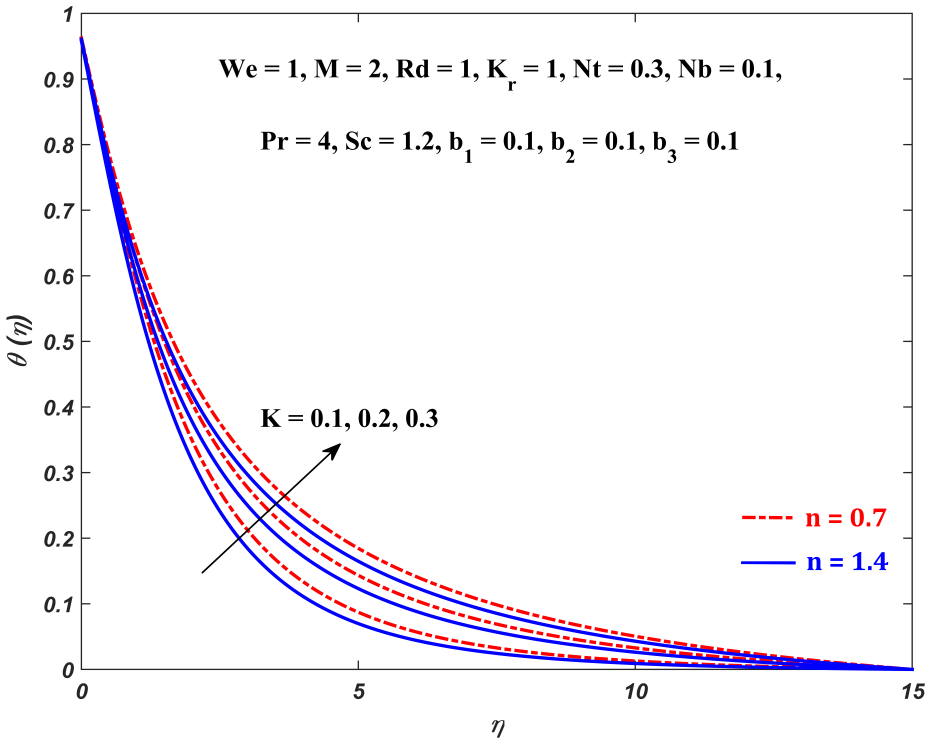

Figure 7.6: $\theta(\eta)$ for differing K values

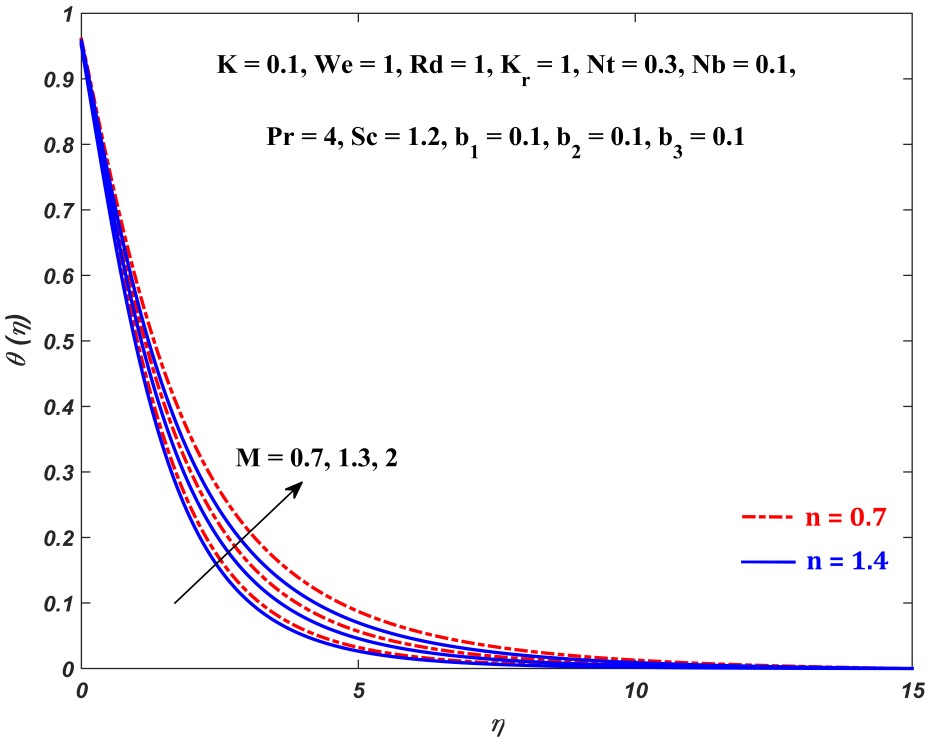

Figure 7.7: $\theta(\eta)$ for differing M values

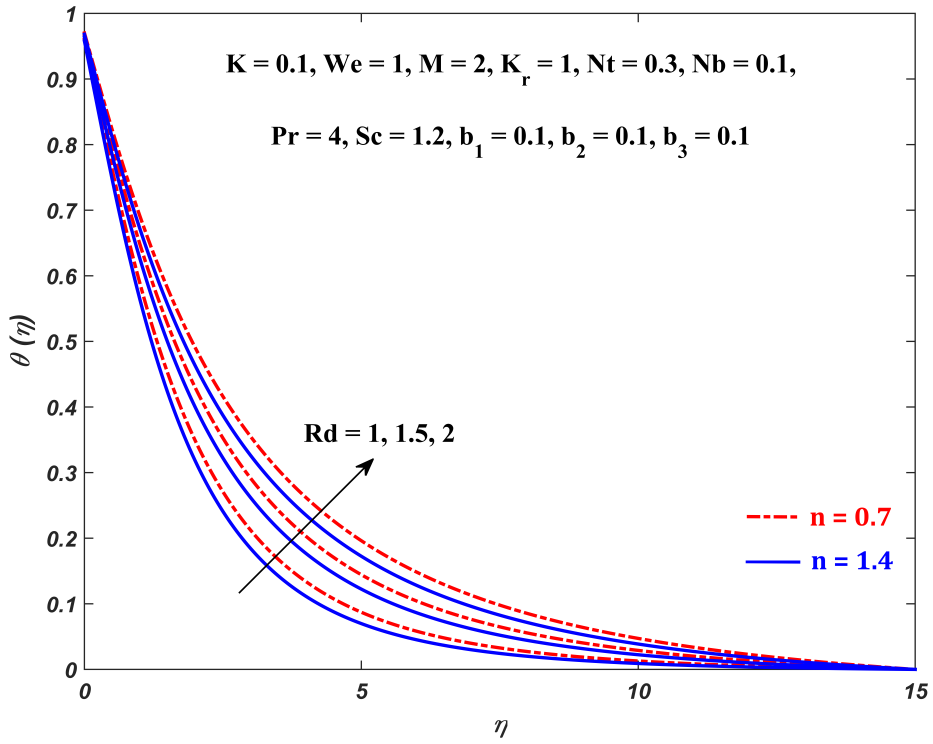

Figure 7.8: $\theta(\eta)$ for differing Rd values

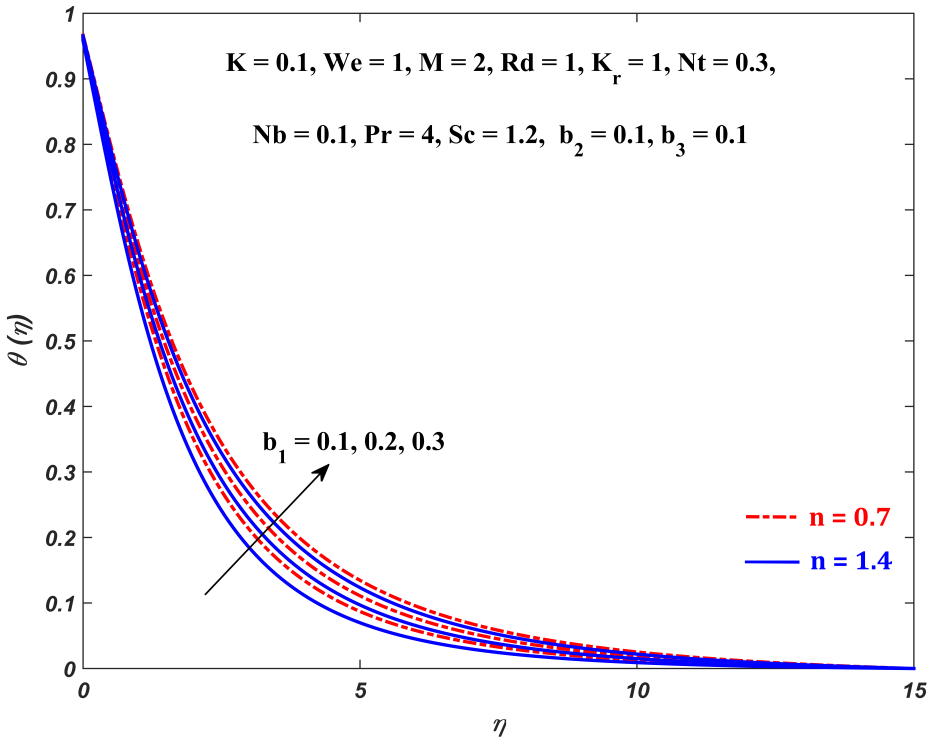

Figure 7.9: $\theta(\eta)$ for differing b_1 values

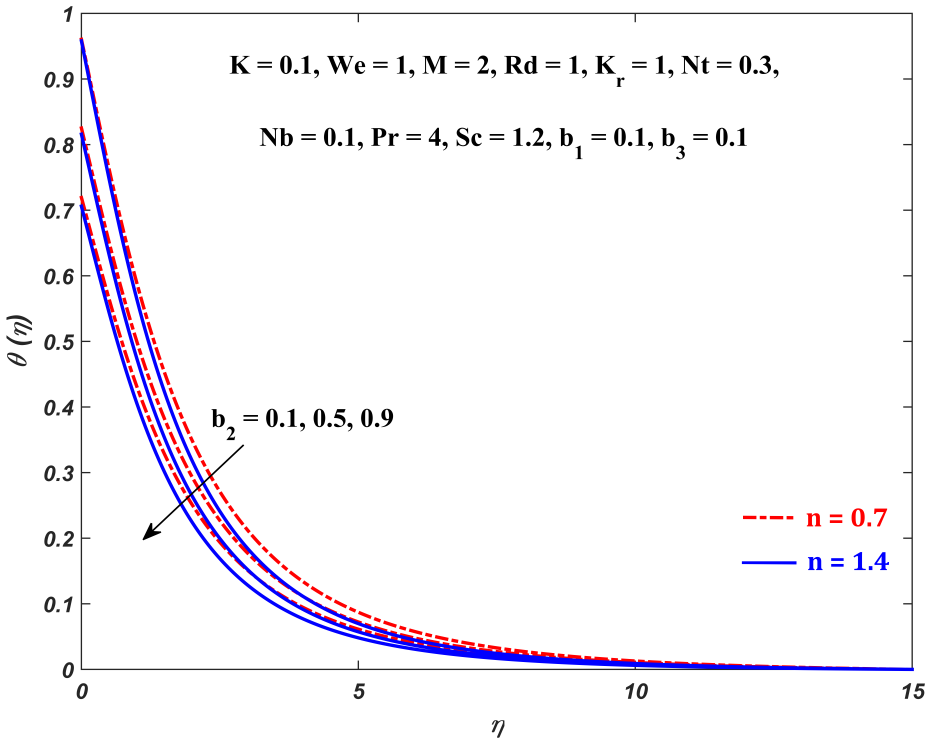

Figure 7.10: $\theta\,(\eta)$ for differing b_2 values

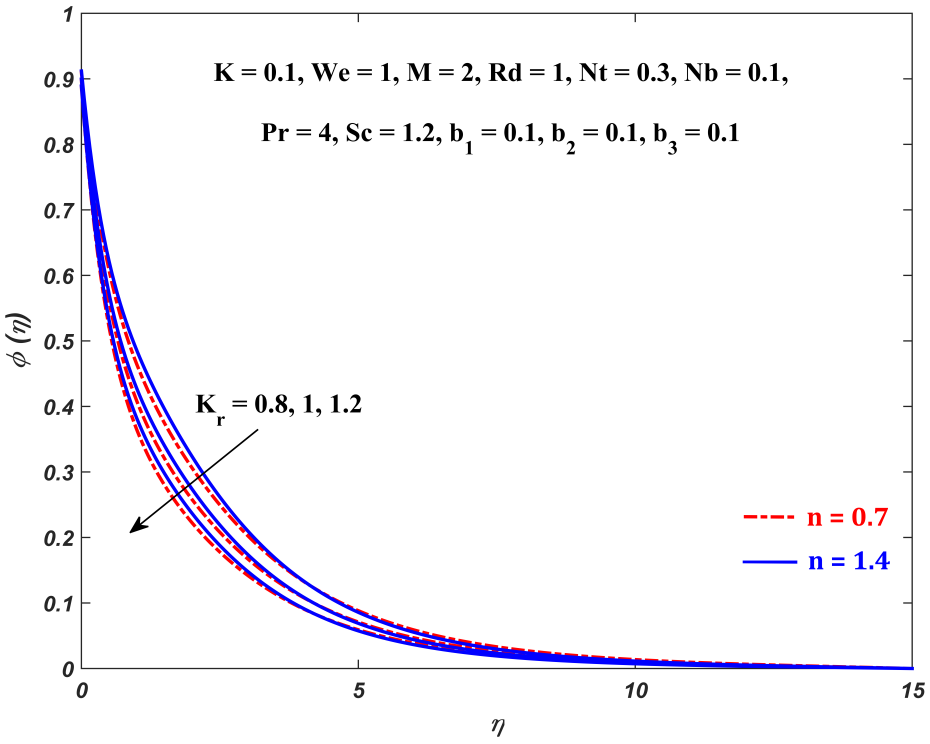

Figure 7.11: $\phi\,(\eta)$ for differing K_r values

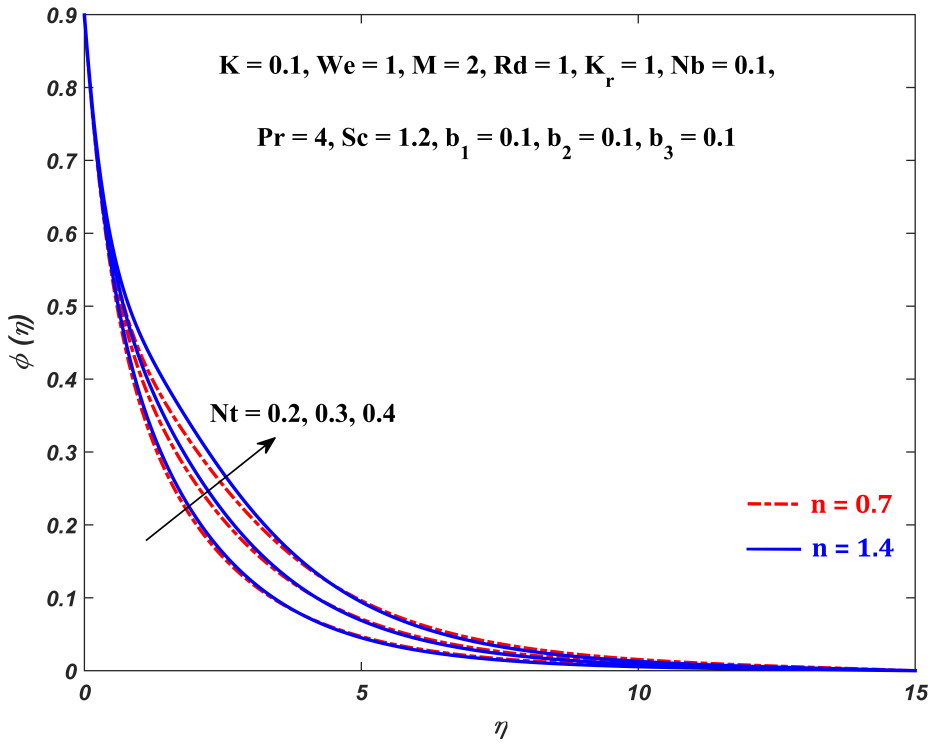

Figure 7.12: $\phi(\eta)$ for differing Nt values

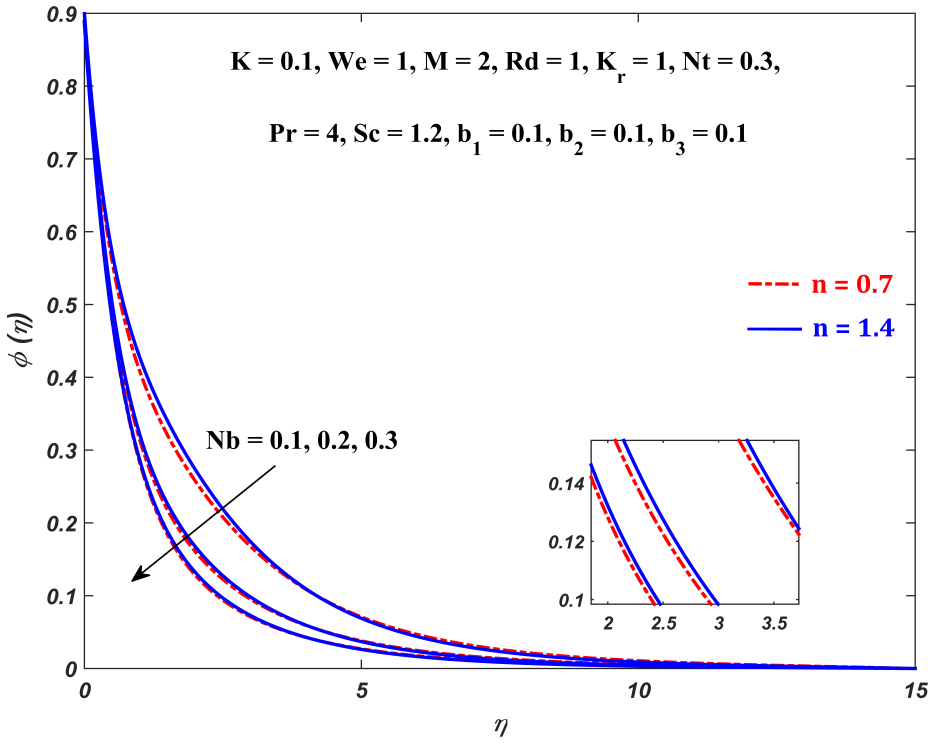

Figure 7.13: $\phi(\eta)$ for differing Nb values

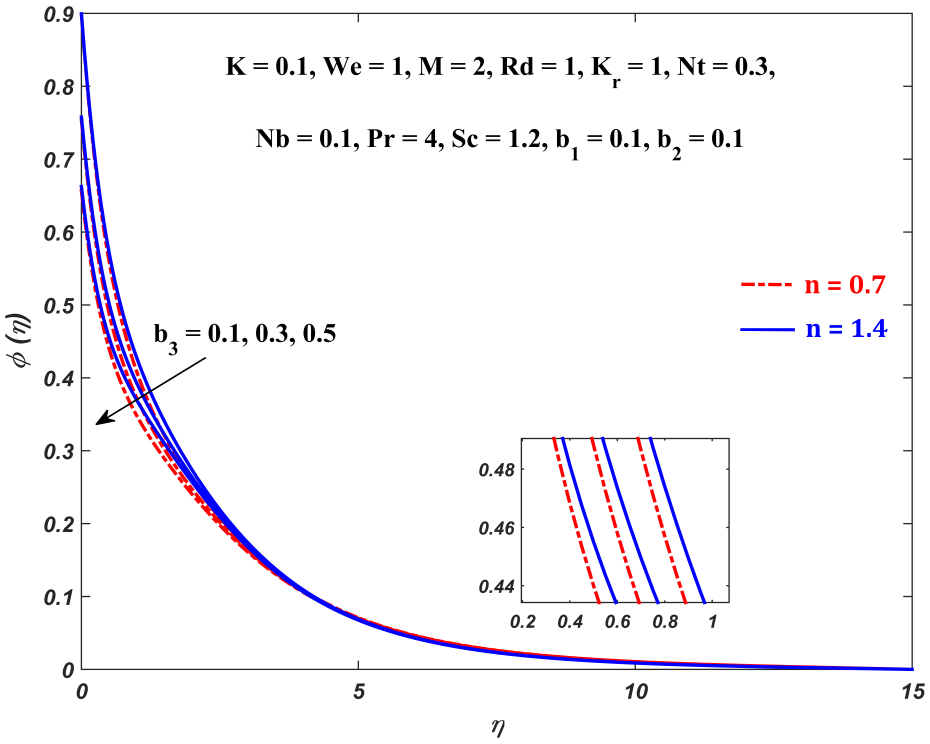

Figure 7.14: $\phi(\eta)$ for differing b_3 values

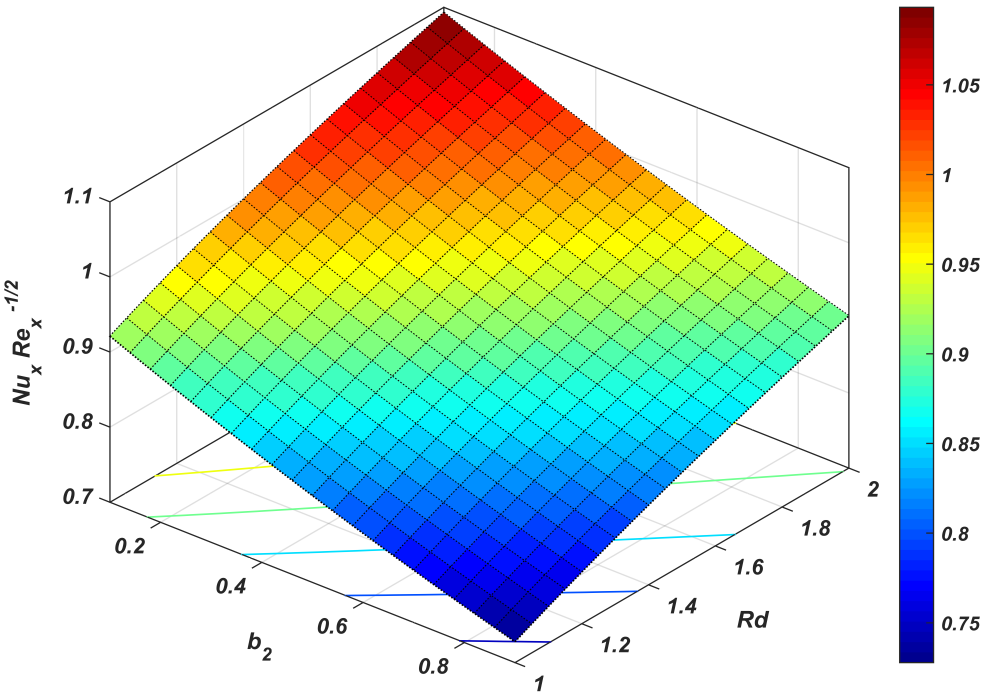

Figure 7.15: Simultaneous effect of Rd & b_2 on $Nu_x\ Re_x^{-1/2}$ $(n = 0.7)$

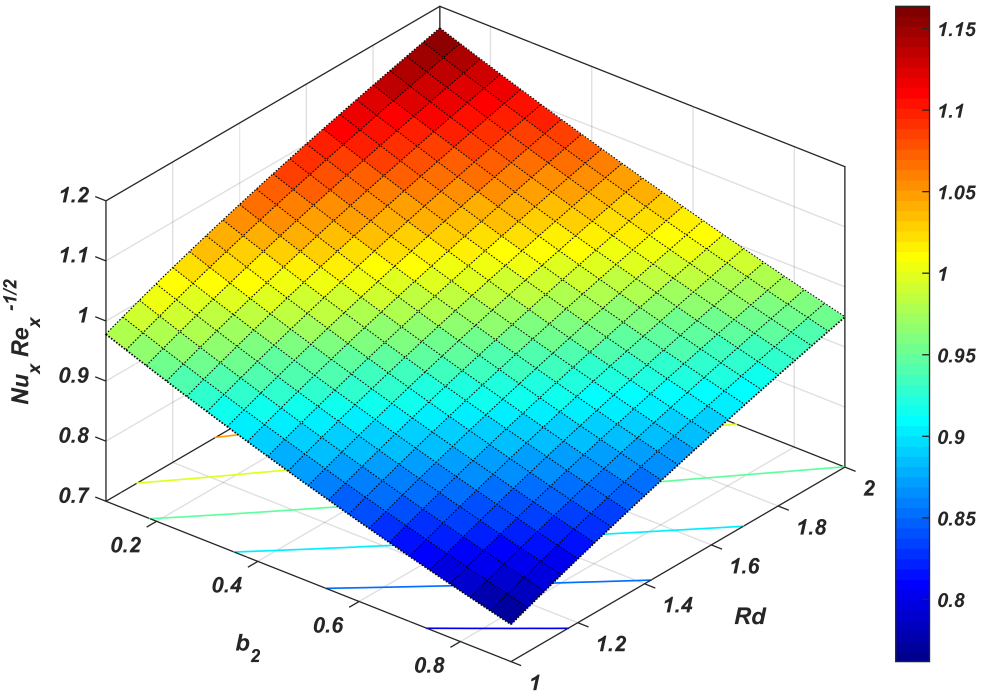

Figure 7.16: Simultaneous effect of Rd & b_2 on $Nu_x\ Re_x^{-1/2}$ $(n = 1.4)$

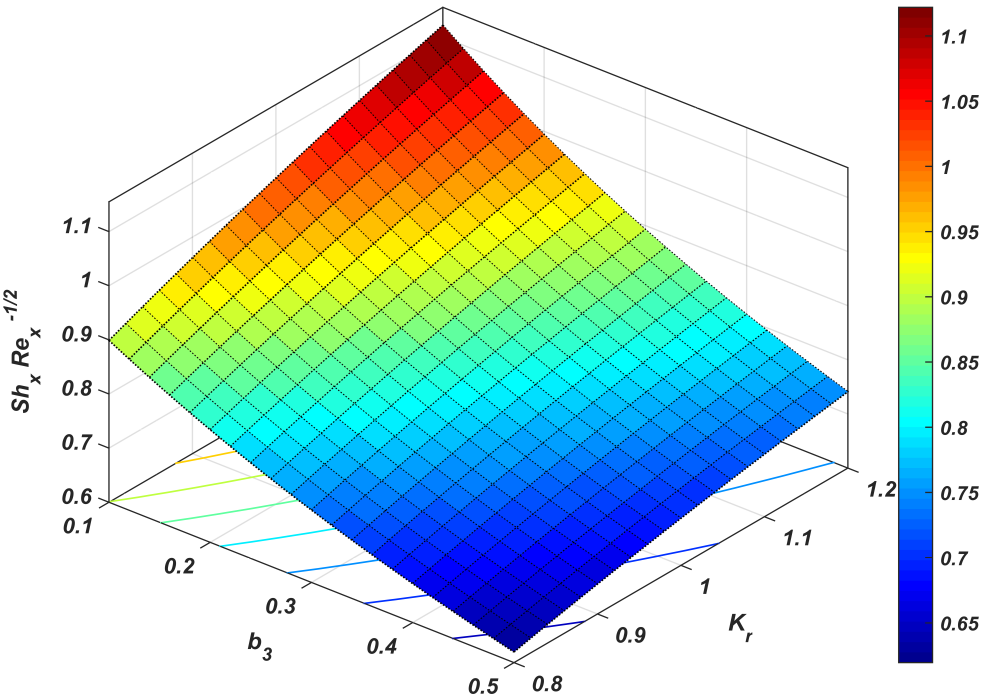

Figure 7.17: Simultaneous effect of K_r & b_3 on $Sh_x\ Re_x^{-1/2}$ $(n = 0.7)$

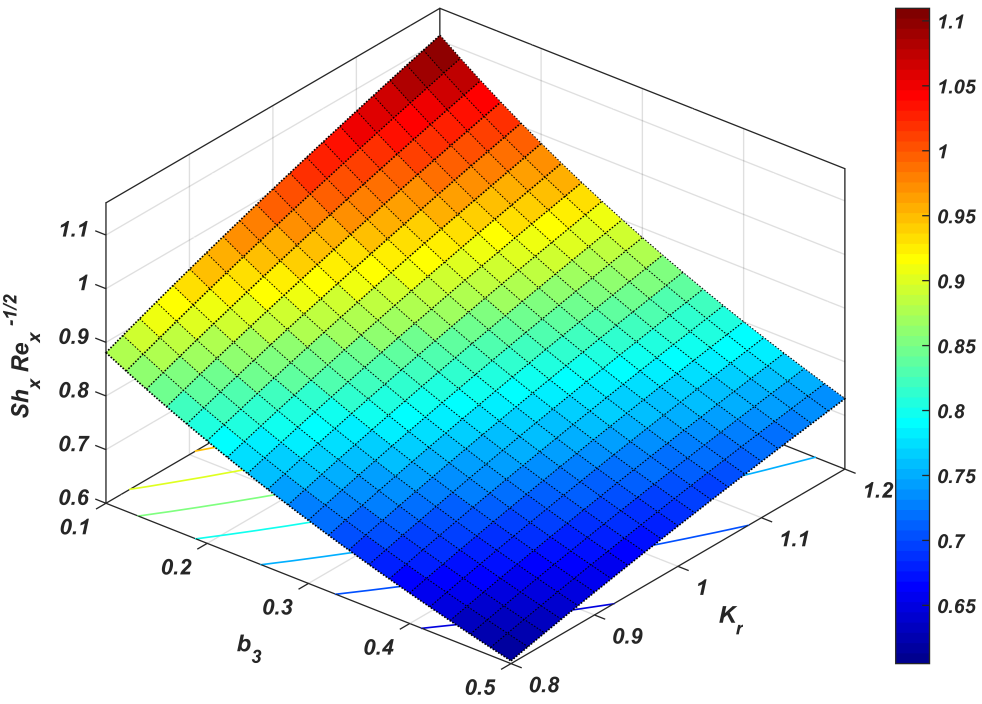

Figure 7.18: Simultaneous effect of K_r & b_3 on $Sh_x\ Re_x^{-1/2}$ $(n = 1.4)$

The simultaneous effect of effectual parameters (two at a time) on heat and mass transfer rate of pseudo-plastic and dilatant fluids is expressed using surface plots in Figures 7.15 - 7.18. It is understood from Figures 7.15 & 7.16 that the heat transfer rate is highest for larger values of Rd and lower values of b_2. It can also be interpreted that $Nu_x\ Re_x^{-1/2}$ is inversely proportional to b_2 and directly proportional to Rd. It is also understood from Figures 7.17 & 7.18 that Sherwood number is highest for larger values of K_r and lower values o fb_3 meaning $Sh_x\ Re_x^{-1/2}$ is inversely proportional to b_3 and directly proportional to K_r. $Nu_x\ Re_x^{-1/2}$ and $Sh_x\ Re_x^{-1/2}$ is higher for dilatant and pseudo-plastic fluids, respectively.

The variation in $\frac{1}{2}Cf_x\ Re_x^{1/2}$ for dilatant and pseudo-plastic fluids with various parameters is exhibited in Table 7.2. The impact of parameters on drag coefficient is analysed when $Pr = 4$ and $Sc = 1.2$. It is noted that We and b_1 have a constructive impact on $\frac{1}{2}Cf_x\ Re_x^{1/2}$ while K and M have a destructive result on $\frac{1}{2}Cf_x\ Re_x^{1/2}$ when $n < 1$. When $n > 1$, it is seen that b_1 has a constructive impact and We, K and M have a destructive impact on the $\frac{1}{2}Cf_x\ Re_x^{1/2}$.

Table 7.2: Variation in $\frac{1}{2}Cf_x\ Re_x^{1/2}$ for various parameters when $Pr = 4$ and $Sc = 1.2$

n	**K**	**We**	**M**	$\mathbf{b_1}$	$\mathbf{\frac{1}{2}Cf_x\ Re_x^{1/2}}$
0.7	0.1	1	2	0.1	1.401116065
0.7	0.4	1	2	0.1	1.474059753
0.7	0.8	1	2	0.1	1.563215753
Slope					**0.231101741**
0.7	0.1	0.5	2	0.1	1.453286406
0.7	0.1	1	2	0.1	1.401116065
0.7	0.1	1.5	2	0.1	1.349602648
Slope					**-0.103683758**
0.7	0.1	1	0.7	0.1	1.107507373
0.7	0.1	1	1.3	0.1	1.257426226
0.7	0.1	1	2	0.1	1.401116065
Slope					**0.225285629**
0.7	0.1	1	2	0.1	1.401116065
0.7	0.1	1	2	0.15	1.306473791
0.7	0.1	1	2	0.2	1.223891623
Slope					**-1.77224442**
1.4	0.1	1	2	0.1	1.562975764
1.4	0.4	1	2	0.1	1.684069593
1.4	0.8	1	2	0.1	1.832448022
Slope					**0.384202839**
1.4	0.1	0.5	2	0.1	1.509404611
1.4	0.1	1	2	0.1	1.562975764
1.4	0.1	1.5	2	0.1	1.61370417
Slope					**0.104299559**
1.4	0.1	1	0.7	0.1	1.203372386
1.4	0.1	1	1.3	0.1	1.384930015
1.4	0.1	1	2	0.1	1.562975764
Slope					**0.276004328**
1.4	0.1	1	2	0.1	1.562975764
1.4	0.1	1	2	0.15	1.43082423
1.4	0.1	1	2	0.2	1.321305561
Slope					**-2.41670203**

The respective impact rates of various parameters (slope of linear regression) are also shown in Table 7.2. The slope of linear regression indicates the nature of variation in $\frac{1}{2}Cf_x\ Re_x^{1/2}$. A negative slope implies that the varying parameter has a destructive effect on $\frac{1}{2}Cf_x\ Re_x^{1/2}$ meaning, an increase in the parameter will reduce the value of $\frac{1}{2}Cf_x\ Re_x^{1/2}$. The rate of decrease/increase of $\frac{1}{2}Cf_x\ Re_x^{1/2}$ per unit value of the varying parameter is explained using the magnitude of slope.

7.5 Statistical Frame

7.5.1 Response Surface Methodology

Response surface methodology (RSM) is a statistical technique that analyses the collaborative impact of influential parameters (independent variables) on the physical quantity of interest (response/dependent variable). RSM estimates a model for the physical quantity of interest using the central composite design (CCD) based data. In this chapter, the impact of Hartmann number ($1 \leq M \leq 2$), thermal radiation ($1 \leq Rd \leq 2$) and temperature slip parameter ($0.1 \leq b_2 \leq 0.3$) on $Nu_{0.7}$ (Nusselt number when $n = 0.7$) and $Nu_{1.4}$ (Nusselt number when $n = 1.4$) are statistically scrutinized. Table 7.3 bespeaks the effective parameters and their levels.

The general model (adopting CCD) for response variable involving linear, interactive and quadratic terms is expressed by:

$$\text{Response} = \xi_0 + \xi_1 A + \xi_2 B + \xi_3 C + \xi_4 AB + \xi_5 BC + \xi_6 AC + +\xi_7 A^2 + \xi_8 B^2 + \xi_9 C^2$$

where ξ_i $(i = 0, 1, \ldots, 9)$ represents the regression coefficients. The experimental design and the response for the 20 runs (according to CCD) are given in Table 7.4. Rows 15-20 of Table 7.4 are repeated for increased model accuracy.

The ANOVA table (Tables 7.5 & 7.6) illustrates the efficiency of the estimated model. A parameter is claimed to be significant if the corresponding F-value is greater than 1 and the corresponding p-value is less than 0.05. It is observed that the quadratic term in b_2 and the interactive term $Rd * b_2$ are not significant. Hence, these terms are removed from the model. The coefficient of determination (R^2) for the model is found to be 99.9% which boosts the model accuracy.

The fitted quadratic models are given by:

$$Nu_{0.7} = 0.96050 - 0.19996\ M + 0.40566\ Rd - 0.4992\ b_2 + 0.03113\ M^2 - 0.04707\ Rd^2 - 0.04660\ M\ Rd + 0.09600\ M\ b_2 \quad (7.5.1)$$

$$Nu_{1.4} = 0.95707 - 0.17183\ M + 0.43809\ Rd - 0.5313\ b_2 + 0.02684\ M^2 - 0.05256\ Rd^2 - 0.04760\ M\ Rd + 0.09300\ M\ b_2 \quad (7.5.2)$$

The reliability of the estimated models for the Nusselt number is further clarified using residual plots (see Figures 7.19 & 7.20). All points in the normal probability plot are situated beside a straight line with an insignificant deflection and the residual histogram is approximately bell-shaped confirming the normal nature of residuals. Furthermore, a maximum error of 0.002 can be observed from the fitted versus residual plot which also contributes to the accuracy of the model.

From Equations (7.5.1) and (7.5.2), it can be inferred that M & b_2 descends Nusselt number (both cases) and Rd has a positive effect on Nusselt number (both cases). The parallel interaction of two parameters on the Nusselt number is graphed using surface and contour plots (see Figures 7.21 - 7.24) by fixing the third parameter at the medium level. From Figures 7.21 - 7.24, it is perceived that the heat transfer rate is highest for smaller values of M & b_2 and larger values of Rd.

Table 7.3: Effectual parameter levels

Parameter	**Symbol**	**Levels**		
		-1 (low)	**0 (medium)**	**1 (high)**
M	A	1	1.5	2
Rd	B	1	1.5	2
b_2	C	0.1	0.2	0.3

Table 7.4: CCD experimental design and the corresponding responses

Run	Coded Values			Actual Values			Response	
	A	**B**	**C**	**M**	**Rd**	$\mathbf{b_2}$	$\mathbf{Nu_{0.7}}$	$\mathbf{Nu_{1.4}}$
1	-1	-1	-1	1.0	1.0	0.1	1.0635	1.1063
2	1	-1	-1	2.0	1.0	0.1	0.9211	0.9779
3	-1	1	-1	1.0	2.0	0.1	1.283	1.3407
4	1	1	-1	2.0	2.0	0.1	1.0932	1.1636
5	-1	-1	1	1.0	1.0	0.3	0.9898	1.0265
6	1	-1	1	2.0	1.0	0.3	0.8658	0.9156
7	-1	1	1	1.0	2.0	0.3	1.2093	1.2603
8	1	1	1	2.0	2.0	0.3	1.0395	1.1029
9	-1	0	0	1.0	1.5	0.2	1.1494	1.1974
10	1	0	0	2.0	1.5	0.2	0.989	1.0506
11	0	-1	0	1.5	1.0	0.2	0.9537	1.001
12	0	1	0	1.5	2.0	0.2	1.1456	1.2073
13	0	0	-1	1.5	1.5	0.1	1.0939	1.1534
14	0	0	1	1.5	1.5	0.3	1.0304	1.0829
15	0	0	0	1.5	1.5	0.2	1.0614	1.1173
16	0	0	0	1.5	1.5	0.2	1.0614	1.1173
17	0	0	0	1.5	1.5	0.2	1.0614	1.1173
18	0	0	0	1.5	1.5	0.2	1.0614	1.1173
19	0	0	0	1.5	1.5	0.2	1.0614	1.1173
20	0	0	0	1.5	1.5	0.2	1.0614	1.1173

Table 7.5: ANOVA table ($Nu_{0.7}$)

Source	Deg. of freedom	Adj. sum of squares	Adj. mean squares	Regression Coefficient	F-Value	p-Value
Model	9	0.169172	0.018797		13479.2	0
Linear	3	0.16747	0.055823		40030.91	0
M	1	0.061842	0.061842	-0.19996	44347.14	0
Rd	1	0.095394	0.095394	0.40566	68407.08	0
b_2	1	0.010234	0.010234	-0.4992	7338.5	0
Square	3	0.000431	0.000144		103.01	0
$M * M$	1	0.000167	0.000167	0.03113	119.42	0
$Rd * Rd$	1	0.000381	0.000381	-0.04707	273.11	0
$b_2 * b_2$	1	0.000001	0.000001	0.0732	1.06	**0.328**
2-Way Interaction	3	0.00127	0.000423		303.67	0
$M * Rd$	1	0.001086	0.001086	-0.0466	778.61	0
$M * b_2$	1	0.000184	0.000184	0.096	132.18	0
$Rd * b_2$	1	0	0	0.004	0.23	**0.642**
Constant				0.9605		
Error	10	0.000014	0.000001			
Lack-of-Fit	5	0.000014	0.000003		*	*
Pure Error	5	0	0			
Total	19	0.169186				
$R^2 = 99.99\%$				Adjusted $R^2 = 99.98\%$		

Table 7.6: ANOVA table ($Nu_{1.4}$)

Source	Deg. of freedom	Adj. sum of squares	Adj. mean squares	Regression Coefficient	F-Value	p-Value
Model	9	0.176	0.01956		16960	0
Linear	3	0.17416	0.05805		50349.3	0
M	1	0.05193	0.05193	-0.1718	45034.9	0
Rd	1	0.10973	0.10973	0.43809	95163.1	0
b_2	1	0.01251	0.01251	-0.5313	10850	0
Square	3	0.00053	0.00018		153.23	0
$M * M$	1	0.00012	0.00012	0.02684	107.35	0
$Rd * Rd$	1	0.00048	0.00048	-0.0526	411.85	0
$b_2 * b_2$	1	0.000002	0.000002	0.0859	1.76	**0.214**
2-Way Interaction	3	0.00131	0.00044		377.55	0
$M * Rd$	1	0.00113	0.00113	-0.0476	982.53	0
$M * b_2$	1	0.00017	0.00017	0.093	150.02	0
$Rd * b_2$	1	0	0	0.0025	0.11	**0.749**
Constant				0.95707		
Error	10	0.000012	0.000001			
Lack-of-Fit	5	0.000012	0.000002		*	*
Pure Error	5	0	0			
Total	19	0.17601				
$R^2 = 99.99\%$				Adjusted $R^2 = 99.99\%$		

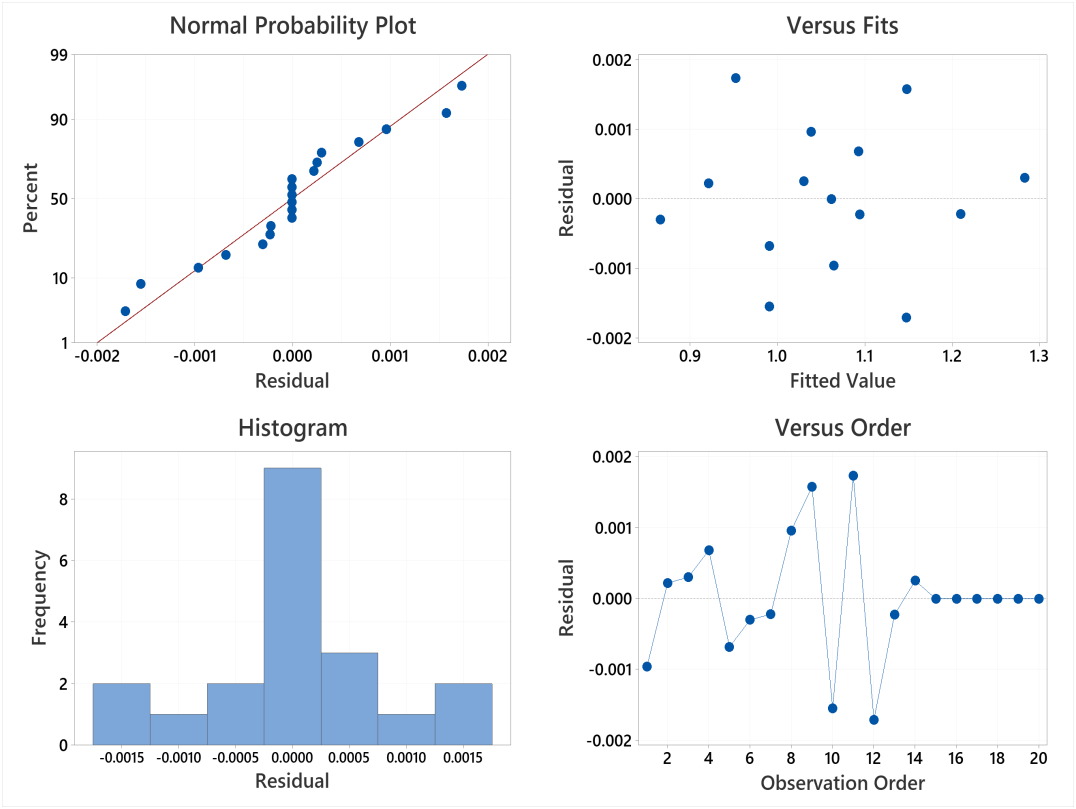

Figure 7.19: Residual plots for $Nu_{0.7}$

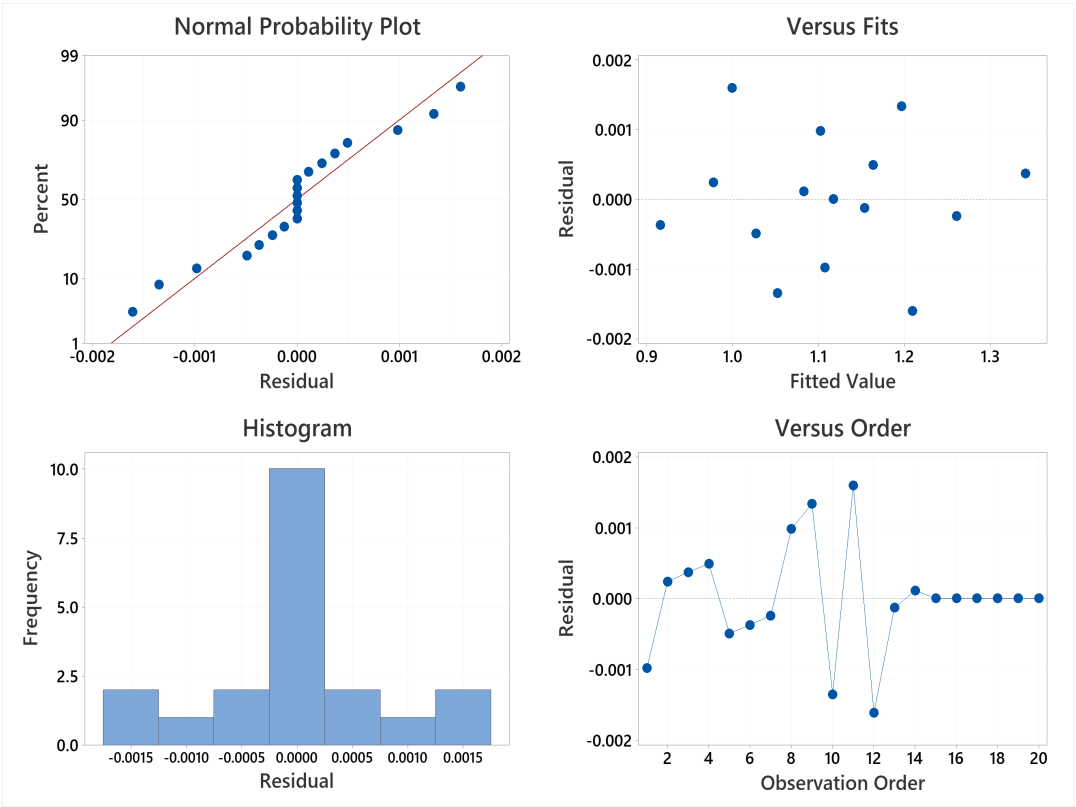

Figure 7.20: Residual plots for $Nu_{1.4}$

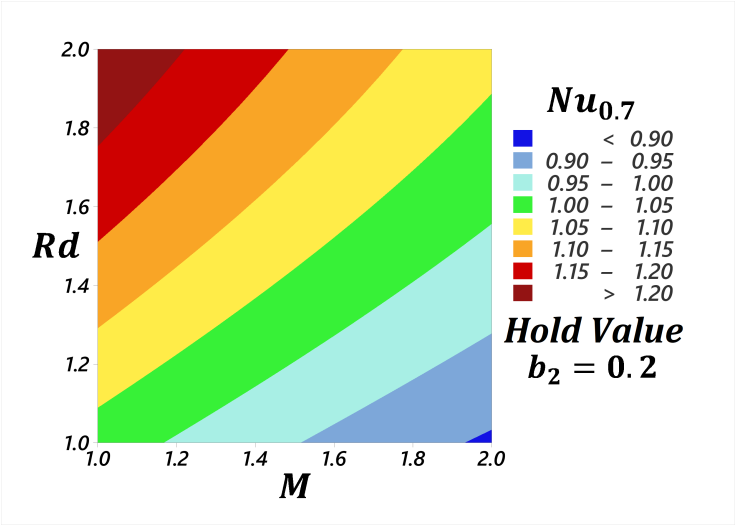

(a)

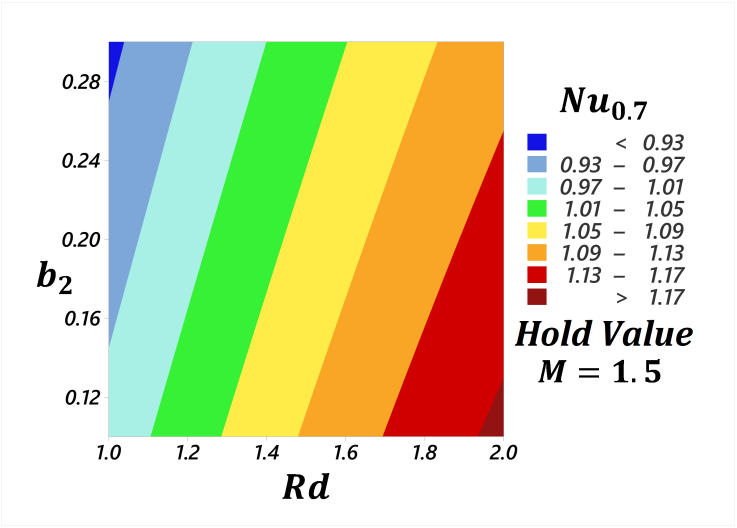

(b)

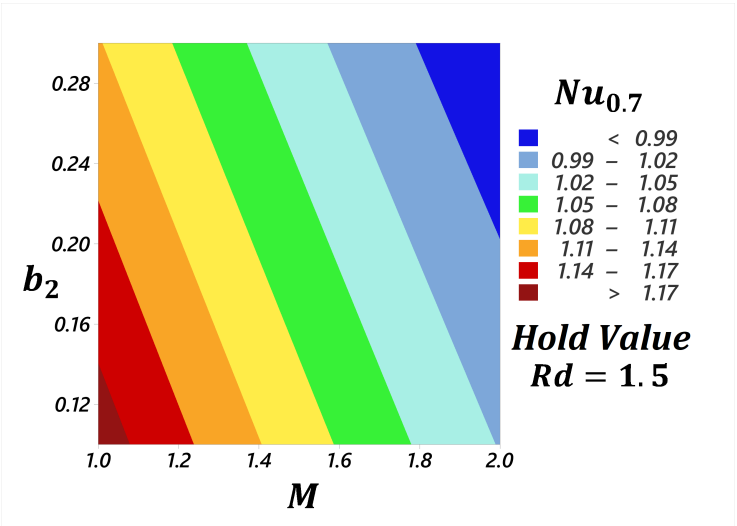

(c)

Figure 7.21: Contour plots for $Nu_{0.7}$

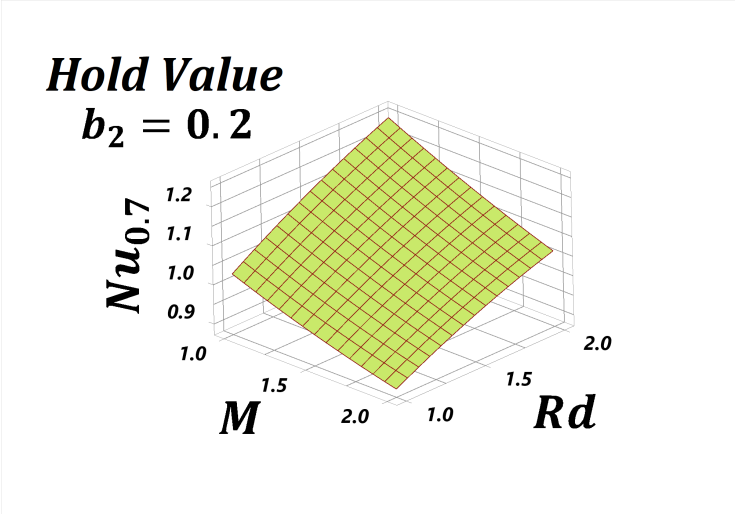

(a)

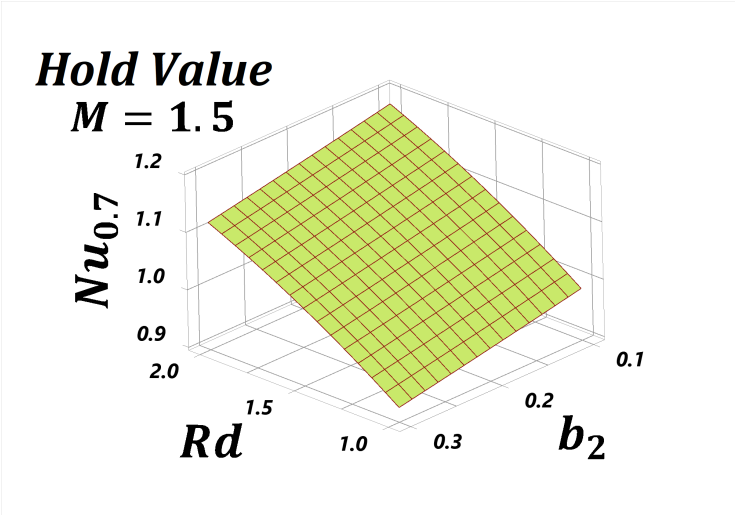

(b)

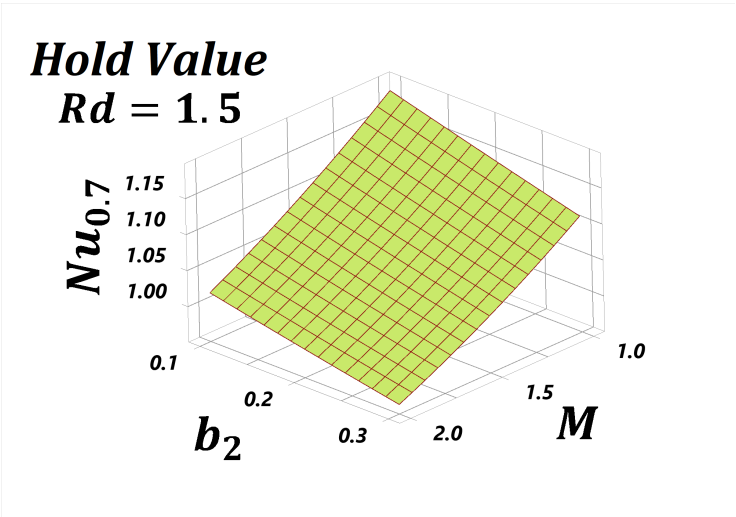

(c)

Figure 7.22: Surface plots for $Nu_{0.7}$

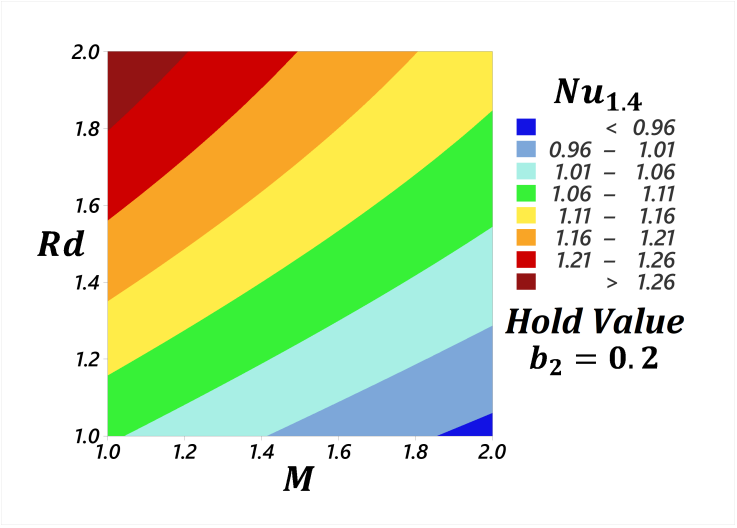

(a)

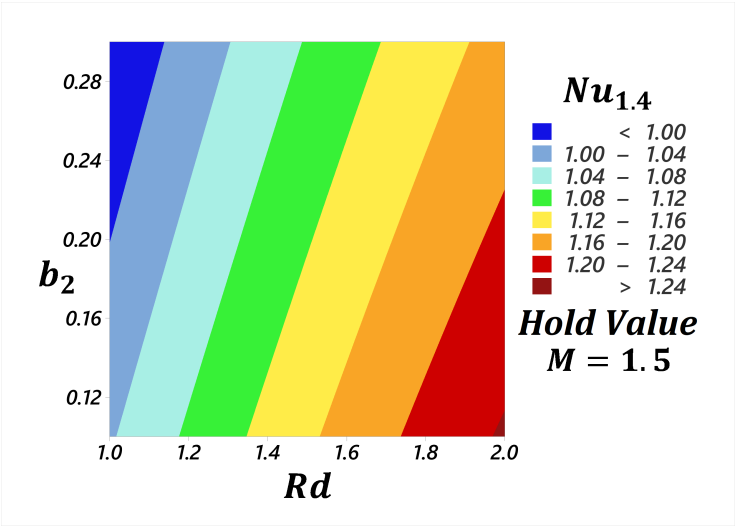

(b)

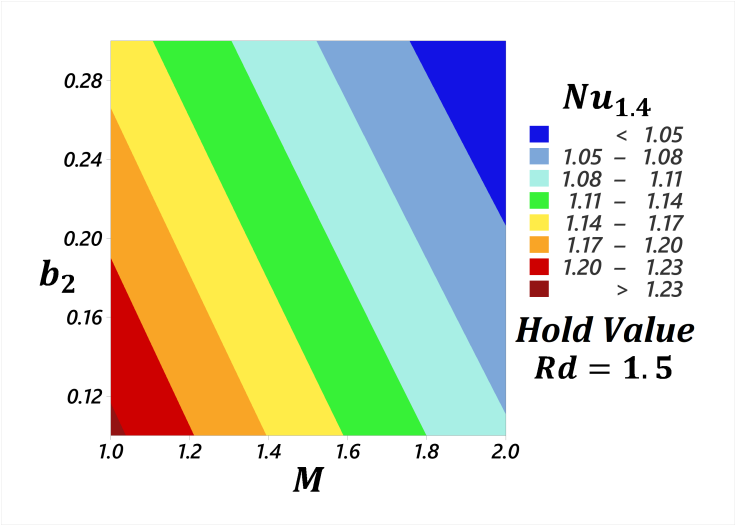

(c)

Figure 7.23: Contour plots for $Nu_{1.4}$

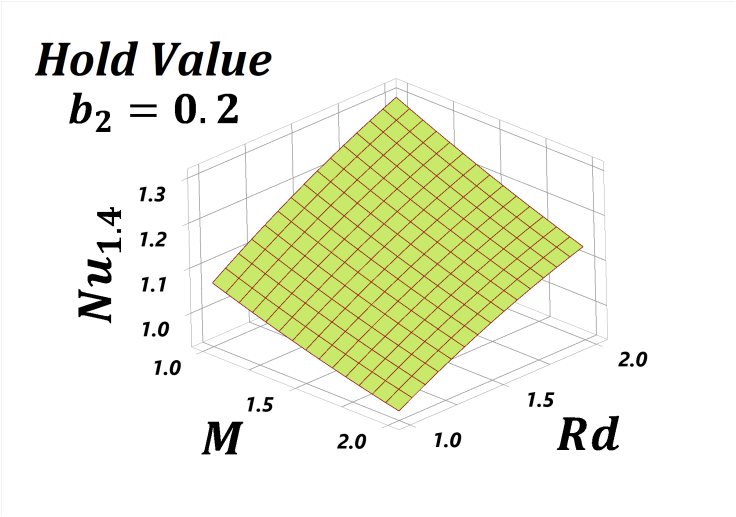

(a)

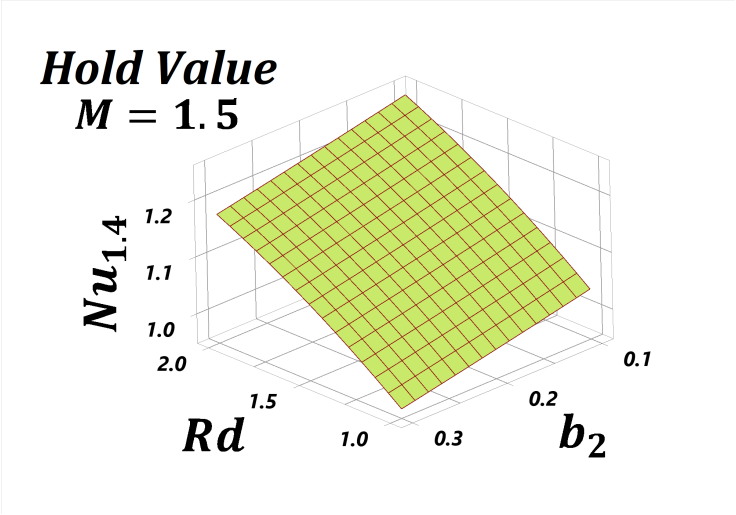

(b)

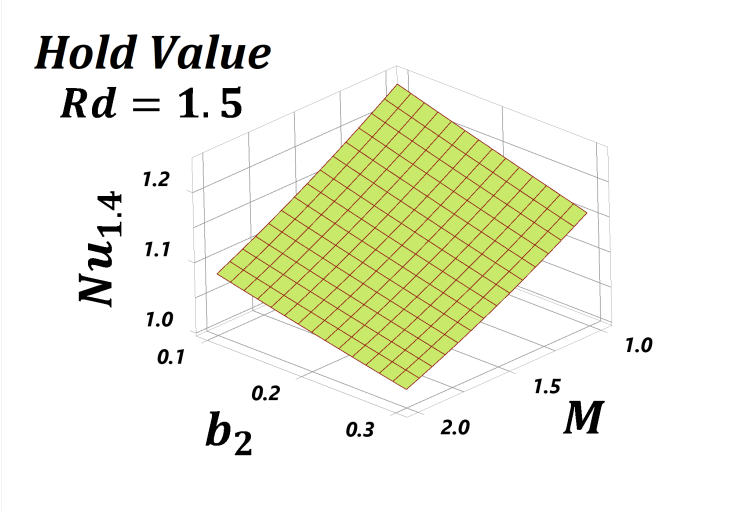

(c)

Figure 7.24: Surface plots for $Nu_{1.4}$

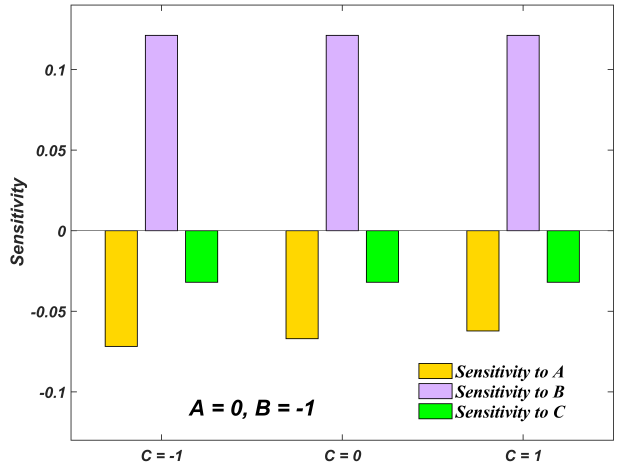

(a)

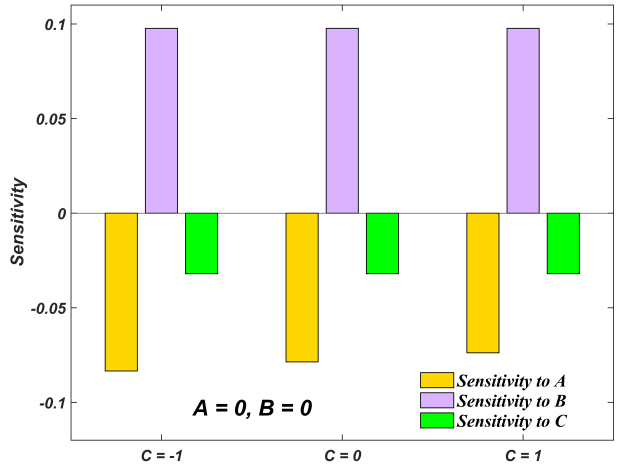

(b)

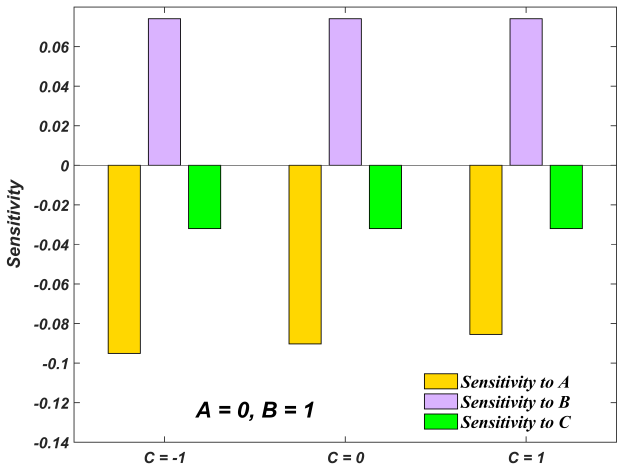

(c)

Figure 7.25: Bar charts showcasing the sensitivity of $Nu_{0.7}$

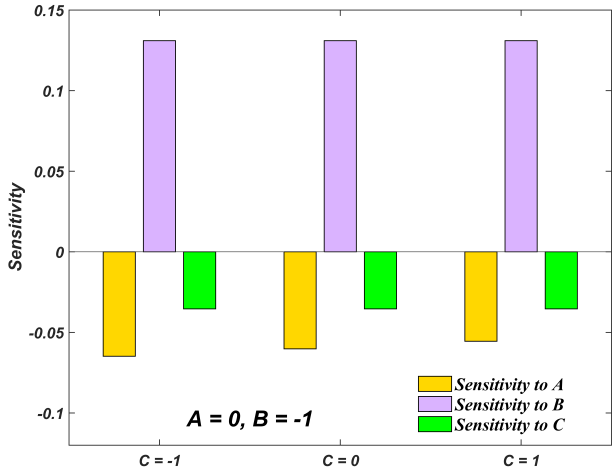

(a)

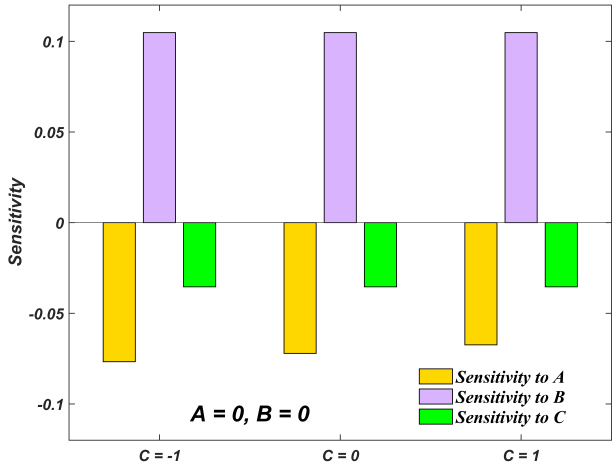

(b)

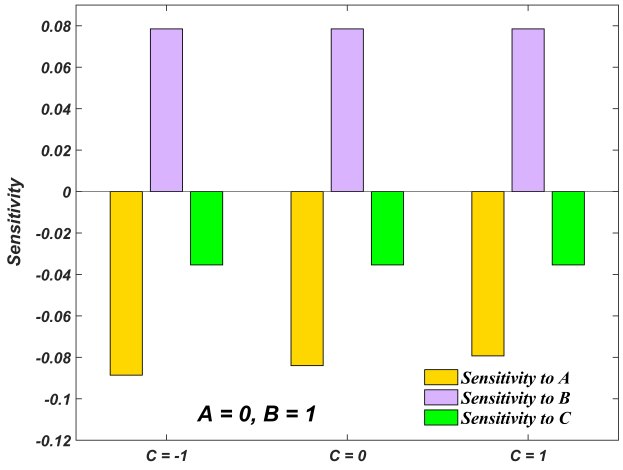

(c)

Figure 7.26: Bar charts showcasing the sensitivity of $Nu_{1.4}$

7.5.2 Sensitivity Analysis

The quadratic models (in coded form) after neglecting the insignificant terms are given by:

$$Nu_{0.7} = 1.06141 - 0.07864\ A + 0.09767\ B - 0.03199\ C + 0.007782\ A^2 - 0.011768\ B^2 - 0.01165\ A\ B + 0.0048\ A\ C \tag{7.5.3}$$

$$Nu_{1.4} = 1.1173 - 0.07206\ A + 0.10475\ B - 0.03537\ C + 0.006709\ A^2 - 0.013141\ B^2 - 0.0119\ A\ B + 0.00465\ A\ C \tag{7.5.4}$$

Then the sensitivity functions are:

$$\frac{\partial Nu_{0.7}}{\partial A} = -0.07864 + 0.015564\ A - 0.01165\ B + 0.0048\ C$$

$$\frac{\partial Nu_{0.7}}{\partial B} = 0.09767 - 0.023536\ B - 0.01165\ A$$

$$\frac{\partial Nu_{0.7}}{\partial C} = -0.03199 + 0.0048\ A$$

$$\frac{\partial Nu_{1.4}}{\partial A} = -0.07206 + 0.013418\ A - 0.0119\ B + 0.00465\ C$$

$$\frac{\partial Nu_{1.4}}{\partial B} = 0.10475 - 0.026282\ B - 0.0119\ A$$

$$\frac{\partial Nu_{1.4}}{\partial C} = -0.03537 + 0.00465\ A$$

Sensitivity analysis accounts for the variation induced by the augmenting parameter on the remaining effectual parameter. The nature of the sensitivity is indicated by a positive or negative sign which means that the response term is positively or negatively correlated with the change in the effective parameter values. The magnitude of sensitivity indicates the intensity of this relationship. The sensitivity for Nusselt number (both cases) is tabulated in Table 7.7 keeping M in the medium level. It is noted that M & b_2 exhibits negative sensitivity and Rd exhibits a positive sensitivity towards $Nu_{0.7}$ & $Nu_{1.4}$.

The sensitivity of the Nusselt number (both cases) is also visualized using bar charts (Figure 7.25 & 7.26). It is seen that the results of sensitivity analysis are in

perfect harmony with the results inferred using RSM. It is also noticed that the Nusselt number is most sensitive with Rd (for low and medium levels of Rd) and M (when Rd is at the high level).

Table 7.7: Sensitivity of $Nu_{0.7}$ & $Nu_{1.4}$ when $A = 0$

B	C	Sensitivity					
		$\frac{\partial \mathbf{Nu_{0.7}}}{\partial \mathbf{A}}$	$\frac{\partial \mathbf{Nu_{0.7}}}{\partial \mathbf{B}}$	$\frac{\partial \mathbf{Nu_{0.7}}}{\partial \mathbf{C}}$	$\frac{\partial \mathbf{Nu_{1.4}}}{\partial \mathbf{A}}$	$\frac{\partial \mathbf{Nu_{1.4}}}{\partial \mathbf{B}}$	$\frac{\partial \mathbf{Nu_{1.4}}}{\partial \mathbf{C}}$
	-1	-0.0718	0.1212	-0.032	-0.0648	0.131	-0.0354
-1	0	-0.067	0.1212	-0.032	-0.0602	0.131	-0.0354
	1	-0.0622	0.1212	-0.032	-0.0555	0.131	-0.0354
	-1	-0.0834	0.0977	-0.032	-0.0767	0.1048	-0.0354
0	0	-0.0786	0.0977	-0.032	-0.0721	0.1048	-0.0354
	1	-0.0738	0.0977	-0.032	-0.0674	0.1048	-0.0354
	-1	-0.0951	0.0741	-0.032	-0.0886	0.0785	-0.0354
1	0	-0.0903	0.0741	-0.032	-0.084	0.0785	-0.0354
	1	-0.0855	0.0741	-0.032	-0.0793	0.0785	-0.0354

7.6 Conclusion

The key points noted from the study are:

- Hartmann number and velocity slip exhibit a destructive nature on the axial velocity profile.
- Increasing Weissenberg number improves the velocity of dilatant fluids and reduces the velocity in the case of pseudo-plastic fluids.
- The curvature parameter is directly proportional to axial velocity and temperature profile.
- Velocity slip has a positive effect while Hartmann number descends skin friction coefficient.

- The slip effect reduces the temperature, velocity and concentration profiles.
- Nusselt number is elevated due to radiation parameter and lowered with thermal slip.
- Chemical reaction parameter promotes and solutal slip demotes mass transfer.
- Temperature is enhanced due to Hartmann number and linear thermal radiation.
- The concentration profile is inversely proportional to the chemically reactive species.
- Heat transfer rate is highest for smaller values of Hartmann number.
- Hartmann number and thermal slip parameter exhibit negative sensitivity towards heat transfer rate (both cases) whereas radiation parameter showcase positive sensitivity towards heat transfer rate (both cases).

Appendix I: Non-dimensional qunatities

$We = \sqrt{\frac{\Gamma^2\ a^3\ x^2\ r^2}{\vartheta_f\ l^3\ R^2}}$	Weissenberg number
$M = \frac{\sigma_f\ B_0^2\ l}{\rho_f\ a}$	Hartmann number
$Nb = \frac{(\rho C)_p\ D_B\ (\mathcal{C}_w - \mathcal{C}_\infty)}{\vartheta_f\ (\rho C)_f}$	Brownian motion parameter
$Pr = \frac{(\mu C_p)_f}{k_f} = \frac{\vartheta_f}{\alpha_f}$	Prandtl number
$K_r = \frac{K_l}{a}$	Chemical reaction parameter
$Sc = \frac{\vartheta_f}{D_B}$	Schmidt number
$Rd = \frac{4\ \sigma^*\ T_\infty^3}{k_f\ k^*}$	Thermal radiation parameter
$Nt = \frac{(\rho C)_p\ D_T\ (T_w - T_\infty\ )}{T_\infty\ \ \vartheta_f\ (\rho C)_f}$	Thermophoresis parameter
$K = \frac{1}{R}\sqrt{\frac{l\ \vartheta_f}{a}}$	Curvature parameter
$b_1 = N_1\sqrt{\frac{a}{l\ \vartheta_f}}$	Velocity slip parameter
$b_2 = N_2\sqrt{\frac{a}{l\ \vartheta_f}}$	Thermal slip parameter
$b_3 = N_3\sqrt{\frac{a}{l\ \vartheta_f}}$	Solutal slip parameter

Appendix II: Nomenclature

a	Reference velocity	k^*	Mean absorption coefficient
l	Characteristic length	B_0	Strength of magnetic field
R	Radius of the cylinder	T_∞	Ambient fluid temperature
$\mathcal{C}$	Fluid concentration	T	Fluid temperature
x, r	Cylindrical coordinates	N_i	Slip factor; i=1, 2, 3
n	Power law index	$\mathcal{C}_w$	Nanoparticle concentration near wall
T_w	Wall fluid temperature	$\mathcal{C}_\infty$	Ambient nanoparticle concentration
$(\rho C_p)_f$	Heat capacity of fluid	Cf_x	Local drag coefficient
K_l	Reaction rate constant	Nu_x	Local Nusselt number
Sh_x	Local Sherwood number	σ_f	Fluid's electrical conductivity
u, v	Velocity components	Γ	Time material constant
η	Dimensionless variable	D_B	Brownian diffusion coefficient
α_f	Thermal diffusivity	D_T	Thermophoretic diffusion coefficient
k_f	Thermal conductivity	ϑ_f	Fluid's kinematic viscosity
ρ_f	Fluid density	$\frac{(\rho C_p)_p}{(\rho C_p)_f}$	Effective heat capacity ratio

Chapter 8

Bioconvective stagnation-point flow over a rotating stretchable disk *

8.1 Introduction

The striking point at which the fluid's local velocity is zero is denominated as the stagnation-point. The phenomenon caused by the unpredictable movement of microorganisms is termed bioconvection. Owing to its practical application in pharmaceuticals, biosensors, medical instruments, bio-chromatography, microchip pump, biomedical science, micro-actuators, and aerodynamics, the bioconvective stagnation-point flow over a whirling extendible disk is investigated. Ferro-nanofluid has been particularly chosen in this work since water-based magnetite nanofluid and rotating disk share similar applications. The nanomaterial flow has been modelled using the modified Buongiorno nanofluid model (MBNM). The impact of the stratification constraints and magnetic field are also accounted. Von Kármán's similarity transformations are employed and the transmuted nonlinear ODEs are resolved using the finite-difference based *bvp5c* routine. MATLAB generated flow profiles have been analyzed for augmentations in the influential parameter values. The influence of magnetic field parameter ($0.2 \leq M \leq 1.8$), thermal stratification parameter ($0.1 \leq S_1 \leq 0.5$), volume fraction of magnetite nanoparticles ($0.01 \leq \phi \leq 0.09$), and velocity ratio parameter ($0.1 \leq S \leq 0.5$) on the heat transfer rate has been scrutinized statistically using a five-level four-factor response surface optimized model. The main objectives of the current chapter are to:

*Published in: Journal of the Indian Chemical Society (Elsevier), 2022; 99(8); 100615.

- Model the bioconvective stagnation-point flow of ferro-nanofluid over a rotating stretchable disk using the modified Buongiorno nanofluid model.
- Analyze the MATLAB generated flow profiles for augmentations in the effectual parameter values.
- Depict the simultaneous effect of influential parameters on the physical quantities with the aid of three-dimensional surface plots.
- Estimate the interactive effects of the key parameters on the heat transfer rate utilizing the five-level four-factor response surface optimized model.

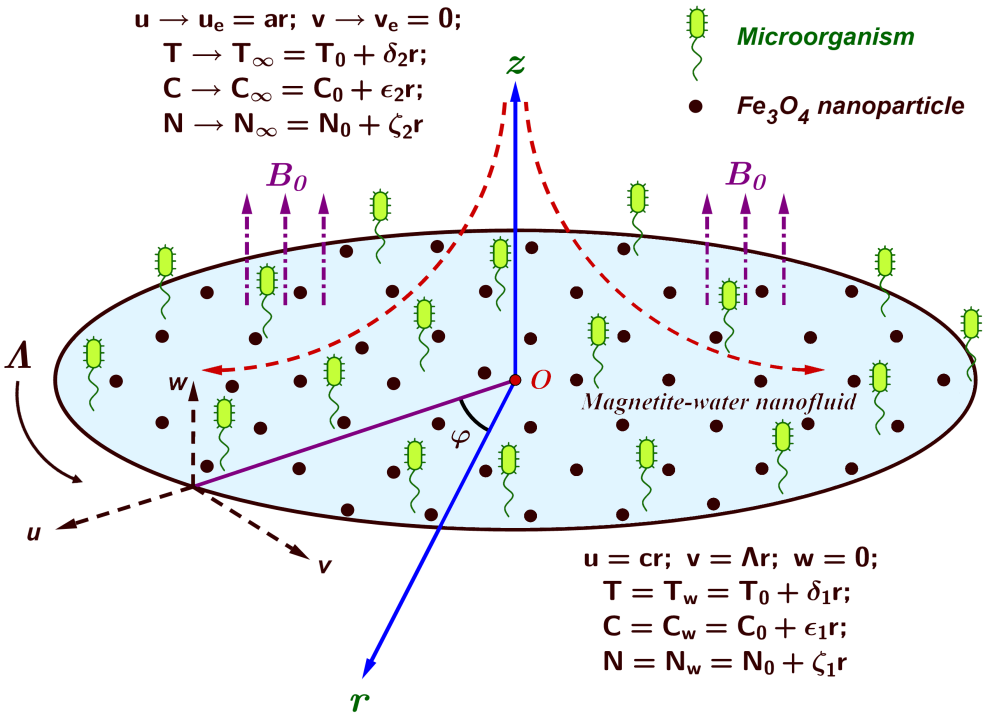

Figure 8.1: Geometrical Frame

8.2 Mathematical Frame

Consider an incompressible, steady and axisymmetric stagnation-point flow of water-based magnetite nanofluid containing gyrotactic microorganisms past a circular disk with a stretching velocity, cr and a constant angular velocity, Λ that imparts swirling flow in the neighbouring fluid layers (see Figure 8.1). The velocity components (u, v, w) denotes the nanofluid flow in the radial (r), azimuthal (φ), and

axial (z) directions, respectively. An external magnetic field (of uniform intensity B_0) is applied along the axial direction. Let ($T,\ T_0,\ T_w,\ T_\infty$) denote the nanomaterial temperature, the reference temperature, the temperature at the disk, and the ambient temperature, respectively. Let ($C,\ C_0,\ C_w,\ C_\infty$) indicate the nanoparticle volume fraction, the reference nanoparticle volume fraction, the nanoparticle volume fraction at the disk, and the ambient nanoparticle volume fraction, correspondingly and also let ($N,\ N_0,\ N_w,\ N_\infty$) denote the microbial concentration, the reference microbial concentration, the microbial concentration at the disk, and the ambient microbial concentration, respectively. The effects of Joule heating and viscous dissipation are negligible and hence not considered. The thermal, solutal, and motile density stratification constraints and linear chemical reaction effects are also incorporated. The induced magnetic field has been neglected due to the assumption of a small magnetic Reynolds number.

Following the two-phase MBNM and the aforementioned assumptions, the governing equations take the form (see Mustafa et al., 2016; Waqas et al., 2021):

$$\frac{\partial u}{\partial r}+\frac{u}{r}+\frac{\partial w}{\partial z}=0 \tag{8.2.1}$$

$$u\frac{\partial u}{\partial r}-\frac{v^2}{r}+w\frac{\partial u}{\partial z}=u_e\frac{du_e}{dr}+\left(\frac{\mu_{nf}}{\rho_{nf}}\right)\frac{\partial^2 u}{\partial z^2}-\left(\frac{\sigma_{nf}}{\rho_{nf}}\right)B_o^2\left(u-u_e\right) \tag{8.2.2}$$

$$u\frac{\partial v}{\partial r}+\frac{uv}{r}+w\frac{\partial v}{\partial z}=\left(\frac{\mu_{nf}}{\rho_{nf}}\right)\frac{\partial^2 v}{\partial z^2}-\left(\frac{\sigma_{nf}}{\rho_{nf}}\right)B_o^2 v \tag{8.2.3}$$

$$u\frac{\partial T}{\partial r}+w\frac{\partial T}{\partial z}=\frac{k_{nf}}{\left(\rho C_p\right)_{nf}}\ \frac{\partial^2 T}{\partial z^2}+\frac{\left(\rho C_p\right)_p}{\left(\rho C_p\right)_{nf}}\left(D_B\left(\frac{\partial T}{\partial z}\frac{\partial C}{\partial z}\right)+\frac{D_T}{T_\infty}\left(\frac{\partial T}{\partial z}\right)^2\right) \tag{8.2.4}$$

$$u\frac{\partial C}{\partial r}+w\frac{\partial C}{\partial z}=D_B\frac{\partial^2 C}{\partial z^2}+\frac{D_T}{T_\infty}\ \frac{\partial^2 T}{\partial z^2}-k_r\left(C-C_\infty\right) \tag{8.2.5}$$

$$u\frac{\partial N}{\partial r}+w\frac{\partial N}{\partial z}+\frac{bW_c}{C_w-C_0}\left(\frac{\partial}{\partial z}\left(N\frac{\partial C}{\partial z}\right)\right)=D_m\frac{\partial^2 N}{\partial z^2} \tag{8.2.6}$$

subject to the boundary conditions (see Mustafa et al., 2016; Waqas et al., 2021):

$$u=cr,\ v=\Lambda \mathrm{r}\ ,\ w=0,\ T=T_w=T_0+\delta_1 r,$$
$$C=C_w=C_0+\epsilon_1 r,\ N=N_w=N_0+\zeta_1 r;\ \text{ at } z=0.$$
$$u\to u_e=ar,\ v\to v_e=0,\ T\to T_\infty=T_0+\delta_2 r,$$

$$C \to C_\infty = C_0 + \epsilon_2 r,\ N \to N_\infty = N_0 + \zeta_2 r;\ \text{ as } z \to \infty.$$

where D_B is the Brownian diffusion coefficient, D_T is the thermophoresis diffusion coefficient, D_m is the microorganism diffusion coefficient, and $(u_e,\ v_e)$ are the free stream velocities along $(r,\ \varphi)$ directions.
Consider the following similarity transformations (see Mustafa et al., 2016; Waqas et al., 2021):

$$\eta = \left(\frac{c}{\vartheta_f}\right)^{\frac{1}{2}} z,\ u = cr\ F(\eta),\ v = cr\ G(\eta),\ w = (c\vartheta_f)^{\frac{1}{2}}\ H(\eta),$$

$$\theta(\eta) = \frac{T - T_\infty}{T_w - T_0},\ \psi(\eta) = \frac{C - C_\infty}{C_w - C_0},\ \chi(\eta) = \frac{N - N_\infty}{N_w - N_0}$$

Employing the similarity transformations into Equations (8.2.1) – (8.2.6), we get:

$$H' = -2F \tag{8.2.7}$$

$$F'' = \left(\frac{A_2}{A_1}\right)\left(F^2 - G^2 - S^2 + HF'\right) + \left(\frac{A_3}{A_1}\right) M\ (F - S) \tag{8.2.8}$$

$$G'' = \left(\frac{A_2}{A_1}\right)(2FG + HG') + \left(\frac{A_3}{A_1}\right) M\ G \tag{8.2.9}$$

$$\theta'' = \left(\frac{Pr}{A_4}\right)\left(A_5\ H\theta' - Nb\ \theta'\ \psi' - Nt\ (\theta')^2\right) \tag{8.2.10}$$

$$\psi'' = Le\ Pr\ H\psi' + Le\ Pr\ Kr\ \psi - \left(\frac{Nt}{Nb}\right)\theta'' \tag{8.2.11}$$

$$\chi'' = Lb\ Pr\ H\chi' + Pe\ ((\chi + \Omega)\psi'' + \psi'\ \chi') \tag{8.2.12}$$

subject to the boundary conditions

$$F(0) = 1,\ G(0) = \omega\ ,\ H(0) = 0,\ \theta(0) = 1 - S_1,\ \psi(0) = 1 - S_2,$$
$$\chi(0) = 1 - S_3,\ F(\infty) \to S,\ G(\infty) \to 0,\ \theta(\infty) \to 0,\ \psi(\infty) \to 0,\ \chi(\infty) \to 0.$$

where the dimensionless parameters are given in appendix I.

The nanofluid models incorporated are (see Alghamdi et al., 2021):

Effective Dynamic Viscosity : $\dfrac{\mu_{nf}}{\mu_f} = \dfrac{1}{(1-\phi)^{2.5}} = A_1$

Effective Density : $\dfrac{\rho_{nf}}{\rho_f} = (1-\phi) + \phi\left(\dfrac{\rho_{np}}{\rho_f}\right) = A_2$

Effective Specific Heat : $\dfrac{(\rho C_p)_{nf}}{(\rho C_p)_f} = (1-\phi) + \phi\left(\dfrac{(\rho C_p)_{np}}{(\rho C_p)_f}\right) = A_3$

Effective Thermal Conductivity : $\dfrac{k_{nf}}{k_f} = \dfrac{k_{np} + 2k_f - 2\phi\,(k_f - k_{np})}{k_{np} + 2k_f + \phi\,(k_f - k_{np})} = A_4$

Effective Electrical Conductivity : $\dfrac{\sigma_{nf}}{\sigma_f} = 1 + \dfrac{3\left(\frac{\sigma_{np}}{\sigma_f} - 1\right)\phi}{\left(\frac{\sigma_{np}}{\sigma_f} + 2\right) - \left(\frac{\sigma_{np}}{\sigma_f} - 1\right)\phi} = A_5$

The physical quantities are given by (see Turkyilmazoglu, 2012; Mustafa et al., 2016):

Local drag coefficient : $C_f = \dfrac{\sqrt{{\tau_r}^2 + {\tau_\varphi}^2}}{\rho_f (cr)^2}$

$where\ \tau_r = \mu_{nf}\ \left.\dfrac{\partial u}{\partial z}\right|_{z=0}$ and $\tau_\varphi = \mu_{nf}\ \left.\dfrac{\partial v}{\partial z}\right|_{z=0}$

$\Rightarrow\ C_f\ Re^{1/2} = A_1\ \sqrt{(F\,'(0))^2 + (G\,'(0))^2}$

Local Nusselt number : $Nu_r = \dfrac{r q_w}{k_f\,(T_w - T_0)}$

$where\ q_w = -k_{nf}\ \left.\dfrac{\partial T}{\partial z}\right|_{z=0}$

$\Rightarrow\ Nu_r\ Re^{-1/2} = -A_4\ \theta\,'(0)$

Local Sherwood number : $Sh_r = \dfrac{rq_m}{D_B\,(C_w - C_0)}$

$$where\ q_m = -D_B\ \left.\frac{\partial C}{\partial z}\right|_{z=0}$$

$$\Rightarrow\ Sh_r\ Re^{-1/2} = -\psi\,'(0)$$

Local motile density number : $Nn_r = \dfrac{rq_n}{D_m\,(N_w - N_0)}$

$$where\ q_n = -D_m\ \left.\frac{\partial N}{\partial z}\right|_{z=0}$$

$$\Rightarrow\ Nn_r\ Re^{-1/2} = -\chi\,'(0)$$

where $Re = \frac{cr^2}{\vartheta_f}$ is the local Reynold's number.

8.3 Numerical Frame & Validation

Equations (8.2.7) - (8.2.12) together with the boundary conditions are numerically resolved in MATLAB employing the *bvp5c* routine. This is accomplished by initially assuming:

$$F = I_1,\ F\,' = I_2,\ F\,'' = I_2^{'},\ G = I_3,\ G\,' = I_4,\ G\,'' = I_4^{'},$$
$$H = I_5,\ H\,' = I_5^{'},\ \theta = I_6,\ \theta\,' = I_7,\ \theta\,'' = I_7^{'},$$
$$\psi = I_8,\ \psi\,' = I_9,\ \psi\,'' = I_9^{'},\ \chi = I_{10},\ \chi\,' = I_{11},\ \chi\,'' = I_{11}^{'}.$$

The reduced system of the first-order ODE is given by:

$$I_1\,' = I_2,\ I_2^{'} = \left(\frac{A_2}{A_1}\right)\left(I_1{}^2 - I_3{}^2 - S^2 + I_2 I_5\right) + \left(\frac{A_3}{A_1}\right) M\,(I_1 - S)\,,$$

$$I_3\,' = I_4,\ I_4^{'} = \left(\frac{A_2}{A_1}\right)(2I_1 I_3 + I_4 I_5) + \left(\frac{A_3}{A_1}\right) M\ I_3,\ I_5^{'} = -2I_1,$$

$$I_6\,' = I_7,\ I_7^{'} = \left(\frac{Pr}{A_4}\right)\left(A_5 I_5 I_7 - Nb\ I_7 I_9 - Nt\ (I_7)^2\right),$$

$$I_8\,' = I_9,\ I_9^{'} = Le\ Pr\ I_5 I_9 + Le\ Pr\ Kr\ I_8 - \left(\frac{Nt}{Nb}\right) I_7^{'},$$

$$I_{10}\,' = I_{11},\ I_{11}^{'} = Lb\ Pr\ I_5 I_{11} + Pe\ \left((I_{10} + \Omega)\, I_9^{'} + I_9 I_{11}\right).$$

with

$$I_1(0) = 1,\ I_3(0) = \omega\ ,\ I_5(0) = 0,\ I_6(0) = 1 - S_1,\ I_8(0) = 1 - S_2,$$
$$I_{10}(0) = 1 - S_3,\ I_1(\infty) \to S,\ I_3(\infty) \to 0,\ I_6(\infty) \to 0,\ I_8(\infty) \to 0,\ I_{10}(\infty) \to 0.$$

Since the flow fields satisfy the boundary conditions asymptotically and also since there are no perceptible changes in the results when using larger values for the similarity variable, the conditions at infinity are scaled to 3. The transmuted set of first-order ODEs is resolved using the *bvp5c* routine, a built-in MATLAB function, with an error tolerance of 10^{-10}. The *bvp5c* routine is an efficient numerical scheme that executes a code based on the finite-difference algorithm which utilizes the four-step sixth-order Lobatto IIIA formula. The *bvp5c* routine directly solves the algebraic equations and examines the true error. This process is continued until the appropriate level of error tolerance is reached. The reliability and the accuracy of the proposed numerical technique have been adjudged through a restrictive correspondence with the already published work of Mustafa et al., 2016. For this, the results of $F'(0)$ and $-G'(0)$ are compared when M and ω values are augmented (see Table 8.1).

Table 8.1: Resemblance of $F'(0)$ and $-G'(0)$ with the work of Mustafa et al., 2016 when $S = \phi = Nt = Le = Lb = \Omega = Pe = Kr = S_1 = S_2 = S_3 = 0,\ Nb \to 0$, and $Pr = 1$

M	ω	**Mustafa et al., 2016**		**Present Study**	
		$\mathbf{F'(0)}$	$\mathbf{-G'(0)}$	$\mathbf{F'(0)}$	$\mathbf{-G'(0)}$
0	0	-1.1737	0	-1.173779499	0
	1	-0.9483	1.487	-0.948365298	1.486962505
	2	-0.3263	3.1278	-0.326275283	3.127830777
2	0	-1.8305	0	-1.830489699	0
	1	-1.6635	2.0239	-1.663452576	2.02394492
	2	-1.1754	4.1135	-1.175347049	4.11349385

Table 8.2: Thermophysical properties of water and magnetite nanoparticles

Property	**Water (base fluid)**	**Fe_3O_4 (nanoparticle)**
$\boldsymbol{\rho}$	997.1	5180
$\boldsymbol{C_p}$	4179	670
$\boldsymbol{k}$	0.613	9.7
$\boldsymbol{\sigma}$	0.05	25000

8.4 Results & Discussion

The consequence of pertinent parameters on the flow profiles and the physical quantities are depicted through the contour-styled graphs given in Figures 8.2 - 8.11 and three-dimensional surface plots given in Figures 8.12 - 8.18, respectively. The base values of the dimensionless parameters are chosen as $Pr = 6.2,\ Nt = Nb = 0.05,\ \phi = 0.01,\ \omega = S = \Omega = Kr = 0.5,\ M = 1,\ Le = 2,\ Lb = 0.3,$ and $Pe = S_1 = S_2 = S_3 = 0.1$. In addition, Table 8.2 lists the thermophysical characteristics of water (base fluid) and magnetite nanoparticles.

The positive response of velocity ratio parameter (S) on the radial velocity ($F(\eta)$) and the negative impact of S on the azimuthal velocity ($G(\eta)$) have been graphed in Figures 8.2 and 8.3, respectively. This can be physically associated to the fact that the elongation of the disk weakens the rotational effect causing the velocity to drop in the azimuthal direction whereas the stretching of the disk accelerates the fluid drawn towards the disk causing a rise in the radial velocity. An escalation in the magnetic field parameter (M) causes for the creation of a resistive force (termed Lorentz force) that slows the flow velocities (see Figures 8.4 and 8.5). Figure 8.6 describes the positive deviations in $G(\eta)$ concerning ω (rotation parameter). Physically, an increase in ω enhances the centrifugal force that enlarges the rotational phenomenon of neighbouring fluid layers.

The introduction of magnetite nanoparticles enhances the thermal conductivity of the nanomaterial, raising the nanofluid temperature ($\theta(\eta)$) profile (illustrated in Figure 8.7). Figure 8.8 depicts the decreasing nature of $\theta(\eta)$ with S_1 (thermal

stratification parameter). Physically, this is due to the drop in temperature variation between the ambient and fluid surface with augmenting S_1 values.

Increasing Kr (chemical reaction parameter) values intensify the nanoparticle consumption, thereby causing a decline in the nanoparticle volume fraction ($\psi(\eta)$) (see Figure 8.9). Figure 8.10 elucidates the negative deviation in $\psi(\eta)$ with respect to S_2 (solutal stratification parameter). This decline in $\psi(\eta)$ with mounting values of S_2 can be physically attributed to the decrease in the volumetric fraction between the surface and reference nanoparticles. From Figure 8.11, it can be perceived that the microbial concentration ($\chi(\eta)$) descends with mounting values of S_3 (microbial stratification parameter). This is because an increase in S_3 descends the microbial concentration difference between the surface and away from the surface.

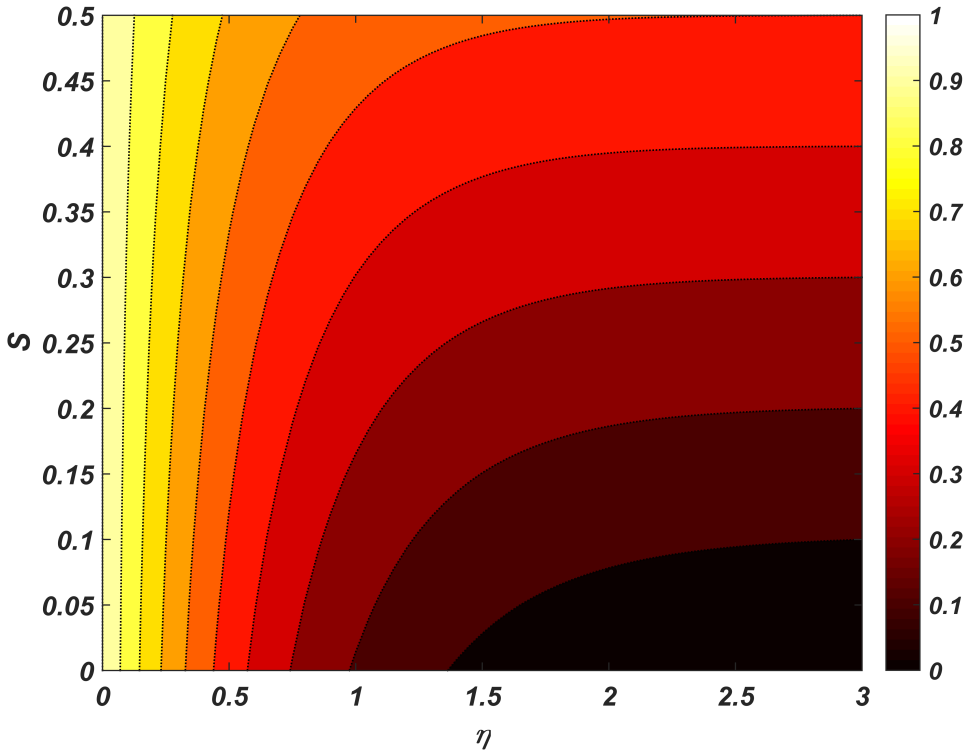

Figure 8.2: Impression of S on $F(\eta)$

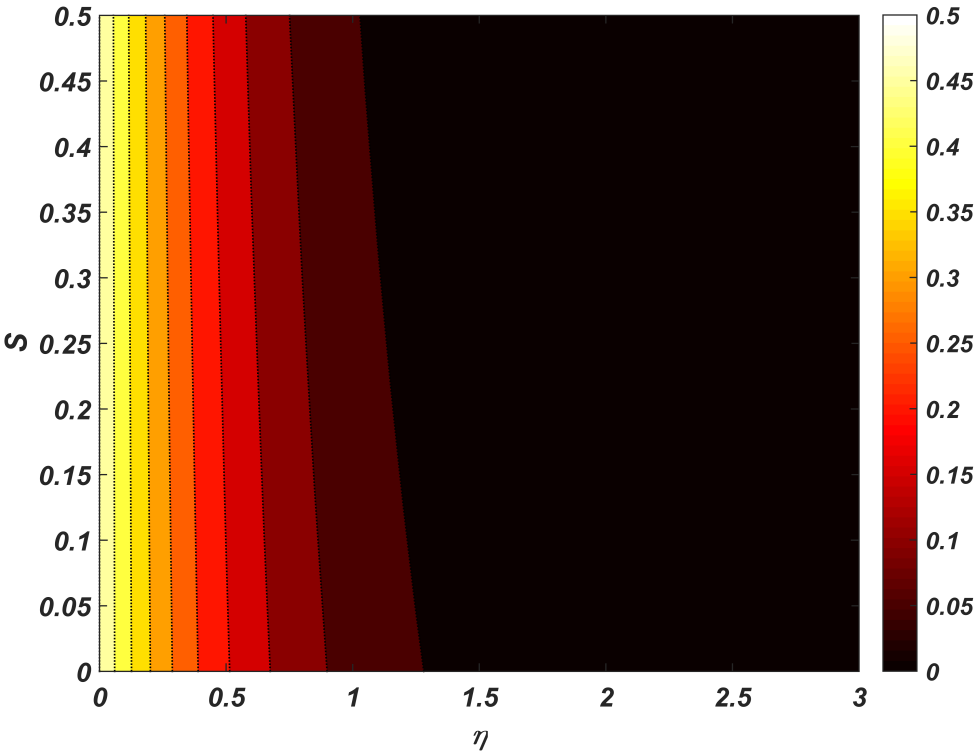

Figure 8.3: Impression of S on $G(\eta)$

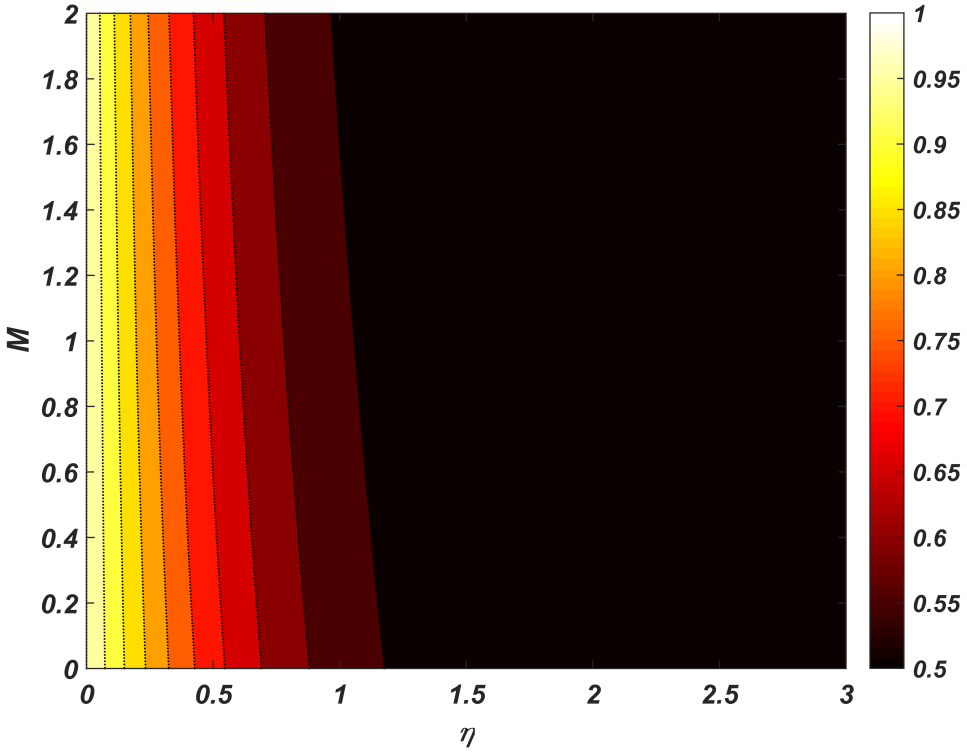

Figure 8.4: Impression of M on $F(\eta)$

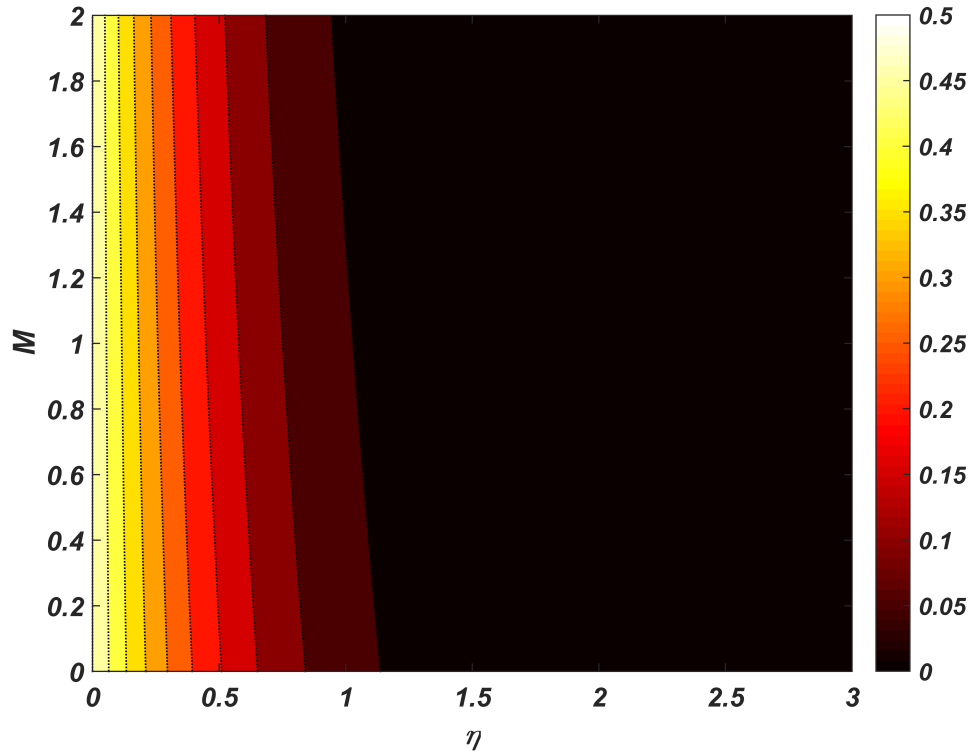

Figure 8.5: Impression of M on $G(\eta)$

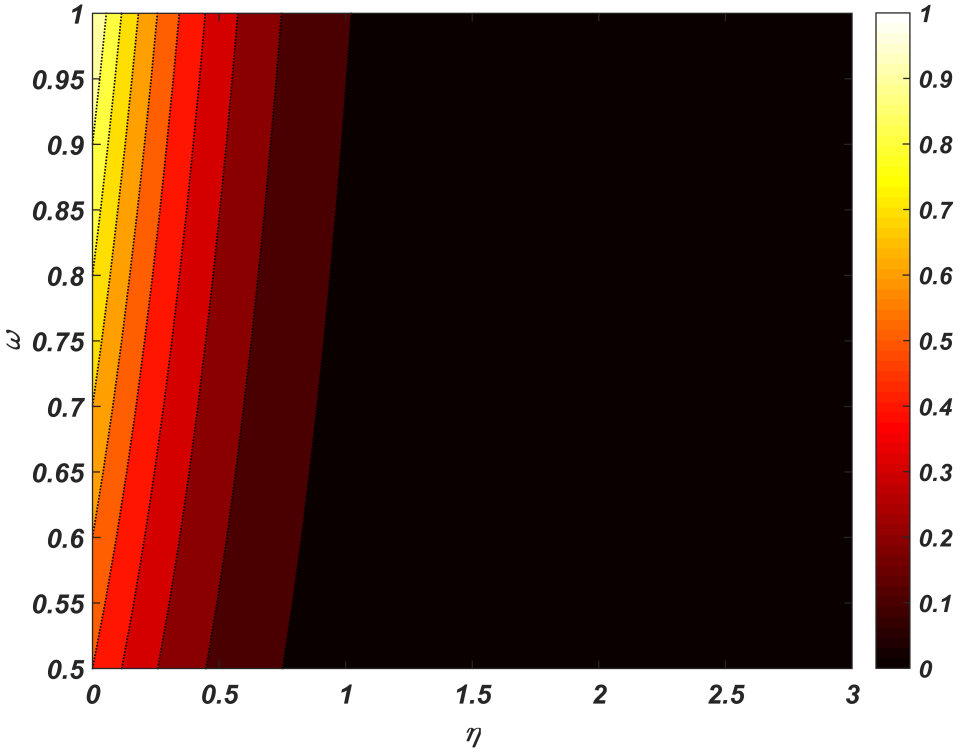

Figure 8.6: Impression of ω on $G(\eta)$

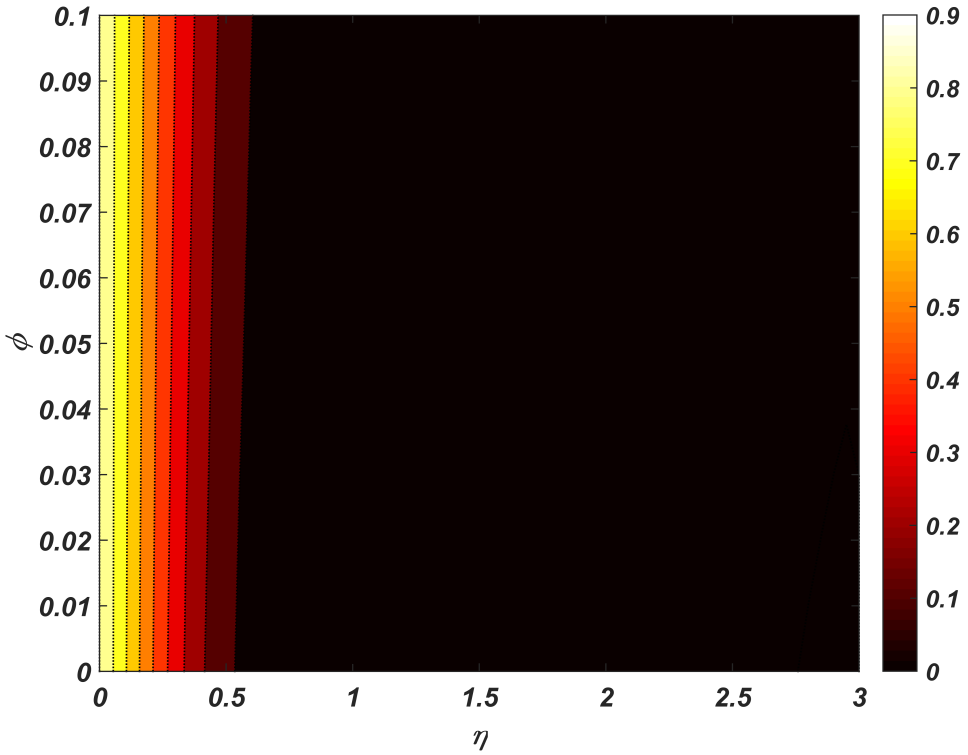

Figure 8.7: Impression of ϕ on $\theta(\eta)$

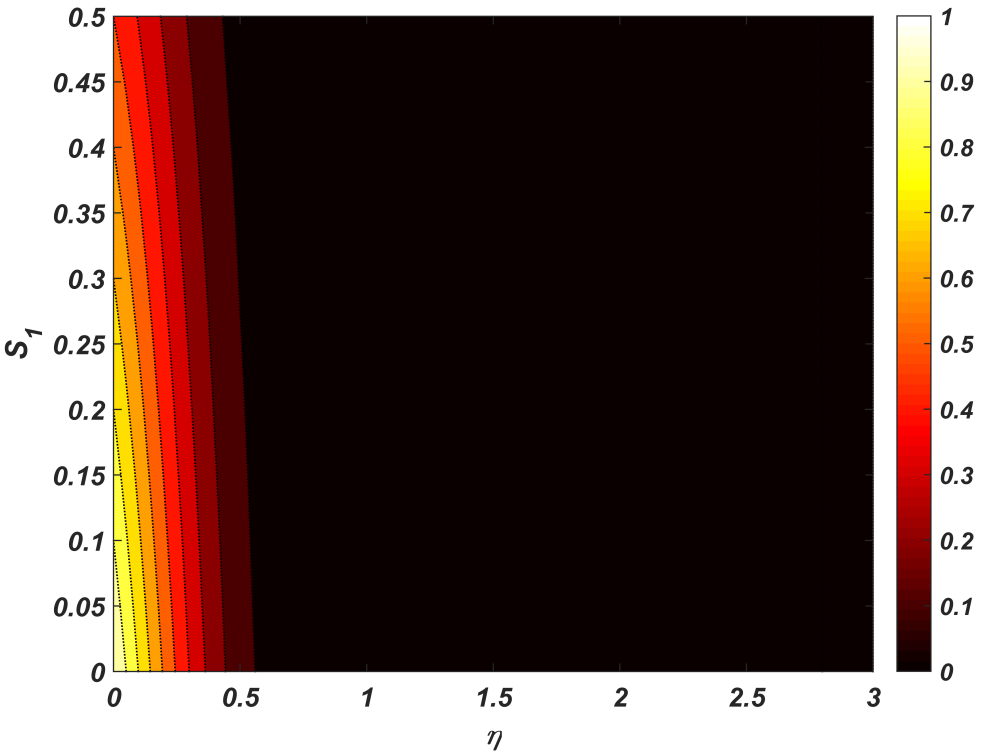

Figure 8.8: Impression of S_1 on $\theta(\eta)$

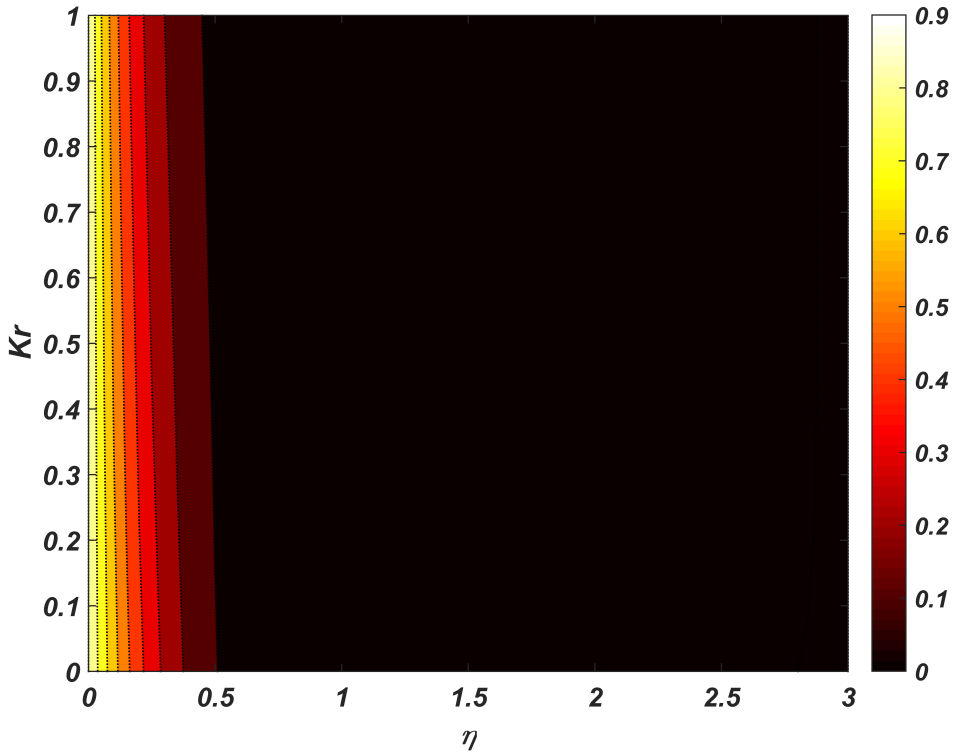

Figure 8.9: Impression of Kr on $\psi(\eta)$

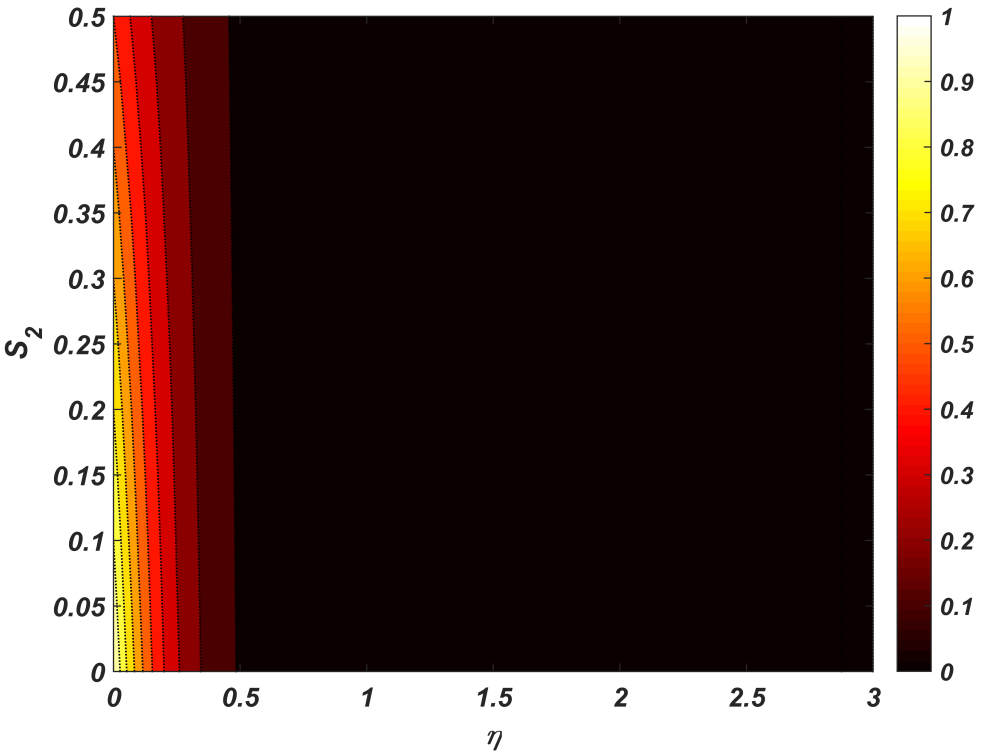

Figure 8.10: Impression of S_2 on $\psi(\eta)$

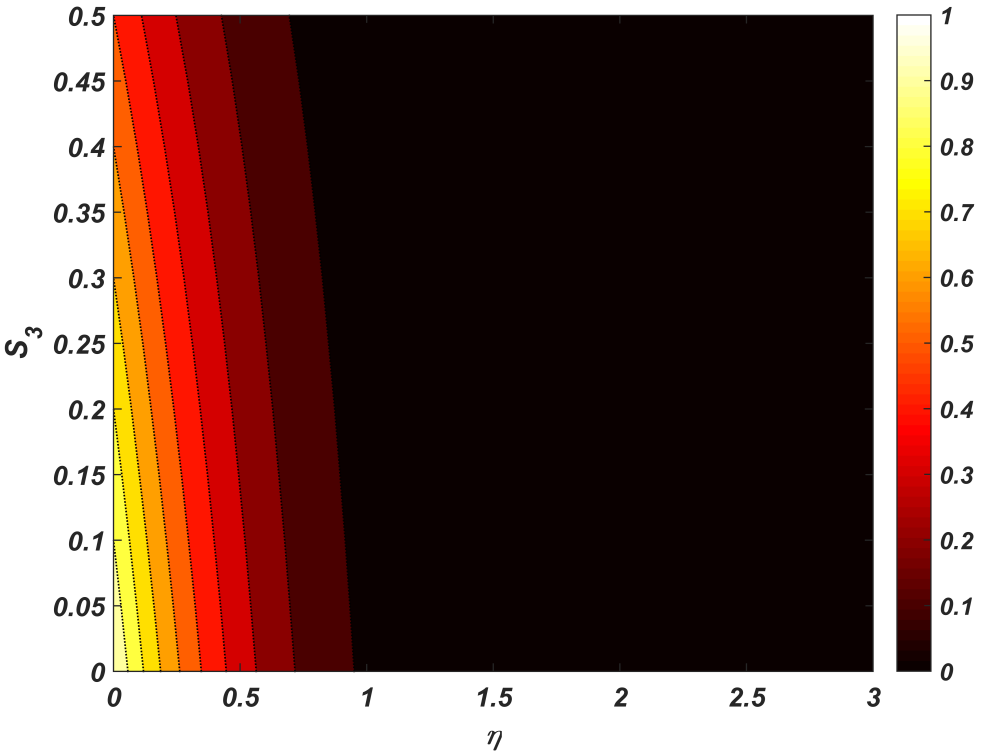

Figure 8.11: Impression of S_3 on $\chi\,(\eta)$

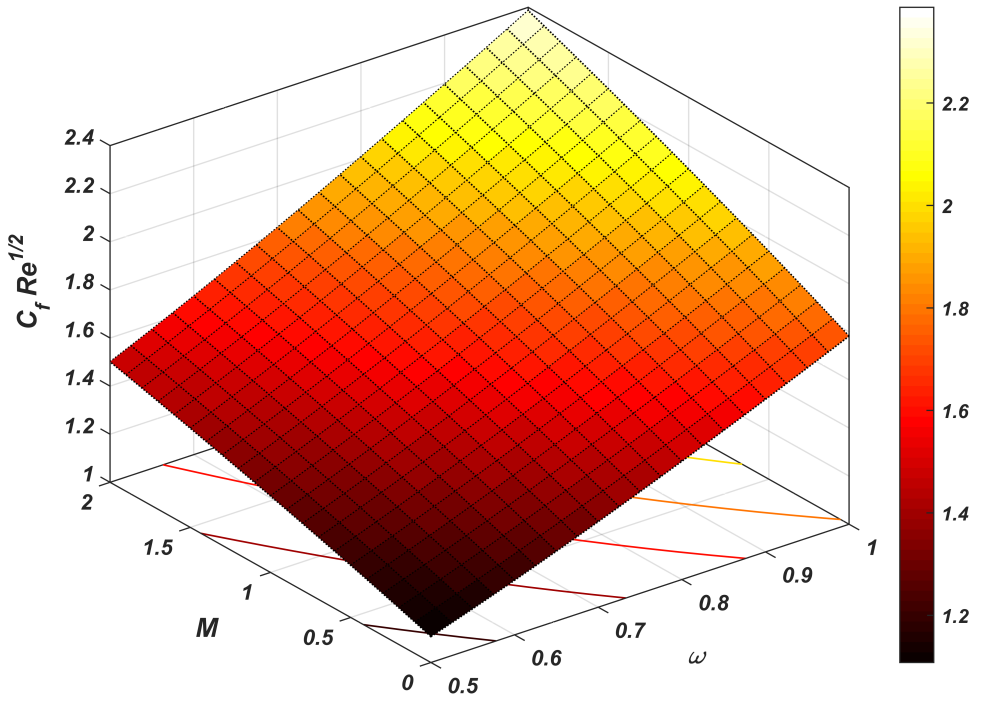

Figure 8.12: Simultaneous impression of ω and M on $C_f\ Re^{1/2}$

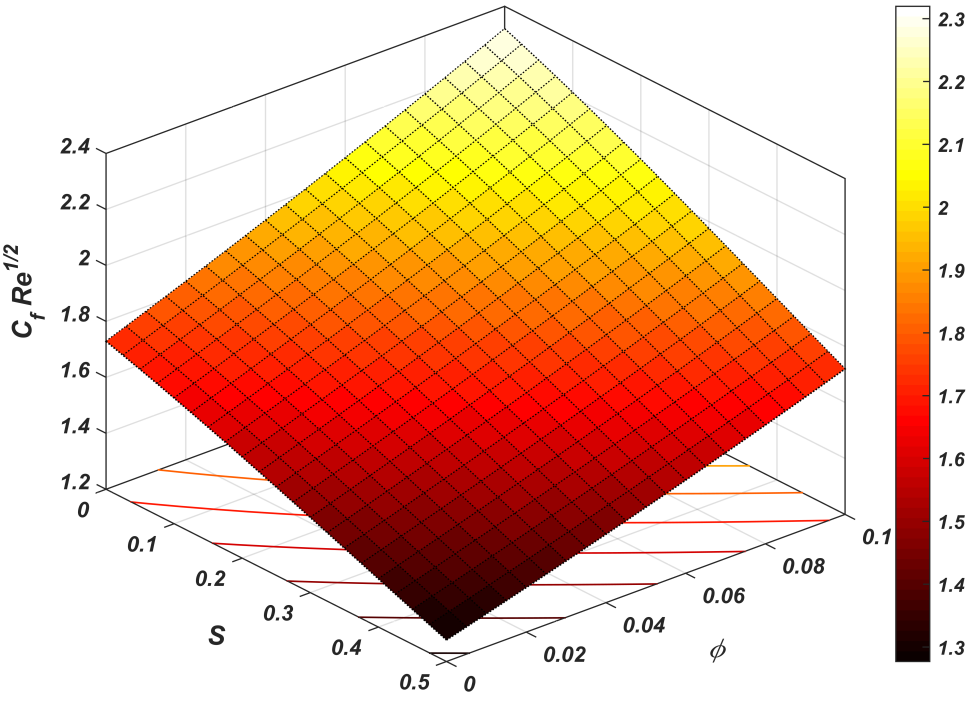

Figure 8.13: Simultaneous impression of ϕ and S on $C_f\ Re^{1/2}$

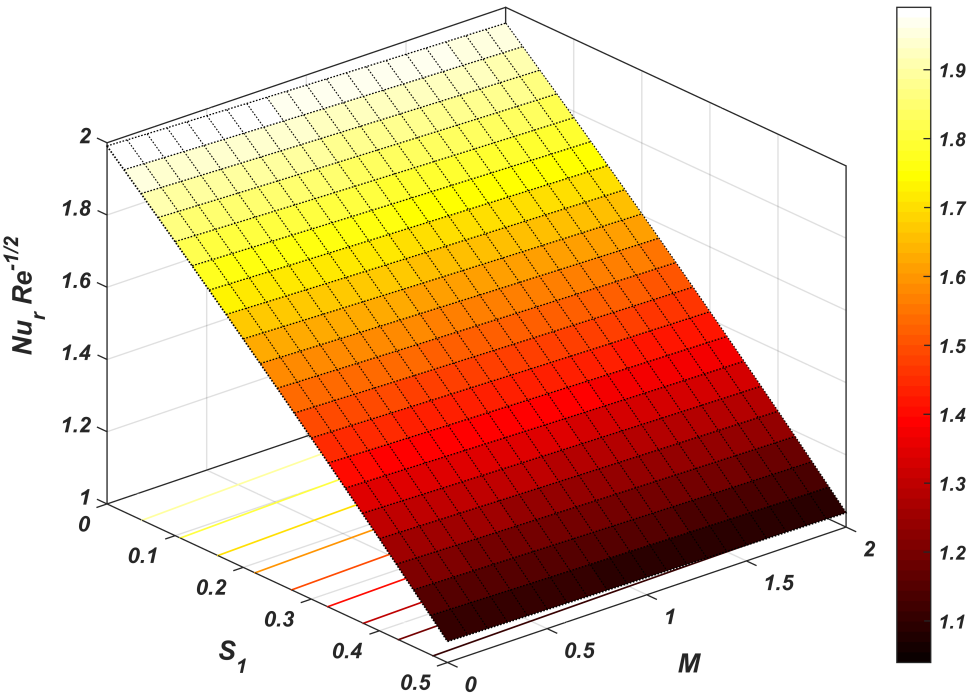

Figure 8.14: Simultaneous impression of S_1 and M on $Nu_r\ Re^{-1/2}$

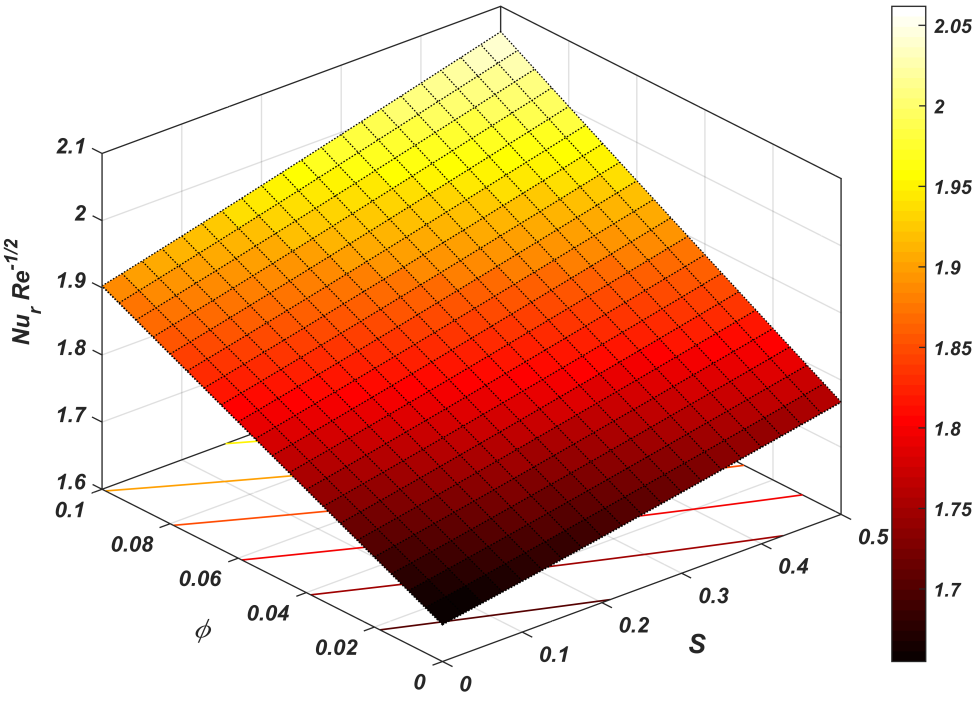

Figure 8.15: Simultaneous impression of ϕ and S on $Nu_r\ Re^{-1/2}$

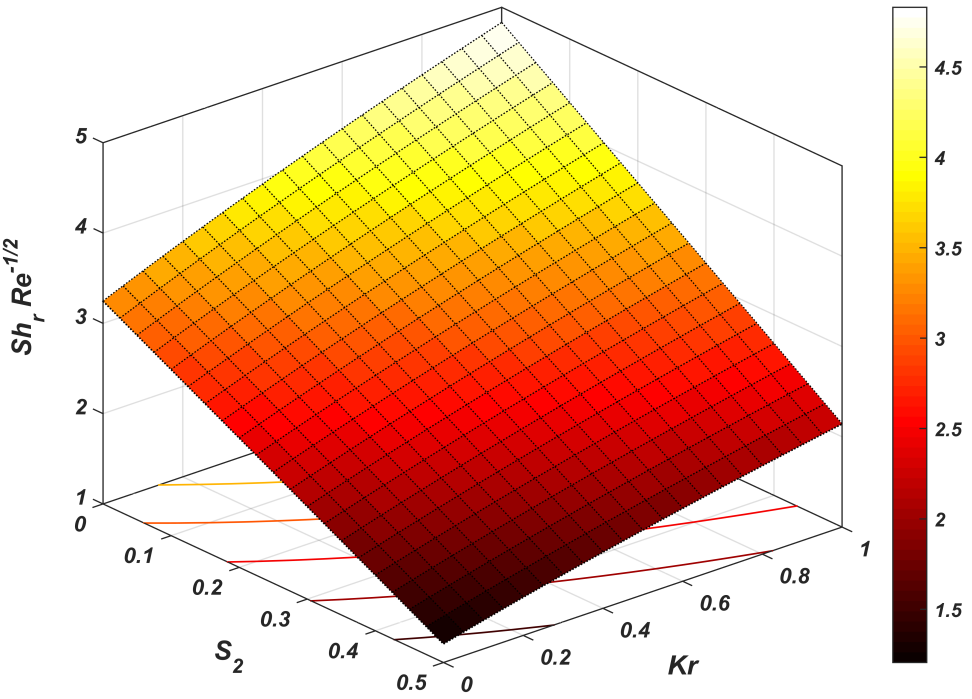

Figure 8.16: Simultaneous impression of S_2 and Kr on $Sh_r\ Re^{-1/2}$

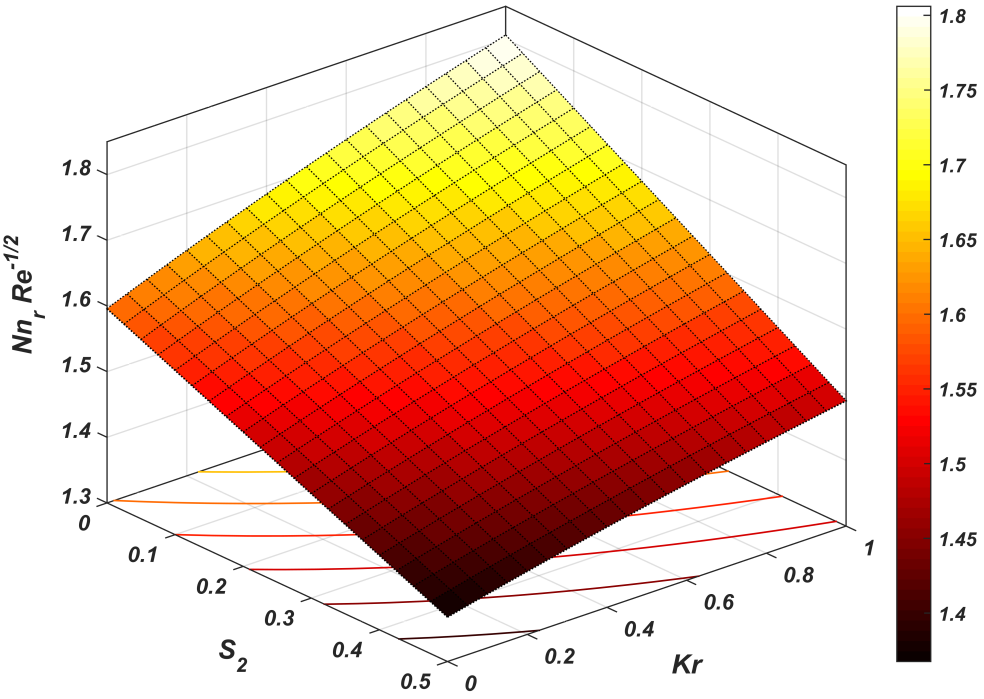

Figure 8.17: Simultaneous impression of S_2 and Kr on $Nn_r\ Re^{-1/2}$

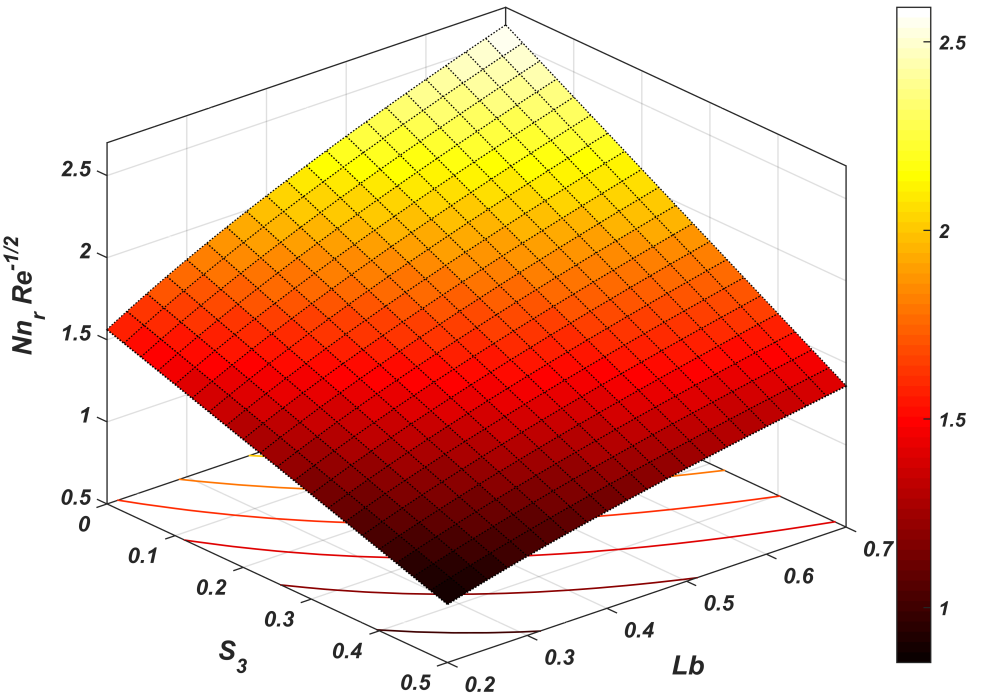

Figure 8.18: Simultaneous impression of S_3 and Lb on $Nn_r\ Re^{-1/2}$

The simultaneous outcome of influential parameters on the physical quantities is depicted with the aid of surface plots (see Figures 8.12 - 8.18). The key observations are:

- Skin friction coefficient $\left(C_f\ Re^{1/2}\right)$ is a decreasing function of S and an increasing function of $\omega,\ M$, and ϕ.
- Highest heat transport $\left(Nu_r\ Re^{-1/2}\right)$ is observed for curtailing values of M and S_1.
- The heat transfer rate ascends with an increase in S and ϕ values.
- Highest mass transfer rate $\left(Sh_r\ Re^{-1/2}\right)$ is observed for curtailed values of S_2 and augmented values of Kr.
- The motile microorganism density number $\left(Nn_r\ Re^{-1/2}\right)$ is an increasing function of Kr and Lb (bioconvection Lewis number).
- $Nn_r\ Re^{-1/2}$ descends with an increase in S_2 and S_3 values.

8.5 Statistical Frame

The four-factor response surface methodology (RSM) is a statistical mechanism that analyzes the mutual response of four independent variables on a dependent variable. In this problem, the impact of magnetic field parameter ($0.2 \leq M \leq 1.8$), thermal stratification parameter ($0.1 \leq S_1 \leq 0.5$), volume fraction of magnetite nanoparticles ($0.01 \leq \phi \leq 0.09$), and velocity ratio parameter ($0.1 \leq S \leq 0.5$) on the heat transport $\left(Nu_r\ Re^{-1/2}\ \right)$ is scrutinized statistically using the Design-Expert software (see Alben, 2002; Montgomery, 2010) and a five-level four-factor response surface optimized model. The effectual parameters and their levels are displayed in Table 8.3.

Table 8.3: Effectual parameter levels

Parameter	**Symbol**	**Levels**				
		$-\mathbf{2}\,(-\alpha)$	**-1 (low)**	**0 (medium)**	**1 (high)**	$\mathbf{2}\,(+\alpha)$
M	$\mathbb{A}$	0.2	0.6	1	1.4	1.8
S_1	$\mathbb{B}$	0.1	0.2	0.3	0.4	0.5
ϕ	$\mathbb{C}$	0.01	0.03	0.05	0.07	0.09
S	$\mathbb{D}$	0.1	0.2	0.3	0.4	0.5

The four-factor response surface optimized model (espousing CCD) for response variable involving linear, quadratic, and interactive terms is couched by:

$$\text{Response} = \mathbb{k}_0 + \mathbb{k}_1\ \mathbb{A} + \mathbb{k}_2\ \mathbb{B} + \mathbb{k}_3\ \mathbb{C} + \mathbb{k}_4\ \mathbb{D} + \mathbb{k}_5\ \mathbb{A}^2 + \mathbb{k}_6\ \mathbb{B}^2 + \mathbb{k}_7\ \mathbb{C}^2 + \mathbb{k}_8\ \mathbb{D}^2 + \mathbb{k}_9\ \mathbb{A}\ \mathbb{B} + \mathbb{k}_{10}\ \mathbb{A}\ \mathbb{C} + \mathbb{k}_{11}\ \mathbb{A}\ \mathbb{D} + \mathbb{k}_{12}\ \mathbb{B}\ \mathbb{C} + \mathbb{k}_{13}\ \mathbb{B}\ \mathbb{D} + \mathbb{k}_{14}\ \mathbb{C}\ \mathbb{D}$$

where $\mathbb{k}_i\ \ (i = 0, 1, \ldots, 14)$ portrays the regression coefficients. The experimental design and the response for the 30 runs (in line with the four-factor CCD) are showcased in Table 8.4.

Table 8.5 (ANOVA table) explains the coherence of the approximated model. A parameter is asserted to be significant if the corresponding p-value is less than 0.05 and the corresponding F-value is greater than 1. It is noticed that the quadratic term in ϕ is not significant for $Nu_r\ Re^{-1/2}$ and hence the term is deleted from the model. The coefficient of determination (R^2) for the model is estimated to be 99.99% which also boosts the model's reliability. The reliability and accuracy of the estimated heat transfer rate model are further elucidated using residual versus predicted plot (see Figure 8.19). Further, a maximum error of 0.0008 is noted from Figure 8.19 which also accounts for the correctness of the model.

The fitted quadratic model is given by:

$$\begin{aligned} Nu_r\ Re^{-1/2}\ (in\ coded\ form) &= 1.47729 - 0.00927\mathbb{A} - 0.19447\mathbb{B} + 0.04253\mathbb{C} \\ &+ 0.02185\mathbb{D} + 0.00035\mathbb{A}^2 - 0.00227\mathbb{B}^2 + 0.00021\mathbb{D}^2 + 0.00123\mathbb{A}\mathbb{B} - 0.00043\mathbb{A}\mathbb{C} \\ &+ 0.00218\mathbb{A}\mathbb{D} - 0.00628\mathbb{B}\mathbb{C} - 0.00286\mathbb{B}\mathbb{D} + 0.00147\mathbb{C}\mathbb{D} \end{aligned} \tag{8.5.1}$$

$$Nu_r\ Re^{-1/2}\ (in\ actual\ form) = 1.85770 - 0.05044M - 1.59627S_1 + 2.86282\phi + 0.20021S + 0.00220M^2 - 0.22688{S_1}^2 + 0.02123S^2 + 0.03065MS_1 - 0.05408M\phi + 0.05459MS - 3.14150S_1\phi - 0.28623S_1S + 0.73642\phi S \quad (8.5.2)$$

The fitted model (Equations (8.5.1) and (8.5.2)) reveals that S_1 and M reduce whereas ϕ and S increase the heat transfer rate. The parallel effect of two parameters on the heat transfer rate is delineated using surface plots (see Figure 8.20) by anchoring the remaining two parameters at their corresponding median level. From Figure 8.20, it is inferred that the heat transfer rate is highest for curtailed values of S_1 & M and augmented values of ϕ & S.

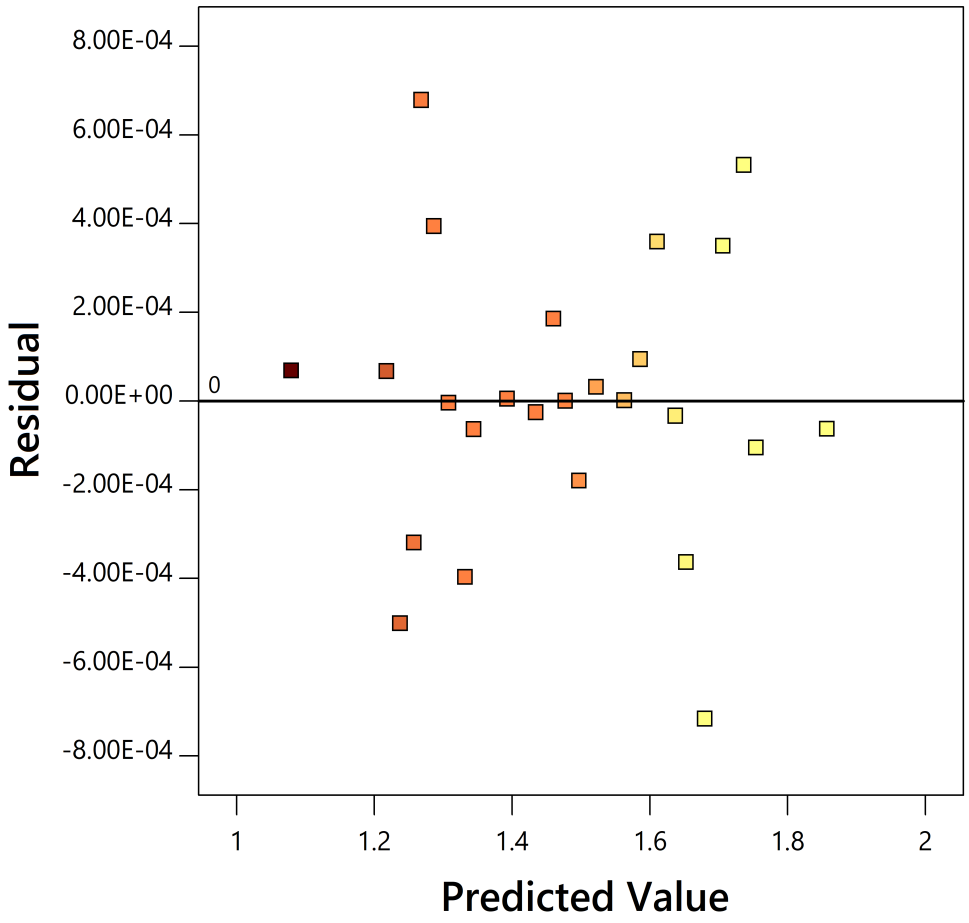

Figure 8.19: Residual versus Predicted value

Table 8.4: Four-factor CCD experimental design and the corresponding responses

Run	M	S_1	ϕ	S	$Nu_r\ Re^{-1/2}$
1	0.6 (-1)	0.2 (-1)	0.03 (-1)	0.2 (-1)	1.610761713
2	1.4 (1)	0.2 (-1)	0.03 (-1)	0.2 (-1)	1.585998024
3	0.6 (-1)	0.4 (1)	0.03 (-1)	0.2 (-1)	1.236802131
4	1.4 (1)	0.4 (1)	0.03 (-1)	0.2 (-1)	1.217775854
5	0.6 (-1)	0.2 (-1)	0.07 (1)	0.2 (-1)	1.70630398
6	1.4 (1)	0.2 (-1)	0.07 (1)	0.2 (-1)	1.679008737
7	0.6 (-1)	0.4 (1)	0.07 (1)	0.2 (-1)	1.307718566
8	1.4 (1)	0.4 (1)	0.07 (1)	0.2 (-1)	1.286791893
9	0.6 (-1)	0.2 (-1)	0.03 (-1)	0.4 (1)	1.652149555
10	1.4 (1)	0.2 (-1)	0.03 (-1)	0.4 (1)	1.636715167
11	0.6 (-1)	0.4 (1)	0.03 (-1)	0.4 (1)	1.268642663
12	1.4 (1)	0.4 (1)	0.03 (-1)	0.4 (1)	1.256785193
13	0.6 (-1)	0.2 (-1)	0.07 (1)	0.4 (1)	1.753850765
14	1.4 (1)	0.2 (-1)	0.07 (1)	0.4 (1)	1.736993024
15	0.6 (-1)	0.4 (1)	0.07 (1)	0.4 (1)	1.344211711
16	1.4 (1)	0.4 (1)	0.07 (1)	0.4 (1)	1.331287872
17	0.2 (-2)	0.3 (0)	0.05 (0)	0.3 (0)	1.49705729
18	1.8 (2)	0.3 (0)	0.05 (0)	0.3 (0)	1.46033275
19	1 (0)	0.1 (-2)	0.05 (0)	0.3 (0)	1.857086312
20	1 (0)	0.5 (2)	0.05 (0)	0.3 (0)	1.07934181
21	1 (0)	0.3 (0)	0.01 (-2)	0.3 (0)	1.392855907
22	1 (0)	0.3 (0)	0.09 (2)	0.3 (0)	1.562984781
23	1 (0)	0.3 (0)	0.05 (0)	0.1 (-2)	1.434411677
24	1 (0)	0.3 (0)	0.05 (0)	0.5 (2)	1.521865896
25	1 (0)	0.3 (0)	0.05 (0)	0.3 (0)	1.477286276
26	1 (0)	0.3 (0)	0.05 (0)	0.3 (0)	1.477286276
27	1 (0)	0.3 (0)	0.05 (0)	0.3 (0)	1.477286276
28	1 (0)	0.3 (0)	0.05 (0)	0.3 (0)	1.477286276
29	1 (0)	0.3 (0)	0.05 (0)	0.3 (0)	1.477286276
30	1 (0)	0.3 (0)	0.05 (0)	0.3 (0)	1.477286276

Table 8.5: ANOVA table

Source	**Deg. of freedom**	**Sum of squares**	**Mean squares**	**F-Value**	**p-Value**
Model	14	0.9656	0.069	4.29E+05	< 0.0001
M	1	0.0021	0.0021	12834.51	< 0.0001
S_1	1	0.9076	0.9076	5.65E+06	< 0.0001
ϕ	1	0.0434	0.0434	2.70E+05	< 0.0001
S	1	0.0115	0.0115	71266.13	< 0.0001
$M * S_1$	1	0	0	149.6	< 0.0001
$M * \phi$	1	2.99E-06	2.99E-06	18.63	0.0006
$M * S$	1	0.0001	0.0001	474.55	<0.0001
$S_1 * \phi$	1	0.0006	0.0006	3928.7	<0.0001
$S_1 * S$	1	0.0001	0.0001	815.36	< 0.0001
$\phi * S$	1	0	0	215.89	< 0.0001
$M * M$	1	3.39E-06	3.39E-06	21.07	0.0004
$S_1 * S_1$	1	0.0001	0.0001	878.23	< 0.0001
$\phi * \phi$	1	6.82E-07	6.82E-07	**4.24**	**0.0572**
$S * S$	1	1.24E-06	1.24E-06	7.69	0.0142
Residual	15	2.41E-06	1.61E-07		
Lack-of-Fit	10	2.41E-06	2.41E-07	*	*
Pure Error	5	0	0		
Total	29	0.9656			
$R^2 = 0.9999975$			Adjusted $R^2 = 0.9999952$		

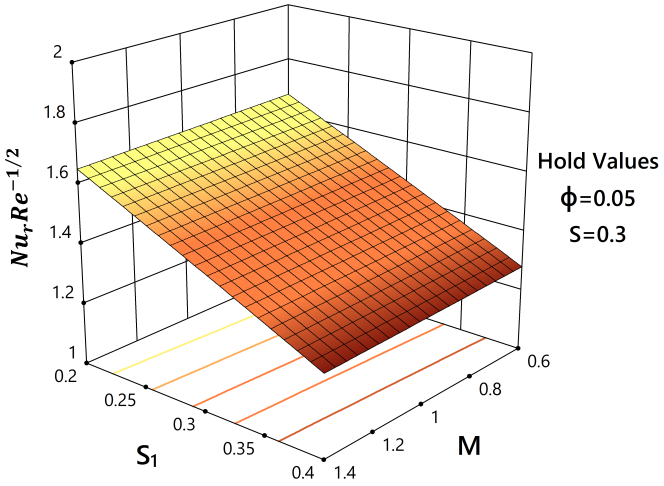

(a)

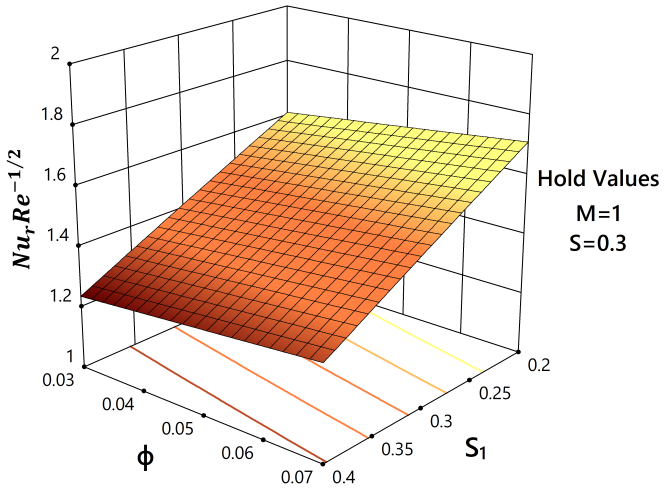

(b)

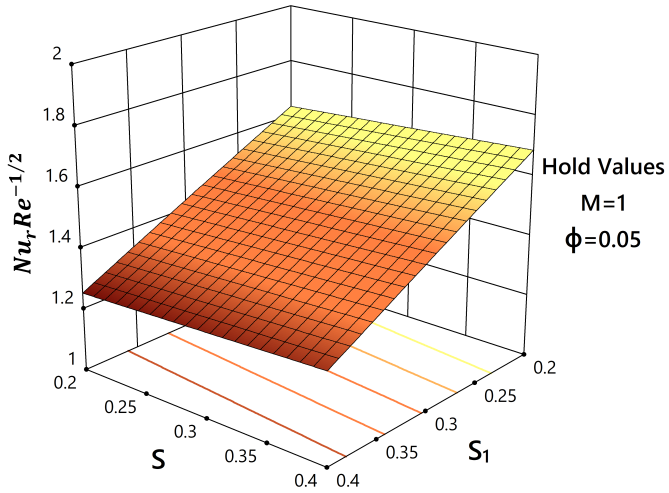

(c)

Figure 8.20: Surface plots for $Nu_r\ Re^{-1/2}$

8.6 Conclusion

In view of its practical application in pharmaceuticals, biosensors, medical instruments, bio-chromatography, microchip pump, biomedical science, micro-actuators, and aerodynamics, the significance of magnetic field and stratification effects on the bioconvective stagnation-point flow over a whirling stretchable disk has been numerically simulated with the help of the finite-difference based *bvp5c* routine. The nanofluid flow has been modelled using MBNM. Further, the impact of magnetic field parameter ($0.2 \leq M \leq 1.8$), thermal stratification parameter ($0.1 \leq S_1 \leq 0.5$), volume fraction of magnetite nanoparticles ($0.01 \leq \phi \leq 0.09$), and velocity ratio parameter ($0.1 \leq S \leq 0.5$) on the heat transport has been scrutinized statistically using a five-level four-factor response surface optimized model. The major conclusions of the present study are:

- The magnetic field parameter has a destructive effect on the radial and azimuthal velocity profiles.
- The drag coefficient increases and the heat transfer rate decreases with growing values of magnetic field parameter.
- Increments in the velocity ratio parameter tend to escalate and curtail the radial velocity and the azimuthal velocity profiles, respectively.
- The nanofluid temperature elevates with an increase in the volume fraction of magnetite nanoparticles and depletes with augmentation in the thermal stratification parameter.
- The solutal and microbial stratification parameters have a negative effect on the nanoparticle volume fraction and the microbial concentration, respectively.
- Augmentation in the chemical reaction parameter increases the nanoparticle consumption, thereby reducing the nanoparticle volume fraction.
- The motile microorganism density number descends with ascending values of solutal and microbial stratification parameters.
- The heat transport is negatively correlated with the thermal stratification parameter and the magnetic field parameter.

Appendix I: Non-dimensional qunatities

$M = \frac{\sigma_f \ B_0^2}{\rho_f \ \mathrm{c}}$	Magnetic field parameter
$S = \frac{a}{c}$	Velocity ratio parameter
$\omega = \frac{\Lambda}{c}$	Rotation parameter
$Nb = \frac{\tau \ D_B \ (C_w - C_0)}{\vartheta_f}$	Brownian motion parameter
$Nt = \frac{\tau \ D_T \ (T_w - T_0)}{T_\infty \ \vartheta_f}$	Thermophoresis parameter
$Pr = \frac{(\mu C_p)_f}{k_f} = \frac{\vartheta_f}{\alpha_f}$	Prandtl number
$Kr = \frac{k_r}{c}$	Chemical reaction parameter
$\tau = \frac{(\rho \ C_P)_p}{(\rho \ C_P)_f}$	Effective heat capacity ratio
$Le = \frac{\alpha_f}{D_B}$	Lewis number
$Lb = \frac{\alpha_f}{D_m}$	Bioconvection Lewis number
$Pe = \frac{bW_c}{D_m}$	Bioconvection Peclet number
$\Omega = \frac{N_\infty}{N_w - N_0}$	Microorganism concentration difference parameter
$S_1 = \frac{\delta_2}{\delta_1}$	Thermal stratification parameter
$S_2 = \frac{\epsilon_2}{\epsilon_1}$	Solutal stratification parameter
$S_3 = \frac{\zeta_2}{\zeta_1}$	Motile density stratification parameter

Appendix II: Nomenclature

a, c, Λ	Positive constants	W_c	Maximum cell swimming speed
u, v, w	Velocity components	B_0	Strength of magnetic field
Nn_r	Local motile density	T_∞	Ambient fluid temperature
T_0	Reference temperature	N_∞	Ambient microbial concentration
C	Fluid concentration	C_0	Reference nanoparticle concentration
T	Fluid temperature	N_0	Reference microbial concentration
r, φ, z	Polar coordinates	N_w	Microbial concentration near wall
b	Chemotaxis constant	C_w	Nanoparticle concentration near wall
T_w	Wall fluid temperature	C_∞	Ambient nanoparticle concentration
ρC_p	Heat capacity	C_f	Local drag coefficient
k_r	Reaction rate constant	Nu_r	Local Nusselt number
Sh_r	Local Sherwood number	N	Microorganism concentration
σ	Electrical conductivity	μ	Dynamic viscosity
η	Dimensionless variable	D_B	Chemical molecular diffusivity
ϑ	Kinematic viscosity	D_m	Microorganism diffusion coefficient
$\delta_i, \epsilon_i, \zeta_i$	Dimensional constants	D_T	Thermophoretic diffusion coefficient
k	Thermal conductivity	u_e, v_e	Free stream velocity
α	Thermal diffusivity	R^2	Coefficient of determination
ρ	Fluid density	ϕ	Volume fraction of Fe_3O_4

Chapter 9

Nanoliquid flow with irregular heat source and realistic boundary conditions *

9.1 Introduction

Photothermal therapy is a method of heat ablation which uses light energy to induce localised heat within the tissue and destroy the diseased cells. Skin is considered as the nonlinear stretched surface and water-based titanium dioxide nanomaterial as the working fluid. Titanium dioxide plays a vital role in cancer therapy methods (including photothermal therapy and photodynamic therapy), skincare products, heat exchangers, and car radiators. Therefore, the dynamics of the $TiO_2 - H_2O$ nanomaterial over a nonlinearly stretched surface is investigated.

For realistic nanoliquid modelling, the conventional Buongiorno model has been improvised (called modified Buongiorno model) by incorporating the effective thermophysical properties of the nanoliquid. Experimentally derived correlations of the thermal conductivity and dynamic viscosity of the nanomaterial are utilized. The significance of passive control of nanoparticles is also studied. The heat transfer analysis includes the mechanism of Rosseland heat flux and exponential heat source. Similarity theory is used to obtain nonlinear ordinary differential equations (ODEs) from the governing partial differential equations which are solved numerically using *bvp*5*c*, a finite difference-based routine in MATLAB. Further, the heat transfer rate is statistically scrutinized for the consequence of magnetic field ($0.5 \leq M \leq 1.5$), thermal radiation ($0.5 \leq R_d \leq 1.5$) and exponential heat source ($0.2 \leq Q_E \leq 0.4$) by employing Response Surface Methodology (RSM) and sensitivity analysis. The

*Published in: ZAMM - Journal of Applied Mathematics and Mechanics (Wiley), 2022; 102(3); e202100167.

main objectives of the present chapter are to:

- Construct a mathematical model to study the MHD flow of a nanomaterial over a nonlinearly elongated surface in the presence of radiation and exponential heat source using the modified Buongiorno model and passive control of nanoparticles.
- Conduct a comparative analysis of the nanomaterial flow using the traditional Buongiorno model and modified Buongiorno model.
- Study the impact of pertinent parameters on flow profiles.
- Utilize the RSM analysis to estimate the interactive effects of the key parameters on the heat transport.
- Evaluate the sensitivity of the heat transfer rate.

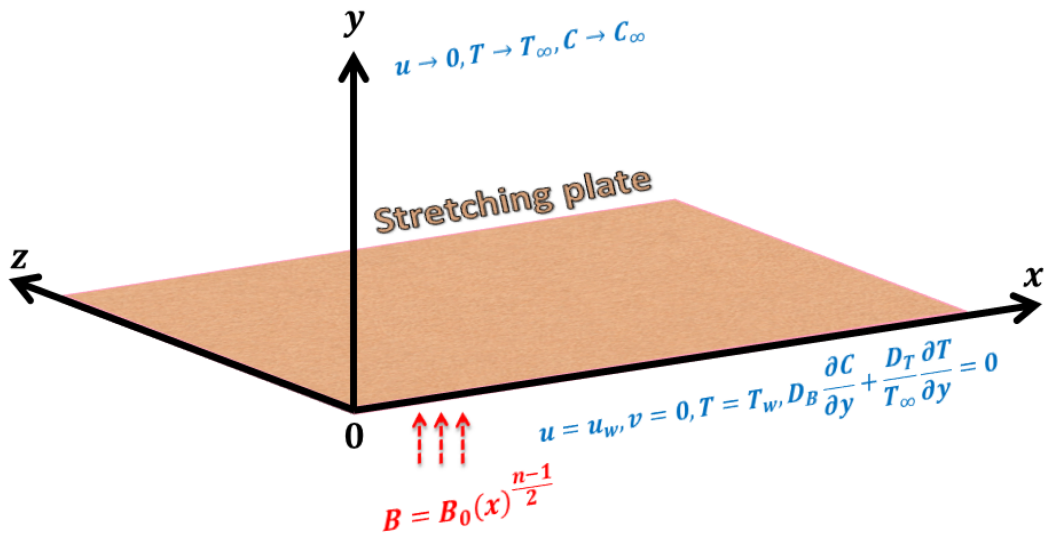

Figure 9.1: Geometrical Frame

9.2 Mathematical Frame

Consider a steady-state laminar flow of an incompressible nanomaterial on a non-linear stretching plate which is placed on the x-axis (see Figure 9.1). Let (u, v) be the velocity components along (x, y) directions. Let $u_w = ax^n$ and $Q_e^* = Q_e(x)^{n-1}$ be the stretching velocity and ESHS intensity, respectively. An external magnetic field $\left(B = B_0(x)^{\frac{n-1}{2}}\right)$ is administered in the y-direction. The induced magnetic field was neglected due to the small magnetic Reynolds number. The nanomaterial is modelled using the modified Buongiorno model and experimentally derived nanomaterial models (see Duangthongsuk & Wongwises, 2009). The normal mass flow of the nanoparticles at the boundary is kept at zero (passive control of the nanoparticles), which improves the practicality of the model. The radiative heat flux applied to the system is modelled using the Rosseland approximation. It is also assumed that no slip occurs on the surface. The effects of viscous dissipation and Joule heating are negligible and therefore not considered.

Under the boundary layer theory, the governing equations are as follows (see Hayat, Aziz, Muhammad, & Ahmad, 2016; Jafar et al., 2020; Abo-Dahab, Abdelhafez, Mebarek-Oudina, & Bilal, 2021):

$$\frac{\partial u}{\partial x} + \frac{\partial v}{\partial y} = 0 \tag{9.2.1}$$

$$\rho_{nm}\left(u\frac{\partial u}{\partial x} + v\frac{\partial u}{\partial y}\right) = \mu_{nm}\ \frac{\partial^2 u}{\partial y^2} - (\sigma_e)_{nm}\ B^2\ u \tag{9.2.2}$$

$$\begin{aligned}(\rho C_p)_{nm}\left(u\frac{\partial T}{\partial x} + v\frac{\partial T}{\partial y}\right) &= \left(\kappa_{nm} + \frac{16\sigma^* T_\infty^3}{3k^*}\right)\frac{\partial^2 T}{\partial y^2} + (\rho C_p)_{np}\left(D_B\ \frac{\partial C}{\partial y}\ \frac{\partial T}{\partial y}\right)\\ &+ (\rho C_p)_{np}\left(\frac{D_T}{T_\infty}\ \left(\frac{\partial T}{\partial y}\right)^2\right) + Q_e^*\ (T_w - T_\infty)\ exp\left(-m\sqrt{\frac{a}{\vartheta_f}}\ x^{\frac{n-1}{2}}\ y\right)\end{aligned} \tag{9.2.3}$$

$$u\frac{\partial C}{\partial x} + v\frac{\partial C}{\partial y} = D_B\ \frac{\partial^2 C}{\partial y^2} + \frac{D_T}{T_\infty}\ \frac{\partial^2 T}{\partial y^2} \tag{9.2.4}$$

subject to the boundary conditions (see Jafar et al., 2020; Abo-Dahab et al., 2021):

$$At\ y = 0\ :\ u = u_w\,(x) = ax^n,\ v = 0,\ T = T_w,\ D_B\frac{\partial C}{\partial y} + \frac{D_T}{T_\infty}\frac{\partial T}{\partial y} = 0.$$

$$As\ y \to \infty\ :\ u \to 0,\ T \to T_\infty,\ C \to C_\infty.$$

Consider the following similarity transformations (see Abo-Dahab et al., 2021):

$$u = ax^n f\,'(\zeta)\,,\ v = -ax^{\frac{n-1}{2}}\sqrt{\frac{\vartheta_f}{a}}\ \left\{\left(\frac{n+1}{2}\right) f(\zeta) + \left(\frac{n-1}{2}\right)\zeta\ f\,'(\zeta)\right\},$$

$$\zeta = \sqrt{\frac{a}{\vartheta_f}}\ x^{\frac{n-1}{2}}\ y,\ \theta(\zeta) = \frac{T - T_\infty}{T_w - T_\infty},\ \psi(\zeta) = \frac{C - C_\infty}{C_\infty}.$$

Using the above defined similarity transformations, Equations (9.2.1) – (9.2.4) are converted into:

$$\left(\frac{A_1}{A_3}\right) f\,''' - \left(\frac{A_5}{A_3}\right) M f\,' + \left(\frac{n+1}{2}\right) f\ f\,'' - n\ (f\,')^2 = 0 \tag{9.2.5}$$

$$\frac{1}{Pr_f}\left(A_2 + \frac{4}{3}R_d\right)\theta\,'' + Q_E\ exp(-m\zeta) + Nb\ \psi\,'\ \theta\,' + Nt\ (\theta\,')^2 + A_4\left(\frac{n+1}{2}\right)\ f\ \theta\,' = 0 \tag{9.2.6}$$

$$\psi\,'' + \left(\frac{Nt}{Nb}\right)\theta\,'' + Le\ Pr_f\ \left(\frac{n+1}{2}\right)\ f\ \psi\,' = 0 \tag{9.2.7}$$

subject to the boundary conditions

$$f(0) = 0,\ f\,'(0) = 1,\ \theta(0) = 1,\ \psi\,'(0) + \left(\frac{Nt}{Nb}\right)\theta\,'(0) = 0,$$

$$f\,'(\infty) \to 0,\ \theta(\infty) \to 0,\ \psi(\infty) \to 0.$$

where the dimensionless parameters are given in appendix I.

The nanofluid models incorporated are (see Jafar et al., 2020; Duangthongsuk & Wongwises, 2009):

$$\text{Effective Dynamic Viscosity} \quad : \quad \frac{\mu_{nm}}{\mu_f} = 1.013 + 0.092\ \phi - 0.015\ \phi^2 = A_1$$

$$\text{Effective Thermal Conductivity} \quad : \quad \frac{k_{nm}}{k_f} = 1.0204 + 0.0249\ \phi = A_2$$

$$\text{Effective Density} \quad : \quad \frac{\rho_{nm}}{\rho_f} = (1-\phi) + \phi\left(\frac{\rho_{np}}{\rho_f}\right) = A_3$$

$$\text{Effective Specific Heat} \quad : \quad \frac{(\rho C_p)_{nm}}{(\rho C_p)_f} = (1-\phi) + \phi\left(\frac{(\rho C_p)_{np}}{(\rho C_p)_f}\right) = A_4$$

$$\text{Effective Electrical Conductivity} \quad : \quad \frac{\sigma_{nm}}{\sigma_f} = 1 + \frac{3\left(\frac{\sigma_{np}}{\sigma_f} - 1\right)\phi}{\left(\frac{\sigma_{np}}{\sigma_f} + 2\right) - \left(\frac{\sigma_{np}}{\sigma_f} - 1\right)\phi} = A_5$$

The physical quantities are given by (see Jafar et al., 2020; Abo-Dahab et al., 2021):

$$\text{Local drag coefficient} \quad : \quad Cf_x = \frac{\tau_\omega}{\rho_f\ (u_w)^2} = \frac{\mu_{nm}\ \left.\frac{\partial u}{\partial y}\right|_{y=0}}{\rho_f\ (u_w)^2},$$

$$\Rightarrow\ Cf_x\ Re_x^{\frac{1}{2}} = A_1\ f\,''(0).$$

$$\text{Local Nusselt number} \quad : \quad Nu_x = \frac{x\ q_\omega}{k_f\ (T_w - T_\infty)} = \frac{-x\ \left.\left(k_{nm}\frac{\partial T}{\partial y} - q_r\right)\right|_{y=0}}{k_f\ (T_w - T_\infty)},$$

$$\Rightarrow\ Nu_x Re_x^{-\frac{1}{2}} = -\left(A_2 + \frac{4}{3}R_d\right)\ \theta\,'(0).$$

where $Re_x = \frac{xu_w}{\vartheta_f}$ is the local Reynold's number.

9.3 Numerical Frame & Validation

The nonlinear ordinary differential equations given in Equations (9.2.5) – (9.2.7) are reduced to a system of single-order ODEs by setting:

$$\Gamma_1 = f,\ \Gamma_2 = f\,',\ \Gamma_3 = f\,'',\ \Gamma_4 = \theta,\ \Gamma_5 = \theta\,',\ \Gamma_6 = \psi,\ \Gamma_7 = \psi\,'.$$

The reduced system of the first-order ODE is given by:

$$\Gamma_1{}' = \Gamma_2,\ \Gamma_2{}' = \Gamma_3$$

$$\Gamma_3{}' = \left(\frac{A_3}{A_1}\right)\left\{\ \left(\frac{A_5}{A_3}\right) M\ \Gamma_2 - \left(\frac{n+1}{2}\right)\Gamma_1\ \Gamma_3 + n\ (\Gamma_2)^2\ \right\}$$

$$\Gamma_4{}' = \Gamma_5$$

$$\Gamma_5{}' = \frac{-Pr_f\ \left\{Q_E\ e^{-m\ \zeta} + Nb\ \Gamma_5\ \Gamma_7 + Nt\ (\Gamma_5)^2 + A_4\left(\frac{n+1}{2}\right)\ \Gamma_1\ \Gamma_5\right\}}{A_2 + \frac{4}{3}R_d}$$

$$\Gamma_6{}' = \Gamma_7$$

$$\Gamma_7{}' = -\left\{\left(\frac{Nt}{Nb}\right)\ \Gamma_5{}' + Le\ Pr_f\ \left(\frac{n+1}{2}\right)\Gamma_1\ \Gamma_7\right\}$$

with

$$\Gamma_1(0) = 0,\ \Gamma_2(0) = 1,\ \Gamma_4(0) = 1,\ \Gamma_7(0) + \left(\frac{Nt}{Nb}\right)\Gamma_5(0) = 0,$$
$$\Gamma_2(\infty) \to 0, \Gamma_4(\infty) \to 0, \Gamma_6(\infty) \to 0.$$

Table 9.1: Comparison of $Nu_x Re_x^{-1/2}$ for different values of Pr_f with the work of W. A. Khan et al., 2010 when $n = 1$. $Nb \to 0$ and $M = Nt = \phi = R_d = Q_E = Le = 0$

$\mathbf{Pr_f}$	$\mathbf{Nu_x Re_x^{-1/2}}$	
	W. A. Khan et al., 2010	**Present Study**
0.7	0.4539	0.45395
2	0.9113	0.91136
7	1.8954	1.89542
20	3.3539	3.35391
70	6.4621	6.46220

Table 9.2: Thermophysical properties of water and titanium dioxide

Property	**Water (base fluid)**	**TiO_2 (nanoparticle)**
$\boldsymbol{\rho}$	997.1	4250
$\boldsymbol{C_p}$	4179	686.2
$\boldsymbol{\sigma_e}$	$5.5 * 10^{-6}$	$2.38 * 10^6$

The conditions at infinity are scaled to 5 since there are no appreciable changes in the results when using larger values of the similarity variable, and the flow fields satisfy the boundary conditions asymptotically. The reduced system of first-order differential equations is solved numerically with the help of *bvp5c* in MATLAB, with an absolute error tolerance of 10^{-6}. The *bvp5c* scheme employs a code based on finite differences that implements the Lobatto IIIA formula of the sixth order in four steps which is a positioning formula whose polynomial positioning provides a C^1-continuous solution with uniform precision of the fifth order in the considered closed interval. Lobatto IIIA's sixth-order four-step formula is implemented as an implicit Runge-Kutta formula. The *bvp5c* scheme solves the algebraic equations directly and checks the true error (positive difference between real and approximate solutions). The accuracy of the method used was also judged through a restrictive correspondence with previously published work of W. A. Khan et al., 2010. A commendable agreement is shown in Table 9.1.

9.4 Results & Discussion

The consequence of key parameters on velocity ($f'(\zeta)$), nanoparticle volume fraction ($\psi(\zeta)$), temperature ($\theta(\zeta)$) profiles and the physical quantities (surface drag and Nusselt number) are illustrated in Figures 9.2 - 9.14. The Prandtl number (Pr_f) and Lewis number (Le) are set at 6.0674 and 2 respectively, which are suitable for the $TiO_2 - H_2O$ nanomaterial. The thermophysical properties of base fluid (water) and TiO_2 (nanoparticle) are given in Table 9.2. Results are presented to compare the flow phenomenon for the Buongiorno model and modified Buongiorno model cases. It is observed that the modified Buongiorno model exhibits higher temperature and lower velocity profiles.

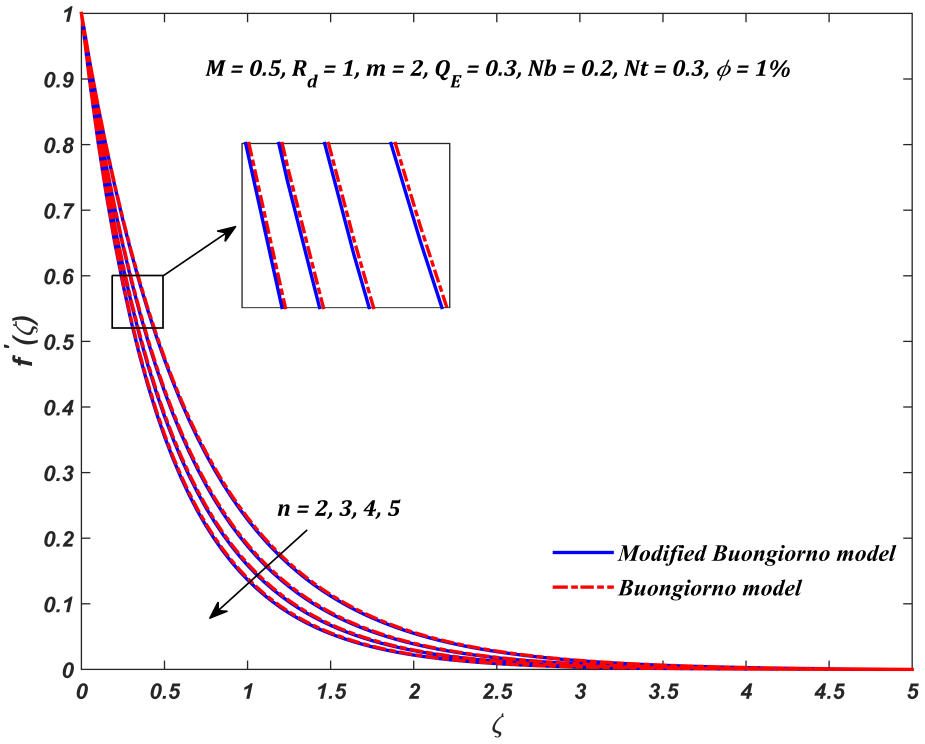

Figure 9.2: $f'(\zeta)$ for distinct values of n

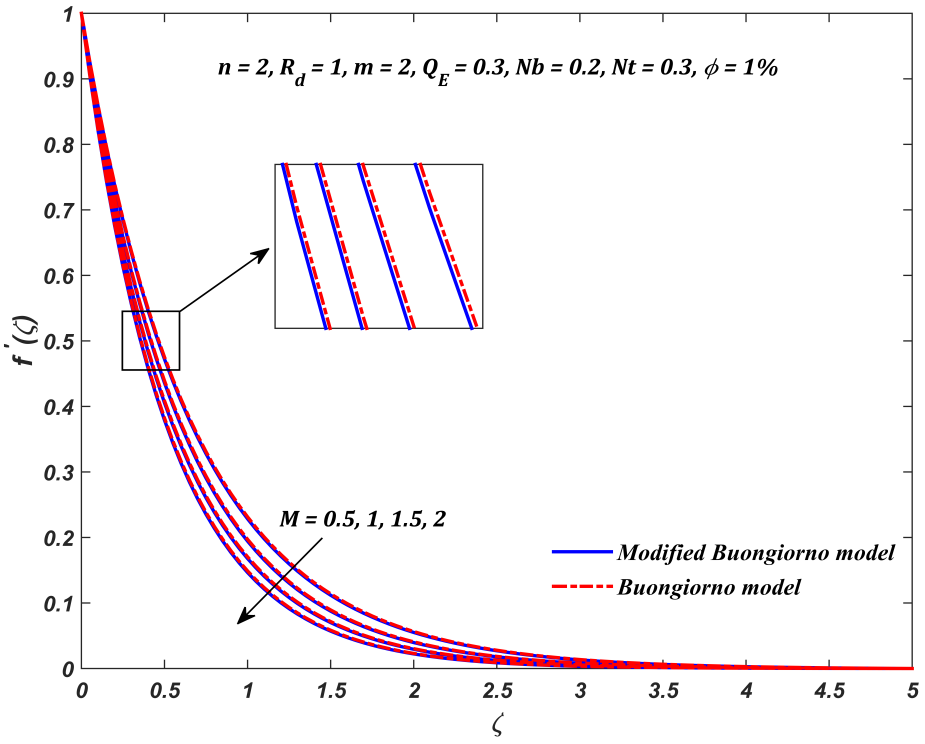

Figure 9.3: $f'(\zeta)$ for distinct values of M

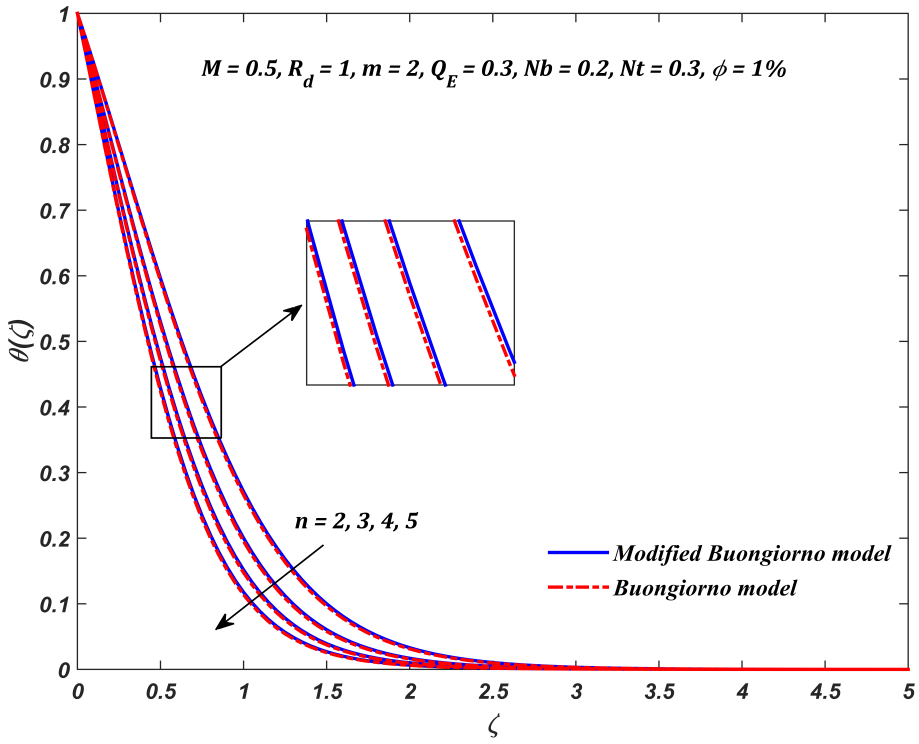

Figure 9.4: $\theta(\zeta)$ for distinct values of n

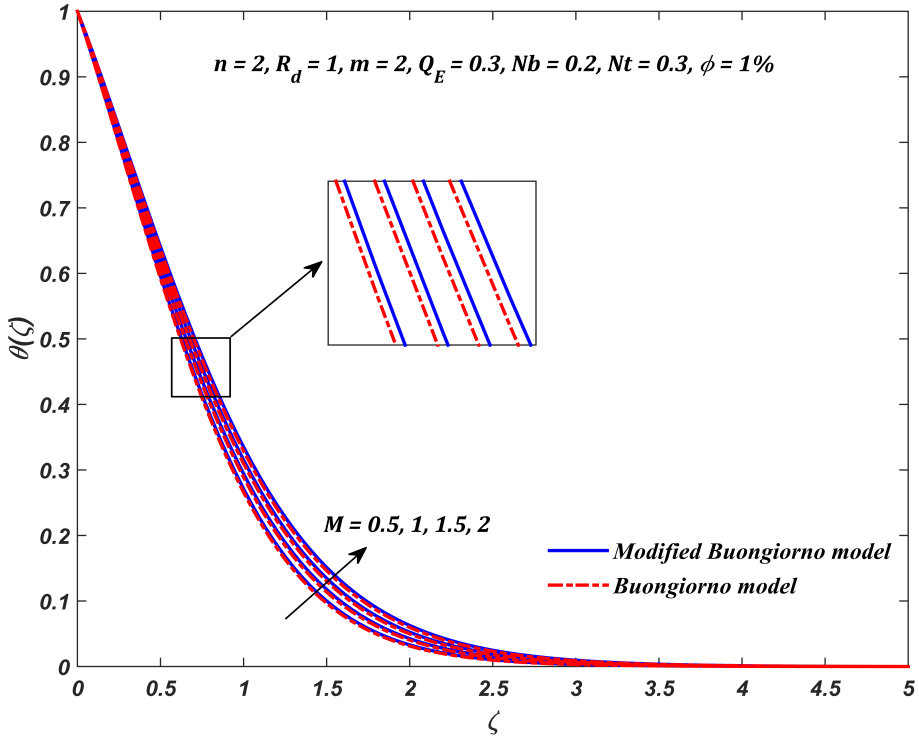

Figure 9.5: $\theta(\zeta)$ for distinct values of M

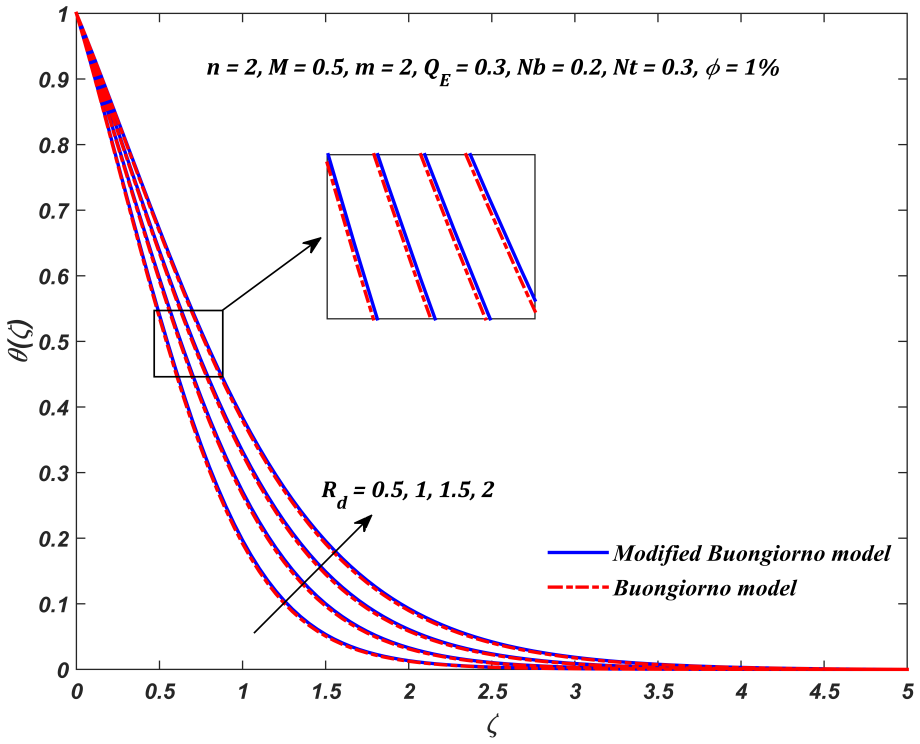

Figure 9.6: $\theta(\zeta)$ for distinct values of R_d

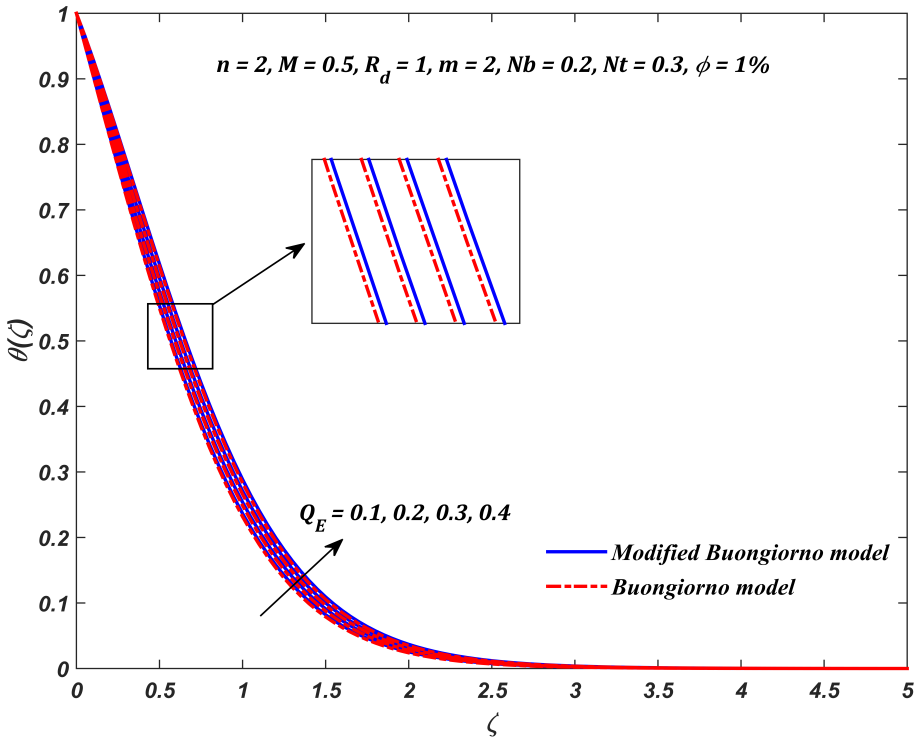

Figure 9.7: $\theta(\zeta)$ for distinct values of Q_E

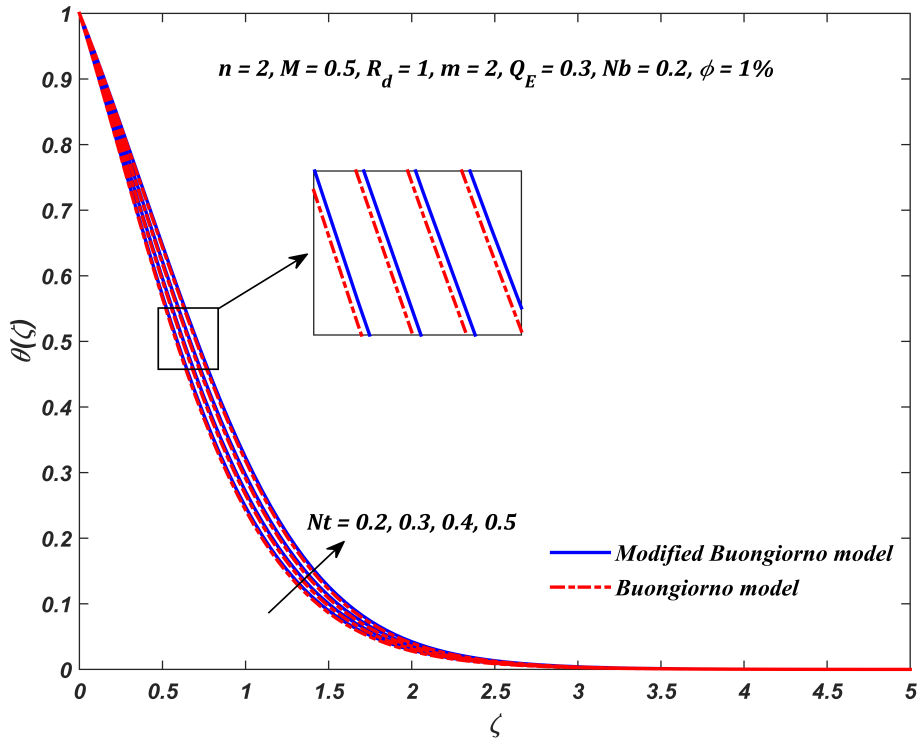

Figure 9.8: $\theta(\zeta)$ for distinct values of Nt

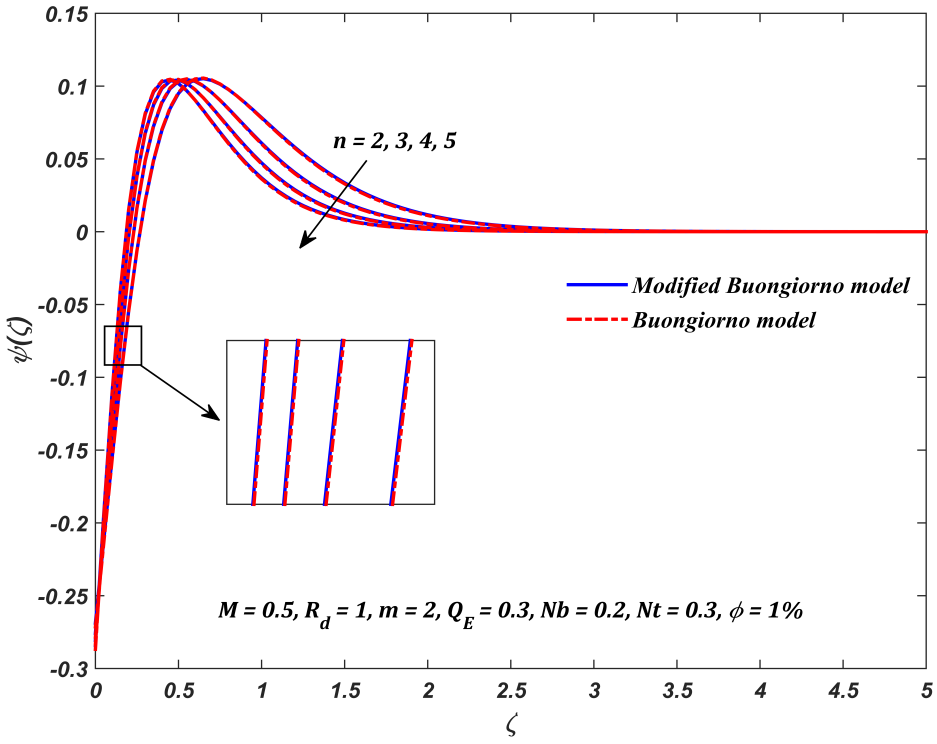

Figure 9.9: $\psi(\zeta)$ for distinct values of n

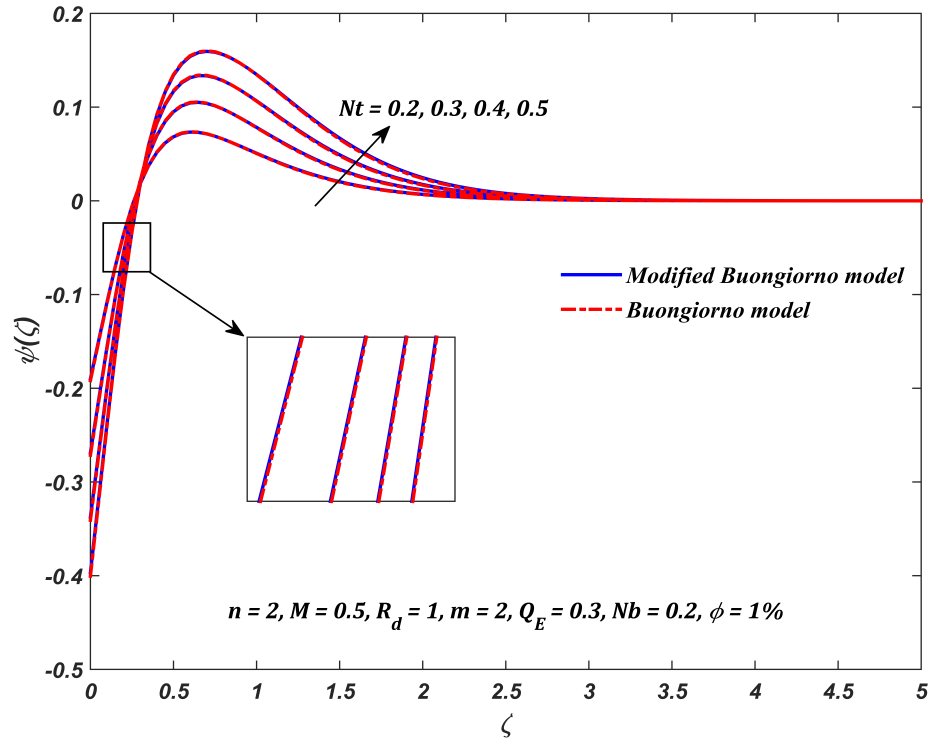

Figure 9.10: $\psi(\zeta)$ for distinct values of Nt

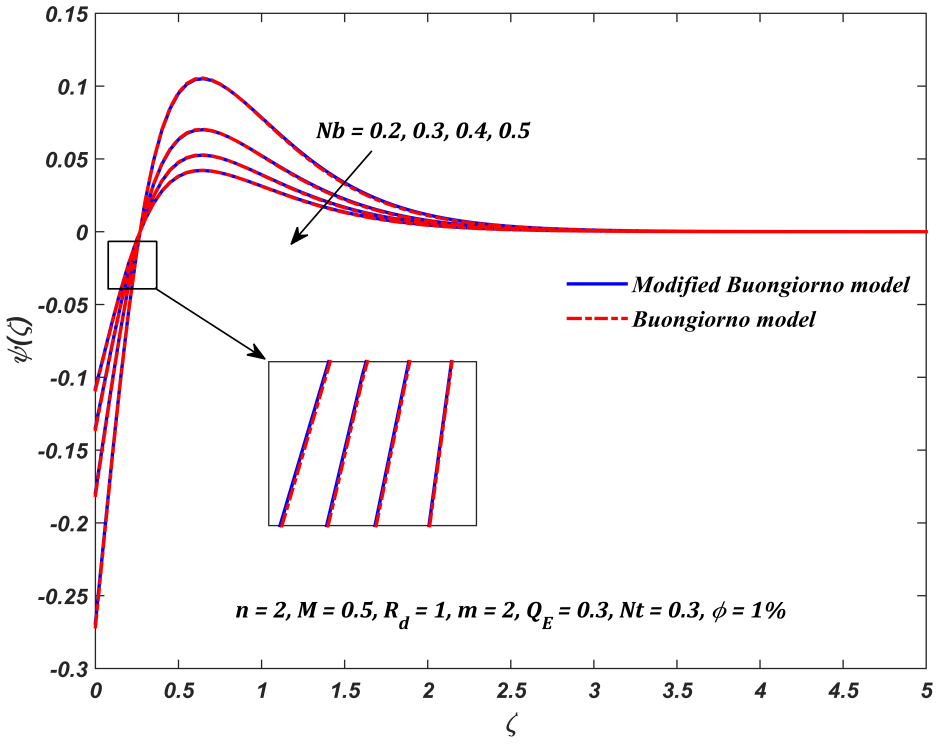

Figure 9.11: $\psi(\zeta)$ for distinct values of Nb

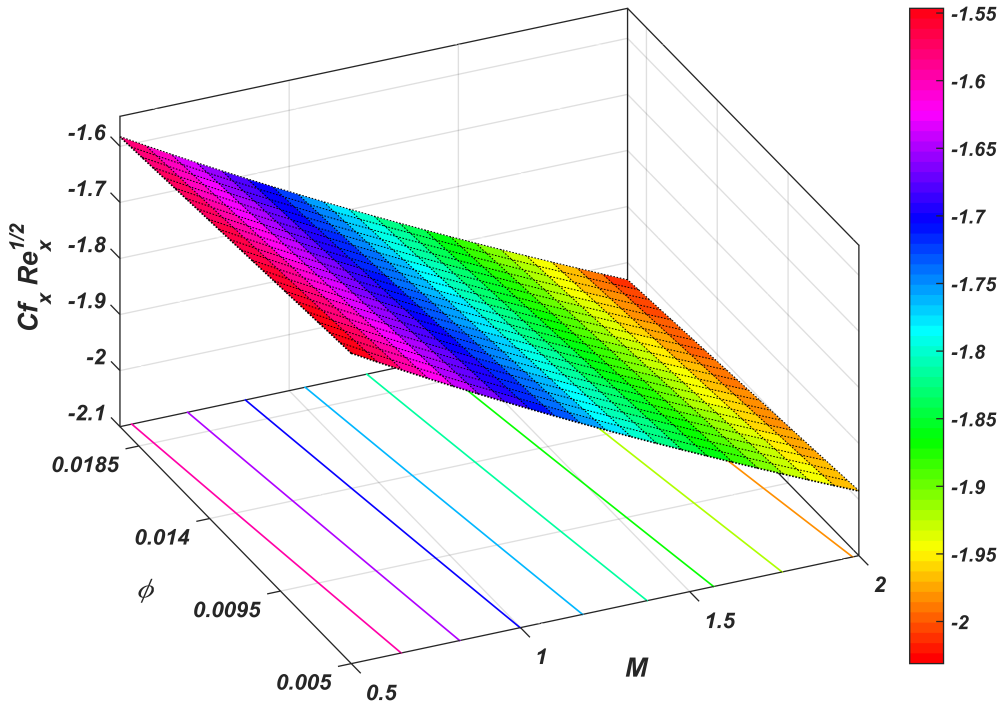

Figure 9.12: Simultaneous effect of M and ϕ on $Cf_x\ Re_x^{1/2}$

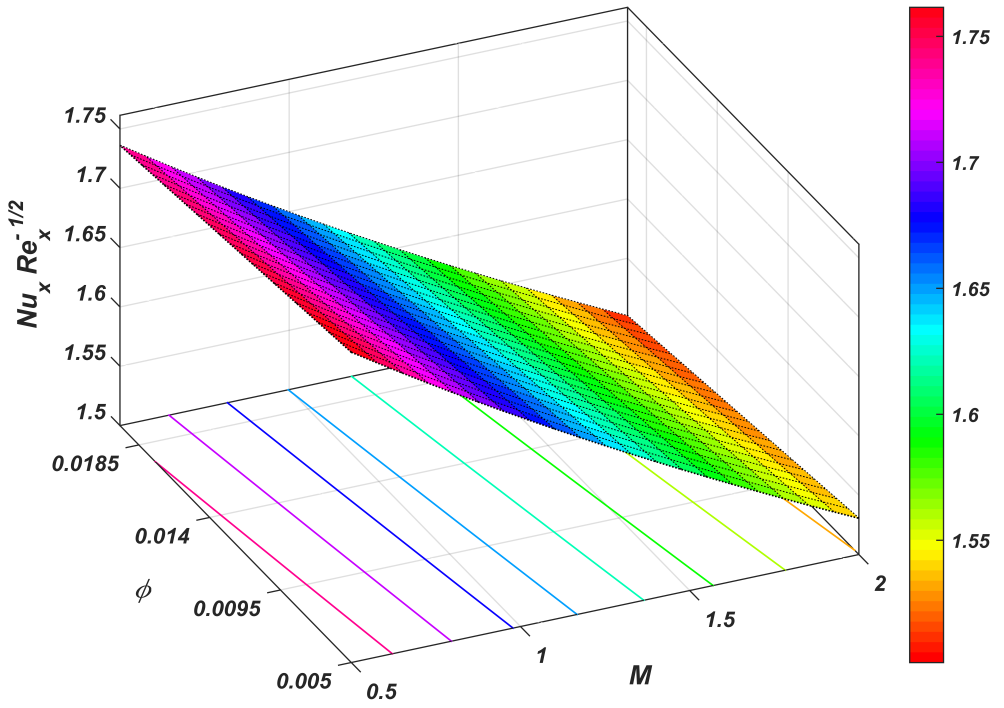

Figure 9.13: Simultaneous effect of M and ϕ on $Nu_x\ Re_x^{-1/2}$

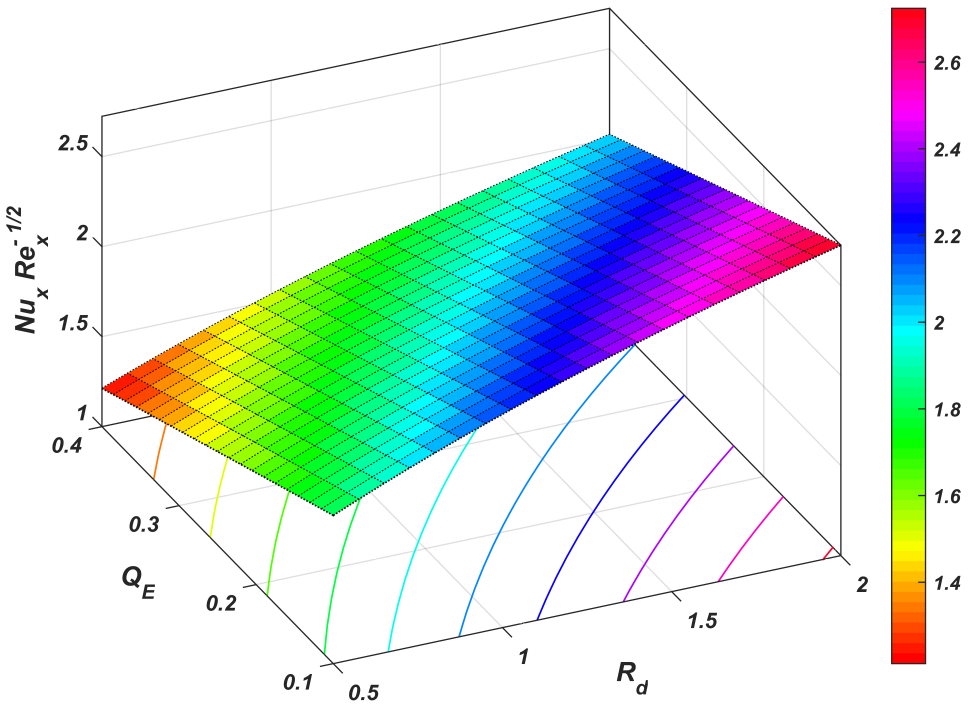

Figure 9.14: Simultaneous effect of R_d and Q_E on $Nu_x\ Re_x^{-1/2}$

Figure 9.2 elucidates the negative impact of the nonlinear stretching parameter (n) on $f\,'(\zeta)$ which implies that an augmentation in the nonlinear stretching parameter will result in a decrease in $f\,'(\zeta)$. Figure 9.3 describes the deviations in $f\,'(\zeta)$ concerning M (magnetic parameter). An increase in M tends to decrease $f\,'(\zeta)$. Physically, this can be associated with the generation of the Lorentz force (retarding force) which retards the magnitude of the nanomaterial's velocity.

The negative impact of n on $\theta\,(\zeta)$ is illustrated in Figure 9.4, implying that greater non-linearity in the stretch leads to lower thermal profiles. Figure 9.5 bespeaks the deviations in $\theta\,(\zeta)$ with respect to M. It can be perceived that $\theta\,(\zeta)$ increases as M values increase. This is because of the Lorentz force generated by the applied magnetic field. The influence of R_d (thermal radiation parameter) and Q_E (ESHS parameter) on $\theta\,(\zeta)$ is analyzed by means of Figures 9.6 and 9.7 respectively. Both parameters tend to improve $\theta\,(\zeta)$. This is because an increase in R_d and Q_E supplies secondary energy which triggers an increase in $\theta\,(\zeta)$. Figure 9.8 illustrates the increase in $\theta\,(\zeta)$ due to mounting Nt (thermophoresis parameter)

values. Physically, this is due to the increased movement of nanoparticles from a warm region to the colder region of the system.

The effect of n on $\psi(\zeta)$ is depicted in Figure 9.9. Dual nature is observed for augmenting n values. For the major part of ζ variation, $\psi(\zeta)$ decreases with augmenting n values. Figure 9.10 elucidates the dual nature observed on $\psi(\zeta)$ for increasing Nt values. For larger values of ζ, an increase in $\psi(\zeta)$ is noted. Physically, this is due to the leap in nanoparticle diffusion caused by temperature differences. The impact of Nb on $\psi(\zeta)$ is represented graphically in Figure 9.11. For the major portion of ζ, Nb has a negative impact on $\psi(\zeta)$. Physically, this decrease in $\psi(\zeta)$ is due to the improved nanoparticle random motion initiated by the increase in Nb values. It is worth mentioning that $\psi(\xi)$ at the boundary is negative due to zero nanoparticle mass flux at the plate and the migration of nanoparticles from the plate to the ambient region which leads to a lower concentration at the vicinity of the plate than the ambient region.

Simultaneous effect of the pertinent parameters on physical quantities is studied with the aid of three-dimensional surface plots which have been graphed in Figures 9.12 - 9.14. Figure 9.12 explains the impact of M and ϕ on $Cf_x\ Re_x^{1/2}$ (drag coefficient). It is observed that both parameters have a negative impact on $Cf_x\ Re_x^{1/2}$. The friction at the area of a solid and a fluid in relative motion is termed drag coefficient. In addition, the negative sign of drag coefficient represents the orientation. From Figures 9.13 and 9.14, it is seen that M, ϕ, and Q_E demotes the heat transfer rate $\left(Nu_x\ Re_x^{-1/2}\right)$ whereas R_d promotes $Nu_x\ Re_x^{-1/2}$.

9.5 Statistical Frame

9.5.1 Response Surface Methodology

RSM is a statistical technique used to measure the level of interaction exerted by the pertinent parameters chosen on the response variable. The influential parameters chosen here are the magnetic parameter ($0.5 \leq M \leq 1.5$), the ESHS parameter ($0.2 \leq Q_E \leq 0.4$) the thermal radiation parameter ($0.5 \leq R_d \leq 1.5$). The heat transfer rate $\left(Nu_x\ Re_x^{-1/2}\right)$ is chosen as the response variable. Table 9.3 bespeaks the effective parameters and their levels. The face-centered central composite design (CCD) is adopted to design the experimental runs. A quadratic model (including linear, quadratic, and interaction terms) is obtained for the response variable whose

general model is given by:

$$\text{Response} = \xi_1 A + \xi_2 B + \xi_3 C + \xi_4 AB + \xi_5 BC + \xi_6 AC + \xi_7 A^2 + \xi_8 B^2 + \xi_9 C^2 + \xi_{10}$$

where ξ_i $(i = 1\ to\ 10)$ represents the regression coefficients. The experimental design and the response for the 20 runs according to CCD are given in Table 9.4.

Table 9.3: Effectual parameter levels

Parameter	**Symbol**	**Levels**		
		-1 (low)	**0 (medium)**	**1 (high)**
M	A	0.5	1	1.5
R_d	B	0.5	1	1.5
Q_E	C	0.2	0.3	0.4

The quadratic model fitted for heat transfer rate with significant terms is given by:

$$Nu_x\ Re_x^{-1/2} = 1.64315 - 0.0995\ M + 0.95605\ R_d - 1.8646\ Q_E + 0.0176\ M^2 - 0.1209\ {R_d}^2 - 0.07569\ M\ R_d\ -\ 0.07147\ M\ Q_E\ -\ 0.22489\ R_d\ Q_E \quad (9.5.1)$$

The accuracy of the fitted model is guaranteed with the aid of the ANOVA table (Table 9.5). A parameter is statistically significant if its p-value is less than 0.05. It can be inferred that the quadratic term in Q_E is not significant and is therefore removed from the quadratic model. The coefficient of determination (R^2) for the model is found to be 99.99% which affirms the accuracy of the model. The residual plots in Figure 9.15 help to evaluate the accuracy of the model. It can be observed that all the data points are roughly distributed along the straight line (from normal probability plot) and the residual histogram is roughly bell-shaped, suggesting the normal nature of the residuals. Furthermore, a maximum error of 0.002 can be observed from the fitted versus residual plot, which also contributes to the accuracy of the model.

Table 9.4: Experimental design with actual and estimated response values

Run	Coded Values			Actual Values			$Nu_x\ Re_x^{-1/2}$	
	A	B	C	M	R_d	Q_E	Actual	Estimated
1	-1	-1	-1	0.5	0.5	0.2	1.62105	1.62183
2	1	-1	-1	1.5	0.5	0.2	1.50475	1.50539
3	-1	1	-1	0.5	1.5	0.2	2.25297	2.25325
4	1	1	-1	1.5	1.5	0.2	2.06122	2.06112
5	-1	-1	1	0.5	0.5	0.4	1.21226	1.21238
6	1	-1	1	1.5	0.5	0.4	1.08191	1.08165
7	-1	1	1	0.5	1.5	0.4	1.79944	1.79883
8	1	1	1	1.5	1.5	0.4	1.59315	1.59241
9	-1	0	0	0.5	1	0.3	1.75286	1.75237
10	1	0	0	1.5	1	0.3	1.59041	1.59094
11	0	-1	0	1	0.5	0.3	1.35272	1.35148
12	0	1	0	1	1.5	0.3	1.9213	1.92258
13	0	0	-1	1	1	0.2	1.88777	1.88622
14	0	0	1	1	1	0.4	1.44556	1.44714
15	0	0	0	1	1	0.3	1.66725	1.66726
16	0	0	0	1	1	0.3	1.66725	1.66726
17	0	0	0	1	1	0.3	1.66725	1.66726
18	0	0	0	1	1	0.3	1.66725	1.66726
19	0	0	0	1	1	0.3	1.66725	1.66726
20	0	0	0	1	1	0.3	1.66725	1.66726

Table 9.5: ANOVA table and regression coefficients

Source	Deg. of freedom	Adj. sum of squares	Adj. mean squares	Regression Coefficient	F-Value	p-Value
Model	9	1.37041	0.152268		142902.72	< 0.0001
Linear	3	1.36247	0.454158		426225.62	< 0.0001
M	1	0.06515	0.065147	-0.0995	61139.97	< 0.0001
R_d	1	0.81533	0.81533	0.95605	765184.48	< 0.0001
Q_E	1	0.482	0.481997	-1.8646	452352.4	< 0.0001
Square	3	0.00396	0.001319		1237.99	< 0.0001
$M * M$	1	0.00005	0.000053	0.0176	49.97	< 0.0001
$R_d * R_d$	1	0.00251	0.002512	-0.1209	2357.85	< 0.0001
$Q_E * Q_E$	1	0	0.000001	-0.0574	**0.85**	**0.378**
2-Way Interaction	3	0.00398	0.001326		1244.56	< 0.0001
$M * R_d$	1	0.00286	0.002865	-0.07569	2688.48	< 0.0001
$M * Q_E$	1	0.0001	0.000102	-0.07147	95.87	< 0.0001
$R_d * Q_E$	1	0.00101	0.001012	-0.22489	949.33	< 0.0001
Constant				1.64315		
Error	10	0.00001	0.000001			
Lack-of-Fit	5	0.00001	0.000002		*	*
Pure Error	5	0	0			
Total	19	1.37042				
$R^2 = 99.99\%$				Adjusted $R^2 = 100\%$		

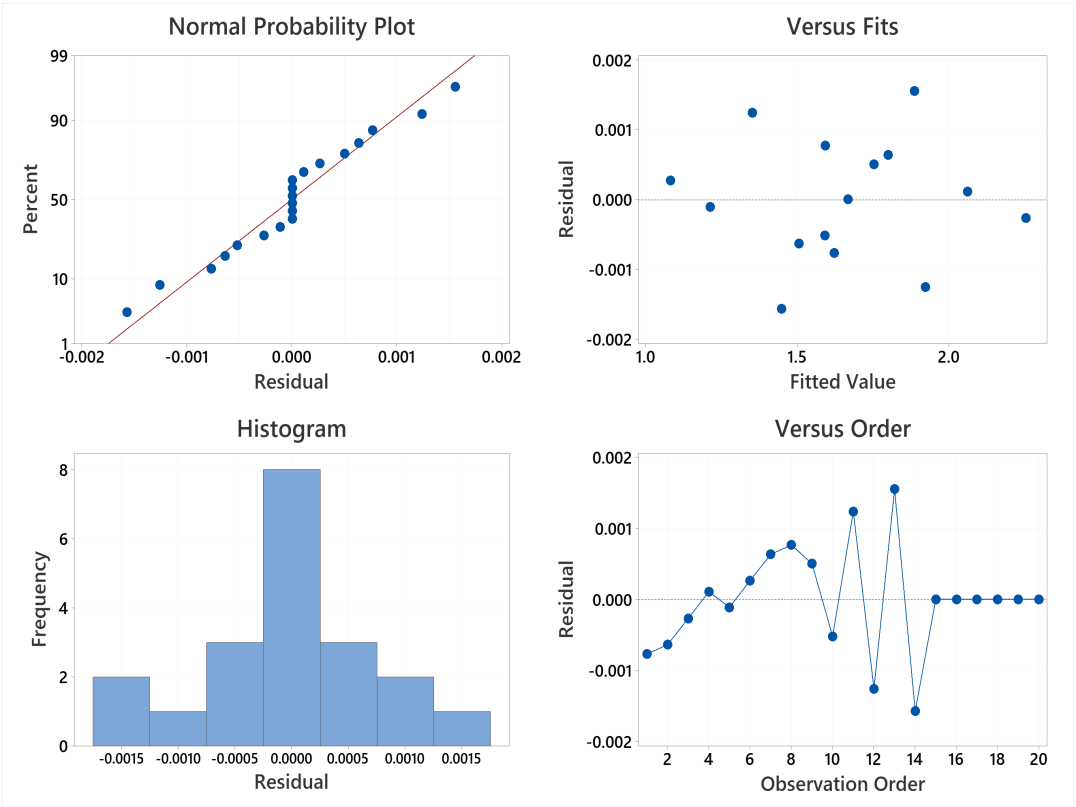

Figure 9.15: Residual plots

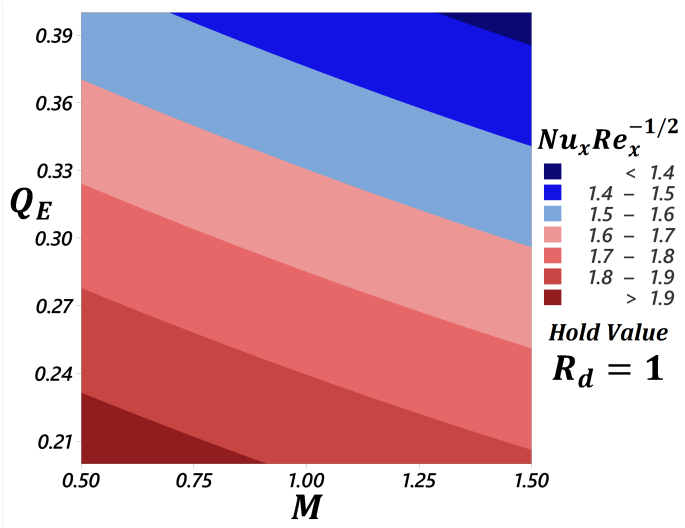

(a)

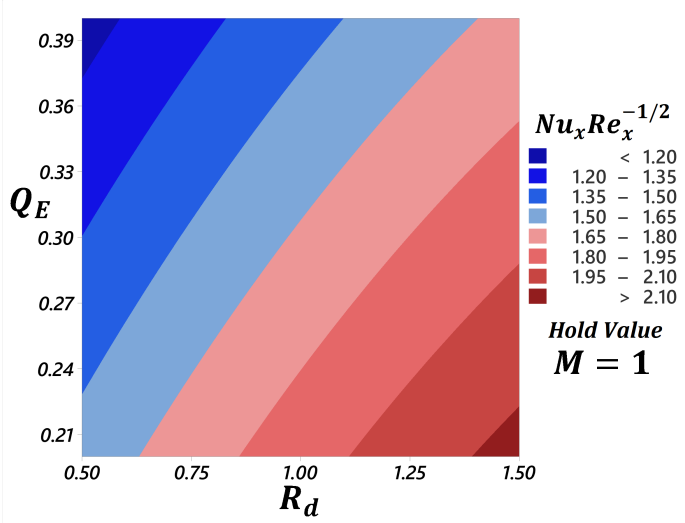

(b)

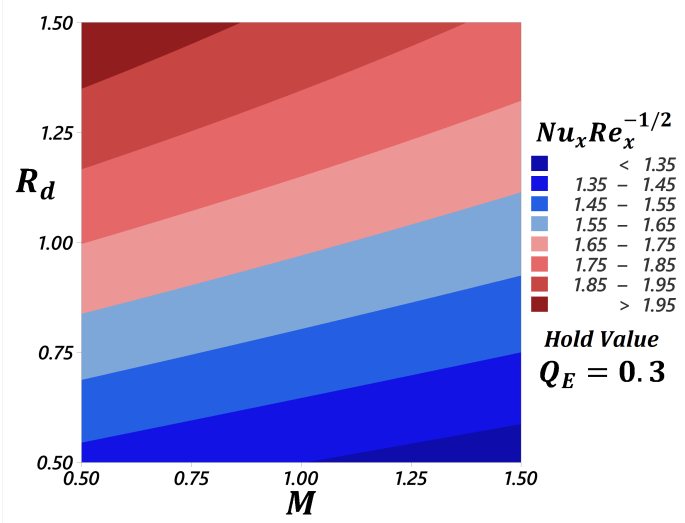

(c)

Figure 9.16: Contour plots for on $Nu_x\ Re_x^{-1/2}$

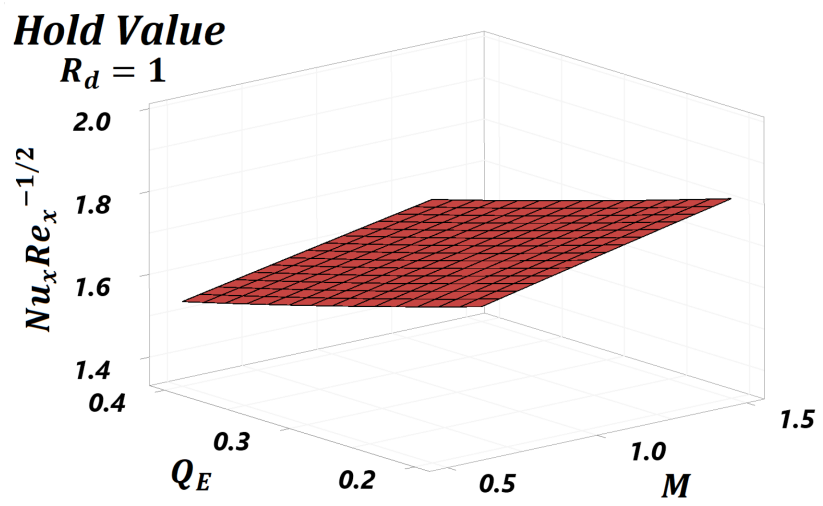

(a)

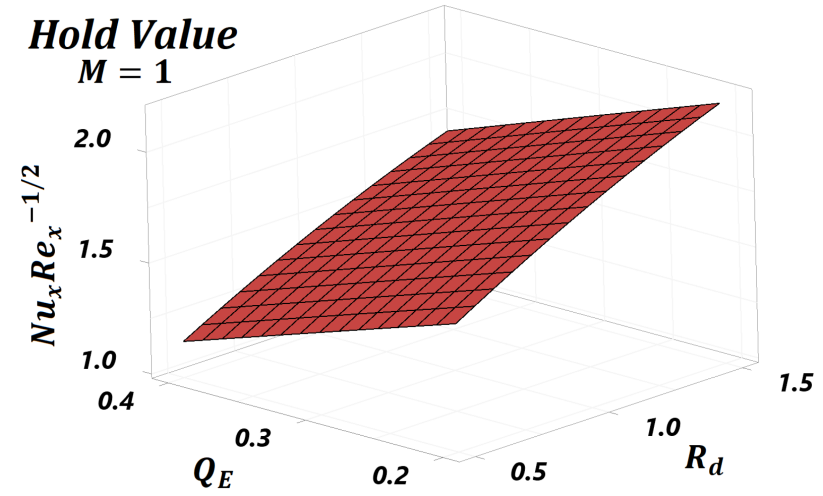

(b)

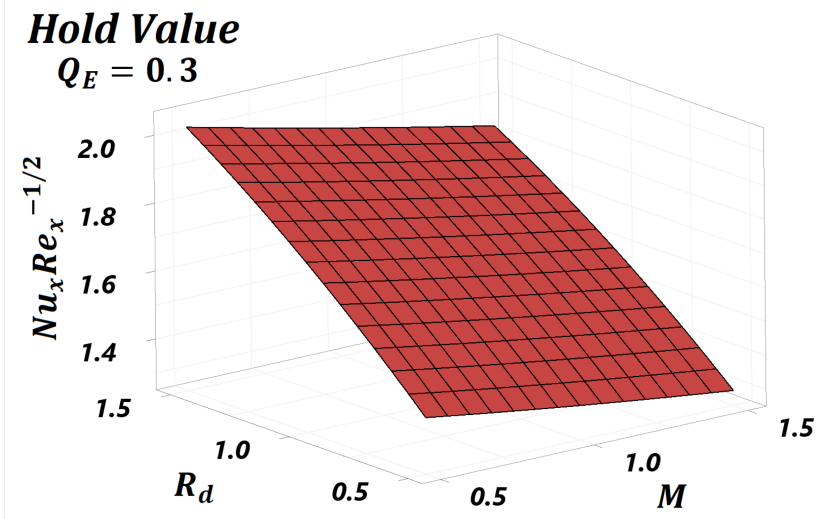

(c)

Figure 9.17: Surface plots for on $Nu_x\ Re_x^{-1/2}$

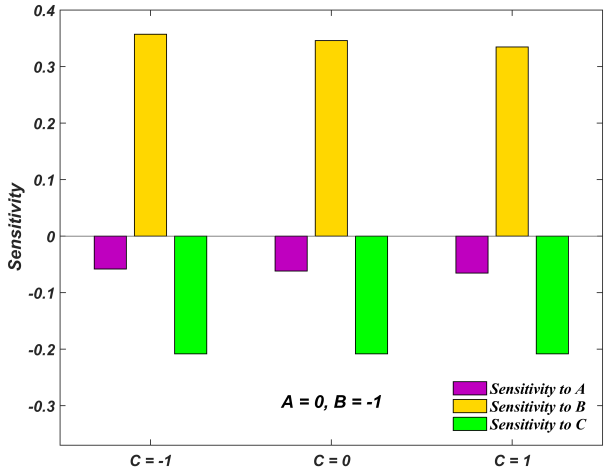

(a)

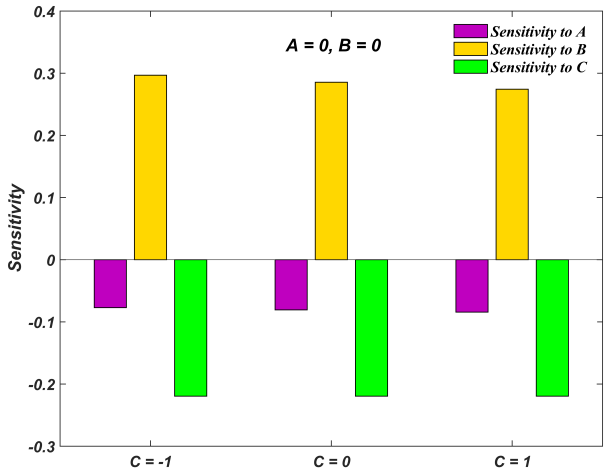

(b)

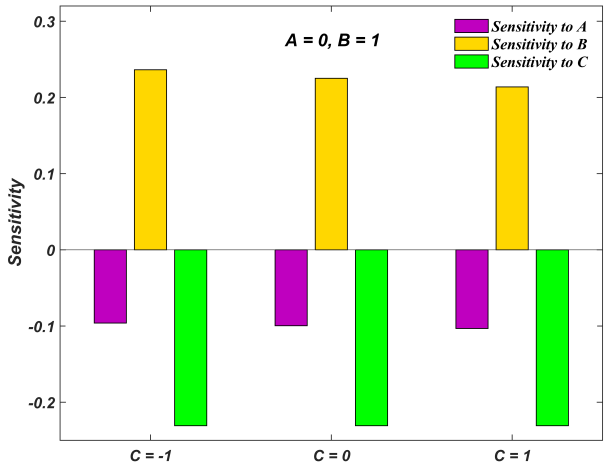

(c)

Figure 9.18: Bar charts showcasing the sensitivity of on $Nu_x\ Re_x^{-1/2}$

From Equation (9.5.1), it can be deduced that M and Q_E have a negative impact on the heat transfer rate, while R_d has a positive impact. The interactive impact of two parameters on $Nu_x Re_x^{-1/2}$ is visualized with the aid of contour and surface plots (see Figures 9.16 and 9.17) by keeping the third parameter at the mid-level. From Figures 9.16 and 9.17, it is evident that $Nu_x\ Re_x^{-1/2}$ is highest for lower values of M & Q_E and for higher values of R_d. Moreover, the interactive impact of the parameters on the heat transfer rate can be deduced using the plots in Figures 9.16 and 9.17. It is worth mentioning that complete synchronization is observed between statistical and numerical results.

9.5.2 Sensitivity Analysis

Sensitivity accounts for the level of change brought in the response variable by the variations in the independent parameters. The quadratic model (in coded form) with the significant regression coefficients takes the following form:

$$Nu_x\ Re_x^{-1/2} = 1.66724 - 0.080714\ A + 0.285540\ B - 0.219544\ C + 0.004400\ A^2 - 0.030226\ B^2 - 0.018923\ AB\ -\ 0.003573\ AC\ -\ 0.011245\ BC \tag{9.5.2}$$

Then the sensitivity functions are:

$$\frac{\partial\left(Nu_x\ Re_x^{-1/2}\right)}{\partial A} = -0.080714 + 0.008800\ A - 0.018923\ B\ -\ 0.003573\ C$$

$$\frac{\partial\left(Nu_x\ Re_x^{-1/2}\right)}{\partial B} = 0.285540 - 0.018923\ A\ - 0.060452\ B - \ 0.011245\ C$$

$$\frac{\partial\left(Nu_x\ Re_x^{-1/2}\right)}{\partial C} = -0.219544\ -\ 0.003573\ A\ -\ 0.011245\ B$$

The sensitivity of $Nu_x\ Re_x^{-1/2}$ is tabulated in Table 9.6 by keeping the magnetic parameter at the medium level ($A = 0$). A positive sensitivity value corresponds to the constructive nature of the augmentation in the parameter toward the response variable and its magnitude measures the intensity of the effect on the response variable. Here, M and Q_E exhibit negative sensitivity and R_d exhibits a positive sensitivity on $Nu_x\ Re_x^{-1/2}$ which is also in agreement with the numeric results obtained earlier.

Sensitivity of $Nu_x\ Re_x^{-1/2}$ is also visualized using bar charts (see Figure 9.18). In Figure 9.18(a), when the thermal radiation parameter is at the low level, the

sensitivity of $Nu_x\ Re_x^{-1/2}$ toward M and Q_E is negative whereas the sensitivity of $Nu_x\ Re_x^{-1/2}$ toward R_d is positive. When R_d is at the low level ($B = -1$), the negative sensitivity of $Nu_x\ Re_x^{-1/2}$ toward M gets intensified and the positive sensitivity of $Nu_x\ Re_x^{-1/2}$ decreases with R_d when Q_E is increased from low to high level. It is also noted that the sensitivity of $Nu_x\ Re_x^{-1/2}$ with Q_E remains constant irrespective of ESHS parameter level. Similar conclusions can be drawn from Figures 9.18(b) and 9.18(c).

Table 9.6: Sensitivity of $Nu_x\ Re_x^{-1/2}$ when $A = 0$

B	**C**	**Sensitivity** $\frac{\partial\left(\mathbf{Nu_x\ Re_x^{-1/2}}\right)}{\partial \mathbf{A}}$	$\frac{\partial\left(\mathbf{Nu_x\ Re_x^{-1/2}}\right)}{\partial \mathbf{B}}$	$\frac{\partial\left(\mathbf{Nu_x\ Re_x^{-1/2}}\right)}{\partial \mathbf{C}}$
	-1	-0.0582	0.3572	-0.2083
-1	0	-0.0618	0.3460	-0.2083
	1	-0.0654	0.3347	-0.2083
	-1	-0.0771	0.2968	-0.2195
0	0	-0.0807	0.2855	-0.2195
	1	-0.0843	0.2743	-0.2195
	-1	-0.0961	0.2363	-0.2308
1	0	-0.0996	0.2251	-0.2308
	1	-0.1032	0.2138	-0.2308

9.6 Conclusion

In view of its biomedical applications in targeted biomedical imaging, and cancer therapy (like photothermal therapy and photodynamic therapy); the significance of an external magnetic field and irregular heat source on the dynamics of $TiO_2 - H_2O$ nanomaterial over a nonlinearly stretched surface has been examined. A realistic model is used by considering the modified Buongiorno model and passive control of nanoparticles. The effect of pertinent parameters on the nanomaterial flow profiles

has been numerically investigated using the *bvp5c* scheme. Further, the influence of pertinent parameters on the heat transfer rate has been scrutinized utilizing the RSM and sensitivity analysis. The key conclusions from the present study are:

- The magnetic field has a constructive effect on the temperature of the nanomaterial and a destructive effect on the velocity of the nanomaterial.
- The temperature of nanomaterial ascends with the exponential space-based heat source, thermal radiation, and thermophoresis mechanisms.
- The thermal field of the nanomaterial when using the modified Buongiorno model is higher than when the traditional Buongiorno model is used.
- The velocity field is lower in the case of the modified Buongiorno model than in the conventional Buongiorno model.
- Surface drag coefficient at the surface decreases for higher nanoparticle volume fraction and magnetic field intensity.
- Increasing the intensity of the magnetic field and exponential heat source decreases heat transport, while increasing radiation increases the rate of heat transfer.
- Heat transfer rate is higher for lower values of magnetic field intensity and exponential heat source in the presence of medium radiative heat flux.
- The heat transport in the nanomaterial is more positively sensitive to thermal radiation and most negatively sensitive to the exponential heat source.

Appendix I: Non-dimensional qunatities

$\tau = \frac{(\rho C_p)_{np}}{(\rho C_p)_f}$	Effective heat capacity ratio
$M = \frac{(\sigma_e)_f \ B_0^2}{a \ \rho_f}$	Magnetic field parameter
$Nb = \frac{\tau \ D_B \ C_\infty}{\vartheta_f}$	Brownian motion parameter
$Pr_f = \frac{(\mu C_p)_f}{k_f}$	Prandtl number
$Q_E = \frac{Q_e}{a \ (\rho C_p)_f}$	Exponential space-based heat source parameter
$Le = \frac{\alpha_f}{D_B}$	Lewis number
$R_d = \frac{4 \ \sigma^* \ T_\infty^3}{k^* \ k_f}$	Thermal radiation parameter
$Nt = \frac{\tau \ D_T \ (T_w - T_\infty)}{T_\infty \vartheta_f}$	Thermophoresis parameter

Appendix II: Nomenclature

a, n, m	Positive constants	Q_e	Uniform heat source intensity
u, v	Velocity components	B_0	Strength of magnetic field
q_r	Radiative heat flux	T_∞	Ambient temperature
T	Fluid temperature	C	Nanoparticle volume fraction
x, y	Cartesian coordinates	u_w	Stretching velocity
τ_w	Wall shear stress	Nu_x	Local Nusselt number
T_w	Wall temperature	C_∞	Ambient nanoparticle volume fraction
ρC_p	Heat capacity	Cf_x	Local drag coefficient
σ_e	Electrical conductivity	τ	Effective heat capacity ratio
ζ	Similarity variable	D_B	Brownian diffusion coefficient
ϑ	Kinematic viscosity	D_T	Thermophoretic diffusion coefficient
k	Thermal conductivity	Q_e^*	Coefficient of exponential
α	Thermal diffusivity		space-based heat source
ρ	Density	ϕ	Volume fraction of TiO_2
μ	Dynamic viscosity	σ^*	Stefan- Boltzmann constant
q_w	Heat flux	k^*	Mean absorption coefficient

Chapter 10

Bioconvective magnetized nanomaterial flow subjected to convective thermal heating and Stefan blowing *

10.1 Introduction

The diffusion of nanoparticles (or species) from the lengthening surface to the ambient region creates a blowing effect. This blowing effect, derived from the Stefan problem, is dissimilar from the mass injection or blowing resulting from transpiration on a permeable surface. Theranostic is a novel procedure that integrates therapy and diagnosis in a single platform. Skin is considered as a nonlinear stretched surface. For its application in theranostic and photothermal therapy for melanoma skin cancer, the hydromagnetic bioconvective flow of a nanomaterial over a lengthening surface is investigated. Realistic nanomaterial modelling is achieved by incorporating passive control of the nanoparticles at the boundary. The impact of the Newtonian heating and Stefan blowing constraints are also accounted. Apposite transformations are employed and then transmuted nonlinear ODEs are resolved using the Bulirsch-Stoer and Newton-Raphson methods. The influence of Stefan blowing parameter ($-3 \leq Sb \leq 3$), the magnetic field parameter ($0.8 \leq M \leq 1.2$) and the Biot number ($0.2 \leq Bi \leq 0.4$) on the heat transfer rate has been scrutinized and optimized utilizing the response surface methodology (RSM). The sensitivity of heat transport rate is computed. The present chapter aims to address the following research questions with numerical and statistical procedures:

*Published in: Waves in Random and Complex Media (Taylor & Francis), 2022; (*early access*).

- What is the effect of pertinent parameters on the flow profiles for different levels of Stefan blowing parameter?
- What is the effect of an applied magnetic field on the flow profiles?
- How does the change in effectual parameters affect the heat transfer for different levels of Stefan blowing parameter?
- How does the interactive effects of magnetic field parameter, Biot number, and Stefan blowing parameter influence the heat transport?
- What is the optimized level of the parameters for maximum heat transport?

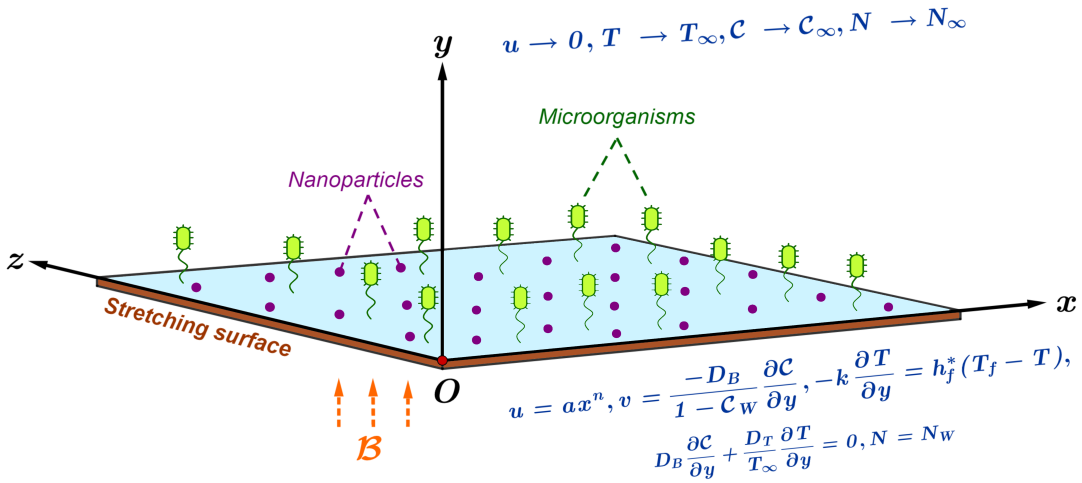

Figure 10.1: Geometrical Frame

10.2 Mathematical Frame

The two-dimensional bioconvective flow of nanoliquid on a lengthening surface (with velocity $u_w = ax^n$) is considered. The plate is placed on the x-axis and the nanoliquid embodied with microorganisms occupies the region $y > 0$. A uniform magnetic field of intensity $\mathcal{B} = \mathcal{B}_0(x)^{\frac{n-1}{2}}$ is administered externally in the y-direction. The Rosseland radiative heat flux is applied. Let $Q_t^* = Q_t x^{n-1}$, $Q_e^* = Q_e x^{n-1}$, $k_r^* = k_r x^{n-1}$ and $h_f^* = h_f x^{\frac{n-1}{2}}$ be the linear heat source (LHS) intensity, exponential space-based heat source (ESHS) intensity, chemical reaction rate, and heat transfer coefficient, respectively. The geometrical scheme of the flow has been shown in Figure 10.1.

Based on the aforementioned assumptions and revised Buongiorno nanoliquid model, the governing equations are given by (see Rana & Bhargava, 2012; Basir et al., 2021):

$$\frac{\partial u}{\partial x}+\frac{\partial v}{\partial y}=0 \tag{10.2.1}$$

$$u\frac{\partial u}{\partial x}+v\frac{\partial u}{\partial y}=\vartheta\frac{\partial^2 u}{\partial y^2}-\frac{\sigma_e \mathcal{B}^2}{\rho}u \tag{10.2.2}$$

$$\begin{aligned} u\frac{\partial T}{\partial x}+v\frac{\partial T}{\partial y}=\alpha\frac{\partial^2 T}{\partial y^2} &+\tau\left\{D_B\,\frac{\partial \mathcal{C}}{\partial y}\frac{\partial T}{\partial y}+\frac{D_T}{T_\infty}\left(\frac{\partial T}{\partial y}\right)^2\right\}-\frac{1}{\rho C_p}\frac{\partial q_r}{\partial y} \\ &+\frac{Q_t^*}{\rho C_p}\left(T-T_\infty\right)+\frac{Q_e^*}{\rho C_p}\left(T_f-T_\infty\right)\exp\left(-m\,\sqrt{\frac{a\left(n+1\right)}{2\vartheta}}\,yx^{\frac{n-1}{2}}\right) \end{aligned} \tag{10.2.3}$$

$$u\frac{\partial \mathcal{C}}{\partial x}+v\frac{\partial \mathcal{C}}{\partial y}=D_B\,\frac{\partial^2 \mathcal{C}}{\partial y^2}+\frac{D_T}{T_\infty}\,\frac{\partial^2 T}{\partial y^2}-k_r^*\left(\mathcal{C}-\mathcal{C}_\infty\right) \tag{10.2.4}$$

$$u\frac{\partial N}{\partial x}+v\frac{\partial N}{\partial y}+\frac{bW_c}{\mathcal{C}_\infty}\left(\frac{\partial}{\partial y}\left(N\frac{\partial \mathcal{C}}{\partial y}\right)\right)=D_m\frac{\partial^2 N}{\partial y^2} \tag{10.2.5}$$

subject to the boundary conditions (see Rana & Bhargava, 2012; Basir et al., 2021):

$$At\ y=0\ :\ u=u_w\left(x\right)=ax^n\ ,\ v=-\frac{D_B}{\left(1-\mathcal{C}_w\right)}\left(\frac{\partial \mathcal{C}}{\partial y}\right),$$

$$-k\,\frac{\partial T}{\partial y}=h_f^*\left(T_f-T\right),\ D_B\,\frac{\partial \mathcal{C}}{\partial y}+\frac{D_T}{T_\infty}\,\frac{\partial T}{\partial y}=0\ ,\ N=N_w.$$

$$As\ y\to\infty\ :\ u\to 0\ ,\ T\to T_\infty\ ,\ \mathcal{C}\to\mathcal{C}_\infty\ ,\ N\to N_\infty.$$

Consider the following similarity transformations (see Mabood et al., 2015; Basir et al., 2021):

$$u=ax^n f'\left(\xi\right),\ v=-\sqrt{\frac{a\vartheta\left(n+1\right)}{2}}\,x^{\frac{n-1}{2}}\left[f\left(\xi\right)+\left(\frac{n-1}{n+1}\right)\xi\ f\ '\left(\xi\right)\right],$$

$$\xi=\sqrt{\frac{a\left(n+1\right)}{2\vartheta}}\,y\,x^{\frac{n-1}{2}},\ T=\left(T_f-T_\infty\right)\theta\left(\xi\right)+T_\infty,$$

$$\mathcal{C}=\psi\left(\xi\right)\mathcal{C}_\infty+\mathcal{C}_\infty,\ N=\chi\left(\xi\right)\left(N_w-N_\infty\right)+N_\infty.$$

Using the above defined similarity transformations, Equations (10.2.1) – (10.2.5) are converted into:

$$f\,''' = \left(\frac{2n}{n+1}\right)(f\,')^2 - ff\,'' + \left(\frac{2}{n+1}\right)Mf\,' \tag{10.2.6}$$

$$\theta\,'' = \frac{-Pr_f}{1+\frac{4}{3}Rd}\left(f\theta' + \left(\frac{2}{n+1}\right)\left(Q_T\theta + Q_E e^{-m\xi}\right) + Nb\theta'\psi' + Nt(\theta')^2\right) \tag{10.2.7}$$

$$\psi\,'' = Le\ Pr_f\ \left(\left(\frac{2}{n+1}\right)Kr\ \psi - f\psi\,'\right) - \left(\frac{Nt}{Nb}\right)\theta\,'' \tag{10.2.8}$$

$$\chi\,'' = Pe\left((\chi+\Omega)\,\psi\,'' + \chi\,'\psi\,'\right) - Lb\ Pr_f\ f\chi\,' \tag{10.2.9}$$

subject to the boundary conditions

$$f\,(0) = \frac{Sb}{Le\ Pr_f}\ \psi\,'(0)\,,\ f\,'(0) = 1,\ \theta\,'(0) = -Bi\,(1-\theta\,(0))\,,$$

$$\psi\,'(0) + \left(\frac{Nt}{Nb}\right)\theta\,'(0) = 0,\ \chi\,(0) = 1.$$

$$f\,'(\infty) \to 0,\ \theta\,(\infty) \to 0,\ \psi\,(\infty) \to 0,\ \chi\,(\infty) \to 0.$$

where the dimensionless parameters are given in appendix I.

The physical quantities are given by (see Mabood et al., 2015; Basir et al., 2021; Ahmad, Ashraf, & Ali, 2020):

$$\text{Local drag coefficient} \quad : \quad Cf_x = \frac{\tau_\omega}{\rho\ (u_w)^2} = \frac{\mu\ \frac{\partial u}{\partial y}\Big|_{y=0}}{\rho\ (u_w)^2},$$

$$\Rightarrow Cf_x Re_x^{1/2} = \sqrt{\frac{n+1}{2}}\ f\,''(0).$$

$$\text{Local Nusselt number} \quad : \quad Nu_x = \frac{x\ q_\omega}{k\ (T_f - T_\infty)} = \frac{-x\left(k\ \frac{\partial T}{\partial y} - q_r\right)\Big|_{y=0}}{k\ (T_f - T_\infty)},$$

$$\Rightarrow Nu_x Re_x^{-1/2} = -\left(1 + \frac{4}{3}Rd\right)\sqrt{\frac{n+1}{2}}\ \theta\,'(0).$$

$$\text{Local motile density number} \quad : \quad Nn_x = \frac{x\ q_n}{D_m\ (N_w - N_\infty)} = \frac{-x\ D_m\ \frac{\partial N}{\partial y}\Big|_{y=0}}{D_m\ (N_w - N_\infty)},$$

$$\Rightarrow Nn_x Re_x^{-1/2} = -\sqrt{\frac{n+1}{2}}\ \chi\,'(0).$$

where $Re_x = \frac{xu_w}{\vartheta}$ is the local Reynold's number.

10.3 Numerical Frame & Validation

The transformed equations are given in Equations (10.2.6) – (10.2.9) are reduced to a system of first-order ODEs by setting:

$$Z_1 = f,\ Z_2 = f\,',\ Z_3 = f\,'',\ Z_4 = \theta,\ Z_5 = \theta\,',\ Z_6 = \psi,\ Z_7 = \psi\,',\ Z_8 = \chi,\ Z_9 = \chi\,'$$

The transmuted system of the first-order ODES is given by:

$$Z_1{}' = Z_2,\ Z_2{}' = Z_3$$

$$Z_3{}' = \left(\frac{2n}{n+1}\right)(Z_2)^2 - Z_1 Z_3 + \left(\frac{2}{n+1}\right) M Z_2$$

$$Z_4{}' = Z_5$$

$$Z_5{}' = \frac{-Pr_f}{1 + \frac{4}{3}Rd}\left(Z_1 Z_5 + \left(\frac{2}{n+1}\right)\left(Q_T\ Z_4 + Q_E\ e^{-m\xi}\right) + Nb\ Z_5\ Z_7 + Nt\ (Z_5)^2\right)$$

$$Z_6{}' = Z_7$$

$$Z_7{}' = Le\ Pr_f\left(\left(\frac{2}{n+1}\right) Kr\ Z_6 - Z_1\ Z_7\right) - \left(\frac{Nt}{Nb}\right) Z_5{}'$$

$$Z_8{}' = Z_9$$

$$Z_9^{'} = Pe\,(Z_8 + \Omega)\,Z_7^{'} - Lb\;Pr_f\;Z_1\;Z_9$$

with

$$Z_1(0) = \frac{Sb\;Nt\;Bi}{Le\;Pr_f\;Nb}\;(1-\omega_2),\;\; Z_2(0) = 1,\;\; Z_3(0) = \omega_1,$$

$$Z_4(0) = \omega_2,\;\; Z_5(0) = -Bi\,(1-\omega_2),\;\; Z_6(0) = \omega_3,$$

$$Z_7(0) = \left(\frac{Nt\;Bi}{Nb}\right)(1-\omega_2),\;\; Z_8(0) = 1,\;\; Z_9(0) = \omega_4.$$

where $\omega_1,\ \omega_2,\ \omega_3$ and ω_4 are estimated employing the Newton-Raphson technique with the aid of a suitable initial guess.

Table 10.1: Resemblance of $-\theta'(0)$ for ordinary fluid when $Pr_f = 1$

n	$-\theta'(\mathbf{0})$		
	Rana & Bhargava, 2012	**Mabood et al., 2015**	**Present Study**
0.2	0.6113	0.61131	0.6113101753
0.5	0.5967	0.59668	0. 5966869638
1.5	0.5768	0.57686	0.5768695042
2	-	0.57245	0.5724552831
3	0.5672	0.56719	0.5671905097
4	-	0.56415	0.5641562416
10	0.5578	0.55783	0.5578319124

The reduced system of first-order differential equations is numerically resolved by employing Bulirsch-Stoer and Newton-Raphson algorithms in MATLAB with infinity, step size, and error tolerance fixed at 6, 0.01, and 10^{-8}, respectively. The Bulirsch-Stoer algorithm is a numerical procedure based on the Richardson extrapolation and the midpoint method. In place of the original Bulirsch and Stoer technique, a simplified version that holds on to the fundamental ideas of Bulirsch and Stoer has been utilized. The automated step size adjustment has been omitted in the algorithm for increased efficiency. For computations requiring high accuracy

solutions involving smooth functions, the Bulirsch-Stoer algorithm has an upper hand. The accuracy and the reliability of the proposed numerical technique have been adjudged through a restrictive correspondence with the previously published works of Rana & Bhargava, 2012 and Mabood et al., 2015 (see Table 10.1).

10.4 Results & Discussion

The impact of pertinent parameters on the velocity ($f'(\xi)$), nanomaterial temperature ($\theta(\xi)$), volume fraction ($\psi(\xi)$), microbial concentration ($\chi(\xi)$), and the physical quantities (skin friction coefficient, Nusselt number, and motile density number) are depicted in Figures 10.2 - 10.21. $Pr_f = 6.2$, $Q_T = Q_E = Bi = Nt = Nb = Lb = 0.3$, $M = Rd = Pe = 1$, $Kr = \Omega = 0.5$, and $n = m = Le = 2$ have been chosen as the default values throughout the computations. Graphical illustrations are presented to compare the flow profiles for $Sb = -3$ (suction), $Sb = 0$ (impermeable surface), and $Sb = 3$ (injection); where Sb represents the Stefan blowing parameter.

The positive impact of n (nonlinear stretching parameter) on $f'(\xi)$ has been graphed in Figure 10.2, which means that an increase in n will augment the velocity profile. The generation of Lorentz force due to M (magnetic field parameter) serves as a resistive force that clashes with the fluid motion and hence reduces the velocity (see Figure 10.3). The magnetic field is responsible for improving the biomedical imaging capabilities by manipulating the transference of nanomaterial to the preferred location. Further, it is seen that the velocity profile descends with mounting values of Sb.

Figure 10.4 elucidates the decreasing nature of $\theta(\xi)$ with n. Augmentation in M will fuel the generation of Lorentz force (a conflicting force) that retards the fluid flow and thereby intensifying the nanofluid temperature (see Figure 10.5). The positive impact of Q_T (LHS parameter), Q_E (ESHS parameter), and Rd (thermal radiation parameter) on $\theta(\xi)$ is elucidated in Figures 10.6 - 10.8, respectively. An increase in Rd, Q_E and Q_T contributes to the surge in nanomaterial temperature by the supplemental energy to the system. Figure 10.9 describes the positive deviations in $\theta(\xi)$ concerning Bi (Biot number). Physically, an augmentation in Bi implies increased convection that tends to boost $\theta(\xi)$. Biologically, an improvement in the nanomaterial temperature has a positive contribution towards hyperthermia that helps in the termination of cancerous cells or tumors. It is also noted that the $\theta(\xi)$

descends with increasing values of Sb.

Figure 10.10 depicts the dual nature observed on $\psi(\xi)$ for mounting values of n. An increase in the nanoparticle volume fraction is observed initially. Subsequently, n has a negative effect on $\psi(\xi)$. The influence of Kr on $\psi(\xi)$ is analyzed in Figure 10.11. For the major portion of ξ, $\psi(\xi)$ descends with increasing values of Kr. Physically, this shrinkage in $\psi(\xi)$ is due to the increased consumption of nanoparticle initiated by the increasing Kr values. The dual nature of $\psi(\xi)$ for differing Le values is represented graphically in Figure 10.12. For larger values of ξ, augmentation in Le tends to decrease the nanoparticle volume fraction. Lewis number corresponds to the ratio of thermal diffusivity with Brownian motion diffusivity. Physically, an increase in Le lowers the Brownian motion diffusivity that prompts a decrease in the nanoparticle volume fraction. Biologically, a decline in nanoparticle volume fraction implies improved biomedical imaging and medication. It is worth mentioning that $\psi(\xi)$ at the boundary is negative due to zero nanoparticle mass flux at the plate and the migration of nanoparticles from the plate to the ambient region which leads to a lower concentration at the vicinity of the plate than the ambient region.

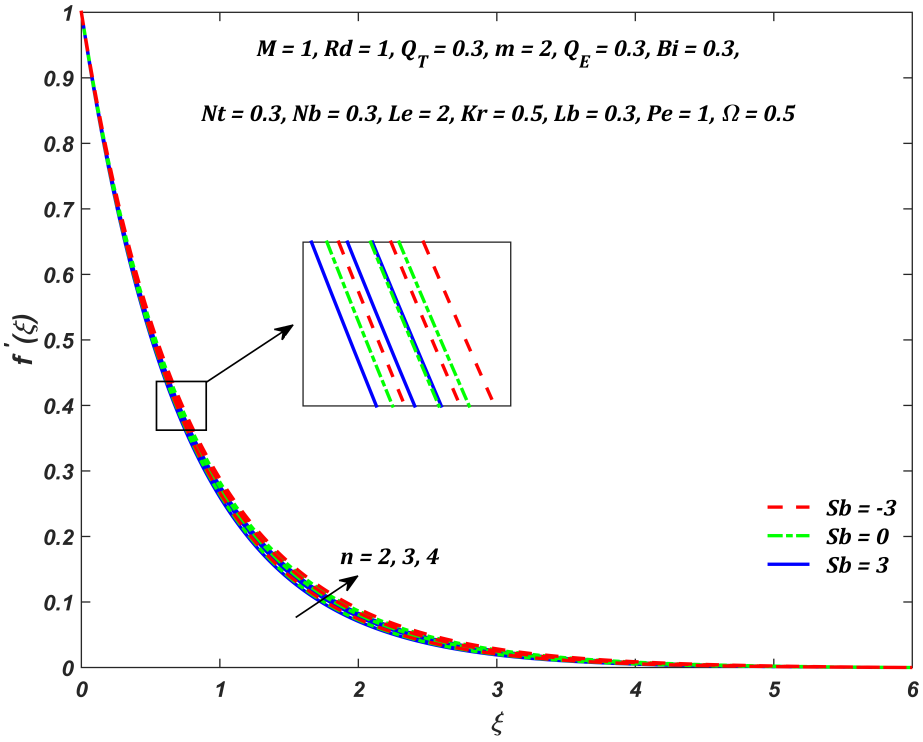

Figure 10.2: $f'(\xi)$ for distinct n values

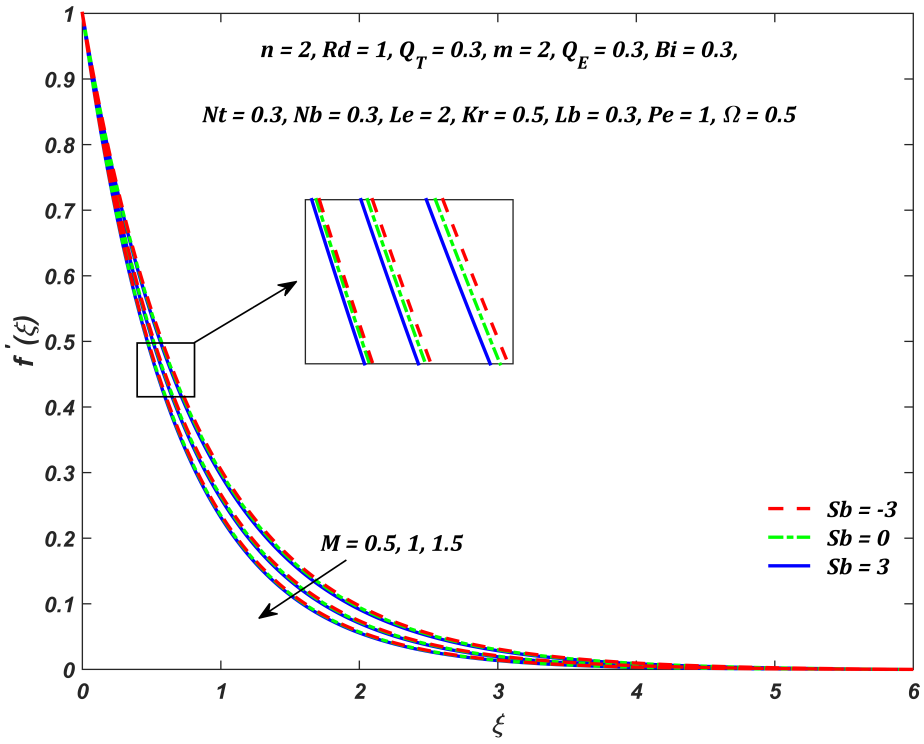

Figure 10.3: $f'(\xi)$ for distinct M values

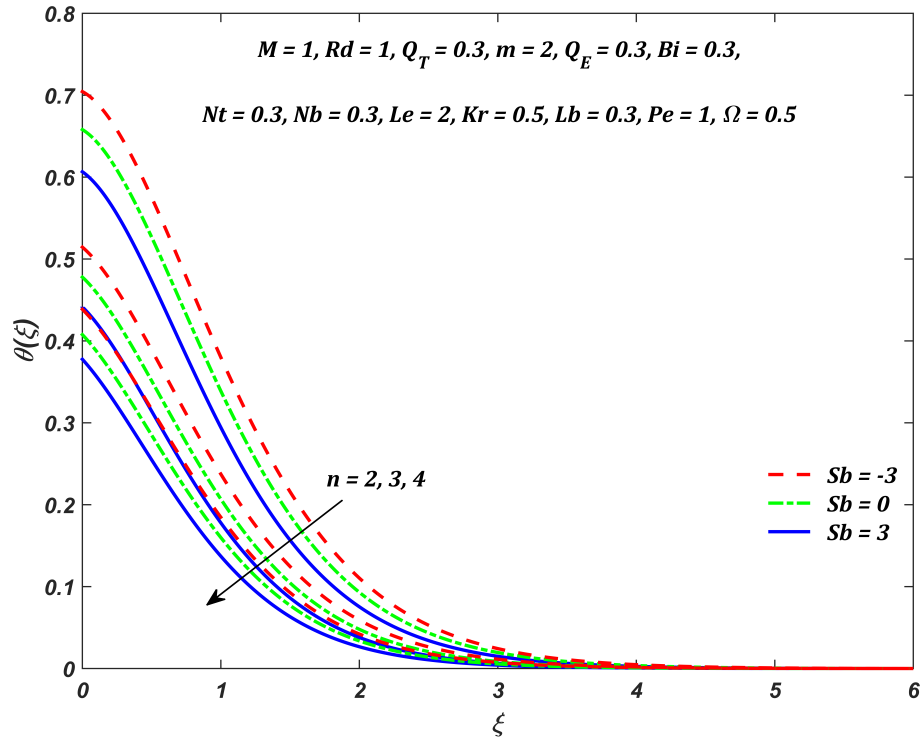

Figure 10.4: $\theta(\xi)$ for distinct n values

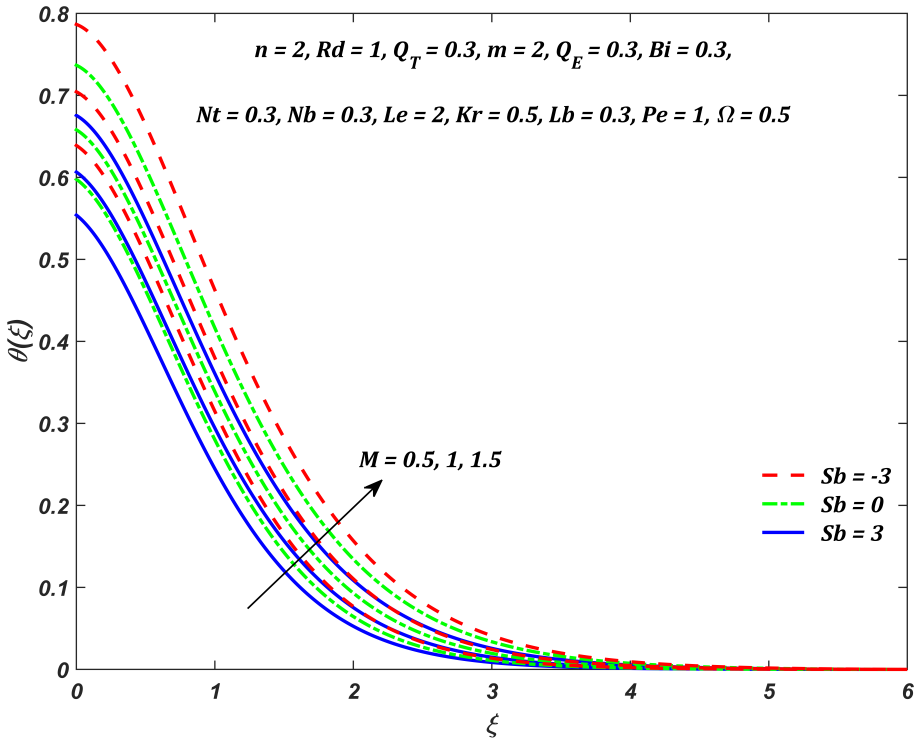

Figure 10.5: $\theta(\xi)$ for distinct M values

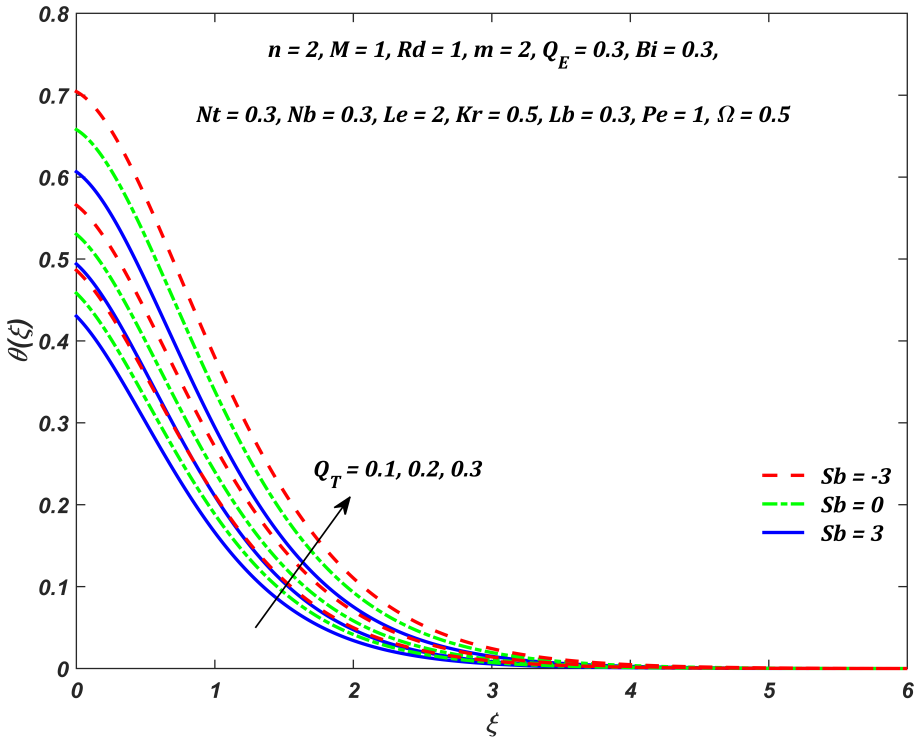

Figure 10.6: $\theta(\xi)$ for distinct Q_T values

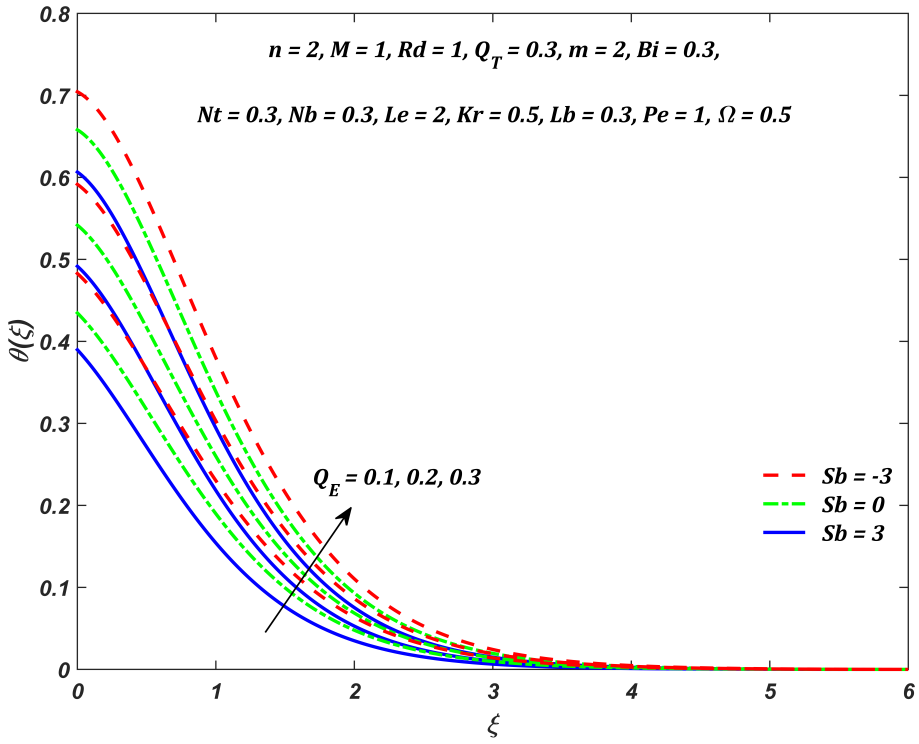

Figure 10.7: $\theta(\xi)$ for distinct Q_E values

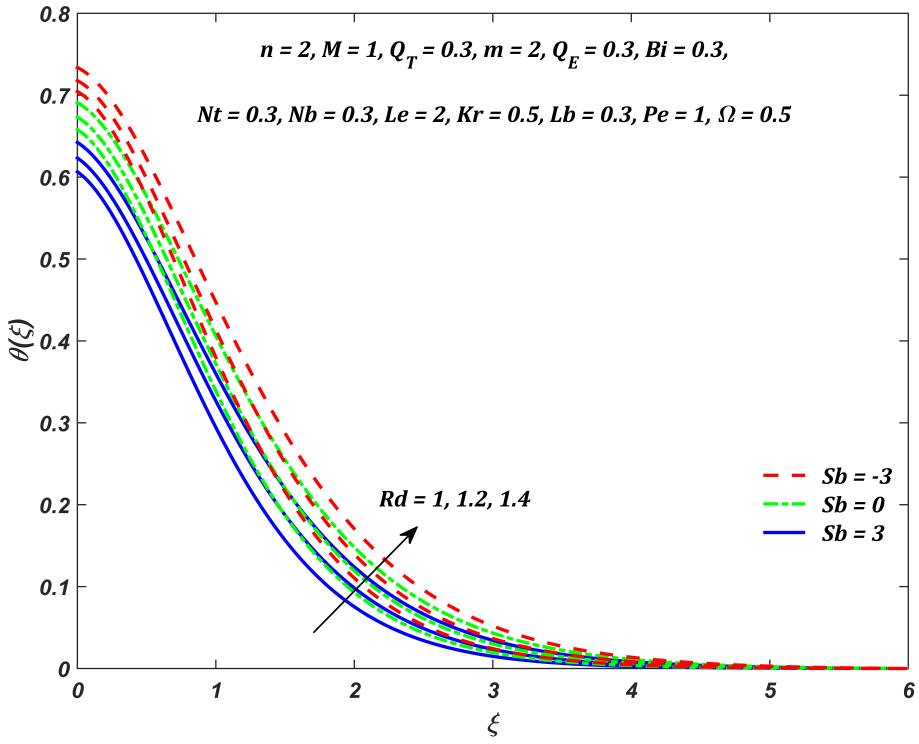

Figure 10.8: $\theta(\xi)$ for distinct Rd values

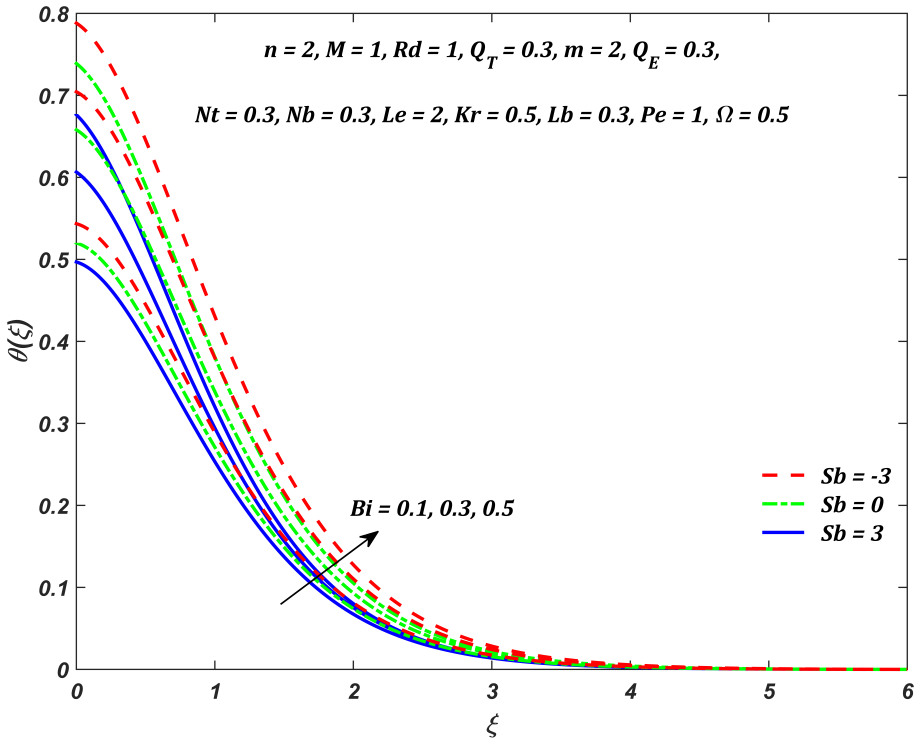

Figure 10.9: $\theta(\xi)$ for distinct Bi values

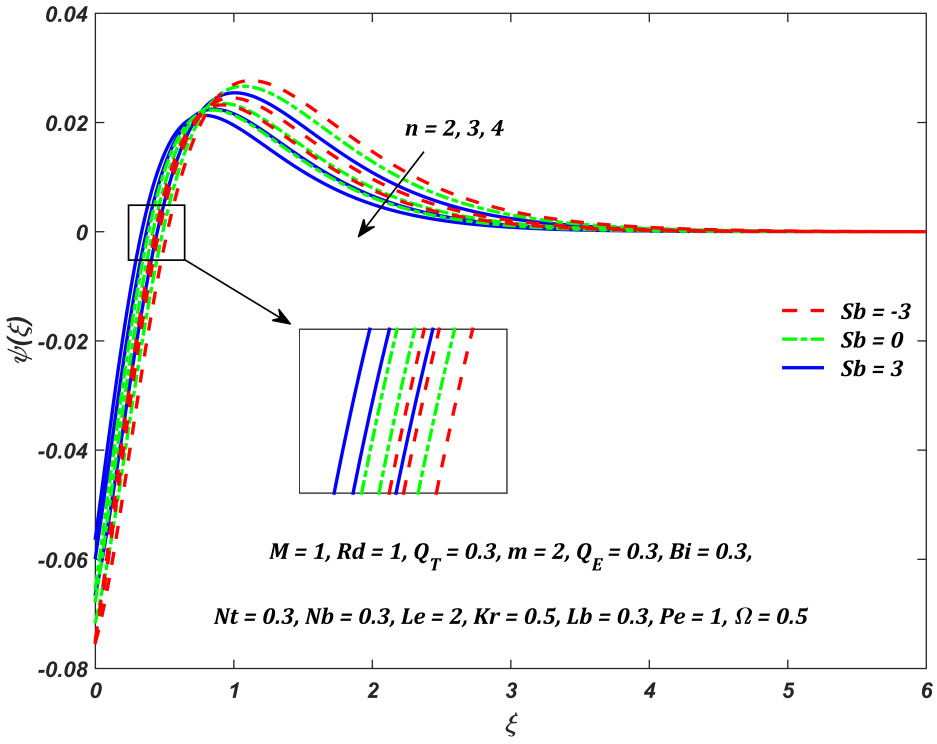

Figure 10.10: $\psi(\xi)$ for distinct n values

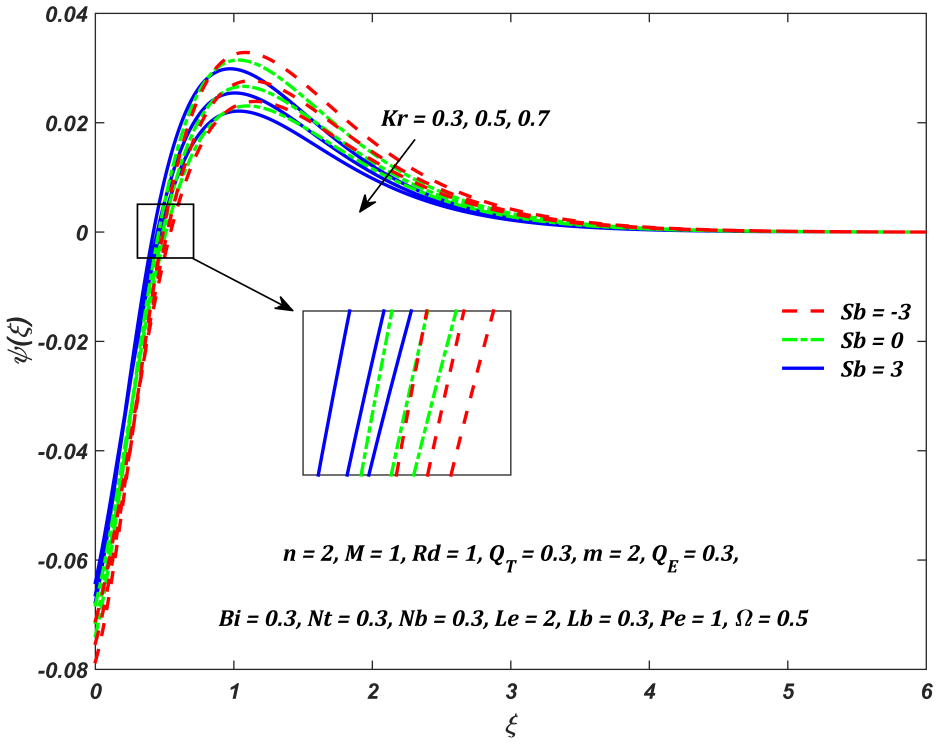

Figure 10.11: $\psi(\xi)$ for distinct Kr values

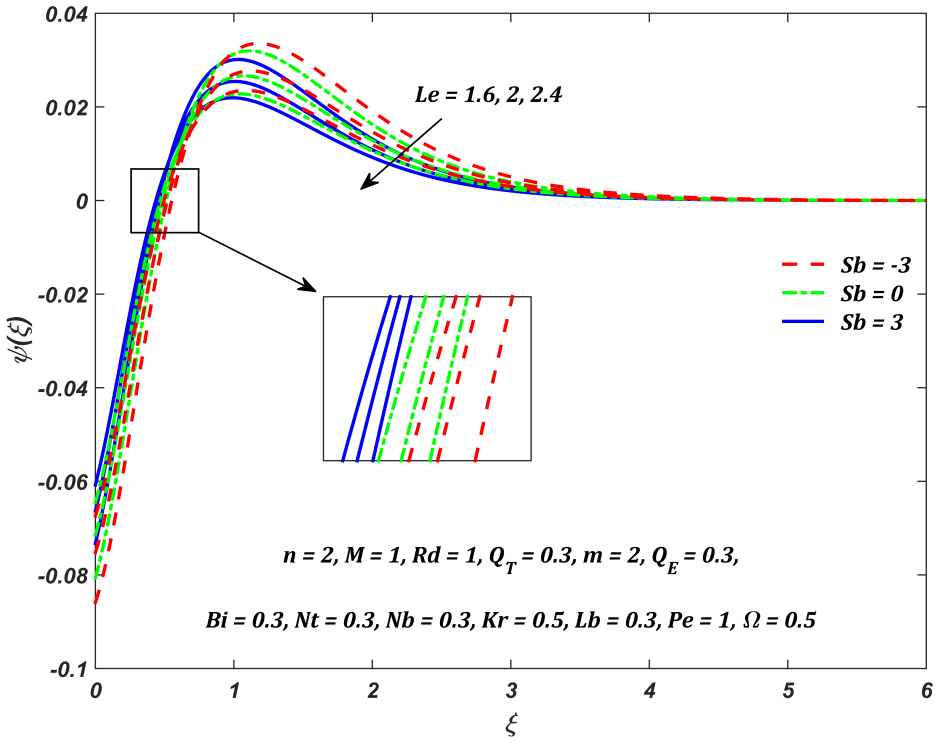

Figure 10.12: $\psi(\xi)$ for distinct Le values

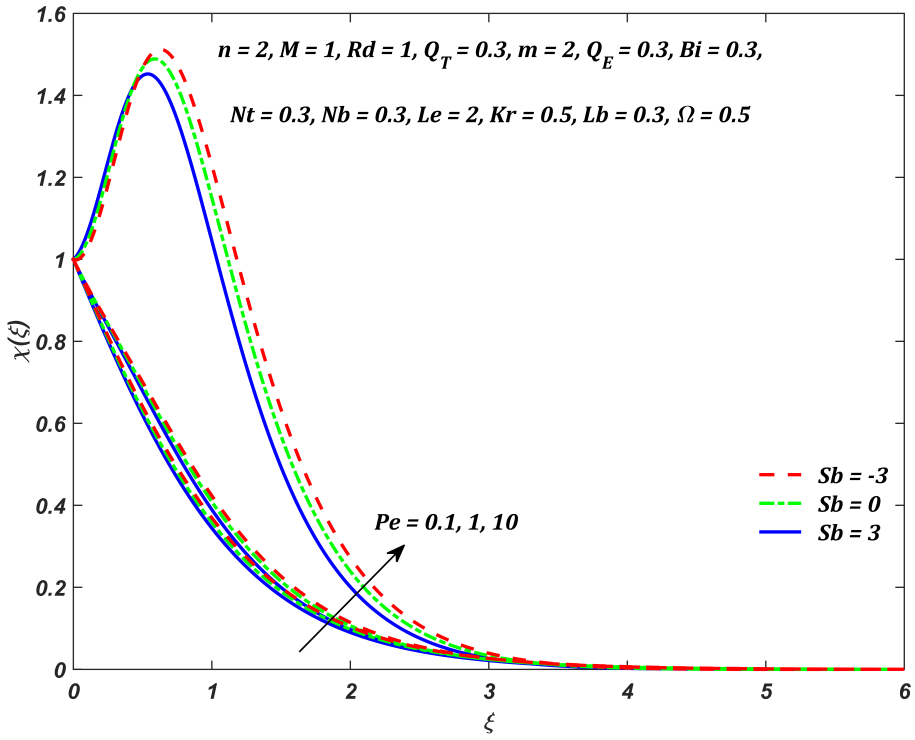

Figure 10.13: $\chi(\xi)$ for distinct Pe values

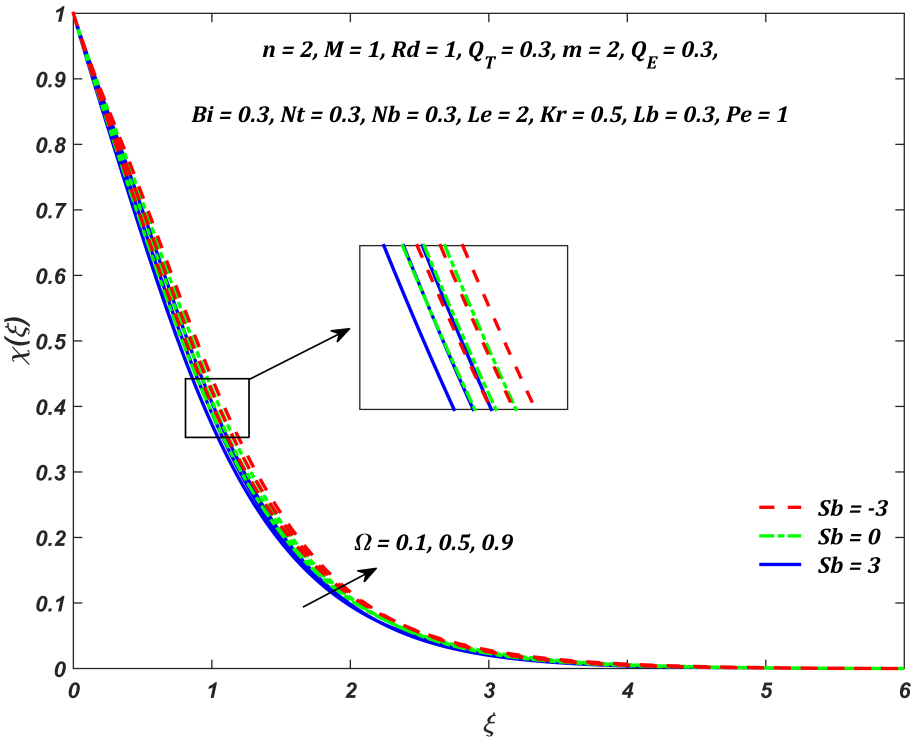

Figure 10.14: $\chi(\xi)$ for distinct Ω values

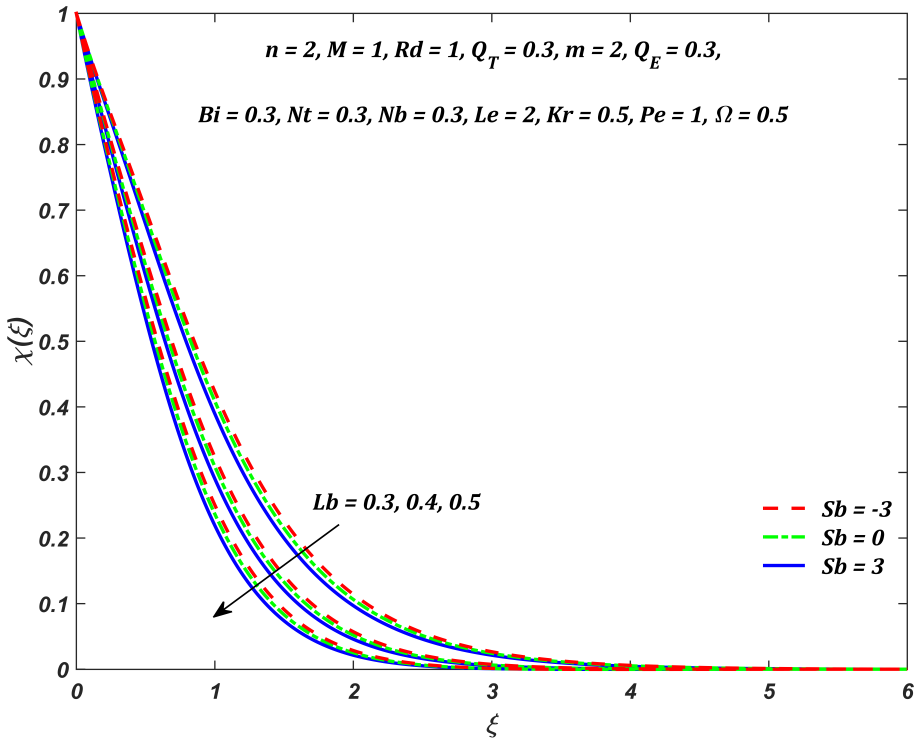

Figure 10.15: $\chi\,(\xi)$ for distinct Lb values

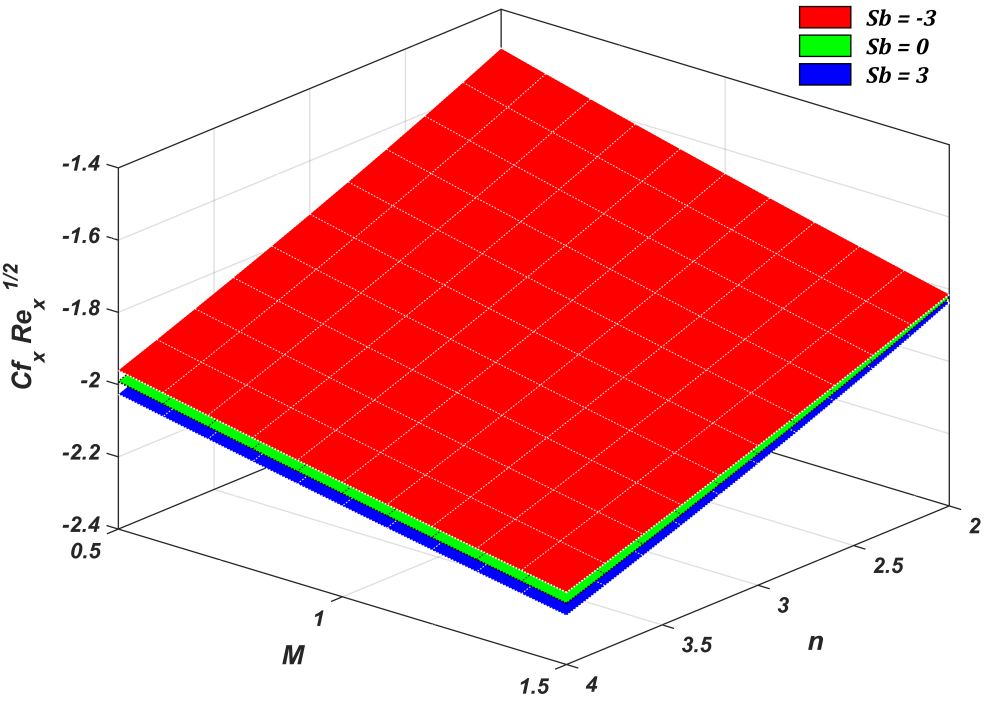

Figure 10.16: Simultaneous impact of M and n on $Cf_x\ Re_x^{1/2}$

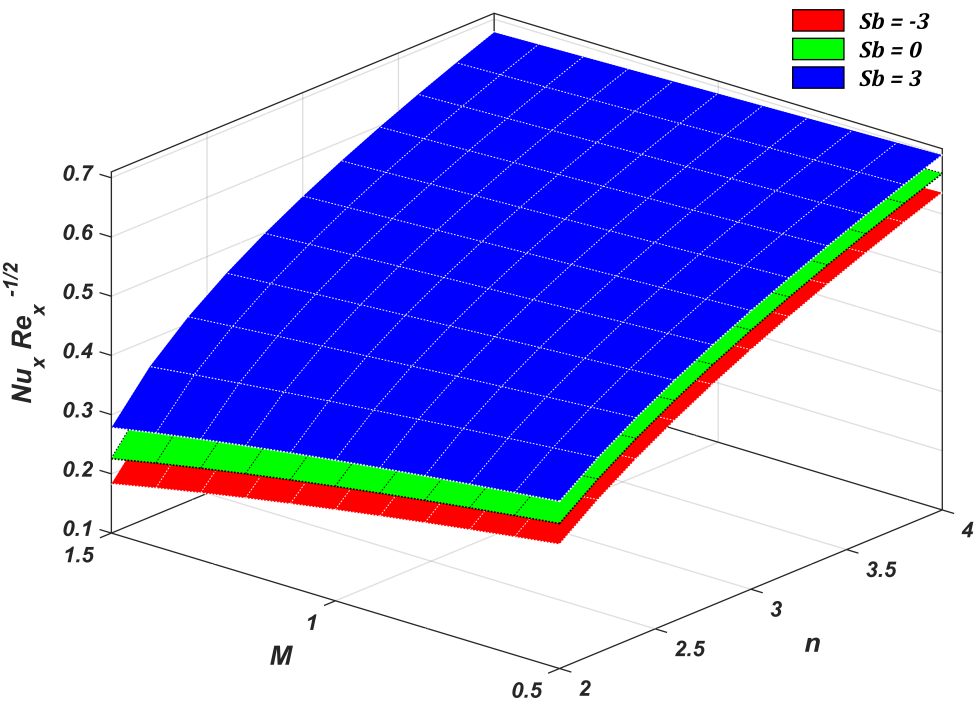

Figure 10.17: Simultaneous impact of M and n on $Nu_x\ Re_x^{-1/2}$

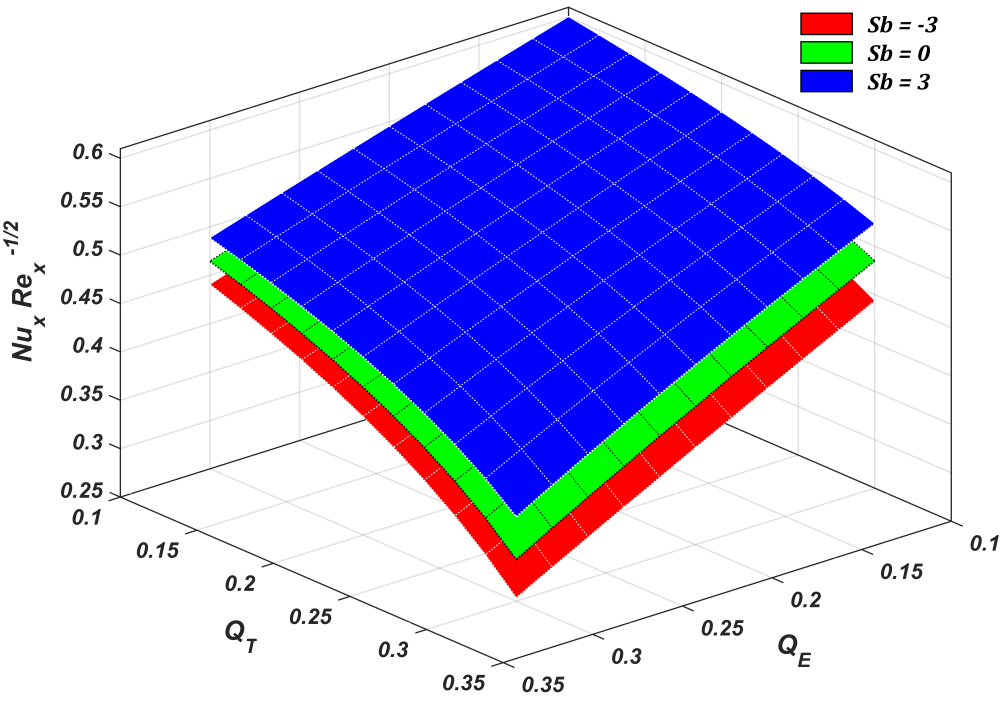

Figure 10.18: Simultaneous impact of Q_T and Q_E on $Nu_x\ Re_x^{-1/2}$

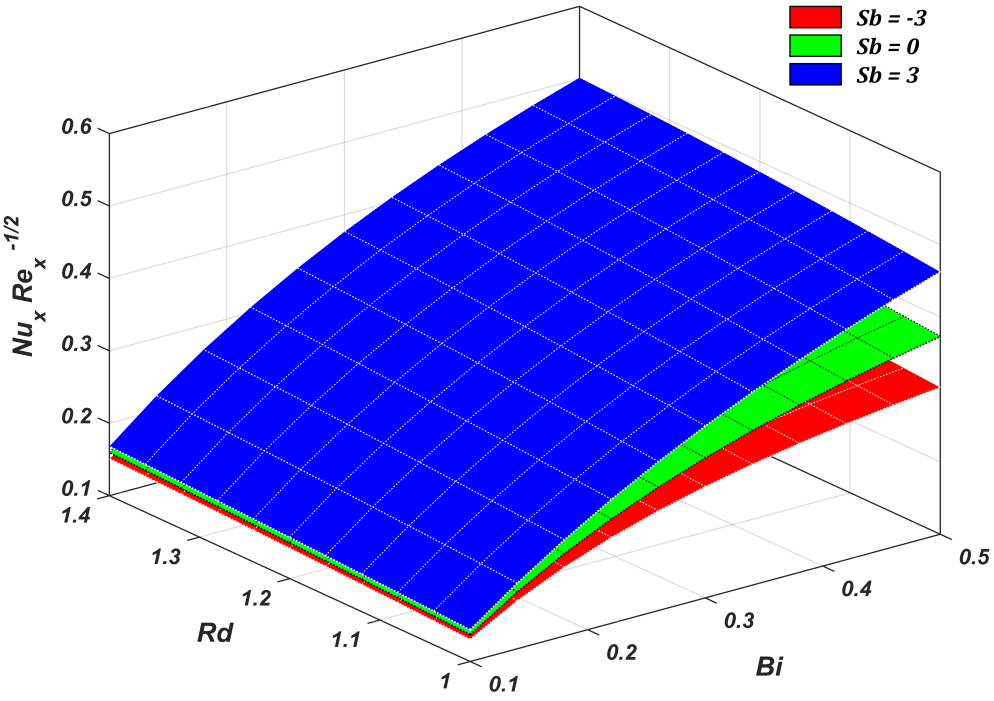

Figure 10.19: Simultaneous impact of Rd and Bi on $Nu_x\ Re_x^{-1/2}$

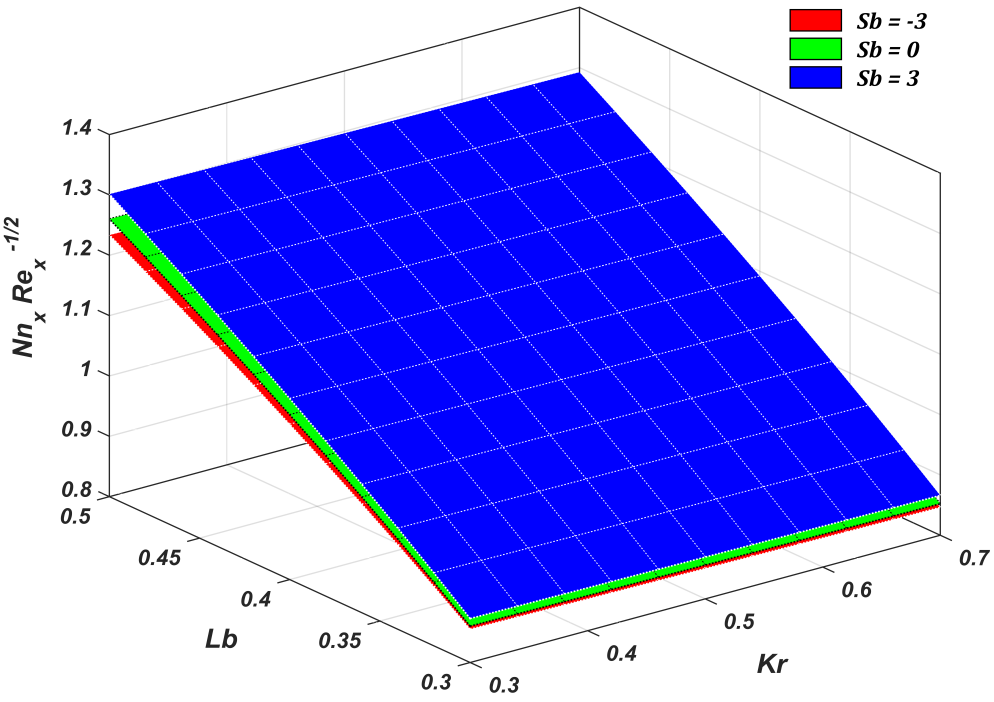

Figure 10.20: Simultaneous impact of Lb and Kr on $Nn_x\ Re_x^{-1/2}$

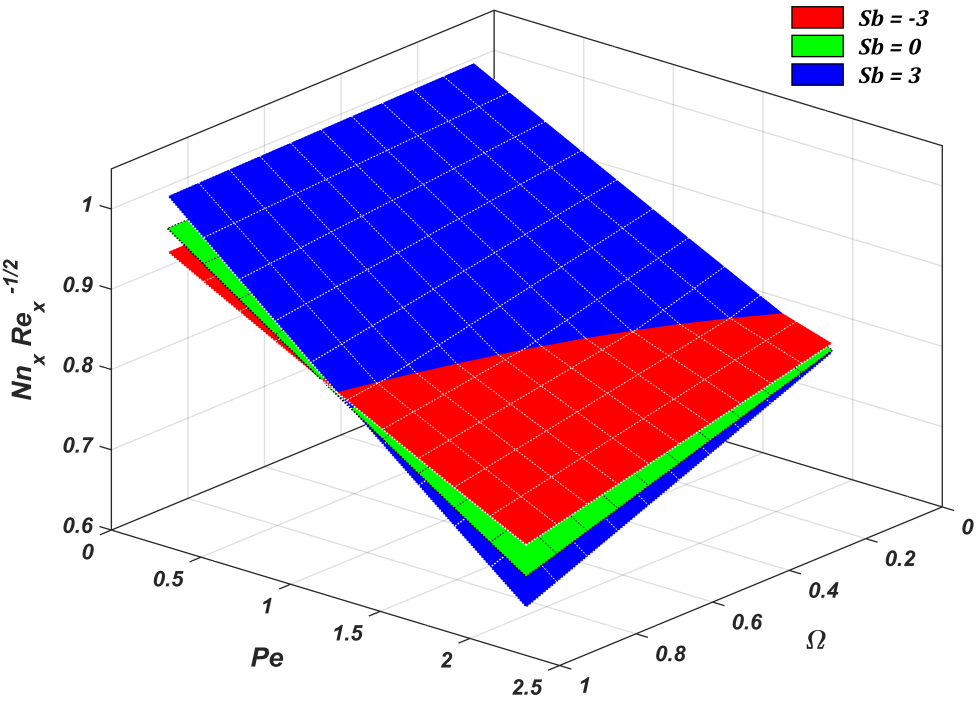

Figure 10.21: Simultaneous impact of Pe and Ω on $Nn_x\ Re_x^{-1/2}$

The increasing nature of $\chi(\xi)$ due to augmenting Pe (bioconvection Peclet number) values is illustrated in Figure 10.13. Pe is the ratio of advective transfer rate to the diffusive transport rate. Physically, an increase in Pe attracts microoraganisms near to the boundary and hence escalates the wall motile microbial flux. Figure 10.14 bespeaks the deviation in $\chi(\xi)$ with respect to Ω (microorganism concentration difference parameter). It can be perceived that $\chi(\xi)$ improves as Ω value is increased. Augmentation in Lb (bioconvection Lewis number) lowers the microorganism diffusivity that prompts a decrease in the microbial concentration profile (see Figure 10.15).

The simultaneous effect of effectual parameters on the physical quantities is presented using three-dimensional surface plots (see Figures 10.16 - 10.21). The impact of M and n on $Cf_x\ Re_x^{1/2}$ (local drag coefficient) is elucidated in Figure 10.16. It is observed that $Cf_x\ Re_x{}^{\frac{1}{2}}$ is a decreasing function of M, n, and Sb. Biologically, drag coefficient is directly proportional to the interaction between the fluid and the surface, which plays a crucial role in biomedical imaging and targeted drug delivery.

From Figures 10.17 - 10.19, it is seen that n, Sb, Rd and Bi promotes

$Nu_x\ Re_x^{-1/2}$ (local heat transfer rate) whereas $Q_E,\ Q_T$, and M demotes $Nu_x\ Re_x^{-1/2}$. Figures 10.20 and 10.21 explain the impact of $Lb,\ Kr,\ Pe$ and Ω on $Nn_x\ Re_x^{-1/2}$ (local motile microorganism density number). It is observed that Lb has a positive effect on $Nn_x\ Re_x^{-1/2}$ whereas $Kr,\ Pe$, and Ω have a negative effect on $Nn_x\ Re_x^{-1/2}$.

10.5 Statistical Frame

10.5.1 Response Surface Methodology (RSM)

The optimized heat transport level and interactive relationship of the chosen influential parameters on the response variable are evaluated with the aid of the robust statistical technique named RSM. The Stefan blowing parameter ($-3 \leq Sb \leq 3$), the magnetic field parameter ($0.8 \leq M \leq 1.2$) the Biot number($0.2 \leq Bi \leq 0.4$) are chosen as the independent variables and the local heat transfer rate $\left(Nu_x\ Re_x^{-1/2}\right)$ is chosen as the dependent (response) variable. The levels of the independent variables are given in Table 10.2.

The experimental runs have been designed using the face-centered central composite design (CCD). The general quadratic model (including linear, quadratic, and interaction terms) for the response variable is given by:

$$\text{Response} = t_1 + t_2\ A + t_3\ B + t_4\ C + t_5\ A^2 + t_6\ B^2 + t_7\ C^2 + t_8\ AB + t_9 BC + t_{10}\ AC$$

where $t_s\ \ (s = 1\ to\ 10)$ represents the regression coefficients. The experimental design and the response for the 20 runs according to CCD are given in Table 10.3.

Table 10.2: Effectual parameter levels

Parameter	Symbol	Levels		
		-1 (low)	**0 (medium)**	**1 (high)**
Sb	A	-3	0	3
M	B	0.8	1	1.2
Bi	C	0.2	0.3	0.4

The fitted quadratic model for local heat transfer rate with significant terms (in coded form) is given by:

$$Nu_x\ Re_x^{-1/2} = 0.293036 + 0.042015\ A - 0.022261\ B + 0.056708\ C + 0.002502\ A^2 - 0.008696\ C^{\ 2} + 0.002051\ AB + 0.019377\ AC - 0.006122\ BC \qquad (10.5.1)$$

The ANOVA table (Table 10.4) explains the efficiency of the approximated model. A parameter is asserted to be significant if the corresponding p-value is less than 0.05 and the corresponding F-value is greater than 1. It is noticed that the quadratic term in M is not significant and hence the term is deleted from the model. The coefficient of determination (R^2) for the model is estimated to be 99.98% which also boosts the model accuracy. The reliability and accuracy of the estimated models are further elucidated using the residual plots (see Figure 10.22). From Figure 10.22 (normal probability plot), it is perceived that all the data points are roughly distributed along the straight line and the residual histogram is roughly bell-shaped, implying the normal nature of the residuals. Further, a maximum error of 0.002 can be noted from the fitted versus residual plot which also accounts to the correctness of the model.

From Equation (10.5.1), it can be inferred that Sb and Bi increase the heat transfer rate and M decreases the heat transfer rate. The concurrent interaction of two parameters on the heat transfer rate by fixing the third parameter at the medium level is delineated using contour and surface plots (see Figures 10.23 and 10.24). From Figures 10.23 and 10.24, it is evident that maximum heat transfer rate is observed for lower values of M and higher values of Sb and Bi. It is also worth mentioning that a perfect agreement is observed between the statistical and numerical results.

The optimized heat transport rate is estimated by achieving maximum desirability value via the RSM model. The optimum level of $Nu_x\ Re_x^{-1/2}$ is estimated to be 0.4304 with desirability of 1. This optimum heat transport occurs when $Sb = 3,\ M = 0.8,\ Bi = 0.4$. Hence, the high levels of Sb and Bi along with the low level of M will make the heat transfer efficiency.

Table 10.3: Experimental design with actual and estimated response values

Run	Coded Values			Actual Values			$Nu_x\ Re_x^{-1/2}$	
	A	B	C	Sb	M	Bi	Actual	Estimated
1	-1	-1	-1	-3	0.8	0.2	0.2237733	0.2248078
2	1	-1	-1	3	0.8	0.2	0.2656219	0.2659882
3	-1	1	-1	-3	1.2	0.2	0.1885512	0.1884582
4	1	1	-1	3	1.2	0.2	0.2373189	0.2378418
5	-1	-1	1	-3	0.8	0.4	0.3122365	0.3117058
6	1	-1	1	3	0.8	0.4	0.430308	0.4303942
7	-1	1	1	-3	1.2	0.4	0.2512449	0.2508682
8	1	1	1	3	1.2	0.4	0.3788019	0.3777598
9	-1	0	0	-3	1	0.3	0.2534004	0.2535600
10	1	0	0	3	1	0.3	0.3373035	0.3375960
11	0	-1	0	0	0.8	0.3	0.3152371	0.3144180
12	0	1	0	0	1.2	0.3	0.2686524	0.2699260
13	0	0	-1	0	1	0.2	0.2292774	0.2276760
14	0	0	1	0	1	0.4	0.3390302	0.3410840
15	0	0	0	0	1	0.3	0.2931598	0.2930760
16	0	0	0	0	1	0.3	0.2931598	0.2930760
17	0	0	0	0	1	0.3	0.2931598	0.2930760
18	0	0	0	0	1	0.3	0.2931598	0.2930760
19	0	0	0	0	1	0.3	0.2931598	0.2930760
20	0	0	0	0	1	0.3	0.2931598	0.2930760

Table 10.4: ANOVA table and regression coefficients

Source	Deg. of freedom	Adj. sum of squares	Adj. mean squares	Regression Coefficient	F-Value	p-Value
Model	9	0.058419	0.006491		5322.35	< 0.0001
Linear	3	0.054766	0.018255		14968.42	< 0.0001
Sb	1	0.017652	0.017652	-0.008789	14474.15	< 0.0001
M	1	0.004955	0.004955	0.0258	4063.2	< 0.0001
Bi	1	0.032158	0.032158	1.3949	26367.91	< 0.0001
Square	3	0.000317	0.000106		86.55	< 0.0001
$Sb * Sb$	1	0.000017	0.000017	0.000278	14.11	0.004
$M * M$	1	0.000002	0.000002	-0.0226	1.85	**0.204**
$Bi * Bi$	1	0.000208	0.000208	-0.8696	170.53	< 0.0001
2-Way Interaction	3	0.003337	0.001112		912.07	< 0.0001
$Sb * M$	1	0.000034	0.000034	0.003418	27.58	< 0.0001
$Sb * Bi$	1	0.003004	0.003004	0.06459	2462.81	< 0.0001
$M * Bi$	1	0.0003	0.0003	-0.3061	245.81	< 0.0001
Constant				0.0415		
Error	10	0.000012	0.000001			
Lack-of-Fit	5	0.000012	0.000002		*	*
Pure Error	5	0	0			
Total	19	0.058432				
$R^2 = 99.98\%$				Adjusted $R^2 = 99.96\%$		

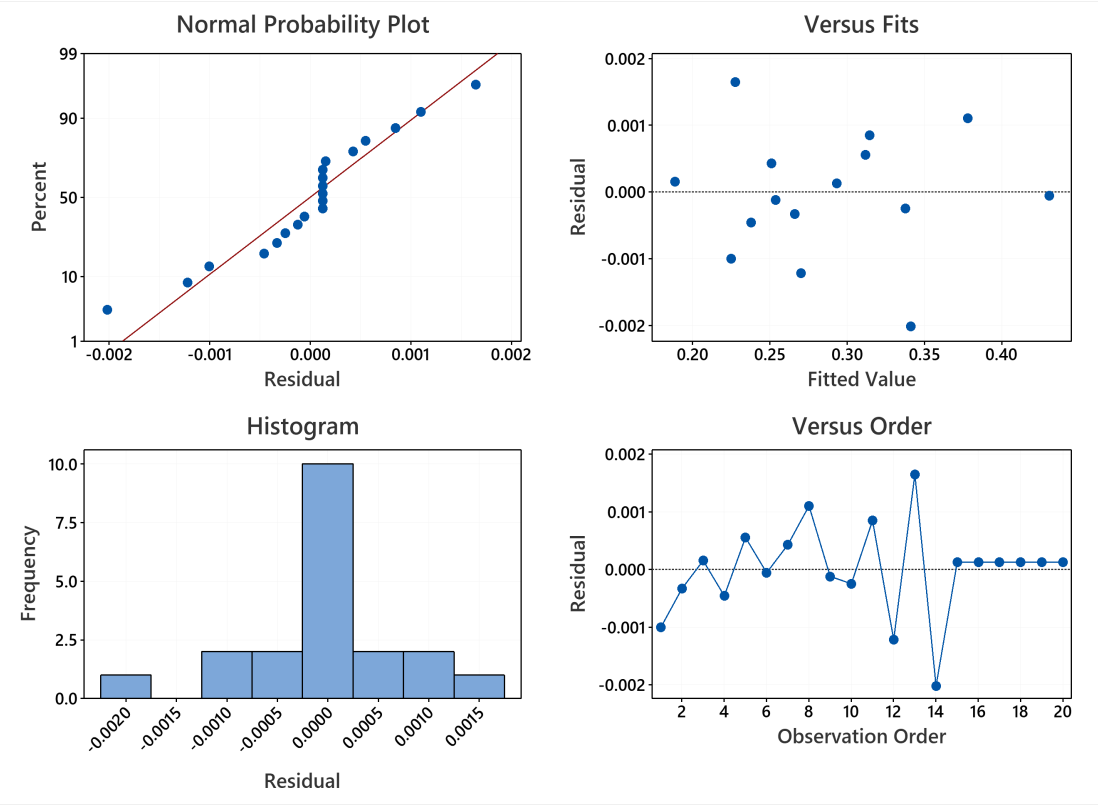

Figure 10.22: Residual plots

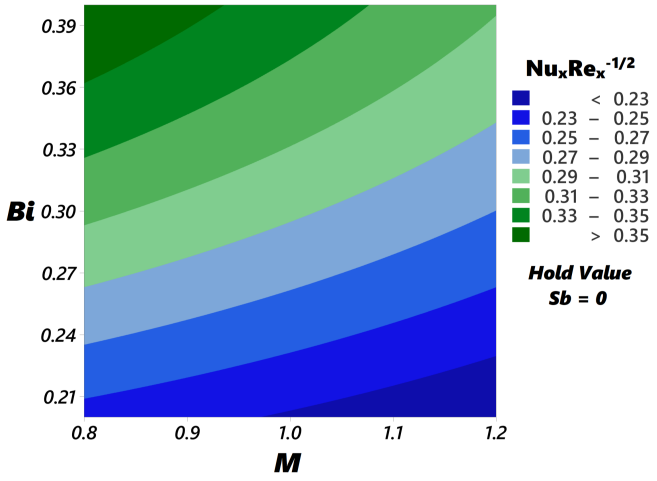

(a)

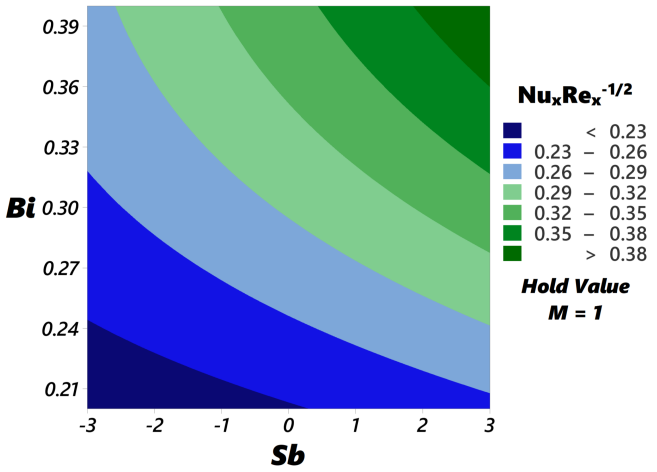

(b)

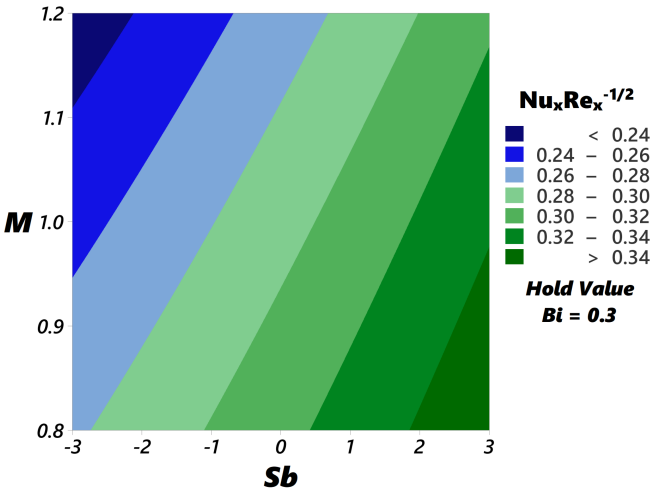

(c)

Figure 10.23: Contour plots for on $Nu_x\ Re_x^{-1/2}$

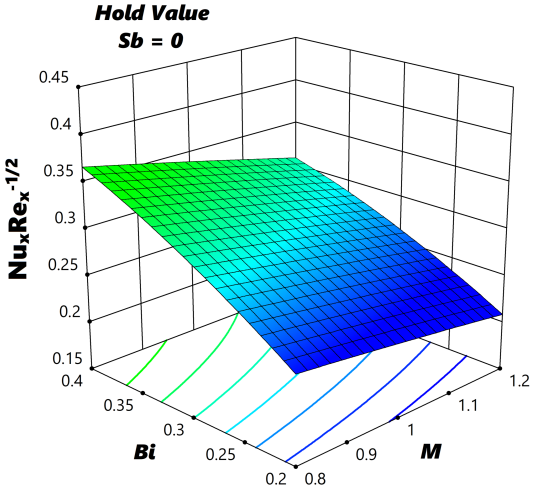

(a)

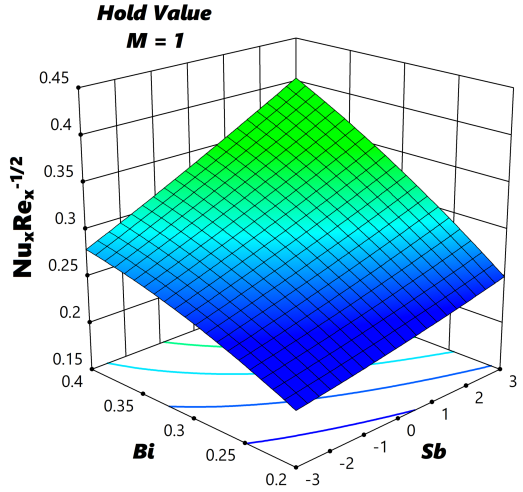

(b)

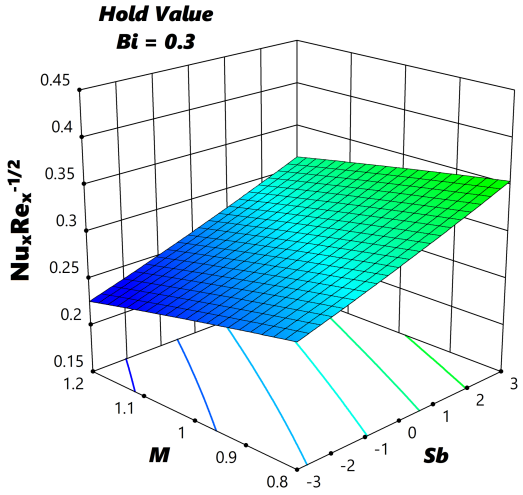

(c)

Figure 10.24: Surface plots for on $Nu_x\ Re_x^{-1/2}$

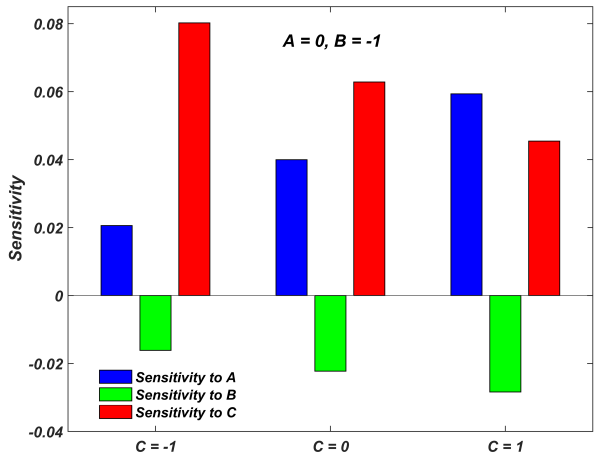

(a)

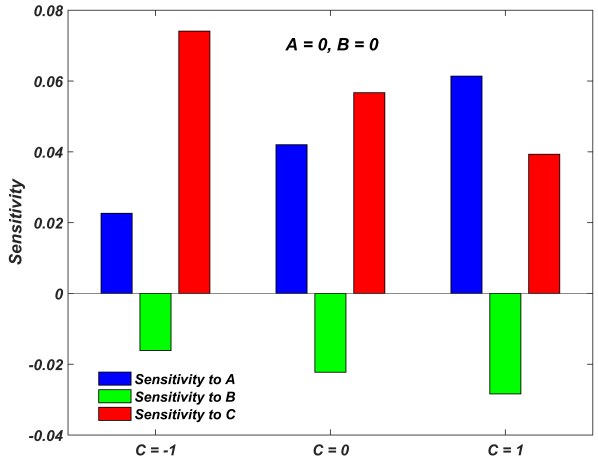

(b)

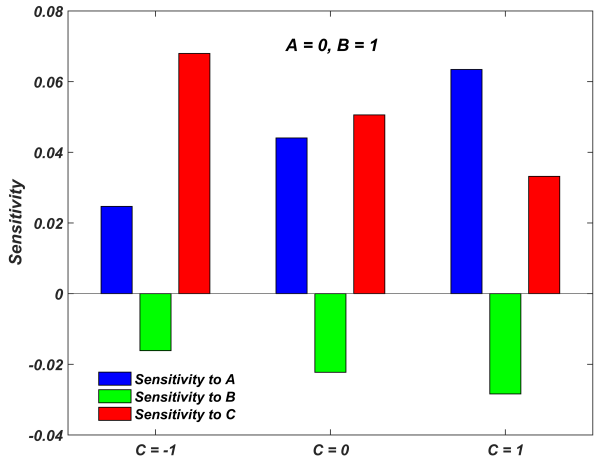

(c)

Figure 10.25: Bar charts showcasing the sensitivity of on $Nu_x\ Re_x^{-1/2}$

10.5.2 Sensitivity Analysis

Sensitivity quantifies the degree of change in the response variable concerning the independent variables. The partial derivatives of the fitted quadratic model (in coded form) with respect to the independent variables are termed sensitivity functions. The sensitivity functions of $Nu_x\ Re_x)^{-1/2}$ are given by:

$$\frac{\partial\left(Nu_x\ Re_x^{-1/2}\right)}{\partial A} = 0.042015 + 0.005004A + 0.002051B + 0.019377C$$

$$\frac{\partial\left(Nu_x\ Re_x^{-1/2}\right)}{\partial B} = -0.022261 + 0.002051A - 0.006122C$$

$$\frac{\partial\left(Nu_x\ Re_x^{-1/2}\right)}{\partial C} = 0.056708 + 0.019377A - 0.006122B - 0.017392C$$

Table 10.5: Sensitivity of $Nu_x\ Re_x^{-1/2}$ when $A = 0$

B	**C**	**Sensitivity** $\frac{\partial\left(\mathbf{Nu_x\ Re_x^{-1/2}}\right)}{\partial \mathbf{A}}$	$\frac{\partial\left(\mathbf{Nu_x\ Re_x^{-1/2}}\right)}{\partial \mathbf{B}}$	$\frac{\partial\left(\mathbf{Nu_x\ Re_x^{-1/2}}\right)}{\partial \mathbf{C}}$
	-1	0.020587	-0.016139	0.080222
-1	0	0.039964	-0.022261	0.062830
	1	0.059341	-0.028383	0.045438
	-1	0.022638	-0.016139	0.074100
0	0	0.042015	-0.022261	0.056708
	1	0.061392	-0.028383	0.039316
	-1	0.024689	-0.016139	0.067978
1	0	0.044066	-0.022261	0.050586
	1	0.063443	-0.028383	0.033194

Table 10.5 bespeaks the sensitivity of $Nu_x\ Re_x^{-1/2}$ generated by keeping the Stefan blowing parameter at the mid-level ($A = 0$). The nature of the correlation between

$Nu_x\ Re_x^{-1/2}$ and the effectual parameters revealed by the sign (positive or negative) of sensitivity, while the intensity of this correlation is measured using the magnitude of sensitivity. Here, Sb and Bi exhibit positive sensitivity and M exhibits a negative sensitivity on $Nu_x\ Re_x^{-1/2}$ which is also in synchronization with the observed numerical results.

Figure 10.25 visualizes the sensitivity of $Nu_x\ Re_x^{-1/2}$ with the aid of bar charts. In Figure 10.25 (a), when M is at the low level ($B = -1$), the sensitivity of $Nu_x\ Re_x^{-1/2}$ towards Sb and Bi is positive whereas the sensitivity of $Nu_x\ Re_x^{-1/2}$ towards M is negative. Further, it is observed that the negative sensitivity of $Nu_x\ Re_x^{-1/2}$ toward M and the positive sensitivity of $Nu_x\ Re_x^{-\frac{1}{2}}$ toward Sb gets intensified whereas the positive sensitivity of $Nu_x\ Re_x^{-1/2}$ descends with Bi, when Bi is augmented from low to high level. Identical conclusions can be drawn from Figure 10.25 (b) and Figure 10.25 (c). It is also noted that $Nu_x\ Re_x^{-1/2}$ is least sensitive to the changes in M at all levels.

10.6 Conclusion

Owing to applications in theranostics and photothermal therapy for melanoma skin cancer, the bioconvective MHD nanomaterial flow over a nonlinearly lengthened surface is analyzed. The flow has been mathematically modelled by considering the Buongiorno model and realistic boundary conditions (like Stefan blowing, passive control of the nanoparticles, and Newtonian boundary constraint). The influence of effectual parameters on the flow profiles has been numerically investigated using the Bulirsch-Stoer algorithm combined with the shooting technique. Further, the influence of Stefan blowing parameter ($-3 \leq Sb \leq 3$), the magnetic field parameter ($0.8 \leq M \leq 1.2$) the Biot number($0.2 \leq Bi \leq 0.4$) on the heat transfer rate has been scrutinized utilizing the RSM and sensitivity analysis. The major conclusions from the present study are:

- Augmenting Stefan blowing parameter curtails the velocity and nanomaterial temperature profiles.

- The magnetic field parameter exhibits a negative impact on the velocity profile which helps in improving the biomedical imaging capabilities by manipulating the transference of nanomaterial to the preferred location.

- Ascending Biot number intensifies the nanomaterial temperature that serves a crucial role in the termination of cancerous cells or tumors.
- The chemical reaction parameter has a destructive effect on the nanoparticle volume fraction that contributes towards improved biomedical imaging and medication.
- The maximum drag coefficient is experienced for lower values of the magnetic field parameter and Stefan blowing parameter.
- The heat transfer rate is an increasing function of the Stefan blowing parameter and Biot number.
- The heat transfer rate is least sensitive to the magnetic field parameter.
- Increasing the intensity of the chemical reaction decreases the motile microorganism density number.
- The optimum level of heat transport is estimated to be 0.4304 which occurs when Stefan blowing and Biot number are maintained at the high levels and magnetic field is kept at the low level.

Appendix I: Non-dimensional qunatities

$Lb = \dfrac{\alpha}{D_m}$	Bioconvection Lewis number
$Nt = \dfrac{\tau\ D_T\ (T_f - T_\infty)}{T_\infty\ \vartheta}$	Thermophoresis parameter
$Kr = \dfrac{k_r}{a}$	Chemical reaction parameter
$Bi = \dfrac{h_f}{k}\sqrt{\dfrac{2\vartheta}{a\,(n+1)}}$	Biot number
$Pe = \dfrac{bW_c}{D_m}$	Bioconvection Peclet number
$Nb = \dfrac{\tau D_B \mathcal{C}_\infty}{\vartheta}$	Brownian motion parameter
$Q_E = \dfrac{Q_e}{a\rho C_p}$	Exponential space-based heat source parameter
$Le = \dfrac{\alpha}{D_B}$	Lewis number
$M = \dfrac{\sigma_e \mathcal{B}_0^2}{a\rho}$	Magnetic field parameter
$Sb = \dfrac{\mathcal{C}_\infty}{1 - \mathcal{C}_w}$	Stefan blowing parameter
$Q_T = \dfrac{Q_t}{a\rho C_p}$	Linear heat source parameter
$\Omega = \dfrac{N_\infty}{N_w - N_\infty}$	Microorganism concentration difference parameter
$Pr_f = \dfrac{\vartheta}{\alpha}$	Prandtl number
$Rd = \dfrac{4\ \sigma^* T_\infty^3}{k^* k}$	Thermal radiation parameter

Appendix II: Nomenclature

a, n, m	Positive constants	N_w	Wall microbial concentration
u, v	Velocity components	$\mathcal{B}_0$	Strength of magnetic field
u_w	Stretching velocity	T_∞	Ambient temperature
T	Fluid temperature	$\mathcal{C}$	Nanoparticle volume fraction
x, y	Cartesian coordinates	h_f^*	Reaction rate constant
τ_w	Wall shear stress	Nu_x	Local Nusselt number
μ	Dynamic viscosity	$\mathcal{C}_\infty$	Ambient nanoparticle volume fraction
ρC_p	Heat capacity	Cf_x	Local drag coefficient
σ_e	Electrical conductivity	T_f	Convective fluid temperature
ξ	Similarity variable	D_B	Brownian diffusion coefficient
ϑ	Kinematic viscosity	D_T	Thermophoretic diffusion coefficient
k	Thermal conductivity	Q_t^*	Coefficient of thermal heat source
α	Thermal diffusivity	Q_e^*	Coefficient of exponential
A, B, C	Coded symbols		space-based heat source
ρ	Density	ω_i	Shooting variables i=1,2,3,4
μ	Dynamic viscosity	σ^*	Stefan- Boltzmann constant
Nn_x	Local motile density	τ	Effective heat capacity ratio
q_w	Heat flux	k^*	Mean absorption coefficient
q_n	Microbial flux	D_m	Stefan- Boltzmann constant
b	Chemotaxis constant	N_∞	Microorganism diffusion coefficient
N	Microbial Concentration	$\mathcal{C}_w$	Wall nanoparticle volume fraction
q_r	Radiative heat flux	k^*	Mean absorption coefficient
k_r^*	Reaction rate constant	W_c	Maximum cell swimming speed

Chapter 11

Electro-magnetohydrodynamic Casson nanomaterial flow over a nonlinearly stretched surface *

11.1 Introduction

Casson fluid, proposed by Casson in 1959, is a shear thinning fluid that assumes infinite viscosity at zero shear-rate, and vice versa. Human blood, honey, tomato sauce, jelly, and concentrated fruit juices are a few examples that follow the Casson nanofluid model. Different nanoparticle shape and radius exhibit different thermal properties that are beneficial in industrial and biomedical fields. The relative movement of the fluid with the boundary is characterized with the aid of slip constraint. For its biomedical applicability, the dynamics of electro-magnetohydrodynamic flow of blood-gold nanomaterial over a nonlinearly stretching surface utilizing the Casson model has been elucidated numerically. The impact of second-order hydrodynamic-slip, nanoparticle radius, first-order thermal-slip, inter-particle spacing and non-uniform heat source are also accounted. The modeled flow equations are transmuted into a nonlinear system of first-order ODEs (with the aid of apposite similarity variables) which are then resolved numerically utilizing the finite-difference based *bvp*5*c* scheme. The current chapter finds its application in radiofrequency ablation, magnetic resonance imaging, cancer therapy, and targeted drug delivery. This numerical exploration makes an attempt in answering the following research questions:

- How does the administration of external electric-field affect the flow?

*Communicated in: Numerical Heat Transfer, Part B: Fundamentals (Taylor & Francis).

- What impact does the addition of gold nanoparticles with varying radius and inter-particle spacing have on Casson nanofluid flow?
- How does second-order hydrodynamic-slip constraint affect the flow?
- What effect does non-uniform heat source have on the thermal field?
- How does the physical quantities sequel to the changes in key parameters?

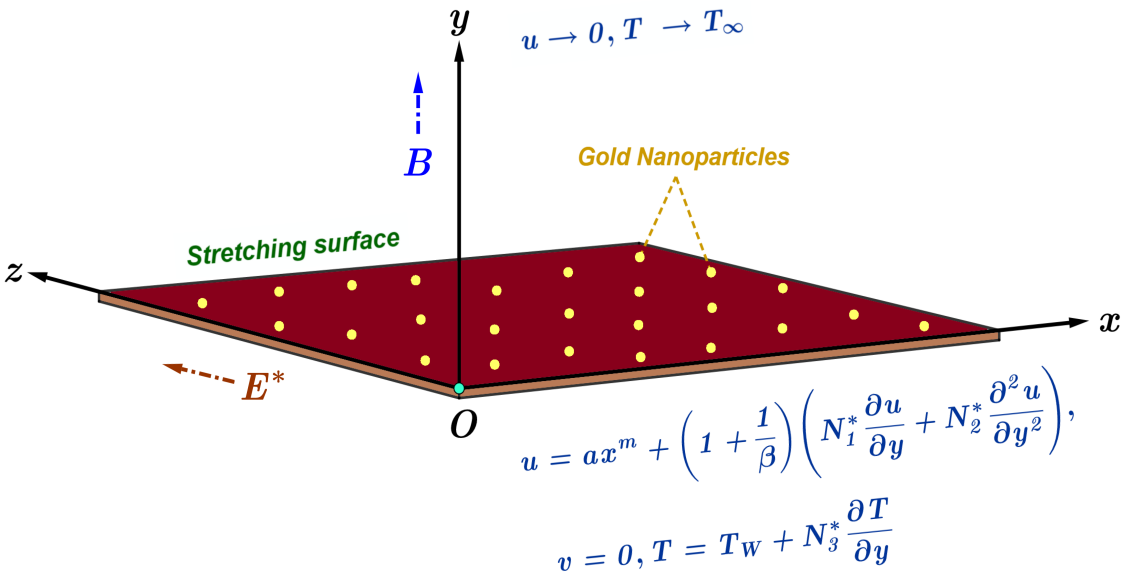

Figure 11.1: Geometrical Frame

11.2 Mathematical Frame

The two-dimensional steady electro-magnetohydrodynamic flow of blood-gold nanomaterial over a nonlinearly stretching surface (with velocity $u_w = ax^m$) utilizing the Casson model is considered. A magnetic-field of intensity $B = B_0\, x^{\frac{m-1}{2}}$ and an electric-field of intensity $E^* = E_0\, x^{\frac{m-1}{2}}$ are administered externally normal to the fluid flow (see Daniel et al., 2018). The impact of 2nd order hydrodynamic-slip, gold nanoparticles of different inter-particle spacing and radius, first order thermal-slip and non-uniform heat source (NHS) are also accounted. The geometrical scheme of the flow has been shown in Figure 11.1.

The governing equations modelled using the above assumptions are given by (see J. Raza, Farooq, Mebarek-Oudina, & Mahanthesh, 2019; Zhou et al., 2021; Fang & Aziz, 2010):

$$\frac{\partial u}{\partial x}+\frac{\partial v}{\partial y}=0 \tag{11.2.1}$$

$$u\frac{\partial u}{\partial x}+v\frac{\partial u}{\partial y}=\frac{\mu_{nf}}{\rho_{nf}}\left(1+\frac{1}{\beta}\right)\frac{\partial^2 u}{\partial y^2}+\frac{\sigma_{nf}}{\rho_{nf}}\left(E^*B-B^2u\right) \tag{11.2.2}$$

$$u\frac{\partial T}{\partial x}+v\frac{\partial T}{\partial y}=\frac{k_{nf}}{(\rho C_p)_{nf}}\frac{\partial^2 T}{\partial y^2}+\frac{q'''}{(\rho C_p)_{nf}} \tag{11.2.3}$$

subject to the boundary conditions (see Abdelmalek et al., 2020; J. Raza et al., 2019):

$$At\ y=0\ :\ u=ax^m+\left(1+\frac{1}{\beta}\right)\left(N_1^*\frac{\partial u}{\partial y}+N_2^*\frac{\partial^2 u}{\partial y^2}\right)\ ,\ v=0\ ,\ T=T_w+N_3^*\frac{\partial T}{\partial y}$$

$$As\ y\to\infty\ :\ u\to 0,\ T\to T_\infty$$

where $q'''=\frac{k_{nf}}{x\ \vartheta_{nf}}\left\{A^*\left(T_w-T_\infty\right)u+B^*\left(T-T_\infty\right)u_w\right\}$ with $A^*>0,\ B^*>0$ is the non-uniform heat source, $N_1^*\left(>0\right)=N_1x^{\frac{1-m}{2}}$ is the first order velocity-slip factor, $N_2^*\left(<0\right)=N_2\ x^{1-m}$ is the second order velocity-slip factor, and $N_3^*\left(>0\right)=N_3\ x^{\frac{1-m}{2}}$ is the first order thermal-slip factor.

Consider the following similarity transformations (see Mabood et al., 2015; Basir et al., 2021):

$$u=ax^m f\,'\left(\eta\right),\ v=-\sqrt{\frac{a\vartheta_f\left(m+1\right)}{2}}\ x^{\frac{m-1}{2}}\left(f\left(\eta\right)+\left(\frac{m-1}{m+1}\right)\eta\ f\,'\left(\eta\right)\right),$$

$$\eta=\sqrt{\frac{a\left(m+1\right)}{2\vartheta_f}}\ yx^{\frac{m-1}{2}},\ \theta\left(\eta\right)=\frac{T-T_\infty}{T_w-T_\infty}$$

Using the above defined similarity transformations, Equations (11.2.1) – (11.2.3) are converted into:

$$f'''=\frac{1}{1+\frac{1}{\beta}}\left\{\frac{A_2}{A_1}\left(\frac{2m}{m+1}\ (f'\ )^2-ff''\right)-\frac{A_3}{A_1}\left(\frac{2}{m+1}\right)M\left(E-f'\right)\right\} \tag{11.2.4}$$

$$\theta''=-\left\{\frac{A_5}{A_4}\ Pr\ f\ \theta'+\frac{A_2}{A_1}\left(\frac{2}{m+1}\right)\left(A^*\ f'+B^*\ \theta\right)\right\} \tag{11.2.5}$$

subject to the boundary conditions

$$f\left(0\right)=0,\ f'\left(0\right)=1+\left(1+\frac{1}{\beta}\right)\left(\sqrt{\frac{m+1}{2}}\ L_1\ f''\left(0\right)+\left(\frac{m+1}{2}\right)L_2\ f'''\left(0\right)\right),$$

$$\theta\left(0\right)=1+\sqrt{\frac{m+1}{2}}\ L_3\ \theta'\left(0\right),\ f'\left(\infty\right)\to 0,\ \theta\left(\infty\right)\to 0.$$

where the dimensionless parameters are given in appendix I.

The nanofluid models incorporated are (see Sun et al., 2022):

$$\text{Effective Dynamic Viscosity}\ :\ \frac{\mu_{nf}}{\mu_f}=1+2.5\ \phi+4.5\left\{\frac{1}{\left(\frac{h}{R_{np}}\right)\left(2+\frac{h}{R_{np}}\right)\left(1+\frac{h}{R_{np}}\right)^2}\right\}=A_1$$

$$\text{Effective Density}\ :\ \frac{\rho_{nf}}{\rho_f}=(1-\phi)+\phi\left(\frac{\rho_{np}}{\rho_f}\right)=A_2$$

$$\text{Effective Electrical Conductivity}\ :\ \frac{\sigma_{nf}}{\sigma_f}=1+\frac{3\left(\frac{\sigma_{np}}{\sigma_f}-1\right)\phi}{\left(\frac{\sigma_{np}}{\sigma_f}+2\right)-\left(\frac{\sigma_{np}}{\sigma_f}-1\right)\phi}=A_3$$

$$\text{Effective Thermal Conductivity}\ :\ \frac{k_{nf}}{k_f}=\frac{k_{np}+2k_f-2\phi\left(k_f-k_{np}\right)}{k_{np}+2k_f+\phi\left(k_f-k_{np}\right)}=A_4$$

$$\text{Effective Specific Heat}\ :\ \frac{(\rho C_P)_{nf}}{(\rho C_P)_f}=(1-\phi)+\phi\left(\frac{(\rho C_p)_{np}}{(\rho C_p)_f}\right)=A_5$$

The physical quantities are given by (see Daniel et al., 2018; J. Raza et al., 2019; Zhou et al., 2021):

$$\text{Local drag coefficient} \quad : \quad Cf_x = \frac{\tau_\omega}{\rho_f \ (u_w)^2} = \frac{\mu_{nf}}{\rho_f \ (u_w)^2} \ \left(1 + \frac{1}{\beta}\right) \ \left.\frac{\partial u}{\partial y}\right|_{y=0}$$

$$\Rightarrow \ Cf_x \ Re_x^{1/2} = A_1 \ \sqrt{\frac{m+1}{2}} \left(1 + \frac{1}{\beta}\right) f \ ''(0)$$

$$\text{Local Nusselt number} \quad : \quad Nu_x = \frac{x \ q_\omega}{k_f \ (T_w - T_\infty)} = \frac{-\ x \ k_{nf}}{k_f \ (T_w - T_\infty)} \ \left.\frac{\partial T}{\partial y}\right|_{y=0}$$

$$\Rightarrow \ Nu_x \ Re_x^{-1/2} = -A_4 \ \sqrt{\frac{m+1}{2}} \ \theta \ '(0).$$

where $Re_x = \frac{x u_w}{\vartheta_f}$ is the local Reynold's number.

11.3 Numerical Frame & Validation

The nonlinear ordinary differential equations given in Equations (11.2.4) − (11.2.5) are reduced to a system of first order ODEs by setting:

$$\Gamma_1 = f, \ \Gamma_2 = f \ ', \ \Gamma_3 = f \ '', \ \Gamma_4 = \theta, \ \Gamma_5 = \theta \ '$$

The reduced system of the first-order ODE is given by:

$\Gamma_1^{'} = \Gamma_2, \ \Gamma_2^{'} = \Gamma_3,$

$\Gamma_3^{'} = \frac{1}{\left(1+\frac{1}{\beta}\right)} \left\{ \left(\frac{A_2}{A_1}\right) \left(\frac{2m}{m+1}\right) (\Gamma_2)^2 - \left(\frac{A_2}{A_1}\right) \Gamma_1 \ \Gamma_3 - \left(\frac{A_3}{A_1}\right) \left(\frac{2}{m+1}\right) M \ (E - \Gamma_2) \right\},$

$\Gamma_4^{'} = \Gamma_5,$

$\Gamma_5^{'} = -\left\{ \left(\frac{A_5 \ Pr}{A_4}\right) \Gamma_1 \ \Gamma_5 + \left(\frac{A_2}{A_1}\right) \left(\frac{2}{m+1}\right) (A^* \ \Gamma_2 + B^* \ \Gamma_4) \right\}.$

with

$$\Gamma_1 (0) = 0, \ \Gamma_2 (0) = 1 + \left(1 + \tfrac{1}{\beta}\right) \left(\sqrt{\tfrac{m+1}{2}} \ L_1 \ \Gamma_3 (0) + \left(\tfrac{m+1}{2}\right) L_2 \ \Gamma_3^{'} (0) \right),$$

$$\Gamma_4 (0) = 1 + \sqrt{\tfrac{m+1}{2}} \ L_3 \ \Gamma_5 (0), \ \Gamma_2 (\infty) \to 0, \ \Gamma_4 (\infty) \to 0.$$

Table 11.1: Resemblance of $-\theta'(0)$ for ordinary fluid when $Pr_f = 1$

n	$-\theta'(\mathbf{0})$		
	Rana & Bhargava, 2012	**Mabood et al., 2015**	**Present Study**
0.2	0.6113	0.61131	0.6113101754
0.5	0.5967	0.59668	0.5966869638
1.5	0.5768	0.57686	0.5768695043
2	-	0.57245	0.5724552833
3	0.5672	0.56719	0.5671905106
4	-	0.56415	0.5641562432
10	0.5578	0.55783	0.5578319176

Table 11.2: Thermophysical properties of blood and gold

Property	**Blood (base fluid)**	**Gold (nanoparticle)**
$\boldsymbol{\rho}$	1050	19300
$\boldsymbol{C_p}$	3617	129
$\boldsymbol{k}$	0.52	318
$\boldsymbol{\sigma}$	1090	$4.1 * 10^6$

The boundary constraints at infinity are dimensioned to 4 since there is no substantial difference in the numerical outcomes on using higher values of the similarity variable, and the flow fields follow the boundary constraints asymptotically. $Pr = 21$, $\phi = 0.02$, $m = 2$, $M = A^* = B^* = L_1 = L_3 = 0.5$, $E = 0.05$, $\beta = 5$, $L_2 = -0.5$, and $h = R_{np} = 1$ have been chosen as the default values. The above system of 1st order ODEs is solved numerically with the aid of *bvp*5*c* scheme in MATLAB with an absolute error tolerance of 10^{-8}. The accuracy of the numerical scheme has been validated through a restrictive analysis with the previously published works of (Rana & Bhargava, 2012) and (Mabood et al., 2015) [see Table 11.1] and a notable covenant is noted.

11.4 Results & Discussion

The impact of pertinent parameters on the velocity profile ($f'(\eta)$) and the temperature profile ($\theta(\eta)$) has been illustrated through Figures 11.2 - 11.16. The thermophysical properties of blood and gold nanoparticle are mentioned in Table 11.2.

The reduction in $f'(\eta)$ with respect to the augmenting values of m has been depicted in Figure 11.2. The introduction of M activates the generation of Lorentz force that reduces $f'(\eta)$ (see Figure 11.3). A reverse nature is observed for $f'(\eta)$ with the introduction of E (see Figure 11.4). Figure 11.5 elucidates the negative impact of β on the nanofluid velocity. The addition of gold-nanoparticles increases the fluid's viscosity and thereby reduces $f'(\eta)$ (see Figure 11.6). The negative impact of inter-particle spacing of gold-nanoparticles on $f'(\eta)$ has been illustrated via Figure 11.7. An increase in the radius of gold-nanoparticles reduces the nanofluid viscosity and thereby augments $f'(\eta)$ (see Figure 11.8). The destructive effect of 1st order velocity-slip parameter and the constructive effect of 2nd order velocity-slip parameter on $f'(\eta)$ have been depicted using Figure 11.9 and Figure 11.10, respectively.

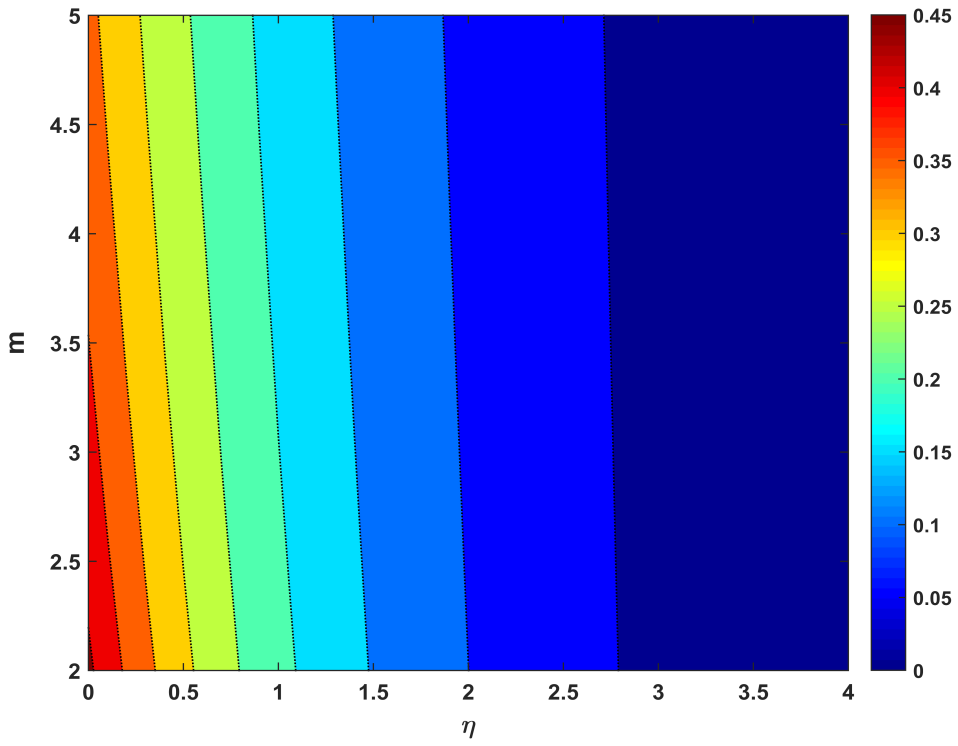

Figure 11.2: Deviations in $f'(\eta)$ with m

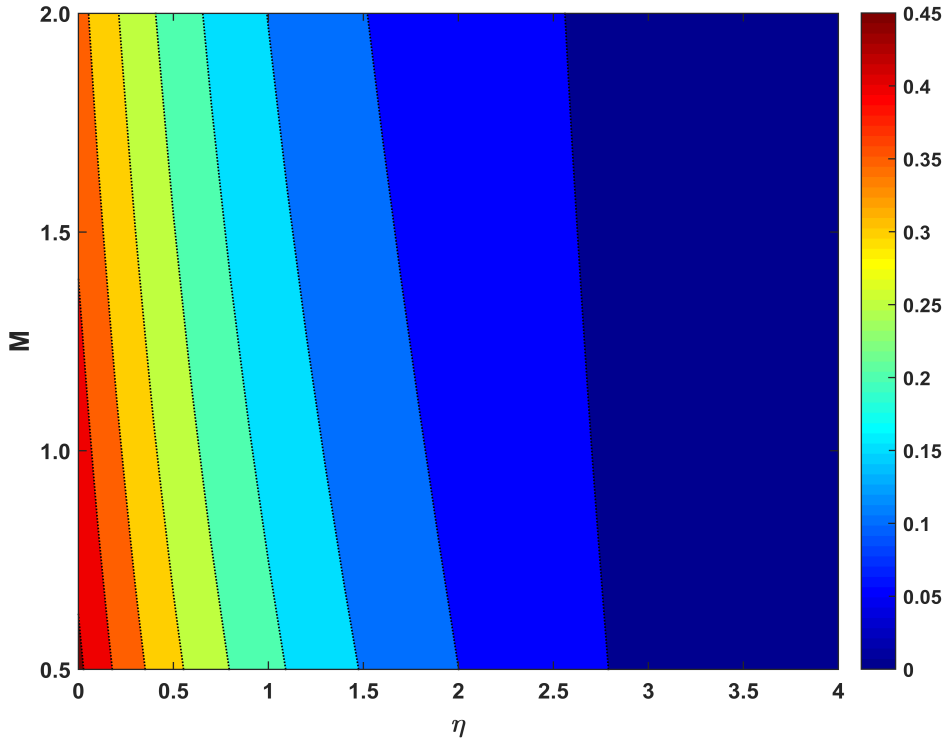

Figure 11.3: Deviations in $f'(\eta)$ with M

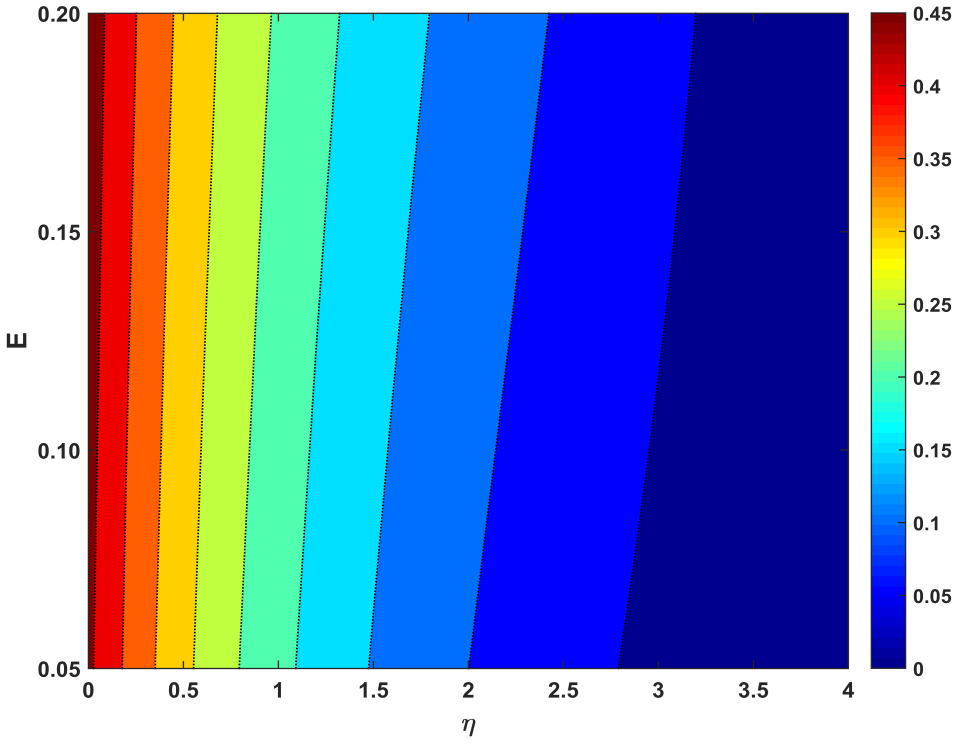

Figure 11.4: Deviations in $f'(\eta)$ with E

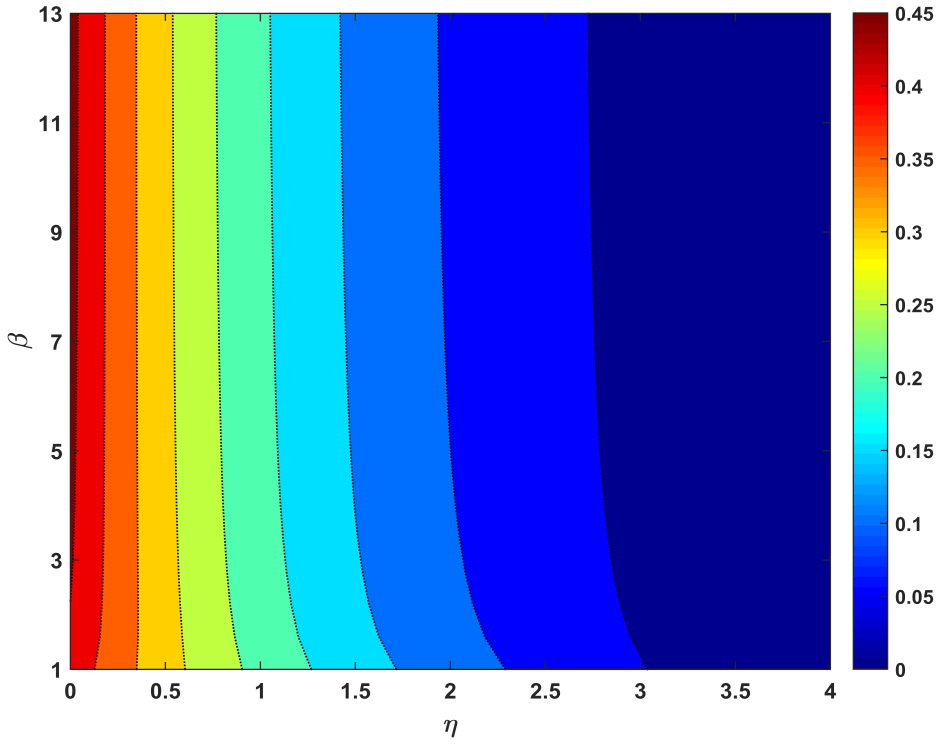

Figure 11.5: Deviations in $f'(\eta)$ with β

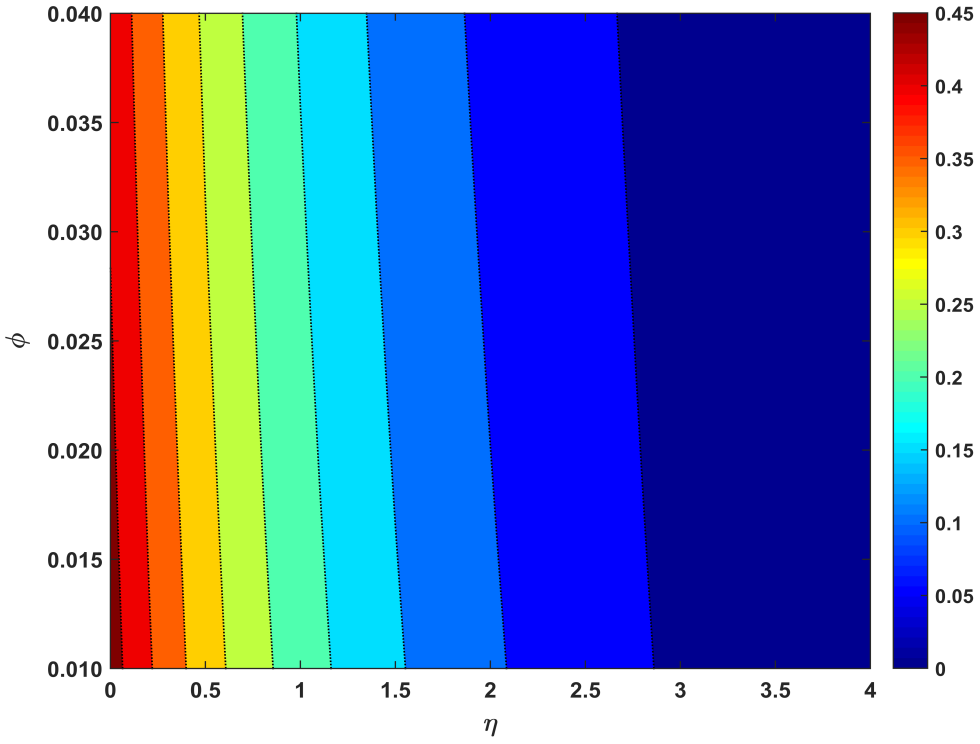

Figure 11.6: Deviations in $f'(\eta)$ with ϕ

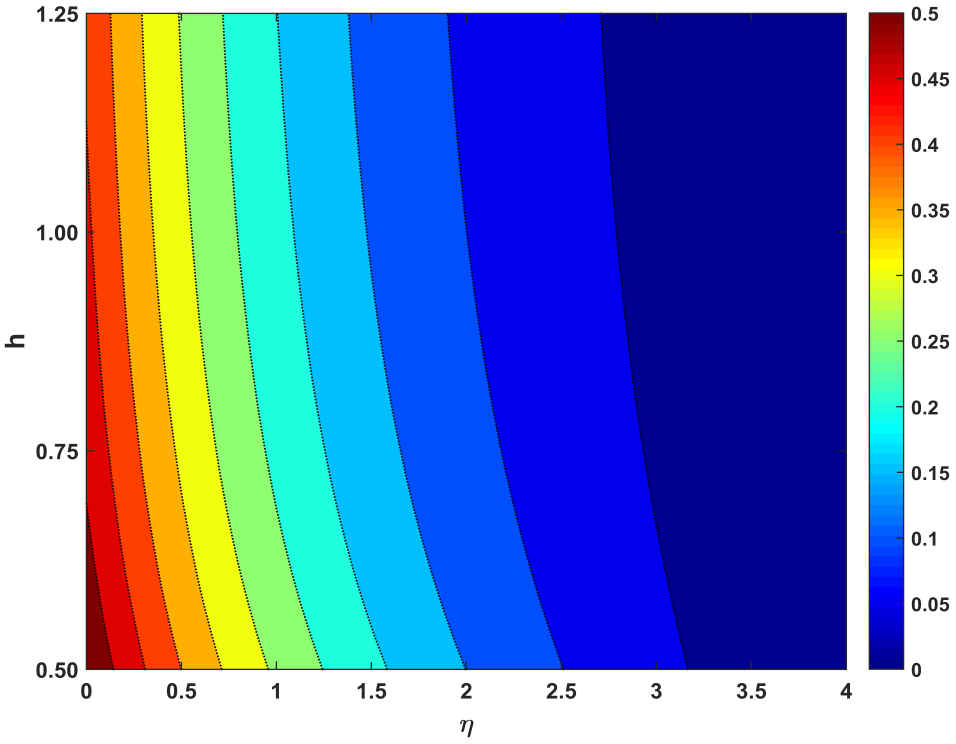

Figure 11.7: Deviations in $f'(\eta)$ with h

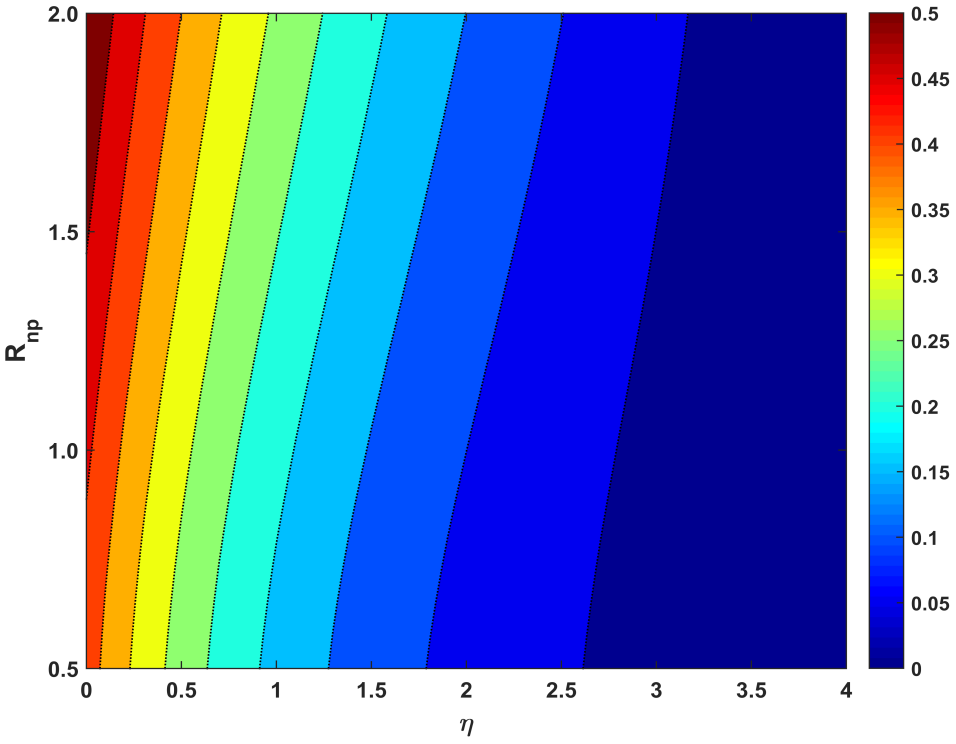

Figure 11.8: Deviations in $f'(\eta)$ with R_{np}

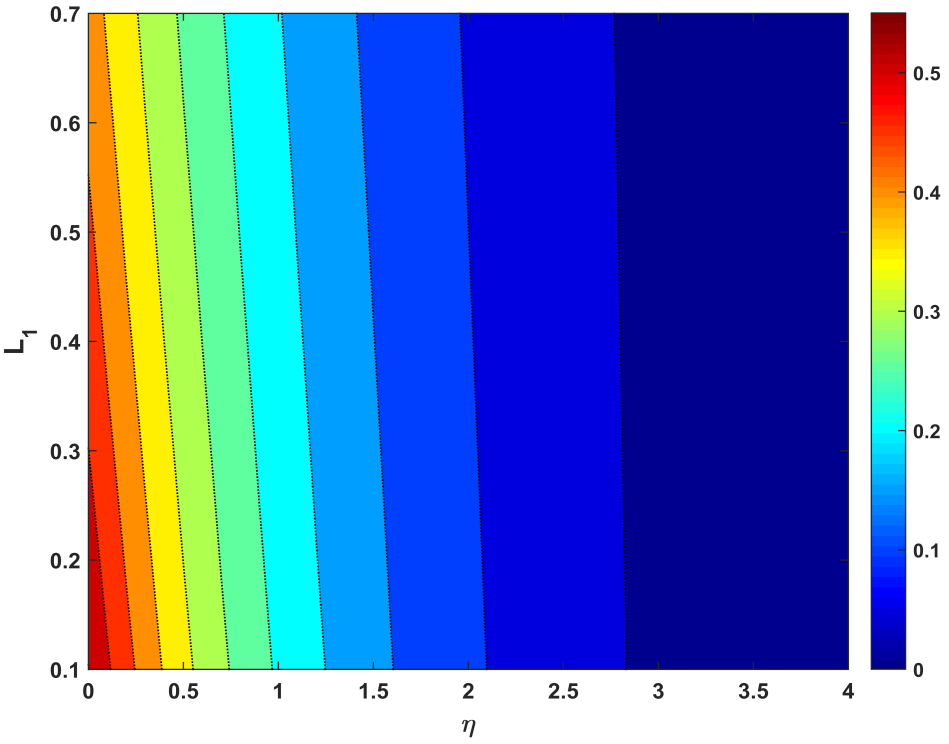

Figure 11.9: Deviations in $f'(\eta)$ with L_1

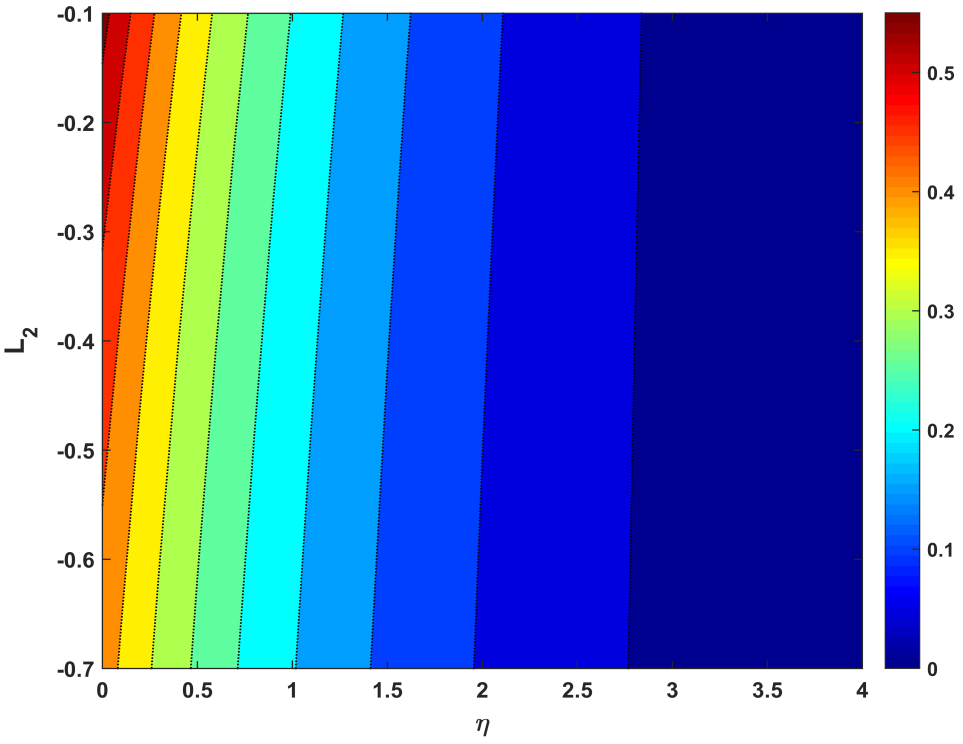

Figure 11.10: Deviations in $f'(\eta)$ with L_2

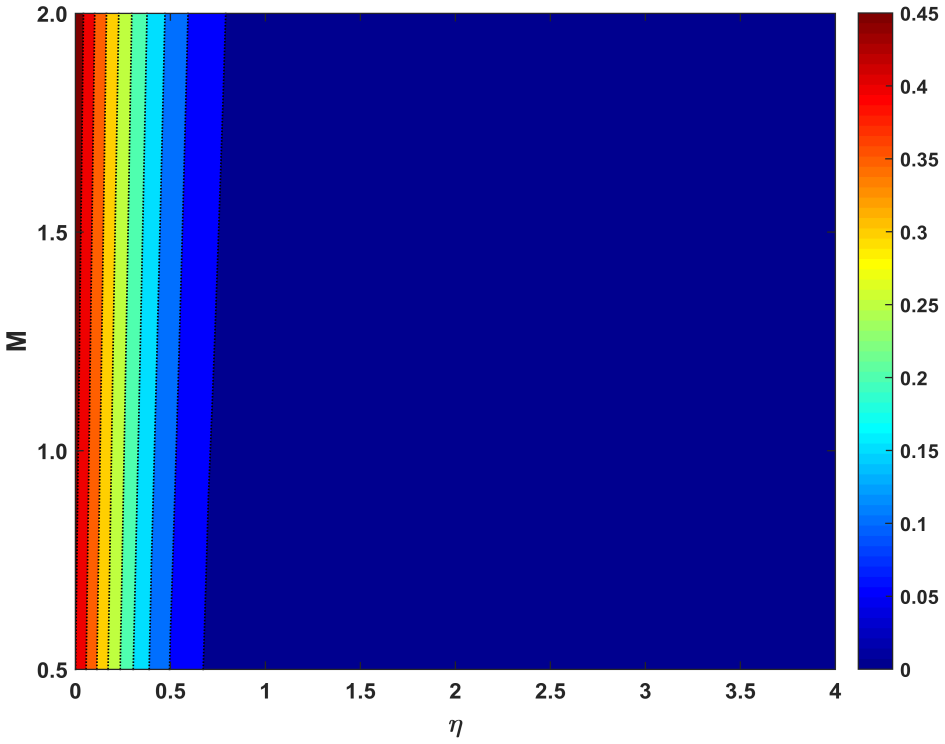

Figure 11.11: Deviations in $\theta(\eta)$ with M

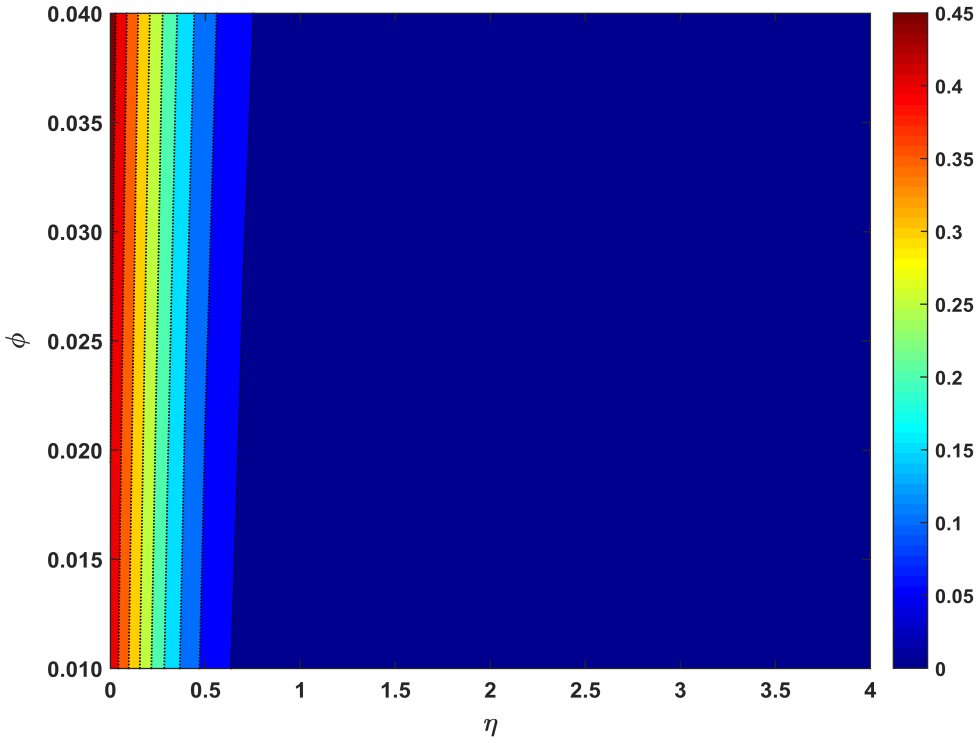

Figure 11.12: Deviations in $\theta(\eta)$ with ϕ

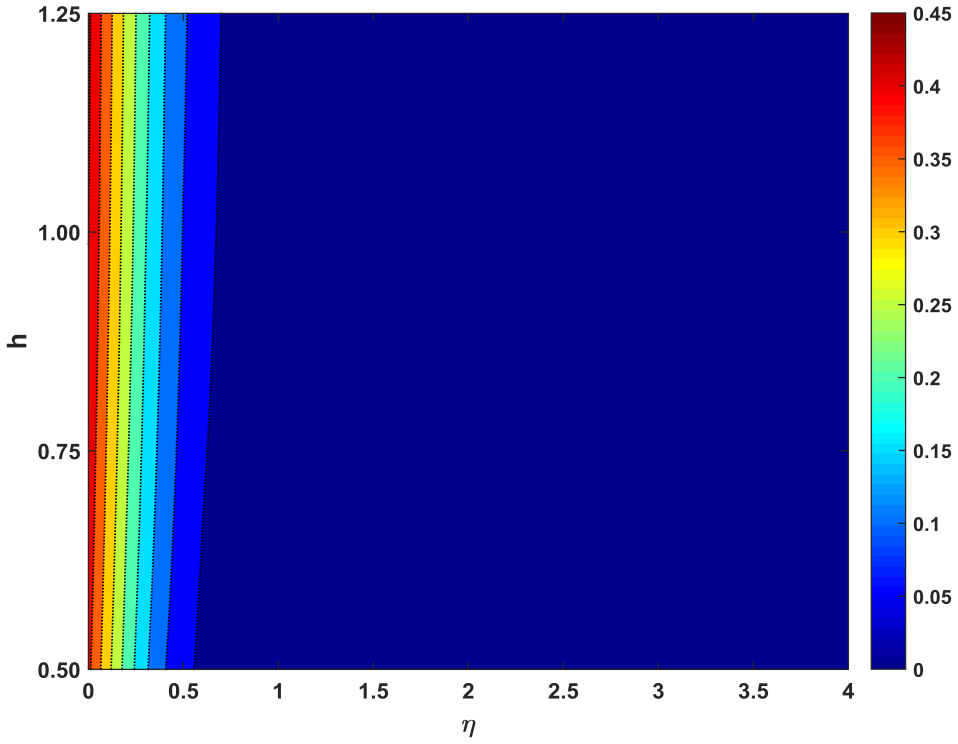

Figure 11.13: Deviations in $\theta(\eta)$ with h

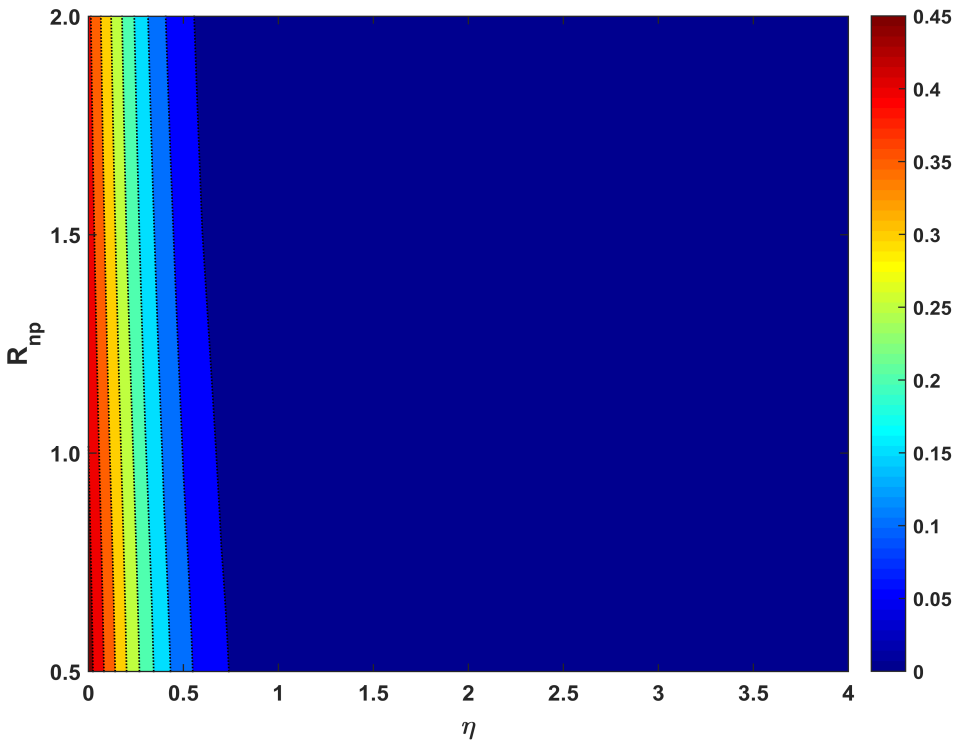

Figure 11.14: Deviations in $\theta(\eta)$ with R_{np}

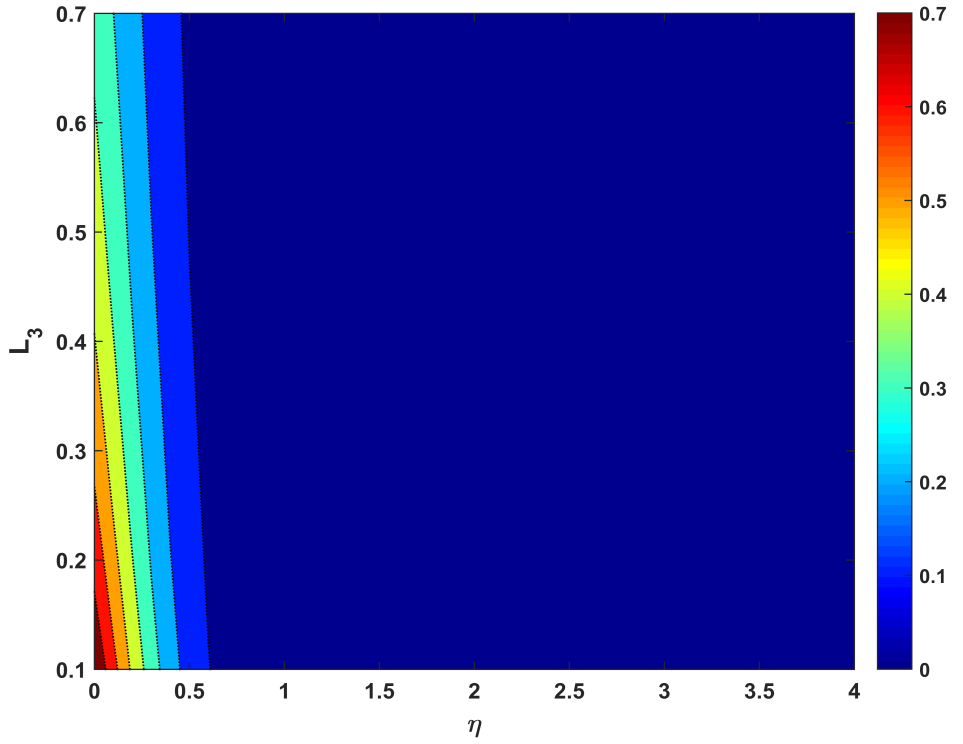

Figure 11.15: Deviations in $\theta(\eta)$ with L_3

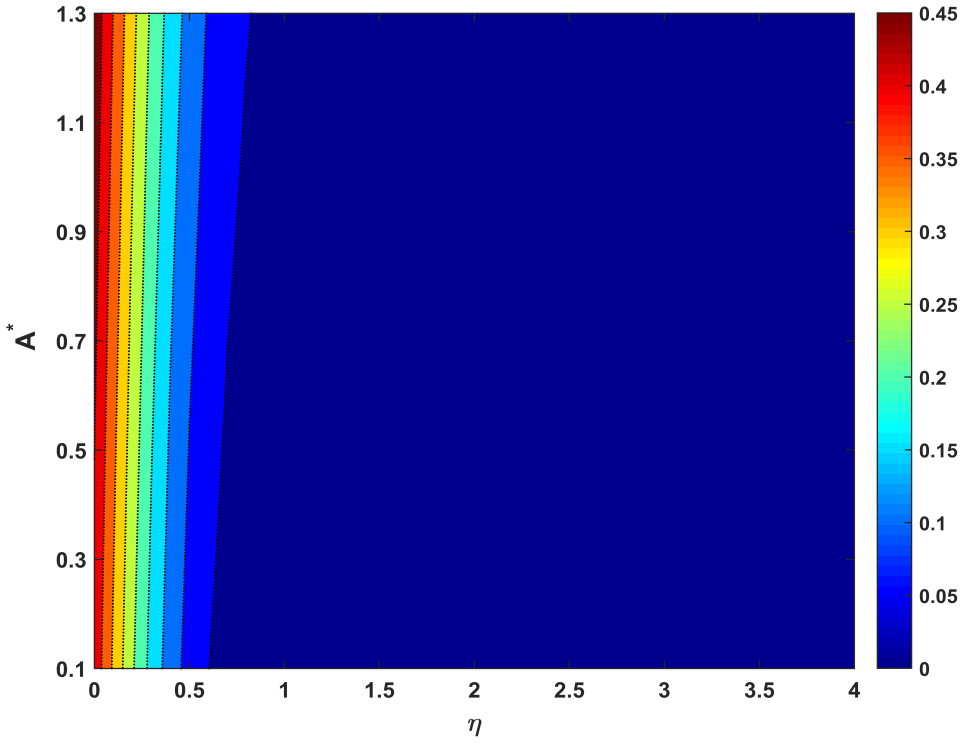

Figure 11.16: Deviations in $\theta(\eta)$ with A^*

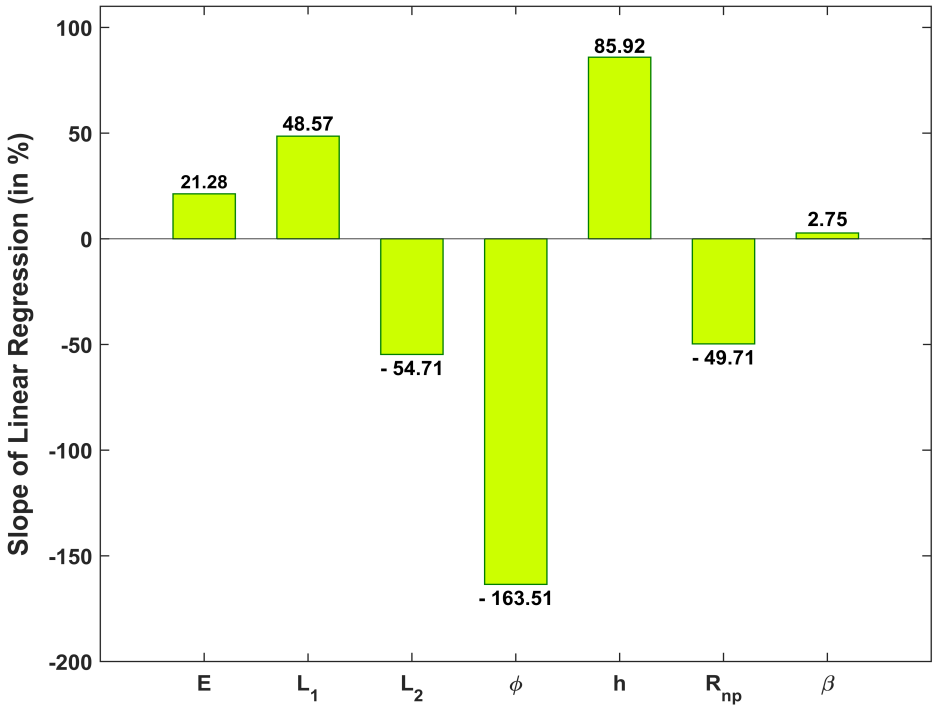

Figure 11.17: Deviations in $Cf_x Re_x^{1/2}$ with differing parameters

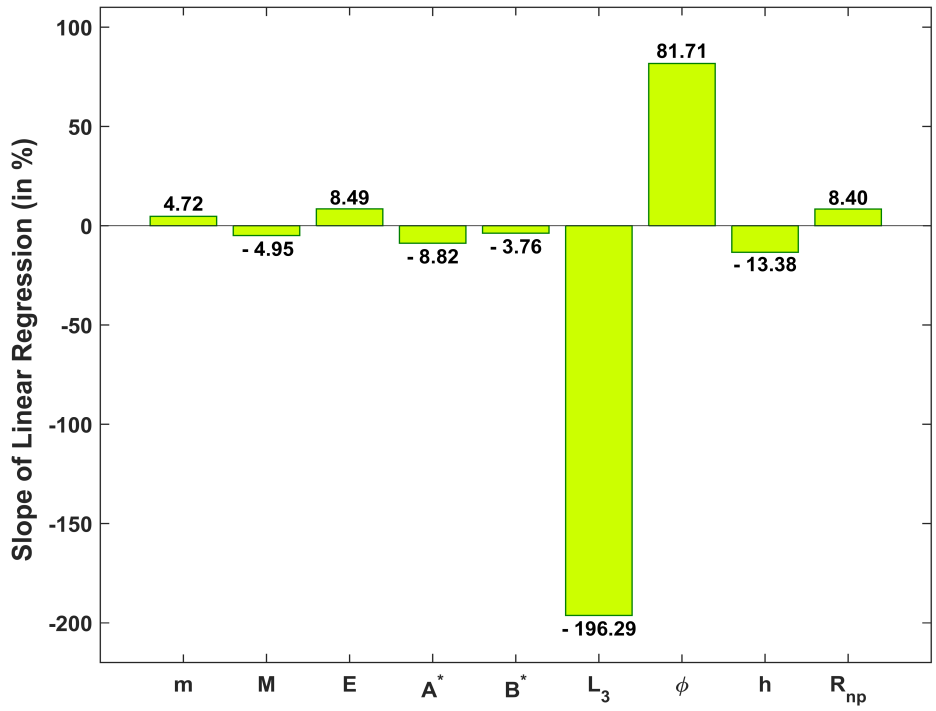

Figure 11.18: Deviations in $Nu_x Re_x^{-1/2}$ with differing parameters

The generation of Lorentz force with the supply of M tends to increase $\theta(\eta)$ (see Figure 11.11). The addition of gold-nanoparticles alters the thermophysical properties that in-turn increases the thermal field (see Figure 11.12). The constructive of inter-particle spacing of gold-nanoparticles on $\theta(\eta)$ has been elucidated through Figure 11.13. Figure 11.14 depicts the destructive effect of the radius of gold-nanoparticle on $\theta(\eta)$. From Figure 11.15, it is evident that the change in 1st order thermal slip parameter is inversely proportional to the thermal field. The augmentation of SHS parameter values induces a supplement energy that increases the temperature profile (see Figure 11.16).

Figures 11.17 - 11.18 graphically represent the trend and magnitude of the change in the drag rate and heat transfer rate with respect to effectual parameters. The following are inferred from Figures 11.17 - 11.18:

- Per unit increase in E augments $Cf_x Re_x^{1/2}$ and $Nu_x Re_x^{-1/2}$ by 21.28% and 8.49%, respectively.

- Per unit increase in the volume fraction of gold nanoparticles augments the $Nu_x Re_x^{-1/2}$ by 81.71% and reduces $Cf_x Re_x^{1/2}$ by 163.51%. Physically, this is due to the improved thermophysical properties of the nanofluid.

- Per unit increase in the inter-particle spacing of gold nanoparticles augments $Cf_x Re_x^{1/2}$ by 85.92% and decreases $Nu_x Re_x^{-1/2}$ by 13.38%.

- Per unit increase in the radius of gold nanoparticles augments $Nu_x Re_x^{-1/2}$ by 8.40% and reduces $Cf_x Re_x^{1/2}$ by 49.71%. Physically, an increase in nanoparticle radius implies an increase in the net amount of nanoparticle in the nanofluid mixture that results in the improvement of nanofluid's thermophysical properties.

- Per unit increase in the 1st order velocity-slip parameter augments the drag coefficient by 48.57% whereas the 2nd order velocity-slip parameter decreases the surface drag by 54.71%.

- Per unit increase in the thermal-slip parameter reduces the heat transfer rate by 196.29%.

- $Nu_x Re_x^{-1/2}$ is maximum for smaller values of $M,\ A^*,\ B^*,\ L_3,\ h$ and larger values of $m,\ E,\ \phi,\ R_{np}$.

- $Cf_x Re_x^{1/2}$ is minimum for smaller values of $E,\ L_1,\ h,\ \beta$ and larger values of $L_2,\ \phi,\ R_{np}$.

11.5 Conclusion

The significance of 2nd order velocity slip, nanoparticle radius, 1st order thermal slip and non-uniform heat source on the electro-magnetohydrodynamic blood-gold Casson nanofluid flow over a nonlinearly stretched surface has been numerically elucidated. The present study finds its application in radiofrequency ablation, magnetic resonance imaging, cancer therapy, and targeted drug delivery. The major findings of the study are:

- The administration of an external electric-field ascends the velocity profile.

- The nanofluid velocity is observed to descend with an increase in the Casson parameter.

- The addition of gold-nanoparticles and an increase in the inter-particle spacing of gold-nanoparticles descends the velocity profile. However, a reverse trend is observed when the radius of gold-nanoparticles is augmented.

- The 2nd order hydrodynamic-slip parameter ascends the nanofluid velocity whereas the 1st order hydrodynamic-slip parameter descends the velocity profile.

- The lowest surface drag is noted for smaller values of Casson parameter.

- The addition of gold-nanoparticles and an increase in the inter-particle spacing of gold-nanoparticles ascends the thermal field. However, a reverse trend is observed when the radius of gold-nanoparticles is augmented.

- The highest heat transfer rate is noticed for lower values of SHS and THS parameters.

- Per unit increase in the electric-field parameter augments the drag coefficient and heat transfer rate by 21.28% and 8.49%, respectively.

- Per unit increase in the volume fraction of gold nanoparticles augments the heat transfer rate by 81.71% and reduces the surface drag by 163.51%.
- Per unit increase in the inter-particle spacing of gold nanoparticles augments the drag coefficient by 85.92% and decreases the heat transfer rate by 13.38%.
- Per unit increase in the radius of gold nanoparticles augments the heat transfer rate by 8.40% and reduces the surface drag by 49.71%.
- Per unit increase in the 1st order velocity-slip parameter augments the drag coefficient by 48.57% whereas the 2nd order velocity-slip parameter decreases the surface drag by 54.71%.

Appendix I: Non-dimensional qunatities

$E = \dfrac{E_0}{B_0\ u_w}$	Electric-field parameter
$L_1 = N_1\sqrt{\dfrac{a}{\vartheta_f}}$	1st order velocity-slip parameter
$L_2 = N_2\ \dfrac{a}{\vartheta_f}$	2nd order velocity-slip parameter
$L_3 = N_3\sqrt{\dfrac{a}{\vartheta_f}}$	1st order thermal-slip parameter
$M = \dfrac{\sigma_f\ {B_0}^2}{a\ \rho_f}$	Magnetic-field parameterr
$Pr = \dfrac{(\mu\ C_p)_f}{k_f}$	Prandtl numberr

Appendix II: Nomenclature

a	Positive constant	E_0	Strength of electric-field
u, v	Velocity components	B_0	Strength of magnetic field
q'''	Non-uniform heat source	T_∞	Ambient temperature
T	Fluid temperature	T_w	Wall temperature
x, y	Cartesian coordinates	u_w	Stretching velocity
τ_w	Wall shear stress	Nu_x	Local Nusselt number
ρC_p	Heat capacity	Cf_x	Local drag coefficient
σ	Electrical conductivity	μ	Dynamic viscosity
η	Similarity variable	ϑ	Kinematic viscosity
k	Thermal conductivity	β	Casson parameter
ρ	Density	ϕ	Nanoparticle volume fraction
R_{np}	Nanoparticle radius	N_1^*, N_2^*	Velocity-slip factors
N_3^*	Thermal-slip factor	m	Non-linear stretching parameter
h	Inter-particle spacing	A^*	Space-dependent heat source
q_w	Heat flux	B^*	Temperature-dependent heat source

Chapter 12

Conclusion and Future Scope

12.1 Concluding Remarks

Owing to the practical applications (like biomedical imaging, targeted drug delivery, hyperthermia, biosensors, medical instruments, pharmaceuticals, bio-chromatography, theranostic, microchip pump, biomedical science, and cancer therapy), nine fluid flow problems (over a flat surface, cylinder and disk) are modelled and investigated in this thesis. The transport phenomena of Newtonian and non-Newtonian fluids (Carreau and Casson fluids) considering various effects like MHD, EMHD, radiation, multiple slip, stratification, geometric effects of nanoparticles, heat source, viscous dissipation, chemical reaction, Stefan blowing, convective heating and passive control of nanoparticles have been investigated. The salient features of the current theoretical/numerical exploration can be summarized as below:

- The augmenting volume fraction of single-wall carbon nanotube and magnetite nanoparticles raises the nanofluid temperature. Addition of gold-nanoparticles and an increase in the inter-particle spacing of gold-nanoparticles descends the velocity profile. However, a reverse trend is observed when the radius of gold-nanoparticles is augmented. The addition of gold-nanoparticles and an increase in the inter-particle spacing of gold-nanoparticles ascends the thermal field.

- Velocity and induced magnetic field profiles are least affected by spherical-shaped silver nanoparticles and highly affected by cylinder-shaped silver nanoparticles. Blade shaped silver nanoparticles contribute the most whereas cylinder-shaped silver nanoparticles contribute the least towards the

nanofluid temperature. Blade shaped silver nanoparticles offer an increased heat transfer rate over the other nanoparticle shapes and cylinder-shaped silver nanoparticles exhibit the highest mass transfer rate. A significant rise in the surface drag is brought out by the spherical-shaped silver nanoparticles followed by blade, platelet, and cylinder-shaped nanoparticles.

- Per unit increase in the electric-field parameter augments the drag coefficient and heat transfer rate by 21.28% and 8.49%, respectively. Per unit increase in the volume fraction of gold nanoparticles augments the heat transfer rate by 81.71% and reduces the surface drag by 163.51%. Per unit increase in the inter-particle spacing of gold nanoparticles augments the drag coefficient by 85.92%. Per unit increase in the radius of gold nanoparticles reduces the surface drag by 49.71%.

- The magnetic field parameter exhibits a negative impact on the velocity profile which helps in improving the biomedical imaging capabilities by manipulating the transference of nanomaterial to the preferred location. Descending electric field parameter retards the velocity profile, which helps in improving the efficiency of targeted drug delivery and biomedical imaging.

- Ascending Biot number intensifies the nanomaterial temperature that serves a crucial role in the termination of cancerous cells or tumors. An increase in the chemical reaction parameter consumes more nanoparticles and hence concentration decreases. Biologically, consumption of more nanoparticles is directly proportional to improved medication and biomedical imaging.

- Increasing Weissenberg number improves the velocity of dilatant fluids and reduces the velocity in the case of pseudo-plastic fluids. The nanofluid velocity is observed to descend with an increase in the Casson parameter.

- The thermal field of the nanomaterial when using the modified Buongiorno model is higher than when the traditional Buongiorno model is used. Further, the velocity field is lower in the case of the modified Buongiorno model than in the conventional Buongiorno model.

- Augmenting Stefan blowing parameter curtails the velocity and nanomaterial temperature profiles. The maximum drag coefficient is experienced for lower

values of the magnetic field parameter and Stefan blowing parameter. The heat transfer rate is an increasing function of the Stefan blowing parameter and Biot number. Further, the optimum level of heat transport is estimated to be 0.4304 which occurs when Stefan blowing and Biot number are maintained at the high levels and magnetic field is kept at the low level.

- The second-order hydrodynamic-slip parameter ascends the nanofluid velocity whereas the first-order hydrodynamic-slip parameter descends the velocity profile. Moreover, the drag coefficient is maximum for higher values of electric field parameter and lower values of magnetic field parameter.

- A decline in nanofluid temperature, microorganism concentration and nanofluid concentration profiles is observed due to ascending thermal, motile density and solutal stratification parameters, respectively.

- The maximum drag coefficient (when stretching parameter is less than 1) is experienced for higher values of the magnetic parameter and lower volume fraction of single-wall carbon nanotube and magnetite nanoparticles. However, the maximum drag coefficient (when stretching parameter is greater than 1) is experienced for lower values of the magnetic parameter and higher volume fraction of single-wall carbon nanotube and magnetite nanoparticles.

- Hartmann number and thermal slip parameter exhibit negative sensitivity towards heat transfer rate whereas radiation parameter showcase positive sensitivity towards heat transfer rate. The heat transport in the nanomaterial is more positively sensitive to thermal radiation and most negatively sensitive to the exponential heat source.

- It is noted that the curvature parameter is directly proportional to axial velocity. The magnetic field parameter has a destructive effect on the radial and azimuthal velocity profiles. Furthermore, increments in the velocity ratio parameter tend to escalate and curtail the radial velocity and the azimuthal velocity profiles, respectively.

12.2 Future Research Work

The use of mathematical modelling to elucidate the biological variations in body fluids due to the application of nanofluids is a growing field with lot of demand on the application scenario. There is a lot of work to be done in this area and the work presented in the thesis only considers a few of these application-oriented sense. It is only natural that this topic can be extended upon to incorporate diverse geometries and more advantageous effects. The use of ternary-hybrid nanofluids and various non-Newtonian (shear thinning) fluids will benefit the future explorations. Entropy generation of a modelled flow and the significance of nanoparticle density on the flow profiles can also be examined. Furthermore, the use of artificial neural networking to optimize the physical quantity of choice can also advance the present work.

List of Publications

1. Sujesh A.S., J. Mackolil, B. Mahanthesh, and Alphonsa Mathew; "Bulirsch-Stoer computations for bioconvective magnetized nanomaterial flow subjected to convective thermal heating and Stefan blowing: a revised Buongiorno model for theranostic applications", *Waves in Random and Complex Media* (Taylor & Francis), 2022. DOI: 10.1080/17455030.2022.2102692

2. Alphonsa Mathew, Sujesh A.S., and A.S. Sabu; "Significance of magnetic field and stratification effects on the bioconvective stagnation-point flow of ferro-nanofluid over a rotating stretchable disk: Four-factor response surface methodology", *Journal of the Indian Chemical Society* (Elsevier), 99(8), 100615, 2022. DOI: 10.1016/j.jics.2022.100615

3. Sujesh A.S., J. Mackolil, B. Mahanthesh, Alphonsa Mathew, and P. Rana; "A study on nanoliquid flow with irregular heat source and realistic boundary conditions: A modified Buongiorno model for biomedical applications", *ZAMM - Journal of Applied Mathematics and Mechanics / Zeitschrift für Angewandte Mathematik und Mechanik* (Wiley), 102(3), e202100167, 2022. DOI: 10.1002/zamm.202100167

4. Alphonsa Mathew, Sujesh A.S., and A.S. Sabu; "Sensitivity analysis on radiative heat transfer of hydromagnetic Carreau nanoliquid flow over an elongating cylinder using Bulirsch-Stoer algorithm", *Thermal Science and Engineering Progress* (Elsevier), 25, 101038, 2021. DOI: 10.1016/j.tsep.2021.101038

5. Sujesh A.S., A.S. Sabu, Alphonsa Mathew, and B. Saravanan; "Statistical analysis on the stratification effects of bioconvective EMHD nanofluid flow past a stretching sheet: Application in theranostics", *Heat Transfer* (Wiley), 50(7), 6680-6702, 2021. DOI: 10.1002/htj.22198

6. Alphonsa Mathew, Sujesh A.S., A.S. Sabu, and S. Saleem; "Significance of multiple slip and nanoparticle shape on stagnation point flow of silver-blood nanofluid in the presence of induced magnetic field", *Surfaces and Interfaces* (Elsevier), 25, 101267, 2021. DOI: 10.1016/j.surfin.2021.101267

7. Sujesh A.S., F. Mabood, A.S. Sabu, Alphonsa Mathew, and I.A. Badruddin; "Dynamics of water conveying single-wall carbon nanotubes and magnetite nanoparticles subject to induced magnetic field: A bioconvective model for theranostic applications", *International Communications in Heat and Mass Transfer* (Elsevier), 126, 105484, 2021. DOI: 10.1016/j.icheatmasstransfer.2021.105484

8. Sujesh A.S., A.S. Sabu, R. Kumar, and Alphonsa Mathew; "Triple stratification effects on bioconvective stagnation point flow pertaining carbon nanotubes due to induced magnetic field", *ZAMM - Journal of Applied Mathematics and Mechanics / Zeitschrift für Angewandte Mathematik und Mechanik* (Wiley), 101(11), e202000375, 2021. DOI: 10.1002/zamm.202000375

List of Presentations

1. Presented the paper entitled “Significance of ESHS and LHS on the MHD hybrid nanofluid flow towards a stagnation point on a stretching/shrinking cylinder" in the 2nd Online International Conference on Advances in Physical, Mathematical and Computational Sciences organized by the Faculty of Physical Sciences, St. Aloysius’ College (Autonomous), Jabalpur; during 23 - 24 July 2021.

2. Presented the paper entitled “Thermal Radiation and Chemical Reaction Effects on Three Dimensional MHD Hybrid Nanofluid Flow past a Stretching Sheet" in the 28th International Conference (Virtual) of Forum for Interdisciplinary Mathematics jointly organized by FIM, SSN & Stella Maris College, Chennai, during 23 - 27 November 2020.

Bibliography

Abbas, N., Malik, M., Alqarni, M., & Nadeem, S. 2020. Study of three dimensional stagnation point flow of hybrid nanofluid over an isotropic slip surface. *Physica A: Statistical Mechanics and its Applications*, *554*, 124020.

Abbas, T., Hayat, T., Ayub, M., Bhatti, M. M., & Alsaedi, A. 2019. Electromagnetohydrodynamic nanofluid flow past a porous riga plate containing gyrotactic microorganism. *Neural Computing and Applications*, *31*(6), 1905–1913.

Abbas, Z., Naveed, M., Tabassum, R., & Ahmad, I. 2021. Influence of hall and joule heating on a magnetic nanofluid (fe3o4) flow on a rotating disk with generalized slip condition. *Heat Transfer*, *50*(7), 7271–7290.

Abbasi, F., Hayat, T., & Ahmad, B. 2015. Peristalsis of silver-water nanofluid in the presence of hall and ohmic heating effects: applications in drug delivery. *Journal of Molecular Liquids*, *207*, 248–255.

Abdelmalek, Z., Mahanthesh, B., Basir, M. F. M., Imtiaz, M., Mackolil, J., Khan, N. S., ... Tlili, I. 2020. Mixed radiated magneto casson fluid flow with arrhenius activation energy and newtonian heating effects: Flow and sensitivity analysis. *Alexandria Engineering Journal*, *59*(5), 3991–4011.

Abdul Halim, N., & Mohd Noor, N. F. 2021. Mixed convection flow of powell–eyring nanofluid near a stagnation point along a vertical stretching sheet. *Mathematics*, *9*(4), 364.

Abo-Dahab, S., Abdelhafez, M., Mebarek-Oudina, F., & Bilal, S. 2021. Mhd casson nanofluid flow over nonlinearly heated porous medium in presence of extending surface effect with suction/injection. *Indian Journal of Physics*, *95*(12), 2703–2717.

Agrawal, P., Dadheech, P. K., Jat, R., Baleanu, D., & Purohit, S. D. 2021. Radiative mhd hybrid-nanofluids flow over a permeable stretching surface with heat source/sink embedded in porous medium. *International Journal of Numerical Methods for Heat & Fluid Flow*, *31*(8), 2818–2840.

Ahmad, S., Ashraf, M., & Ali, K. 2020. Bioconvection due to gyrotactic microbes in a nanofluid flow through a porous medium. *Heliyon*, *6*(12), e05832.

Ahmad, S., Ijaz Khan, M., Hayat, T., & Alsaedi, A. 2020. Numerical analysis of

copper-water and copper-oxide-water nanofluids flow over a stretching sheet. *International Journal of Modern Physics B*, *34*(13), 2050130.

Ahmad, S., Nadeem, S., Muhammad, N., & Issakhov, A. 2020. Radiative swcnt and mwcnt nanofluid flow of falkner–skan problem with double stratification. *Physica A: Statistical Mechanics and its Applications*, *547*, 124054.

Akbar, A. A., Ahammad, N. A., Awan, A. U., Hussein, A. K., Gamaoun, F., Tag-ElDin, E. M., & Ali, B. 2022. Insight into the role of nanoparticles shape factors and diameter on the dynamics of rotating water-based fluid. *Nanomaterials*, *12*(16), 2801.

Al-Amri, F., & Muthtamilselvan, M. 2020. Stagnation point flow of nanofluid containing micro-organisms. *Case Studies in Thermal Engineering*, *21*, 100656.

Alben, K. T. 2002. *Books and software: design, analyze, and optimize with design-expert.* ACS Publications.

Alfvén, H. 1942. Existence of electromagnetic-hydrodynamic waves. *Nature*, *150*(3805), 405–406.

Alghamdi, M., Wakif, A., Thumma, T., Khan, U., Baleanu, D., & Rasool, G. 2021. Significance of variability in magnetic field strength and heat source on the radiative-convective motion of sodium alginate-based nanofluid within a darcy-brinkman porous structure bounded vertically by an irregular slender surface. *Case Studies in Thermal Engineering*, *28*, 101428.

Ali, B., Hussain, S., Abdal, S., & Mehdi, M. M. 2020. Impact of stefan blowing on thermal radiation and cattaneo–christov characteristics for nanofluid flow containing microorganisms with ablation/accretion of leading edge: Fem approach. *The European Physical Journal Plus*, *135*(10), 1–18.

Ali, F. M., Nazar, R., Arifin, N. M., & Pop, I. 2011a. Mhd boundary layer flow and heat transfer over a stretching sheet with induced magnetic field. *Heat and Mass transfer*, *47*(2), 155–162.

Ali, F. M., Nazar, R., Arifin, N. M., & Pop, I. 2011b. Mhd stagnation-point flow and heat transfer towards stretching sheet with induced magnetic field. *Applied Mathematics and Mechanics*, *32*(4), 409–418.

Ali, R., Asjad, M. I., & Akgül, A. 2021. An analysis of a mathematical fractional model of hybrid viscous nanofluids and its application in heat and mass transfer. *Journal of Computational and Applied Mathematics*, *383*, 113096.

Alqarni, M., Waqas, H., Alghamdi, M., & Muhammad, T. 2022. Importance of bioconvection in 3d viscoelastic nanofluid flow due to exponentially stretching surface with nonlinear radiative heat transfer and variable thermal conductivity. *Journal of Thermal Analysis and Calorimetry*, *147*(7), 4805–4819.

Al-Rashed, A. A., Shahsavar, A., Rasooli, O., Moghimi, M., Karimipour, A., & Tran, M. D. 2019. Numerical assessment into the hydrothermal and entropy generation characteristics of biological water-silver nano-fluid in a wavy walled microchannel heat sink. *International Communications in Heat and Mass Transfer*, *104*, 118–126.

Alsaedi, A., Khan, M. I., Farooq, M., Gull, N., & Hayat, T. 2017. Magnetohydrodynamic (mhd) stratified bioconvective flow of nanofluid due to gyrotactic microorganisms. *Advanced Powder Technology*, *28*(1), 288–298.

Alshomrani, A. S., Ullah, M. Z., & Baleanu, D. 2020. Importance of multiple slips on bioconvection flow of cross nanofluid past a wedge with gyrotactic motile microorganisms. *Case Studies in Thermal Engineering*, *22*, 100798.

Aly, E. H., & Pop, I. 2020. Mhd flow and heat transfer near stagnation point over a stretching/shrinking surface with partial slip and viscous dissipation: Hybrid nanofluid versus nanofluid. *Powder Technology*, *367*, 192–205.

Amanulla, C., Saleem, S., Wakif, A., & AlQarni, M. 2019. Mhd prandtl fluid flow past an isothermal permeable sphere with slip effects. *Case Studies in Thermal Engineering*, *14*, 100447.

Amjad, M., Zehra, I., Nadeem, S., Abbas, N., Saleem, A., & Issakhov, A. 2020. Influence of lorentz force and induced magnetic field effects on casson micropolar nanofluid flow over a permeable curved stretching/shrinking surface under the stagnation region. *Surfaces and Interfaces*, *21*, 100766.

Ankamwar, B. 2012. Size and shape effect on biomedical applications of nanomaterials. *Biomedical Engineering-Technical Applications in Medicine*(1).

Ashraf, M. U., Qasim, M., Wakif, A., Afridi, M. I., & Animasaun, I. L. 2022. A generalized differential quadrature algorithm for simulating magnetohydrodynamic peristaltic flow of blood-based nanofluid containing magnetite nanoparticles: a physiological application. *Numerical Methods for Partial Differential Equations*, *38*(3), 666–692.

Azizian, R., Doroodchi, E., McKrell, T., Buongiorno, J., Hu, L., & Moghtaderi, B.

2014. Effect of magnetic field on laminar convective heat transfer of magnetite nanofluids. *International Journal of Heat and Mass Transfer*, *68*, 94–109.

Bachok, N., Ishak, A., & Pop, I. 2011. Flow and heat transfer over a rotating porous disk in a nanofluid. *Physica B: Condensed Matter*, *406*(9), 1767–1772.

Bai, R. G., Muthoosamy, K., & Manickam, S. 2015. Nanomedicine in theranostics. In *Nanotechnology applications for tissue engineering* (pp. 195–213). Elsevier.

Bansal, J. 1977. *Viscous fluid dynamics*. Oxford & IBH Publishing Company.

Barik, A. K., Mishra, S. K., Mishra, S., & Pattnaik, P. 2020. Multiple slip effects on mhd nanofluid flow over an inclined, radiative, and chemically reacting stretching sheet by means of fdm. *Heat Transfer—Asian Research*, *49*(1), 477–501.

Basir, M. F. M., Bilal, M., Choudhary, R., Mackolil, J., Mahanthesh, B., & Nisar, K. S. 2021. Numerical and sensitivity analysis of mhd bioconvective slip flow of nanomaterial with binary chemical reaction and newtonian heating. *Heat Transfer*, *50*(6), 5439–5466.

Bég, O. A., Kabir, M. N., Uddin, M. J., Izani Md Ismail, A., & Alginahi, Y. M. 2021. Numerical investigation of von karman swirling bioconvective nanofluid transport from a rotating disk in a porous medium with stefan blowing and anisotropic slip effects. *Proceedings of the Institution of Mechanical Engineers, Part C: Journal of Mechanical Engineering Science*, *235*(19), 3933–3951.

Behnam, M. A., Emami, F., Sobhani, Z., & Dehghanian, A. R. 2018. The application of titanium dioxide (tio2) nanoparticles in the photo-thermal therapy of melanoma cancer model. *Iranian Journal of Basic Medical Sciences*, *21*(11), 1133.

Benkhedda, M., Boufendi, T., Tayebi, T., & Chamkha, A. J. 2020. Convective heat transfer performance of hybrid nanofluid in a horizontal pipe considering nanoparticles shapes effect. *Journal of Thermal Analysis and Calorimetry*, *140*(1), 411–425.

Besthapu, P., Haq, R. U., Bandari, S., & Al-Mdallal, Q. M. 2019. Thermal radiation and slip effects on mhd stagnation point flow of non-newtonian nanofluid over a convective stretching surface. *Neural Computing and Applications*, *31*(1), 207–217.

Bhanvase, B. A., & Barai, D. 2021. *Nanofluids for heat and mass transfer:*

Fundamentals, sustainable manufacturing and applications. Academic Press.

Bhatti, M., & Michaelides, E. E. 2021. Study of arrhenius activation energy on the thermo-bioconvection nanofluid flow over a riga plate. *Journal of Thermal Analysis and Calorimetry*, *143*(3), 2029–2038.

Bhatti, M. M., Shahid, A., Abbas, T., Alamri, S. Z., & Ellahi, R. 2020. Study of activation energy on the movement of gyrotactic microorganism in a magnetized nanofluids past a porous plate. *Processes*, *8*(3), 328.

Bilal, M., Sagheer, M., & Hussain, S. 2018. Numerical study of magnetohydrodynamics and thermal radiation on williamson nanofluid flow over a stretching cylinder with variable thermal conductivity. *Alexandria Engineering Journal*, *57*(4), 3281–3289.

Blasiak, B., van Veggel, F. C., & Tomanek, B. 2013. Applications of nanoparticles for mri cancer diagnosis and therapy. *Journal of Nanomaterials*, *2013*, 1–12.

Box, G. E., & Wilson, K. B. 1992. On the experimental attainment of optimum conditions. In *Breakthroughs in statistics* (pp. 270–310). Springer.

Brinkman, H. C. 1952. The viscosity of concentrated suspensions and solutions. *The Journal of Chemical Physics*, *20*(4), 571.

Bulirsch, R., Stoer, J., & Stoer, J. 2002. *Introduction to numerical analysis* (Vol. 3). Springer.

Buongiorno, J. 2006. Convective transport in nanofluids. *Journal of Heat Transfer*, *128*(3), 240–250.

Casson, N. 1959. A flow equation for pigment-oil suspensions of the printing ink type. *Rheology of Disperse Systems*, 84–104.

Cengel, Y., & Cimbala, J. 2013. *Fluid mechanics fundamentals and applications.* McGraw Hill.

Choi, S. U. S., & Eastman, J. A. 1995. Enhancing thermal conductivity of fluids with nanoparticles. *Proceedings of the 1995 International Mechanical Engineering Congress and Exposition, ASME, San Francisco*, *66*, 99-105.

Chu, Y.-M., Khan, M. I., Khan, N. B., Kadry, S., Khan, S. U., Tlili, I., & Nayak, M. 2020. Significance of activation energy, bio-convection and magnetohydrodynamic in flow of third grade fluid (non-newtonian) towards stretched surface: A buongiorno model analysis. *International Communications in Heat and Mass Transfer*, *118*, 104893.

Chugh, H., Sood, D., Chandra, I., Tomar, V., Dhawan, G., & Chandra, R. 2018. Role of gold and silver nanoparticles in cancer nano-medicine. *Artificial Cells, Nanomedicine, and Biotechnology*, *46*(sup1), 1210–1220.

Comparetti, E. J., Pedrosa, V. d. A., & Kaneno, R. 2017. Carbon nanotube as a tool for fighting cancer. *Bioconjugate Chemistry*, *29*(3), 709–718.

Cortell, R. 2007. Viscous flow and heat transfer over a nonlinearly stretching sheet. *Applied Mathematics and Computation*, *184*(2), 864–873.

Daniel, Y. S., Aziz, Z. A., Ismail, Z., & Bahar, A. 2020. Unsteady emhd dual stratified flow of nanofluid with slips impacts. *Alexandria Engineering Journal*, *59*(1), 177–189.

Daniel, Y. S., Aziz, Z. A., Ismail, Z., & Salah, F. 2017a. Double stratification effects on unsteady electrical mhd mixed convection flow of nanofluid with viscous dissipation and joule heating. *Journal of Applied Research and Technology*, *15*(5), 464–476.

Daniel, Y. S., Aziz, Z. A., Ismail, Z., & Salah, F. 2017b. Effects of thermal radiation, viscous and joule heating on electrical mhd nanofluid with double stratification. *Chinese Journal of Physics*, *55*(3), 630–651.

Daniel, Y. S., Aziz, Z. A., Ismail, Z., & Salah, F. 2018. Effects of slip and convective conditions on mhd flow of nanofluid over a porous nonlinear stretching/shrinking sheet. *Australian Journal of Mechanical Engineering*, *16*(3), 213–229.

Daniel, Y. S., Aziz, Z. A., Ismail, Z., & Salah, F. 2019. Thermal radiation on unsteady electrical mhd flow of nanofluid over stretching sheet with chemical reaction. *Journal of King Saud University-Science*, *31*(4), 804–812.

Dinarvand, S., Rostami, M. N., Dinarvand, R., & Pop, I. 2019. Improvement of drug delivery micro-circulatory system with a novel pattern of cuo-cu/blood hybrid nanofluid flow towards a porous stretching sheet. *International Journal of Numerical Methods for Heat & Fluid Flow*, *29*(11), 4408–4429.

Doh, D.-H., Muthtamilselvan, M., Swathene, B., & Ramya, E. 2020. Homogeneous and heterogeneous reactions in a nanofluid flow due to a rotating disk of variable thickness using ham. *Mathematics and Computers in Simulation*, *168*, 90–110.

Duangthongsuk, W., & Wongwises, S. 2009. Measurement of temperature-dependent

thermal conductivity and viscosity of tio2-water nanofluids. *Experimental Thermal and Fluid Science*, *33*(4), 706–714.

Eid, M. R. 2020. Effects of np shapes on non-newtonian bio-nanofluid flow in suction/blowing process with convective condition: Sisko model. *Journal of Non-Equilibrium Thermodynamics*, *45*(2), 97–108.

Eid, M. R., Al-Hossainy, A., & Zoromba, M. S. 2019. Fem for blood-based swcnts flow through a circular cylinder in a porous medium with electromagnetic radiation. *Communications in Theoretical Physics*, *71*(12), 1425.

Eid, M. R., Mahny, K., Dar, A., & Muhammad, T. 2020. Numerical study for carreau nanofluid flow over a convectively heated nonlinear stretching surface with chemically reactive species. *Physica A: Statistical Mechanics and its Applications*, *540*, 123063.

Einstein, A. 1906. Eine neue bestimmung der moleküldimensionen. *Annalen der Physik*, *324*(2), 289–306.

El-Aziz, M. A., & Afify, A. A. 2018. Influences of slip velocity and induced magnetic field on mhd stagnation-point flow and heat transfer of casson fluid over a stretching sheet. *Mathematical Problems in Engineering*, *2018*, 9402836.

Ellahi, R., Hassan, M., & Zeeshan, A. 2017. Shape effects of spherical and nonspherical nanoparticles in mixed convection flow over a vertical stretching permeable sheet. *Mechanics of Advanced Materials and Structures*, *24*(15), 1231–1238.

Elnaqeeb, T., Animasaun, I. L., & Shah, N. A. 2021. Ternary-hybrid nanofluids: significance of suction and dual-stretching on three-dimensional flow of water conveying nanoparticles with various shapes and densities. *Zeitschrift für Naturforschung A*, *76*(3), 231–243.

Fang, T., & Aziz, A. 2010. Viscous flow with second-order slip velocity over a stretching sheet. *Zeitschrift für Naturforschung A*, *65*(12), 1087–1092.

Fang, T., & Jing, W. 2014. Flow, heat, and species transfer over a stretching plate considering coupled stefan blowing effects from species transfer. *Communications in Nonlinear Science and Numerical Simulation*, *19*(9), 3086–3097.

Farooq, U., Waqas, H., Khan, M. I., Khan, S. U., Chu, Y.-M., & Kadry, S. 2021. Thermally radioactive bioconvection flow of carreau nanofluid with

modified cattaneo-christov expressions and exponential space-based heat source. *Alexandria Engineering Journal*, *60*(3), 3073–3086.

Farrokhi, H., Otuya, D. O., Khimchenko, A., & Dong, J. 2019. Magnetohydrodynamics in biomedical applications. *Nanofluid Flow in Porous Media*.

Fisher, R. 1950. *On the'probable error'of a coeficient of correlation deduced from a small sample, metron i (1921). reprinted in: Contributions to mathematical statistics. 3–32.* Wiley, New York.

Foulkes, R., Ali Asgari, M., Curtis, A., & Hoskins, C. 2019. Silver-nanoparticle-mediated therapies in the treatment of pancreatic cancer. *ACS Applied Nano Materials*, *2*(4), 1758–1772.

Gangadhar, K., Ramana, K., Makinde, O. D., & Kumar, B. R. 2018. Mhd flow of a carreau fluid past a stretching cylinder with cattaneo-christov heat flux using spectral relaxation method. *Defect and Diffusion Forum*, *387*, 91–105.

Gellci, K., & Mehrmohammadi, M. 2014. Photothermal therapy. *Encyclopedia of Cancer; Schwab, M., Ed.; Springer: Berlin/Heidelberg, Germany*, 1–5.

Gholinia, M., Hoseini, M., & Gholinia, S. 2019. A numerical investigation of free convection mhd flow of walters-b nanofluid over an inclined stretching sheet under the impact of joule heating. *Thermal Science and Engineering Progress*, *11*, 272–282.

Gireesha, B., Mahanthesh, B., Shivakumara, I., & Eshwarappa, K. 2016. Melting heat transfer in boundary layer stagnation-point flow of nanofluid toward a stretching sheet with induced magnetic field. *Engineering Science and Technology, an International Journal*, *19*(1), 313–321.

Gireesha, B., Umeshaiah, M., Prasannakumara, B., Shashikumar, N., & Archana, M. 2020. Impact of nonlinear thermal radiation on magnetohydrodynamic three dimensional boundary layer flow of jeffrey nanofluid over a nonlinearly permeable stretching sheet. *Physica A: Statistical Mechanics and its Applications*, *549*, 124051.

Gowda, R. P., Kumar, R. N., Prasannakumara, B., Nagaraja, B., & Gireesha, B. 2021. Exploring magnetic dipole contribution on ferromagnetic nanofluid flow over a stretching sheet: An application of stefan blowing. *Journal of Molecular Liquids*, *335*, 116215.

Graham, A. L. 1981. On the viscosity of suspensions of solid spheres. *Applied Scientific Research*, *37*(3), 275–286.

Gunawan, E. R., & Suhendra, D. 2008. Four-factor response surface optimization of the enzymatic synthesis of wax ester from palm kernel oil. *Indonesian Journal of Chemistry*, *8*(1), 83–90.

Hady, F. M., Ibrahim, F. S., Abdel-Gaied, S. M., & Eid, M. R. 2012. Radiation effect on viscous flow of a nanofluid and heat transfer over a nonlinearly stretching sheet. *Nanoscale Research Letters*, *7*(1), 1–13.

Hafeez, A., Khan, M., & Ahmed, J. 2020. Stagnation point flow of radiative oldroyd-b nanofluid over a rotating disk. *Computer Methods and Programs in Biomedicine*, *191*, 105342.

Halim, N., Sivasankaran, S., & Noor, N. M. 2017. Active and passive controls of the williamson stagnation nanofluid flow over a stretching/shrinking surface. *Neural Computing and Applications*, *28*(1), 1023–1033.

Hamilton, R. L., & Crosser, O. 1962. Thermal conductivity of heterogeneous two-component systems. *Industrial & Engineering Chemistry Fundamentals*, *1*(3), 187–191.

Hayat, T., Aziz, A., Muhammad, T., & Ahmad, B. 2016. On magnetohydrodynamic flow of second grade nanofluid over a nonlinear stretching sheet. *Journal of Magnetism and Magnetic Materials*, *408*, 99–106.

Hayat, T., Farooq, M., & Alsaedi, A. 2015. Homogeneous-heterogeneous reactions in the stagnation point flow of carbon nanotubes with newtonian heating. *AIP Advances*, *5*(2), 027130.

Hayat, T., Haider, F., Muhammad, T., & Alsaedi, A. 2017. On darcy-forchheimer flow of carbon nanotubes due to a rotating disk. *International Journal of Heat and Mass Transfer*, *112*, 248–254.

Hayat, T., Haider, F., Muhammad, T., & Alsaedi, A. 2020. Darcy-forchheimer flow by rotating disk with partial slip. *Applied Mathematics and Mechanics*, *41*(5), 741–752.

Hayat, T., Khan, M. I., Qayyum, S., & Alsaedi, A. 2018. Entropy generation in flow with silver and copper nanoparticles. *Colloids and Surfaces A: Physicochemical and Engineering Aspects*, *539*, 335–346.

Hayat, T., Muhammad, K., Farooq, M., & Alsaedi, A. 2016. Melting heat transfer in

stagnation point flow of carbon nanotubes towards variable thickness surface. *AIP Advances*, *6*(1), 015214.

Hayat, T., Qayyum, S., Imtiaz, M., & Alsaedi, A. 2016. Comparative study of silver and copper water nanofluids with mixed convection and nonlinear thermal radiation. *International Journal of Heat and Mass Transfer*, *102*, 723–732.

Hazarika, S., Ahmed, S., & Chamkha, A. J. 2021. Investigation of nanoparticles cu, ag and fe3o4 on thermophoresis and viscous dissipation of mhd nanofluid over a stretching sheet in a porous regime: a numerical modeling. *Mathematics and Computers in Simulation*, *182*, 819–837.

Hepokur, C., Kariper, İ. A., Mısır, S., Ay, E., Tunoğlu, S., Ersez, M. S., ... Yaylım, İ. 2019. Silver nanoparticle/capecitabine for breast cancer cell treatment. *Toxicology in Vitro*, *61*, 104600.

Hiemenz, K. 1911. Die grenzschicht an einem in den gleichformigen flussigkeitsstrom eingetauchten geraden kreiszylinder. *Dinglers Polytech. J.*, *326*, 321–324.

Hussain, M., Farooq, U., & Sheremet, M. 2022. Nonsimilar convective thermal transport analysis of emhd stagnation casson nanofluid flow subjected to particle shape factor and thermal radiations. *International Communications in Heat and Mass Transfer*, *137*, 106230.

Hussanan, A., Salleh, M. Z., Alkasasbeh, H. T., & Khan, I. 2018. Mhd flow and heat transfer in a casson fluid over a nonlinearly stretching sheet with newtonian heating. *Heat Transfer Research*, *49*(1185–1198).

Ibrahim, S., Lorenzini, G., Kumar, P. V., & Raju, C. 2017. Influence of chemical reaction and heat source on dissipative mhd mixed convection flow of a casson nanofluid over a nonlinear permeable stretching sheet. *International Journal of Heat and Mass Transfer*, *111*, 346–355.

Ibrahim, W., & Negera, M. 2020. Mhd slip flow of upper-convected maxwell nanofluid over a stretching sheet with chemical reaction. *Journal of the Egyptian Mathematical Society*, *28*(1), 1–28.

Iqbal, M. S., Malik, F., Mustafa, I., Khan, I., Ghaffari, A., Riaz, A., & Nisar, K. S. 2020. Impact of induced magnetic field on thermal enhancement in gravity driven fe3o4 ferrofluid flow through vertical non-isothermal surface. *Results in Physics*, *19*, 103472.

Iqbal, Z., Azhar, E., & Maraj, E. 2017. Transport phenomena of carbon nanotubes

and bioconvection nanoparticles on stagnation point flow in presence of induced magnetic field. *Physica E: Low-Dimensional Systems and Nanostructures*, *91*, 128–135.

Iqbal, Z., Maraj, E., Azhar, E., & Mehmood, Z. 2017. Framing the performance of induced magnetic field and entropy generation on cu and tio2 nanoparticles by using keller box scheme. *Advanced Powder Technology*, *28*(9), 2332–2345.

Isa, S., Arifin, N., Nazar, R., Bachok, N., Ali, F., & Pop, I. 2017. Mhd mixed convection boundary layer flow of a casson fluid bounded by permeable shrinking sheet with exponential variation. *Scientia Iranica*, *24*(2), 637–647.

Jafar, A. B., Shafie, S., & Ullah, I. 2020. Mhd radiative nanofluid flow induced by a nonlinear stretching sheet in a porous medium. *Heliyon*, *6*(6), e04201.

Jakeer, S., & Reddy, P. B. A. 2020. Entropy generation on emhd stagnation point flow of hybrid nanofluid over a stretching sheet: Homotopy perturbation solution. *Physica Scripta*, *95*(12), 125203.

Jamaludin, A., Naganthran, K., Nazar, R., & Pop, I. 2020. Mhd mixed convection stagnation-point flow of cu-al2o3/water hybrid nanofluid over a permeable stretching/shrinking surface with heat source/sink. *European Journal of Mechanics-B/Fluids*, *84*, 71–80.

Jamiatia, M. 2019. Numerical investigation in comparing the influence of water-silver-magnesium oxide hybrid nanofluid and water-silver normal nanofluid on fluid flow, heat transfer and entropy generation in an enclosure with rotating heat sources. *The European Physical Journal Plus*, *134*(8), 1–15.

Junoh, M. M., Ali, F. M., Arifin, N. M., Bachok, N., & Pop, I. 2019. Mhd stagnation-point flow and heat transfer past a stretching/shrinking sheet in a hybrid nanofluid with induced magnetic field. *International Journal of Numerical Methods for Heat & Fluid Flow*, *30*(3), 1345–1364.

Kameswaran, P., Narayana, M., Sibanda, P., & Murthy, P. 2012. Hydromagnetic nanofluid flow due to a stretching or shrinking sheet with viscous dissipation and chemical reaction effects. *International Journal of Heat and Mass Transfer*, *55*(25-26), 7587–7595.

Kármán, T. v. 1921. Über laminare und turbulente reibung. *ZAMM-Journal of Applied Mathematics and Mechanics/Zeitschrift für Angewandte Mathematik und Mechanik*, *1*(4), 233–252.

Khalid, A., Khan, I., Khan, A., Shafie, S., & Tlili, I. 2018. Case study of mhd blood flow in a porous medium with cnts and thermal analysis. *Case Studies in Thermal Engineering*, *12*, 374–380.

Khan, I., Malik, M., Hussain, A., & Khan, M. 2017. Magnetohydrodynamics carreau nanofluid flow over an inclined convective heated stretching cylinder with joule heating. *Results in Physics*, *7*, 4001–4012.

Khan, J., Mustafa, M., Hayat, T., & Alzahrani, F. 2017. Numerical study for bödewadt flow of water based nanofluid over a deformable disk: Buongiorno model. *Indian Journal of Physics*, *91*(5), 527–533.

Khan, M., Irfan, M., & Khan, W. 2019. Heat transfer enhancement for maxwell nanofluid flow subject to convective heat transport. *Pramana*, *92*(2), 1–9.

Khan, M. I., Hayat, T., Shah, F., & Haq, F. 2019. Physical aspects of cnts and induced magnetic flux in stagnation point flow with quartic chemical reaction. *International Journal of Heat and Mass Transfer*, *135*, 561–568.

Khan, S. A., Nie, Y., & Ali, B. 2020. Multiple slip effects on mhd unsteady viscoelastic nano-fluid flow over a permeable stretching sheet with radiation using the finite element method. *SN Applied Sciences*, *2*(1), 1–14.

Khan, U., Bilal, S., Zaib, A., Makinde, O., & Wakif, A. 2022. Numerical simulation of a nonlinear coupled differential system describing a convective flow of casson gold–blood nanofluid through a stretched rotating rigid disk in the presence of lorentz forces and nonlinear thermal radiation. *Numerical Methods for Partial Differential Equations*, *38*(3), 308–328.

Khan, U., Shafiq, A., Zaib, A., Sherif, E.-S. M., & Baleanu, D. 2020. Mhd radiative blood flow embracing gold particles via a slippery sheet through an erratic heat sink/source. *Mathematics*, *8*(9), 1597.

Khan, U., Zaib, A., Khan, I., & Nisar, K. S. 2021. Insight into the dynamics of transient blood conveying gold nanoparticles when entropy generation and lorentz force are significant. *International Communications in Heat and Mass Transfer*, *127*, 105415.

Khan, W., & Pop, I. 2010. Boundary-layer flow of a nanofluid past a stretching sheet. *International Journal of Heat and Mass Transfer*, *53*(11-12), 2477–2483.

Khanafer, K., Vafai, K., & Lightstone, M. 2003. Buoyancy-driven heat transfer enhancement in a two-dimensional enclosure utilizing nanofluids. *International*

Journal of Heat and Mass Transfer, *46*(19), 3639–3653.

Kierzenka, J., & Shampine, L. F. 2008. A bvp solver that controls residual and error. *JNAIAM J. Numer. Anal. Ind. Appl. Math*, *3*(1-2), 27–41.

Kiusalaas, J. 2005. *Numerical methods in engineering with matlab®*. Cambridge university press.

Koriko, O., Omowaye, A., Animasaun, I. L., & Bamisaye, M. E. 2017. Melting heat transfer and induced-magnetic field effects on the micropolar fluid flow towards stagnation point: Boundary layer analysis. *International Journal of Engineering Research in Africa*, *29*, 10–20.

Koriko, O. K., Adegbie, K. S., Shah, N. A., Animasaun, I. L., & Olotu, M. A. 2021. Numerical solutions of the partial differential equations for investigating the significance of partial slip due to lateral velocity and viscous dissipation: the case of blood-gold carreau nanofluid and dusty fluid. *Numerical Methods for Partial Differential Equations*, 1–29.

Koriko, O. K., Animasaun, I., Mahanthesh, B., Saleem, S., Sarojamma, G., & Sivaraj, R. 2018. Heat transfer in the flow of blood-gold carreau nanofluid induced by partial slip and buoyancy. *Heat Transfer—Asian Research*, *47*(6), 806–823.

Krishnamurthy, M., Gireesha, B., Prasannakumara, B., & Gorla, R. S. R. 2016. Thermal radiation and chemical reaction effects on boundary layer slip flow and melting heat transfer of nanofluid induced by a nonlinear stretching sheet. *Nonlinear Engineering*, *5*(3), 147–159.

Kumar, A., Tripathi, R., Singh, R., & Sheremet, M. A. 2021. Entropy generation on double diffusive mhd casson nanofluid flow with convective heat transfer and activation energy. *Indian Journal of Physics*, *95*(7), 1423–1436.

Kumar, M. A., Reddy, Y. D., Rao, V. S., & Goud, B. S. 2021. Thermal radiation impact on mhd heat transfer natural convective nano fluid flow over an impulsively started vertical plate. *Case Studies in Thermal Engineering*, *24*, 100826.

Kumar, R., Bhattacharyya, A., Seth, G., & Chamkha, A. J. 2021. Transportation of magnetite nanofluid flow and heat transfer over a rotating porous disk with arrhenius activation energy: Fourth order noumerov's method. *Chinese Journal of Physics*, *69*, 172–185.

Kumar, R., Kumar, R., Sharma, T., & Sheikholeslami, M. 2021. Mathematical modeling of stagnation region nanofluid flow through darcy–forchheimer space taking into account inconsistent heat source/sink. *Journal of Applied Mathematics and Computing*, *65*(1), 713–734.

Kumar, R., Kumar, R., Shehzad, S. A., & Sheikholeslami, M. 2018. Rotating frame analysis of radiating and reacting ferro-nanofluid considering joule heating and viscous dissipation. *International Journal of Heat and Mass Transfer*, *120*, 540–551.

Kumar, R., Kumar, R., Sheikholeslami, M., & Chamkha, A. J. 2019. Irreversibility analysis of the three dimensional flow of carbon nanotubes due to nonlinear thermal radiation and quartic chemical reactions. *Journal of Molecular Liquids*, *274*, 379–392.

Kumar, R., Kumar, R., Vajravelu, K., & Sheikholeslami, M. 2020. Three dimensional stagnation flow of casson nanofluid through darcy-forchheimer space: a reduction to blasius/sakiadis flow. *Chinese Journal of Physics*, *68*, 874–885.

Kumari, M., Takhar, H. S., & Nath, G. 1990. Mhd flow and heat transfer over a stretching surface with prescribed wall temperature or heat flux. *Wärme-und Stoffübertragung*, *25*(6), 331–336.

Kundu, P. K., Cohen, I. M., & Dowling, D. R. 2015. *Fluid mechanics*. Academic press.

Kuznetsov, A., & Avramenko, A. 2004. Effect of small particles on this stability of bioconvection in a suspension of gyrotactic microorganisms in a layer of finite depth. *International Communications in Heat and Mass Transfer*, *31*(1), 1–10.

Kuznetsov, A., & Nield, D. 2013. The cheng–minkowycz problem for natural convective boundary layer flow in a porous medium saturated by a nanofluid: a revised model. *International Journal of Heat and Mass Transfer*, *65*, 682–685.

Li, Y.-X., Rehman, M. I. U., Huang, W.-H., Khan, M. I., Khan, S. U., Chinram, R., & Kadry, S. 2022. Dynamics of casson nanoparticles with non-uniform heat source/sink: a numerical analysis. *Ain Shams Engineering Journal*, *13*(1), 101496.

Liu, Y., Jian, Y., & Tan, W. 2018. Entropy generation of electromagnetohydrodynamic (emhd) flow in a curved rectangular

microchannel. *International Journal of Heat and Mass Transfer*, *127*, 901–913.

Łukasiewicz, K., & Fol, M. 2018. Microorganisms in the treatment of cancer: advantages and limitations. *Journal of Immunology Research*, *2018*, 1–8.

Lund, L. A., Omar, Z., Raza, J., & Khan, I. 2021. Magnetohydrodynamic flow of cu–fe3o4/h2o hybrid nanofluid with effect of viscous dissipation: dual similarity solutions. *Journal of Thermal Analysis and Calorimetry*, *143*(2), 915–927.

Mabood, F., Ashwinkumar, G., & Sandeep, N. 2022. Effect of nonlinear radiation on 3d unsteady mhd stagnancy flow of fe3o4/graphene–water hybrid nanofluid. *International Journal of Ambient Energy*, *43*(1), 3385–3395.

Mabood, F., Ibrahim, S., Kumar, P., & Lorenzini, G. 2020. Effects of slip and radiation on convective mhd casson nanofluid flow over a stretching sheet influenced by variable viscosity. *Journal of Engineering Thermophysics*, *29*(2), 303–315.

Mabood, F., Khan, W., & Ismail, A. M. 2015. Mhd boundary layer flow and heat transfer of nanofluids over a nonlinear stretching sheet: a numerical study. *Journal of Magnetism and Magnetic Materials*, *374*, 569–576.

Mabood, F., Yusuf, T., & Khan, W. 2021. Cu–al2o3–h2o hybrid nanofluid flow with melting heat transfer, irreversibility analysis and nonlinear thermal radiation. *Journal of Thermal Analysis and Calorimetry*, *143*(2), 973–984.

Mackolil, J., & Mahanthesh, B. 2019. Sensitivity analysis of radiative heat transfer in casson and nano fluids under diffusion-thermo and heat absorption effects. *The European Physical Journal Plus*, *134*(12), 619.

Mackolil, J., & Mahanthesh, B. 2021. Sensitivity analysis of marangoni convection in tio2–eg nanoliquid with nanoparticle aggregation and temperature-dependent surface tension. *Journal of Thermal Analysis and Calorimetry*, *143*(3), 2085–2098.

Madhu, M., Mahanthesh, B., Shashikumar, N., Shehzad, S., Khan, S., & Gireesha, B. 2020. Performance of second law in carreau fluid flow by an inclined microchannel with radiative heated convective condition. *International Communications in Heat and Mass Transfer*, *117*, 104761.

Mahanthesh, B., Animasaun, I., Rahimi-Gorji, M., & Alarifi, I. M. 2019. Quadratic convective transport of dusty casson and dusty carreau fluids past a stretched surface with nonlinear thermal radiation, convective condition and non-uniform

heat source/sink. *Physica A: Statistical Mechanics and its Applications*, *535*, 122471.

Mahanthesh, B., Gireesha, B., Animasaun, I., Muhammad, T., & Shashikumar, N. 2019. Mhd flow of swcnt and mwcnt nanoliquids past a rotating stretchable disk with thermal and exponential space dependent heat source. *Physica Scripta*, *94*(8), 085214.

Mahanthesh, B., Gireesha, B. J., Gorla, R. S., & Makinde, O. D. 2018. Magnetohydrodynamic three-dimensional flow of nanofluids with slip and thermal radiation over a nonlinear stretching sheet: a numerical study. *Neural Computing and Applications*, *30*(5), 1557–1567.

Mahanthesh, B., Gireesha, B. J., PrasannaKumara, B. C., & Shashikumar, N. S. 2017. Marangoni convection radiative flow of dusty nanoliquid with exponential space dependent heat source. *Nuclear Engineering and Technology*, *49*(8), 1660–1668.

Mahanthesh, B., & Mackolil, J. 2021. Flow of nanoliquid past a vertical plate with novel quadratic thermal radiation and quadratic boussinesq approximation: sensitivity analysis. *International Communications in Heat and Mass Transfer*, *120*, 105040.

Mahanthesh, B., Mackolil, J., & Shehzad, S. A. 2020. Statistical analysis of stagnation-point heat flow in williamson fluid with viscous dissipation and exponential heat source effects. *Heat Transfer*, *49*(8), 4580–4591.

Mahanthesh, B., Thriveni, K., & Lorenzini, G. 2021. Significance of nonlinear boussinesq approximation and non-uniform heat source/sink on nanoliquid flow with convective heat condition: sensitivity analysis. *The European Physical Journal Plus*, *136*(4), 1–18.

Mahapatra, T., & Gupta, A. 2002. Heat transfer in stagnation-point flow towards a stretching sheet. *Heat and Mass transfer*, *38*(6), 517–521.

Manzoor, U., Muhammad, T., Farooq, U., & Waqas, H. 2022. Investigation of thermal stratification and nonlinear thermal radiation in darcy-forchheimer transport of hybrid nanofluid by rotating disk with marangoni convection. *International Journal of Ambient Energy*, *43*(1), 1–8.

Mathur, P., Jha, S., Ramteke, S., & Jain, N. 2018. Pharmaceutical aspects of silver nanoparticles. *Artificial Cells, Nanomedicine, and Biotechnology*, *46*(sup1),

115–126.

Maxwell, J. C. 1873. *A treatise on electricity and magnetism* (Vol. 1). Clarendon press.

Md Basir, M. F., Kumar, R., Md Ismail, A. I., Sarojamma, G., Narayana, P. V. S., Raza, J., & Mahmood, A. 2019. Exploration of thermal-diffusion and diffusion-thermal effects on the motion of temperature-dependent viscous fluid conveying microorganism. *Arabian Journal for Science and Engineering*, *44*(9), 8023–8033.

Mehmood, Z., & Iqbal, Z. 2016. Interaction of induced magnetic field and stagnation point flow on bioconvection nanofluid submerged in gyrotactic microorganisms. *Journal of Molecular Liquids*, *224*, 1083–1091.

Minkowycz, W., Sparrow, E. M., & Abraham, J. P. 2012. *Nanoparticle heat transfer and fluid flow* (Vol. 4). CRC press.

Montgomery, D. 2010. *Design and analysis of experiments, with design expert.* John Wiley 9. Course Policies.

Muhammad, T., Alamri, S. Z., Waqas, H., Habib, D., & Ellahi, R. 2021. Bioconvection flow of magnetized carreau nanofluid under the influence of slip over a wedge with motile microorganisms. *Journal of Thermal Analysis and Calorimetry*, *143*(2), 945–957.

Mukhopadhyay, S. 2013. Casson fluid flow and heat transfer over a nonlinearly stretching surface. *Chinese Physics B*, *22*(7), 074701.

Mustafa, I., Javed, T., & Ghaffari, A. 2016. Heat transfer in mhd stagnation point flow of a ferrofluid over a stretchable rotating disk. *Journal of Molecular Liquids*, *219*, 526–532.

Nadeem, S., Hayat, T., & Khan, A. U. 2019. Numerical study of 3d rotating hybrid swcnt–mwcnt flow over a convectively heated stretching surface with heat generation/absorption. *Physica Scripta*, *94*(7), 075202.

Nakayama, Y. 2018. *Introduction to fluid mechanics.* Butterworth-Heinemann.

Nandeppanavar, M. M., Vajravelu, K., Abel, M. S., & Siddalingappa, M. 2012. Second order slip flow and heat transfer over a stretching sheet with non-linear navier boundary condition. *International Journal of Thermal Sciences*, *58*, 143–150.

Naramgari, S., & Sulochana, C. 2016. Dual solutions of radiative mhd nanofluid

flow over an exponentially stretching sheet with heat generation/absorption. *Applied Nanoscience*, *6*(1), 131–139.

Nasir, S., Islam, S., Gul, T., Shah, Z., Khan, M. A., Khan, W., ... Khan, S. 2018. Three-dimensional rotating flow of mhd single wall carbon nanotubes over a stretching sheet in presence of thermal radiation. *Applied Nanoscience*, *8*(6), 1361–1378.

Nazeer, M., Irfan, M., Hussain, F., & Siddique, I. 2022. Entropy generation analysis in blood-gold casson nanofluid through horizontal wavy channel with velocity and thermal slips: Applications in skin diseases. *Journal of Computational Biophysics and Chemistry*, 1–14.

Obalalu, A. M. 2022. Chemical entropy generation and second-order slip condition on hydrodynamic casson nanofluid flow embedded in a porous medium: a fast convergent method. *Journal of the Egyptian Mathematical Society*, *30*(1), 1–25.

Oke, A., Animasaun, I., Mutuku, W., Kimathi, M., Shah, N. A., & Saleem, S. 2021. Significance of coriolis force, volume fraction, and heat source/sink on the dynamics of water conveying 47 nm alumina nanoparticles over a uniform surface. *Chinese Journal of Physics*, *71*, 716–727.

Pal, D., & Mondal, S. K. 2018. Mhd nanofluid bioconvection over an exponentially stretching sheet in the presence of gyrotactic microorganisms and thermal radiation. *BioNanoScience*, *8*(1), 272–287.

Platt, J. R. 1961. " bioconvection patterns" in cultures of free-swimming organisms. *Science*, *133*(3466), 1766–1767.

Pordanjani, A. H., Vahedi, S. M., Aghakhani, S., Afrand, M., Öztop, H. F., & Abu-Hamdeh, N. 2019. Effect of magnetic field on mixed convection and entropy generation of hybrid nanofluid in an inclined enclosure: sensitivity analysis and optimization. *The European Physical Journal Plus*, *134*(8), 1–20.

Puneeth, V., Manjunatha, S., Madhukesh, J., & Ramesh, G. 2021. Three dimensional mixed convection flow of hybrid casson nanofluid past a non-linear stretching surface: A modified buongiorno's model aspects. *Chaos, Solitons & Fractals*, *152*, 111428.

Ramesh, G., Shehzad, S., & Izadi, M. 2020. Thermal transport of hybrid liquid over thin needle with heat sink/source and darcy–forchheimer porous medium

aspects. *Arabian Journal for Science and Engineering*, *45*(11), 9569–9578.

Ramesh, G., Shehzad, S., & Tlili, I. 2020. Hybrid nanomaterial flow and heat transport in a stretchable convergent/divergent channel: a darcy-forchheimer model. *Applied Mathematics and Mechanics*, *41*(5), 699–710.

Ramly, N., Sivasankaran, S., & Noor, N. 2017. Zero and nonzero normal fluxes of thermal radiative boundary layer flow of nanofluid over a radially stretched surface. *Scientia Iranica*, *24*(6), 2895–2903.

Ramzan, M., Riasat, S., Shah, Z., Kumam, P., & Thounthong, P. 2020. Unsteady mhd carbon nanotubes suspended nanofluid flow with thermal stratification and nonlinear thermal radiation. *Alexandria Engineering Journal*, *59*(3), 1557–1566.

Rana, P., & Bhargava, R. 2012. Flow and heat transfer of a nanofluid over a nonlinearly stretching sheet: a numerical study. *Communications in Nonlinear Science and Numerical Simulation*, *17*(1), 212–226.

Rana, P., Mahanthesh, B., Mackolil, J., & Al-Kouz, W. 2021. Nanofluid flow past a vertical plate with nanoparticle aggregation kinematics, thermal slip and significant buoyancy force effects using modified buongiorno model. *Waves in Random and Complex Media*, 1–25.

Rana, P., Shukla, N., Bég, O. A., & Bhardwaj, A. 2021. Lie group analysis of nanofluid slip flow with stefan blowing effect via modified buongiorno's model: entropy generation analysis. *Differential Equations and Dynamical Systems*, *29*(1), 193–210.

Raval, J. P., Joshi, P., & Chejara, D. R. 2018. Carbon nanotube for targeted drug delivery. In *Applications of nanocomposite materials in drug delivery* (pp. 203–216). Elsevier.

Raza, J., Farooq, M., Mebarek-Oudina, F., & Mahanthesh, B. 2019. Multiple slip effects on mhd non-newtonian nanofluid flow over a nonlinear permeable elongated sheet: numerical and statistical analysis. *Multidiscipline Modeling in Materials and Structures*, *15*(5), 913–931.

Raza, M., Ellahi, R., Sait, S. M., Sarafraz, M., Shadloo, M. S., & Waheed, I. 2020. Enhancement of heat transfer in peristaltic flow in a permeable channel under induced magnetic field using different cnts. *Journal of Thermal Analysis and Calorimetry*, *140*(3), 1277–1291.

Rout, H., Mohapatra, S., Shaw, S., Muhammad, T., Nayak, M., & Makinde, O. D. 2021. Entropy optimization for darcy–forchheimer electro-magneto-hydrodynamic slip flow of ferronanofluid due to stretching/shrinking rotating disk. *Waves in Random and Complex Media*, 1–33.

Sadiq, M. A., Haider, F., Hayat, T., & Alsaedi, A. 2020. Partial slip in darcy-forchheimer carbon nanotubes flow by rotating disk. *International Communications in Heat and Mass Transfer*, *116*, 104641.

Salahuddin, T. 2020. Carreau fluid model towards a stretching cylinder: Using keller box and shooting method. *Ain Shams Engineering Journal*, *11*(2), 495–500.

Salahuddin, T., Hussain, A., Malik, M., Awais, M., & Khan, M. 2017. Carreau nanofluid impinging over a stretching cylinder with generalized slip effects: using finite difference scheme. *Results in Physics*, *7*, 3090–3099.

Sampath Kumar, P., Gireesha, B., Mahanthesh, B., & Chamkha, A. J. 2019. Thermal analysis of nanofluid flow containing gyrotactic microorganisms in bioconvection and second-order slip with convective condition. *Journal of Thermal Analysis and Calorimetry*, *136*(5), 1947–1957.

Sandeep, N., Chamkha, A. J., & Animasaun, I. 2017. Numerical exploration of magnetohydrodynamic nanofluid flow suspended with magnetite nanoparticles. *Journal of the Brazilian Society of Mechanical Sciences and Engineering*, *39*(9), 3635–3644.

Sarkar, G., & Sahoo, B. 2021. On dual solutions of the unsteady mhd flow on a stretchable rotating disk with heat transfer and a linear temporal stability analysis. *European Journal of Mechanics-B/Fluids*, *85*, 149–157.

Schlichting, H., & Kestin, J. 1961. *Boundary layer theory* (Vol. 121). Springer.

Sembulingam, K., & Sembulingam, P. 2012. *Essentials of medical physiology*. JP Medical Ltd.

Senapati, M., Parida, S. K., Swain, K., & Ibrahim, S. M. 2022. Analysis of variable magnetic field on chemically dissipative mhd boundary layer flow of casson fluid over a nonlinearly stretching sheet with slip conditions. *International Journal of Ambient Energy*, *43*(1), 3712–3726.

Seth, G., Bhattacharyya, A., Kumar, R., & Chamkha, A. 2018. Entropy generation in hydromagnetic nanofluid flow over a non-linear stretching sheet with navier's

velocity slip and convective heat transfer. *Physics of Fluids*, *30*(12), 122003.

Shafiq, A., Sindhu, T. N., & Khalique, C. M. 2020. Numerical investigation and sensitivity analysis on bioconvective tangent hyperbolic nanofluid flow towards stretching surface by response surface methodology. *Alexandria Engineering Journal*, *59*(6), 4533–4548.

Shah, N. A., Animasaun, I., Chung, J. D., Wakif, A., Alao, F., & Raju, C. 2021. Significance of nanoparticle's radius, heat flux due to concentration gradient, and mass flux due to temperature gradient: The case of water conveying copper nanoparticles. *Scientific Reports*, *11*(1), 1–11.

Shah, Z., Bonyah, E., Islam, S., & Gul, T. 2019. Impact of thermal radiation on electrical mhd rotating flow of carbon nanotubes over a stretching sheet. *AIP Advances*, *9*(1), 015115.

Shahid, A., Huang, H., Bhatti, M. M., Zhang, L., & Ellahi, R. 2020. Numerical investigation on the swimming of gyrotactic microorganisms in nanofluids through porous medium over a stretched surface. *Mathematics*, *8*(3), 380.

Shampine, L. F., & Reichelt, M. W. 1997. The matlab ode suite. *SIAM Journal on Scientific Computing*, *18*(1), 1–22.

Shehzad, S., Mabood, F., Rauf, A., Izadi, M., & Abbasi, F. 2021. Rheological features of non-newtonian nanofluids flows induced by stretchable rotating disk. *Physica Scripta*, *96*(3), 035210.

Sheikholeslami, M., & Ganji, D. 2013. Heat transfer of cu-water nanofluid flow between parallel plates. *Powder Technology*, *235*, 873–879.

Sheikholeslami, M., Ganji, D., & Rashidi, M. 2016. Magnetic field effect on unsteady nanofluid flow and heat transfer using buongiorno model. *Journal of Magnetism and Magnetic Materials*, *416*, 164–173.

Sindhu, S., & Gireesha, B. J. 2021. Effect of nanoparticle shapes on irreversibility analysis of nanofluid in a microchannel with individual effects of radiative heat flux, velocity slip and convective heating. *Heat Transfer*, *50*(1), 876–892.

Sk, M. T., Das, K., & Kundu, P. K. 2016. Effect of magnetic field on slip flow of nanofluid induced by a non-linear permeable stretching surface. *Applied Thermal Engineering*, *104*, 758–766.

Song, Y.-Q., Obideyi, B., Shah, N. A., Animasaun, I., Mahrous, Y., & Chung, J. D. 2021. Significance of haphazard motion and thermal migration of alumina

and copper nanoparticles across the dynamics of water and ethylene glycol on a convectively heated surface. *Case Studies in Thermal Engineering*, *26*, 101050.

Spalding, D. B. 1954. Mass transfer in laminar flow. *Proceedings of the Royal Society of London. Series A. Mathematical and Physical Sciences*, *221*(1144), 78–99.

Sravanthi, C. 2019. Effect of nonlinear thermal radiation on silver and copper water nanofluid flow due to a rotating disk with variable thickness in the presence of nonuniform heat source/sink using the homotopy analysis method. *Heat Transfer—Asian Research*, *48*(8), 4033–4048.

Sreedevi, P., & Reddy, P. S. 2019. Effect of swcnts and mwcnts maxwell mhd nanofluid flow between two stretchable rotating disks under convective boundary conditions. *Heat Transfer—Asian Research*, *48*(8), 4105–4132.

Strauss, W. A. 2007. *Partial differential equations: An introduction*. John Wiley & Sons.

Subhani, M., & Nadeem, S. 2019. Numerical analysis of micropolar hybrid nanofluid. *Applied Nanoscience*, *9*(4), 447–459.

Subramanian, K., Rao, T. N., & Balakrishnan, A. 2019. *Nanofluids and their engineering applications*. CRC Press.

Sun, X., Animasaun, I. L., Swain, K., Shah, N. A., Wakif, A., & Olanrewaju, P. O. 2022. Significance of nanoparticle radius, inter-particle spacing, inclined magnetic field, and space-dependent internal heating: The case of chemically reactive water conveying copper nanoparticles. *ZAMM-Journal of Applied Mathematics and Mechanics/Zeitschrift für Angewandte Mathematik und Mechanik*, *102*(4), e202100094.

Suresh Reddy, E., & Panda, S. 2022. Heat transfer of mhd natural convection casson nanofluid flows in a wavy trapezoidal enclosure. *The European Physical Journal Special Topics*, *231*(13-14), 2733–2747.

Thriveni, K., & Mahanthesh, B. 2021. Significance of variable fluid properties on hybrid nanoliquid flow in a micro-annulus with quadratic convection and quadratic thermal radiation: response surface methodology. *International Communications in Heat and Mass Transfer*, *124*, 105264.

Thumma, T., & Mishra, S. 2020. Effect of nonuniform heat source/sink, and viscous and joule dissipation on 3d eyring–powell nanofluid flow over a stretching sheet.

Journal of Computational Design and Engineering, *7*(4), 412–426.

Timofeeva, E. V., Routbort, J. L., & Singh, D. 2009. Particle shape effects on thermophysical properties of alumina nanofluids. *Journal of Applied Physics*, *106*(1), 014304.

Tiwari, R. K., & Das, M. K. 2007. Heat transfer augmentation in a two-sided lid-driven differentially heated square cavity utilizing nanofluids. *International Journal of Heat and Mass transfer*, *50*(9-10), 2002–2018.

Tlili, I., Ramzan, M., Nisa, H. U., Shutaywi, M., Shah, Z., & Kumam, P. 2020. Onset of gyrotactic microorganisms in mhd micropolar nanofluid flow with partial slip and double stratification. *Journal of King Saud University-Science*, *32*(6), 2741–2751.

Tripathi, D., Prakash, J., Tiwari, A. K., & Ellahi, R. 2020. Thermal, microrotation, electromagnetic field and nanoparticle shape effects on cu-cuo/blood flow in microvascular vessels. *Microvascular Research*, *132*, 104065.

Truong, N. P., Whittaker, M. R., Mak, C. W., & Davis, T. P. 2015. The importance of nanoparticle shape in cancer drug delivery. *Expert Opinion on Drug Delivery*, *12*(1), 129–142.

Turkyilmazoglu, M. 2012. Three dimensional mhd stagnation flow due to a stretchable rotating disk. *International Journal of Heat and Mass Transfer*, *55*(23-24), 6959–6965.

Turkyilmazoglu, M. 2014. Nanofluid flow and heat transfer due to a rotating disk. *Computers & Fluids*, *94*, 139–146.

Uddin, I., Khan, M. A., Ullah, S., Islam, S., Israr, M., & Hussain, F. 2018. Characteristics of buoyancy force on stagnation point flow with magneto-nanoparticles and zero mass flux condition. *Results in Physics*, *8*, 160–168.

Uddin, M., Khan, W., Qureshi, S., & Bég, O. A. 2017. Bioconvection nanofluid slip flow past a wavy surface with applications in nano-biofuel cells. *Chinese Journal of Physics*, *55*(5), 2048–2063.

Upadhya, S. M., Devi, R., Raju, C., & Ali, H. M. 2021. Magnetohydrodynamic nonlinear thermal convection nanofluid flow over a radiated porous rotating disk with internal heating. *Journal of Thermal Analysis and Calorimetry*, *143*(3), 1973–1984.

ur Rehman, S., Mir, N. A., Farooq, M., Rizwan, M., Ahmad, F., Ahmad, S., & Ahmad, B. 2020. Analysis of thermally stratified flow of sutterby nanofluid with zero mass flux condition. *Journal of Materials Research and Technology*, *9*(2), 1631–1639.

Usman, M., Soomro, F. A., Haq, R. U., Wang, W., & Defterli, O. 2018. Thermal and velocity slip effects on casson nanofluid flow over an inclined permeable stretching cylinder via collocation method. *International Journal of Heat and Mass Transfer*, *122*, 1255–1263.

Vahedi, S. M., Pordanjani, A. H., Raisi, A., & Chamkha, A. J. 2019. Sensitivity analysis and optimization of mhd forced convection of a cu-water nanofluid flow past a wedge. *The European Physical Journal Plus*, *134*(3), 1–21.

Verma, A. K., Rajput, S., Bhattacharyya, K., & Chamkha, A. J. 2022. Nanoparticle's radius effect on unsteady mixed convective copper-water nanofluid flow over an expanding sheet in porous medium with boundary slip. *Chemical Engineering Journal Advances*, *12*, 100366.

Vinita, V., & Poply, V. 2020. Impact of outer velocity mhd slip flow and heat transfer of nanofluid past a stretching cylinder. *Materials Today: Proceedings*, *26*, 3429–3435.

Wager, H. W. T. 1911. Vii. on the effect of gravity upon the movements and aggregation of euglena viridis, ehrb., and other micro-organisms. *Philosophical Transactions of the Royal Society of London. Series B, Containing Papers of a Biological Character*, *201*(274-281), 333–390.

Waini, I., Ishak, A., & Pop, I. 2019a. Hybrid nanofluid flow and heat transfer over a nonlinear permeable stretching/shrinking surface. *International Journal of Numerical Methods for Heat & Fluid Flow*, *29*(9), 3110–3127.

Waini, I., Ishak, A., & Pop, I. 2019b. Unsteady flow and heat transfer past a stretching/shrinking sheet in a hybrid nanofluid. *International Journal of Heat and Mass Transfer*, *136*, 288–297.

Waini, I., Ishak, A., & Pop, I. 2021. Unsteady hybrid nanofluid flow on a stagnation point of a permeable rigid surface. *ZAMM-Journal of Applied Mathematics and Mechanics/Zeitschrift für Angewandte Mathematik und Mechanik*, *101*(6), e202000193.

Wang, C. 1989. Free convection on a vertical stretching surface. *ZAMM-Journal of*

Applied Mathematics and Mechanics/Zeitschrift für Angewandte Mathematik und Mechanik, *69*(11), 418–420.

Waqas, H., Naseem, R., Muhammad, T., & Farooq, U. 2021. Bioconvection flow of casson nanofluid by rotating disk with motile microorganisms. *Journal of Materials Research and Technology*, *13*, 2392–2407.

Wazwaz, A.-M. 2002. *Partial differential equations*. CRC Press.

Wu, L. 2008. A slip model for rarefied gas flows at arbitrary knudsen number. *Applied Physics Letters*, *93*(25), 253103.

Xue, Q. 2005. Model for thermal conductivity of carbon nanotube-based composites. *Physica B: Condensed Matter*, *368*(1-4), 302–307.

Yang, C., Li, W., & Nakayama, A. 2013. Convective heat transfer of nanofluids in a concentric annulus. *International Journal of Thermal Sciences*, *71*, 249–257.

Yusuf, T., Mabood, F., Khan, W., & Gbadeyan, J. 2020. Irreversibility analysis of cu-tio2-h2o hybrid-nanofluid impinging on a 3-d stretching sheet in a porous medium with nonlinear radiation: Darcy-forchhiemer's model. *Alexandria Engineering Journal*, *59*(6), 5247–5261.

Zainal, N. A., Nazar, R., Naganthran, K., & Pop, I. 2021. Unsteady emhd stagnation point flow over a stretching/shrinking sheet in a hybrid al2o3-cu/h2o nanofluid. *International Communications in Heat and Mass Transfer*, *123*, 105205.

Zhang, L. 2021. Application of fractal theory in transient pressure properties of hydrocarbon reservoir. In *Modelling of flow and transport in fractal porous media* (pp. 193–249). Elsevier.

Zhang, L., Bhatti, M. M., & Michaelides, E. E. 2020. Electro-magnetohydrodynamic flow and heat transfer of a third-grade fluid using a darcy-brinkman-forchheimer model. *International Journal of Numerical Methods for Heat & Fluid Flow*, *31*(8), 2623–2639.

Zhou, J.-C., Abidi, A., Shi, Q.-H., Khan, M. R., Rehman, A., Issakhov, A., & Galal, A. M. 2021. Unsteady radiative slip flow of mhd casson fluid over a permeable stretched surface subject to a non-uniform heat source. *Case Studies in Thermal Engineering*, *26*, 101141.